

**DESIGN AND BEHAVIOR OF ANCHORAGE ZONES
IN POST-TENSIONED CONCRETE MEMBERS**

by

David Howard Sanders, B.S., M.S.

DISSERTATION

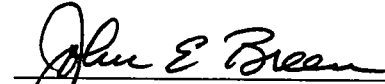
Presented to the Faculty of the Graduate School of
The University of Texas at Austin
in Partial Fulfillment
of the Requirements
for the Degree of
Doctor of Philosophy

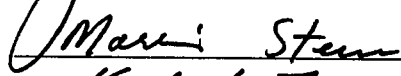
THE UNIVERSITY OF TEXAS AT AUSTIN


August, 1990

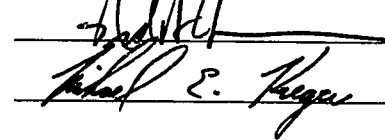
DESIGN AND BEHAVIOR OF ANCHORAGE ZONES
IN POST-TENSIONED CONCRETE MEMBERS

APPROVED BY
DISSERTATION COMMITTEE:









To my wife, Tina, and my Lord, Jesus,
for all their patience and unconditional
support; and to my parents, Wallace and
Julia, for their encouragement and love.

ACKNOWLEDGEMENTS

My five years in Austin and at The University of Texas are filled with good memories and friends. My wife has been with me every step of the way as we have worked on our Ph.D.. I owe her everything, including the first four years of our marriage. Her patience, understanding and love made the tough days much easier. I want to acknowledge all the support and love of my friends that I met while I was in Austin. They have made my days in Austin some of the finest of my life.

Some of my best friends were fellow workers on the anchorage zone research project: Dr. John Breen, Olivier Burdet, Chuck Crisman, Brian Falconer, Carin Roberts and Gregor Wollman. Olivier deserves a big thank you for his technical support and friendship as we both worked toward a research product of which we could be proud. I can't think of words to describe Carin and Gregor. I looked forward to coming to work everyday because I knew those two would be there. Thanks for all the good times at the laboratory: singing, dancing, talking, casting concrete, sweating, testing specimens and sharing. Chuck's work, advice, long-suffering and coffee breaks were essential in the construction and testing of all the specimens. Dr. Breen was a supervisor and a friend that I could go to at anytime, (though sometimes hard to find), if I needed some advise or input. His guidance and assistance on this project were invaluable. A special thanks to Dr. Breen for giving me the opportunity and the time to be a scoutmaster.

I also want to thank the Phil M. Ferguson Laboratory at The University of Texas at Austin. All the staff, students and professors that worked there, I am proud to have as friends. All of their support, patience and tolerance is greatly appreciated. People that deserve special attention include: the computer room crew who were in the computer room night after night and kept me from falling asleep,

(most of the time), the noontime card playing crew that would come get me from my desk when they could find no one else to play, the concrete casting crews which even had to cast without me one time, the upstairs folks (Laurie, Jean, Maxine, Sharon and Irene), the downstairs folks (Dick, Blake, "Crane" Wayne, "Machine" Wayne, Alex, Pat, and Hinkly), all the professors for their advice, support and torment (Drs. Burns, Frank, Jirsa, Klingner, Kreger, and Yura) and Paul Tikalsky. Paul, we made it, thanks for being a great friend.

Finally, a special thanks to National Cooperative Highway Research Program for making this project possible, to my advisory committee for taking the time to help me to complete this dissertation, and to half the Amazon forest which had to be sacrificed to provide the paper necessary for this dissertation.

David H. Sanders

June, 1990

**DESIGN AND BEHAVIOR OF ANCHORAGE ZONES
IN POST-TENSIONED CONCRETE MEMBERS**

Publication No. _____

David Howard Sanders, Ph.D.
The University of Texas at Austin, 1990

Supervisor: John E. Breen

The major emphasis of this research was the development of a generalized approach for the design and proper reinforcement of anchorage zones in post-tensioned concrete members. The approach addresses the serviceability limit state with elastic finite element analysis and the ultimate limit state with a plasticity based solution called the strut-and-tie model (STM).

Experimental tests were conducted to verify the ultimate strength analytical and design models developed. A total of 36 experimental specimens were tested. The specific types of anchorage zones that were tested include: concentric tendon, eccentric tendon, multiple tendons, and inclined tendons with curvature. The basic STM which assumes an elastic stress distribution at the end of the general zone was developed in detail. The model was found to be a very conservative estimate of the anchorage zone capacity and very appropriate for design and analysis of anchorage zones. Examples are given and procedures developed for determining the dimensions and capacities of the nodes and compression struts within the STM. A modified STM was also developed which more accurately represents the ultimate behavior and capacity of the anchorage zone. The model allows a more plastic stress distribution at the end of the anchorage zone than in the basic STM. The serviceability limit state was addressed with the development of methods for predicting the first cracking load. The first cracking

load was found to be difficult to predict but conservative design models were determined.

The document has an extensive state-of-the-art review that examines existing technical literature, product literature, codes, and handbooks. New terminology was introduced which helps to define the anchorage zone. This terminology was also used to propose divisions of responsibilities within the anchorage zone between the engineer-of-record, the anchorage device supplier and the constructor. A proposed revision to the AASHTO Bridge Specification is presented that incorporates the division of responsibilities, the results from this document, and companion research at The University of Texas at Austin conducted by Burdet and Roberts.

TABLE OF CONTENTS

| | Page |
|---|------|
| ACKNOWLEDGEMENTS..... | iv |
| ABSTRACT..... | vi |
| TABLE OF CONTENTS..... | viii |
| CHAPTER 1 INTRODUCTION..... | 1 |
| 1.1 Background..... | 1 |
| 1.2 Definitions and Classifications..... | 5 |
| 1.3 Research Objectives..... | 9 |
| 1.4 Experimental Program..... | 12 |
| CHAPTER 2 STATE-OF-THE-ART..... | 14 |
| 2.1 Introduction..... | 14 |
| 2.2 Technical Literature..... | 14 |
| 2.3 Product Literature..... | 49 |
| 2.4 User Survey and Assessment..... | 53 |
| 2.5 Current Codes and Commentaries..... | 65 |
| CHAPTER 3 CONCENTRIC ANCHORAGE SPECIMENS WITH STRAIGHT TENDONS... | 78 |
| 3.1 Introduction..... | 78 |
| 3.2 Test Program..... | 78 |
| 3.3 Prediction of the First Cracking Load using Elastic Analysis Models..... | 142 |
| 3.4 Ultimate Load Prediction Models..... | 163 |
| 3.5 Conclusions for Concentric Anchorage Zones..... | 216 |
| CHAPTER 4 ECCENTRIC ANCHORAGE SPECIMENS WITH STRAIGHT TENDONS.... | 220 |
| 4.1 Introduction..... | 220 |
| 4.2 Test Program..... | 222 |
| 4.3 Prediction of the First Cracking Load using Elastic Analysis Models..... | 266 |
| 4.4 Strut-and-Tie Model Prediction of the Ultimate Load.. | 277 |
| 4.5 Conclusions for Eccentric Anchorage Zones..... | 305 |
| CHAPTER 5 MULTIPLE ANCHORAGE SPECIMENS WITH STRAIGHT TENDONS..... | 308 |
| 5.1 Introduction..... | 308 |
| 5.2 Test Program..... | 308 |
| 5.3 Prediction of the First Cracking Load using Elastic Analysis Models..... | 362 |
| 5.4 Strut-and-Tie Model Prediction of the Ultimate Load.. | 371 |
| 5.5 Conclusions for Multiple Anchorage Zones..... | 398 |

| | Page |
|--|------|
| CHAPTER 6 SPECIMENS WITH INCLINED ANCHORAGES AND TENDON CURVATURES..... | 401 |
| 6.1 Introduction..... | 401 |
| 6.2 Test Program..... | 401 |
| 6.3 Prediction of the First Cracking Load using Elastic Analysis Models..... | 437 |
| 6.4 Strut-and-Tie Model Prediction of the Ultimate Load.. | 445 |
| 6.5 Conclusions for Specimens with Inclined Anchorages and Tendon Curvatures..... | 471 |
| CHAPTER 7 SUMMARY OF RESULTS AND AASHTO SPECIFICATION PROPOSAL... | 475 |
| 7.1 Introduction..... | 475 |
| 7.2 Experimental Results..... | 475 |
| 7.3 AASHTO Specification and Commentary Proposal..... | 504 |
| CHAPTER 8 CONCLUSIONS AND RECOMMENDATIONS..... | 540 |
| 8.1 Introduction..... | 540 |
| 8.2 First Cracking Prediction..... | 541 |
| 8.3 Ultimate Capacity Prediction Using the Strut-and-Tie Model..... | 543 |
| 8.4 Future Research..... | 546 |
| APPENDIX A SURVEY LETTER..... | 548 |
| BIBLIOGRAPHY..... | 558 |

CHAPTER 1

INTRODUCTION

1.1 Background

The use of post-tensioned construction can be traced back for millennia. Early Egyptian boats and medieval barrels had fitted wooden staves compressed together by iron strips or rings. The iron rings were heated and placed around the wood. When the iron cooled, it contracted and, thus, post-tensioned the wood pieces to induce compression and close the joints to prevent leaks [89]. Using the same principles, designers today post-tension concrete to delay cracking and increase ultimate strength. Eugene Freyssinet patented the basic idea of prestressed construction in 1928-30. The use of post-tensioning was mostly limited to arch structures until the late 1940's. Post-tensioning was used in the rebuilding of European bridges following World War II; and, since then, the use of post-tensioning in construction has been steadily increasing worldwide. Many advances have been made in post-tensioned construction in the last 40 years. Post-tensioning is now widely used in bridge piers, in bridge decks, in building slabs, in containment vessels, and in medium and long-span girders where substantial load-carrying capacity is needed. With increased use has come the need for a better understanding of the components of post-tensioned construction. This has been driven not only by the preference to design logically and rationally but also by economic factors. Economic pressures encourage the structural engineer to "push" the post-tensioning structural system towards the limits. In post-tensioned construction, this results in thinner sections, less reinforcement, higher post-tensioning forces, longer spans and higher applied loads.

One of the most critical aspects of post-tensioned construction and one necessary for the success of the system is the anchorage zone. The anchorage zone is where the concentrated post-tensioning force of

the tendons is applied to the structure. From this point, the forces spread into the structure. Figure 1.1 shows how catastrophic a failure can be when the anchorage zones are not properly designed. Fortunately, in this case, the pedestrian bridge was under construction when the failure occurred. This is common for anchorage zone failures since the highest force applied to the anchorages occurs during the stressing process. This is also a time when the concrete is of lower maturity and lower strength.



Figure 1.1 Failure of an Anchorage Zone in a Pedestrian Bridge during Construction

In a recent paper, Schlaich [151] referred to zones near concentrated loads as "D" regions, where "D" could stand for "discontinuity" or "disturbed." In these areas, standard flexural analyses are not valid because of the high degree of local non-linearity. In the 1950's and 1960's, extensive research was performed on anchorage zones utilizing the theory of elasticity type of analysis and small anchor block tests. These studies helped to give a basic understanding of the forces in simple anchorage zone configurations. However, when anchorage configurations were more complicated, the engineer had difficulty extrapolating from these basic results. Codes and standards provided little guidance. In the 1970's, the situation improved somewhat as the use of finite element analysis became more common. Designers had the option to conduct a finite element analysis of their more complex anchorage zones. Yet, many times this sort of analysis is too time consuming, uneconomical, or difficult to translate into reinforcement patterns. There was still very little guidance in the codes and specifications. In addition, there was no commonly accepted rational and systematic approach to the design of anchorage zones in post-tensioned concrete members.

A survey conducted by the CEB [37] asked engineers to design, according to their own national code or handbook, a beam having six anchorages applying a total force of 2700 kN (607 kips). The engineers were asked to calculate the bursting force (the force caused by the spreading of the applied concentrated force), the length of the bursting zone, and the cross-sectional area of reinforcement necessary to carry the bursting force. The range in responses was rather striking. For the bursting force, the average was 192.5 kN (43.3 kips) with a range from 49.5 kN (11.1 kips) to 440 kN (98.9 kips). The same wide range of values was seen for the length of the bursting zone and reinforcement area. The distribution length for the bursting force ranged from 170 mm (6.69 in.) to 850 mm (33.5 in.) with an average of 508 mm (20.0 in.). The required reinforcement ranged from 207 mm²

(0.32 in²) to 2000 mm² (3.10 in²) with an average of 790 mm² (1.22 in²). The survey makes it clear that progress in the current state-of-the-art in design of anchorage zones is not a matter of refining five or ten percent but rather is at the point of reducing differences that can range from 50 to 500 percent.

The current American Association of State Highway and Transportation Officials (AASHTO) Bridge Design Specification [5] only states that designers should maintain a bearing pressure of less than 3000 psi or $0.9f'_{ci}$, whichever is smaller, ahead of the anchorage device. In most cases, anchorage devices today exceed these requirements, thus, making the requirements meaningless. The specification also does not give any guidance for the other portions of the anchorage zone which, in many cases, are critical. These other portions, which are described in detail later, include the bursting zone, the spalling zone, and the longitudinal edge tension zone. Because of this discrepancy between the specification and what is needed by engineers to design post-tensioned anchorage zones, AASHTO asked the National Cooperative Highway Research Program (NCHRP) to initiate a research project which would develop a rational and systematic approach to the design of anchorage zones and which could eventually be implemented in the AASHTO specification.

The research project, of which this document is one part, began in the fall of 1986 with the overall objective of developing a rational and systematic approach to anchorage zone design. Since this project's purpose is very dependent on practicing engineers, a survey was sent to practicing engineers in April of 1987 to determine what the problems were in anchorage zone design. The survey is discussed in detail in Chapter 2. Three of the most significant conclusions from the survey are listed below.

- 1) The current design provision in Sections 8.15, 8.31, 9.15, 9.21 and 9.26 of the AASHTO Bridge Design Specification [5] are insufficient. Most of the bridge engineers responding

found them inadequate.

- 2) Sufficient information is available for the design of single anchorages with straight tendons but as geometries become complicated there are no well established techniques.
- 3) Inconsistency and confusion exists as to who is responsible for the design and checking of different aspects of the anchorage zone. There is not a clear division of responsibility between the anchorage device supplier, the engineer of record, and the constructor.

Upon completion of a thorough state-of-the-art study, the following research objectives were developed.

- 1) Develop divisions of responsibility for the anchorage zone design and construction between designers, anchorage device manufacturers, and constructors.
- 2) Develop an experimental research program that addresses the problems in design practice today and that can be used to verify a rational limit states approach to the design of the general zone.
- 3) Develop a systematic and rational approach to the design of post-tensioned anchorage zones that is adaptable to many different anchorage zone geometries.
- 4) Prepare a specification provision incorporating the results of this research project for consideration for adoption by the American Association of State Highway and Transportation Officials (AASHTO).

1.2 Definitions and Classifications

Before a detailed research program could be developed, a general design methodology and a corresponding division of responsibility within the anchorage zone were developed using the responses of the survey and other information gathered in the state-of-the-art review. The first step in the division of responsibility was to subdivide the anchorage zone into the local zone and the general zone (see Fig. 1.2). The general zone is defined geometrically as the volume of concrete through which the lateral spreading of post-tensioning forces occurs

from the highly concentrated load at the anchorage device to a more linear force distribution across the entire cross section at some distance from the anchorage device. For anchorage zones at the end of a member, the transverse dimensions are approximately equal to the depth and width of the section, provided that neither are larger than the longitudinal dimension of the member. The longitudinal extent of the general zone in the direction of the tendon is equal to 1 to 1.5 times the larger of the width or the depth of the member. For intermediate anchorage zones (anchorage force application not at the end of a member), the general zone dimensions are approximately the same as for end anchorages, except that the longitudinal dimension also extends in the direction opposite to the anchorage force for a distance at least equal to the larger of the width or the depth of the member. It is important to emphasize that the anchorage zone is a three-dimensional body. The sections in Fig. 1.2 are two-dimensional representations which are valid as long as the two principal directions are considered. In the general zone, the spreading of forces and the tensile stresses induced are the major design considerations. The following terminology is used throughout this report when discussing general zone forces. The various forces are shown in Fig. 1.3.

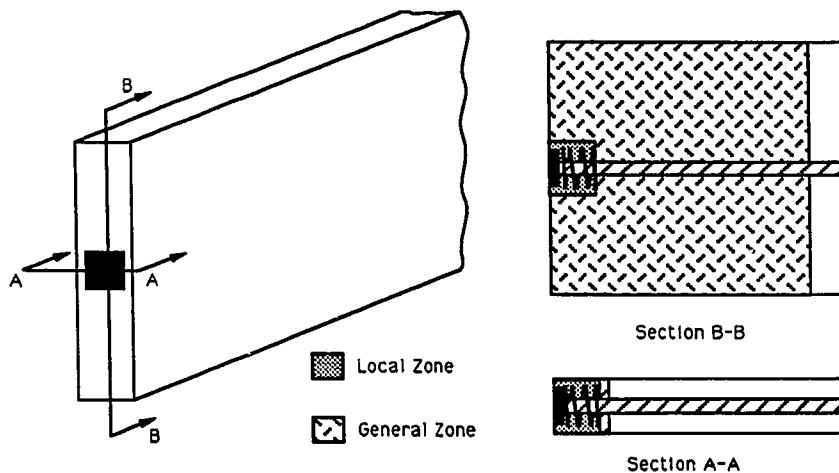


Figure 1.2 Local Zone and General Zone Division in the Anchorage Zone

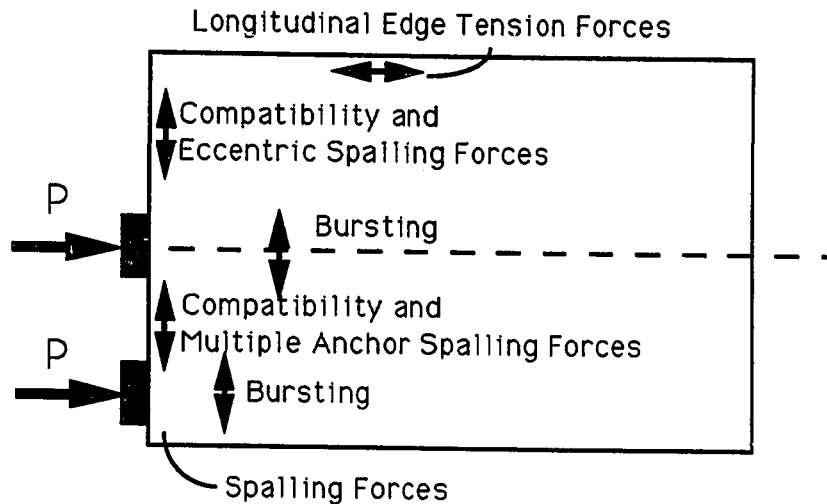


Figure 1.3 Location of Forces in the General Zone

Bursting Forces: Bursting Forces are tensile forces acting transverse to the axis of the tendon and developing ahead of (and, in the case of intermediate anchorages, also behind) the anchorage device. Bursting forces are caused by the lateral spreading of the concentrated post-tensioning force.

Edge Tension Forces: Edge Tension Forces are tensile forces acting parallel and close to the transverse and longitudinal edges of the member. The transverse edge is the surface on which the anchors are loaded. The tensile forces along the transverse edge are referred to as spalling forces. The tensile forces along the longitudinal edge are referred to as longitudinal edge tension forces.

Spalling Forces: Spalling Forces are tensile forces acting in the concrete close to and parallel to the loading surface and in close proximity to the anchorage device. These forces may be induced by the condition of compatibility of displacements, eccentric loads, and/or multiple anchorage configurations. When the resultant of all active tension forces lies outside the kern of the section, spalling forces occur extending from the member's outer longitudinal edge furthest from the axis of the resultant to the resultant of the tendons parallel and close to the loaded

face. When multiple anchors are utilized, spalling forces occur between the anchorages. These forces are similar to the tensile tie forces existing between footings in deep walls supported on individual footings.

Longitudinal Edge Tension Forces: Longitudinal Edge Tension Forces are tensile forces induced parallel and close to the member's outer edge surface which is furthest away from the axis of the resultant of the tendons when the line of action of the resultant of all active tendon forces lies outside the kern of the section.

The local zone is defined geometrically as the volume of concrete surrounding and immediately ahead of the anchorage device throughout which the force in the anchorage device is transferred to the general zone. The lateral dimensions of the local zone are approximately the lateral dimensions of the anchorage device plus twice the applicable cover. The local zone contains any relevant confining reinforcement. The length of the local zone is approximately the larger of its lateral dimensions. The local zone must resist the very high local pressures introduced by the anchorage device and transfer them to the general zone. The behavior of the local zone is strongly influenced by the specific characteristics of the anchorage device and its confining reinforcement, while less influenced by the geometry and loading of the overall structure.

It is understood that these definitions are not clear cut, but they help to clarify the aspects of the anchorage zone design. In cases of thin sections (see Fig. 1.2 Section A-A), the local zone and general zone occupy the same volume of concrete in the transverse direction. However, the definition of the local zone and the general zone can help to fix responsibilities. In Europe, it is current practice for anchorage device suppliers to provide specific verified local confinement reinforcing details with their products and minimum edge distances which are necessary for their anchorage device to reach the design capacity. This should be done because the basic behavior of the local zone is then structure independent if the appropriate edge

distances and local confining reinforcement are provided. For the overall project, it became apparent that the development of either a methodology for local zone analysis or a test certification of anchorage devices that would be independent of specific structural application was both practical and desirable.

If the design responsibilities for the local zone and the general zone could be separated, this would allow the various responsibilities for the proper performance of the anchorage zone to be assigned to the engineer of record, the anchorage device supplier, and the constructor. The engineer of record would be responsible for the overall design and approval of working drawings for the general anchorage zone including the specific location of the tendons, anchorage devices, and general zone reinforcement as well as the specific stressing sequence. The anchorage device supplier would be responsible for furnishing adequate hardware devices and specifying required auxiliary and confining reinforcement to ensure the proper performance of the local zone. The constructor would be responsible for the proper placement of all materials and correct performance of all stressing operations according to the design documents of the engineer of record and the requirements stipulated by the anchorage device supplier.

1.3 Research Objectives

The research project, of which this document is one part, has the overall objective of developing design recommendations and methods for both the local zone and the general zone. The research project is a five-year study funded by the National Cooperative Highway Research Program (NCHRP). The project is divided into two phases. The first phase is to examine the local and general zones for end-surface type anchorages (see Fig. 1.4). The second phase is to examine more complicated geometries such as blisters, ribs, diaphragms and closely spaced slab anchorages. The research reported in this dissertation is largely the experimental aspects of the first phase of the general zone research. The research on the local zone is well documented in a

thesis by Roberts [143]. The elastic finite element analysis, formulation of strut-and-tie model, and study of parameter variations for the general zone are documented in a dissertation by Burdet [25].

The state-of-the-art review indicated that, while a wide range of analytical and experimental investigations have been carried out and while a number of design approaches have been suggested or adopted, there is not a recognized coherent and logical framework for anchorage zone design in North America.

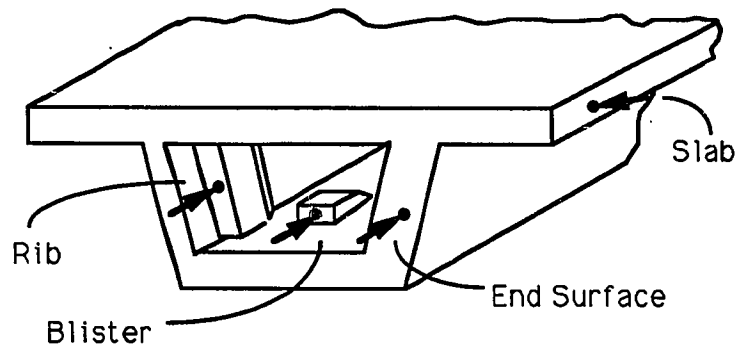


Figure 1.4 Anchorage Types and Locations

It was concluded from the initial studies that the most feasible approach to the development of possible AASHTO criteria lies in the adoption of a limit states approach with a clear division of responsibilities. Criteria to address the serviceability limit state are basically aimed at local zone performance. It was recognized early that it is virtually impossible to predict the onset of surface cracking at realistic tendon stressing levels in typical applications when effects of restraint forces, volume changes, and other loadings

are considered. Thus, while analyses are useful in predicting cracking loads in isolated test specimens, it is more important for actual applications in bridge structures to provide guidelines for providing effective reinforcement to control cracking to acceptable limits. This requires experimental verification of cracking loads and crack widths. The ultimate limit state at maximum tendon force levels will be addressed by establishing general procedures to determine the effective contribution of various reinforcement techniques using strut-and-tie models similar to those recently proposed by Schlaich et al. [151]. However, for some simpler anchorage applications, more useful simple equations might be an alternative. The project is aimed at development of such techniques as well as at comprehensive verification of the adequacy of the strut-and-tie models in accurately predicting anchorage zone capacity.

The study was divided into seven parts as reflected in the following chapters of this document.

- 1) State-of-the-Art (Chapter 2). Examines the technical literature, product information, current codes and commentaries, and a survey that was sent to structural engineers.
- 2) Concentric Single Anchorages with Straight Tendons (Chapter 3). Studies the basic concepts of the simplest anchorage zone design including reinforcement distribution, anchorage width to section depth ratio, lateral post-tensioning, first crack prediction, and ultimate load prediction.
- 3) Eccentric Single Anchorages with Straight Tendons (Chapter 4). Investigates the effect of eccentricity on specimen behavior and then extends the prediction concepts developed for concentric anchorages to eccentric anchorages.
- 4) Multiple Anchorage Specimens with Straight Tendons (Chapter 5). Examines the grouping of anchorages and spacing between anchorages.
- 5) Specimens with Anchorage Inclinations and Curved Tendons (Chapter 6). Investigates different tendon curvatures and inclinations of anchorages. Examines the distribution of the

radial forces.

6) Summary of Results and Proposed Specification (Chapter 7)

7) Conclusions and Recommendations (Chapter 8).

An examination of the survey in Chapter 2 shows a wide variety of post-tensioning applications. Since this project is being funded by NCHRP, the test specimens and the conclusions are made with bridge applications as the major focus. However the results of this study are germane to all post-tensioning applications. This research is the first phase of a continuing study at the University of Texas at Austin. Therefore, not all bridge applications are covered. Topics covered in the continuing study include anchorages in blisters, ribs, diaphragms, and slabs.

1.4 Experimental Program

The study explores the general zone behavior for the most frequently reported anchorage zone configurations. The approach for the design of the test specimens was to select the appropriate strut-and-tie model and proportion the general zone reinforcement. In conjunction with this, a linear elastic analysis was performed to verify the general distribution of stress fields [25]. The critical reinforcement in each test specimen was instrumented to provide confirmation or evaluation of the design model utilized. Specimens were tested to failure with crack development, force distribution patterns, and ultimate loads being monitored. The results were checked against the design assumptions, and the final criteria were developed in such a fashion that designers should be able to implement procedures for design without requiring complex analysis except in the most unusual cases. It is emphasized that the physical tests were being used to verify the strut-and-tie models and not to develop empirical expressions. This has allowed a wide ranging scope of tests with few replications and made the best use of the limited resources.

Reporting of the experimental test program follows the divisions

of the research project as discussed in the previous section. The general zone test program consisted of seventeen concentric single-anchorage specimens, six eccentric single-anchorage specimens, eight multiple-anchorage specimens, and five specimens with tendon curvatures and inclined anchorages. The total number of general zone specimens was thirty-six.

CHAPTER 2 STATE-OF-THE-ART

2.1 Introduction

Considerable previous work has been done in the area of post-tensioned anchorage zones. Information about the design and behavior of anchorage zones can be found from four sources:

- 1) Technical literature,
- 2) Product literature,
- 3) Design engineers, and
- 4) Current codes and commentaries.

Each one of these sources will be outlined in the following sections. The objective of this chapter is to show the current status of post-tensioning anchorage zone design.

2.2 Technical Literature

This section will give a basic overview of the available technical literature for the design and analysis of post-tensioned anchorage zones. Much of the literature dates back to the 1950's and 1960's, but there have been many significant works since then. The technical literature can be divided into six main approaches:

- 1) Analysis utilizing the theory of elasticity,
- 2) Equilibrium methods of analysis,
- 3) Photoelastic investigations,
- 4) Finite element studies,
- 5) Strut-and-tie models, and
- 6) Experimental investigations.

In some cases, studies have incorporated more than one of these approaches (e.g. finite element analysis with an experimental investigation). When this occurs and one approach is more prevalent than the other, the study is mentioned under the prevalent approach.

2.2.1 Analysis Utilizing the Theory of Elasticity. If a reinforced concrete anchorage zone can be assumed to be a homogeneous, isotropic, and linearly elastic body, then the anchorage zone analysis

can be treated as that for the effects of concentrated loads on an elastic body. Such an approach has been shown [65,66] to be valid until the onset of visible cracking. Since the elastic analysis will satisfy equilibrium, the distribution of elastic stresses will indicate a possible load carrying mechanism. If an appropriate criteria is chosen for the tensile and compressive stress limits, the elastic analysis results can be useful in determining the crushing and allowable loads. Such analyses usually do not consider the effect or distribution of anchorage zone reinforcement.

Several authors including Guyon [70] have used a two-dimensional elasticity approach. Guyon's approach to the determination of stresses in the anchorage zone has been widely utilized in design. The classic theory of elasticity solution for the stresses is very complicated and time consuming unless approximated by finite element solutions. Guyon was able to model the spreading of forces in the anchorage zones and then quantify them as bursting stresses and spalling stresses. Bursting stresses are the stresses normal to the axis of loading caused by the lateral spreading of the concentrated load. Spalling stresses are stresses acting normal to the axis of load but along the loaded surface. Guyon determined that the most important variable in determining the magnitude of the stresses and forces in the anchorage zone was the ratio of the plate width to the section depth (a/h). Guyon developed a number of design aids for some of the most common situations to assist the engineer.

In Fig. 2.1a, the general anchorage zone of a rectangular beam is shown subjected to a concentrated load. The depth of the section is equal to " h " with the horizontal load being applied along the line of symmetry. The longitudinal stresses are assumed to be uniformly distributed at a distance of " h " from the anchor. The other dimension shown is the anchor plate width, " a ". Based on a classic theory of elasticity solution, Guyon developed the design aid shown in Fig. 2.1b. Once the ratio a/h is determined, Fig. 2.1b is used to determine the

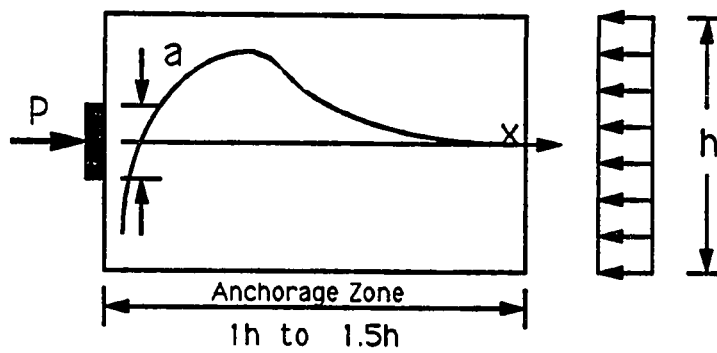


Figure 2.1a Anchorage Zone for a Concentric Anchorage

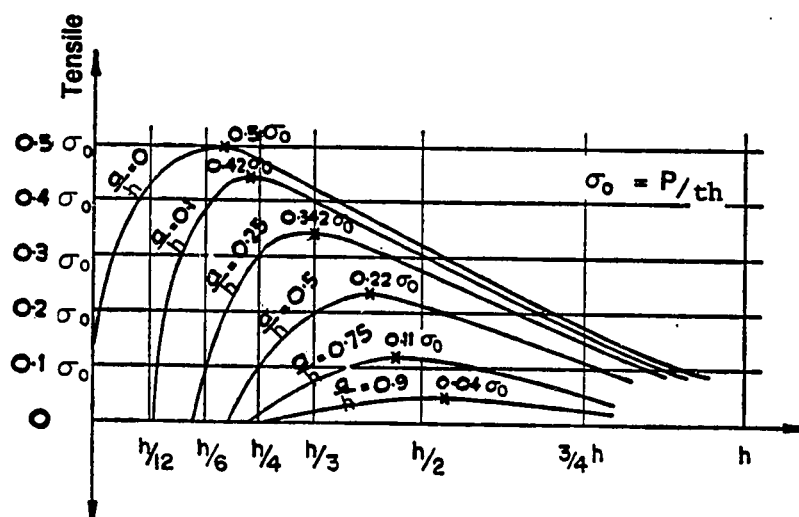


Figure 2.1b Bursting Stress Distribution for Concentric Anchorages [70]

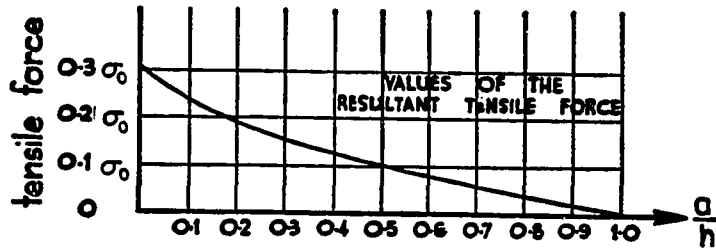
bursting tensile stress distribution beneath the load point. Figure 2.2 shows additional design aids, for bursting force (Fig. 2.2a), for maximum bursting stress (Fig. 2.2b), and for the location of the maximum and zero bursting stresses (Fig. 2.2c).

When the applied load is eccentric, Guyon proposed that the symmetric prism be used to determine the ratio a/h' (see Fig. 2.3a). The premise behind the symmetric prism is that the distribution of bursting stresses calculated for the prism would be equivalent to those in the beam. The width of the prism (h') is equal to twice the minimum distance from the centerline of the tendon to the concrete edge. He also proposed the symmetric prism for use with multiple loads that are closely spaced (see Fig. 2.3b). In this case, the width of the symmetric prism is taken as the smaller of the spacing between the anchors or two times the distance from the concrete edge to the tendon centerline. The a/h' ratio is used in place of a/h in Figs. 2.1 and 2.2 to determine the maximum bursting stress, the magnitude of the bursting force and/or the location of the maximum stress.

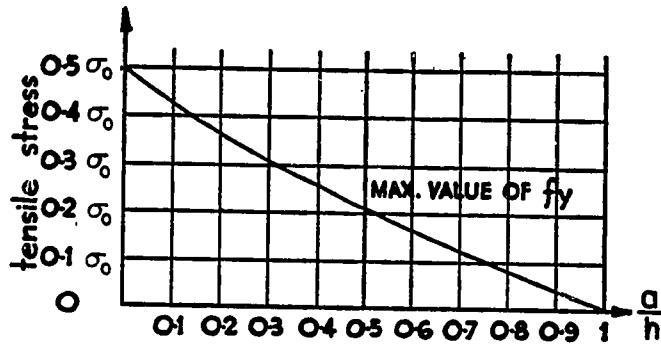
Guyon also determined that spalling tensile stresses existed. Utilizing photoelastic work by Tesar, Guyon calculated the following spalling force magnitudes for various a/h' or a/h ratios.

| a/h' , a/h | 0 | 0.1 | 0.25 | 0.5 |
|----------------|-------|-------|--------|-------|
| Spalling Force | 0.04P | 0.03P | 0.025P | 0.02P |

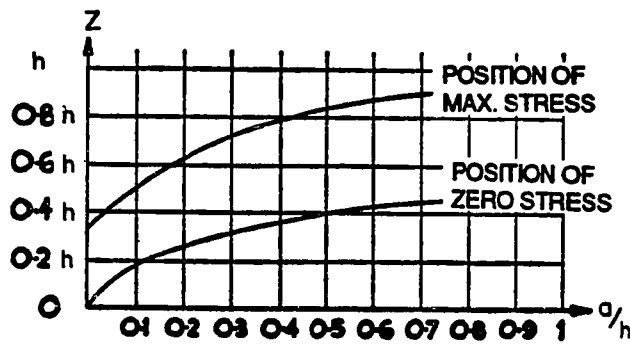
Douglas and Trahair [46] also used an elasticity approach. They investigated the stress distribution for a variety of bearing surface areas and the effect of including the tendon duct in the analysis. Their investigation consisted of a series of tests and elastic analyses with 6 x 12 inch concrete cylinders. Good agreement was found with Guyon's theory except they did not find evidence to support spalling stresses. The presence of the tendon duct reduced the ultimate load by nine percent.



a) Magnitude of Bursting Force



b) Maximum Bursting Stress



c) Location of Maximum and Zero Stress

Figure 2.2 Bursting Zone Data for a Concentric Anchorage Zone [70]

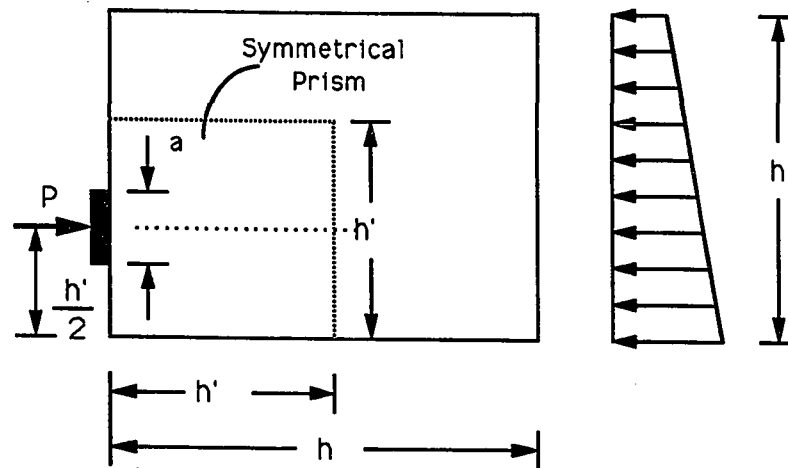


Figure 2.3a Guyon's Symmetrical Prism

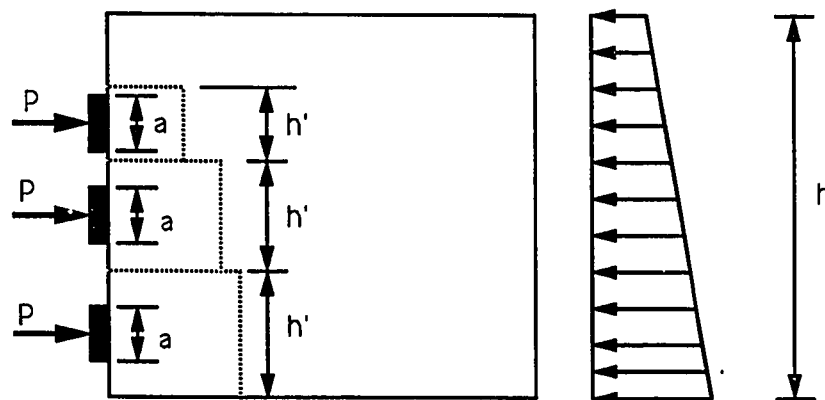


Figure 2.3b Symmetrical Prism for Closely Spaced Anchors

Gergely et al. [65,66] conducted an extensive study that included elasticity principles, equilibrium concepts, and experimental tests. Each approach will be discussed in its related section. Gergely determined the stress contours for a rectangular section with an eccentrically applied distributed load. The solution was developed using two Airy stress functions and finite differences. The results were very close to the levels found by Guyon. Analytical tests were run with several different Poisson's ratios (0.1 to 0.2). When the ratio was changed from 0.1 to 0.15, the bursting stress changed by 20 percent. The change in the ratio also had a considerable influence on bursting strains but only close to the load where the longitudinal stresses were high.

Gerstner and Zienkiewicz [67] solved the problem of a concentrated load at an eccentricity of 0 and $3/8$ of the depth of the section. The problem was divided into a particular solution and a corrective solution. The particular solution was the elasticity solution for stress distribution in a semi-infinite medium, while the corrective solution adjusts the stresses to conform to the boundary conditions and can be solved using finite differences. The solutions were extremely close to those of Guyon. Therefore, Gerstner stopped after only two cases.

Iyengar continued the work on the effect of boundary conditions of the elastic solution. Iyengar [85] did an extensive comparison of the existing analytical models of Guyon [70], Sievers [159], Bleich [20] and Morsch [117]. Iyengar's results agree with Guyon's solution for the bursting stresses. He found that the symmetric prism is a good technique for modeling the zone but believed that the solution was not accurate near the boundaries or for longitudinal and shear stress distributions. Iyengar also conducted a three-dimensional elastic analysis [86] which detected the spalling stresses that were discussed by Guyon. The peak stresses of Guyon's elasticity solution are about 12 percent smaller than those determined by Iyengar. Iyengar detected

the development of spalling stresses. He theorized that Douglas and Trahair [46] did not detect the spalling stresses because they focused on hoop stresses. Spalling stresses are determined from the radial stress component.

Som and Ghosh [162] developed expressions for bursting stresses for concentric, eccentric, and multiple anchors using Airy stress functions. For the concentric case, the calculated bursting stresses are very close to Guyon but differ greatly from Magnel [107]. Magnel [107] and Som [162] showed for concentric multiple anchors a reduction in the maximum bursting stress level from that of the concentric single anchor case; while Guyon showed the same value for constant dimensions of the symmetric prism. The maximum bursting stress predicted by Magnel and Som for eccentric anchors are approximately the same while Guyon is higher.

2.2.2 Equilibrium Methods of Analysis. The distribution of reinforcement to control crack widths in a cracked anchorage zone has been studied based on equilibrium models. Gergely et al. [65,66] developed the following technique to design the spalling reinforcement along the loaded face in addition to the elasticity solution. The equilibrium conditions that are used to determine the spalling force are shown in Fig. 2.4. The first step is to establish a crack length and then determine the moment and shear along plane AB that are necessary for equilibrium. The cracking will usually occur at the position of maximum moment. Reinforcement requirements are determined from the force T which is related to the moment and the crack length. For design purposes they suggested that the crack length can be assumed to be equal to the height of the member.

Lenschow and Sozen [95] introduced an approximate method of analysis for anchorage zone cracking based on the analogy of a beam on an elastic foundation (see Fig. 2.5). A reference plane is selected parallel to the longitudinal axis. The reference plane is where the bursting stresses will be calculated; therefore, it is usually parallel

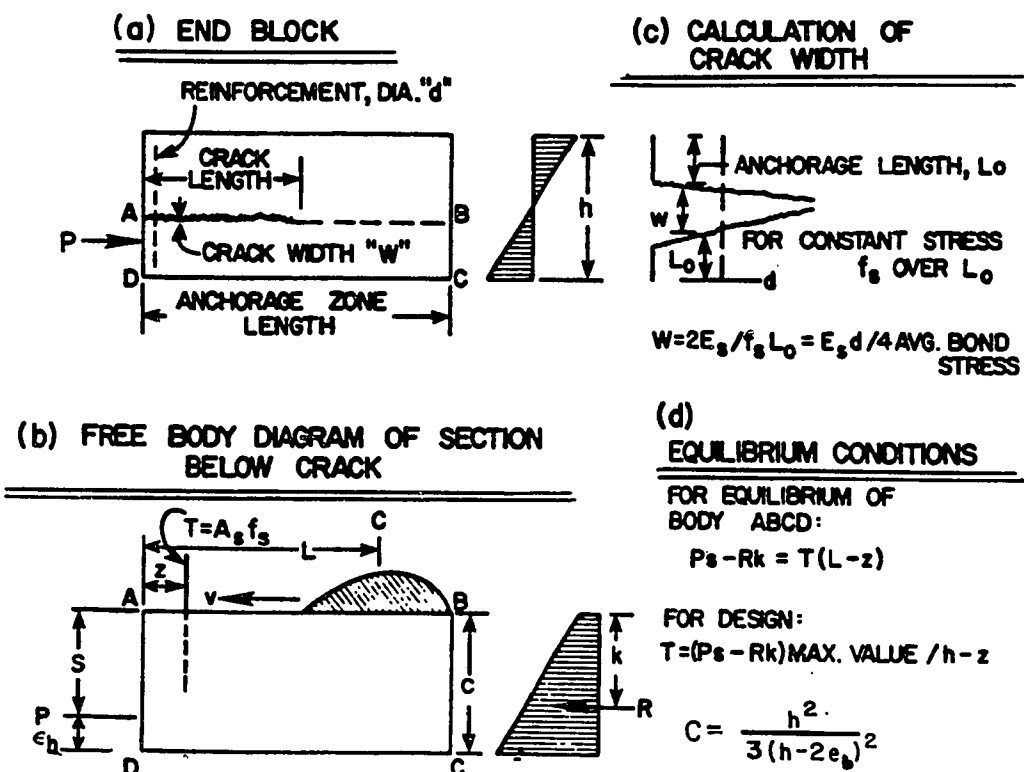


Figure 2.4 Geregly's Beam Analysis [65,66]

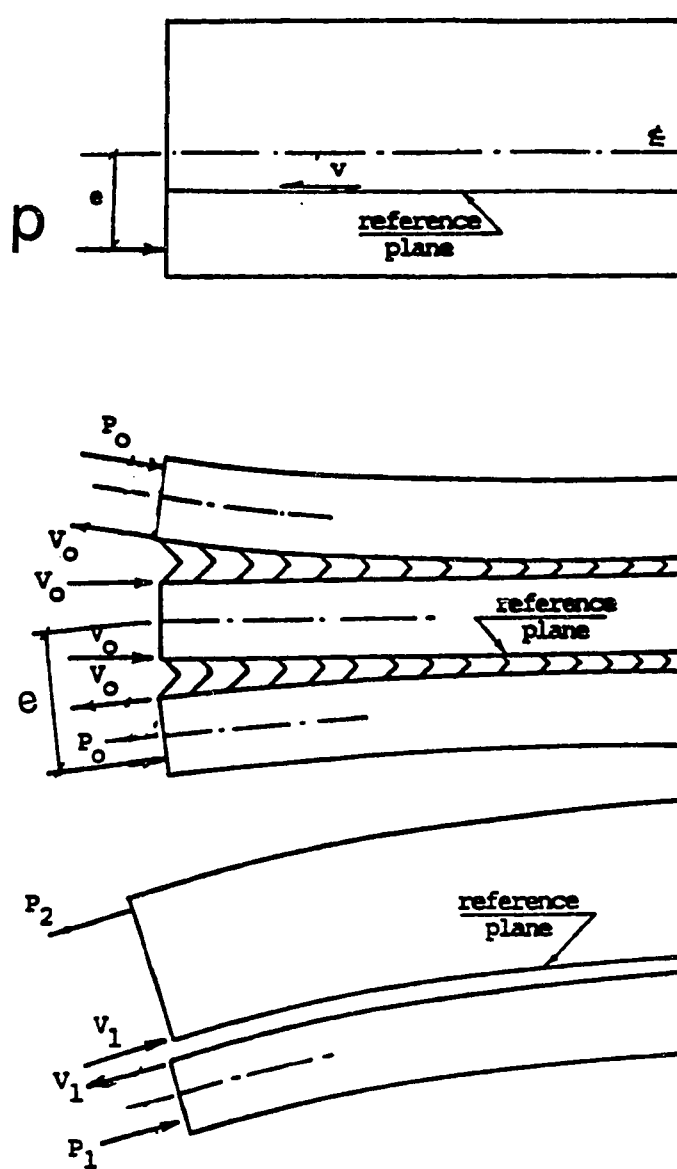


Figure 2.5 Beam on an Elastic Foundation Analogy by Lenschow and Sozen [95]

to but offset from the load. The beam is divided into three beams that are symmetric about the centroid of the beam. Fictitious springs, representing the concrete, are added and the loads are adjusted so that the beams have the same curvature. Since the beams have the same curvature, the springs will no longer come into effect. The method then uses equilibrium and compatibility relations to analyze the beam below the reference plane as a beam on an elastic foundation. The forces in the spring are equal to the bursting forces.

The results of this analysis compare well with the results of Guyon for both concentric and eccentric loads (see Fig. 2.6). The primary difficulty with this method comes with defining the value of the spring stiffness. The advantage of the method occurs in that, once a problem is solved, it is easy to proportion the reinforcement since the engineer knows the force distribution directly.

Magnel [107] developed an approximate method based on equilibrium. Magnel assumed that the stresses became linear at a distance equal to the depth of the member and that the bursting stress distribution along any reference line parallel to the longitudinal axis of the beam had a parabolic distribution. From equilibrium, Magnel determined the moment and the shear on the reference plane then solved the resulting parabolic function. Magnel carried out tests on two unreinforced blocks to show that his results were conservative.

2.2.3 Photoelastic Investigations. Christodoulides [30,31,32,33] performed two-dimensional photoelastic tests to explore the distribution of stresses in a rectangular block with two anchors symmetrically arranged about the centerline of the section. Christodoulides also conducted a three-dimensional photoelastic test on a concrete crane gantry to compare the photoelastic results with strain data. From his tests, he concluded that maximum stresses occur directly in front of the load. He determined that Poisson's ratio had no effect on stresses because his plastic model answers agreed with the results from the concrete gantry beam test. According to the results

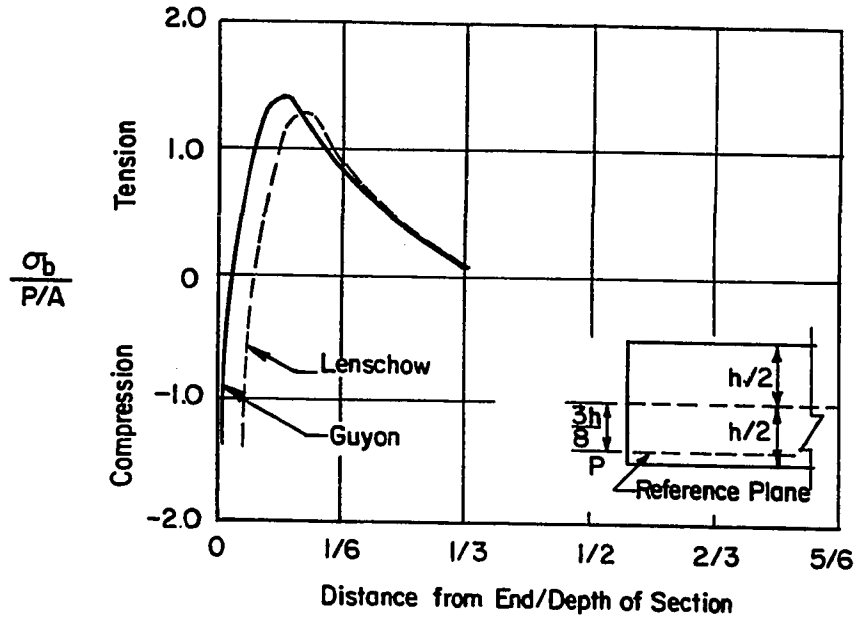


Figure 2.6a Bursting Stress under an Eccentric Load [181]

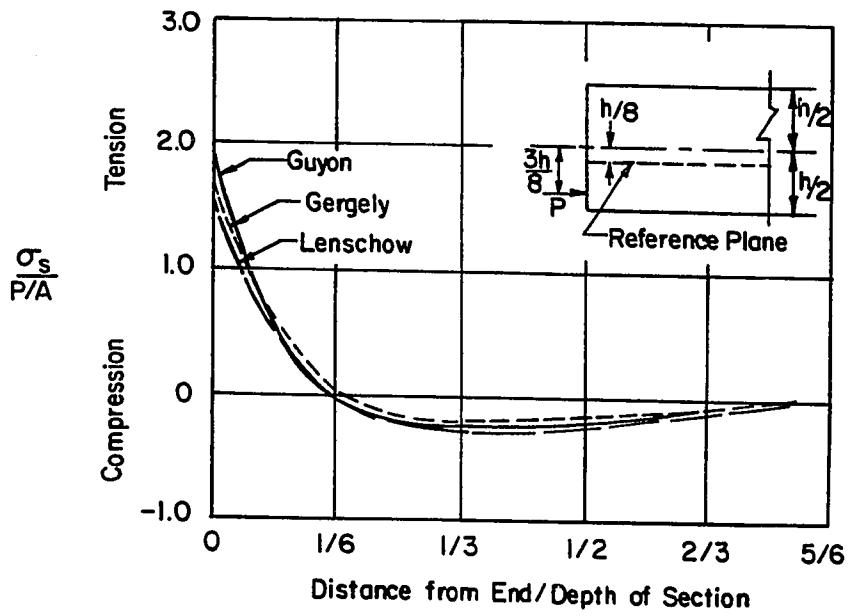


Figure 2.6b Spalling Stresses [181]

of Christodoulides, both the Magnel and Guyon theories underestimated the maximum stresses on the concrete surface.

Leonhardt [96] relied heavily on the symmetrical prism theory of Guyon and on extensive photoelastic studies by Sargious [149] to generalize design theories for reinforcing anchorage zones. While a major proponent of strut-and-tie models for reinforcement proportioning, it is notable that his 1964 English edition did not mention this latter approach in its chapter on anchorage zones.

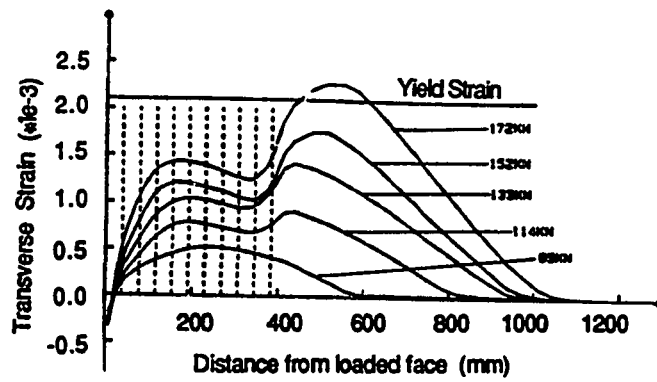
Rasheeduzzafar and Al-Saadoun [139] conducted a three-dimensional photoelastic investigation on anchorage bearing stresses in rectangular blocks. The study looked at embedded anchors versus external anchors and also treated both multiple anchors and edge spacing. The following trends were determined from the program. Embedded anchors allow part of the force to be transferred by shear and part by bearing. The study concluded that one-third of the force can be transferred by shear traction. Embedded anchors have smaller maximum tensions than external plates. Forces become essentially uniform after a longitudinal distance of two-thirds the depth of the block. The stresses that develop on the unloaded faces are very dependent on the location of the anchor; therefore, they predicted that a design formula that does not incorporate the proximity of the anchor to the unloaded faces will not be entirely successful in predicting stresses. In the tests, the geometry of the single and multiple anchorages were not exactly the same but the stress data obtained suggested that, apart from an increase in the bursting tension on the loaded face, there is no significant interaction between adjacent anchor units spaced apart at least a distance equal to twice the largest anchor dimension. They concluded that, in the absence of more comprehensive design criteria, the symmetric prism approach provides the most reasonable model for evaluating the bursting force.

Vaughn [179] investigated two-dimensional photoelastic techniques to model multiple tendons, eccentricity, and inclination. Vaughn

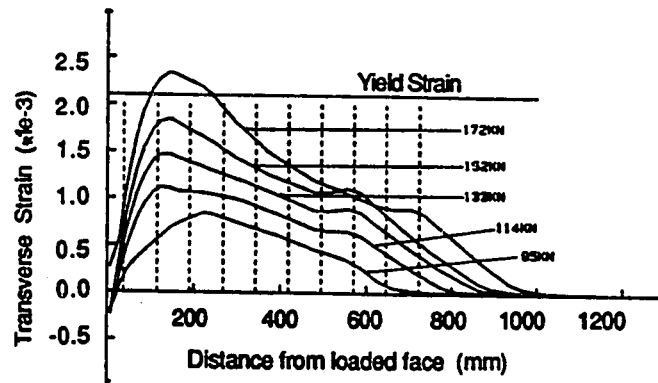
discovered that a conical shaped anchor produced principal tensile stresses approximately 150 percent greater than those for flat bearing anchors and produced maximum shearing stresses approximately 250 percent greater. The spalling stresses increased significantly for increasing eccentricity and for an increasing angle of inclination. Large spalling stresses were also created between multiple anchors along the loaded face.

2.2.4 Finite Element Studies. The development of comprehensive finite element analysis models has opened the way for powerful analytical studies. While results depend on the mesh and the solution techniques used, the linear finite element analysis has great promise for determining uncracked-state stresses. Nonlinear finite element studies can model the cracked anchorage zone state.

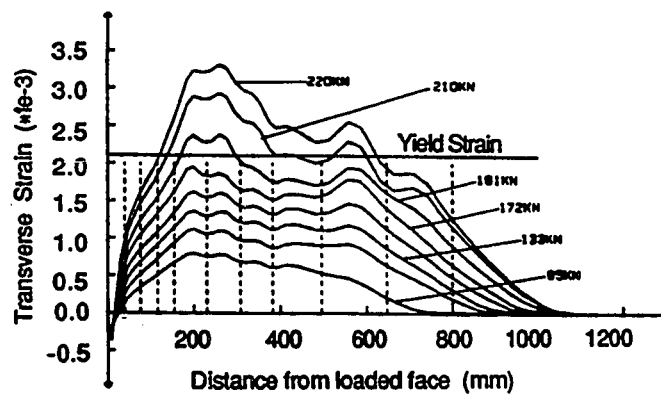
Adeghe and Collins [2] used a nonlinear finite element analysis to study the effect of reinforcement distribution in the bursting region on the strain distribution. The specimens investigated had an a/h of 0.1 and a total length of 1220 mm (48.0 in.). Figure 2.7 shows the results of the three reinforcement distributions. The strain distribution changes significantly for the three reinforcement patterns after the cracking load (95 kN or 21.4 kips). Adeghe and Collins determined that placing all the reinforcement in the high stress region (see Fig. 2.7a) would result in brittle behavior. Spreading the reinforcement along the entire bursting region (see Fig. 2.7c) would make much better use of the reinforcement. Figure 2.8 shows the principal compressive stress trajectories for an elastic analysis and a nonlinear analysis. The dispersion angle of the compression from the bearing surface is steeper in the elastic analysis than in the nonlinear analysis. This indicates that more reinforcement would be required from the elastic analysis because the centroid of the bursting force is closer to the bearing surface. Therefore, the elastic analysis would be conservative.



a) Stirrup Detail 1

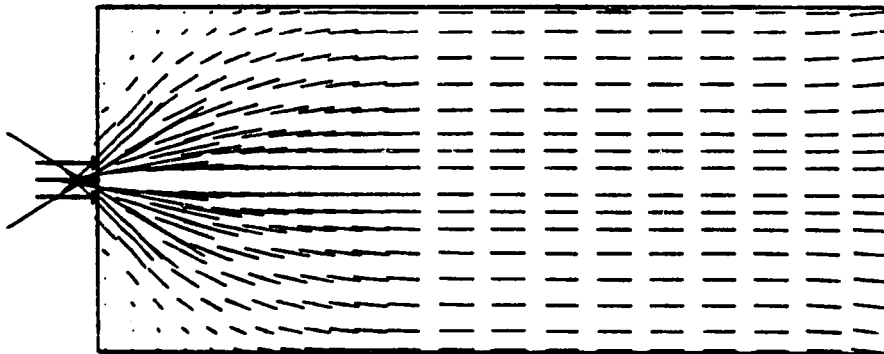


b) Stirrup Detail 2

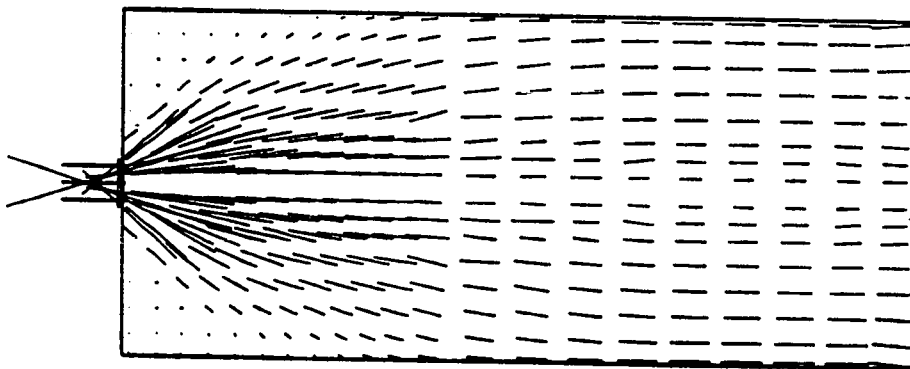


c) Stirrup Detail 3

Figure 2.7 Transverse Tensile Strain Distribution for Three Stirrup Arrangements [2]



a) Compressive Stress Flow, Linear Elastic Analysis



b) Compressive Stress Flow, Nonlinear Analysis

Figure 2.8 Comparison of Linear Elastic and Nonlinear Compressive Stress Flow [2]

finite element analyses which consider continuity effects omitted in the equilibrium based strut-and-tie models. Burdet found that the maximum compressive strength of the anchorage zone could be found by matching the peak compressive stress as determined from the finite element analysis to $0.75f'_c$ at a distance from the loading surface equal to the lateral dimension of the anchorage device.

From the parametric studies, Burdet developed the following formulas to estimate the bursting force and the location of the bursting force. These equations are valid for initial anchorage inclinations of -5 degrees (extrapolated) to 20 degrees.

$$T_{burst} = 0.25 \cdot (1 - a/h) + 0.5 \cdot P \cdot \sin(\theta)$$

$$d_{centroid} = 0.5 \cdot (1 - 2 \cdot e/h) + 5 \cdot e \cdot \sin(\theta)$$

Where

P is the total factored tendon load for the stressing arrangement considered;

a is the lateral dimension of the anchorage device or group of devices in the direction considered;

e is the eccentricity (always taken as positive) of the anchorage device or group of devices;

h is the transverse dimension of the cross section in the direction considered; and

θ is the angle of inclination of the resultant of the tendon or tendons with respect to the centerline of the member, positive for concentric tendons or if the anchor force point towards the centerline of the member, but negative if the anchor force points away from the centroid of the section.

Burdet also formulated procedures to develop strut-and-tie models and correlated the resulting models with his finite element analysis and existing experimental results including those reported in this dissertation. He found that using the strut-and-tie model based on an assumed dispersion angle (α , see Fig. 2.9) of 26 degrees for the compression struts correlated well with the test results for most anchorage zone configurations. Designing with the strut-and-tie model

must include checks of the tension tie capacity and compression capacity at the local zone-general zone interface. He concluded that, for a very complex configuration, it is difficult to determine critical strut patterns and strength so that it appears desirable to use a finite element analysis to determine compressive strength limits.

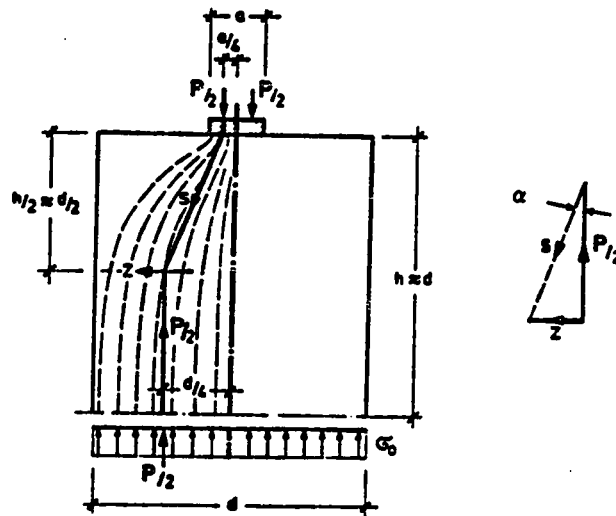


Figure 2.9 Strut-and-Tie Model by Morsch [117]

Egeberg [49] conducted two-dimensional linear finite element studies with concentric and eccentric single tendon anchorage blocks. Cases were run for uncracked, cracked, and reinforced sections. He found very close agreement with Guyon's theories and close agreement with Magnel. The maximum bursting stress level was the same as Guyon's, but the spalling stresses were significantly less. Egeberg determined that the bursting stresses were almost exactly the same for eccentric and concentric cases with the distributions simply shifted to a different location. The introduction of a crack at a prescribed stress level caused the raising of stresses ahead of the crack, propagating the crack. The addition of reinforcement significantly dropped the stress level in the concrete because the force was transferred to steel.

Stone and Breen [166,168] used a combination of finite element analysis and experimental testing to study single anchorage zones in thin web members. This study is discussed in detail in the experimental investigation section. Stone and Breen found good correlation between experimental and analytical results.

A broad investigation using finite elements was conducted by Yettram and Robbins [190,191,192]. The research was presented in a series of three articles with the first addressing the simplest case of concentric anchorage zone stresses in a rectangular section. In the first study, both two- and three-dimensional cases were reported with the following conclusions.

- 1) The distance to form a uniform normal stress field is 1.25 times the height of the prism.
- 2) A variation of Poisson's ratio between 0.125 and 0.2 has little effect upon the stress distribution.
- 3) Iyengar's and Guyon's two-dimensional elastic analysis results give good values for the average stress when compared with Yettram, although they cannot indicate the transverse variations in the stress distribution.
- 4) The experimental results of Zielinski and Rowe were based on surface measurements and significantly over-estimated the maximum bursting stress for all ratios of bearing surface area to cross section area; therefore, Yettram's results were not close to those of Zielinski.

In the second paper, Yettram and Robbins addressed the problem of eccentric and multiple anchorages in rectangular and non-rectangular sections. From the cases studied, it was determined that the symmetric prism method of Guyon gave a satisfactory representation of the bursting stresses for design purposes. They suggested that, if the symmetric prism extends into either or both of the flanges with non-rectangular sections, then the influence of the bursting stresses will extend a further distance in front of the loaded face than the depth of the rectangular symmetric prism. They found that in non-rectangular

sections, the effect of flanges was generally to reduce the importance of spalling stresses.

In their third paper, Yettram and Robbins studied anchorage zone stresses in I section members with end blocks. In the study, the length of the end block was the major variable. They concluded that, in very short end blocks, the lateral (out of plane) bursting stresses should be considered. A longitudinal taper between the block and the web is advantageous. The maximum bending stress is greater than the maximum bursting stress except in very long blocks. Short end blocks (length/depth less than 0.75) are of little advantage because bending stresses overshadow the bursting stress, and this causes an increase in the transverse reinforcement and greater congestion.

2.2.5 Strut-and-Tie Model. The strut-and-tie model is a concept in which elasticity stress trajectory fields or a basic understanding of the flow of forces in the member are used to formulate an equilibrium based model consisting of struts and ties. In these models, the applied loads such as post-tensioning forces are transferred through the structure with the use of compression members (struts) and tension members (ties). The strut-and-tie models stem from the pioneering work of Ritter in 1899 who used such a model to develop the truss analogy to explain the shear-diagonal tension resistance in reinforced concrete beams. It has been developed by many engineers such as Morsch, Leonhardt, Thuerlimann and Schlaich. The most comprehensive treatment in English is the recent paper by Schlaich et al. [151] which shows many applications of the strut and tie model including the modeling of an anchorage zone. Figure 2.9 shows a strut-and-tie model that was used by Morsch [117] in 1924. Even though the model is based on very simplified assumed force trajectories, the analysis of the tie force Z gives an equation for the bursting force that is very close to what many current codes use. An example for an eccentric anchorage is shown in Fig. 2.10. Figures 2.10a and 2.10b show the elastic stress distribution, as determined by theory of

elasticity analysis. Figure 2.10c is the representative strut-and-tie model which is the simplified depiction of the elastic stress fields. The elastic stress fields can be used to determine where the struts and ties should be placed. The strut-and-tie model is gaining popularity because a designer can readily formulate general anchorage zone reinforcement from such a model. Even though very little previous research has been conducted into the direct application of the strut-and-tie model to the ultimate strength design of the anchorage zone, the technique holds much promise.

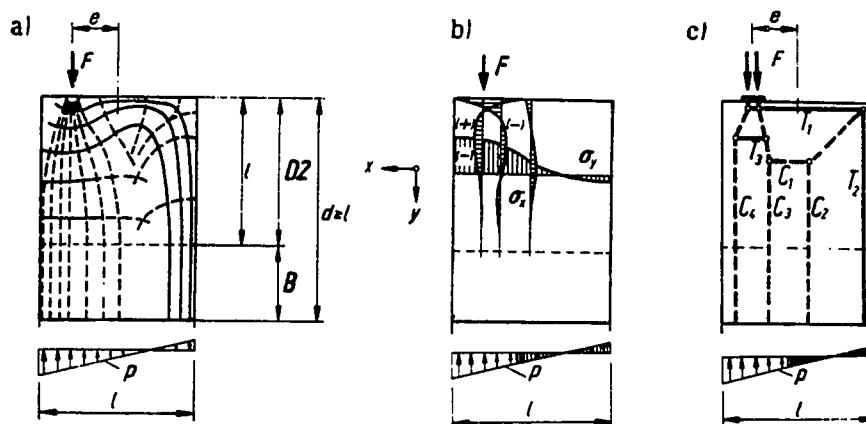


Figure 2.10 Strut-and-Tie Development from an Elastic Stress Distribution [151]

Schlaich divides a member into two types of regions, "B" and "D". "B" regions are zones with linear strain distributions where beam theories apply. The stress states in these regions are easily derived from the sectional forces. "D" regions are zones in which the strain distributions are significantly nonlinear such as near concentrated loads, corners, openings and other discontinuities. The anchorage zone is a "D" region. Saint Vénant's principle can be used to find the approximate length of the disturbed anchorage zone. Therefore, for most applications the length of the anchorage zone can be taken to be

the depth of the section. The following steps are necessary to use the strut-and-tie procedure:

- 1) Develop the strut-and-tie model where the struts and ties model the actual stress trajectories by lines of action and concentrate their curvature in nodes;
- 2) Calculate the strut and tie forces;
- 3) Dimension the struts, ties and nodes; and
- 4) Check stresses and forces.

The strut-and-tie model is a lower bound plasticity theory. The lower bound theory of plasticity assumes that both internal and external equilibrium are satisfied, and that stresses do not exceed the material yield conditions. The theory also assumes that the system has sufficient ductility to develop the yield conditions. Since concrete has limited plastic rotation capabilities, it is important to choose a strut-and-tie model that does not require large rotation in order to mobilize the struts and ties. Struts and ties oriented along the elastic trajectories neglect some potential gain from plastic behavior but also ensure reasonable rotations. If the assumptions of the lower bound theory are met, then the predicted capacity will be smaller than or equal to the collapse load.

Schlaich details the dimensioning of struts, ties, and nodes and their stress limitations. Tension ties carried by reinforcement are essentially linear or one-dimensional elements between two nodes. Compression struts or tension ties carried by concrete between nodes tend to spread or bulge out. This spreading can induce additional tension (see Fig. 2.10). Schlaich defines nodes as simplified idealizations of reality that are defined at the intersection points of three or more straight struts or ties. A node is a sudden change in the direction of the strut that would not occur in the actual structure. Schlaich classifies nodes as either singular or smeared. Singular nodes are caused when a strut or tie is representing a

concentrated stress field. If the stress field is wide or when the tension ties consist of many closely spaced bars, the deviation of the forces may be smeared over some length. If a node is smeared, there is typically not a stress problem at the node, since the forces are spread out over a larger area. Figure 2.11 shows the locations of the smeared and singular nodes.

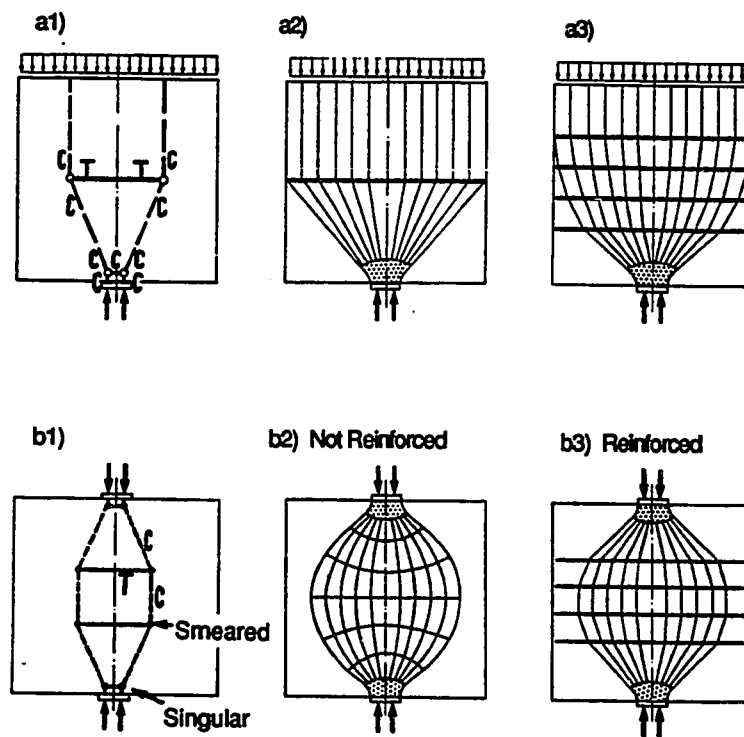


Figure 2.11 Stress Fields for Concentric Strut-and-Tie Models [151]

The concrete compression strength is dependent on the stress state in the concrete. Transverse compression is favorable because it acts as confinement. Transverse tension is very detrimental especially if cracks form parallel to the principal direction of the struts. Schlaich proposes the following strength values for concrete in compression.

- $f_c = 1.0f_{cd}$ for undisturbed and uniaxial compression;
 $f_c = 0.8f_{cd}$ if cracks parallel to the direction of the strut may form or in node regions where a tension tie is anchored;
 $f_c = 0.6f_{cd}$ where there may be skewed cracking;
 $f_c = 0.4f_{cd}$ where there is extensive cracking such as what is necessary for large plastic rotations; and
 f_{cd} is the effective design strength of compression concrete.

According to the CEB Code [36], $f_{cd} = 0.85f'_c/\gamma_c$ where γ_c is a factor of safety and the coefficient of 0.85 accounts for sustained loading. In the CEB Code, $\phi = 1.0$ and the load factors for dead loads and live loads are 1.35 and 1.5 respectively.

Marti [108,109] recommended an average effective compressive strength of $0.6f'_c$. He stressed the importance of visualizing the force flow consistent with the equilibrium assumptions and providing the necessary detailing to develop the required forces.

Collins and Mitchell [34] proposed the following equations for the compressive strength of concrete based on longitudinal (ϵ_1) and transverse strains (ϵ_t).

$$f_c = 5.5f'_c/(4 + \gamma_d/\epsilon_d)$$

$$\text{where } \gamma_d = 2\epsilon_d + \epsilon_1 + \epsilon_t$$

and ϵ_d at failure can be taken as 0.002.

2.2.6 Experimental Investigations. Experimental work can be placed into two groups: those focusing on studying the general zone behavior and those focusing on the study of the local zone behavior. Investigations have been placed in one of these two classifications, even though most studies are not mutually exclusive. The general zone is usually assumed to extend for a length about equal to the overall depth of the member. The local zone extends for a length about equal to the largest dimension of the anchorage device.

2.2.6.1 General Zone. Ban et al. [17] conducted both an experimental and analytical study. The analytical study consisted of two and three-dimensional elastic investigations, while the experimental study consisted of 36 block tests. The main variables in the study were the amount of spiral reinforcement, the size of the anchor plate and the concrete strength. Strain gages were used to measure surface strains on the concrete. The results from the study were then compared with existing theories.

The research had five major conclusions.

- 1) The arrangement of a proper amount of transverse reinforcement is effective in increasing the cracking and ultimate loads of the end block.
- 2) When the bearing surface of the anchor is increased, a slight increase in the ultimate load may occur.
- 3) Linear relationships can be developed to relate both the concrete strength and thickness of the anchorage plate to the cracking load and to the ultimate load.
- 4) In comparing two-dimensional solutions to experimental results, Bleich's solution compared very well while those of Guyon deviated considerably.
- 5) Siever's three-dimensional analysis approximated the experimental distributions.

Breen, Cooper and Galloway [23] tested fifteen "I" section specimens to examine the effects of the anchorage geometry, concrete strength, local reinforcement patterns, length of spirals, lateral post-tensioning, tendon curvature, and percentage of web reinforcement. They concluded the following.

- 1) Formation of cracks along the tendon axis can be accelerated by anchorages with stiff transitional cones and radial forces due to tendon curvatures.
- 2) The cracking load is not affected by increasing the percentage of web reinforcement and is only slightly affected by concrete compressive strength.

- 3) The cracking load is not greatly affected by the size of the bearing plate.
- 4) Very long spirals are effective in delaying the first cracking load.
- 5) Transverse post-tensioning is very effective in controlling and preventing tendon path cracks.

Fenwick and Lee [56,94] loaded a series of 18 rectangular and "I" section anchorage zones. In addition to the shape of the section, other test variables included the bearing surface area and the tie spacing. The researchers concluded that most of the past research has ignored force redistribution after cracking and that most designs are based on the force being sustained in an uncracked member. Consequently, bursting forces are overestimated. In the tests, the bursting force in "I" sections was much higher than in rectangular sections of the same depth and web thickness. Based on the results of the project, a design procedure was developed. The design is based on an average stress to peak stress ratio of 0.76 in uniformly distributed reinforcing ties. This factor would be increased if the reinforcement is placed according to the stress distribution. The procedure was developed for only concentric single anchorages.

$$\begin{aligned}
 \text{Area of Steel} &= 1.32F_{\text{bursting}}/f_{\text{steel}} \\
 F_{\text{bursting}} &= 1.20m_{\tau}M_a/l_a \\
 m_{\tau} &= 1.25 - 0.25(R)^{0.5} \\
 l_a &= 1.73r(2.9 - 1.9(R)^{0.25})
 \end{aligned}$$

Where R equals the stiffness ratio, the ratio of the transverse stiffness after cracking to that existing before cracking (R for one test equaled 0.033); M_a is the maximum anchorage zone bending moment; and r equals the radius of gyration of the section or the equivalent prism.

Gergely et al. [66] conducted 25 tests on anchorage zones in end blocks. The specimens consisted of rectangular and "I" beam sections

conducted using finite differences. The research was very productive and derived the following conclusions:

- 1) In members with low eccentricities, bursting stresses beneath the load are the highest stresses; while, with high eccentricities the spalling stresses at the mid height of the section are highest. The tensile zone is larger for concentric loaded sections, but the stress peaks are higher for eccentric loaded sections.
- 2) In "I" beams, the performance is better if the force goes through the flange.
- 3) Reinforcement cannot be utilized before cracking, therefore, elastic analysis is invalid in a cracked section.
- 4) Bursting stresses are not affected by the behavior of the spalling zone; therefore, the symmetric prism of Guyon is valid.

Higashida and Nakajima [78] tested eight rectangular blocks each with 18 prestressing bars anchored at the end sections in six rows of three anchors. The specimens were loaded by stressing the bars by rows, starting in the middle and moving to the ends. The specimens varied by altering the reinforcement amount and the stressing level of the bars. Higashida and Nakajima concluded that, for design purposes, the amount of reinforcement for multiple anchorages can be calculated by using the theory for single anchorage systems.

Huang [82] tested one "I" beam and did an accompanying finite difference solution. The "I" beam had end block sections with different lengths (depth of the beam and 1.5 times depth of the beam). Stress results agreed with those of Magnel and Guyon. Huang discovered that it is not good to make end blocks too long because they develop high vertical tensile stresses. However, they need to be long enough to distribute the stresses. Huang suggested using a length equal to the depth of the member.

Stone and Breen [166,168] conducted an experimental and analytical study of single anchorage zones in thin web members. The

experimental program investigated the following primary variables: tendon eccentricity and inclination, section height and width, concrete tensile splitting strength, anchor width and geometry, and the effect of supplementary anchorage zone reinforcement, both active (lateral post-tensioning) and passive. The experimental study consisted of three phases. Two phases tested a total of forty one-quarter scale specimens; and, in a third phase, ten tests were performed on five full-scale specimens, one test at each end. The analytical study utilized a three-dimensional linear finite element computer analysis to generalize the experimental results.

The conclusions of the investigation were:

- 1) For increasing eccentricity and inclination, the cracking load decreased. (This contradicts theories which base cracking on critical bursting stresses since both Guyon's symmetrical prism results and finite element analyses indicate that bursting stresses decrease with increasing eccentricity.)
- 2) Bearing stresses as high as 2.5 times the compressive concrete strength were routinely achieved before the ultimate load. The cracking strength raised with the increasing of the ratio of the bearing area to the surrounding concrete surface area.
- 3) Tendon path cracks can occur at locations well outside the general anchorage zone in sections where the tendon profile has significant curvature and multiple strands are used, because of the tendency for the tendon bundle to flatten out and create lateral forces.
- 4) Tests on unreinforced sections using plate-, bell-, and cone-type anchors showed that anchor geometry can affect the cracking load. (A cone anchor has stiff bearing walls in the conical section. Many times plate anchors are equipped with a conical trumpet, but it is flexible.) The cracking load of the bell anchor is equal to 1.08 times that of the plate anchor, and the cracking load of the cone anchor was equal to 0.61 times that of the plate anchor. The ultimate loads for the plate and cone anchors are only slightly above cracking load, while bell anchors could reach loads up to approximately 25 percent above cracking.

- 5) Spiral passive reinforcement exhibits much better performance than standard orthogonal reinforcement both for increasing cracking and ultimate loads and for controlling crack widths. The ultimate load for anchorages with spiral reinforcement is as much as 45 to 60 percent higher than those with orthogonal reinforcement having a reinforcement ratio ten times that of the spiral. Spirals were more effective when smaller wires were used with as short a pitch as possible. In addition, long spirals ($2b$ to $2.5b$ in length, where b is the web width) performed no better than short spirals.
- 6) Lateral post-tensioning reinforcement was the most effective method for controlling cracking in the anchorage zone. The best location for active reinforcement was as close to the loaded face as possible.
- 7) The tensile strengths of micro-concrete used in one-quarter scale models were found to be substantially higher than those of normal concrete. Therefore, cracking and ultimate loads should be normalized with respect to the tensile strength.
- 8) Crack patterns observed in the full-scale specimens could be accurately reproduced in the one-quarter scale models; but crack widths, even after scaling, were 40 percent smaller on the average.

From their conclusions, Stone and Breen developed an empirical design procedure based on the cracking load of the concrete. While applicable to sections similar to those tested, the empirical procedure can give misleading results for extreme values of variables such as eccentricity, section dimensions, etc.

Taylor [173] tested seven anchorages to develop a failure criterion for plain concrete. His values for the bursting stresses were between those of Guyon and those of Zielinski and Rowe. Taylor found that these values could be reduced by applying a compressive load perpendicular to the axis of the post-tensioning force. He also noted the formation of a cone of concrete ahead of the bearing plate. This cone of concrete is formed due to the stiffness provided by the bearing plate. Once the shear forces along the surface of the cone loosen, the cone acts as a wedge in the concrete. This causes bursting forces

perpendicular to the axis of the load.

Trinh [177] tested 24 specimens to investigate lightweight concrete in anchorage zones. He determined that lightweight concrete was less resistant. To adjust for the lower strength he recommends using larger bearing plates or increasing the thickness of the section. He also noted that plate flexibility was important when determining the strength of a specimen. Trinh determined that the best equation for the effective width of the plate was the width of the wedge plate plus two times the bearing plate thickness. A safe lower bound equation was 0.886 times the wedge plate width plus two times the bearing plate thickness. When lightweight concrete was used the effective width was best found by adding three times the thickness instead of two. These equations correlated well when rectangular plates were used but not as well for circular plates. Trinh also developed an equation for the bearing capacity of the local zone.

Virlogeux [180] tested three large specimens that examined the effects of lightweight concrete. The specimens had anchorages that were inclined and had tendons with curvature. He also did an initial study on small blocks of concrete which showed that: the post-tensioning duct reduces the ultimate strength; the bearing capacity of lightweight concrete is less than that of normal weight concrete; and the more rigid a bearing plate, the better the performance of the specimen. In the large specimens, one was cast monolithically while the other two used a precast plug for the anchorage device. This precast plug used normal weight concrete and contained the bearing plate and the confining reinforcement. The two specimens with plugs had different strengths of lightweight concrete in the general zone. The specimen without the plug failed in the local zone, while failure of those with the plugs occurred along the tendon path.

Welsch and Sozen [181] did an extensive number of tests which focused on spalling cracking in both rectangular and "I" sections. The beam tests were either unreinforced or lightly reinforced near the

anchorage. Welsh and Sozen found that spalling cracks did not lead to failure as long as the cracks were small. Since their beams were unreinforced in the bursting region, failure of the specimen was almost simultaneous with the formation of cracks in the bursting region. Welsh and Sozen also did sustained load tests and found that more than one-half of the total crack growth for their specimens occurred in the first week of the eight month tests. Their results correlated well with the basic method of Lenschow.

Zielinski and Rowe [194,195] conducted one of the most extensive experimental programs. The program was divided into two parts: single axial symmetric anchorages and multiple anchorages. The following variables were studied: the ratio of the size of the loading plate to the area of the cross section (A_b/A), the duct size of the post-tensioning cable, the position (external or embedded) of the anchorage device, the shape of the bearing plate (square or circular), and type, position and amount of reinforcement. Stresses were measured using strain gages on the concrete surface. The study investigated both bursting stresses and forces, but only in small specimens. Therefore, their study was a combination of a local zone and general zone study. The study had the following conclusions:

- 1) The distribution of bursting stresses and the ultimate load of an end block are not significantly affected by the anchorage being embedded or external.
- 2) The dominant factor in the distribution of bursting stresses and the ultimate load is the ratio of the loaded area to the cross sectional area of the prism (A_b/A), while the positions at which the maximum and zero bursting stresses occur are not significantly affected by the ratio.
- 3) The maximum bursting stress, which always occurs in the central axis of the prism, is considerably greater than that predicted by any of the existing theories.
- 4) The percent of reinforcement has a significant effect on the bearing capacity of end blocks, and spirals were found to be more efficient than orthogonal reinforcement.

- 5) When two anchors are set apart in an anchorage zone, the deep-beam effect sets up tensile forces between the anchors.
- 6) For a group of anchors, the individual symmetric prism may be used to design reinforcement under each anchor.
- 7) The size of the duct did not seem to be a major factor affecting the bursting stress distribution.

Yong et al. [193] utilized a combination of finite element solutions and 15 experimental tests to investigate how shear forces affect anchorage zone stresses. The specimens were "I" sections with end blocks. The 15 tests included three beams with concentric anchors and end block lengths of 12 inch, 18 inch and 24 inch and 12 tests with eccentric anchors with the same set of three end block lengths. From these tests, it was concluded that a lateral shear force on a beam causes a significant reduction in the value of the lateral tensile strains but has relatively little effect on the transverse tensile strains. If lateral active reinforcement is used to control lateral bursting strains, special attention needs to be paid to potentially high transverse strains in thin web members. Peak lateral bursting strains do not occur at the same location as peak lateral bursting stresses.

2.2.6.2 Local Zone. A major concern in American anchorage zone specifications has been the limitation of anchorage bearing stresses. Much of the research regarding bearing stresses has been originated by concern over bearing capacity.

Hawkins [73,74,75] has done extensive research into the bearing capacity of concrete under both rigid and flexible loading plates as well as with strip loadings. One series [73] addressed loading through rigid plates. The test program consisted of 230 tests in which the loading geometry (R), the size of the specimen, and the type and strength of the concrete were varied. R is a confinement factor equal to the effective unloaded area divided by the loaded area (for an unconfined plate of the same dimension as the concrete, $R = 0$). The

effective unloaded area takes into account the edge distance around the loaded surface and is geometrically similar to the loaded surface. From the tests with R less than 40, the following conservative estimate of the ultimate bearing strength was developed.

$$q = f'_c + K(Rf'_c - f'_c)^{0.5}$$

K is equal to a function of the angle of internal friction that can be conservatively taken to be 50. Hawkins also concluded that any increase in bearing capacity above the compressive strength of the concrete is directly dependent upon the angle of internal friction and that it is essential for the concrete to be densely compacted and for the air voids and shrinkage cracks to be kept to a minimum.

In another research program [74], Hawkins investigated the relationship between flexible, semi-flexible, and rigid plates with 33 tests. From the tests, it was determined that the load capacity versus the thickness of the plate is linear when the plate is flexible. In the semi-flexible range, the capacity rises exponentially until a maximum value is reached, corresponding to the capacity for a rigid plate. In a flexible plate, increasing the bearing area does little to increase the ultimate bearing load. However, increasing the area is very effective in increasing bearing capacity for rigid plates.

Hawkins [75] also reports the results of 39 tests on rigid plates extending across the full width of the block. From the tests, two modes of failure were observed: the corners of the block including the strip plate can shear off, or the crack which develops on the axis of the load can propagate spontaneously and cause the bearing plate to punch down into it. The bearing capacity for design purposes can be predicted by the following equation developed by Kriz and Rath: $q = 5.91f'_c{}^{0.5}(D/W)^{1/3}$ where D is the distance from the edge of the block to the centerline of the bearing plate, W is the width of the bearing plate, f'_c is the compressive strength of the concrete in psi.

Middendorf [113,114] conducted 48 tests with f'_c between 4000 and 6000 psi to investigate the validity of the then current code of

practice, "Criteria for Prestressed Concrete Bridges" by the Bureau of Public Roads. The code of practice used the following equation:

$$q = 0.6f'_{c1}(A/A_b)^{1/3} \leq f'_{c1}$$

A is the effective concrete area and A_b is the bearing area. Middendorf concluded that the cube root formula for design should be replaced with a square root formula, and that the maximum bearing stress should be limited to three times the compressive strength. He also determined that the relationship between effective concrete area and bearing area is valid except in the case of grouped plates where the overall plate area should be used, and that tilting the plate up to five degrees does not affect its bearing ability. Middendorf limited his theories to applications after the concrete is three days old.

Niyogi [120,121] tested 154 reinforced concrete blocks to investigate the problem of bearing stress capacity. He developed three equations to determine the ultimate concentric bearing capacity, ultimate eccentric bearing capacity, and the effect of adding a spiral. He determined that the eccentricity of the load tended to decrease the ultimate bearing strength and that spiral reinforcement increased the bearing strength by increasing the lateral confinement. He also determined that large diameter spirals appeared to be the most effective against cracking, and that large bearing plate performance was enhanced less by additional reinforcement than by smaller plates. In his tests, visible cracking loads were increased by the addition of reinforcement and grid steel increased bearing strength but not as effectively as spiral reinforcement.

Most of the current standards include anchorage bearing stress criteria. A majority of the codes and guidelines, as shown in Section 2.5, utilize a bearing capacity based on the equation $f'_c\sqrt{A/A_b}$.

Roberts [143] examined a wide range of variables that affect the performance of the local zone including concrete strength, plate size, confinement and edge distance. Roberts made the following observations:

- 1) The first cracking load is primarily affected by the ratio a/h and the tensile strength of the concrete. It is not affected by the presence of reinforcement.
- 2) Auxiliary reinforcement can be used to reduce crack size.
- 3) The ultimate load can be raised by increasing the diameter or increasing the pitch of the spiral reinforcement. By increasing the edge distance or including auxiliary reinforcement, the ultimate load is increased.
- 4) An equation was determined for the design of the local zone confinement.

The equation which best fit the data for the bearing capacity was Equation (1). Equation (2) was the recommended design equation.

$$P_b = 0.8f'_c\sqrt{A/A_b}A_b + k \cdot f_{lat} \cdot (1-s/d_c)^2 \cdot A_{core} \leq 3f'_c \cdot A_b \quad (1)$$

$$P_b = 0.7f'_c\sqrt{A/A_b}A_b + k \cdot f_{lat} \cdot (1-s/d_c)^2 \cdot A_{core} \leq 3f'_c \cdot A_b \quad (2)$$

Where $f_{lat} = k \cdot A_s \cdot f_y / (d_c \cdot s)$

And

- A is the supporting area defined as the maximum area geometrically similar to the loaded area and concentric with it;
- A_b is the full net area of the bearing plate;
- A_{core} is the area of the confined portion of concrete;
- A_s is the cross sectional area of the confining reinforcement;
- d_c is the outside dimension of the confining reinforcement;
- f'_c is the compressive strength of concrete;
- f_y is the yield stress of the confining reinforcement;
- k is 2 for spiral reinforcement and 1 for tie reinforcement; and
- s is the center to center spacing of the confining reinforcement.

For f'_c above 8000 psi, the 0.8 in Equation (1) and the 0.7 in Equation (2) should be reduced 0.05 for every 2000 psi increase in f'_c above 8000 psi but should not be taken as less than 0.65. Equation (1) which best fit the data has a standard deviation of 20 percent.

- 5) To fully use the net bearing area of an anchor, the anchor must meet the slenderness requirement of Equations (3) and

(4).

and
$$n/t \leq 0.07 \sqrt[3]{E_b/f_b} \quad (3)$$

$$f_s \leq 3 f_b n^2/t^2 \quad (4)$$

where t is the thickness of the bearing plate;
 n is the distance from the edge of the stiff wedge plate or outer perimeter of wedge holes for plate with integral wedge plates;
 E_b is the Modulus of Elasticity for the bearing plate material; and
 f_b is F_{pu}/A_b , F_{pu} is the guaranteed ultimate load of the tendon.

- 6) When local zone details were tested in the small prism and then tested in a large specimen, the details were always found to be conservative.
- 7) The study recommends test data be furnished by manufacturers on standardized specimens in order to verify reinforcing details and edge distances.

Wurm and Daschner [186,187] conducted an extensive study with 130 specimens. Their study investigated 1) the effects of the A/A_b ratio, 2) the type of confining reinforcement, 3) the amount of reinforcement, 4) sustained loading, 5) post-tensioning duct effects, 6) placing the anchorage at an eccentricity and 7) concrete age. Their major conclusions were that:

- 1) Spiral is the most efficient form of reinforcement;
- 2) If confining reinforcement is too short, a crushing of the concrete will occur at the base of the confinement;
- 3) The post-tensioning duct reduces the ultimate load; and
- 4) Ultimate loads for specimens with sustained loading were 20 percent lower than those loaded short term.

2.3 Product Literature

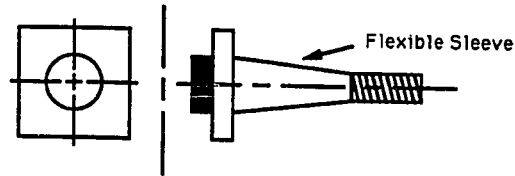
An additional source of information about anchorage zone and anchorage devices is from the product literature of anchorage device

suppliers. For the scope of this study, the type of anchorage that is the focus is multiple strand anchorages. There are many post-tensioning anchorage suppliers in the United States that furnish the multistrand type of anchors predominant in bridge girder construction. Few applications are envisioned in bridge girder construction for the monostrand type of anchors; while they could be used in transverse deck post-tensioning, the difficulty in developing adequate long term corrosion protection and the large number of closely spaced strands required makes the use of monostrands less desirable. Currently, there is a study being conducted at the University of Texas at Austin that is investigating closely spaced anchors in slab applications. Information on monostrand anchorages will be available upon the completion of this study.

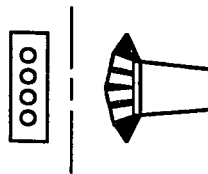
In the initial stages of this program, information was solicited on bridge anchorages from the producer membership of the Post-Tensioning Institute, which represents the majority of suppliers in the United States. Product information was obtained from:

- 1) CCL Division of Nicholson Construction Company,
- 2) CEC Systems, Inc.,
- 3) Continental Concrete Structures,
- 4) Dywidag Systems International,
- 5) Genstar Structures Limited,
- 6) Linden Post-Tensioning Corporation,
- 7) Prescon Corporation,
- 8) Stresstek Division of Conner Corporation, and
- 9) VSL Corporation.

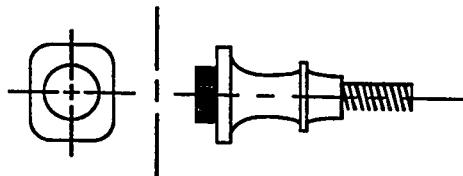
In spite of the large number of hardware suppliers, an examination of their catalog and typical application examples indicated that most of the manufacturers had three basic multistrand anchors: 1) a square flat bearing anchor, 2) a rectangular flat bearing anchor, and 3) a multiple plane anchor (see Fig. 2.12). The square flat bearing anchor comes in various sizes with capacities from three to 55 strands, while the multiple plane anchor is produced in sizes and capacities ranging from three to 61 strands. The rectangular flat bearing anchor is only



a) Square Flat Bearing Anchor



b) Rectangular Flat Bearing Anchor



c) Multiple Plane Anchor

Figure 2.12 Anchor Types

available with a four strand capacity and is widely used for deck slab stressing. Most anchors were available for use with either 0.5 inch strand or 0.6 inch strand.

Some of the anchor devices are equipped with confining spirals. In the copious product data received, only three companies gave information on the local zone confinement reinforcement size or spacing required to ensure satisfactory anchor performance up to the design load. There is a major discrepancy between the local zone information supplied to the engineer in Europe versus that supplied in the United States. Figure 2.13 shows the information provided for one anchor. Figure 2.13a is from a supplier here in the United States while Fig. 2.13b is from the same supplier in West Germany. Figure 2.13a has only

| Anchor Type | | 6812 | 6815 | 6819 |
|--------------------------------|-----------------|---------------------------|------|------|
| Ultimate Load | (kN) | 3180 | 3975 | 5035 |
| Recess Form | Øa(mm) | 300 | 300 | 360 |
| Multi-Surface Anchor | Øb | 220 | 250 | 280 |
| | c | 190 | 200 | 220 |
| | Ød | 160 | 180 | 200 |
| | e | 43 | 50 | 55 |
| Transition Tube | Øg | 120 | 130 | 145 |
| | L | 350 | 400 | 450 |
| Min. Concrete Strength | | B45 (5000 psi) | | |
| Anchorage Spacing | | | | |
| Center Distance | | 300 | 340 | 400 |
| Edge Distance | | 170 | 190 | 220 |
| Cracking Tensile Reinforcement | | Depends on National Spec. | | |

Figure 2.13a Product Information, United States

Anchorage Type 6812

| Concrete Strength | B25 (psi)(3600) | B35 (5000) | B45 (6500) | B45 (6500) | B45 (6500) | B45 (6500) |
|--|--------------------|---------------|---------------|---------------|---------------|---------------|
| Anchor Distances (mm) | | | | | | |
| Center Distance | 380 | 350 | 320 | 370 | 430 | 480 |
| If reduced center distance is then opposite direction must be | 350 | 320 | 290 | 340 | 400 | 450 |
| Edge Distance | 410 | 380 | 350 | 400 | 460 | 510 |
| | 210 | 195 | 180 | 205 | 235 | 260 |
| Stirrups | | | | | | |
| Number | 5 | 5 | 5 | 4 | 5 | 4 |
| Bar Diameter | 10 | 10 | 10 | 10 | 8 | 8 |
| Stirrup Width | 350 | 320 | 290 | 340 | 400 | 450 |
| Initial Distance from Anchor | 70 | 65 | 60 | 75 | 75 | 110 |
| Spacing | 35 | 35 | 35 | 50 | 50 | 50 |
| Spiral | | | | | | |
| Number of Turns | 5 | 5 | 5 | 4 | 4 | 4 |
| Bar Diameter | 14 | 14 | 12 | 12 | 8 | 8 |
| Spiral Diameter | 340 | 310 | 280 | 275 | 400 | 400 |
| Initial Distance from Anchor | 40 | 40 | 40 | 75 | 100 | 100 |
| Spacing | 55 | 50 | 50 | 70 | 70 | 70 |

Figure 2.13b Product Information, West Germany

the basic anchorage geometry and some minimum guidance. Figure 2.13b has extensive information on the reinforcing details to be used to confine the local zone. This is not completely the fault of the supplier because the governing codes in the United States have no requirements that such guidance be provided while it is mandatory under the West German system. In the survey of practitioners discussed in detail in the next section, it was frequently reported that the local zone reinforcement immediately around the anchorage device is designed by the post-tensioning supplier and not by the engineer of record. When the division of responsibility described in Chapter 1 was described to suppliers, all said they were in favor of the design engineer of record taking control of the general zone which would allow the suppliers to concentrate on specifying the required confining reinforcement and concrete cover of the local zone. For anchorage device applications where high stresses are expected or where auxiliary local zone confinement is necessary, a standard test method should be developed so that third party test agencies could certify special anchorage assemblies as acceptable in specified concretes and with specified minimum edge covers, minimum center-to-center spacings, and minimum auxiliary reinforcement. This acceptance procedure is currently used in Europe and would provide the engineer with much needed information.

2.4 User Survey and Assessment

Design techniques, application details, and problems encountered with anchorage zones vary widely throughout the United States and worldwide. To help in formulating the research program, a survey concerning current practices and problems was developed and sent in 1987 to all the bridge division members of AASHTO (state highway departments and province highway departments), a number of firms that design post-tensioned structures, and to active research contributors in the area of anchorage zones. One-hundred forty four surveys were sent out and 66 responses were received.

2.4.1 Survey Description. The amount of knowledge and experience regarding post-tensioning varies greatly from agency to agency. Therefore, the survey had to be flexible enough so that information could be obtained from different levels of experience. The survey document had the following objectives:

- 1) To determine what procedures and criteria are currently being used to analyze, design, and evaluate anchorage zones,
- 2) To determine incidents of failure or severe distress which have occurred in anchorage zones,
- 3) To determine the most commonly used anchorage zone configurations, and
- 4) To determine typical reinforcing patterns.

It was decided that, instead of developing a very detailed series of questions, the format would consist of a set of general requests and a classification system for anchorage zones to help direct the answers to areas of interest. The following information was requested.

- 1) Problems encountered in design, checking or inspection of post-tensioned anchorage zones;
- 2) Analysis procedures, evaluation criteria, or references used in the design or checking anchorage zones;
- 3) Criteria used to judge when special attention had to be paid to the post-tensioning system;
- 4) Knowledge of specific failures or severe distress in post-tensioned anchorage zones including photos or crack pattern sketches; and
- 5) Sample plans or details of typical and special anchorage applications.

The classification system was divided into eight major areas: anchorage zone, location, geometry, loads, concrete, reinforcement, hardware, and design criteria. A copy of the survey document is included in Appendix A.

2.4.2 Survey Results. The response to the survey was very good.

Surveys were sent to 64 bridge engineer members of AASHTO, and 38 responded. Of the 38 responses, 23 (60 percent) use post-tensioning. Eighteen of the responses (80 percent of those who use post-tensioning) were highly informative and included either example plans, design guidelines, or written answers to the questions. Eighty surveys were sent to consulting engineers or researchers. The response was not as good as from the AASHTO members. Only 28 responses were received from consultants or researchers; but, as with AASHTO members, 17 (60 percent) used post-tensioning in design or had research experience with it. Sixteen (95 percent of those who use post-tensioning) gave informative responses.

The most common information included in responses was anchorage zone plans. The responses received included hundreds of pages of plans with reinforcement details. A sampling of various details is included in Figs. 2.14 to 2.24 and is subsequently referred to in order to illustrate terminology. The plans were examined, and it was apparent that there is a broad variety of applications and details being used. However, after further study, it became obvious that there seemed to be some general overall patterns that predominated. While of no statistical significance in strict mathematical terms, the incidence of type of anchorage application furnished by respondents was felt to be a good indication of the diversity of the problem and the general nature of the interests and concerns of the respondents. An examination of the plans and details submitted indicated that the anchorage applications could be classified by:

a) Location,

1. Beam or Slab - End surface (Figs. 2.14, 2.15), transverse tendon (Figs. 2.16, 2.17a) or interior anchors
2. Blister - End surface or interior anchors (Figs. 2.18, 2.19, 2.23)
3. Recess Pocket (Fig. 2.20)
4. Diaphragm - End or transverse anchors (Figs. 2.21 and 2.23)
5. Rib - End or interior anchors (Fig. 2.24)

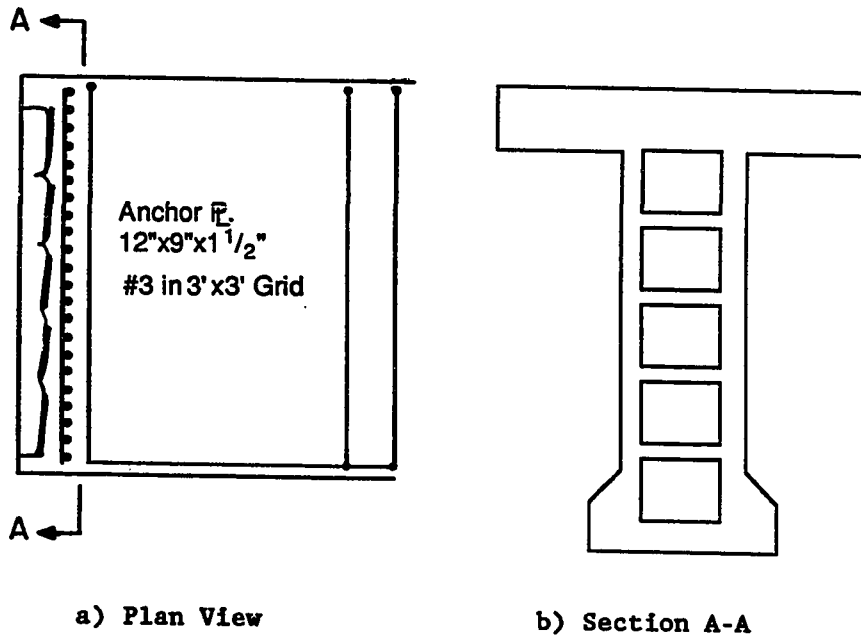


Figure 2.14 Concentric End Anchorage

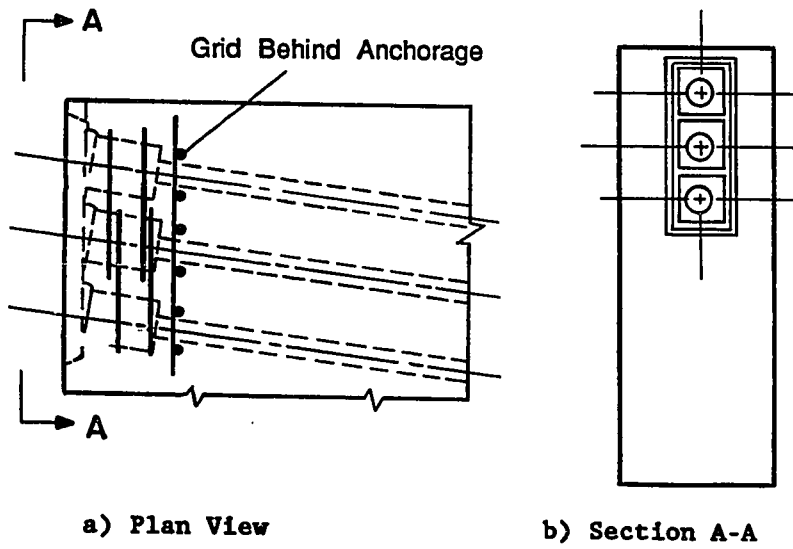


Figure 2.15 Eccentric End Anchorage

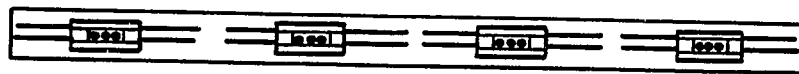


Figure 2.16 Transverse Slab Anchorage

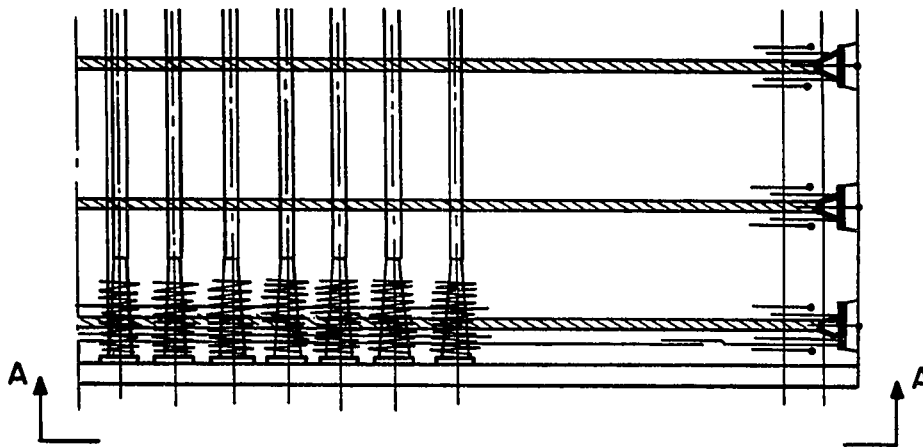


Figure 2.17a Longitudinal and Transverse Deck Tendons

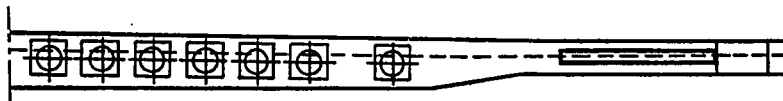


Figure 2.17b Section A-A Longitudinal Deck Tendons

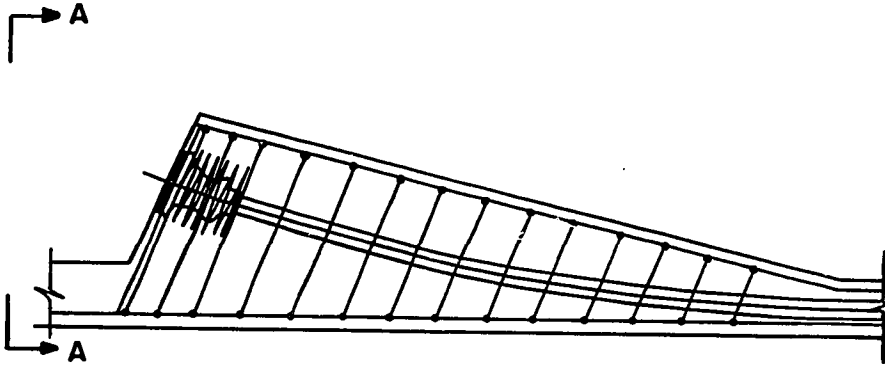


Figure 2.18a Corner Blister

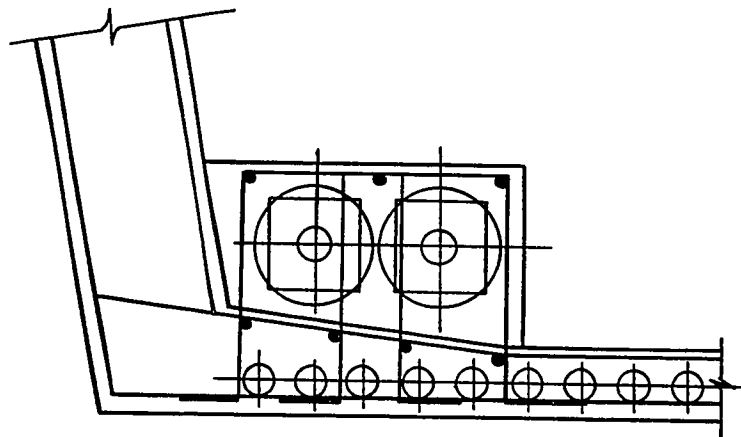
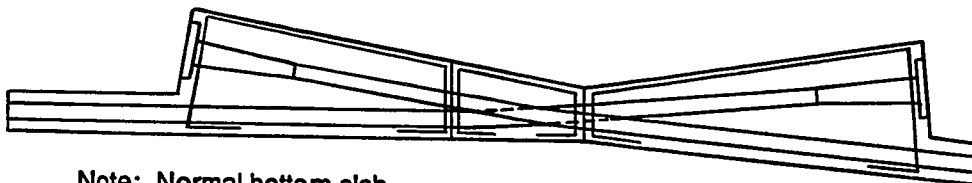


Figure 2.18b Section A-A Corner Blister



Note: Normal bottom slab
reinforcing not shown

Figure 2.19 Double Direction Blister

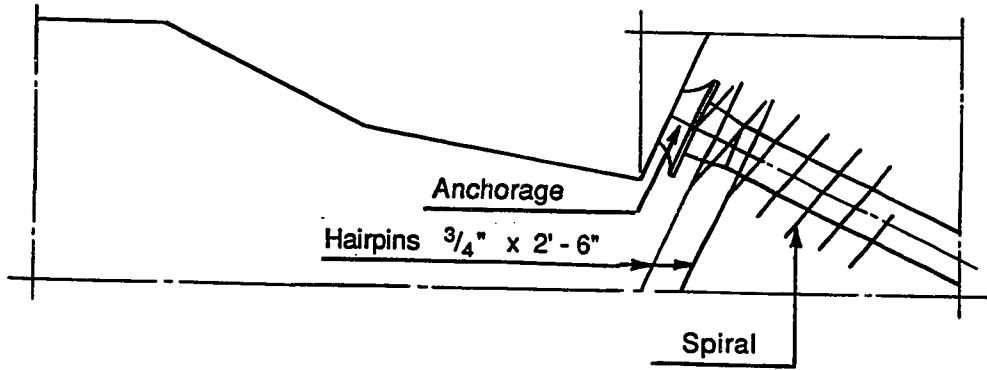


Figure 2.20 Recessed Deck Pocket

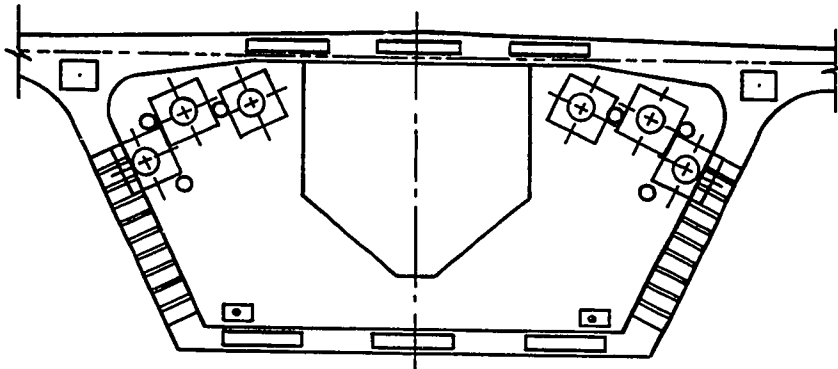


Figure 2.21 Longitudinal Anchorages in Diaphragm

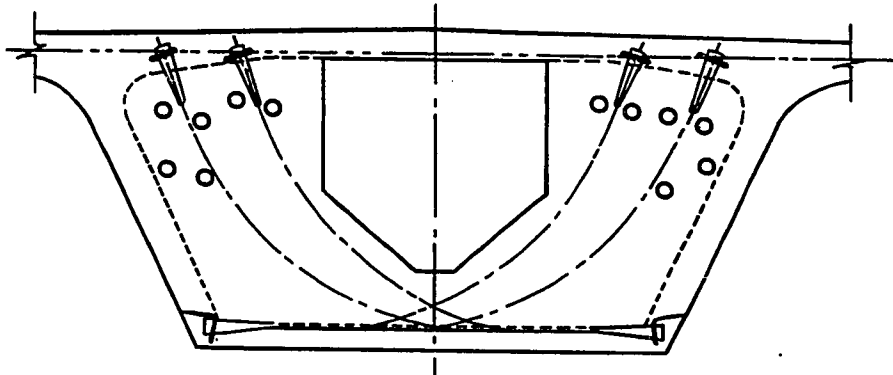


Figure 2.22 Transverse Post-Tensioned Diaphragm

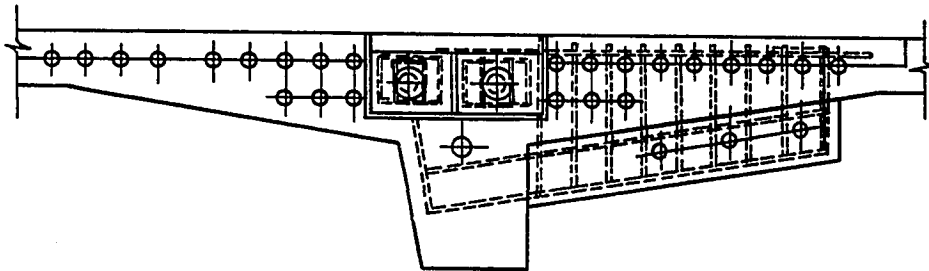


Figure 2.23 End Blister and Deck Anchorages

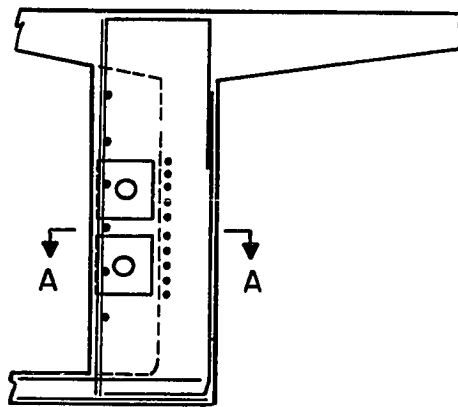


Figure 2.24a Multiple Rib Anchorage

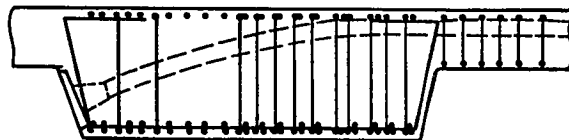


Figure 2.24b Section A-A Multiple Rib Anchorage

- b) Number,
 - 1. Single anchor
 - 2. Multiple anchors
- c) Supplemental Reinforcement, or
 - 1. Orthogonal (Figs. 2.14, 2.15)
 - 2. Spiral (Fig. 2.17a)
 - 3. Mixture of orthogonal and spiral (Fig. 2.18a)
 - 4. No reinforcement specified
- d) Type of Tendon Layout.
 - 1. Concentric (Fig. 2.14)
 - 2. Eccentric (Fig. 2.15)
 - 3. Straight (Fig. 2.17)
 - 4. Curved (Fig. 2.18)
 - 5. Deviation: Horizontal (Fig. 2.24) and Vertical (Fig. 2.14)

Each response was critically examined and the general applications classified using this system. Since respondents had submitted only sample details, the occurrence in a project was counted as a single unit whether the project used that anchorage application once or one hundred times in multiple girders and spans. The detailed tabulations according to these categories are given in Tables 2.1 and 2.2

The plans that were sent were dominated by multiple end anchors (Figs. 2.14 and 2.15) and multiple anchor blisters (Fig. 2.18), with very few anchorage zones having just single anchors. Since the plans that were sent were only small portions of all the plans of a bridge, single anchorages could still be in extensive use. However, the respondents' concern was clearly with multiple anchorages. Besides the different applications, locations, and number of anchorages, there were many other variables. Table 2.1 also shows the number of anchors that utilize either orthogonal, spiral, or mixed supplemental reinforcement. The number of plans showing mixed supplemental reinforcement was very small, and the rest of the plans were divided evenly between orthogonal and spiral reinforcement. Another major

Table 2.1 Frequency of Anchorage Applications Submitted by Respondents

| Application Type | Number of Terminating Tendons in Anchorage Zone | | Supplemental Reinforcement | | | |
|------------------|---|----------|----------------------------|--------|-------|----------------|
| | Single | Multiple | Orthogonal | Spiral | Mixed | None Specified |
| Beam or Slab | | | | | | |
| End | 0 | 19 | 6 | 6 | 4 | 3 |
| Transverse | 0 | 8 | 3 | 3 | 0 | 2 |
| Interior | 0 | 0 | 0 | 0 | 0 | 0 |
| Blister | | | | | | |
| End | 1 | 3 | 2 | 2 | 0 | 0 |
| Interior | 4 | 15* | 7 | 10 | 0 | 2 |
| Recess Pocket | 2 | 0 | 0 | 2 | 0 | 0 |
| Diaphragm | | | | | | |
| End | 0 | 17 | 9 | 8 | 0 | 0 |
| Transverse | 0 | 5 | 0 | 2 | 1 | 2 |
| Rib | | | | | | |
| End | 0 | 1 | 1 | 0 | 0 | 0 |
| Interior | 0 | 2 | 2 | 0 | 0 | 0 |

* Two of these applications were double direction blisters.

Table 2.2 Frequency of Tendon Characteristic Submitted by Respondents

| Application Type | Anchorage Zone Location | | Anchorage Zone Profile | | Initial Deviation | | |
|------------------|-------------------------|-----------|------------------------|--------|-------------------|-------|------|
| | Concentric | Eccentric | Straight | Curved | Horiz. | Vert. | None |
| Beam or Slab | | | | | | | |
| End | 6 | 13 | 12 | 7 | 0 | 14 | 5 |
| Transverse | 8 | 0 | 8 | 0 | 1 | 0 | 7 |
| Blisters | | | | | | | |
| End | — | — | 2 | 2 | 1 | 2 | 1 |
| Interior | — | — | 7 | 12 | 4 | 13 | 2 |
| Recess Pocket | — | — | 2 | 0 | 0 | 2 | 0 |
| Diaphragm | | | | | | | |
| End | 6 | 11 | 8 | 3* | 3 | 7 | 7 |
| Transverse | 1 | 4 | 2 | 3 | 1 | 4 | 0 |
| Rib | | | | | | | |
| End | 0 | 1 | 0 | 1 | 1 | 0 | 0 |
| Interior | 1 | 1 | 1 | 1 | 1 | 1 | 0 |

* Some drawings did not give enough detail to determine.

variable was the angle of inclination of the anchor. For end anchors, the range in deviation from the vertical was 6 to 25 degrees; while the angular deviation of the blisters ranged from 3 to 22 degrees. Table 2.2 shows that, in most cases, the anchor has an initial inclination and that, in many cases, the tendon is not curved in the anchorage zone.

In addition to the geometry of the anchor and the reinforcement, most plans also include stressing instructions. The majority of the stressing instructions came in the form of a minimum concrete strength at the time of stressing, maximum tendon stress levels, and a minimum age of concrete at the time of stressing. Also, instructions were often given to indicate if a specific stressing sequence was assumed in the design and was to be followed in construction. Instructions were frequently given regarding the maximum eccentricity of prestress forces during the various stages of intermediate stressing of multiple tendons, the relation between stressing sequences on adjacent girders, and the necessity of jacking from both ends to minimize friction losses and equalize stress levels.

Besides submitting example plans, many respondents provided thoughtful and informative answers to the questions. Many respondents stated that they had no problems designing anchorage zones but added that, in most cases, they used guidelines in addition to AASHTO. In the case of foreign respondents, they used their more effective national codes. One response said, "The AASHTO post-tensioning anchorage specifications are completely out of date. We design based on CEB/FIP and/or PTI published recommendations and anchorage stresses based on Guyon's theories." Many utilize the classical theories developed by Guyon and Leonhardt. Several did not feel that the use of only orthogonal reinforcement was adequate and regularly require the use of spirals. One response stated that they used spiral confining reinforcement unless there was insufficient room, then they used layers of mat reinforcement. Several respondents said that they order full-

scale tests of the anchorage zone if there was any question in the design of the reinforcement.

One question asked whether there is any situation where no special consideration had to be given to the post-tensioning design. One respondent said that the only anchorage not requiring special consideration are anchors in large diaphragms. Another said, "Post-tensioning details are given the utmost care and attention, perhaps more than any other portion of the structure." A quote that may represent the thoughts of many respondents is that, "Previous experience from jobs that worked well is certainly the best but is not worth a damn in court..."

Several responses mentioned failures but most were attributed to poor concrete or misplaced reinforcement. One response attributed excessive cracking to an incorrect stressing sequence in which large moments were developed. A few failures were caused by the lack of proper containment reinforcement around the anchorage zone.

Some additional comments concerned the limit state guidelines. A question that is very important is what type of safety factor should be used in design. One response said that a safety factor of at least three should be used against crushing and at least 2 1/2 for all other anchorage zone design procedures. Most responses indicated relatively little thought as to the proper safety level regarding strength or cracking. Another major limit state concern is the question of what amount of cracking should be allowed at service loads, if any. The range for allowable crack widths given in the responses was 0.004 inches to 0.01 inches.

Besides providing information on typical details being used in post-tensioned bridge anchorage zones, the survey clarified and dramatized the types of application problems that designers are encountering. It was apparent that American design criteria are fragmented, limited, and not well understood. Studies in the technical literature are primarily directed towards single anchorages, whereas

applications are almost always of multiple anchorages. Actual tendons are frequently eccentric and inclined, although neither application is treated explicitly in present criteria.

2.5 Current Codes and Commentaries

In a post-tensioned anchorage system, very large highly concentrated forces must be transferred to a continuous distribution of stresses at a distance approximately equal to the depth of the member. The anchorage zone consists of two distinct parts: 1) the region immediately surrounding the anchorage device [*the local zone*] and 2) a second region [*the general zone*] where the major transition from highly localized to distributed stresses occurs. The state-of-the-art for design of these zones will be detailed in this section. There are a number of current codes and published guidelines used to design post-tensioned anchorages. Generally, current design techniques do not specifically distinguish between the local and general zones. Therefore, most of the discussion of current design techniques deals with general zone design. The following major codes and guides are reviewed in this study.

- AASHTO Bridge Code '89 [5]
- ACI 318-89 [6]
- Austrian Code '79 [13]
- CEB-FIP Model Code '78 [36]
- CIRIA Anchorage Design '76 [38]
- FIP Recommendations '81 [57]
- Florida DOT Design Criteria [60]
- German Code, DIN 1045 [68]
- North Carolina DOT Design Criteria [122]
- Ontario Bridge Code '83 [123]
- PTI Design and Construction Specification for Segmental Bridges [135]
- Switzerland Code, SIA 162 [171]
- VSL End Block Design '75 [105]

Most of the standards use different notation. In order to permit comparison, this report uses the notation shown in Table 2.3 and Fig. 2.25.

Table 2.3 Notation for Specification Comparison

| | |
|-----------------------|---|
| a | = lateral width of anchor bearing surface (see Fig. 2.25) |
| A | = effective bearing area ($h' \times t'$) |
| A₁ | = anchor bearing area ($a \times b$) |
| A_r | = reinforcement area |
| A_s | = area of hoop reinforcement |
| A₂ | = area of concrete within hoop |
| b | = transverse width of anchor bearing surface (see Fig. 2.25) |
| d | = effective depth of anchorage zone, determined as depth from anchor where stresses become linear, assumed usually to be equal to height of section |
| d₁ | = distance from centerline of tendon to edge of concentric symmetrical prism used for calculation of spalling stresses in CIRIA guide (see Fig. 2.25), where $d_1 > h'$ |
| f_b | = bursting stress |
| f_c | = stress in concrete |
| f'_c | = concrete strength at 28 days |
| f_{ci} | = concrete strength at stressing |
| f_{ck} | = characteristic concrete cube strength at stressing |
| f_{cu} | = concrete cube strength at stressing |
| f_{pu} | = specified tensile strength of prestressing tendons |
| f_{py} | = specified yield strength of prestressing tendons |
| f_t | = tensile strength |
| f_y | = steel yield strength |
| F_b | = bursting force |
| h | = height of section |
| h' | = effective lateral width of bearing surface determined by boundaries of area which is geometrically similar to the anchor bearing area |
| M_H | = maximum moment in hoop reinforcement zone |
| M_{sp} | = maximum difference between the moment caused by the linear stress distribution at $h/2$ from the anchor and the distribution at the anchor |
| N_H | = maximum axial force in hoop reinforcement zone |
| P | = jacking force |
| s | = hoop spacing |
| t | = thickness of the section |
| t' | = effective transverse width of bearing surface determined by boundaries of area which is geometrically similar to the anchor bearing area |
| u | = perimeter of a hoop |

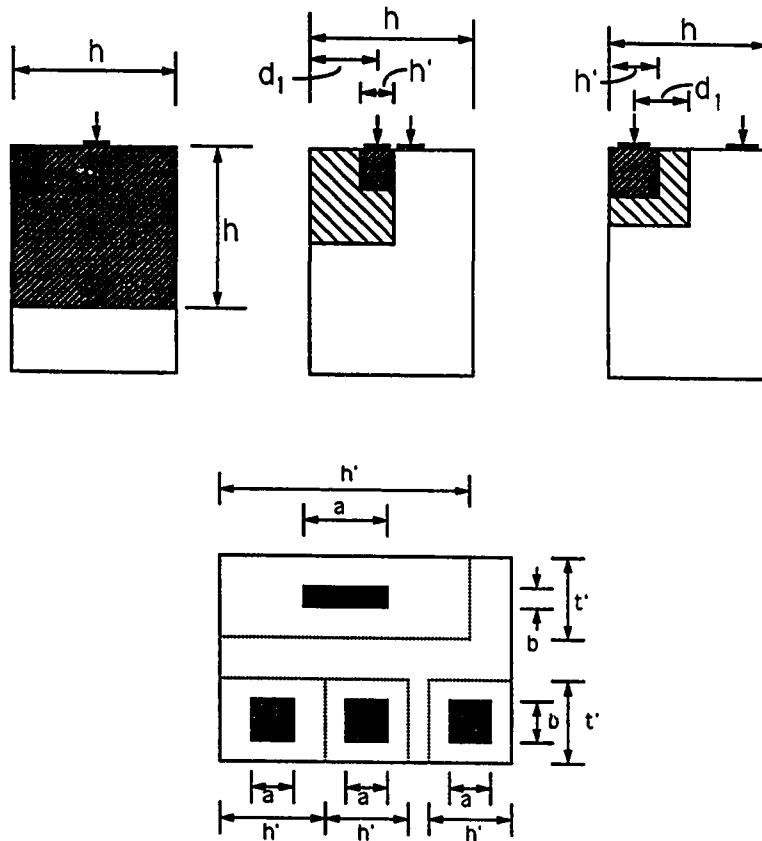


Figure 2.25 Parameter Description for Specification Comparison

2.5.1 Local Zone Criteria. The local zone of a particular anchorage is greatly influenced by the anchor force and is relatively insensitive to surrounding anchors, section geometry, or other applied forces. Tests have shown [168] that this zone is very critical to the behavior of the anchorage zone. In order to properly distribute the forces in the general zone, most anchor devices require local zone confinement. Several of the codes and standards do require tests to determine if the anchor is properly reinforced. This would be classified as a local zone test. Such tests are normally sponsored by the device manufacturers and do not usually need to be conducted for each individual application. Four publications that give guidelines

for tests on the local zone are the PTI Design and Construction Specification [135]*, the Austrian Code [13], the FIP Recommendations [57] and the German Code [68]. A typical local zone test specimen is shown in Fig. 2.26. In the PTI Segmental Bridge Specification [135], the test block has a width that is twice the minimum edge distance from the centerline of the anchor to the face of the concrete or the minimum spacing between anchors plus 3 inches. The length should be three times the largest cross section dimension. The concrete strength at testing shall not exceed 85 percent of concrete strength at the time of the post-tensioning in the actual structure. Three tests should be conducted. The anchorage should not have more than 0.01 inches of permanent distortion after being loaded to 95 percent of the ultimate tendon strength. At a load of 40 percent of the ultimate tendon strength, there should be no concrete cracks. At 70 percent, the width

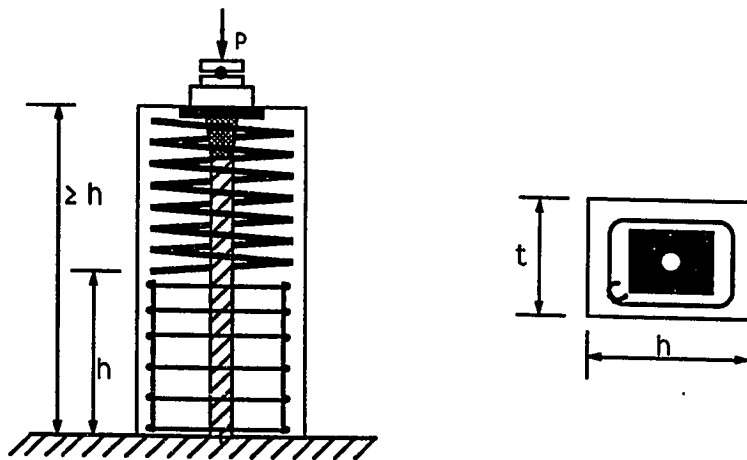


Figure 2.26 Local Zone Test Specimen

* The PTI Design and Construction Specification was developed on a concurrent NCHRP project and had extensive input concerning anchorage zones from personnel of the University of Texas NCHRP project of which this dissertation is a part.

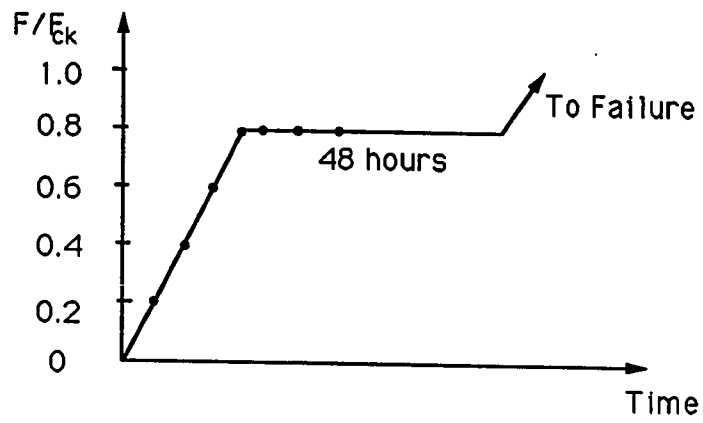
of concrete cracks should not exceed 0.005 inches. After loading to 95 percent, the width of concrete cracks should not exceed 0.015 inches.

In the Austrian Code [13], the test specimen is a rectangular section with a height at least two times the width. The width is twice the shortest distance to the concrete face or is the distance between anchors. All anchors are tested with a spiral and confining reinforcement around the edge of the specimen. Four specimens should be tested with three loaded cyclically and then loaded to failure. The fourth specimen is loaded monotonically until failure. For the cyclic tests, the concrete strength should be 80 percent of the field strength; while, for the static test, the strength should be equal to the field strength. The cyclic test consists of ten cycles between six percent and 60 percent of the guaranteed minimum strand strength (F_n), ten cycles between six percent and 72 percent of F_n , and then increasing of the load until failure of the specimen at 0.2 to 0.3 N/mm²/sec (29 to 44 psi/sec). For the static test, the specimen is loaded at the same rate as the cyclic test (0.2 to 0.3 N/mm²/sec) until failure. At $0.06F_n$, cracks are limited to 0.05 mm (0.002 inches); and, at $0.72F_n$, cracks are limited to 0.12 mm (0.005 inches). Crack limits apply only to cracks that start in the upper or anchor portion of the specimen. The maximum required load is $0.90F_n$ for cyclic loading, F_n for static tests, and $1.2F_n$ if no spiral is ordinarily included with the anchorage device.

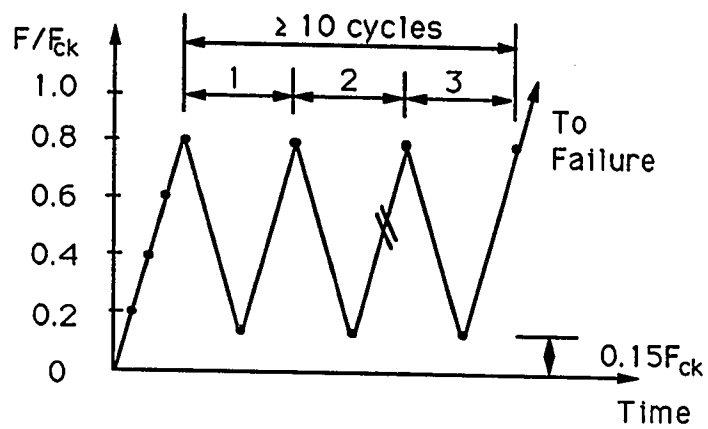
In the FIP Recommendation [57], the specimen is a rectangular section in which the dimensions are taken to be twice the permissible minimum distance of the anchorage to the concrete edges of the structure in the corresponding directions. The height is taken to be two times the maximum section width (see Fig. 2.26). In the upper part of the specimen, bursting reinforcement shall be provided as specified by the manufacturer for the proper use of the particular system. The remaining lower portion of the specimen should be reinforced to prevent premature failure; this portion should have at least a height equal to

the maximum section width. The concrete strength at the start of testing shall not be greater than 85 percent of the specified application concrete characteristic value, which is defined as a statistical value that 95 percent of the concrete test specimens will exceed. During testing, the concrete strength shall not exceed the characteristic strength. Two testing procedures may be used: the static load transfer test and the slow cycle load transfer test. The static load transfer test is illustrated in Fig. 2.27a. The load is applied in steps of 0.20 of the maximum load until a load of 80 percent of the tendon characteristic tensile strength is achieved. Crack measurements and deflections are taken at 20 percent, 40 percent, 60 percent, and 80 percent of the characteristic value of the tendon. The load is maintained at 80 percent of the characteristic value for 48 hours and then increased to failure. The slow cycle load transfer test is shown in Fig. 2.27b. The test starts the same way as the static test; but, once the load of 80 percent is reached, the specimen is cycled between 80 percent and 15 percent for at least ten cycles or until the crack widths have stabilized. Once the crack widths are stable, the specimen is loaded to failure.

The German Code [68] and the FIP Recommendations have the same specimen guidelines but slightly different loading patterns. As with the FIP, the German Code specifies two different loading tests: static load transfer test and slow cycle load transfer test. The only difference in the slow cycle test is the maximum and minimum load level during cycling. The maximum German value is 70 percent of the nominal tendon strength, and the minimum is 10 percent. For the static load transfer test, two sustained load periods are specified. The specimen is first loaded to 55 percent of the nominal tendon strength and held there for 48 hours. It is then loaded to 70 percent and held for another 48 hours. At the conclusion of the time, the specimen is then loaded to failure.



a) Static Load Test



b) Cyclic Load Test

Figure 2.27 Loading Patterns for Local Zone Test

Specific criteria for the testing of anchorages for unsatisfactory performance in the local zone have generally not been used in the United States. The widely utilized bearing stress limitations (the compression stress exerted by the anchor on the concrete) on anchorage devices contained in AASHTO [5] Section 9.15.2.4, ACI Code and Commentary [6] Section 10.15, and Section 4.2 of the PTI Segmental Bridge Construction Specification [135] are indirect local zone criteria. The most widely reported bearing stress formulas are listed in Table 2.4. Most are related to the effective bearing area divided by the anchor force bearing area. The maximum bearing stress allowed is $2.2f_c$ in the CEB-FIP Code. In the United States, AASHTO limits the design to $0.9f'_c$ but not more than 3000 psi, while the criteria of Florida and North Carolina [60,122] and the PTI Specification limit it to $1.25f'_c$, but not more than 6875 psi. The arbitrary maximum upper limits penalize high strength concrete.

2.5.2 General Zone Criteria. The resistance to tensile forces becomes a major concern in the general zone. Tensile forces are induced by the lateral diffusion of forces in the member (bursting stresses) or by moments due to the eccentricity of the anchor force and/or multiple anchors (spalling stresses). The codes and guidelines listed previously address the problems in the general zone in a variety of ways. The methods have been grouped into the following: bursting force estimates, spalling force estimates, and restrictions on concrete stresses, reinforcement stresses, anchorage stresses, and prestress steel stresses.

Most guidelines check the bursting force (see Table 2.5). The bursting force is the tensile force perpendicular to the axis of the tendon. Most use a formula of the form $kP(1 - a/h')$. The German code utilizes two bursting zones when the eccentricity of the anchor is outside the kern ($e/h > 1/6$). Zone 1 occurs directly ahead of the anchor within depth h' , while Zone 2 is centered on the axis of the section at a depth of $2/3h$. In addition to the bursting force, many

Table 2.4 Bearing Stress Estimates

| | |
|-------------------------------------|---|
| AASHTO Bridge Code '89 | At SL $f_c \leq 3000$ psi or $\leq 0.9f'_{ci}$ |
| PTI Segmental PT Guideline Proposal | At PT $f_c \leq 0.8f'_{ci}\sqrt{A/A_b} - 0.2$ or $1.25f'_{ci}$ or 5000 psi At SL $f_c \leq 0.6f'_{ci}\sqrt{A/A_b}$ or $1.25f'_{ci}$ or 6875 psi |
| CIRIA Guide | At PT $f_c \leq 0.40f'_{ci}$ if bearing area is not well defined At PT $f_c \leq 0.80f'_{ci}$ if bearing area is well defined |
| Design Criteria for F1 & NC | At PT $f_c \leq 0.8f'_{ci}\sqrt{A/A_b} - 0.2$ or $1.25f'_{ci}$ or 5000 psi At SL $f_c \leq 0.6f'_{ci}\sqrt{A/A_b}$ or $1.25f'_{ci}$ or 6875 psi |
| CEB-FIP Model Code '78 | $f_c \leq f_{ck}/K \sqrt{A/A_b}$ or $3.3f_{ck}/K$ where $K = 1.5$ for normal conditions and $K = 1.3$ for overload |
| Austrian Code | $f_c \leq 0.90kf'_{cu}$ where for A_b/A 0 0.20 0.40 0.60 0.80 1.0 K 1.60 1.23 0.93 0.69 0.51 0.40 |
| German Code | $f_c \leq K/2.1\sqrt{A/A_b}$ or $1.46\beta_r$ where $t' \leq 3b$ and $h \leq 3a$, $d \geq h - 3b$ and no overlapping of A_2 at depth d in the case of multiple loads for f'_{cu} (MN/mm ²) ≤ 25 35 45 55 β_r 0.70 f'_{cu} 23 27 30 |
| Swiss Code | $f_c \leq 0.65f'_{ci}\sqrt{A/A_b}$ or $1.8f'_{ci}$ limits of $t' \leq 3b$ and $h \leq 3a$ |

At S.L. = At Service Load

At P.T. = At Stressing

Table 2.5 Bursting Force Estimates

| | | | | | | | | | | | | | |
|--|---|--------|------------|------|------------|-----|------------|-----|------|------|------|------|------|
| ACI 358-86 | $F_b = 0.70P e^{-3a/h'}$ | | | | | | | | | | | | |
| PTI Segmental PT Guideline Proposal | $F_b = 0.35P(1 - a/h')$ | | | | | | | | | | | | |
| CIRIA Guide | <p>$F_b = cP/K$ where $K = 1$ for isolated anchors and anchors on the perimeter of the block, $K = 1.5$ for anchor distributed in one direction, and $K = 2.0$ for anchors distributed in two direction and for</p> <table style="margin-left: auto; margin-right: auto;"> <tr> <td>a/h'</td> <td>≤ 0.3</td> <td>0.4</td> <td>0.5</td> <td>0.6</td> <td>≥ 0.7</td> </tr> <tr> <td>c</td> <td>0.23</td> <td>0.20</td> <td>0.17</td> <td>0.14</td> <td>0.11</td> </tr> </table> | a/h' | ≤ 0.3 | 0.4 | 0.5 | 0.6 | ≥ 0.7 | c | 0.23 | 0.20 | 0.17 | 0.14 | 0.11 |
| a/h' | ≤ 0.3 | 0.4 | 0.5 | 0.6 | ≥ 0.7 | | | | | | | | |
| c | 0.23 | 0.20 | 0.17 | 0.14 | 0.11 | | | | | | | | |
| Design Criteria for FL & NC | $F_b = 0.35P(1 - a/h')$ $f_b = 0.7P/td(1 - a/h')$ | | | | | | | | | | | | |
| VSL End Block Design Guide | $F_b = 0.30P(1 - a/h')$ $f_b = \text{See Figure 2.1b}$ | | | | | | | | | | | | |
| Ontario Bridge Code '83 | $F_b = 0.70P e^{-3a/h'}$ $f_b = \frac{P}{(a/h')^2} e^{-3a/h'} \leq 0.8f_t + 20A_r/td$ | | | | | | | | | | | | |
| CEB-FIP Model Code '78 | $F_b = 0.30P(1 - a/h')$ | | | | | | | | | | | | |
| Austrian Code | $F_b = 0.30P(1 - a/h')$ | | | | | | | | | | | | |
| German Code | $F_{b1} = 0.25P(1 - a/h')$ $F_{b2} = 0.30P(e/h - 1/6)$ | | | | | | | | | | | | |

of the publications limit the bursting stress (see Table 2.5). The VSL Guide [105] uses the stress distribution curves shown in Fig. 2.1 to determine the bursting stress level. A loaded face tensile force (spalling force) also develops near the concrete surface next to the anchor for eccentric anchors (see Table 2.6).

Several of the codes give explicit restrictions on concrete tensile stress levels. Such stresses may be computed by comprehensive linear analyses of the anchorage zone such as with application of finite element analysis. The analyses should consider all applied forces and are essentially based on a limiting principal tensile stress. Tensile stresses are limited in AASHTO [5] Section 9.15.2.2 to $7.5\sqrt{f'_c}$, while the PTI [135] Section 13.2.1 limits stresses to $6\sqrt{f'_c}$. The Florida guide [60] is based on research with Florida limestone and limits tensile stresses to 0.8 times the split cylinder test or $5\sqrt{f'_c}$.

In addition to force and stress calculations, many codes have restrictions on the maximum stress levels for at least one of the following: concrete (see Table 2.7), reinforcement (see Table 2.8), anchorages (see Table 2.9), and prestressing steel (see Table 3.0).

Anchorage zone supplemental reinforcement is the last major area specified in several of the criteria for the design of the anchorage zone. AASHTO requires that a grid of #3 bars at 3 inches be placed not more than 1-1/2 inches from the inside face of the anchor bearing plate, if a recommended reinforcement is not given by the manufacturer. In the guide used by Florida and North Carolina, individual anchors must use spirals and anchor groups must use spirals in combination with links or prestressing to contain bursting stresses; grids may not be used. In the Ontario Bridge Code, the bursting reinforcement must extend from $0.281h'(1 - e^{3a/h'})$ to h' ; but in the CEB-FIP Model Code, bursting reinforcement must extend from $0.1h'$ to h' and the allowable load may be increased as hoop reinforcement is added according to: $1.3u/A_s \cdot f_y - (A_b - A) \cdot f_{ck}(1 - M_s/(uNx/\pi))$. In the Austrian Code, reinforcement behind a blister must take $P/4$ in tension, while the VSL

guide says $P/2$ must be taken in tension.

Table 2.6 Spalling Force Estimates

| | |
|----------------------------|---|
| CIRIA Guide | $F_{sp} = 0.2P[(h'/2 - d_1)/(h'/2 + d_1)]^3$ $F_{sp} = 0.04P$ <p style="text-align: right;">if $d_1 > h'$ if $d_1 \leq h'$</p> |
| VSL End Block Design Guide | $F_{sp} = 2M_{sp}/h$ $f_{sp} = 6M_{sp}/th^2 \leq 0.6F_t$ |
| Ontario Bridge Code '83 | $F_{sp} = 0.04P$ |
| German Code | $F_{sp} = P(e/d - 1/6) \geq 0$ |

Table 2.7 Concrete Stress Restrictions

| | |
|-----------------------------|--|
| AASHTO Bridge Code'89 | Unless otherwise stated in plans, at transfer f_{ci} must be ≥ 3500 psi |
| Design Criteria for FL & NC | In precast concrete for transfer PT, f_{ci} must be ≥ 4000 psi and for longitudinal PT must be $\geq f'_c$ 28 days. In cast-in-place concrete before partial PT f'_{ci} must be ≥ 2500 psi and for full PT ≥ 4000 psi |
| Swiss Code | Cannot use greater than f'_{cu} at 28 days for design calculations |

Table 2.8 Reinforcement Stress Restrictions

| | |
|--|---|
| PTI Segmental PT Guideline Proposal | The tensile stress in the anchorage reinforcement is limited to $0.60f_y$ at the jacking. |
| CIRIA Guide | The tensile stress in the anchorage reinforcement is limited to $0.87f_y$ at the jacking. |
| Design Criteria for FL & NC | The tensile stress in the anchorage reinforcement is limited to $0.5f_y$ at jacking and $0.4f_y$ after losses |

Table 2.9 Anchorage Stress Restrictions

| | |
|---------------------------|---|
| AASHTO Bridge Code'89 | Anchorage of unbonded tendons shall develop at least 95% of the minimum specified ultimate tendon strength of the prestressing steel without exceeding anticipated set. |
| ACI 318-89 | Anchorage of unbonded tendons shall develop the minimum specified ultimate tendon strength of the prestressing steel without exceeding anticipated set. The anchorage zone develop the ultimate tendon strength of the prestressing tendon using a strength reduction factor of 0.9 for concrete. |
| CEB-FIP Model Code '78 | Anchorage required to handle 1.2 times the maximum force in the prestress tendons |

Table 2.10 Prestressing Steel Stress Restrictions

| | |
|--------------------------------|---|
| AASHTO Bridge Code'89 | Temporary stress before losses due to creep and shrinkage must be $\leq 0.7f_{pu}$ with allowances for temporary overstressing at seating up to $0.9f_{py}$ |
| ACI 318-89 | Temporary stress due to tendon jacking force must be less than $0.94f_{py}$, $0.8f_{pu}$ or the maximum value recommended by the manufacturer of the prestressing tendon or anchorages |
| Design Criteria for FL & NC | Maximum jacking stress is $0.76f_{pu}$ for stress relieved strand (SRS) and $0.81f_{pu}$ for low relaxation strand (LRS). |

CHAPTER 3
CONCENTRIC ANCHORAGE ZONES WITH STRAIGHT TENDONS

3.1 Introduction

In post-tensioned concrete, the basic anchorage zone configuration includes the anchorage device located on the geometric centroid of the concrete cross section. This chapter examines concentric anchorage zones in detail. Thirteen specimens were used to investigate concentric anchorage variables including reinforcement distribution, the ratio of the anchorage device width (a) to the section depth (h), and the effect of lateral post-tensioning.

In this chapter, the individual test setup and test results are described in detail. The test results are analyzed from both a first cracking and ultimate load standpoint.

3.2 Test Program

The concentric anchorage test series investigated the basic variables of post-tensioned anchorage zones before more complicated section geometries and/or post-tensioning configurations were done. The test program was divided into four test groups. The first two illustrated the reinforcement distribution effect on the load carrying capacity. The third changed the ratio of the anchorage device width to the section depth. The fourth group showed the effects of lateral post-tensioning.

3.2.1 Test Setup. All of the concentric specimens were loaded in a universal testing machine and were supported on two sheets of 1/32-inch teflon to reduce any base friction. The specimens were carefully centered under the ten-inch diameter spherical loading head. Specimens were loaded monotonically with stops to record readings and mark surface concrete cracks. Typical load increments were 25 kips until the applied load approached the cracking load; then the increments were reduced to ten kips. No special methods were used to locate concrete surface cracks other than careful visual observations and the

monitoring of strain gage data. It was determined after several tests that cracking typically occurred when strains in nearby reinforcement reached 250 microstrain. When first seen, a typical crack width would be less than 0.001 inches. Electronic strain gages were placed on the key reinforcement and were monitored with the use of a computer data acquisition system. On most tests, anchorage displacement was recorded; and, on several, crack widths were monitored. Tests were typically completed within three hours. For each test, concrete compression strength and tensile strength were determined with 6 x 12 inch cylinder compression tests and split cylinder tests respectively. The compression cylinder tests were performed utilizing neoprene pad caps. All cylinders were field cured in conditions identical to those of the specimens. The reported compressive and tensile concrete strengths for each specimen were the average of at least three cylinder tests. Concrete was a nominal 3,500 to 5,000 psi concrete with type "I" cement, river sand and 3/8 inch maximum size coarse aggregate. All specimens were cast horizontally as if they were slabs. This facilitated concrete placement and consolidation. Reinforcing bars were tested for their yield strength and modulus of elasticity. The yield point for the reinforcing bar was based on a 0.2% offset. Strain gages were used to determine the load strain relationship. All steels used were ductile in behavior. Concrete strength and reinforcing bar information will be given in each test series section.

3.2.2 Test Series "A". Series "A" consisted of four specimens. Dimensions and reinforcing details are shown in Figs. 3.1 to 3.3. All four specimens had the same geometry and loading configuration, but the centroid and size of the reinforcement varied. The specimens were 6 inches thick and loaded over the full thickness. This was done so that the specimens would behave as two-dimensional as possible. All four specimens were cast from the same batch of concrete, a 3,500 psi concrete mix. The load was applied to specimens through two plates 6 x 12 x 1 inch stacked on top of the specimen. Two loading plates

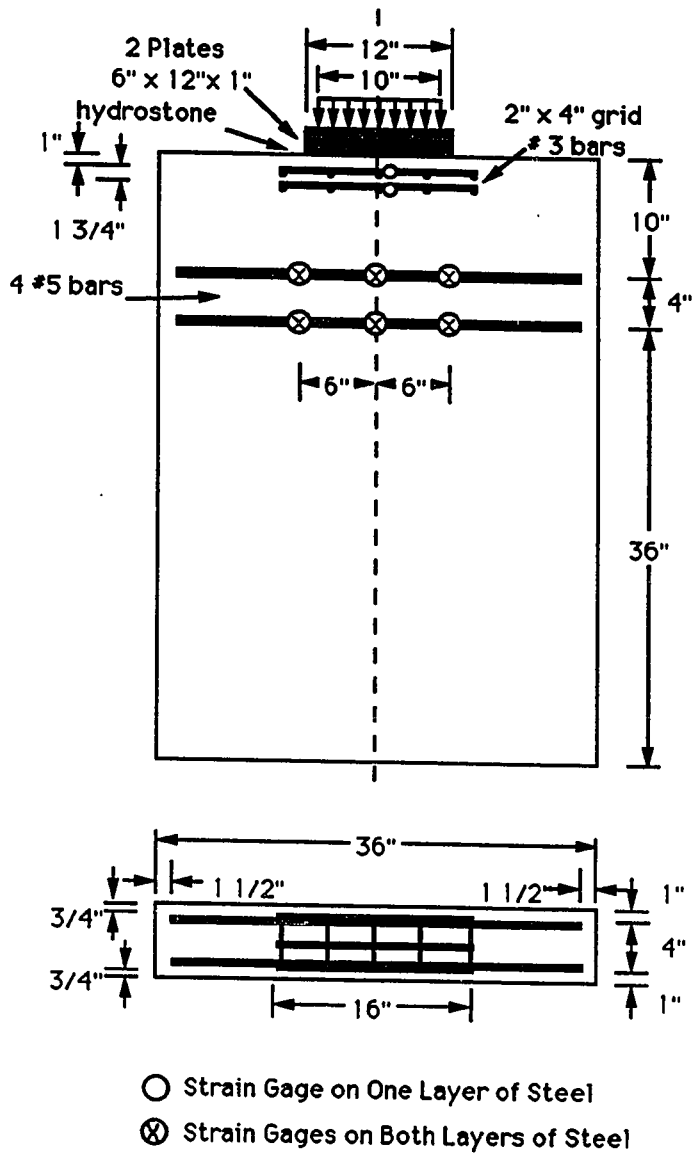
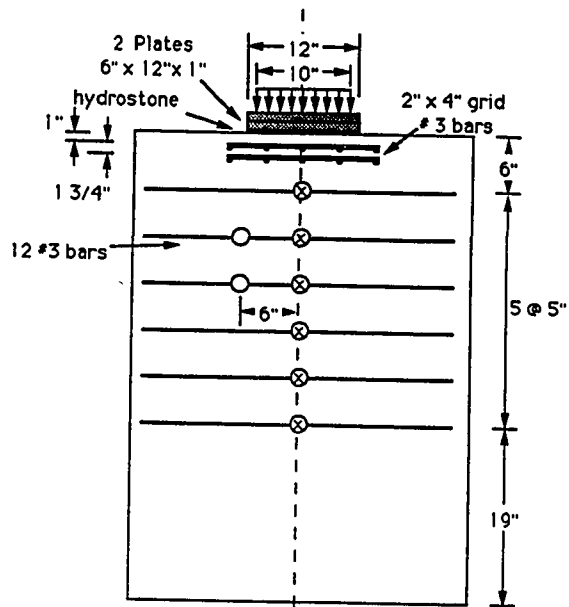
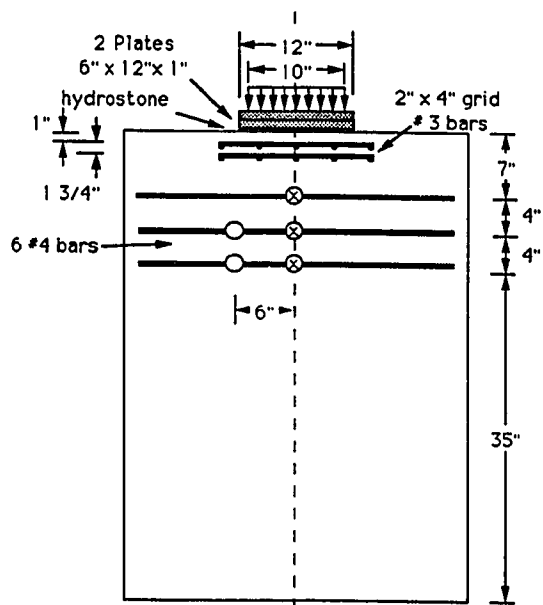


Figure 3.1 Specimen A1 Detail

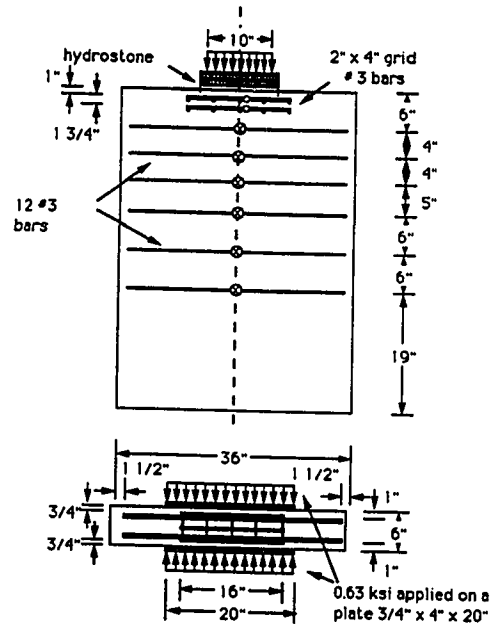


a) Specimen A2

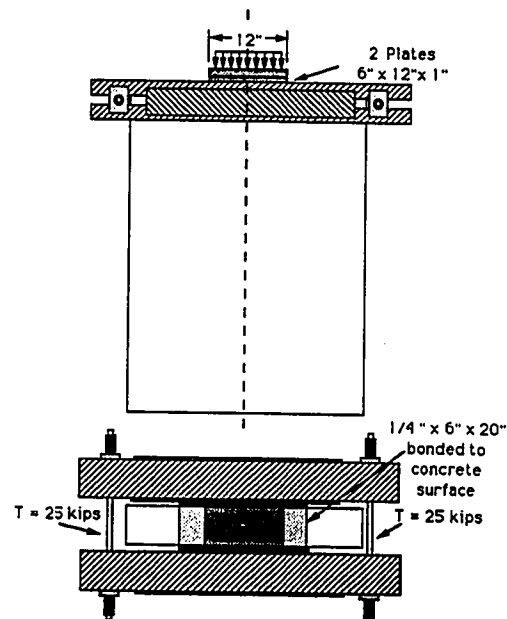


b) Specimen A3

Figure 3.2 Reinforcement Details for Specimens A2 and A3



a) Reinforcement and Transverse Loads



b) Transverse Post-Tensioning Details
Figure 3.3 Details for Specimen A4

ensured that the applied load would spread over the entire plate width before entering the specimen. Before the plates were positioned, hydrostone was placed over the concrete loading area to ensure a level and uniform contact surface between the steel plate and the concrete. During the test, each specimen was braced to prevent any lateral movement (see Fig. 3.4). The local zone reinforcement consisted of two layers of reinforcement located at 1 inch and 2 3/4 inches from the loading surface, and composed of #3 Grade 60 reinforcing bars on 2-inch centers. Table 3.1 shows the compressive strength, tensile strength, and reinforcing bar characteristics for each test.

Table 3.1 Material Information for Specimen A1 to A4

| Specimen | Concrete | | Reinforcing Bar | | | | Yield Strain (microstrain) |
|----------|-------------------|-----------------|-----------------|--------------|-----------------|----------------|-------------------------------|
| | f_{sp} (psi) | f'_c (psi) | Bar Size | E (ksi) | F_y (kips) | f_y (ksi) | |
| A1 | 308 | 3360 | #5 | 27400 | 18.5 | 59.6 | 2180 |
| A2 | 308 | 3360 | #4 | 27200 | 13.3 | 66.7 | 2450 |
| A3 | 314 | 3480 | #3 | 29700 | 8.90 | 80.9 | 2730 |
| A4 | 330 | 3840 | #3 | 29700 | 8.90 | 80.9 | 2730 |

Specimen A1 bursting reinforcement (see Fig. 3.1) consisted of two layers of #5 Grade 60 reinforcing bars at an average depth of 12 inches with a total tension capacity of 73.9 kips. All of the bursting reinforcement was strain gaged along the specimen centerline. The information from these gages is shown in Fig. 3.5. Gages 10"R (Right) and 14"R were on reinforcement on one side of the specimen, while 10"L (Left) and 14"L were on the opposite side. None of the bursting reinforcement yielded before failure. The first surface crack occurred near the centerline at 298 kips. The crack propagated to within 1 3/4 inches of the base on the left side of the specimen (see Fig. 3.6).

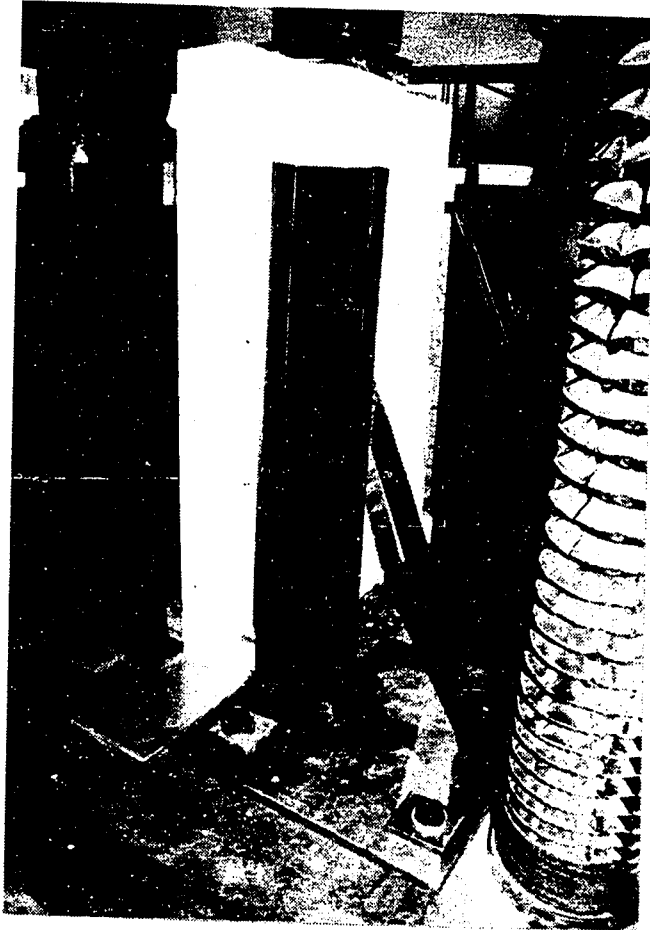


Figure 3.4 Test Setup "A" Series

No cracks occurred on the right side of the specimen at this load stage. After the peak load was reached, the load dropped to 249 kips. The specimen was reloaded but was only able to reach 288 kips. Extensive cracking occurred on the right side of the specimen with several cracks spreading out from the loading plate. A crack opened along the specimen centerline on the right side parallel with the crack seen one load stage earlier on the left side. Additional cracking opened on the right side starting just outside the loading plate and

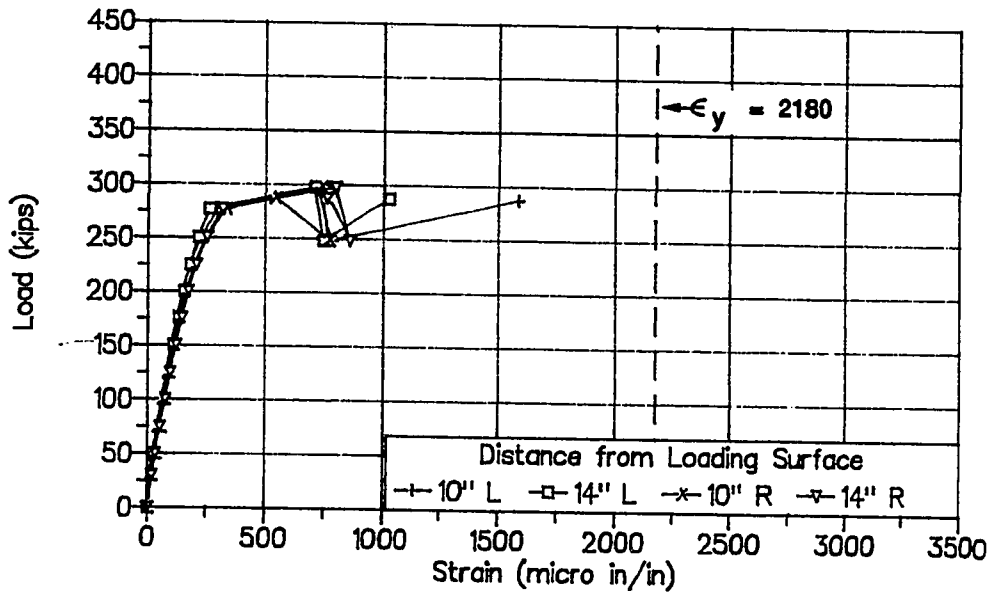
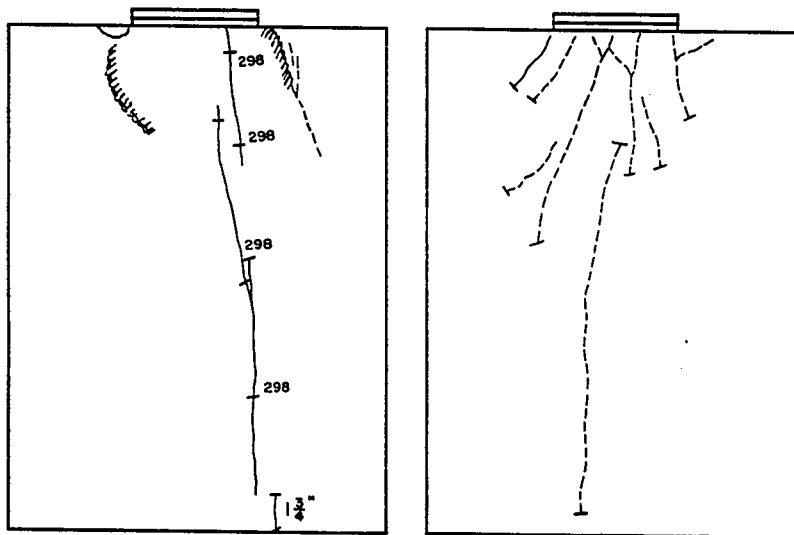


Figure 3.5 Bursting Strain Data, Specimen A1



a) Left Side

b) Right Side

Figure 3.6 Crack Patterns, Specimen A1

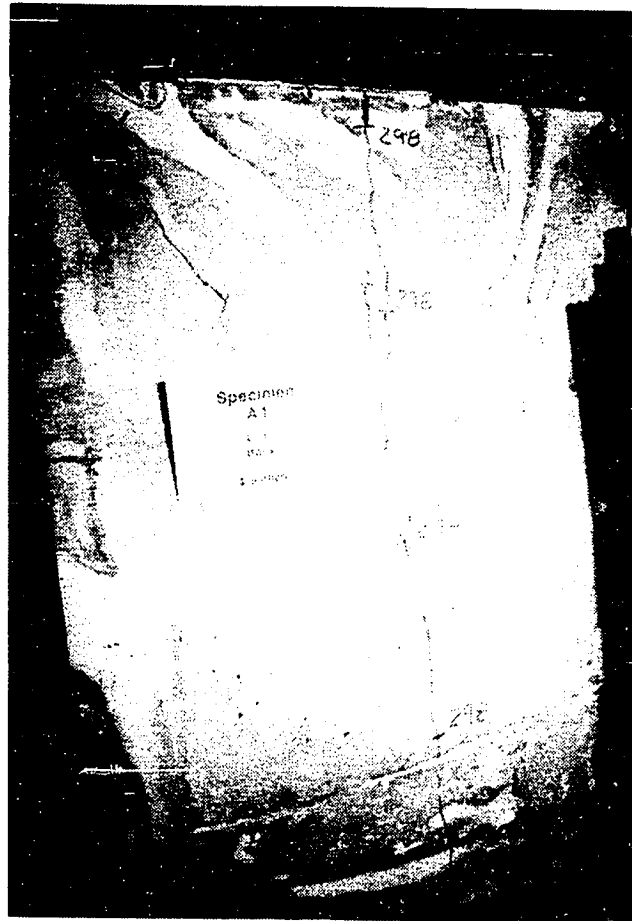


Figure 3.7 Specimen A1 at Ultimate

then propagated down into the specimen (see Fig. 3.7). These were caused by a bulging of the concrete underneath the loading plate. The dotted lines represent cracks that occurred during the reloading stage. The waving line over the dotted line represents the cracks that were caused by bulging of the concrete. A bulging of concrete ahead of the anchor was a typical sign of a local zone failure. As the concrete crushed ahead of the loading plate, the loading plate was pushed into the specimen. This pushing action causes the concrete to spall off. Table 3.2 is a test summary for "A" series specimens. When two first

cracking loads are given, it means that cracks were not seen on both sides of the specimen until the second load.

Table 3.2 Load Summary for Specimen A1 to A4

| Specimen | First Crack (kips) | | Ultimate (kips) |
|----------|-----------------------|-----|--------------------|
| A1 | 298 | | 298 |
| A2 | 225 | | 275 |
| A3 | 250 | | 265 |
| A4 | 300 | 315 | 437 |

Specimen A2 shown in Fig. 3.2a had three layers of bursting reinforcement consisting of #4 Grade 60 reinforcing bars located at an average depth from the loading plate of 11 inches and with a total tension capacity of 79.8 kips. As in Specimen A1, bursting reinforcement strain was measured along the specimen centerline. Figure 3.8 shows the bursting strain for both mats of bursting reinforcement. The values were very similar until approaching the ultimate load. The first cracking load was 225 kips, and the ultimate load was 275 kips. After reaching the peak load, the load dropped to 230 kips. The specimen was reloaded but was only able to reach 268 kips. The cracking pattern was very similar to Specimen A1 (see Fig. 3.9). The first crack was near the specimen centerline. At 275 kips and during the reload to 268 kips, cracks propagated from the edges of the loading plate due to the bulging of the concrete ahead of the loading plate. At the conclusion of the test, approximately 7 inches of concrete below the plate was removed with a slight pull (shaded portion underneath anchor in Fig. 3.9).

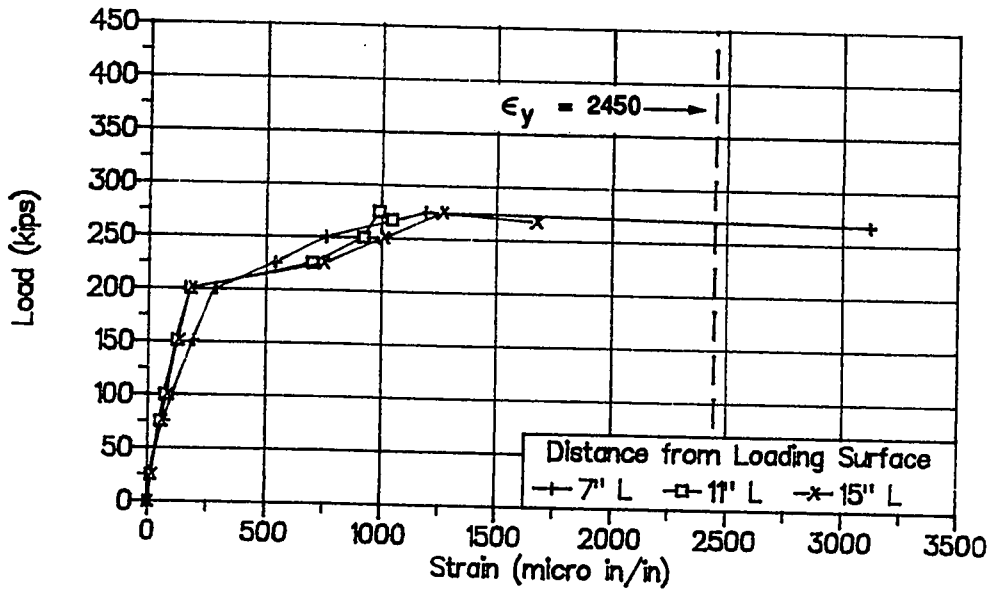


Figure 3.8a Bursting Strain Data, Left Side, Specimen A2

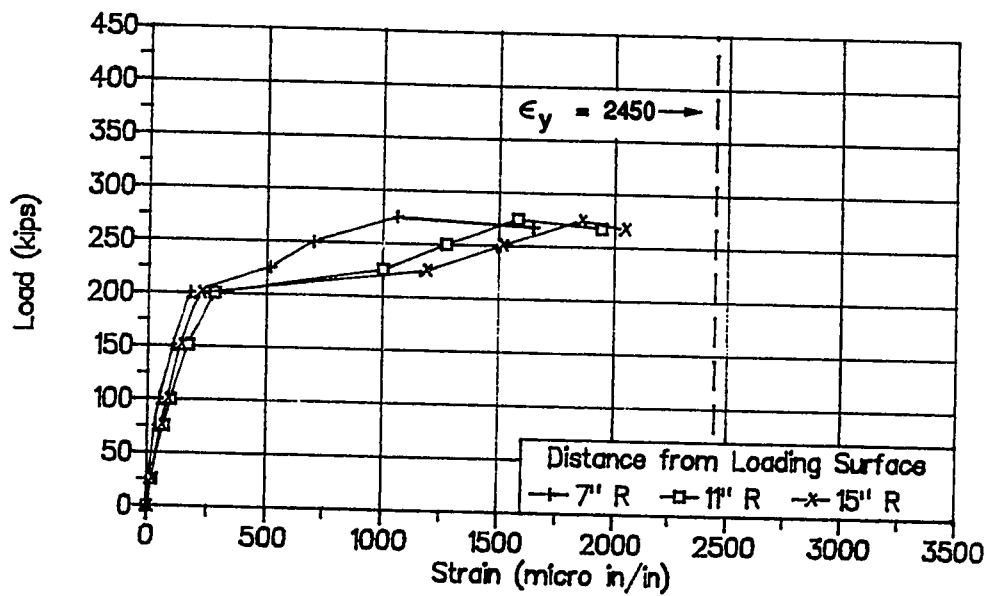


Figure 3.8b Bursting Strain Data, Right Side, Specimen A2

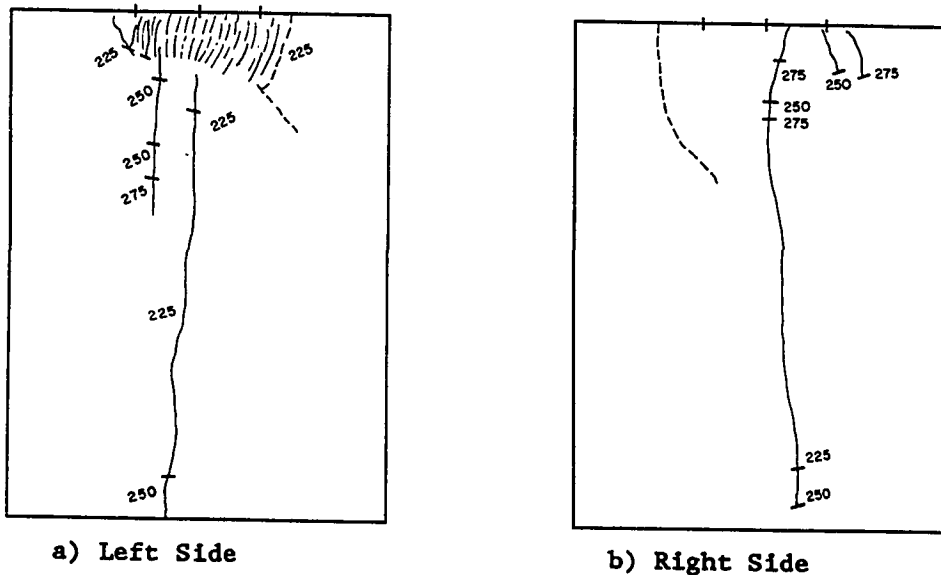


Figure 3.9 Crack Patterns, Specimen A2

The bursting reinforcement of Specimen A3 consisted of six layers of #3 Grade 60 reinforcing bar spaced evenly between 6 and 31 inches (see Fig. 3.2b). The centroid of the bursting reinforcement was at 18-1/2 inches from the loading plate with a total tension capacity of 106.8 kips. The centerline bursting reinforcement strains are shown in Fig. 3.10. The strains in the bursting reinforcement jumped from less than 250 microstrain to over 600 microstrain at 225 kips as the concrete began to crack internally. The first surface cracks were not seen until 250 kips. In Fig. 3.11, the percentage of the total axial force in each bar of the bursting reinforcement shows a substantial increase at the first cracking load of 250 kips. The numbers in parentheses in the legend are the total relative percentages of the bursting force determined from the strain gages relative to the applied axial load. The cracking pattern was very similar to that in Specimens A1 and A2. A specimen centerline crack opened at first crack. At ultimate, distress in the local zone caused extensive cracking immediately ahead of the anchor, crushing of the concrete, and eventually a bulging of the concrete. The ultimate load was 265 kips.

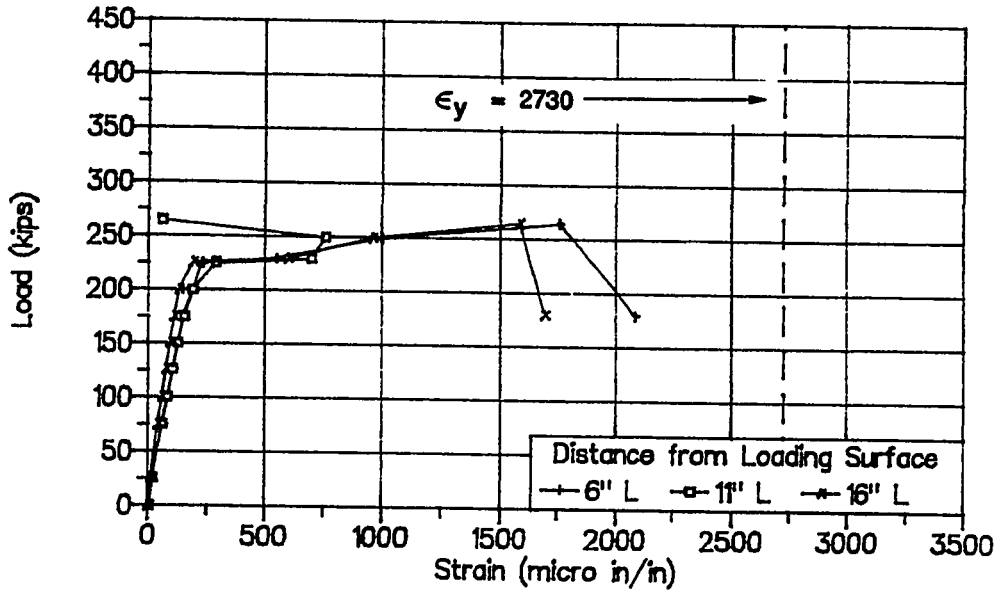


Figure 3.10a Bursting Strain Data, Top Left, Specimen A3

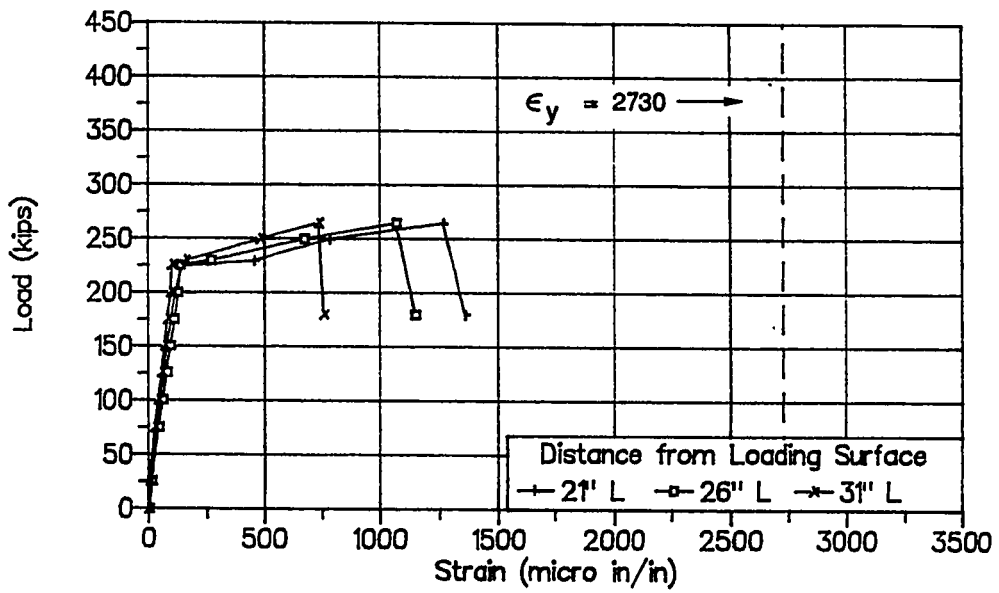


Figure 3.10b Bursting Strain Data, Bottom Left, Specimen A3

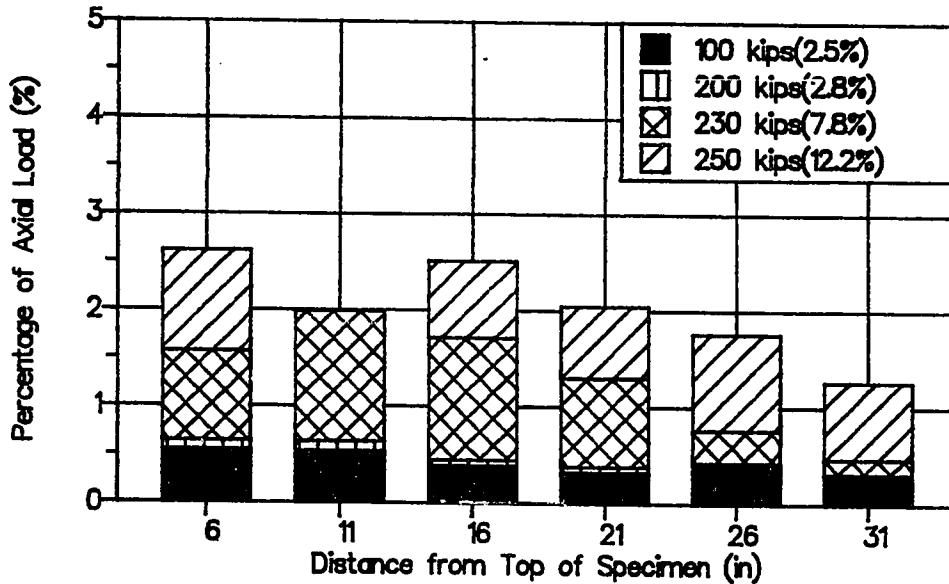


Figure 3.11 Specimen A3 Bursting Tension Force with Respect to the Applied Axial Load

Before testing Specimen A4, the initial three tests were examined in detail. It was determined that the specimens were failing in the local zone due to excessive compressive stresses (see section 3.4), because the specimens had general zone tensile capacities much higher than expected. To increase the local zone capacity of Specimen A4, stiffened beams were used to apply 50 kips of transverse load over a 4 x 20 inch area (625 psi) (see Figs. 3.3 and 3.12), utilizing two 5/8-inch threaded post-tensioning bars.

The total amount of bursting reinforcement in Specimen A4 was the same as in Specimen A3 (see Fig. 3.2b) but was distributed closer to the loading plate. The total tension capacity of the bursting reinforcement was 106.8 kips with a centroid of 17 1/2 inches. Figure 3.13 shows the bursting strains recorded from the strain gages located along the centerline on the bursting reinforcement. The first crack occurred at 300 kips along the specimen centerline. Figure 3.14 is a

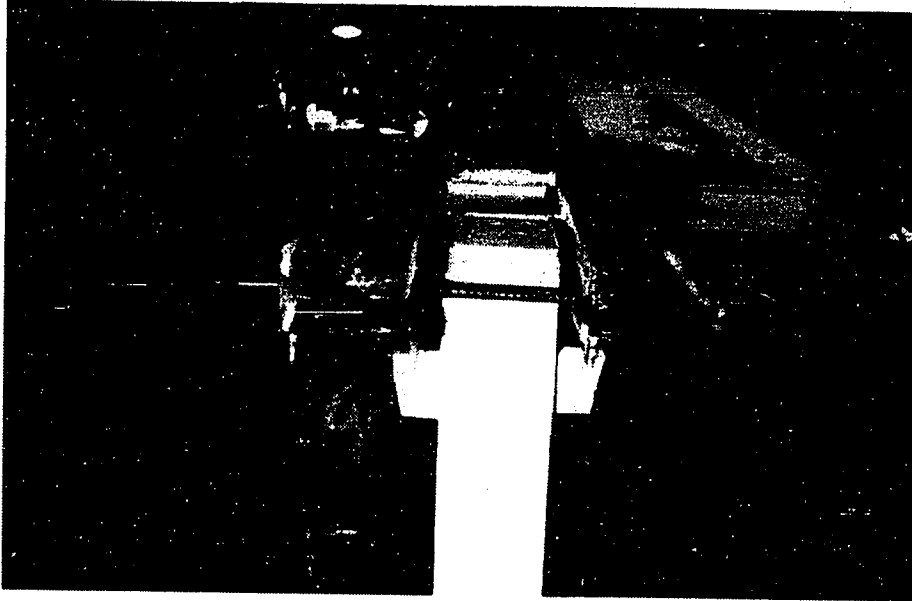


Figure 3.12 Specimen A4 Transverse Post-Tensioning

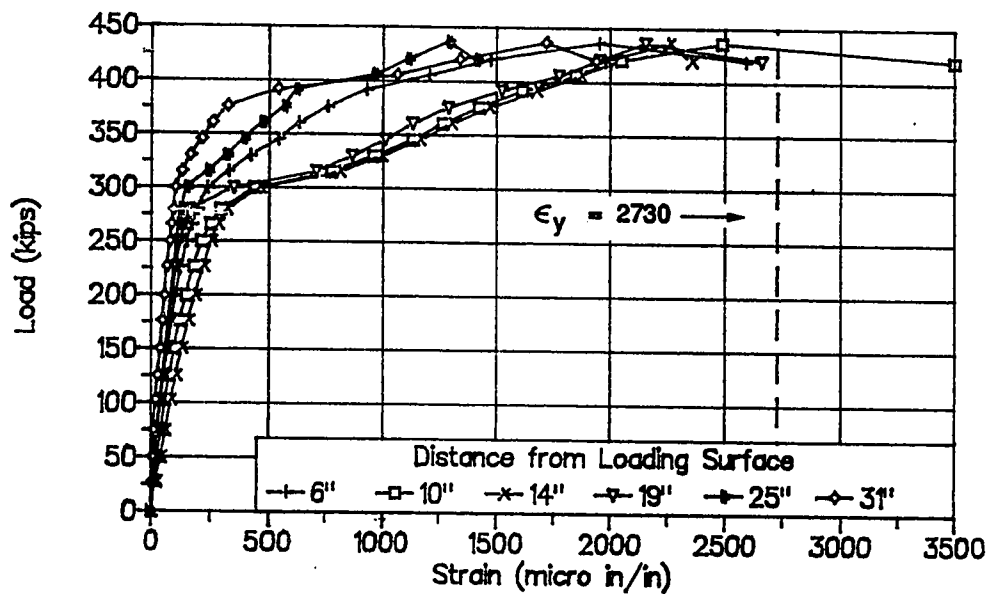


Figure 3.13 Bursting Strain Data, Specimen A4

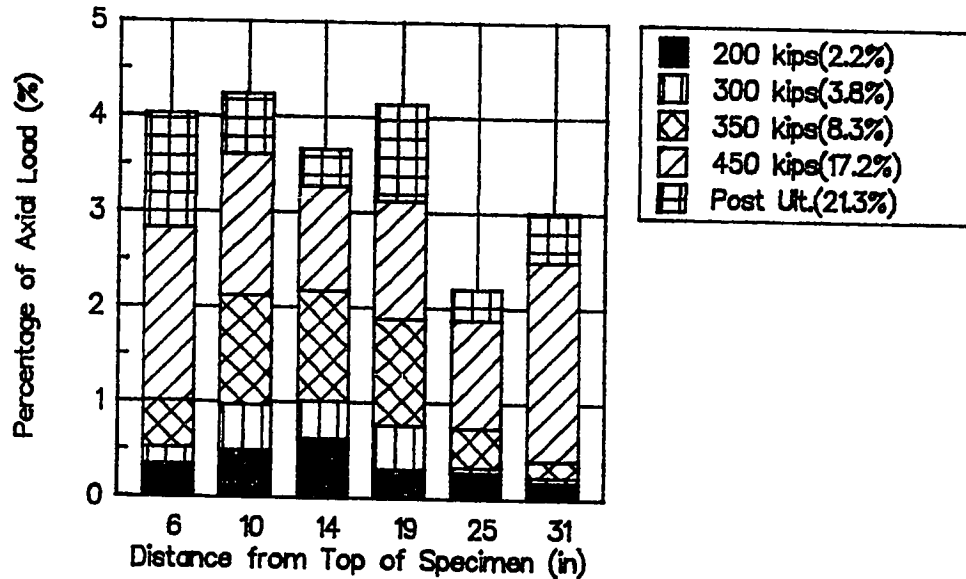
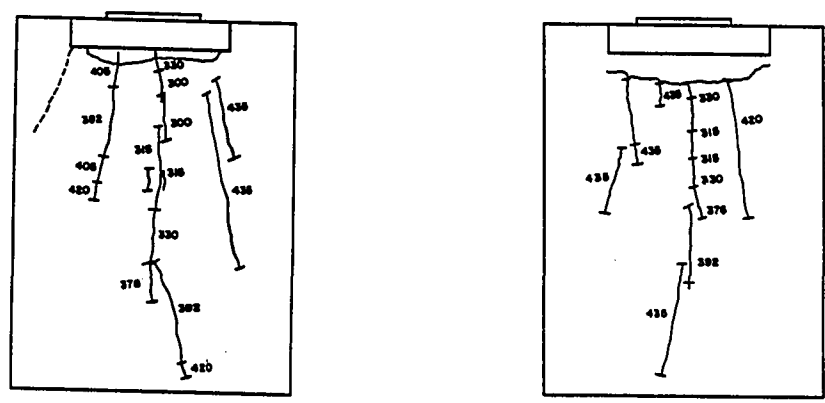


Figure 3.14 Specimen A4 Bursting Tension Force with Respect to the Applied Axial Force

comparison of force in the bursting reinforcement for different load levels. As with Specimen A3, a small percentage of the force was carried by the reinforcement before the first crack occurred. After the first cracking load, the total bursting force being carried by the bursting reinforcement increases substantially and has a shape similar to that predicted by the elastic analysis. As the load approaches ultimate, the stress level in the bursting reinforcement deeper in the section began to increase and the force distribution became more uniform. Cracks in the specimen continued to propagate throughout the test until within 2 inches of the base (see Fig. 3.15). The ultimate load was 437 kips. At the ultimate load, concrete spalled off just below the transverse prestressed area (see Fig. 3.16).

3.2.3 Test Series "B". Series "B" consisted of eight specimens. The "B" series was designed with highly conservative local zone reinforcement to prevent any local zone failure. As in Series "A", a



a) Left Side

b) Right Side

Figure 3.15 Crack Patterns for Specimen A4

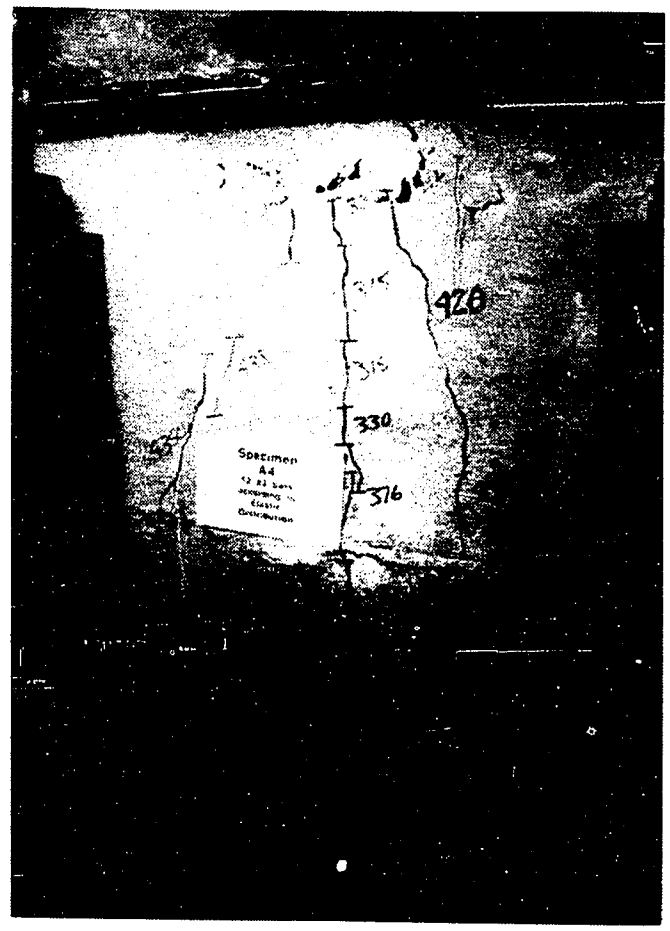


Figure 3.16 Specimen A4 Crack Pattern at Ultimate

determination of the effect of reinforcement distribution was the major objective (Specimens B1 to B4). Other specimens investigated the effect of zero general zone bursting reinforcement (B5), zero local zone reinforcement (B6), the void caused by a post-tensioning duct (B7), and only a partial loading of the bearing plate (B8). The dimensions and reinforcing details for Series "B" specimens are given in Figs. 3.17, 3.18, 3.37 and 3.43. The spiral used for local zone reinforcement (except in B6) consisted of #4 smooth bar with a yield strength of 80.3 ksi and a modulus of elasticity of 26,900 ksi. Each spiral had a 1 1/4-inch pitch and a total of seven turns with the first and last half turn tied to the adjacent turn. All eight specimens had the same outer dimensions and loading plate size. The loading plate was hydrostoned to the top of the specimen after casting. The specimens were made in two casts: B1 to B4 and B5 to B8. The concrete mix used was a 5,000 psi, 3/8 inch aggregate mix. Table 3.3 shows the material properties for each of the specimens. All specimens had electronic strain gages along the specimen centerline on a majority of the bursting reinforcement.

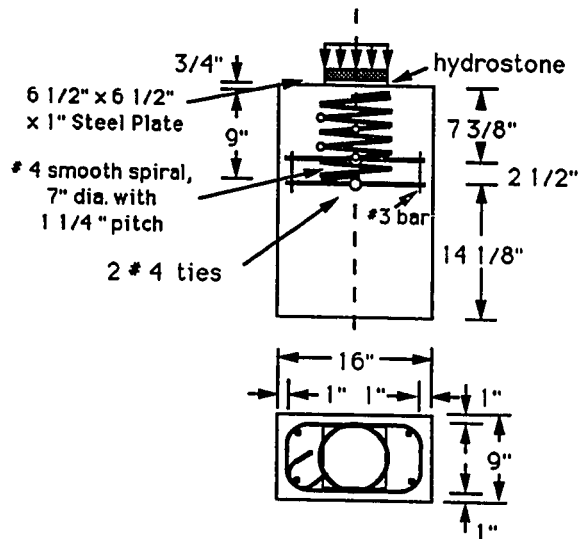
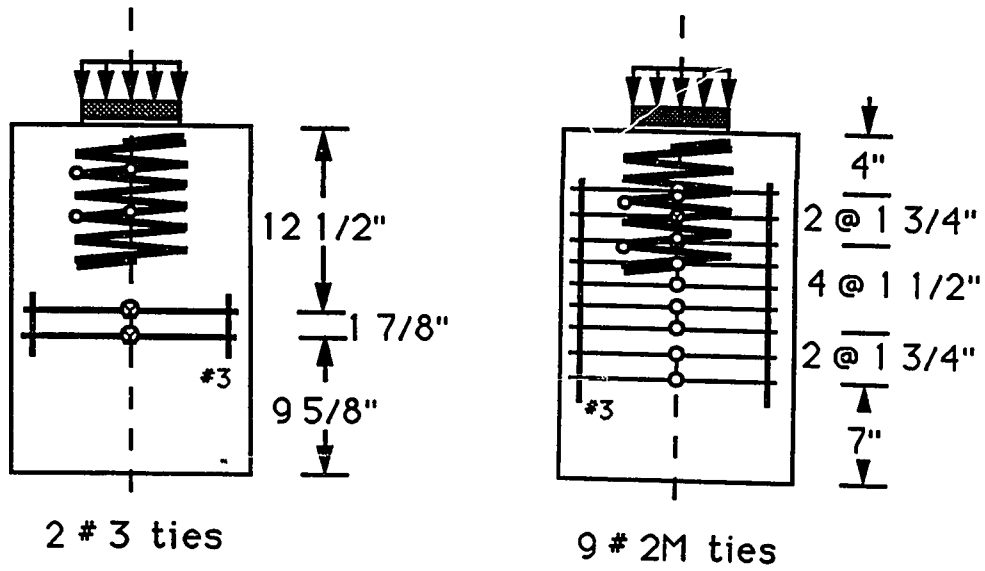


Figure 3.17 Specimen B1 Detail

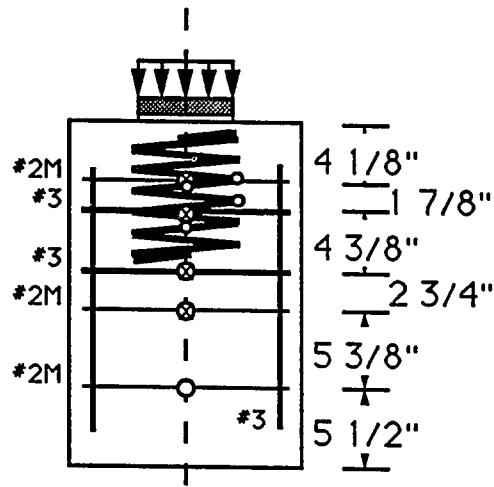


2 # 3 ties

9 # 2M ties

a) Specimen B2

b) Specimen B3



c) Specimen B4

Figure 3.18 Details for Specimens B2, B3 and B4

Table 3.3 Material Information for B1 to B8

| Specimen | Concrete | | Reinforcing Bar | | | | |
|----------|-------------------|-----------------|-------------------------------|--------------|-----------------|----------------|-------------------------------|
| | f_{sp} (psi) | f'_c (psi) | Bar Size | E (ksi) | F_y (kips) | f_y (ksi) | Yield Strain (microstrain) |
| B1 | 464 | 5380 | #4 | 27900 | 12.7 | 63.5 | 2270 |
| B2 | 464 | 5380 | #3 | 28700 | 7.34 | 66.7 | 2320 |
| B3 | 464 | 5380 | #2m | 27600 | 2.20 | 44.9 | 1640 |
| B4 | 464 | 5380 | #2m | 27600 | 2.20 | 44.9 | 1640 |
| | | | #3 | 28700 | 7.34 | 66.7 | 2320 |
| B5 | 420 | 5320 | No General Zone Reinforcement | | | | |
| B6,B7,B8 | 420 | 5320 | Same as B4 | | | | |

#2M has a cross sectional area of 0.049 in²

Specimen B1 (shown in Fig. 3.17) had two layers of #4 Grade 60 reinforcing bars at an average depth of 8 5/8 inches with a total tension capacity of 50.8 kips. The specimen cracked along the specimen centerline at 200 kips (see Table 3.4). The load-displacement curve (see Fig. 3.19) shows a change of specimen axial stiffness at the cracking load from 2,460 kips/in to 1,575 kips/in. Once cracked, the amount of load drop-off after each load stage began to increase. Figure 3.20 shows the cracking pattern on the north side of the specimen at ultimate. The extent of the first crack at 200 kips was marked along the centerline. After the specimen reached an ultimate load of 366 kips, the load decreased to 330 kips but the specimen was able to be reloaded to 365 kips. After reaching the ultimate load for the second time, the specimen appeared to be fully cracked along the specimen centerline and it could be assumed that the amount of concrete tensile capacity being utilized was very small due to the smooth nature

Table 3.4 Load Summary for Specimen B1 to B8

| Specimen | First Crack (kips) | Ultimate(kips) | |
|----------|-----------------------|----------------|-----------|
| | | Peak | Secondary |
| B1 | 200 | 366* | 365 |
| B2 | 186 | 290 | 280 |
| B3 | 217 | 331 | 313 |
| B4 | 200 | 337* | 305 |
| B5 | 170 | 212* | 25 |
| B6 | 171 | 297* | 258 |
| B7 | 170 | 296* | 283 |
| B8 | 156 | 276 | 273 |

* - Load deflection curves at peak value have rounded tops

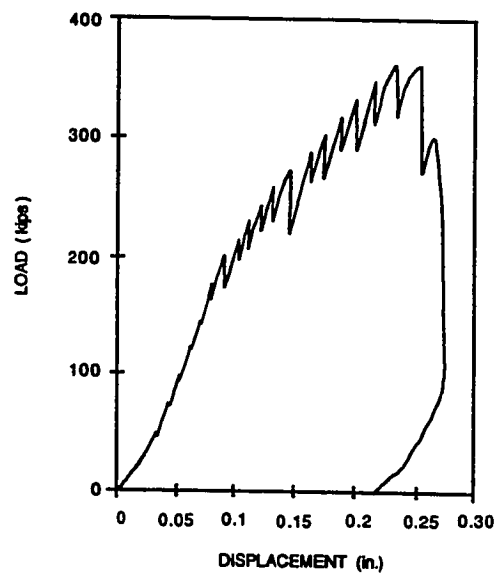


Figure 3.19 Specimen B1 Load-Displacement Curve

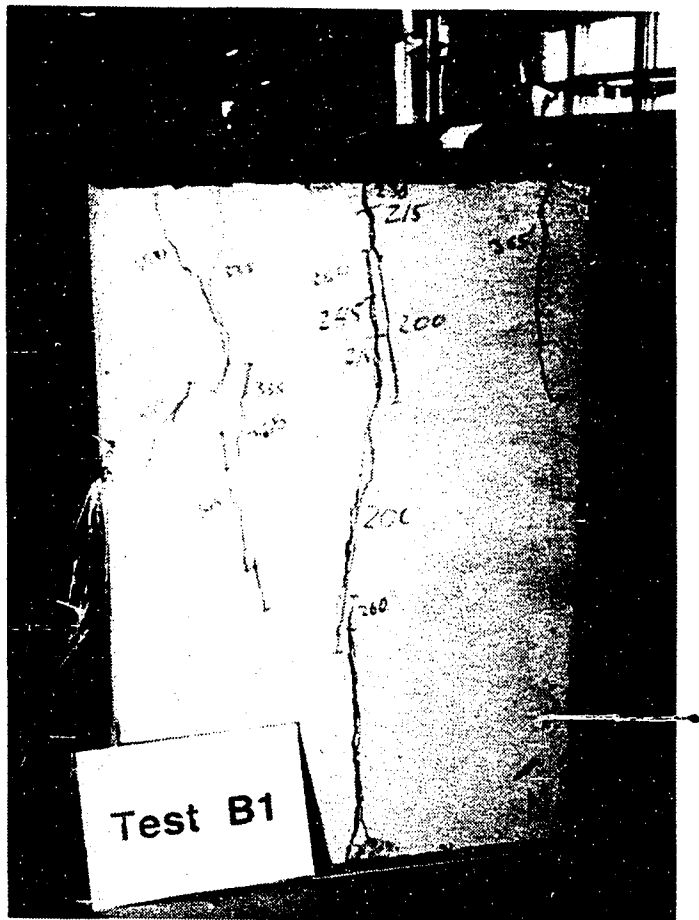


Figure 3.20 Crack Pattern for North Side of Specimen B1 at Ultimate

of the load-displacement plot during the reload to 365 kips. At the peak load, the main centerline crack was 0.0945 inches wide at the top and 0.039 inches wide in the middle of the specimen. The specimen was loaded again but was only able to reach 300 kips before the load began to drop again. Figure 3.21 shows the strain gage data from the bursting reinforcement indicating that yielding was realized. The bursting reinforcement was gaged on only one side of the specimen. However, from the observed cracking patterns, it was assumed that all bursting reinforcement yielded. Figure 3.22 shows the ultimate load

crack pattern for the south side of the specimen. There was a more extensive cracking pattern than was seen on the north side (see Fig. 3.20), with the largest crack still along the specimen centerline. Horizontal cracks opened on the transverse faces at 365 kips. The spiral reinforcement was used to confine the local zone which reached approximately 25 percent of yield (see Fig. 3.23). The strain gages on the spiral were oriented in two directions: in the direction of the major axis (lateral) and in the direction of the specimen thickness (transverse). Since the spiral reinforcement was used mainly for the confinement of the local zone, the strains in both directions were essentially equal. The spiral strains closer to the loading surface were slightly greater than those deeper into the specimen; this was possibly due to the spreading of forces away from the spiral. As the load approached the ultimate load, the displacement of the anchorage device increased along with cracking which was ahead of the anchor and on the top surface (see Fig. 3.24).

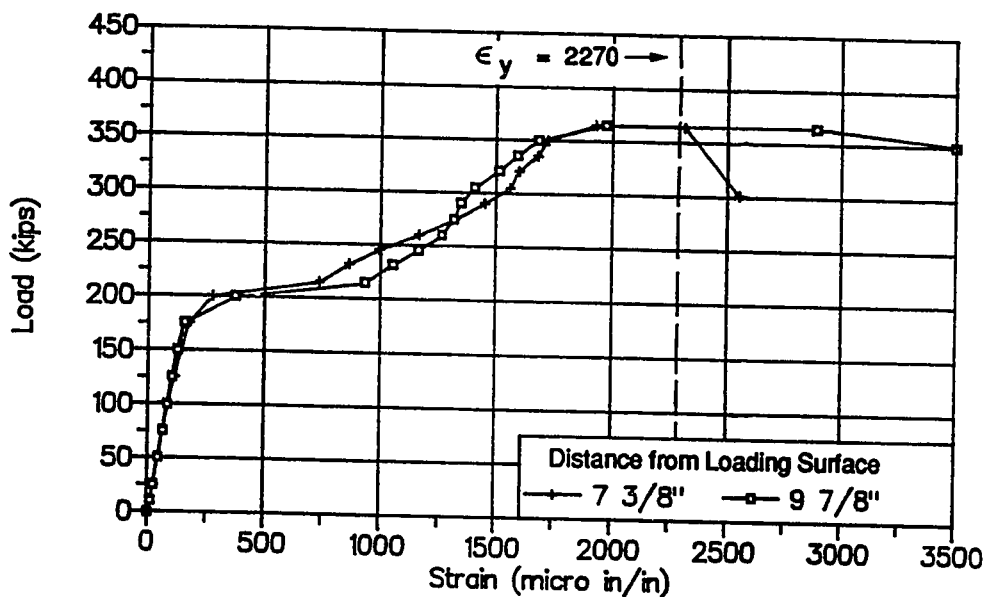


Figure 3.21 Bursting Strain Data, Specimen B1

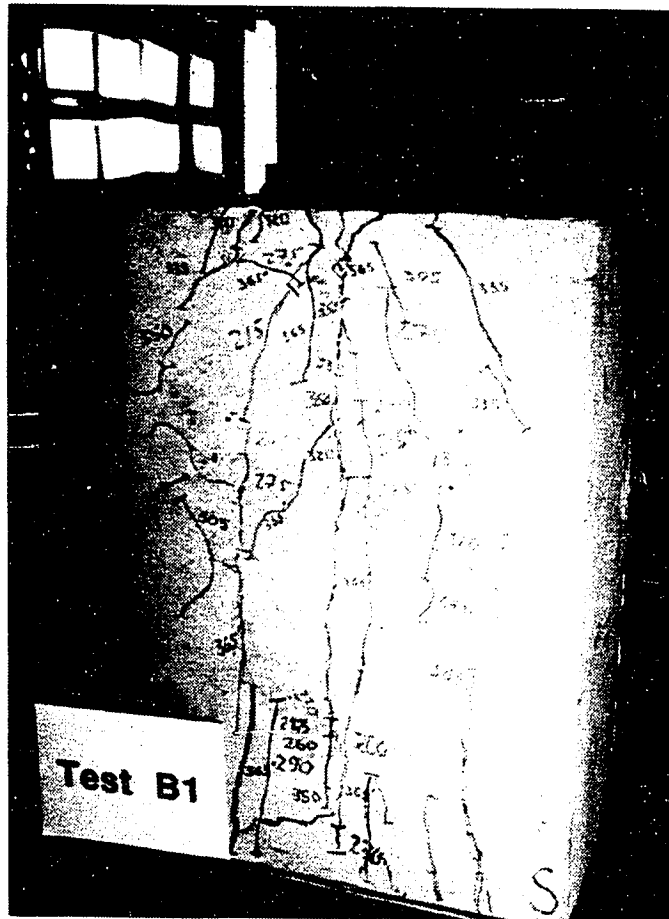


Figure 3.22 Specimen B1 Crack Pattern on South Side at Ultimate

The bursting reinforcement of Specimen B2 (see Fig. 3.18a) consisted of two layers of #3 Grade 60 reinforcing bars at an average depth of 13 15/16 inches with a total tension capacity of 29.36 kips. The total bursting tension capacity of Specimen B2 was 57.8 percent of Specimen B1, but the centroid of the bursting reinforcement was approximately 5 inches deeper. The load-displacement curve for Specimen B2 shows a linear behavior until approaching the ultimate load with an axial stiffness of 2,750 kips/in (see Fig. 3.25). The first cracking load was 186 kips, and the ultimate load was 290 kips. The

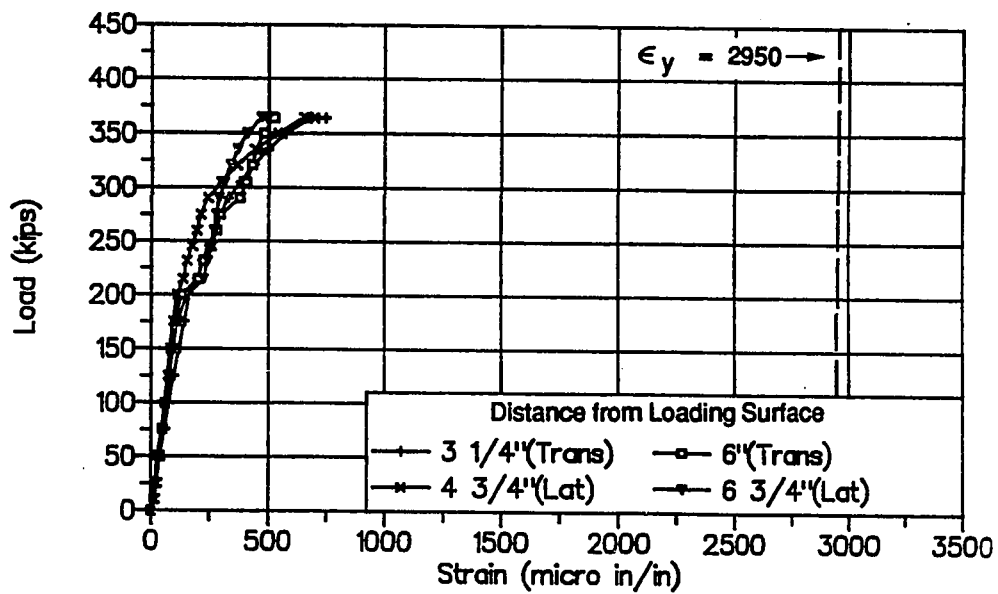


Figure 3.23 Spiral Strain Data, Specimen B1

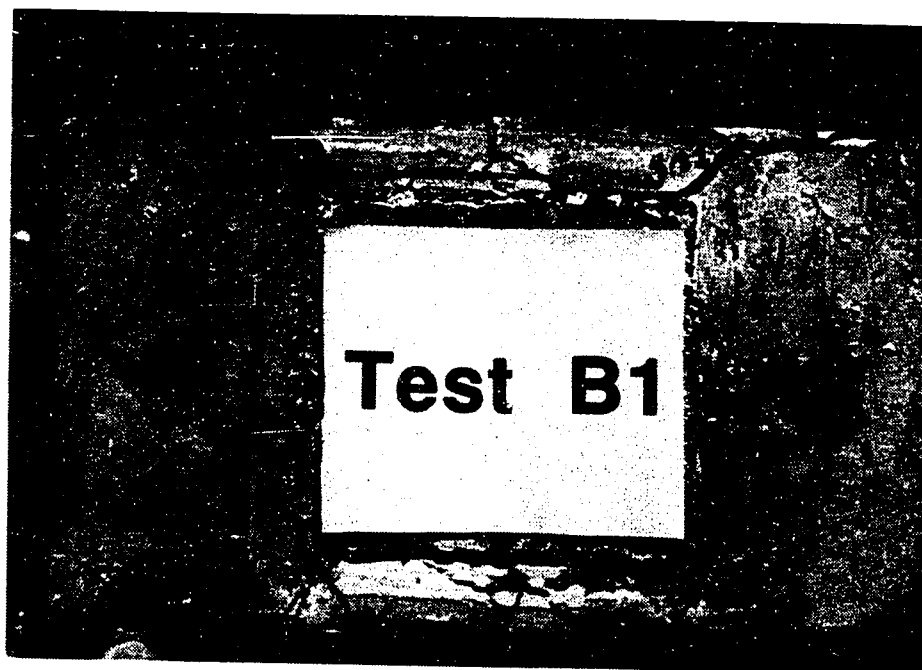


Figure 3.24 Loading Surface of Specimen B1 after Ultimate

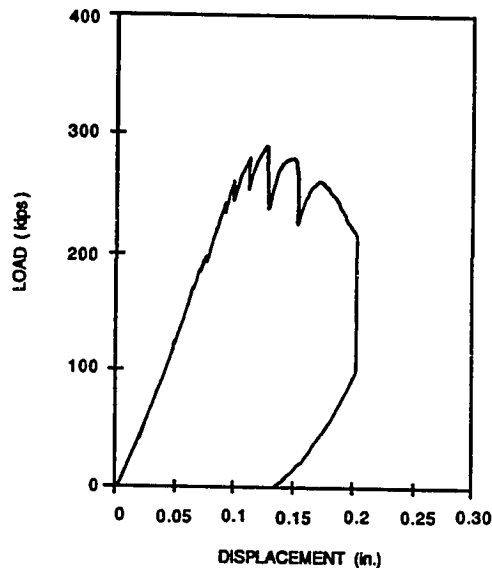


Figure 3.25 Load-Displacement Curve, Specimen B2

load-displacement curve at the ultimate load was very sharp and did not become rounded until reloaded to 280 kips. At 290 kips some concrete still remained uncracked across the specimen centerline and could be utilized to restrain the lateral spreading of the axial force. The load decreased suddenly after reaching 290 kips. The main centerline crack propagated to the base of the specimen as shown in Fig. 3.26. When reloaded to 280 kips, a rounded load displacement curve was seen. At 280 kips, the specimen was fully cracked along the specimen centerline so that the tensile contribution of the concrete was minimal. The strain data from the bursting reinforcement (see Fig. 3.27) shows a significant increase in strains immediately after reaching the first cracking load of 186 kips. This clearly demonstrates that the bursting force was carried previously by the tensile strength of the concrete before cracking and was transferred to the reinforcement after cracking. The spiral behaved in a similar manner as in Specimen B1, reaching a maximum strain of 400 microstrain. The final cracked state of Specimen B2 was similar to Specimen B1. The centerline crack width at 280 kips was 0.063 inches at 4 inches from

the top and 0.055 inches at the mid height of the specimen.

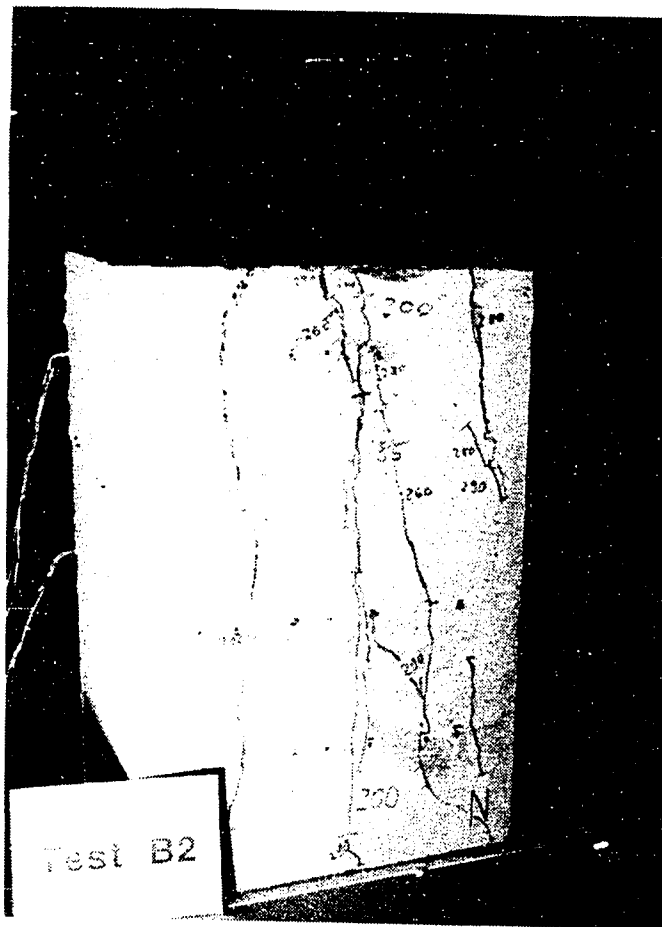


Figure 3.26 Cracking Pattern for Specimen B2 at Ultimate

Specimen B3 (shown in Fig. 3.17b) had #2m reinforcing bars distributed evenly from 4 inches to 17 inches below the loading plate with a centroid at 10 1/2 inches. The total tension bursting reinforcement capacity was 39.6 kips. The load-displacement curve for Specimen B3 shown in Fig. 3.28 was very similar to that of Specimen B2. The initial cracking of the specimen along the centerline occurred at 217 kips and did not alter the axial stiffness of the system, 2,390

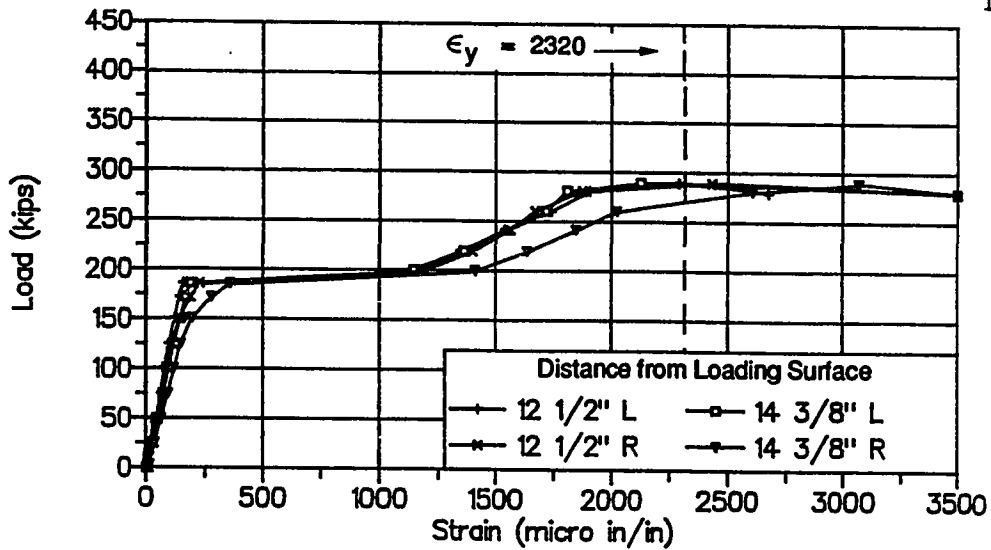


Figure 3.27 Bursting Strain Data, Specimen B2

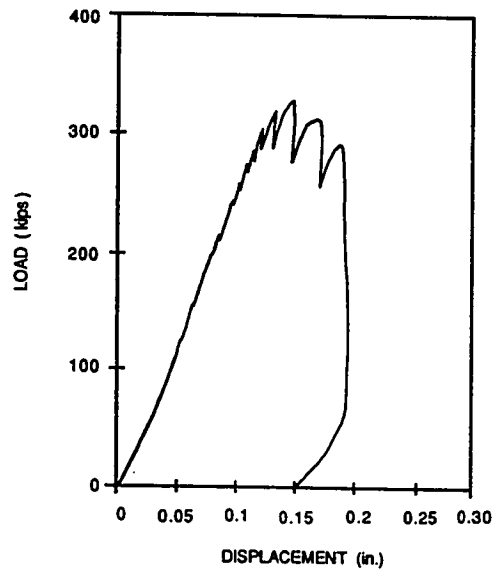


Figure 3.28 Load-Displacement Curve, Specimen B3

kips/in. At the ultimate load of 331 kips, some concrete was still uncracked along the centerline, as indicated by the sharp peak of the load-displacement curve. Strain data from the bursting reinforcement is shown in Figs. 3.29 and 3.30. At the ultimate load, all

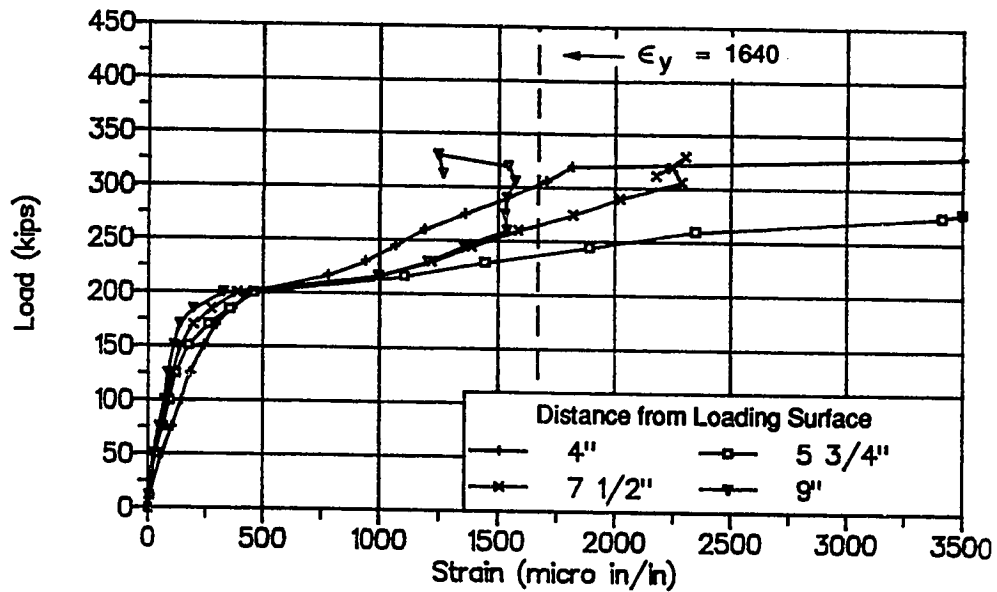


Figure 3.29 Bursting Strain Data, Specimen B3, Close Reinforcement

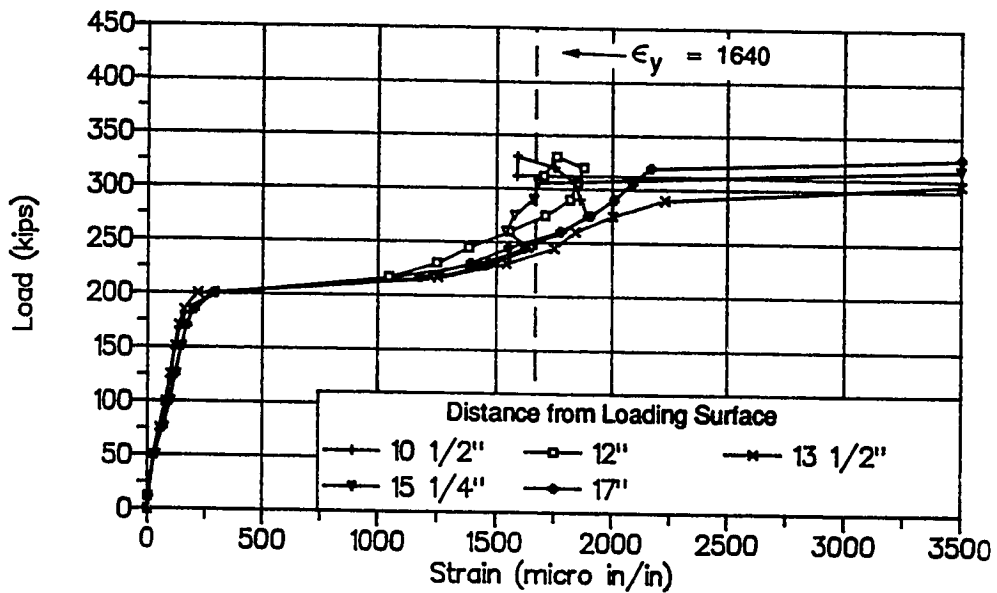


Figure 3.30 Bursting Strain Data, Specimen B3, Distant Reinforcement

the bursting reinforcement had effectively yielded. Bursting reinforcement located at 9 inches and 10 1/2 inches from the loading plate was close to the end of the spiral, which was a #4 smooth bar. The spiral hinders the development of the large strains necessary for yielding. The force in the #2 bar was transferred to the spiral over the crack region. Figure 3.31 shows a uniform percentage of force along the entire length of Specimen B3; this indicates a movement away from the elastic distribution towards a plastic distribution.

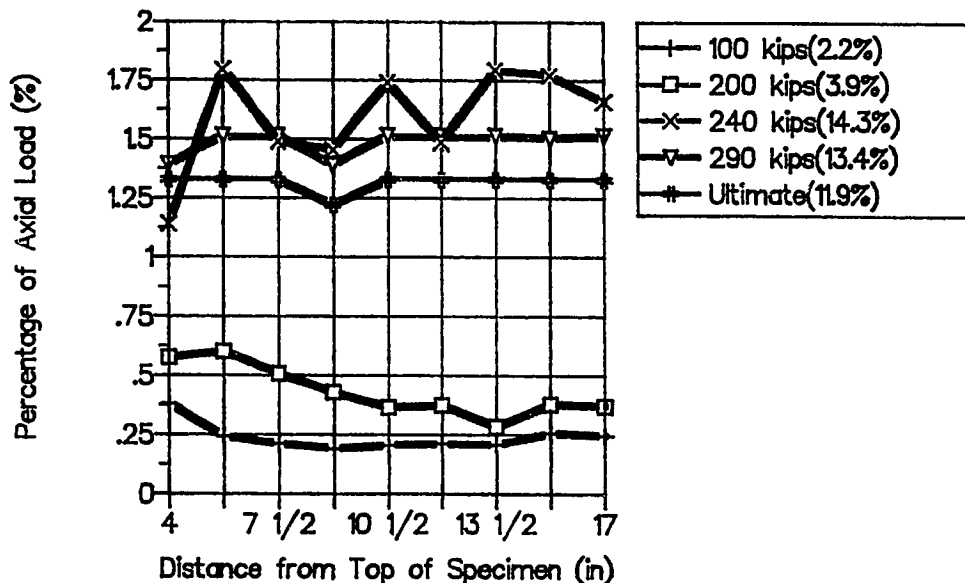


Figure 3.31 Specimen B3 Bursting Force as a Percentage of Applied Axial Load

In Specimen B4, the bursting reinforcement was distributed from 4 1/8 inches to 18 1/2 inches as shown in Fig. 3.17c and described in Table 3.3. The total tension bursting reinforcement capacity was 42.6 kips with a reinforcement centroid of 9 3/8 inches. The bursting reinforcement was distributed according to the elastic analysis distribution. Figure 3.32 shows the bursting reinforcement stress distribution compared to the predicted elastic distribution for

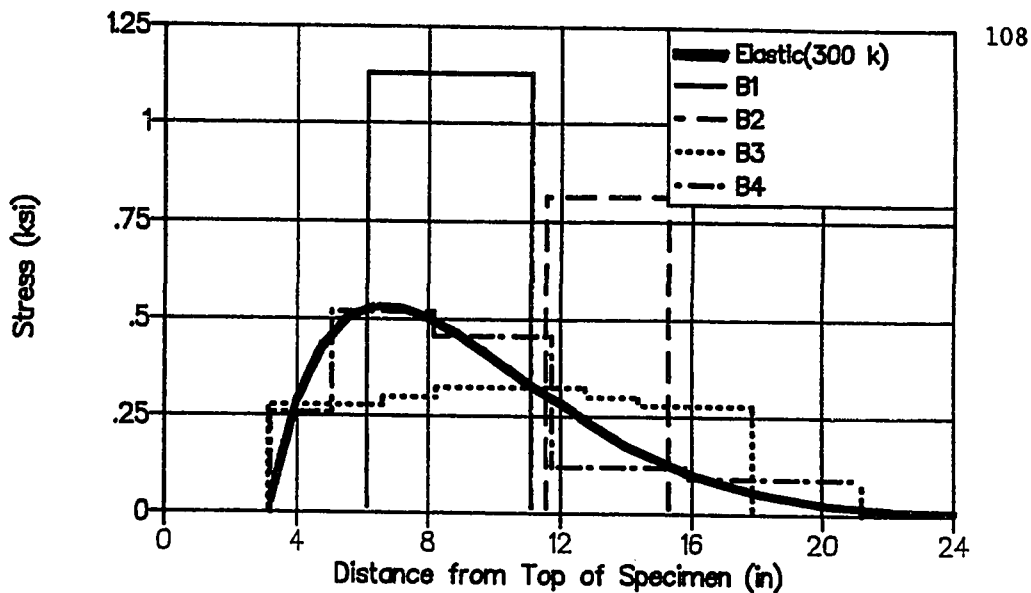


Figure 3.32 Specimen B1 to B4 Bursting Reinforcement Distribution Compared with the Elastic Stress Distribution

Specimens B1 to B4. Specimen B4 was the closest to the elastic distribution, while B2 was the farthest away. The stress distribution determined assumed a full yield of the bursting reinforcement, no tensile concrete stresses across the centerline, and a uniform distribution spread over an area equal to the reinforcement spacing by a unit thickness. The elastic stress distribution was based on an axial load of 300 kips. The load-displacement curve in Fig. 3.33 had a linear behavior well above the first cracking load of 200 kips with an axial stiffness of 2,810 kips/in. The peak load was 337 kips and, as with Specimen B1, had a rounded top on the load-displacement diagram which indicates a fully cracked section along the centerline. The bursting strains of Fig. 3.34 show that all the reinforcement yielded, except the bars in row three, 10 3/8 inches from the loading plate. As in Specimen B3, these bars were located near the end of the spiral which prevents large strains from developing in the bursting reinforcement. Figure 3.35 shows the effective bursting force per bar divided by the applied load for various load stages. Peak strains in

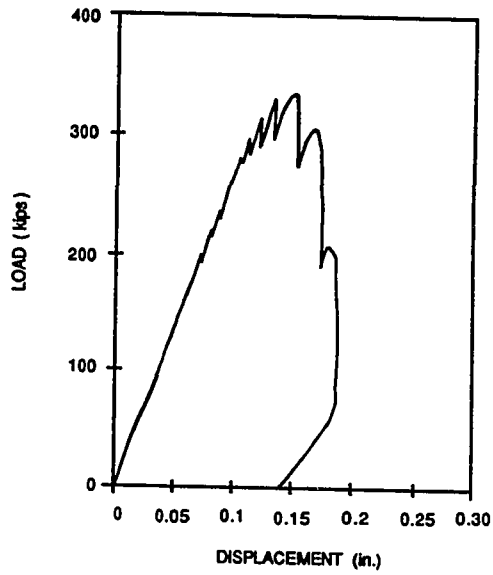


Figure 3.33 Load-Displacement Curve, Specimen B4

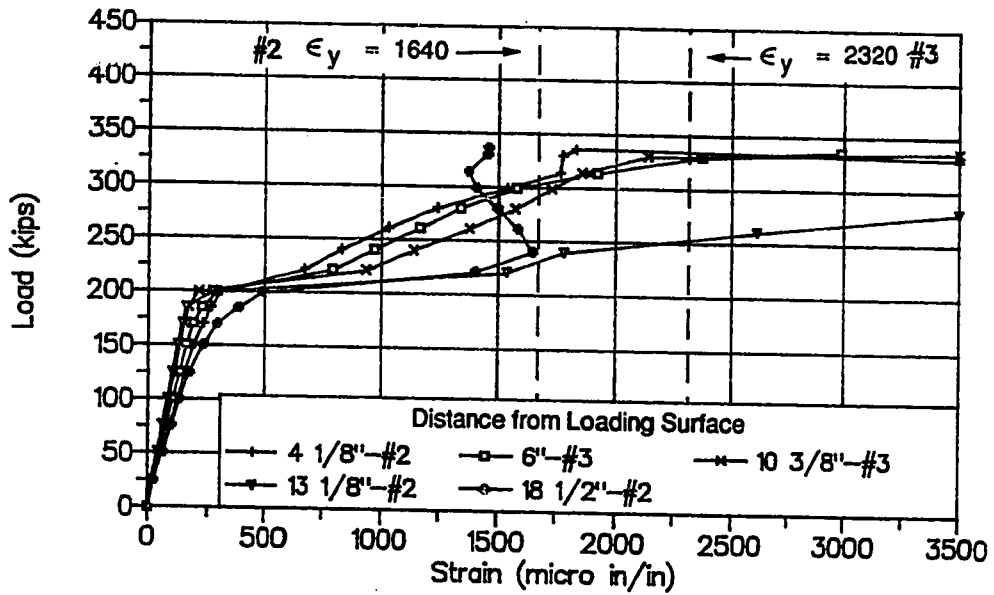


Figure 3.34 Bursting Strain Data, Specimen B4

the local zone spiral were no greater than 675 microstrain. Figure 3.35 shows the final crack state for Specimen B4. The first crack was very similar to those of the previously described tests with the initial crack being along the specimen centerline. During the test, the centerline crack width grew and additional cracks opened near the anchorage plate. The cracked state at ultimate was very extensive with cracks located over a majority of the section. There were also cracks on the transverse face as seen in Fig. 3.36.

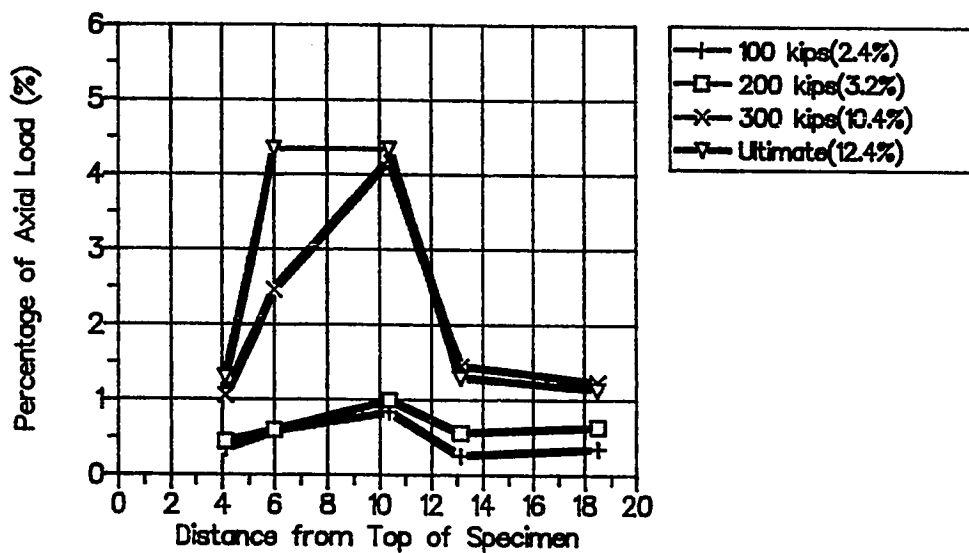


Figure 3.35 Specimen B4 Bursting Force as a Percentage of Applied Axial Load

Specimen B5 had no general zone reinforcement but had a #4 smooth spiral in the local zone (see Fig. 3.37a). The first cracking load was 170 kips, but the specimen was able to reach 212 kips before failure. Figure 3.38 shows the load-displacement curve for Specimen B5 indicating that the overall stiffness stayed near a constant 2,730 kips/in until failure when the load dropped quickly to 25 kips. This

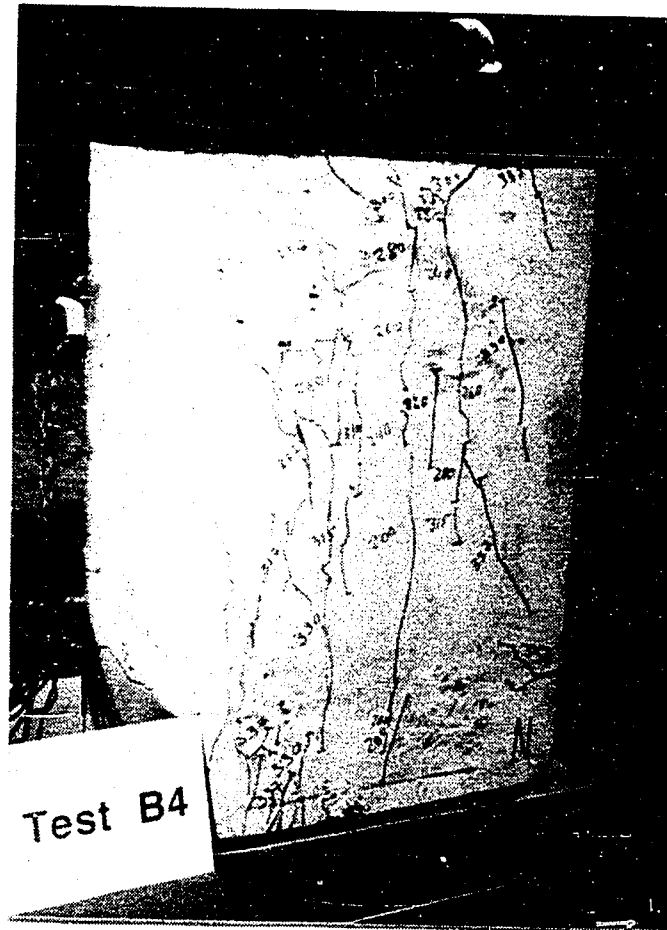


Figure 3.36 Specimen B4 Cracking Pattern at Ultimate

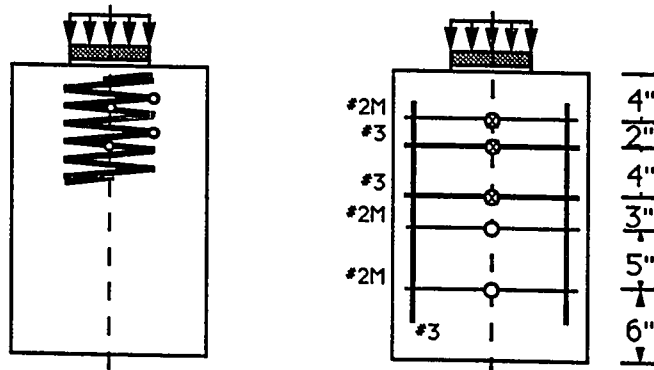


Figure 3.37 Specimen B5 and B6 Details

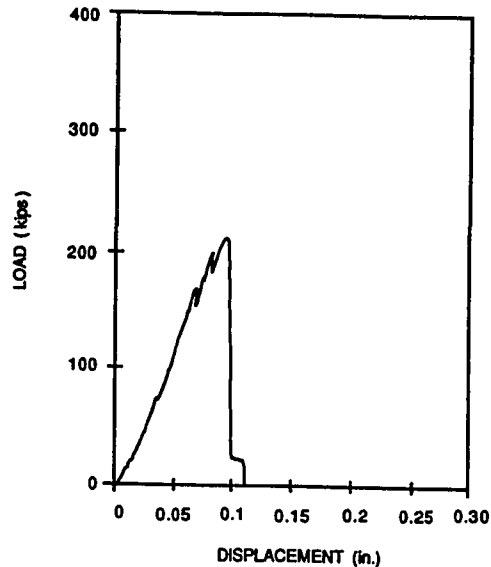


Figure 3.38 Specimen B5 Load-Displacement Curve

behavior can be seen in the comparison of the sizes of cracks in pictures taken just before (Fig. 3.39) and after (Fig. 3.40) the ultimate load. After the ultimate load, the crack along the centerline was significantly wider and assures that there was no uncracked concrete across the centerline. The strain data from the spiral had no strains above 100 microstrain.

Specimen B6 was essentially the same as Specimen B4 except that there was no local zone spiral (see Fig. 3.37b). The centroid of the bursting reinforcement was slightly higher, 9 1/8 inches versus 9 3/8 inches. Figure 3.41 shows a comparison of the load-displacement curves of Specimens B4 and B6 indicating very similar initial loading behavior. Specimen B6 had an axial stiffness of 3,120 kips/in. The first crack for B6 occurred at 171 kips, and the specimen had an ultimate load of 297 kips. The load-displacement curve indicated a substantially less ductile failure than for Specimen B4. The area under the load-displacement curve for Specimen B6 is approximately half of that for Specimen B4. This indicates the importance of the local

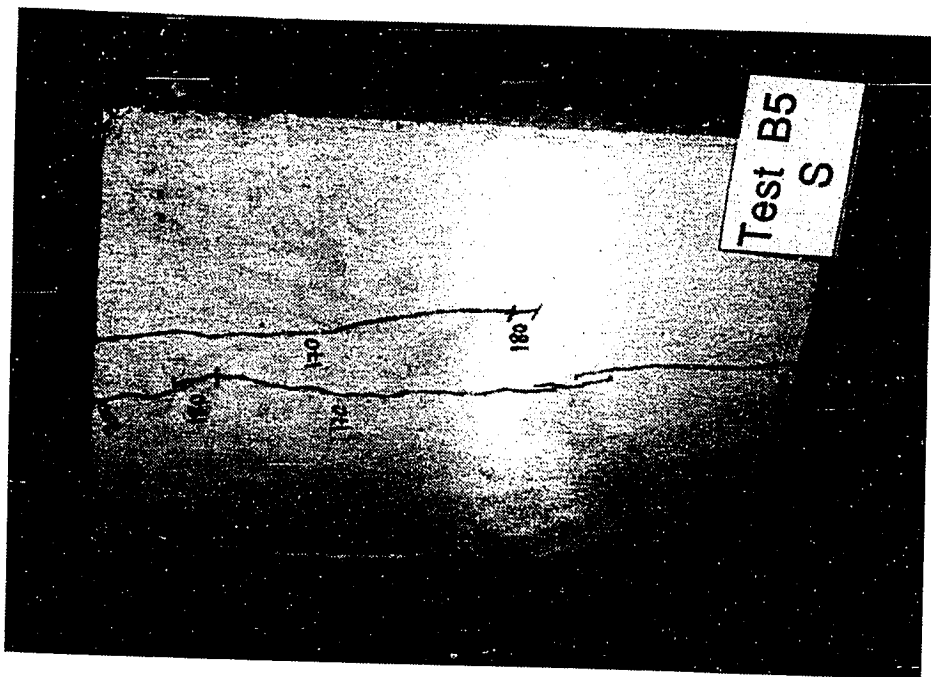


Figure 3.39 Specimen B5 Crack Pattern
Just Before Ultimate Load

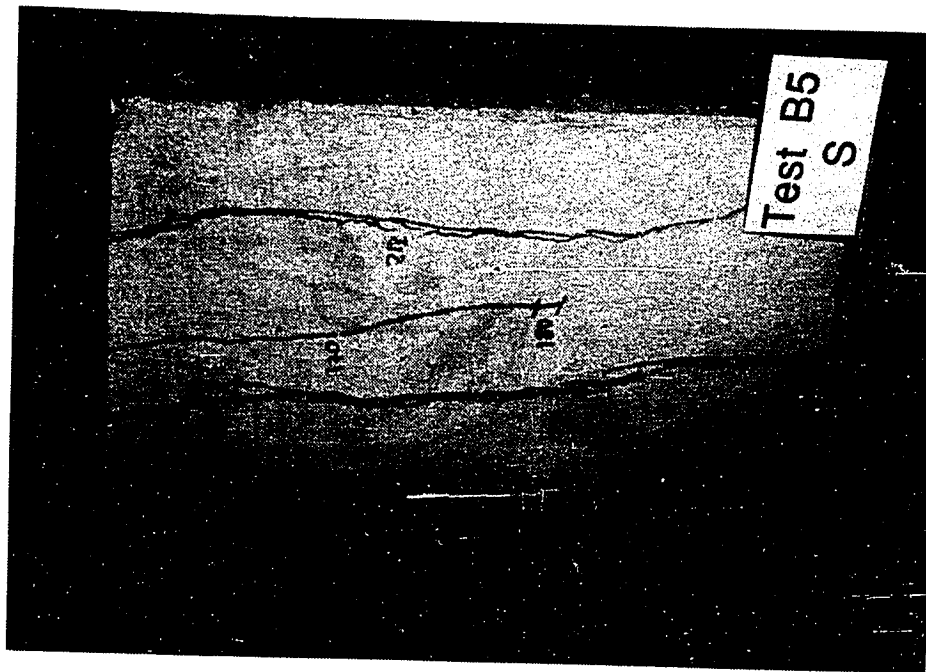


Figure 3.40 Specimen B5 Crack Pattern
After Ultimate Load

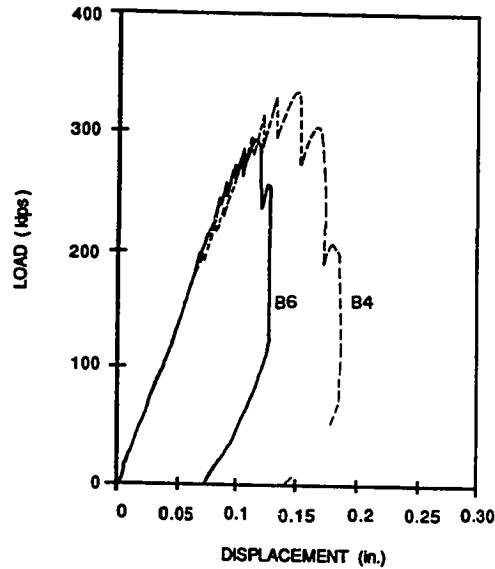


Figure 3.41 Specimen B6 Load-Displacement Curve

zone confining spiral in providing local zone ductility. The bursting reinforcement strain data of Fig. 3.42 indicated that all of the bursting reinforcement had yielded at the peak load. The bursting reinforcement located in the section had yielded by 250 kips. Specimen B6 had a cracking pattern, at first crack and ultimate, comparable to that of Specimen B4.

Specimen B7 was practically the same as Specimen B4 with the exception that B7 included a post-tensioning duct. The duct was added to model more accurately actual post-tensioning applications (see Fig. 3.43a). The duct was 2 inches in diameter, reducing the effective concrete cross section along the section centerline to 7 inches. The comparison of load-displacement curves for Specimens B7 and B4 shown in Fig. 3.44 indicates very similar stiffness (B7-2,970 kips/in and B4-2,810 kips/in) and ultimate load, with Specimen B4 reaching a slightly higher load. The ultimate load for Specimen B7 was 296 kips with a first cracking load of 170 kips. The strain data and cracking patterns from Specimen B7 were very similar to those of Specimens B4 and B6 and,

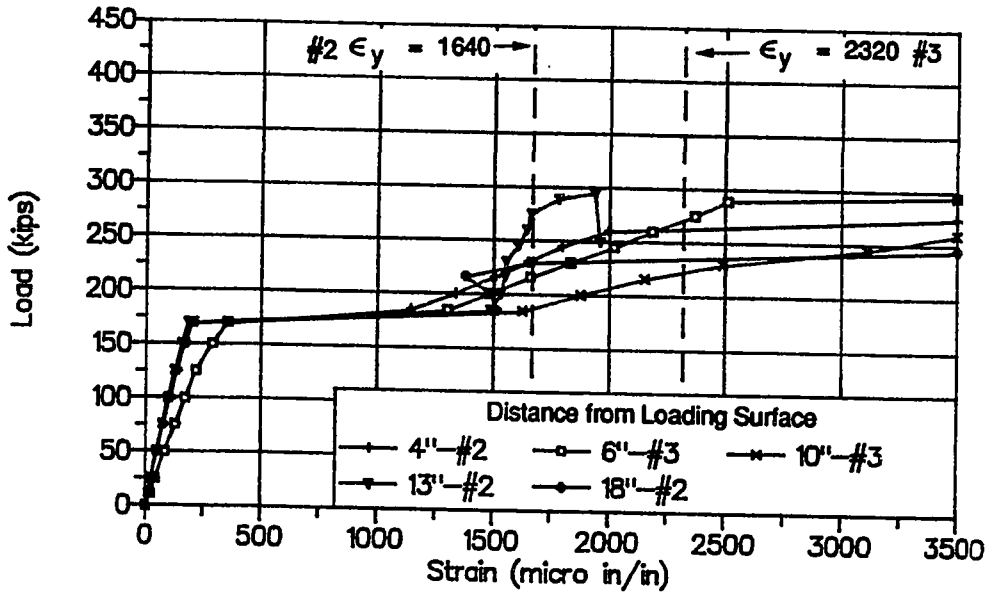
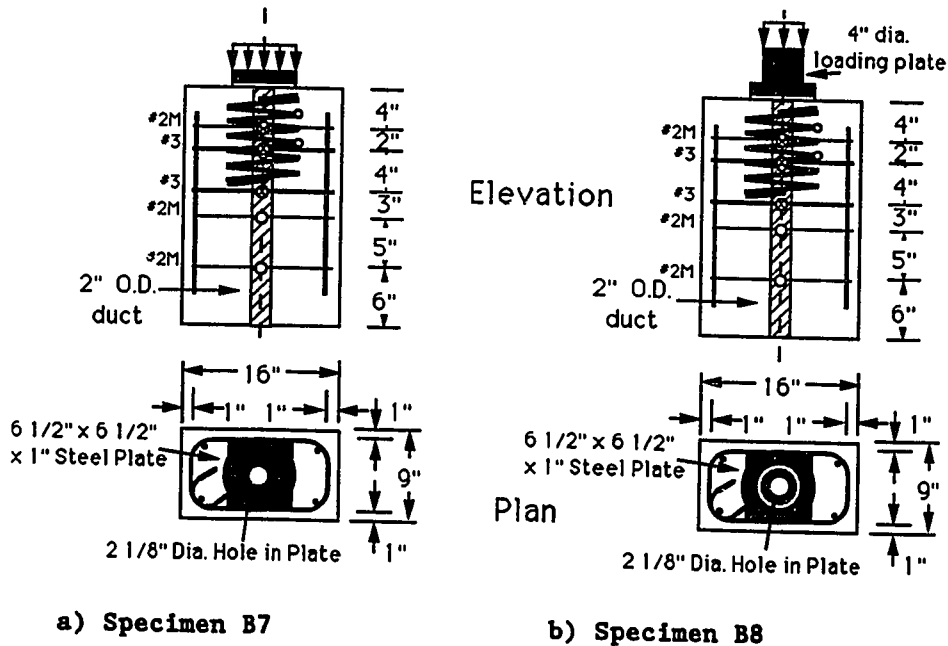


Figure 3.42 Bursting Strain Data, Specimen B6



a) Specimen B7

b) Specimen B8

Figure 3.43 Specimen Details for Specimens B7 and B8

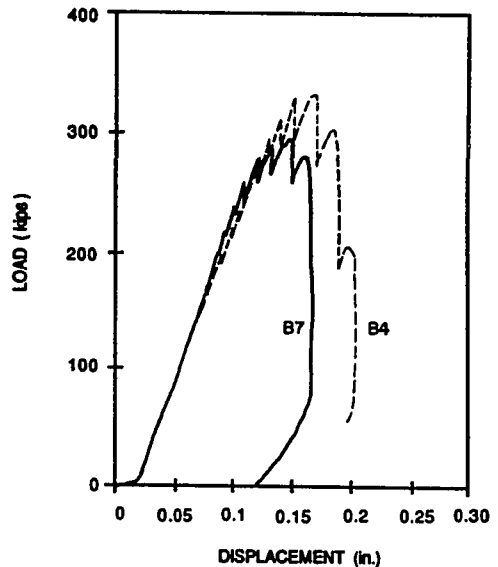


Figure 3.44 Specimen B7 Load-Displacement Curve

therefore, were not shown.

Specimen B8 was identical to Specimen B7, except that it was loaded through a 4-inch diameter pedestal (see Figs. 3.43b and 3.45) placed on top of the 6 1/2 inch square loading plate instead of over the full plate width. Loading the specimen through the pedestal modelled the loading of an anchorage device through a wedge plate with a diameter of 4 inches. The load-displacement curves for B4, B7, and B8 are shown in Fig. 3.46. The axial stiffness of Specimen B8 was reduced to 2,500 kips/in. because of the reduction in the effective width of the bearing plate. The first crack and ultimate loads were also reduced to 156 kips and 276 kips respectively. The load-displacement curve also shows a sharp peak for the ultimate load, but the specimen was reloaded to 273 kips. The bursting reinforcement strain data from Specimen B8 shown in Fig. 3.47 indicate a yielding of all bursting reinforcement. The cracking patterns were again very similar to previous "B" series tests.

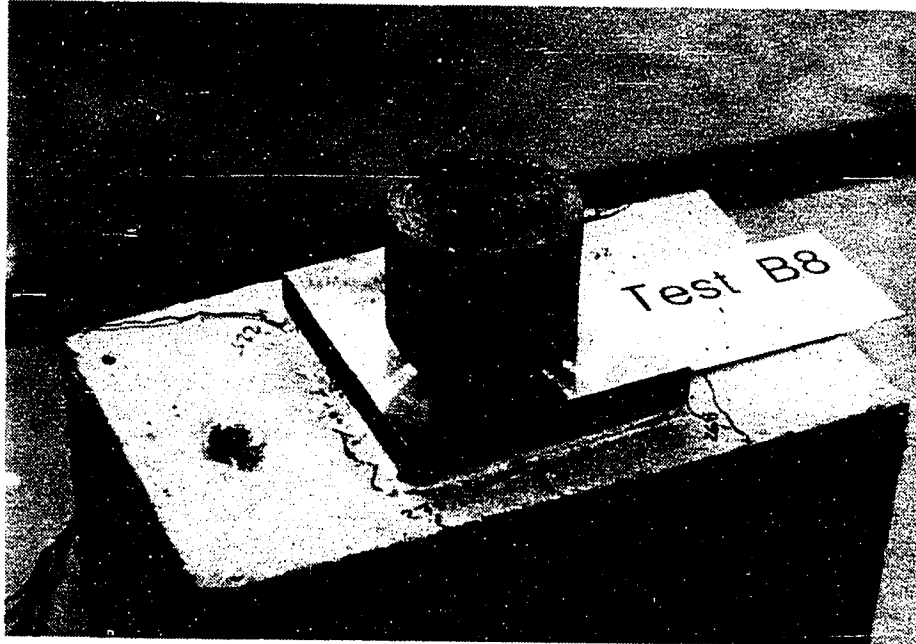


Figure 3.45 Specimen B8 Loading Pedestal

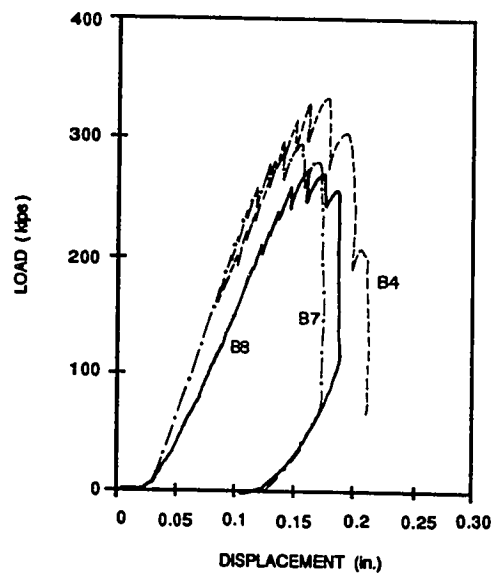


Figure 3.46 Specimen B8 Load-Displacement Curve

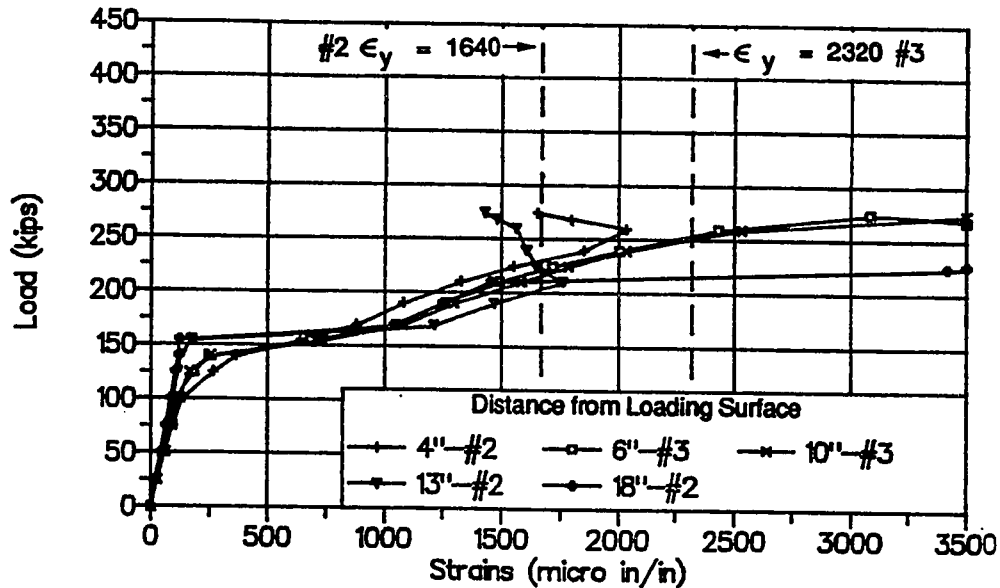


Figure 3.47 Bursting Strain Data, Specimen B8

3.2.3 Specimen C1. The objective of Specimen C1 (see Fig. 3.48) was to test a concentric specimen with a substantially reduced ratio of anchor width to section height (a/h). Series "A" had an a/h ratio of 0.333, while the a/h for Series "B" was 0.406. Specimen C1 had an a/h of 0.181. The anchorage device used was a multiple-plane anchorage for seven 1/2-inch diameter strands with outer dimensions of 6.5 x 6.5 inches (see Fig. 3.49). The bursting reinforcement for the specimen consisted of four layers of #3 Grade 60 (see Table 3.5) reinforcing bars which were at an average depth of 15 inches. The bursting reinforcement had a total tension capacity of 52.8 kips. The local zone reinforcement for Specimen C1 was a #4 smooth spiral with a 7-inch diameter and a 1 3/4-inch pitch. There were a total of six turns with the first half turn, and the last half turn tied to the adjacent turn. The modulus of elasticity of the spiral was 26,900 ksi with a yield strength of 80.3 ksi. As with the other concentric specimens, strain gages were located along the specimen centerline. One bar also

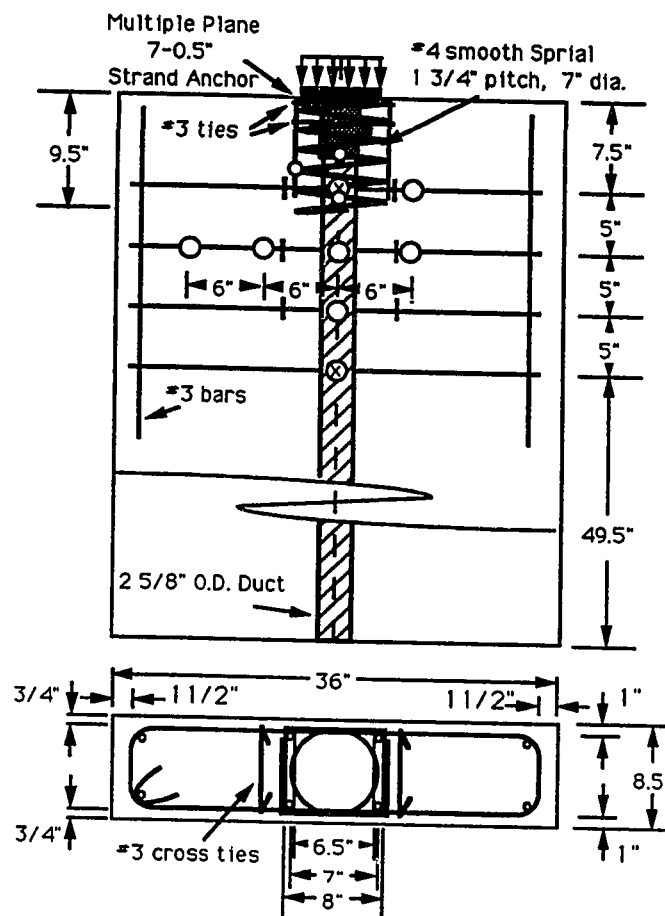


Figure 3.48 Specimen C1 Detail

Table 3.5 Specimen C1 Material and Test Information

| Concrete (psi) | | E (ksi) | #3 Bursting Reinforcement | | | First Crack (kips) | | Ultimate (kips) | |
|-------------------|--------|--------------|---------------------------|----------------|-------------------------------|-----------------------|------|--------------------|--|
| f_{sp} | f'_c | | F_y (kips) | f_y (ksi) | Yield Strain (microstrain) | | Peak | Secondary | |
| 379 | 5190 | 27500 | 6.60 | 60.0 | 2430 | 225 290 | 370 | 345 | |

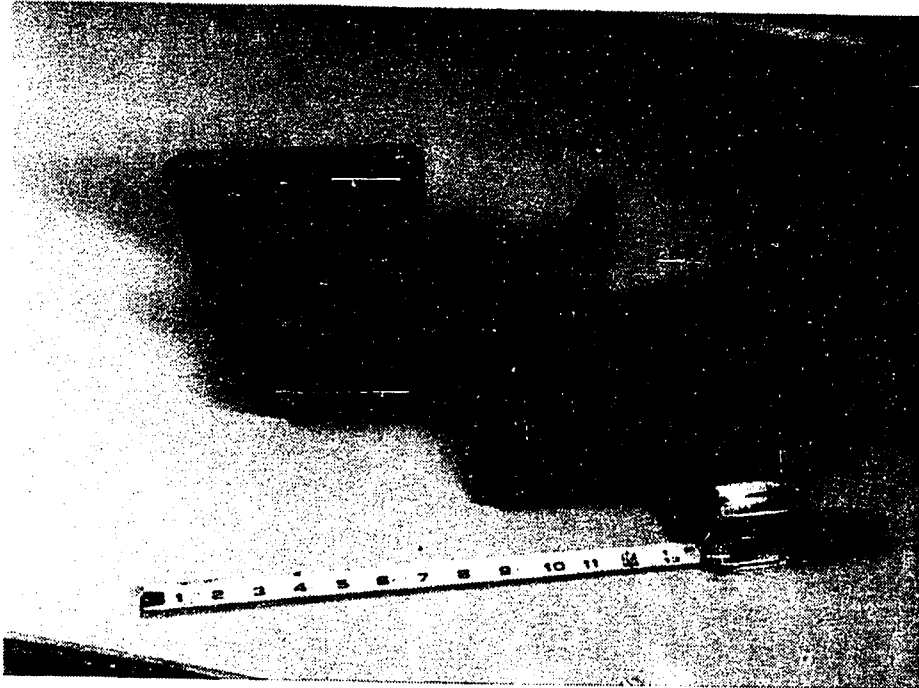


Figure 3.49 Photographs of Multiple-Plane Anchorages

had strain gages along its length at 6-inch intervals (see Fig. 3.48). The concrete used for Specimen C1 was a nominal 4,000 psi 3/8 inch maximum aggregate mix.

The load-displacement curve (see Fig. 3.50) was very similar to the other concentric specimens. Specimen C1 had an initial axial stiffness of 1650 kips/in. The loss of load after each load stage became more pronounced as the applied load increased. The first surface crack occurred along the specimen centerline at 225 kips. Figure 3.51 shows the width of the main centerline crack at various load stages. The crack was measured with a 60-power hand-held microscope. The smallest division on the microscope was 0.001 inches. Measurement of the crack was very subjective. A mark was placed on the concrete, so that the crack width was measured at the same location every time. The crack surfaces were jagged. The width measurement of the crack can change very easily by 0.005 inches within a short

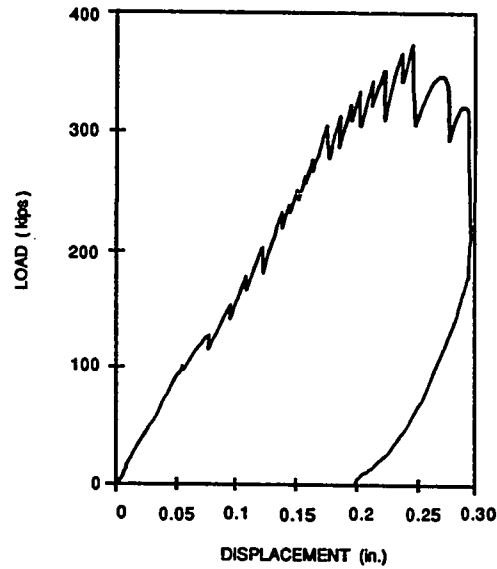


Figure 3.50 Specimen C1 Load-Displacement Curve

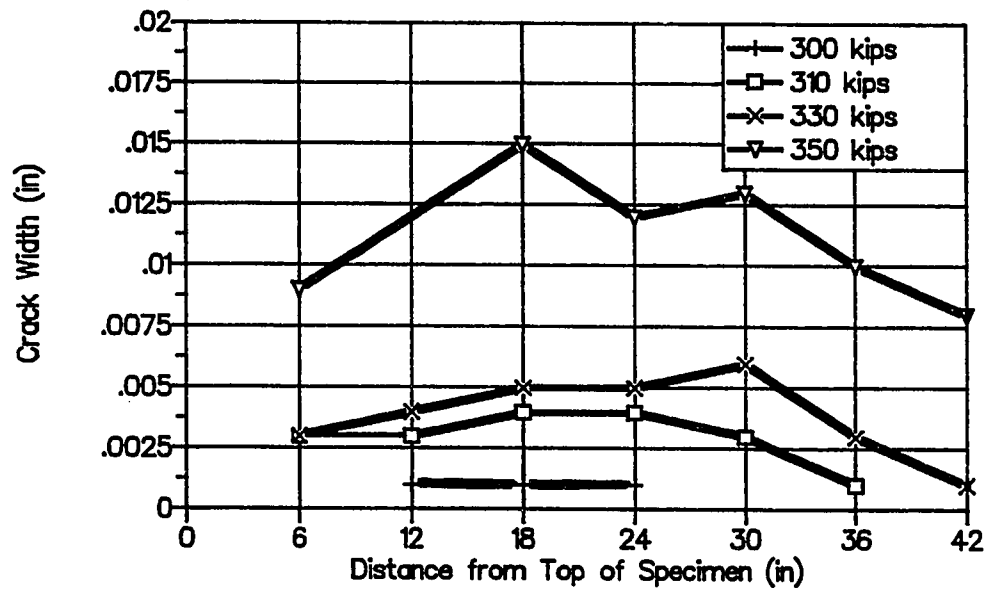


Figure 3.51 Specimen C1 Crack Widths along Centerline

distance. The crack width was fairly well controlled until 350 kips, when the centerline crack propagated to the base of the specimen. Figure 3.52 is a summary of bursting strain data. The strains in the bursting reinforcement were almost identical until first cracking at 225 kips. They continued to be small until just after 300 kips when the concrete became sufficiently cracked so as to clearly transfer substantial force to the bursting reinforcement. Figure 3.53 shows the strains in the bursting reinforcement bar 12 1/2 inches from the top of the specimen. The figure shows the importance of extending the bars across the full width of the specimen and providing full development. The strains in the local spiral were higher than in the "B" series (see Fig. 3.54) with the strains in the lateral direction reaching 800 microstrain. The transverse spiral gage indicated very small strains. The ultimate load was 370 kips. The load-displacement diagram of Fig. 3.50 had a sharp peak at ultimate indicating that the concrete was

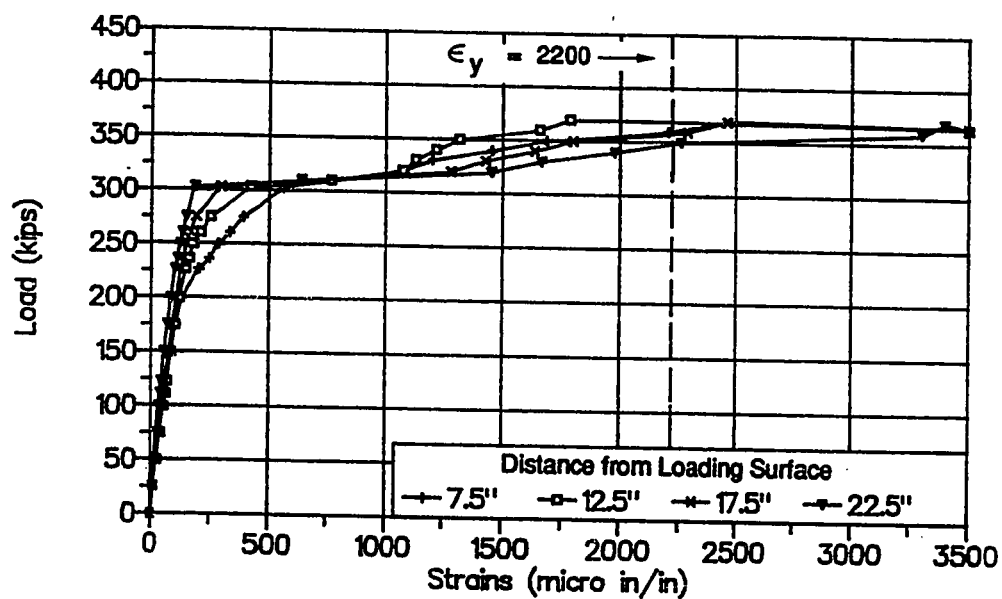


Figure 3.52 Bursting Strain Data along the Centerline, Specimen C1

still contributing significantly to the bursting force resistance across the centerline. The specimen was reloaded to 345 kips and a rounded load peak occurred. Figure 3.55 is a photo of Specimen C1 at ultimate. The crack pattern indicates that the load spread immediately from the anchorage device. As in previous tests, the largest crack was still the centerline crack. Since the specimen was tall and thin, transverse support was provided. The supports consisted of stiff steel frames with 3 x 4 inch support pads at the top and bottom of the frames. However, the pads were pressed against the specimen with a threaded rod and a nut that was only hand tight. In addition, there were two sheets of teflon between the pad and the concrete surface to allow lateral movement without transverse movement.

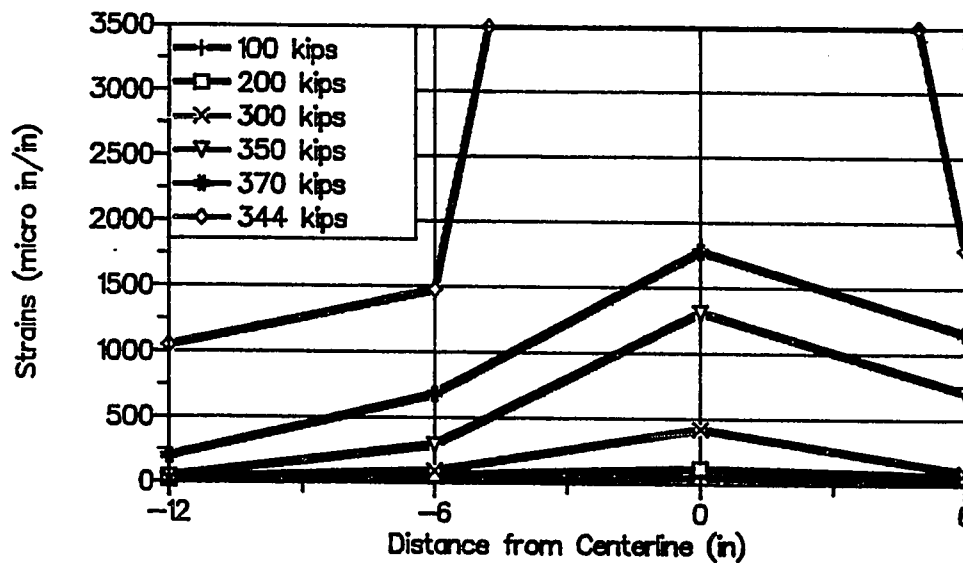


Figure 3.53 Bursting Strain Data along a Reinforcing Bar at 12 1/2 inches from the Loading Surface

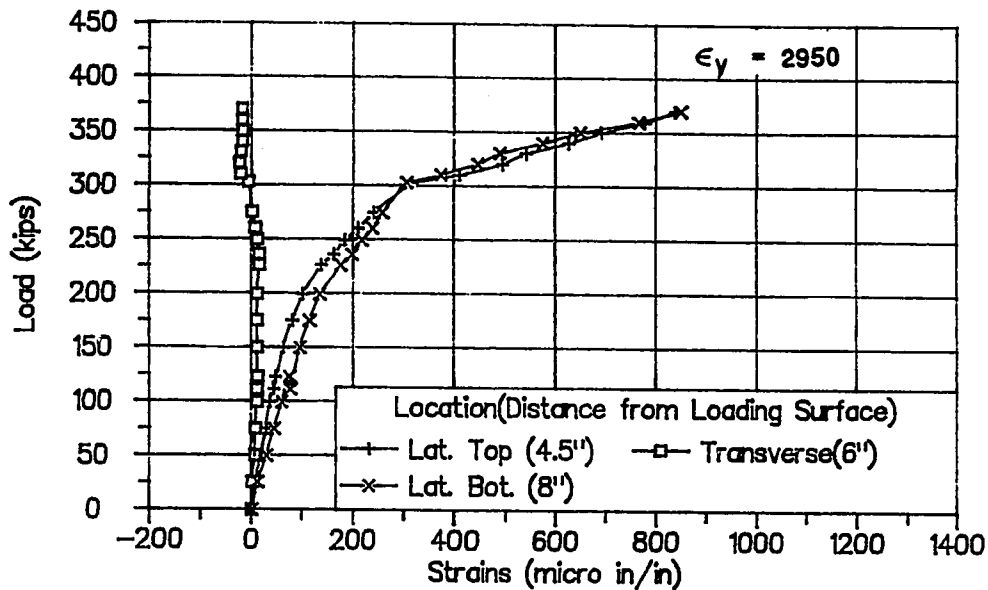


Figure 3.54 Spiral Strain Data, Specimen C1

3.2.4 Test Series "TPT". In test Series "TPT", the influence of lateral post-tensioning was studied. The four specimens had identical geometry (see Figs. 3.56 and 3.57) and non-prestressed reinforcement. The only variables were the position and the amount of lateral post-tensioning. The non-prestressed bursting reinforcement of each specimen had a total tension capacity of 26.2 kips at a centroid of 11 1/2 inches. All of the tests used a multiple-plane seven 1/2-inch diameter strand anchorage device described in section 3.2.3.

In the original test program, four specimens were planned as follows:

- TPT1) No Lateral Post-Tensioning,
- TPT2) 5/16-inch, 250-ksi strand stressed to 70 percent (10.2 kips) of ultimate at 10 1/2 inches below the loading surface,
- TPT3) Same force as in Specimen TPT2, but at 5 inches below the loading surface, and
- TPT4) Same location as in Specimen TPT3 but twice as much force by using two 5/16-inch, 250-ksi strands (20.3 kips).

Due to the behavior of Specimens TPT1 and TPT2, Specimen TPT3 was

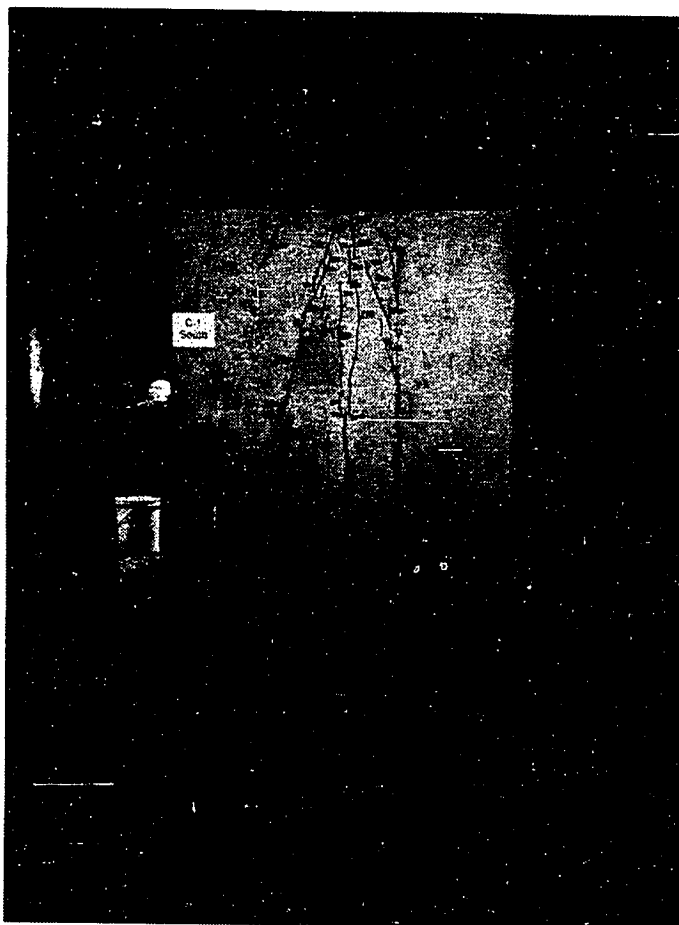
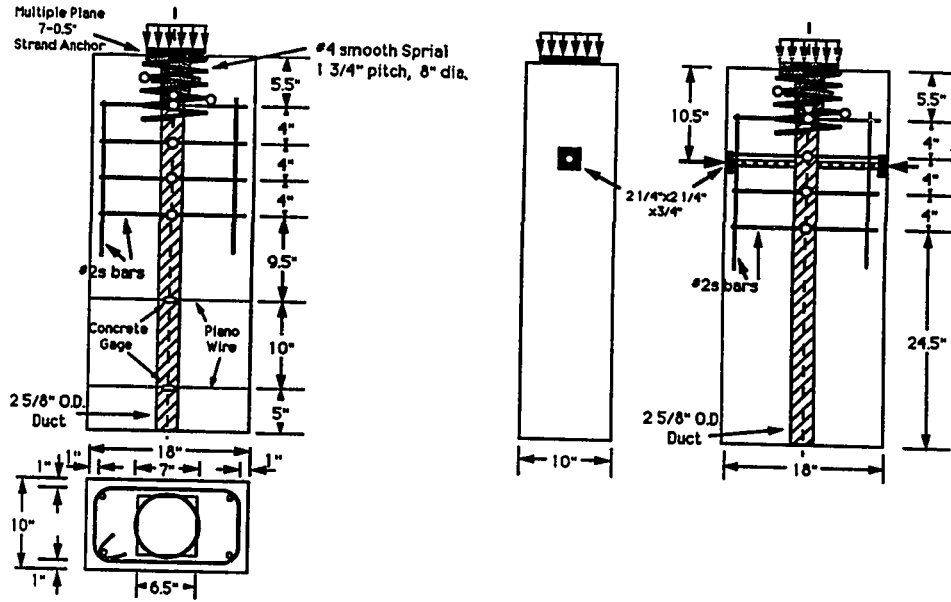


Figure 3.55 Specimen C1 Test Setup and Crack Pattern at Ultimate

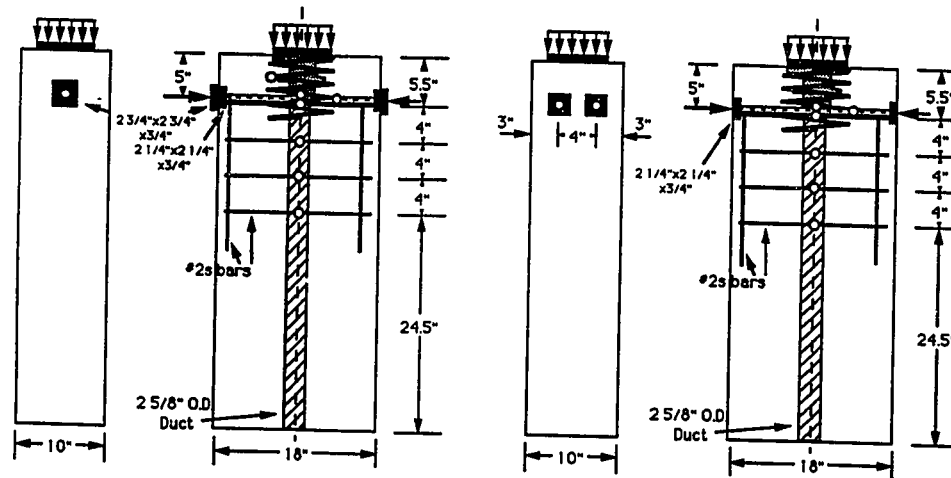
changed to a single 1/2-inch 270-ksi strand stressed to 70 percent of the ultimate tendon strength for a total force of 28.9 kips instead of the originally planned 10.2 kips. The reason for the change is discussed later. The local zone spirals used in all the tests were smooth #4 bars with a modulus of elasticity of 26,900 ksi and a yield strength of 80.3 ksi. The spiral had a 1 3/4-inch pitch, a diameter of 8 inches, and a total of five turns with the first half turn and the last half turn tied to the adjacent turn. Table 3.6 shows the material properties for Specimens TPT1 to TPT4.



a) Specimen TPT1

b) Specimen TPT2

Figure 3.56 Specimens TPT1 and TPT2 Details



a) Specimen TPT3

b) Specimen TPT4

Figure 3.57 Specimens TPT3 and TPT4 Details

Table 3.6 Material Information for Specimen TPT1 to TPT4

| Specimen | #2s Bursting Reinforcing Bar | | | | |
|----------|------------------------------|-----------------|-----------------------|-------------------------------|-----------------------|
| | E (ksi) | F_y (kips) | f_y (ksi) | Yield Strain (microstrain) | |
| All | 28900 | 3.57 | 75.1 | 2600 | |
| Specimen | Concrete | | Prestressing Steel | | |
| | f_{sp} (psi) | f'_c (psi) | Strand Size | E (ksi) | $0.7F_{pu}$ (kips) |
| TPT1 | 326 | 4950 | No Prestressing Steel | | |
| TPT2 | 326 | 4950 | 5/16 | 30200 | 10.2 |
| TPT3 | 409 | 5150 | 1/2 | - | 28.9 |
| TPT4 | 326 | 4950 | 2-5/16 | 30200 | 20.3 |

#2s has a cross sectional area of 0.0475 in^2

In order to accurately control the load in the very short length of the lateral post-tensioning strands, the application of the lateral post-tensioning was done with the use of a screw chuck (see Fig. 3.58) and strand strain gages for Specimen TPT2 and TPT4. A screw chuck was made by utilizing a standard chuck and a wedge system and then threading the outside surface to fit into a high strength nut. The top of the chuck was flattened to facilitate the use of a wrench. The strand was tightened by holding the chuck stationary, while the nut was turned to increase the elongation of the strand. The threads of the screw chuck were coated with an anti-seize material, and the bottom of the nut was sprayed with liquid teflon to help with the turning of the nut. The strain of the strand was measured with two strain gages placed on the strand. The modulus of elasticity of the strand was an effective modulus determined by placing gages on the strand and testing to 80 percent of F_{pu} .

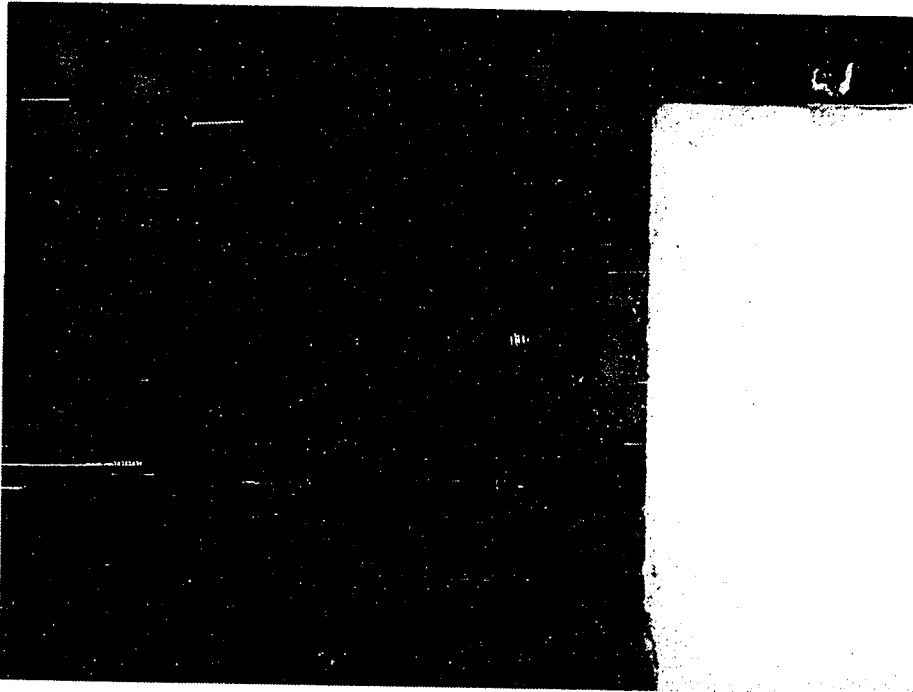


Figure 3.58 Screw Chucks

In Specimen TPT3, the diameter of the lateral duct was too small to allow both the strand and strain gages to fit, since a 1/2-inch strand was used instead of a 5/16-inch strand. Therefore, a load cell was utilized to measure the strand load. All strands were stressed with a hydraulic ram and pump.

Specimen TPT1 was the control specimen with no lateral post-tensioning. The load-displacement curve for Specimen TPT1 had an initial stiffness of 1860 kips/in (see Fig. 3.59). The first cracking load was 200 kips, and the ultimate load was 310 kips (see Table 3.7). As with other concentric specimens, the initial crack was along the specimen centerline. As the load was increased, the crack propagated down the specimen to the base (275 kips) resulting in an increase in the width of crack. Figure 3.60 shows the crack width for several load stages. The bursting strain data in Fig. 3.61 shows that all the bursting reinforcement yielded. Two concrete strain meters were cast into the concrete at the base of the specimen (see Fig. 3.62). The

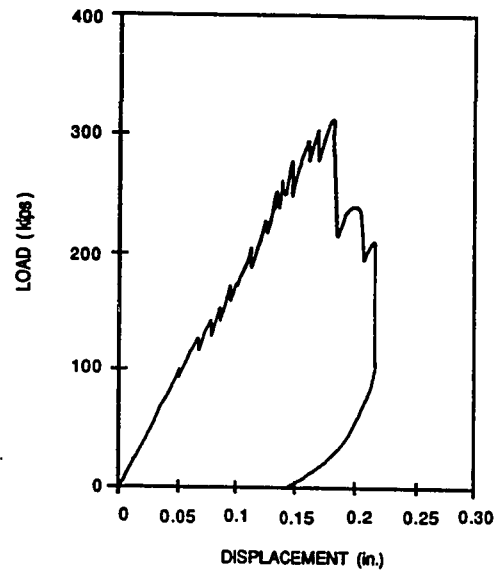


Figure 3.59 Specimen TPT1 Load-Displacement Curve

Table 3.7 Test Summary for Specimens TPT1 to TPT4

| Specimen | First Crack Loads | | Ultimate Loads | | | |
|----------|-------------------|---------------------|----------------|---------------------|----------------------|------------|
| | Axial (kips) | Lateral (kips)** | Peak (kips) | Secondary (kips) | Lateral (kips)*** | |
| TPT1 | 200 | 225 | NA | 310 | 240 | NA |
| TPT2 | 225 | 225 | 10.2 | 300* | 300 | 11.8 |
| TPT3 | 270 | 280 | 29.3 | 370* | 370 | 29.3 |
| TPT4 | 240 | 240 | 10.2, 10.3 | 332* | 326 | 11.2, 11.4 |

* - Load deflection curves at peak value have rounded tops

** - Lateral load at first cracking load

*** - Lateral load at ultimate load

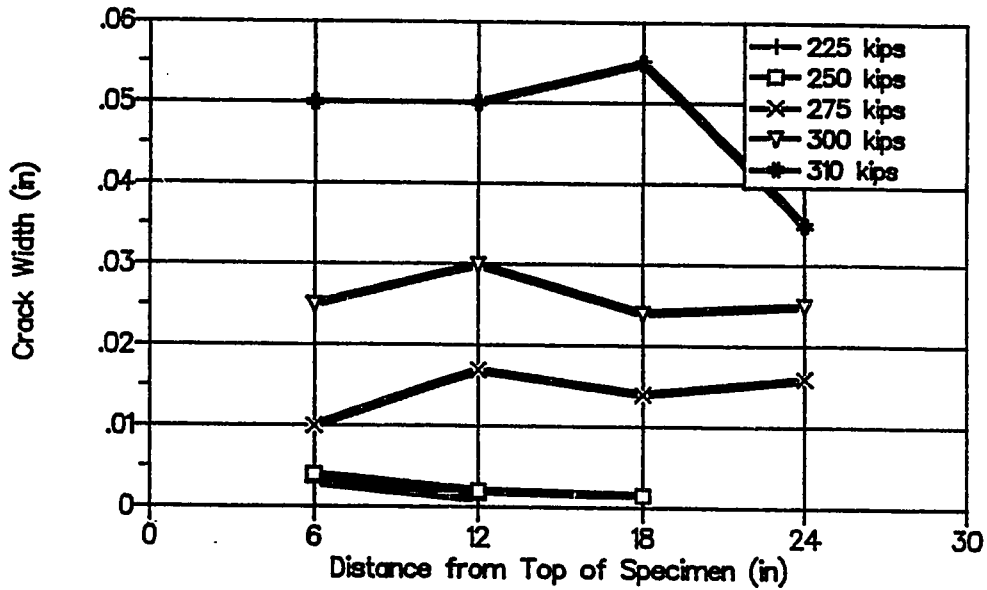


Figure 3.60 Specimen TPT1 Crack Width along Centerline

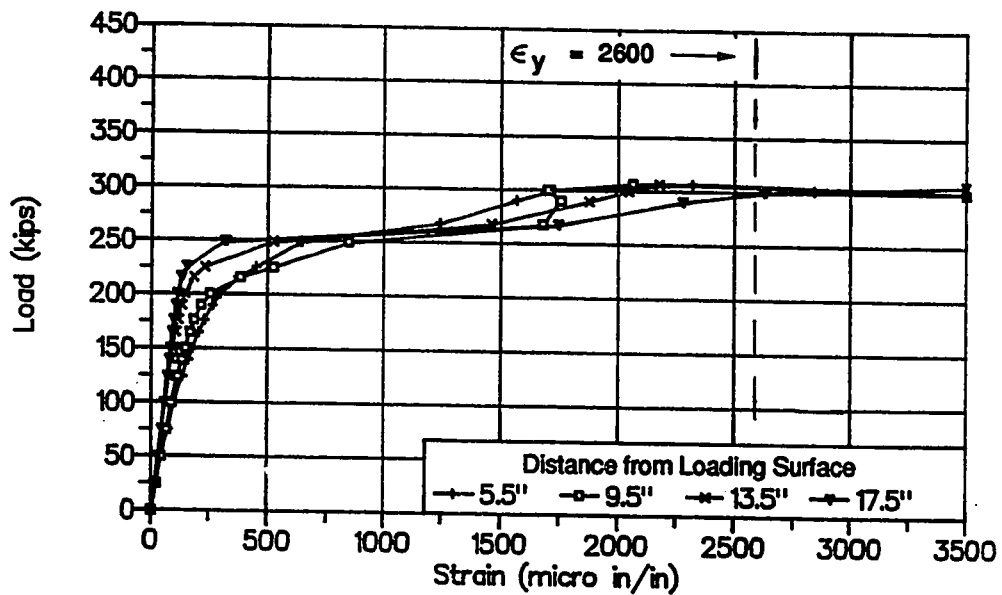


Figure 3.61 Bursting Strain Data, Specimen TPT1

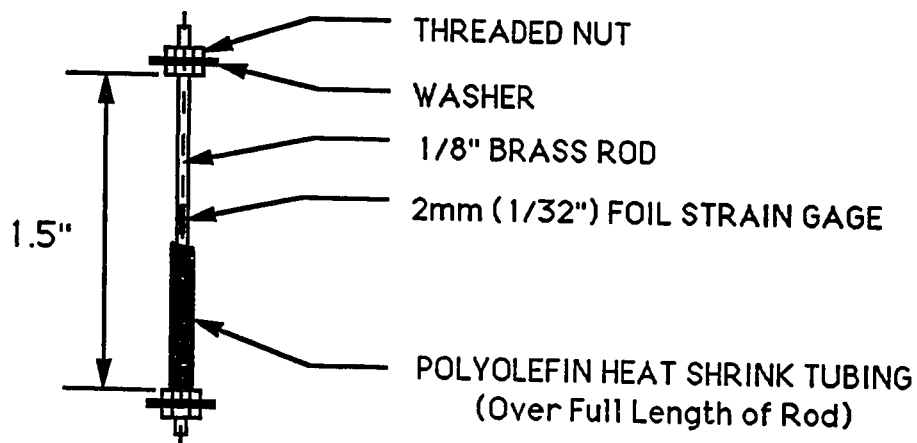


Figure 3.62 Concrete Strain Meter Detail

gage consisted of a brass rod with washers at each end and a strain gage in the middle that was protected with shrink tubing. Figure 3.63 shows the results of the concrete strain meters in comparison to the lowest layer of reinforcement strains. The strains in the concrete gages were very linear until a load of 250 kips and a strain of 90 microstrain. At 275 kips, when the centerline crack propagated to the base, the strains jump to 2,800 and 1,400 microstrain for the concrete gages located at 27 and 37 inches from the top of the specimen respectively. The strains continue to increase for the gage at 27 inches from the loading surface until 300 kips and 307 kips for the gage at 37 inches; when the strain reached these values, the readings became erratic. At the ultimate load, horizontal cracks formed on the transverse face of the specimen (see Fig. 3.64). The load-displacement curve of Fig. 3.59 reveals a steep drop after reaching the peak load of 310 kips. The specimen was reloaded to 240 kips. This load was the peak load that could be achieved upon reloading.

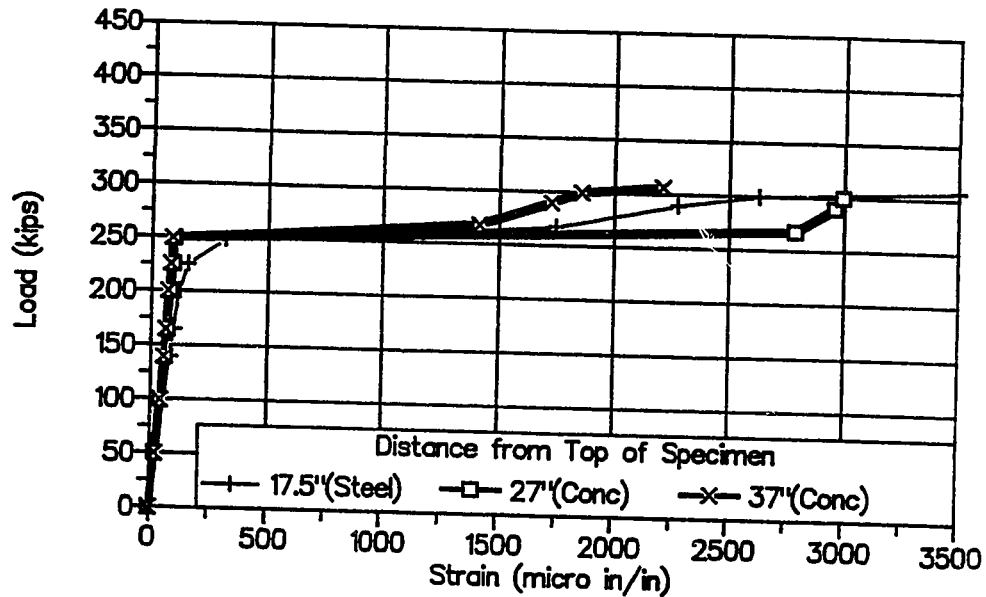


Figure 3.63 Concrete Gage Results from Specimen TPT1

Specimens TPT2 to TPT4 had lateral post-tensioning applied before the major axis loading. Figure 3.65 shows the predicted stress distribution from Burdet's [25] elastic finite element analysis along the specimen centerline for all the "TPT" series. Figure 3.66 shows the calculated reduction in the bursting stress for Specimen TPT4 at 240 kips due to the lateral post-tensioning. The application of lateral post-tensioning should raise not only the ultimate load but also the cracking load. Specimen TPT2 had 10.2 kips of lateral post-tensioning applied at a depth of 10 1/2 inches from the loading surface. The load-displacement curve for TPT2 (see Fig. 3.67) had an initial stiffness of 2,820 k/in with a peak load of 300 kips and was reloaded back to 300 kips after dropping to 250 kips. The bursting strains and cracking patterns were very similar to that of TPT1. Figure 3.68 shows the crack width for Specimen TPT2. A comparison with TPT1 at 300 kips shows a reduction in maximum crack width measured from

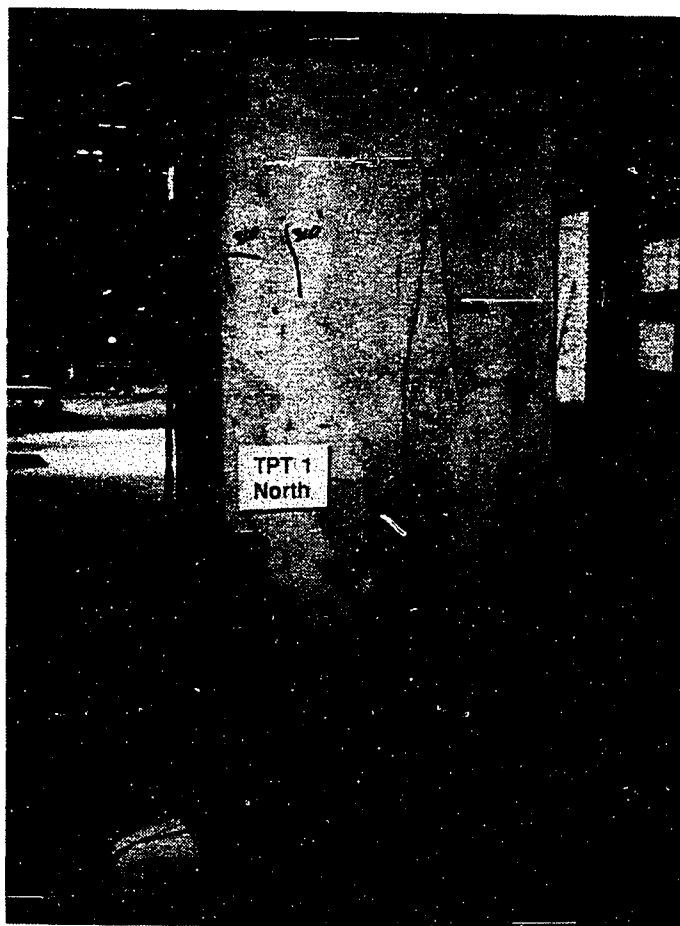


Figure 3.64 Specimen TPT1 Crack Pattern at Ultimate

0.03 inches to 0.015 inches. From TPT1 to TPT2, the cracking load increased from 200 to 225 kips but the ultimate load dropped from 310 kips to 300 kips. At the time of testing, it was decided that the lateral post-tensioning amount scheduled for TPT3 might not be large enough to show a difference in the effect on the capacity. Therefore, the 1/2-inch strand was used instead of the 5/16-inch strand for Specimen TPT3.

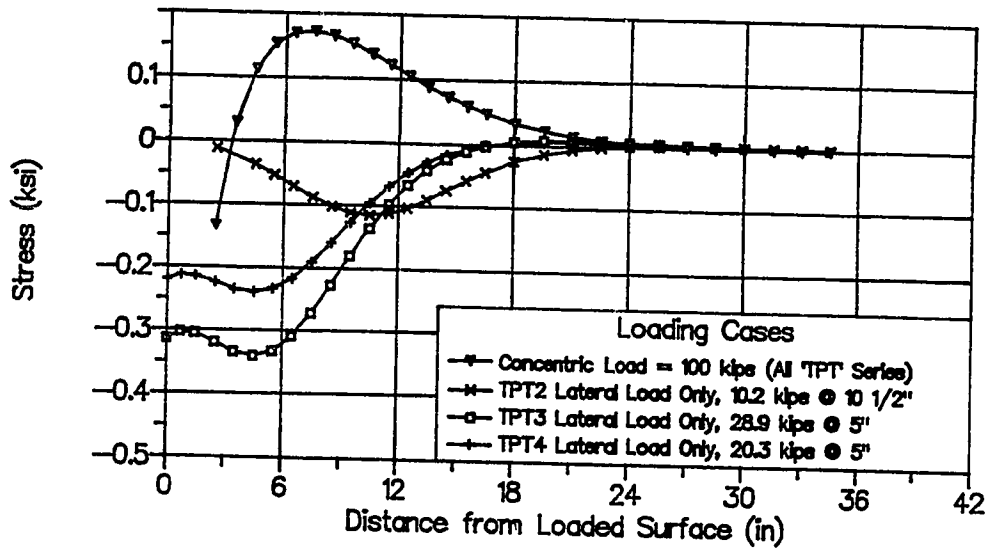


Figure 3.65 Lateral Post-Tensioning Stress Results

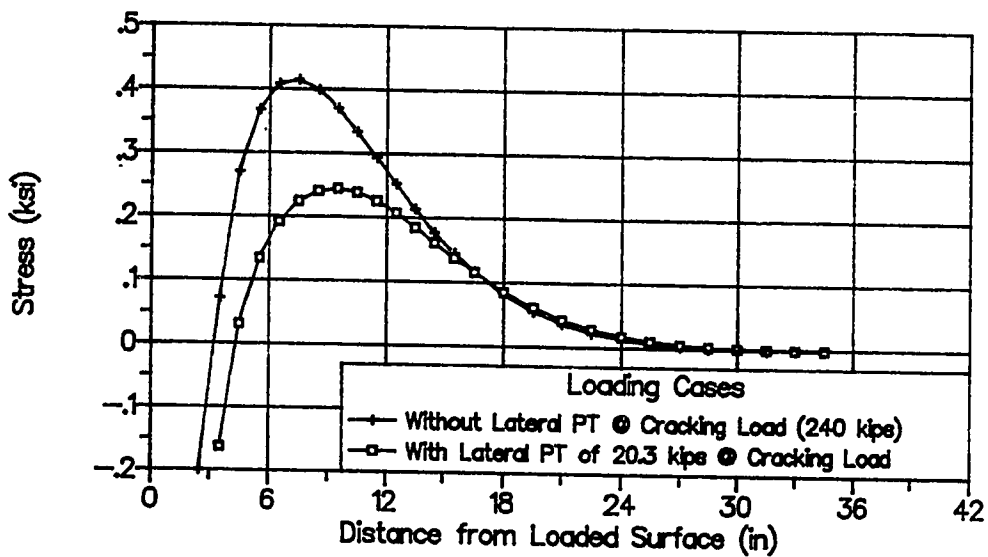


Figure 3.66 Effect of Lateral Post-Tensioning on Bursting Stress Distribution, Specimen TPT4

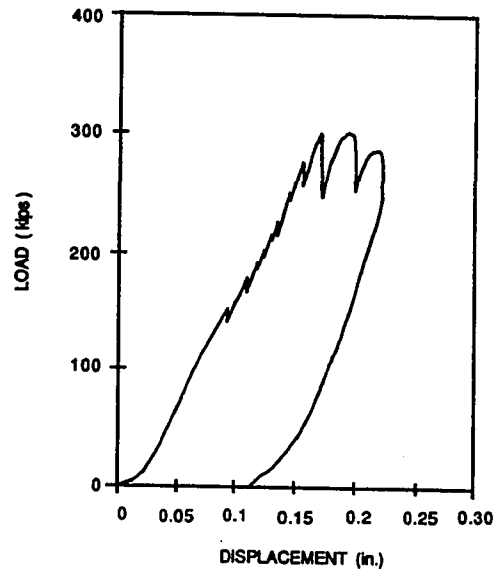


Figure 3.67 Specimen TPT2 Load-Displacement Curve

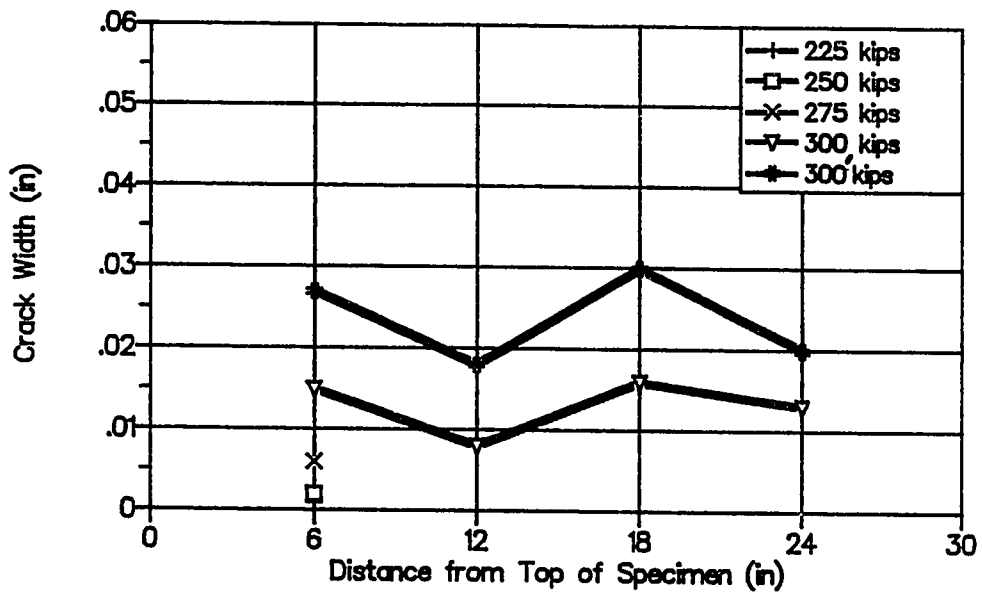


Figure 3.68 Specimen TPT2 Crack Widths along Centerline

Specimens TPT3 and TPT4 shifted the lateral post-tensioning to 5 inches from the loading surface and increased the amount of post-tensioning. Figures 3.69 and 3.70 are the load-displacement diagrams for TPT3 and TPT4 respectively. Both specimens were able to be reloaded to the peak load several times before the capacity began to decrease. The cracking patterns were again much the same as in the cases of Specimens TPT1 and TPT2. The first crack occurred down the center, and there were horizontal cracks along the transverse face at the conclusion of the test (see TPT1, Fig. 3.64). Figure 3.71 shows Specimen TPT3 at ultimate. The hydraulic ram is on the left side of the picture, and the load cell is on the right. In addition to the horizontal crack seen in other specimens, a vertical crack was formed on the transverse face due to the spreading of the highly concentrated force away from the anchor (see Fig. 3.72). There was a slight difference between Specimens TPT4 and TPT2, and Specimen TPT3 in the way in which the lateral post-tensioning behaved at ultimate. Since the lateral load for Specimen TPT3 was provided by a constant force hydraulic ram instead of by a constant displacement fixed screw chuck, there was no increase in transverse load as the cracks grew; this can be seen by comparing Figs. 3.73 (TPT3) and 3.74 (TPT4). In Specimen TPT3 as the cracks grew, the lateral force was controlled by hydraulic pressure and did not change. The lateral force shown in Fig. 3.73 is the average of the load cell and pressure transducer readings. In Specimen TPT4 as well as in Specimen TPT2, the strand was locked off in the screw chucks; so, as the cracks grew, the strand length and the strain in the strand increased. The two lines in Fig. 3.74 are for each of the two 5/16-inch strands in Specimen TPT4. The strain measurements are the average of readings from two gages on each strand. Figures 3.75 and 3.76 give the crack data for Specimens TPT3 and TPT4 respectively. Using 300 kips as the bench mark, the crack size continued to decrease over that recorded in Specimen TPT1 and TPT2 (see Table 3.8). At 300 kips, the maximum crack width measured for Specimen

TPT4 was 0.005 inches while for TPT3 it was 0.001 inch. These crack sizes were much less than those of TPT1 and TPT2 at 300 kips.

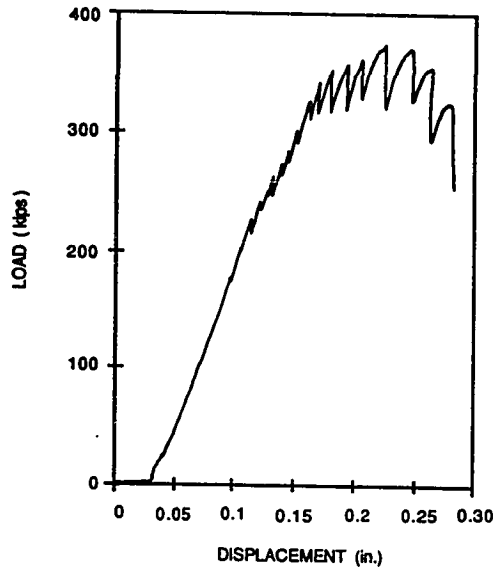


Figure 3.69 Specimen TPT3 Load-Displacement Curve

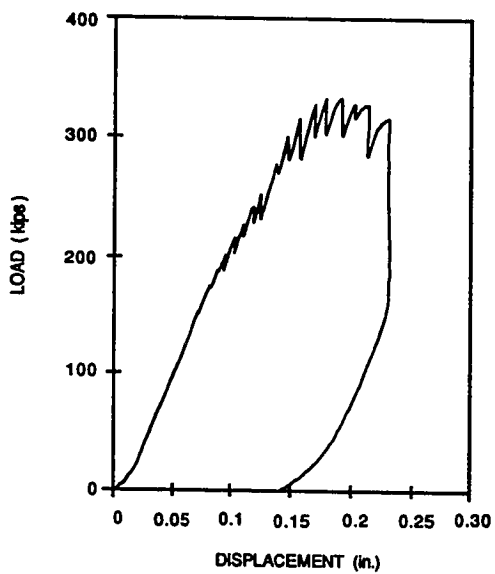


Figure 3.70 Specimen TPT4 Load-Displacement Curve

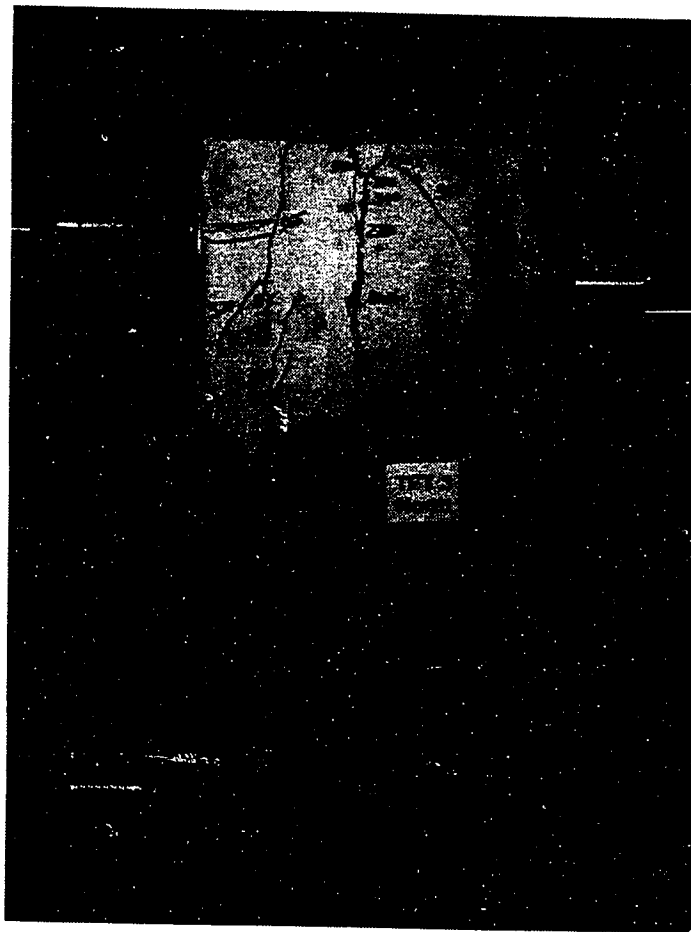


Figure 3.71 Specimen TPT3 Crack Pattern at Ultimate

Table 3.8 Crack Summary for "TPT" Series

| Specimen | Maximum Bursting Crack Width (in) | | |
|----------|-----------------------------------|----------|----------|
| | 275 kips | 300 kips | Ultimate |
| TPT1 | 0.010 | 0.025 | 0.055 |
| TPT2 | 0.006 | 0.016 | 0.030 |
| TPT3 | No Crack | 0.001 | 0.038 |
| TPT4 | 0.002 | 0.005 | 0.033 |

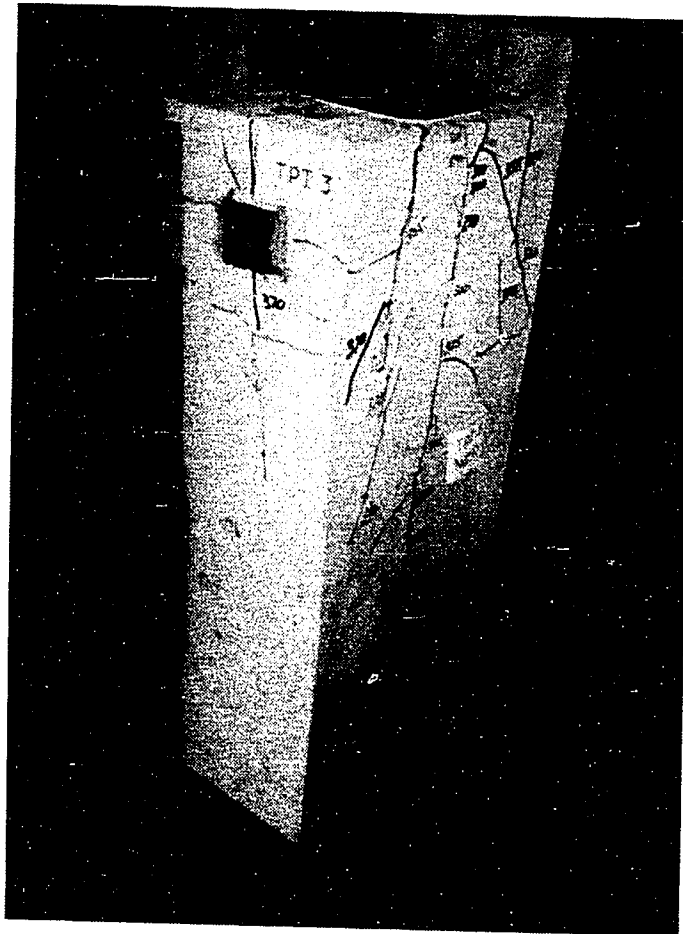


Figure 3.72 Specimen TPT3 Crack Pattern on Transverse Face

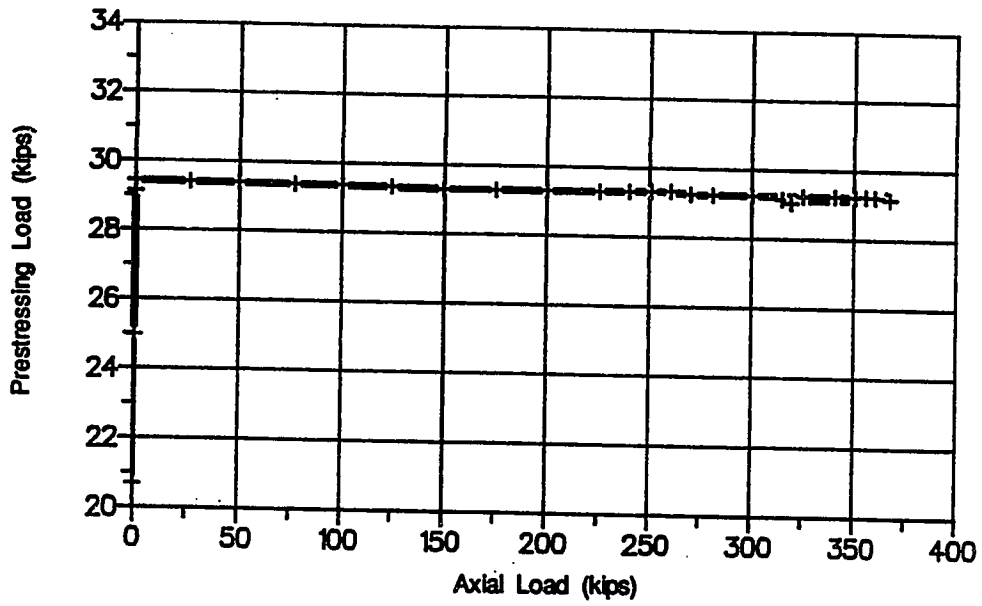


Figure 3.73 Lateral Load for Specimen TPT3

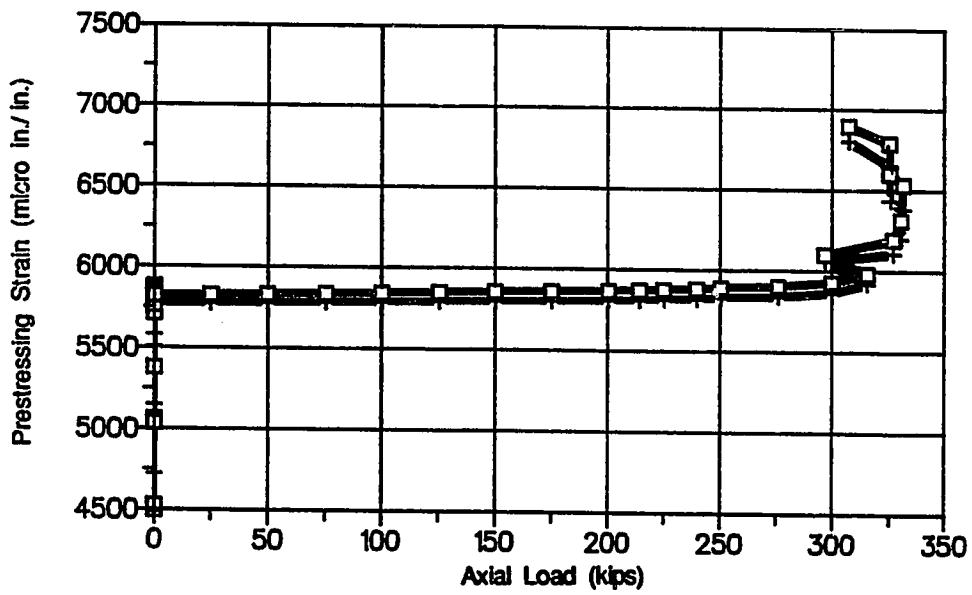


Figure 3.74 Lateral Prestressing Strain for Specimen TPT4

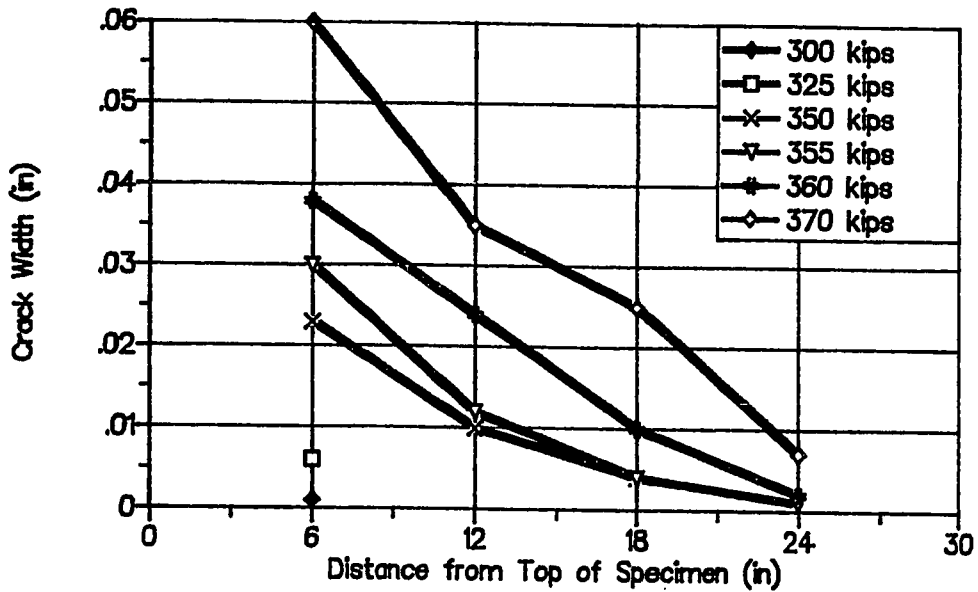


Figure 3.75 Specimen TPT3 Crack Width along Centerline

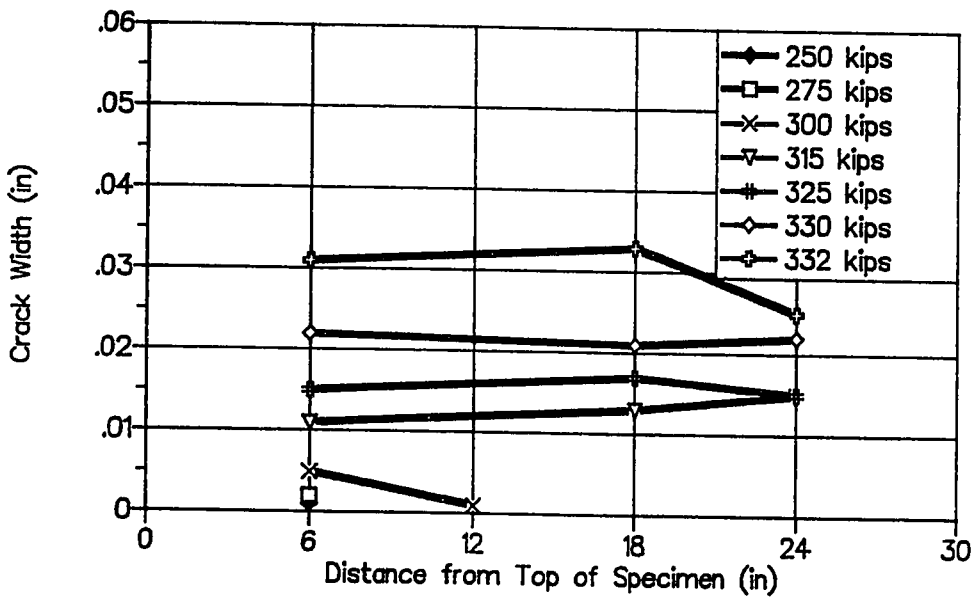


Figure 3.76 Specimen TPT4 Crack Width along Centerline

3.3 Prediction of the First Cracking Load using Elastic Analysis Models

The prediction of the first cracking load is important in many applications of post-tensioned construction. There are instances when post-tensioned concrete is used in highly corrosive environments because of its ability to stay uncracked or to have very well controlled and very narrow cracks. In those applications, it is important for the anchorage zone to remain uncracked or to have, at most, very fine cracks. Post-tensioned tendons are very susceptible to corrosion damage. In less corrosive environments, cracking is not as critical from a serviceability perspective but may be critical from a visual perspective. Therefore, an uncracked section may be desired.

Even for concentric anchors, the prediction of the first cracking load involves several variables. Some of these variables are known, some can be determined by simple approximation or by complicated analysis, and others are difficult to determine. What is difficult to determine is: 1) how the microstructure of the concrete is behaving, 2) how imperfections will affect the first cracking load, and 3) how to determine the actual concrete tensile strength. An accurate determination of the concrete tensile strength in the structure in contrast to what can be assumed or determined by companion tests is a difficult task. The companion material tests that are most commonly used are the split cylinder, modulus of rupture, or pure tension tests. Additional uncertainties are: the effect of the three-dimensional state of stress on the tension capacity in the plane being considered, and the effect of the discontinuity due to a post-tensioning duct on the stress distribution and on the first cracking load.

Even if a reasonably accurate prediction model is found, what load should be used in test comparisons for the first cracking load of the test specimen? Unlike the ultimate load which is clearly determined in tests, the appearance of the first crack depends on visual observations affected by the techniques and equipment used or on an indirect determination from concrete or reinforcement strains.

An even larger question is whether first cracking prediction equations based on tests of an unrestrained specimen have general validity in actual anchorage applications in structures where other cracking forces can be set up by restraint conditions or alternate loading cases.

In this test program, the first cracking loads for the concentric specimens were determined by a combination of observations of the changes in strain readings on the bursting reinforcement and visual observations of the cracks on the concrete surface. As strains on the bursting reinforcement approached 250 microstrain, the observation of the concrete surface was intensified. When first seen, cracks were typically less than 0.001 inches in width. The condition of the concrete surface greatly influences the size of the crack which can be seen. If the surface is rough, then the crack can be hidden until higher loads. Since the concrete sections were cast as slabs, one of the major axis sides had to be finished by troweling the concrete. Much care was taken to create as smooth a surface as possible. As the project progressed, the skill of the finishers improved and the finished side approached the formed side in its smoothness.

Several times, even though the specimens were loaded concentrically, there were discrepancies in the detection of the first cracking for each face and in the pattern of the cracking on opposite faces of the specimen. Contributing factors to these discrepancies are flaws or stress concentrations in the concrete that could cause premature cracking, a non uniform distribution of the forces on each side of the specimen, or differential microcracking. Microcracking is the cracking that occurs beneath the concrete surface between individual concrete particles. The first cracking load that will be reported in this section might be more accurately termed the first observed surface cracking load. For simplicity, it will be referred to as the first cracking load.

The objective of the following section will be to determine a model that best predicts the first cracking load and then to select a

lower bound equation suitable for design. In addition, trends due to the variables that affect the first cracking load will be discussed.

3.3.1 Prediction Model. Before significant cracking occurs, the theory of elasticity can be used to model the stress distribution in concrete. Once cracks occur, the stress distribution begins to change. A large number of elastic studies have been presented involving anchorage zones. Guyon's [70] studies from the 1940's have been well documented and are the most utilized tool for the design of anchorage zones. Burdet [25], in conjunction with this current study, has examined the anchorage zone from both an elasticity and a plasticity perspective. The elastic finite element results used in the chapter were developed from Burdet's data which is discussed in detail in Reference 25.

Figure 3.77a shows the elastic bursting stress distribution determined by Guyon for various a/h ratios. The value of most interest for the prediction of the first cracking load is the peak tensile bursting stress. Figure 3.77b is a summary of the peak stress value. As the a/h value increases, the peak stress value decreases relative to the uniform stress at the far end of the general anchorage zone ($\sigma_o = P/th$). The ordinary hypothesis for the prediction of the cracking load is that the concrete will crack when the maximum local stress exceeds the measured tensile capacity of the concrete. The split cylinder appears to be the best companion material test to determine the tensile strength of the concrete in anchorage zones. In the split cylinder test, concentrated axial loads are applied on opposite diameters of the cylinder (see Fig. 3.78). The spreading of the forces induces a tension along the centerline of the cylinder, which causes the cylinder to split. In an anchorage zone, the same process is causing the anchorage zone to split. An axial load is applied; and, as the forces spread laterally from the anchorage device, a tension force is caused internally along the tendon axis.

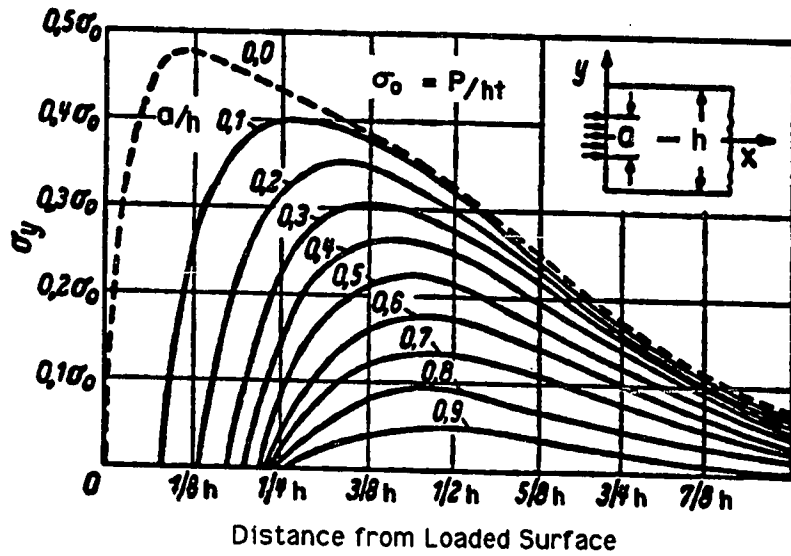


Figure 3.77a Bursting Stress Distribution [70]

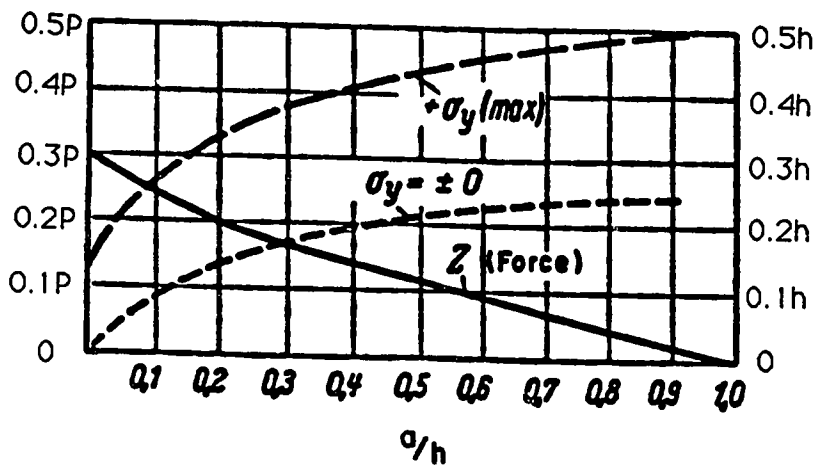


Figure 3.77b Bursting Stresses and Forces [70]

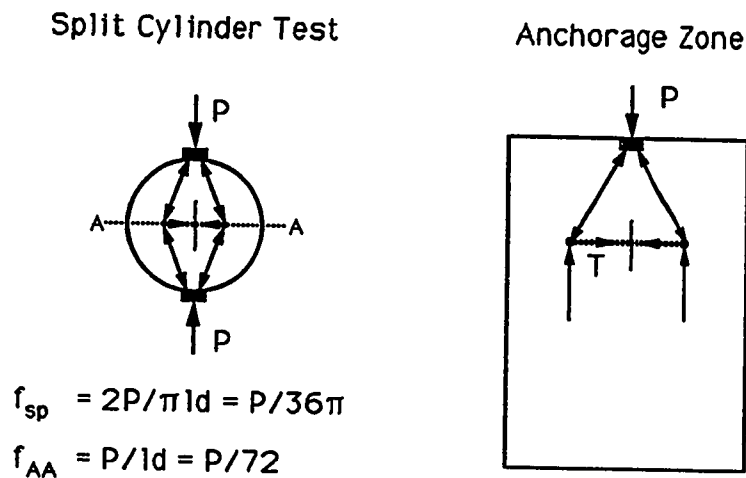


Figure 3.78 Split Cylinder Test

The split cylinder value reported for each test in the previous section is the average of at least three cylinders. However, behind the reported single value for the split cylinder test results inaccuracies are hidden. In many cases there were five to six thousand pounds of difference in the splitting loads between the three cylinders averaged for a test value report. A typical final average would be 45,000 pounds. This represents a coefficient of variance of about ten percent. On one occasion when split cylinders from the same concrete batch were tested at various ages, the split cylinder strength decreased although the compression strength went up with an additional week of aging. This is not to say that the split cylinder test data is totally unreliable but rather to indicate that it is not possible to know the mix split cylinder tensile strength more accurately than within 10 to 15 percent.

Table 3.9 Split Cylinder Analysis

| Date of Tests | Compressive Strength (kips) | Average f'_c (ksi) | Split Cylinder Load (kips) | Tensile Strength (fsp) (psi) | $f_{sp}k/\sqrt{f'_c}$ k | Modified Tensile Strength $k_{ave}/\sqrt{f'_c}$ |
|---------------------------------|-----------------------------|----------------------|----------------------------------|------------------------------|-------------------------|---|
| 6/14/89 TPT1 TPT2 TPT4 | 139 141 140 | 4.95 | 35.90 34.00 34.50 43.10 | 326 | 4.63 | 366 |
| 6/16/89 TPT3 | 146 145 146 | 5.15 | 50.20 44.90 43.50 | 408 | 5.69 | 373 |
| 6/20/89 C1 | 145 145 150 | 5.19 | 43.50 44.40 40.80 | 379 | 5.27 | 374 |
| k ave = | | | | | 5.20 | |

The case where there was a loss in split cylinder strength over time is reported in Table 3.9. The "TPT" series and Specimen C1 were cast from the same batch of concrete on June 2, 1989. On June 14th Specimens TPT1, TPT2 and TPT4 were tested. The compressive strength on that day was 4.95 ksi, and the split cylinder strength was 326 psi. Two days later, on June 16th, the compressive strength had increased by four percent to 5.15 ksi while the split cylinder strength had increased 25 percent to 408 psi. By June 20th, the test day for Specimen C1, the compressive strength had increased an additional one percent to 5.19 ksi but the split cylinder strength had decreased by seven percent to 379 psi. The compressive strength increased at a steady rate, but the split cylinder results were inconsistent. It is unlikely that the tensile strength of concrete would rise sharply and then fall. To determine a more realistic tensile strength for each test day, an average factor (k_{ave}) was calculated which, when multiplied by the $\sqrt{f'_c}$, would determine a modified tensile strength for each compressive strength value. The $\sqrt{f'_c}$ was used because it is the most common estimation of the relationship between the tensile strength and the compressive strength of concrete.

Table 3.10 First Cracking Load using Split Cylinder Strength

| Specimen | Split Cylinder (psi) | Lateral P.T. (psi) | Peak Stress / σ_o | Predicted Cracking Load (kips) | Test Cracking Load (kips) | Test/Predicted |
|----------|----------------------|--------------------|--------------------------|--------------------------------|---------------------------|----------------|
| A1 | 308 | 0 | 0.294 | 226 | 298 | 1.32 |
| A2 | 308 | 0 | 0.294 | 226 | 226 | 1.00 |
| A3 | 314 | 0 | 0.294 | 230 | 250 | 1.08 |
| A4 | 330 | 0 | 0.294 | 242 | 300 | 1.24 |
| B1 | 464 | 0 | 0.256 | 261 | 200 | 0.77 |
| B2 | 464 | 0 | 0.256 | 261 | 186 | 0.71 |
| B3 | 464 | 0 | 0.256 | 261 | 217 | 0.83 |
| B4 | 464 | 0 | 0.256 | 261 | 200 | 0.77 |
| B5 | 420 | 0 | 0.256 | 236 | 170 | 0.72 |
| B6 | 420 | 0 | 0.256 | 236 | 171 | 0.72 |
| B7 | 420 | 0 | 0.256 | 236 | 170 | 0.72 |
| B8 | 420 | 0 | 0.289 | 209 | 156 | 0.75 |
| C1 | 374 | 0 | 0.372 | 308 | 225 | 0.73 |
| TPT1 | 366 | 0 | 0.311 | 212 | 200 | 0.95 |
| TPT2 | 366 | 107 | 0.311 | 273 | 225 | 0.82 |
| TPT3 | 373 | 216 | 0.311 | 340 | 270 | 0.79 |
| TPT4 | 366 | 191 | 0.311 | 322 | 240 | 0.75 |
| | | | | | Average | 0.86 |
| | | | | | Standard Deviation | 0.18 |
| | | | | | Coef. of Variance | 0.21 |

$$\sigma_o = P/ht$$

Table 3.10 shows the measured and calculated first cracking values determined by matching the elastic peak bursting stress predicted by a two-dimensional finite element analysis to the split cylinder strength. The reduction in the concrete thickness due to the duct in Specimens B7, B8, C1 and the "TPT" series was neglected. For Specimens TPT2, TPT3, and TPT4, the lateral post-tensioning compression stress along the specimen centerline is taken into account by adding the precompression stress determined from the finite element analysis (see Fig. 3.65) to the split cylinder strength. For example, due to the precompression, the effective tensile strength of TPT4 is increased from 366 psi to 557 psi. The prediction of the first crack load based on elastic analysis and the split cylinder strength yields unconservative answers for all but four tests and a coefficient of variance of 21 percent.

As was discussed earlier, the process of visually detecting the first crack is difficult. Theoretically, Specimens A1 and A2 should have the same cracking load since they are geometrically the same, have only slight differences in reinforcement, were cast from the same mix, and, therefore, have the same split cylinder strength. Instead, there is a 72-kip difference, which is 32 percent. This shows the inconsistencies that can exist in crack detection and/or actual cracking load. In the "B" series, the cracking loads were much more consistent. Specimens B1 through B4 should have the same cracking load. Two of the specimens cracked at 200 kips, one at 186 kips, and the other at 217 kips for an average of 201 kips and a coefficient of variance of six percent. It is not the author's contention that crack prediction is futile but rather that a large coefficient of variance must be accepted.

A closer look at the split cylinder test reveals a significant difference between the split cylinder test and the splitting phenomenon in the anchorage zone. This difference is the relative amount of compression along an axis normal to the splitting. The axial compressive stress at the midpoint of the split cylinder for a concrete with a split cylinder strength of 400 psi is 628 psi (see Fig. 3.78). Figure 3.79 shows the axial compressive stress along the specimen centerline as computed by Burdet's finite element analysis [25] for a range of a/h values. The axial compressive stress at the location of the peak bursting stress can be three times higher than that applied in the split cylinder test. Ottosen [125] has developed a failure criterion for concrete in the biaxial and triaxial states of stress. Figure 3.80 shows a failure surface determined by Ottosen. Slicing planes through the failure surface would yield the curves shown in Fig. 3.81. Figure 3.81 shows two failure curves for Specimen B1. One assumes there is only a biaxial state of stress. The second includes the stresses caused by the forces spreading in the transverse direction, a triaxial state of stress. The compressive strength of B1

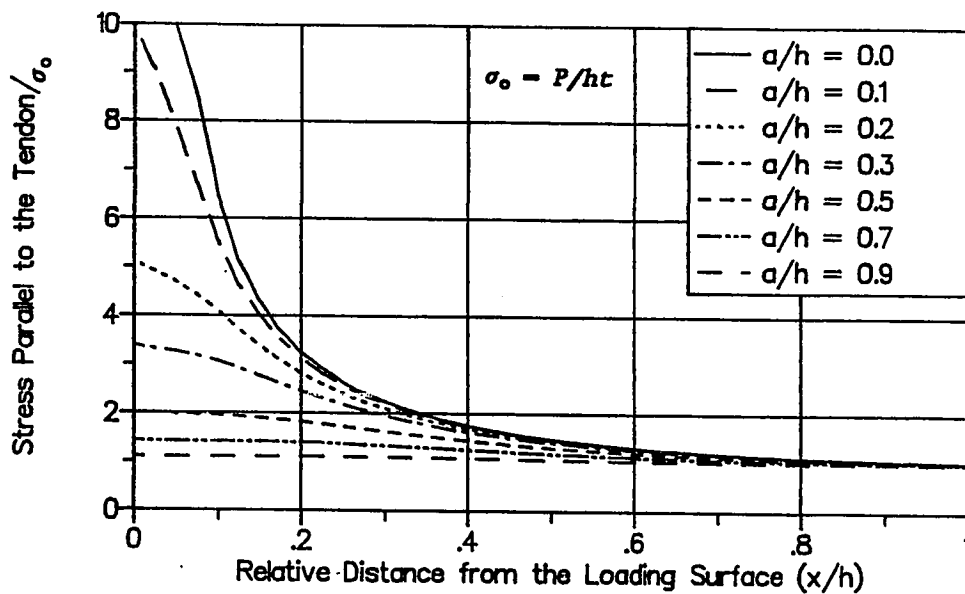


Figure 3.79 Compressive Stress along the Specimen Centerline according to the Finite Element Analysis [25]

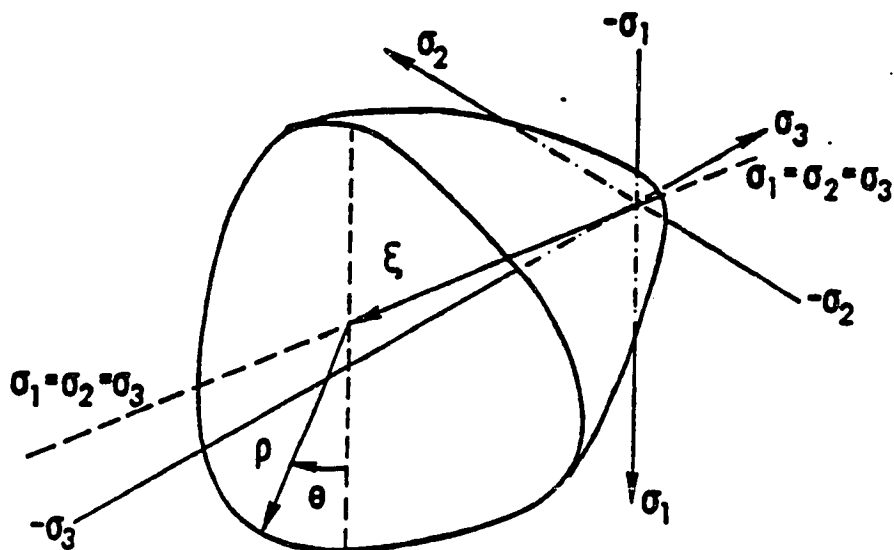


Figure 3.80 Ottosen's Failure Surface [125]

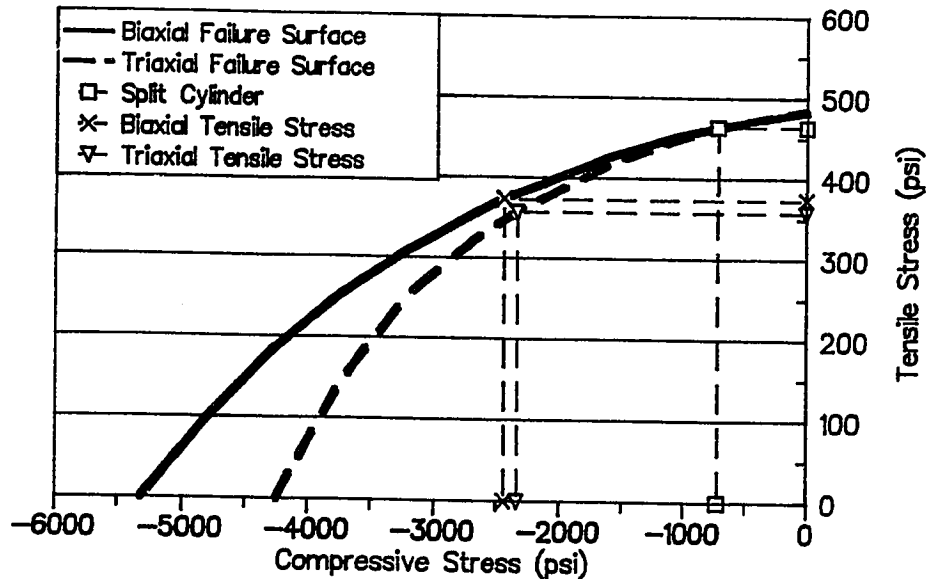


Figure 3.81 Specimen B1 Failure Curves for Biaxial and Triaxial Stress States

was 5,380 psi, and the split cylinder strength was 464 psi. The major parameters of Ottosen's criteria are determined directly from the ratio of the pure tensile strength (no compression) to the compressive strength. The pure tensile strength is not known, but the split cylinder strength is. Therefore, two points are known on the failure surface: a compressive stress of 729 psi with a tensile stress of 464 psi and a compressive stress of 5,380 psi with a tensile stress of 0 psi. Assuming different values for the ratio of the pure tensile strength to the compressive strength, a curve can be found that intersects both of these points (see Fig. 3.81). The triaxial curve utilizes the same pure tensile strength to compressive strength ratio but includes the third stress tensor.

An iterative process must be used to determine the effective tensile strength for a given specimen. An axial load must be assumed to determine the values of the compressive stress and the transverse

stress at the location of the peak lateral stress. Once those stresses are known, the effective tensile strength is determined along with the corresponding cracking load. If this cracking load does not match the load assumed initially, another cracking load must be assumed until the two loads converge.

The transverse stress is small for all the concentric specimens because the specimens are thin. For the "A" series, the triaxial stress is zero because the load is applied over the full thickness of the specimen. The transverse stress for Specimen C1 at the peak lateral stress location is zero because the transverse spreading of forces is completed before the peak stress in the lateral direction is reached. Table 3.11 shows the crack predictions if the limiting tensile stress is based on the biaxial state of stress criteria. Table 3.12 is based on the triaxial state of stress criteria. By utilizing the biaxial stress criteria, the tensile strength is reduced about 15 percent. The statistical analysis shows that the average of the test-to-predicted ratio is much closer to one, but the coefficient of variance stays at 21 percent. The coefficient of variance stays high due mainly to the "A" series. Neglecting the "A" series, the average of test-to-predicted ratio drops to 0.92 and the coefficient of variance drops to 8.1 percent. Including the triaxial effect can further reduce the predicted tensile strength by another five percent. The variation does not change because of the domination of the "A" series specimens which have a transverse stress of zero. If the "A" series is not included, the average of the test-to-predicted ratio increases to 0.95 and the coefficient of variance is 8.3 percent. By more accurately modeling the state of stress in the anchorage zone, the prediction of the first cracking load improved but can be still unconservative.

In the preceding computations, the reduction in cross-sectional area and possible stress concentration effects due to the effect of the post-tensioning duct have been ignored. A direct comparison of the

Table 3.11 First Crack Prediction, Biaxial Stress State

| Specimen | Compression Stress (psi) | Reduced Tensile Capacity (psi) | Change in Tensile Capacity (psi) | Lateral P.T. (psi) | Predicted Cracking Load (kips) | Test Cracking Load (kips) | Test/Predicted |
|--------------------|--------------------------|--------------------------------|----------------------------------|--------------------|--------------------------------|---------------------------|----------------|
| A1 | 1400 | 258 | -50 | 0 | 189 | 298 | 1.57 |
| A2 | 1400 | 258 | -50 | 0 | 189 | 226 | 1.19 |
| A3 | 1440 | 264 | -50 | 0 | 194 | 250 | 1.29 |
| A4 | 1530 | 282 | -48 | 0 | 207 | 300 | 1.45 |
| B1 | 2440 | 374 | -90 | 0 | 210 | 200 | 0.95 |
| B2 | 2440 | 374 | -90 | 0 | 210 | 186 | 0.88 |
| B3 | 2440 | 374 | -90 | 0 | 210 | 217 | 1.03 |
| B4 | 2440 | 374 | -90 | 0 | 210 | 200 | 0.95 |
| B5 | 2280 | 350 | -70 | 0 | 197 | 170 | 0.86 |
| B6 | 2280 | 350 | -70 | 0 | 197 | 171 | 0.87 |
| B7 | 2280 | 350 | -70 | 0 | 197 | 170 | 0.86 |
| B8 | 1900 | 371 | -49 | 0 | 185 | 156 | 0.84 |
| C1 | 1940 | 329 | -45 | 0 | 271 | 225 | 0.83 |
| TPT1 | 1790 | 323 | -43 | 0 | 187 | 200 | 1.07 |
| TPT2 | 2259 | 299 | -67 | 107 | 235 | 225 | 0.96 |
| TPT3 | 2715 | 273 | -100 | 216 | 283 | 270 | 0.96 |
| TPT4 | 2596 | 277 | -89 | 191 | 271 | 240 | 0.89 |
| Average | | | | | | | 1.03 |
| Standard Deviation | | | | | | | 0.22 |
| Coef. of Variance | | | | | | | 0.21 |

Table 3.12 First Crack Prediction, Triaxial Stress State

| Specimen | Transverse Stress (psi) | Compression Stress (psi) | Reduced Tensile Strength (psi) | Change in Tensile Capacity (psi) | Lateral P.T. (psi) | Predicted Cracking Load (kips) | Test Cracking Load (kips) | Test/Predicted |
|--------------------|-------------------------|--------------------------|--------------------------------|----------------------------------|--------------------|--------------------------------|---------------------------|----------------|
| A1 | 0 | 1400 | 258 | -50 | 0 | 189 | 298 | 1.57 |
| A2 | 0 | 1400 | 258 | -50 | 0 | 189 | 226 | 1.19 |
| A3 | 0 | 1440 | 264 | -50 | 0 | 194 | 250 | 1.29 |
| A4 | 0 | 1530 | 282 | -48 | 0 | 207 | 300 | 1.45 |
| B1 | 199 | 2340 | 358 | -106 | 0 | 201 | 200 | 0.99 |
| B2 | 199 | 2340 | 358 | -106 | 0 | 201 | 186 | 0.92 |
| B3 | 199 | 2340 | 358 | -106 | 0 | 201 | 217 | 1.08 |
| B4 | 199 | 2340 | 358 | -106 | 0 | 201 | 200 | 0.99 |
| B5 | 188 | 2210 | 339 | -81 | 0 | 191 | 170 | 0.89 |
| B6 | 188 | 2210 | 339 | -81 | 0 | 191 | 171 | 0.90 |
| B7 | 188 | 2210 | 339 | -81 | 0 | 191 | 170 | 0.89 |
| B8 | 208 | 1868 | 364 | -56 | 0 | 181 | 156 | 0.86 |
| C1 | 0 | 1940 | 329 | -45 | 0 | 271 | 225 | 0.83 |
| TPT1 | 119 | 1770 | 319 | -47 | 0 | 184 | 200 | 1.08 |
| TPT2 | 148 | 2210 | 290 | -76 | 107 | 230 | 225 | 0.98 |
| TPT3 | 175 | 2718 | 254 | -119 | 216 | 272 | 270 | 0.99 |
| TPT4 | 163 | 2510 | 261 | -105 | 191 | 261 | 240 | 0.92 |
| Average | | | | | | | 1.05 | |
| Standard Deviation | | | | | | | 0.21 | |
| Coef. of Variance | | | | | | | 0.20 | |

effect of the duct is possible from Specimens B4, B6, and B7. Specimen B7 had a post-tensioning duct, while the other two did not. Specimens B6 and B7 were cast at the same time, had the same general zone reinforcement, and had practically identical cracking loads (171 versus 170 kips) even though the post-tensioning duct in Specimen B7 reduces the effective concrete width by 22 percent. A substantial reduction in cracking load (200 kips versus 170 kips or a 15 percent decrease) was seen from Specimens B4 to B7, but there was also a fairly large reduction in split cylinder tensile strength (464 psi to 420 psi or a 10 percent decrease). Burdet [25] did a comparison between a two-dimensional finite element analysis and a three-dimensional analysis with a hole equal to a quarter of the specimen thickness at the center of the section. The hole was made by removing elements. The analysis gives an indication of the trends. Figure 3.82 shows a comparison of the lateral stresses for several cuts through the three-dimensional analysis and the two-dimensional analysis. Two-dimensional stresses were calculated using an effective thickness equal to the specimen thickness minus the hole (duct) width (see Fig. 3.83, concrete section). The effective width correction reasonably adjusts the two-dimensional stress value to the calculated value of the stress near the surface. This slightly contradicts the experimental results which showed very little change in the cracking load with the inclusion of the duct in a specimen.

Table 3.13 gives the duct dimensions for Specimens B7, B8, C1, TPT1, TPT2, TPT3, and TPT4. Table 3.14 shows the triaxial stress crack predictions removing the full duct width from the effective thickness. The prediction is 15 percent conservative, but the coefficient of variance drops to 16 percent. If the "A" series is not included, the average of the test-to-predicted ratio is 1.08 and the coefficient of variance is 13 percent. To remove the full duct width seems to be overly conservative and may not be very logical.

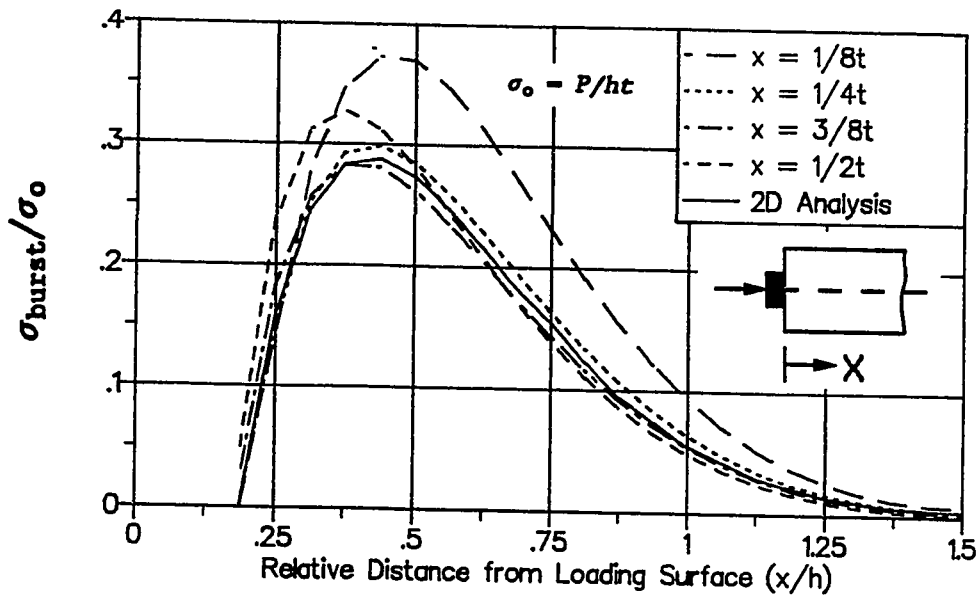


Figure 3.82 Bursting Stresses: Comparison of 3-D Analysis Including a Duct Hole with a 2-D Analysis (with correction) [25]

Table 3.13 Post-Tensioning Duct Dimensions

| Specimen | Outside Diameter (in) | Inside Diameter (in) | Thickness (in) |
|---------------------|-----------------------|----------------------|----------------|
| B7, B8 | 2 | 1 15/16 | 1/32 |
| C1 and "TPT" Series | 2 5/8 | 2 3/8 | 1/32 |

Table 3.14 First Crack Prediction Including Full Duct Effect and Triaxial Stress State

| Specimen | Effective Thickness (in) | Transverse Stress (psi) | Compression Stress (psi) | Reduced Tensile Strength (psi) | Lateral P.T. (psi) | Predicted Cracking Load (kips) | Test Cracking Load (kips) | Test/Predicted |
|----------|--------------------------|-------------------------|--------------------------|--------------------------------|--------------------|--------------------------------|---------------------------|----------------|
| A1 | 6 | | | | | 189 | 298 | 1.57 |
| A2 | 6 | | | | | 189 | 226 | 1.19 |
| A3 | 6 | | | | | 194 | 250 | 1.29 |
| A4 | 6 | | | | | 207 | 300 | 1.45 |
| B1 | 9 | | | | | 201 | 200 | 0.99 |
| B2 | 9 | | | | | 201 | 186 | 0.92 |
| B3 | 9 | | | | | 201 | 217 | 1.08 |
| B4 | 9 | | | | | 201 | 200 | 0.99 |
| B5 | 9 | | | | | 191 | 170 | 0.89 |
| B6 | 9 | | | | | 191 | 171 | 0.90 |
| B7 | 7 | 155 | 1834 | 368 | 0 | 158 | 170 | 1.08 |
| B8 | 7 | 145 | 1513 | 386 | 0 | 147 | 156 | 1.06 |
| C1 | 5.63 | 0 | 1430 | 351 | 0 | 200 | 225 | 1.13 |
| TPT1 | 7.13 | 93 | 1390 | 339 | 0 | 145 | 200 | 1.38 |
| TPT2 | 7.13 | 118 | 1750 | 321 | 107 | 183 | 225 | 1.23 |
| TPT3 | 7.13 | 142 | 2120 | 302 | 216 | 221 | 270 | 1.22 |
| TPT4 | 7.13 | 135 | 2020 | 303 | 191 | 210 | 240 | 1.14 |
| | | | | | | | Average | 1.15 |
| | | | | | | | Standard Deviation | 0.19 |
| | | | | | | | Coef. of Variance | 0.16 |

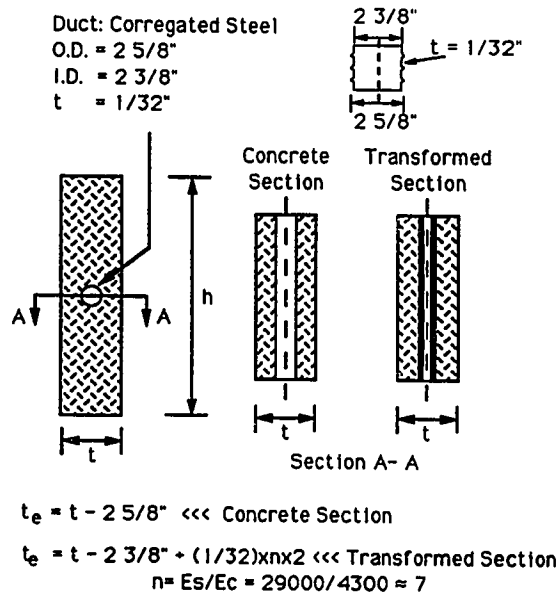


Figure 3.83 Effective Concrete Thickness

At low loads, the bond between the duct and the concrete is quite effective. Therefore, some of the tensile force can be carried by the corrugated steel post-tensioning duct. It would be more accurate to model the cross section including the duct as a composite section (see Fig. 3.83). Table 3.15 shows the first cracking prediction utilizing this modified effective thickness. The average of the test to model value is 1.11, and the coefficient of variance is 17 percent. If the "A" series is not included, the average of the test-to-predicted ratio is 1.03 and the coefficient of variance is 11 percent. Some of the predictions are still unconservative.

Table 3.15 First Crack Prediction using Modified Effective Thickness and Triaxial Stress State

| Specimen | Effective Thickness (in) | Transverse Stress (psi) | Compression Stress (psi) | Reduced Tensile Strength (psi) | Lateral P.T. (psi) | Predicted Cracking Load (kips) | Test Cracking Load (kips) | Test/Predicted |
|----------|-----------------------------|----------------------------|-----------------------------|-----------------------------------|-----------------------|-----------------------------------|------------------------------|----------------|
| A1 | 6 | | | | | 189 | 298 | 1.57 |
| A2 | 6 | | | | | 189 | 226 | 1.19 |
| A3 | 6 | | | | | 194 | 250 | 1.29 |
| A4 | 6 | | | | | 207 | 300 | 1.45 |
| B1 | 9 | | | | | 201 | 200 | 0.99 |
| B2 | 9 | | | | | 201 | 186 | 0.92 |
| B3 | 9 | | | | | 201 | 217 | 1.08 |
| B4 | 9 | | | | | 201 | 200 | 0.99 |
| B5 | 9 | | | | | 191 | 170 | 0.89 |
| B6 | 9 | | | | | 191 | 171 | 0.90 |
| B7 | 7.52 | 166 | 1958 | 359 | 0 | 169 | 170 | 1.01 |
| B8 | 7.52 | 156 | 1626 | 379 | 0 | 158 | 156 | 0.99 |
| C1 | 6.62 | 0 | 1529 | 345 | 0 | 221 | 225 | 1.02 |
| TPT1 | 8.12 | 101 | 1506 | 334 | 0 | 157 | 200 | 1.28 |
| TPT2 | 8.12 | 127 | 1890 | 312 | 107 | 197 | 225 | 1.14 |
| TPT3 | 8.12 | 153 | 2277 | 289 | 216 | 237 | 270 | 1.14 |
| TPT4 | 8.12 | 146 | 2176 | 292 | 191 | 227 | 240 | 1.06 |
| | | | | | | | Average | 1.11 |
| | | | | | | | Standard Deviation | 0.19 |
| | | | | | | | Coef. of Variance | 0.17 |

The last model examined required using the triaxial analysis modification of the split cylinder data as well as modifying the section thickness considering the duct inside diameter and transforming

the wall thickness. After all this effort the average predicted value is above the test load, but the coefficient of variance is still high.

Since there may be applications when a totally crack free anchorage zone is felt essential or when a conservative result is very satisfactory, the following method was developed to yield conservative results. The prediction of first cracking load assumes a 30% reduction in the split cylinder strength due to the triaxial effects and is determined from the compressive strength, $0.7 \cdot 6\sqrt{F'_c}$ which equals $4.2\sqrt{F'_c}$. This is very close to the results of the equation used by ACI Committee 209 to estimate concrete tensile strength, $1/3 w^{0.5}\sqrt{F'_c}$, where w is the weight of the concrete (145 lbs./ft³). Substituting into the equation recommended by ACI Committee 209, the concrete tensile strength is $4\sqrt{F'_c}$. The effective thickness for those specimens with ducts was determined by subtracting the inside diameter of duct from the section thickness. This assumption determines higher stresses than the transformed section but lower values than obtained by subtracting the outside diameter of the duct. The predictions (see Table 3.16) are essentially conservative for all cases. The calculations are much simpler than using a triaxial analysis with a transformed section but do predict more conservative results.

3.3.2 Trends in the First Cracking Load. When developing the first test series, it was seen that for some a/h ratios the cracking load could be quite high and the specimen would fail locally before a general zone failure could occur. In this subsection, several figures (Figs. 3.84 to 3.87) are shown that compare the local zone maximum load to the cracking load for different b/t ratios and the ratio of the plate width in the transverse direction to the specimen thickness. The cracking load is determined by setting the maximum predicted stress from Guyon's curves equal to the reduced tensile strength of the concrete ($4.2\sqrt{F'_c}$) developed in the previous subsection. The local zone maximum load is shown for three criteria: 1) $0.4f'_c\sqrt{A/A_b} \cdot A_b$, 2) $1.5f'_cA_b$, and 3) $3f'_cA_b$. The first criterion is the equation of an unreinforced

local zone [143] where A_b is the bearing area and A is the effective concrete area that is geometrically similar to the bearing area. The second criterion is a compression level that was easily obtained in this test program with proper confinement. The third criterion is the maximum local zone load, according to Roberts [143], even when the local zone is well confined. The graph range is limited to 1.0 for $P/f_c t h$ because, at this load, the compression failure of the general zone is controlling the design.

Table 3.16 Lower Bound Crack Prediction

| Specimen | Effective Thickness (in) | f'_c (psi) | $4.2\sqrt{f'_c}$ (psi) | Lateral P.T. (psi) | Predicted Cracking Load (kips) | Test Cracking Load (kips) | Test/ Predicted |
|----------|-----------------------------|-----------------|---------------------------|-----------------------|-----------------------------------|------------------------------|--------------------|
| A1 | 6 | 3360 | 243 | 0 | 179 | 298 | 1.67 |
| A2 | 6 | 3360 | 243 | 0 | 179 | 226 | 1.26 |
| A3 | 6 | 3480 | 248 | 0 | 182 | 250 | 1.37 |
| A4 | 6 | 3840 | 260 | 0 | 191 | 300 | 1.57 |
| B1 | 9 | 5380 | 308 | 0 | 173 | 200 | 1.15 |
| B2 | 9 | 5380 | 308 | 0 | 173 | 186 | 1.07 |
| B3 | 9 | 5380 | 308 | 0 | 173 | 217 | 1.25 |
| B4 | 9 | 5380 | 308 | 0 | 173 | 200 | 1.15 |
| B5 | 9 | 5317 | 306 | 0 | 172 | 170 | 0.99 |
| B6 | 9 | 5317 | 306 | 0 | 172 | 171 | 0.99 |
| B7 | 7.06 | 5317 | 306 | 0 | 135 | 170 | 1.26 |
| B8 | 7.06 | 5317 | 306 | 0 | 120 | 156 | 1.30 |
| C1 | 6.18 | 5188 | 303 | 0 | 181 | 225 | 1.24 |
| TPT1 | 7.68 | 4953 | 296 | 0 | 131 | 200 | 1.53 |
| TPT2 | 7.68 | 4953 | 296 | 107 | 179 | 225 | 1.26 |
| TPT3 | 7.68 | 5151 | 301 | 216 | 230 | 270 | 1.18 |
| TPT4 | 7.68 | 4953 | 296 | 191 | 216 | 240 | 1.11 |
| | | | | | | Average | 1.26 |
| | | | | | | Standard Deviation | 0.18 |
| | | | | | | Coef. of Variance | 0.15 |

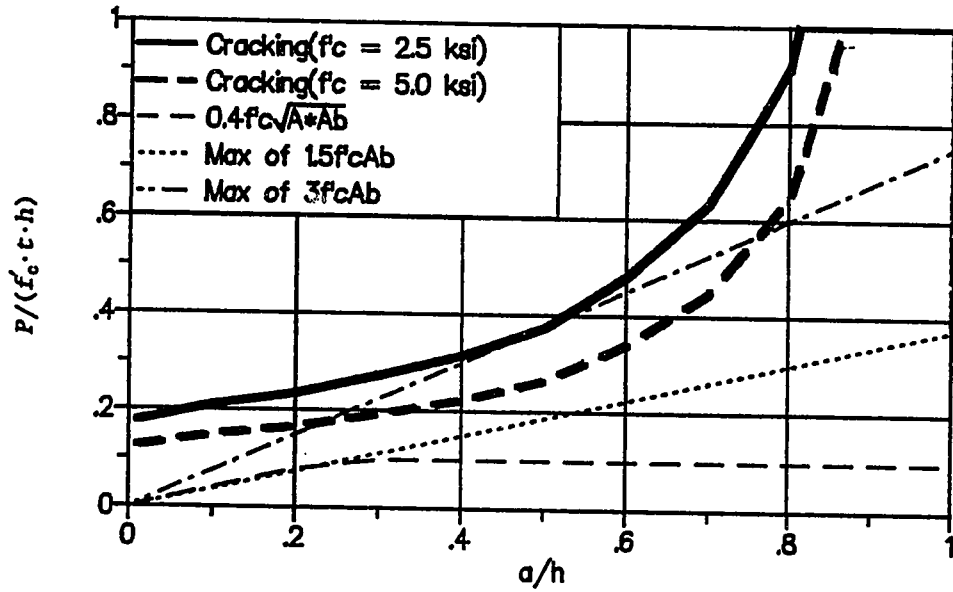


Figure 3.84 First Crack Load versus Local Zone Capacity $b/t = 0.25$

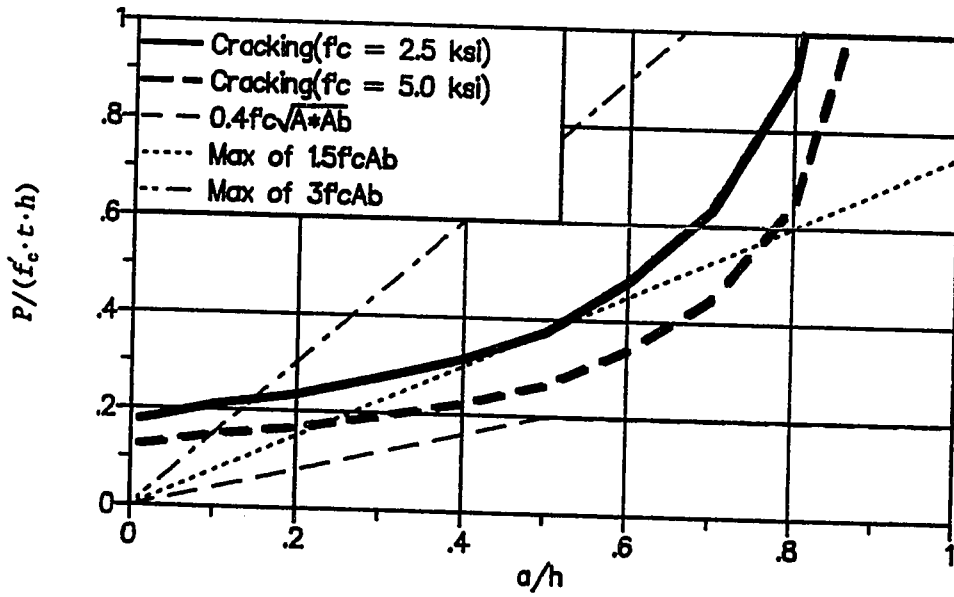


Figure 3.85 First Crack Load versus Local Zone Capacity $b/t = 0.50$

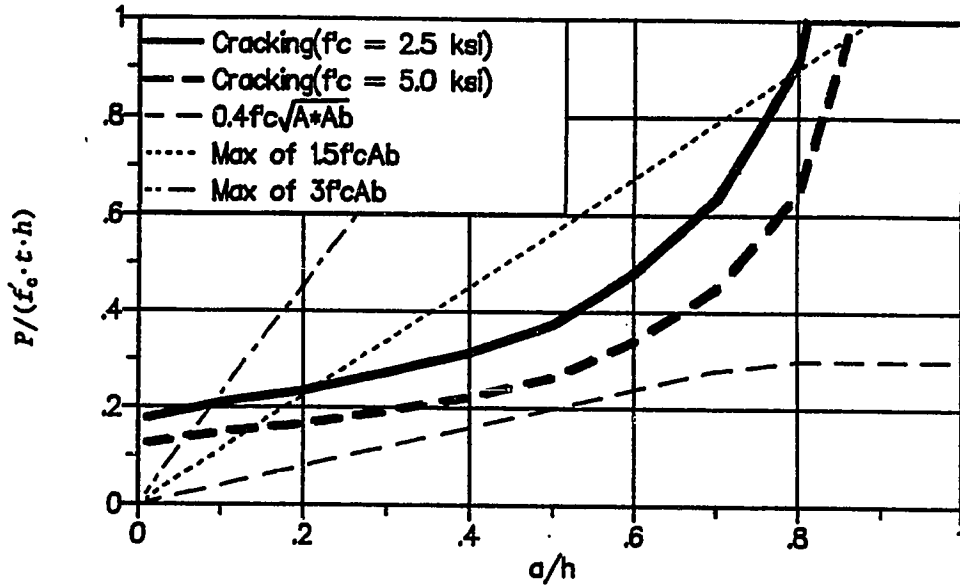


Figure 3.86 First Crack Load versus Local Zone Capacity $b/t = 0.75$

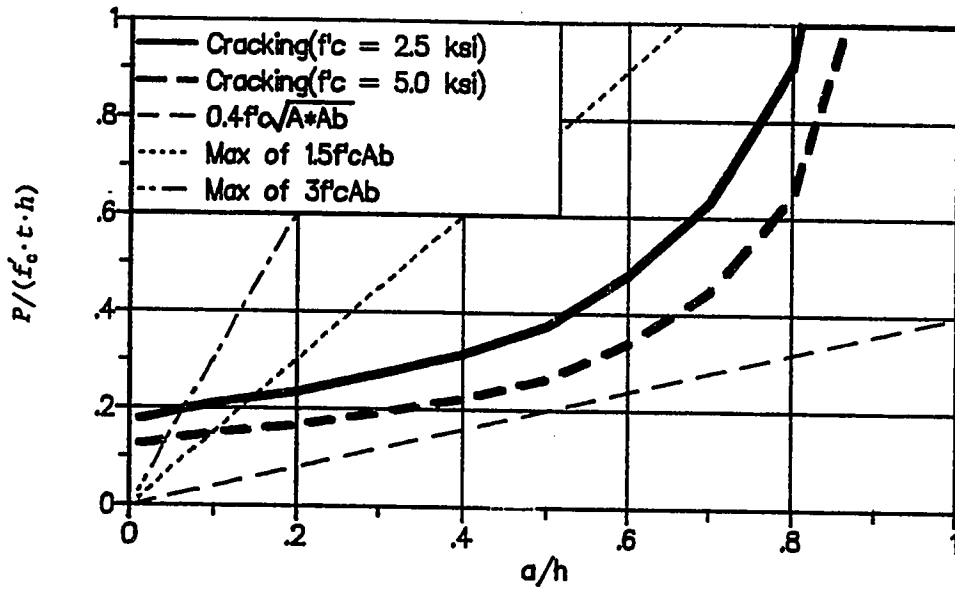


Figure 3.87 First Crack Load versus Local Zone Capacity $b/t = 1.00$

Figure 3.84 ($b/t = 0.25$) shows that for small b/t ratios the local zone will dominate the design, especially for very small and very large a/h ratios. An unconfined local zone would fail before the general zone cracking occurs. In order to obtain a general zone crack, the local zone stress must be very high. If a low strength concrete is used, it is still questionable whether the general zone will ever crack before the local zone fails. Since the local zone strength increases with f'_c and the general zone strength increases only with the $\sqrt{f'_c}$, the higher the concrete strength becomes, the more likely the general zone will crack before local zone failure. The most common post-tensioning applications have a/h values between 0.2 and 0.4. In this zone for $b/t = 0.25$, the local zone will fail first unless very high bearing stresses are achieved. As the b/t ratio becomes larger, the strength of the local zone increases in comparison to that of the general zone. When the anchorage device is as wide as the section ($b/t = 1$, See Fig. 3.87), and the local zone is able to reach $1.5f'_c$, the general zone will crack before the local zone fails for a/h ratios between 0.1 and 0.9. In the a/h region between 0.2 and 0.4, the general zone will crack when the bearing stresses are around f'_c .

3.3.3 Conclusions. The prediction of the cracking load has shown that there are many uncertainties involved in the calculation. The most complicated model, which included the triaxial effects and a transformed duct width had results shown in Table 3.15 and was 11 percent conservative. However, it had a coefficient of variance of 17 percent. A much simpler, approximate method was also developed which based the tensile strength on the cylinder compressive strength and included the duct thickness. This method was essentially conservative for all the tests. Overall, it was 26 percent conservative on the average and had a coefficient of variance of 15 percent. Cracking trends were investigated analytically. The investigation showed that, for many a/h ratios, the local zone bearing resistance will need to be above f'_c for there to be cracking in the general zone before the local

zone fails.

It is difficult to extrapolate these techniques to an actual beam where there are other loads causing changes in the stress distribution. Since these models do not predict the cracking caused by creep, shrinkage, or temperature effects, other first cracking procedures must be used, if these effects are present. Similarly, if an analysis is conducted that models actual beam conditions, the matching of the peak stress with a reduced or modified tensile strength ($4.2\sqrt{F_c}$) should produce conservative answers. If Guyon's elastic curves or some other simplified stress distribution is used, the effect of other loads on the stress distribution must be considered. In simply supported beams where the support reaction is small relative to the post-tensioning force and the anchorage zone is near the end of the beam, the methods discussed in previous subsections are applicable because the stress distribution in the anchorage region should be only slightly altered from the isolated anchorage specimen analysis. In more complicated post-tensioning applications, the effects of other loads on the anchorage zone stress distribution may increase or decrease the tensile stresses and must, therefore, be considered.

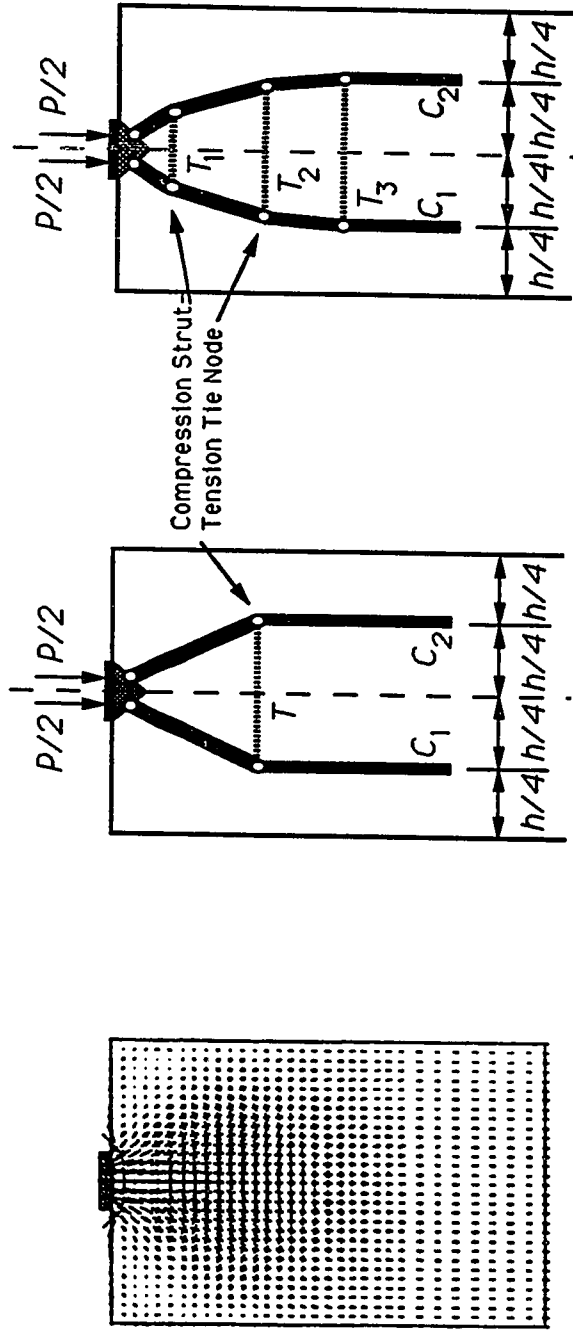
3.4 Ultimate Load Prediction Models

This section examines methods for predicting the ultimate load of concentric anchorage zones. The first subsection will closely examine the components of the strut-and-tie model (STM) and the failure modes which must be checked. The second and third subsections examine the applicability of the basic STM that assumes a uniform stress distribution at the end of the anchorage zone and illustrate the checks necessary for compressive struts and nodes. The fourth subsection examines two methods which incorporate beam bending and additional plasticity to model the extra capacity observed above the basic STM prediction. The fifth subsection demonstrates the current technique for ultimate load prediction.

3.4.1 Components of the Strut-and-Tie Model (STM). As discussed

in Chapter 2, the basic STM is comprised of three components: tension ties, nodes and compression struts. Figure 3.88a shows the pattern of the force distribution in a concentric anchorage zone as predicted by an elastic analysis. Figure 3.88b shows a very simplified STM which crudely represents the force flow, while Fig. 3.88c shows a STM which better models the pattern of the compressive force distribution. To construct a STM for a concentric anchorage zone, the load on the bearing plate is divided into two equal loads located at the quarter points of the plate. The force at the end of the general zone is assumed to be balanced by a uniform resistance. From equilibrium, the point of application of struts C_1 and C_2 can be located at the quarter points of the section. Compression struts carry the load from the bearing plate into the section. Tension ties are necessary in order to satisfy equilibrium as the forces spread out into the section. The tension ties are provided by reinforcing steel, and the compressive forces are carried by the concrete.

The location and magnitude of the tension ties are determined by the location and properties of the reinforcing bars used. The more complicated task is the definition of the size and capacity of the compression struts and nodes. The local zone surrounding the anchorage device contains the node which transfers the tendon force onto the concrete. Based on failure observations, the shape of the node was assumed to be a pyramid. In this and several previous studies [73,143,166], a pyramid or cone was observed under the loading plate when a bearing failure occurred. The depth of the pyramid can be determined from the width of the anchorage device in each of the principal directions. Figure 3.89 shows the idealization of the pyramid in a principal direction. The height of the triangle is taken to be half of the plate width in the direction under consideration. In a concentric anchorage zone, the forces in both the elastic state and the plastic state divide evenly on either side of the specimen centerline. Therefore, the node is symmetrical. Compression struts



a) Elastic Stresses

b) Single-Tie STM

c) Multiple-Tie STM

Figure 3.88 Strut-and-Tie Model Development

initiate from the node, and their width is determined by the node shape. The applied loads intersect the node-strut boundary (line MN, Fig. 3.89) at a distance of $1/4$ of the anchorage width from the loaded surface. The intersection points (A and B) are called the secondary local zone nodes and are the working points for the STM.

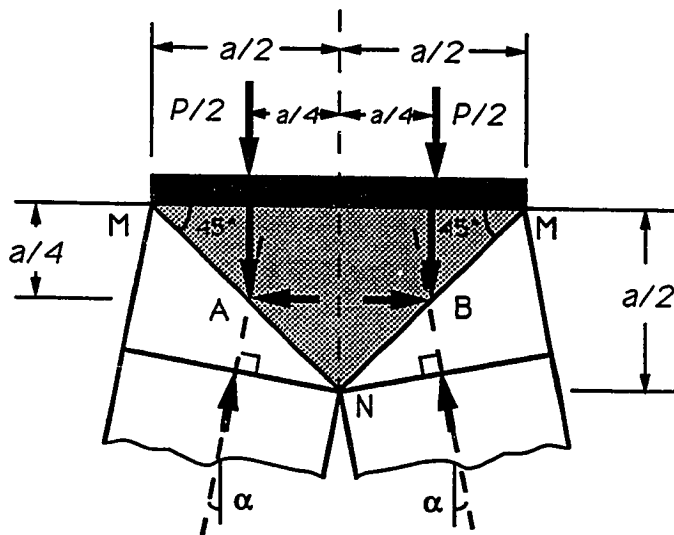


Figure 3.89 Idealized Concentric Local Zone Node

Once the local zone node is defined, the capacity of the STM can be determined by summation of moments about a secondary local zone node (see Fig. 3.90). The reinforcement (tie) crossing the tendon path can be included in the equilibrium equation if the reinforcement can be fully developed where the tension tie intersects the compression strut (node) (see Fig. 3.89). Caution should be used when including long spirals. Spirals that extend for a length greater than a plate width will, in most cases, not be wide enough to develop the tension tie out to the compression strut tension tie node. It will always be conservative to neglect the spiral. In most cases neglecting the spiral as a tension tie will have a very small effect because of its close proximity to the plate. The compression force (C_3) between the

secondary nodes is determined by summing the forces along the specimen centerline. The initial dispersion angle (α) of the compression strut is determined by the summation of forces at one of the secondary nodes (see Fig. 3.91). The angle (α) at the secondary node is also the slope of the line of action of the strut from the secondary node to another node located at the centroid of the bursting reinforcement (see Fig. 3.91).

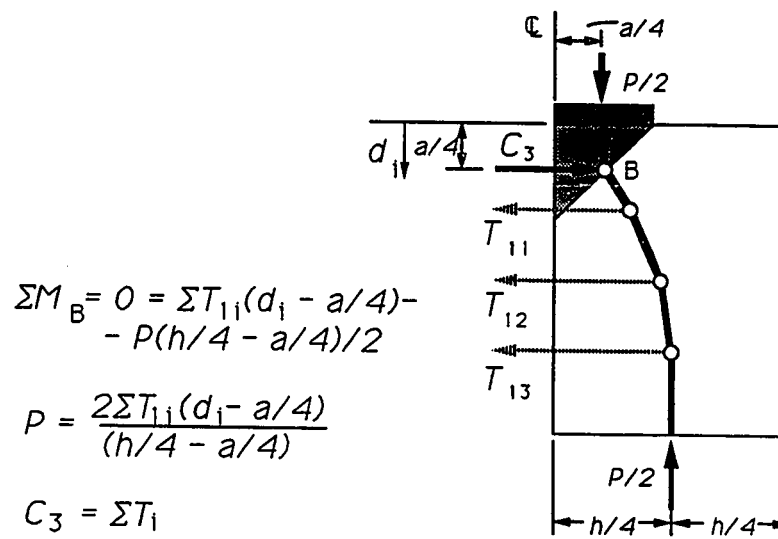


Figure 3.90 Strut-and-Tie Model Free Body Diagram

The struts in the anchorage zone are excellent examples of Schlaich's [151] bottle struts shown in Fig. 3.92a. The struts will continue to increase in width as the compressive forces move away from the anchorage device until they reach a uniform stress distribution. An approximation of this spreading is shown in Fig. 3.92b. The width of the compression strut is assumed to be equal to twice the distance from the section centerline to the centerline of the strut as measured normal to the strut axis. However, the struts cannot overlap or extend outside the section.

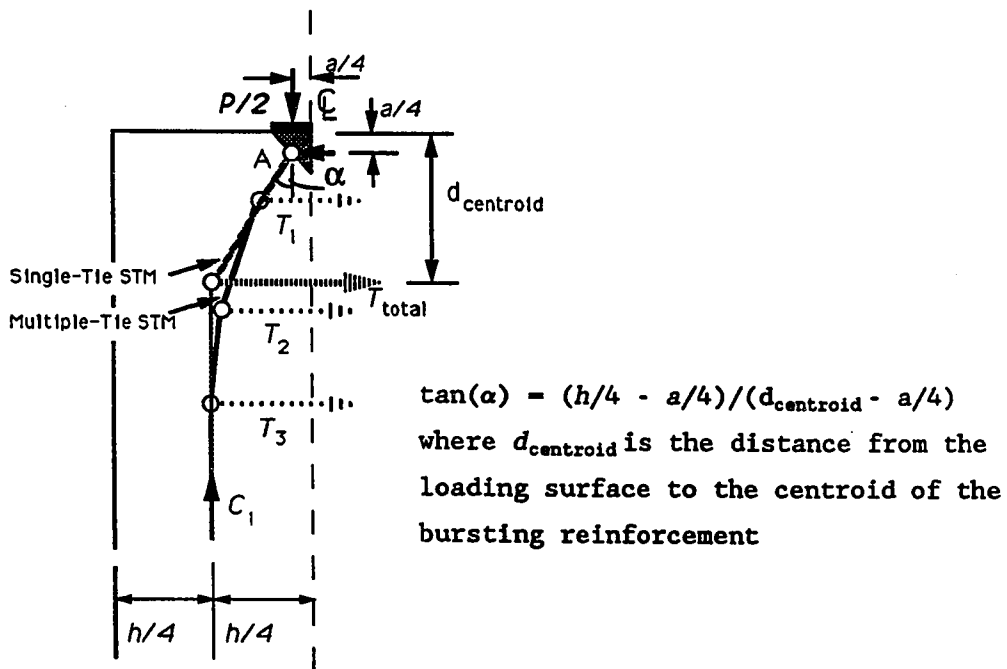
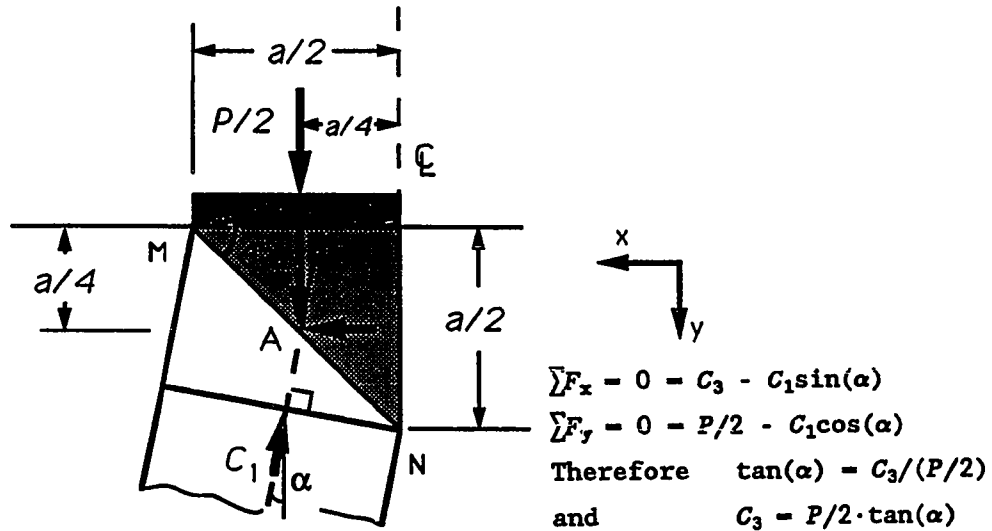
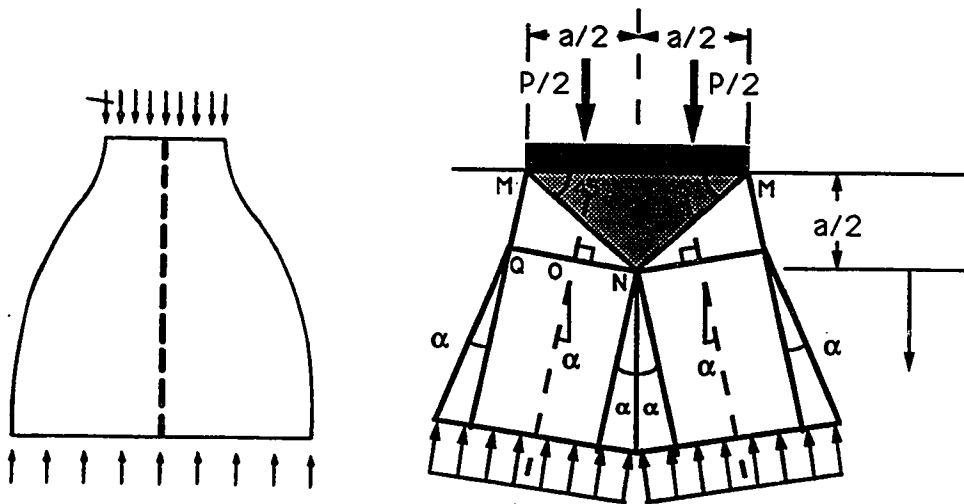


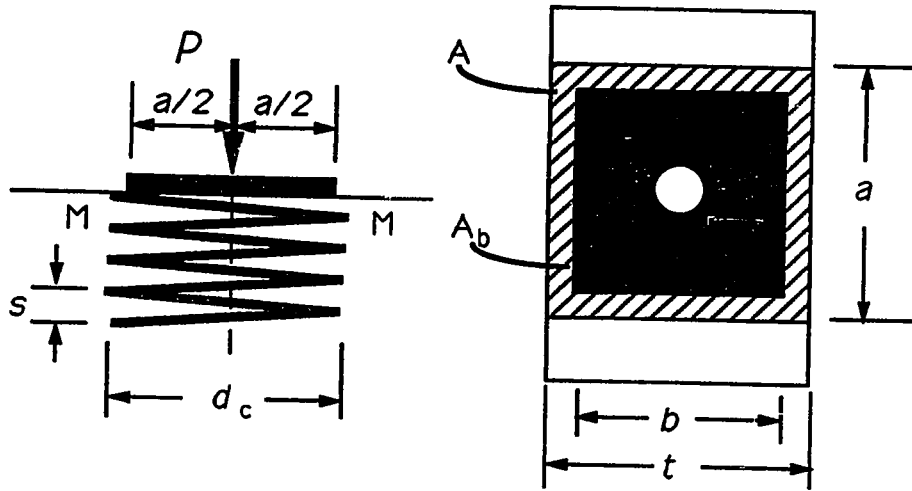
Figure 3.91 Local Zone Node Equilibrium



a) Bottle Struts [151] b) Simple Strut Approximation
Figure 3.92 Strut Development

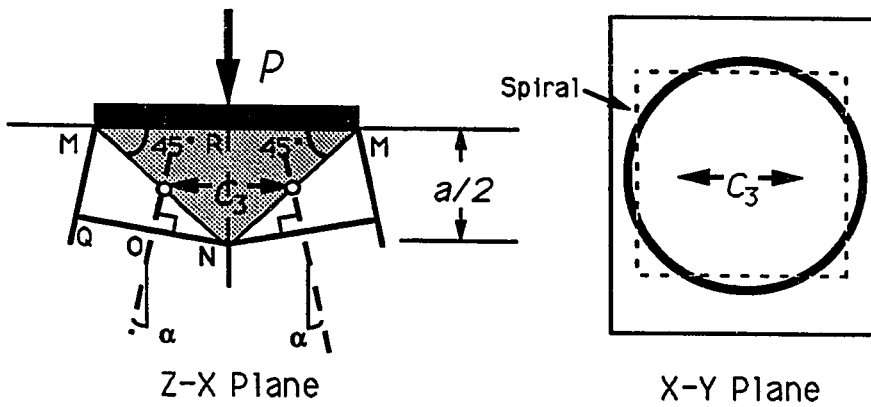
With the definition of the compression strut and nodes, there are four checks that must be made to verify the strength of the nodes and compressive struts to carry the ultimate load of the anchorage zone. The four checks are as follows:

- 1) Local zone bearing capacity ahead of the loading surface including confinement effects (see Fig. 3.93a plane MM),
- 2) Compression capacity perpendicular to the tendon path and centered on the secondary nodes assumed located at $a/4$ ahead of the plate for concentric anchorage as shown in Fig. 3.93b (plane NR),
- 3) Compressive strut capacity at the node-strut interface (plane QN in Fig. 3.94, and
- 4) Strut compressive capacity as the strut leaves the confined local zone and/or when the section thickness changes (plane KL in Fig. 3.95).



$$P_b = 0.7f'_c \sqrt{A/A_g} A_b + k \cdot f_y \cdot A_s / (s \cdot d) \cdot (1 - s/d_c)^2 \cdot A_{core} \leq 3f'_c \cdot A_b$$

a) Bearing Capacity



| | |
|-----------|---|
| Z-Y Plane | $C_3 = [0.7f'_c + 4P/A_b] ab/2$ |
| X-Y Plane | $C_3 = [0.7f'_c \sqrt{A/A_g} A_b + k \cdot f_y \cdot A_s / (s \cdot d) \cdot (1 - s/d_c)^2] ab/2$ |

b) Node Compression Capacity

Figure 3.93 Bearing and Node Compression Capacity

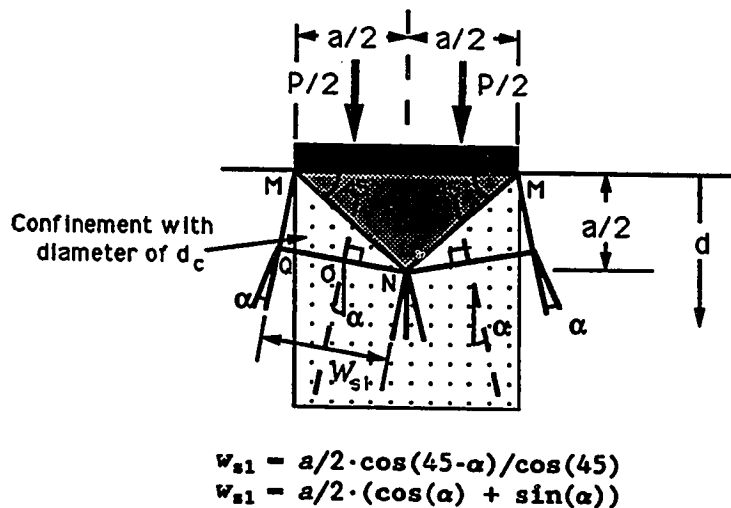
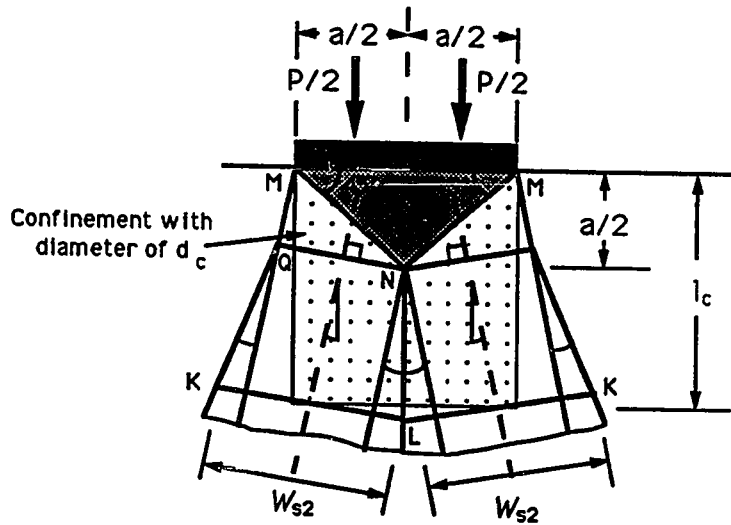


Figure 3.94 Node-Strut Interface Capacity

The capacity of the confined concrete in compression was the focus of the study by Roberts [143]. She concluded that the best equation for the bearing and strut capacity was the following:

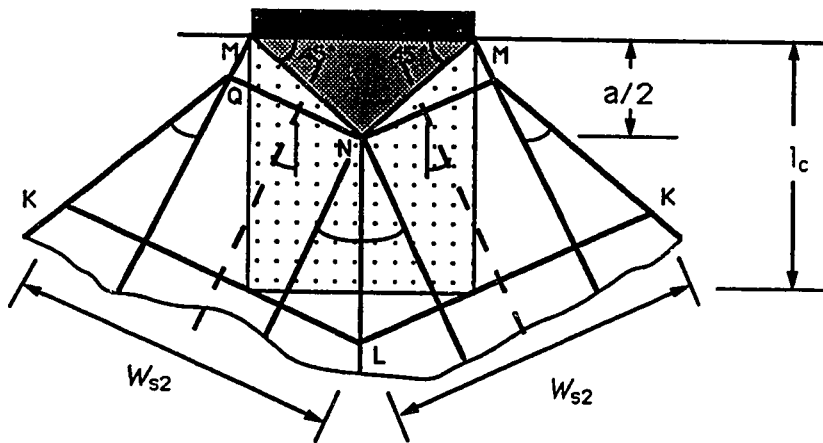
$$P_{b,s} = 0.7f'_c \sqrt{A/A_g} A_b + k \cdot f_y \cdot A_s / (s \cdot d) \cdot (1-s/d_c)^2 \cdot A_{core} \leq 3f'_c \cdot A_b$$

- where
- A - the effective area, which is the maximum area of the supporting surface that is geometrically similar to the loaded area and concentric with it;
 - A_b - the bearing or strut area;
 - A_{core} - the area confined by the local confining reinforcement;
 - A_g - gross area of the bearing plate;
 - A_s - the area of the confining reinforcement with the spacing "s";
 - d_f - the diameter of the spiral or the width of the ties;
 - f'_c - concrete compressive strength at the time of stressing;
 - f_y - the yield strength of the confining reinforcement;
 - k - 4 for spirals or active confinement and 2 for ties; and
 - s - the pitch of the spiral or the spacing of the ties.



$$w_{s2} = 2 \cdot (a/4 + (l_c - a/4) \tan(\alpha)) \cos(\alpha) \leq h/2 \cdot \cos(\alpha)$$

a) Strut Exit through Base of Confinement



$$w_{s2} = 2 \cdot (a/4 + (l_c - a/4) \tan(\alpha)) \cos(\alpha) \leq h/2 \cdot \cos(\alpha)$$

$$l = l_c - ((l_c - a/4) \tan(\alpha) + a/4 - d_c/2) \cos(\alpha) \sin(\alpha)$$

b) Strut Exit through Side of Confinement

Figure 3.95 Local Zone-General Zone Interface Capacity

The width of the strut at the node-strut interface is defined from the geometry of the node and is dependent on the plate size and the strut angle. The stress distribution across the strut is taken to be nonuniform when the strut is partially outside the confined region. In this case, the portion of the strut within the confined zone can utilize the additional concrete compressive capacity available because of the confinement. The portion of the strut outside the confined zone is restricted to the unconfined concrete compressive strength. As the compressive strut spreads away from the node, the average strut stress decreases since the percentage of the strut which is confined decreases. The actual strut compressive stress must be below the unconfined compressive strength of the concrete before the strut leaves the confined zone.

The width of the strut when it leaves the confined zone is dependent on the strut angle, the plate size, and the size of the confined zone. Figure 3.95a shows the case where the strut axis exits through the base of the confinement. The width of the strut, w_{s2} , is determined where the strut becomes fully unconfined. Figure 3.95b shows the other case where the strut axis exits through the side of the confinement zone. The equation for the strut width, w_{s2} , at the end of the confinement is more complicated. As long as a portion of the strut is confined and the confined zone has a constant width, the critical section for compression check number 4) will be at the base of the confinement. Figure 3.96 shows the ratio of the strut capacity as a function of the distance from the loading surface. The ratio of the strut capacity is the strength of the appropriate contributions of both the confined and unconfined concrete to the strength of the strut, assuming all concrete unconfined. The concentric anchorage zone on which Fig. 3.96 is based has the following characteristics: 1) the confined to unconfined concrete strength ratio is two, 2) the confinement has the same width as the bearing plate, and 3) the confinement has a length equal to the width of the bearing plate. When

the strut angle, α , is zero, the strut does not spread out and is completely confined (confined to unconfined strength ratio is equal to two) until it is a plate width away from the loading surface where the strut exits the confinement. For angles greater than zero, there is a gradual reduction in the capacity relationship until the strut capacity reaches the unconfined strength.

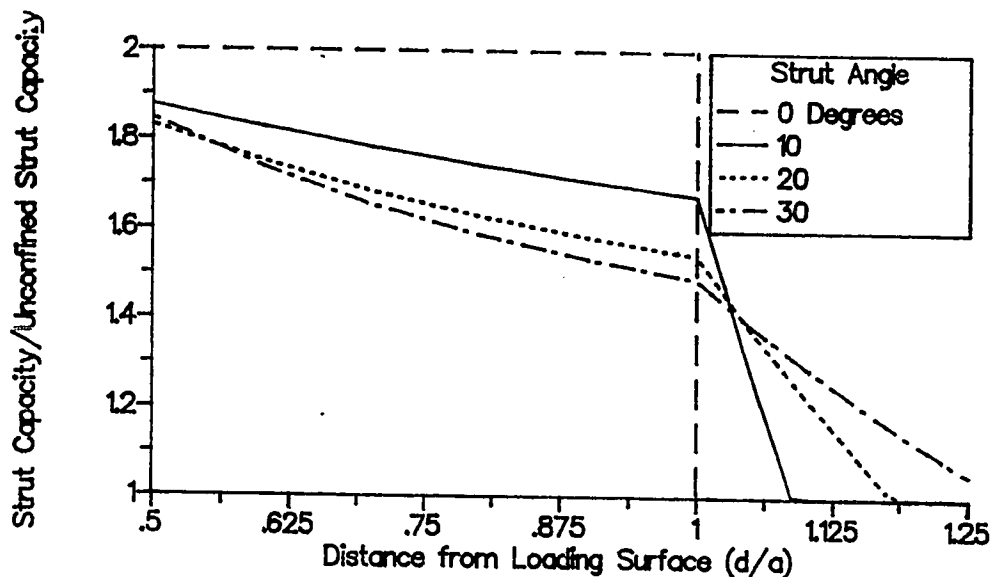
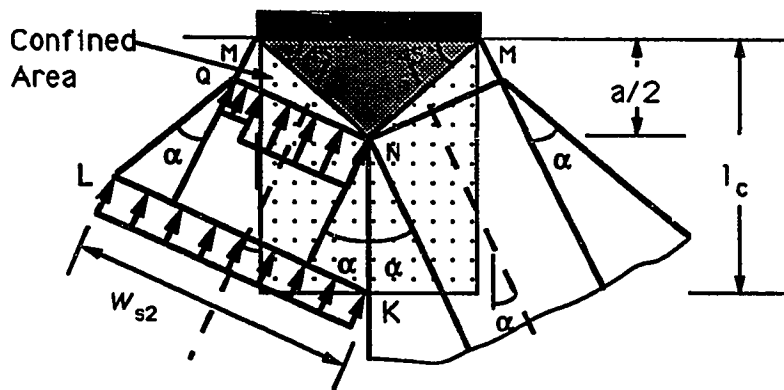


Figure 3.96 Strut Compression Capacity Relative to Unconfined Strut Capacity

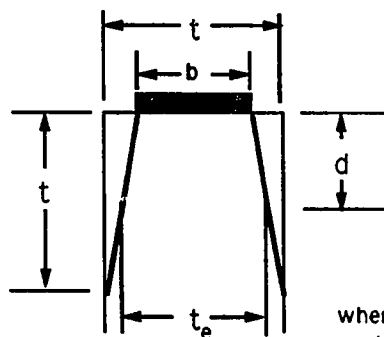
Figure 3.97 shows simplified assumptions that can be used to determine the strut size. To avoid determining where the strut exits the confined zone, it is conservative to use a strut width corresponding to the last location, "k", where the strut is confined along the tendon path (see Fig. 3.97a) but has a strut strength completely based on the unconfined concrete strength. This strut will always have a smaller width than the more accurate equations in Fig. 3.95. Since the strut width is smaller and the compressive strength is taken to be the unconfined compressive concrete strength, the capacity will also be smaller.



$$w_{s2} = a/2 \cdot (\cos(\alpha) + \sin(\alpha)) + 2 \cdot (l_c - a/2) \sin(\alpha) \leq h/2 \cdot \cos(\alpha)$$

$$w_{s2} = a/2 \cdot \cos(\alpha) + (2 \cdot l_c - a/2) \sin(\alpha)$$

a) Local Zone-General Zone Interface



$$t_e = b + (t - b) \cdot d/t$$

where d is distance to the centerline of the strut measured perpendicular to and from the loading surface

b) Strut Transverse Thickness

Figure 3.97 Simplified Equations

In Fig. 3.97b, the width of the strut in the transverse direction varies from the plate transverse width, (b), to the section transverse thickness, (t). The rate at which the strut transverse width increases can be determined from the STM in the transverse direction or can be conservatively assumed to increase linearly from the plate width at the loaded surface to the section transverse thickness at a depth from the loaded surface equal to the section thickness (see Fig. 3.97b) of thin sections. The transverse width of the inclined strut is calculated at the centerline of the strut; therefore, it is an average strut thickness over the entire width.

Figure 3.98 shows two different strut paths that could be used in determining the strut width. The outer dashed line, (a), is the line of action of the strut based on a single-tie STM with the lower node assumed to be at the centroid of the bursting reinforcement. The solid wide line, (b), represents the line of action of the strut from a more accurate multiple-tie STM. When determining the strut width at a location more than a distance equal to the plate width below the loaded surface, the two struts begin to separate. The assumption that the strut width is equal to two times the distance from the specimen centerline yields different answers for the strut width, (w_1), depending on which strut path is used. Fig. 3.98 shows estimates for the strut width for the two cases. There can be a significant difference between the strut widths, w_a and w_b . Since it takes a detailed analysis to determine the line of action of the strut for the multiple-tie STM, the strut path based on the reinforcement centroid will be used (path "a" and width w_a). The use of this strut is within the accuracy of the model as long as the location of the calculated strut width is within approximately two plate widths of the loading surface.

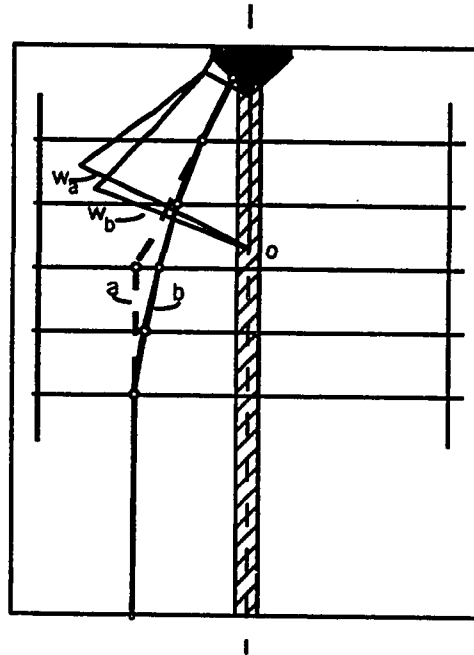


Figure 3.98 Strut Line of Action and Width

Roberts [143] has proposed the testing and certification of anchorage devices as the practical way of utilizing anchorage devices that require high bearing stresses to reach their design capacity. Her recommendations require that anchorage device manufacturers or users test load any anchorage devices that have a rated capacity in excess of a certain bearing pressure to at least the maximum load of the tendons. In addition, they must provide designers with the minimum edge distances and confining reinforcement details required to develop the test loads. In design practice, if an engineer uses an anchorage device that has been so tested and certified, it is not necessary to check the bearing capacity, the node-strut interface capacity or the nodal compression capacity (C_3 in Fig. 3.93b, strut perpendicular to the tendon path within the node) as long as strut angles are less than 40 degrees. Strut angles for most post-tensioning application are less than 30 degrees. When the strut angles become larger than 40 degrees, the angle is so much greater than the strut angle in the certification

test that a more detailed analysis is necessary. In the specimens tested in this research project, the largest strut angle was approximately 35 degrees. The engineer must always check the capacity at the local zone-general zone interface at the end of the confinement.

Because of the certification test, the safety factor in the local zone is somewhat lower than in the rest of the anchorage zone. If the maximum permissible temporary stressing load for a bridge is 0.8 times the capacity of the tendon, then the required load factor in the test is $1/0.8$ or 1.25. No ϕ factor is required. The maximum load was accepted for the certification test since, in load tests with tendons, the test specimens may be limited to the maximum capacity of the tendons. In the general zone, a load factor of 1.3 similar to that used for dead load is required because of the high degree of knowledge about the maximum tendon load that can be applied to the structure. A ϕ factor of 0.7 for compression is recommended, which is similar to that of tied columns, and matches the high standard deviation of the compression test results when correlated with theoretical predictions. Roberts found this to be true in her investigation. The load factor and ϕ factor combine to yield a safety factor of $1.3/0.7$ or 1.86. This is some 50 percent higher than that required for local zone test for anchorage devices. Therefore, the engineer must check the local zone-general zone interface to verify that the unconfined concrete capacity is high enough to handle the applied load. In the certification test proposed by Roberts, anchorage device suppliers are allowed to place confining reinforcement in the base of the test specimen outside the local zone up to a volumetric ratio of 0.013. If such reinforcement has been placed in the test specimen, the engineer must place at least the equivalent reinforcement in the general anchorage zone. Roberts did find that the failure load of the general zone tests were always higher than the isolated local zone tests results.

In the following subsection, a concentric anchorage specimen will be analyzed utilizing the concepts just described. Then, ultimate load

predictions for all the concentric test specimens will be compared with test loads.

3.4.2 Basic Strut-and-Tie Model for Ultimate Load Prediction

Example Calculations. As stated in the previous subsection, it is important, when designing with the strut-and-tie model, that all possible failure modes are checked. The following calculations demonstrate the procedures that were necessary to select the general zone bursting reinforcement, to check the local zone, and to check the compression struts of Specimen B1 (see Fig. 3.17). The compression strut checks were as follows:

- 1) The local zone bearing capacity ahead of the loading surface including the confinement effects (see Fig. 3.93a plane MM),
- 2) The compression capacity perpendicular to the tendon path and centered on the secondary nodes assumed to be located at $a/4$ ahead of the plate for concentric anchorage as shown in Fig. 3.93b (plane NR),
- 3) The compressive strut capacity at the node-strut interface (plane QN in Fig. 3.94), and
- 4) The strut compressive capacity as the strut leaves the confined local zone and/or when the section thickness changes (plane KL in Fig. 3.95).

As is customary in design of laboratory test specimens, ϕ was assumed to be one and no load factors were used because the tests were conducted under laboratory conditions. The calculations were carried out prior to the test and are reported as if the ultimate test load is unknown. This is the same procedure that would be used by an engineer who is checking an anchorage detail proposal when knowing only the concrete strength, proposed reinforcement layout and anchorage size. In design the engineer would include the proper load factors and ϕ factors.

The calculations are divided into six parts. First, the known physical dimensions and properties are given. Based on the given

proposed reinforcement distribution, the ultimate load is computed assuming the tension ties would control. Any contribution of the spiral to the tension tie forces is neglected. Then, the four compression checks are compared against the tension tie governing load prediction. The first compression capacity check is for failure immediately ahead of the bearing surface (see Fig. 3.93a). Then, the strut capacity between the secondary nodes must be checked (see Fig. 3.93b). The final two checks verify the capacity at the node-strut interface (see Fig. 3.94), and at the interface between the local and the general zones (see Fig. 3.97a). For the compression strut checks, the spiral in the local zone is assumed to confine an equivalent square area concentric with the spiral.

- 1) Given: Plate Size = 6.5" x 6.5" (a x b)
 Specimen Thickness (t) = 9 inches
 Depth of Section (h) = 16 inches
 $f'_c = 5.38$ ksi
 Spiral = #4 ($f_y = 80.3$ ksi) smooth bar,
 $d_c = 7$ inches, $s = 1.25$ inches, and $l_c = 9.75$ inches
 Bursting Reinforcement: #4 ties at 7 3/8 inches and 9 7/8 inches with $F_y = 12.7$ kips/bar (two legs of a closed hoop at each level)

- 2) Determination of Ultimate Load assuming Tension Ties Control with a uniform stress distribution at the end of the anchorage zone (see Fig. 3.90)

$$P = 2 \sum [T_i(d_i - a/4)] / (h/4 - a/4) \text{ where } i \text{ is the number of the reinforcement layer}$$

$$P = 2[12.7 \cdot 2 \cdot (7.375 - 6.5/4) + 12.7 \cdot 2 \cdot (9.875 - 6.5/4)] / (16/4 - 6.5/4) = \underline{299 \text{ kips}}$$

Therefore, the capacity of the anchorage zone if the tension ties control, and the stress distribution at the end of the anchorage zone is uniform, is 299 kips.

- 3) Bearing Capacity Immediately Ahead of the Anchorage Device

$$P_b = 0.7f'_c \sqrt{A/A_s} A_b + k \cdot f_y \cdot A_s / (s \cdot d) \cdot (1 - s/d_c)^2 \cdot A_{cor} \leq 3f'_c \cdot A_b$$

where A = the effective area which is the maximum area of the supporting surface that is geometrically similar to the

- loaded area and concentric with it;
- A_b - the bearing or strut area (A_{st});
- A_{core} - the area confined by the local confining reinforcement (A_{stc} for struts);
- A_g - gross area of the bearing plate;
- A_s - the area of the confining reinforcement with the spacing "s";
- d_f - the diameter of the spiral or the width of the ties;
- f'_c - concrete compressive strength at the time of stressing;
- f_y - the yield strength of the confining reinforcement;
- k - 4 for spirals or active confinement and 2 for ties; and
- s - the pitch of the spiral or the spacing of the ties.

$$A_b = A_g = 6.5 \cdot 6.5 = 42.3 \text{ in}^2$$

$$A_{core} = \pi \cdot 7^2 / 4 = 38.5 \text{ in}^2$$

$$A = 9.0 \cdot 9.0 = 81.0 \text{ in}^2$$

$$P_b = 0.7 \cdot 5.38 \cdot \sqrt{81.0 / 42.3} \cdot 42.3 +$$

$$4 \cdot (80.3 \cdot 0.2 \cdot 2) / (1.25 \cdot 7) \cdot (1 - 1.25/7)^2 \cdot 38.5$$

$$= \underline{602 \text{ kips}} >> \text{ tension tie load still controls (299 kips)}$$

4) Force Between Secondary Nodes

$$P_s = 0.7 f'_c \sqrt{A/A_{st}} A_{st} + k \cdot f_y \cdot A_s / (s \cdot d) \cdot (1 - s/d_c)^2 \cdot A_{stc} \leq 3 f'_c \cdot A_{st}$$

where A_{st} - the total strut area

A_{stc} - the area of the strut which is confined

$$A = A_{st} = A_{stc} = (a/2) \cdot b = (6.5/2) \cdot 6.5 = 21.1 \text{ in}^2$$

$$P_s = 0.7 \cdot 5.38 \cdot \sqrt{21.1/21.1} \cdot 21.1 +$$

$$4 \cdot (80.3 \cdot 0.2 \cdot 2) / (1.25 \cdot 7) \cdot (1 - 1.25/7)^2 \cdot 21.1 = \underline{289 \text{ kips}}$$

$$P_s \leq 3 \cdot 5.38 \cdot 21.1 = 341 \text{ kips}$$

$$P_s \geq C_3 \text{ ??}$$

where C_3 = Total Bursting Reinforcement Tension Force determined from summation of tension capacity of bursting reinforcement

$$C_3 = 4 \cdot 12.7 = 50.8 \text{ kips}$$

$$\leq 289 \text{ kips} \quad \text{Therefore, strut will not fail.}$$

5) Strut Capacity at the Node-Strut Interface

Since the depth of the node-strut interface ($a/2 = 6.5/2$) is 3.25 inches, which is less than the length of the spiral (9.75 inches), the compressive capacity at the node-strut interface is a combination of

the confined and unconfined concrete.

$$P_s = 2 \cdot (\text{Confined Concrete Capacity} + \text{Unconfined Concrete Capacity}) \cdot \cos(\alpha)$$

** equation is multiplied by two to include struts on either side of the specimen centerline and is multiplied by $\cos(\alpha)$ to compare with the axial force

$$P_s = 2 \cdot (\sigma_{s\text{-confined}} \cdot A_{stc} + \sigma_{s\text{-unconfined}} \cdot A_{stU}) \cdot \cos(\alpha)$$

where A_{stc} = confined strut area
 A_{stU} = $A_{st} - A_{stc}$ = unconfined strut area
 A_{st} = total strut area
 $\sigma_{s\text{-confined}}$ = maximum stress in confined concrete
 $\sigma_{s\text{-unconfined}}$ = maximum stress in unconfined concrete

Determine Strut Angle (α):

The strut angle can be determine from equilibrium or from specimen geometry.

$$\text{atan}(\alpha) = C_3 / (\text{Axial Load} / 2)$$

$$\text{atan}(\alpha) = 50.8 / (299 / 2)$$

$$\alpha = 18.8 \text{ degrees}$$

or

$$\text{atan}(\alpha) = (h/4 - a/4) / (d_{\text{centroid}} - a/4)$$

where d_{centroid} = the distance from the loading surface to the centroid of the bursting reinforcement

$$\text{atan}(\alpha) = (16/4 - 6.5/4) / (8.625 - 6.5/4)$$

$$\alpha = 18.8 \text{ degrees}$$

Determine the portion of the strut which is confined and unconfined:

Determine Equivalent Width of Confined Area (Since a spiral is round, it is easier to convert spiral into an equivalent square to compare it with rectangular struts. This is especially true when the struts are not symmetrical as they are in eccentric and multiple anchorages.)

$d_c = \sqrt{\pi \cdot 7 \cdot 7 / 4} = 6.2$ inches >> Therefore the distance from the specimen centerline to the confined boundary is 3.1 inches.

Determine the Width (w_{s1} , see Fig. 3.94) and Thickness (t_s , see Fig. 3.97b) of the Strut

$$\begin{aligned}
 w_{s1} &= a/2 \cdot \cos(45-\alpha)/\cos(45) \\
 &= 6.5 \cdot \cos(45-18.8)/(2 \cdot \cos(45)) = 4.12 \text{ inches} \\
 t_e &= b + (t-b) \cdot d/t \\
 d &= \text{distance to the centroid of plane } w_{s1} \text{ from the} \\
 &\quad \text{loading surface perpendicular to the tendon axis} \\
 &= a/2 - w_{s1}/2 \cdot \sin(\alpha) = 6.5/2 - 4.12/2 \cdot \sin(18.8) \\
 &= 2.59 \text{ inches} \\
 t_e &= 6.5 + (9-6.5) \cdot 2.59/9 = 7.22 \text{ inches} \\
 A_{st} &= w_{s1} \cdot t_e = 4.12 \cdot 7.22 = 29.7 \text{ in}^2 \\
 A_{stc} &= d_c \cdot (d_c/2/\cos(\alpha)) = 6.2 \cdot (6.2/2/\cos(18.8)) = 20.3 \text{ in}^2 \\
 A_{stu} &= A_{st} - A_{stc} = 29.7 - 20.3 = 9.4 \text{ in}^2
 \end{aligned}$$

Determine Maximum Compressive Strut Stress:

Maximum Stress in the Confined Zone

$$\begin{aligned}
 \sigma_s &= 0.7f'_c \sqrt{A/A_{st}} + k \cdot f_y \cdot A_s / (s \cdot d) \cdot (1-s/d_c)^2 \leq 3f'_c \\
 A &= \text{the effective area, which in most cases is} \\
 &\quad \text{restricted by the ratio of the section} \\
 &\quad \text{thickness to the strut thickness} \\
 A &= t \cdot (w_{s1} \cdot t/t_e) = 9 \cdot (4.12 \cdot 9/7.12) = 46.2 \text{ in}^2 \\
 \sigma_s &= 0.7 \cdot 5.38 \sqrt{46.2/29.7} + \\
 &\quad 4 \cdot (80.3 \cdot 0.2 \cdot 2) / (1.25 \cdot 7) \cdot (1-1.25/7)^2 \\
 &= 14.9 \text{ ksi} \leq 3f'_c = 3 \cdot 5.38 = 16.1 \text{ ksi}
 \end{aligned}$$

Maximum Stress in the Unconfined Zone

$$\sigma_s = 0.7 \cdot 5.38 \sqrt{46.2/29.7} + 0 = 4.70 \text{ ksi}$$

Maximum Axial Load:

$P_s = 2 \cdot [14.9 \cdot 20.3 + 4.70 \cdot 9.4] \cdot \cos(18.8) = \underline{656}$ kips This is greater than the load predicted by the tension ties (299 kips). Therefore, the node-strut interface does not control.

It is conservative to neglect any contribution from the unconfined concrete as shown by the following calculation.

$$\begin{aligned}
 A_{st} &= 6.2 \cdot (3.1/\cos(18.8)) = 20.3 \text{ in}^2 \\
 A/A_{st} &= 1 \\
 \sigma_s &= 0.7 \cdot 5.38 \cdot \sqrt{(1) +} \\
 &\quad 4 \cdot (80.3 \cdot 0.2 \cdot 2) / (1.25 \cdot 7) \cdot (1-1.25/7)^2 = 13.8 \text{ ksi}
 \end{aligned}$$

$$P_s = 2 \cdot [13.8 \cdot 20.3] \cdot \cos(18.8) = \underline{532} \text{ kips}$$

6) Strut Capacity at Interface between the Local Zone and the General Zone (Base of the Spiral)

The width of the strut is conservatively estimated in accordance with Fig. 3.97a.

$$\begin{aligned} w_{s2} &= a/2 \cdot \cos(\alpha) + (2l_c - a/2) \sin(\alpha) \\ &= 6.5/2 \cdot \cos(18.8) + (2 \cdot 9.75 - 6.5/2) \cdot \sin(18.8) \\ &= 8.31 \text{ inches} \end{aligned}$$

$$w_{s2} \leq h/2/\cos(\alpha) = 16/2/\cos(18.8) = 8.45 \text{ inches}$$

Therefore, $w_{s2} = 8.31$ inches

$$\begin{aligned} t_e &= 6.5 + (9 - 6.5) \cdot (9.75 - 8.31/2 \cdot \sin(18.8))/9 \\ &= 8.84 \text{ inches} \end{aligned}$$

$$A_{st} = 8.84 \cdot 8.31 = 73.4 \text{ in}^2$$

$$A = t \cdot (w_{s2} \cdot t/t_e) = 9 \cdot (8.31 \cdot 9/8.84) = 76.1 \text{ in}^2$$

$$\sigma_s = 0.7 \cdot 5.38 \sqrt{76.1/73.4} + 0 = 3.90 \text{ ksi}$$

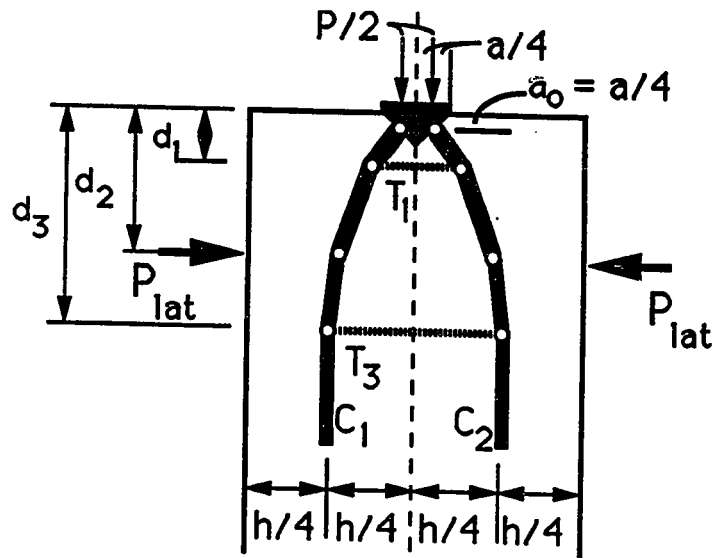
$$P_s = 2 \cdot [3.90 \cdot 73.4] \cdot \cos(18.8) = \underline{542} \text{ kips} \gg \text{ This is greater than the load predicted by the tension ties (299 kips). Therefore, the local zone-general zone interface does not control.}$$

Thus, based on these calculations, this specimen would be governed by the tension tie and the predicted capacity would be 299 kips.

Calculations similar to those just demonstrated will be used in the following subsection to determine the capacity for all the concentric anchorage specimens.

3.4.3 Basic Strut-and-Tie Model for Ultimate Load Prediction Summary. The following information is needed before determining the ultimate load prediction for the concentric anchorage specimens. In specimens with lateral post-tensioning, the lateral forces are treated as a compression force applied to the STM (see Fig. 3.99a). In Specimen B8, the plate was only loaded through a four-inch diameter pedestal instead of using uniform loading over the entire width as in all other specimens. The dimensions of the effective bearing plate

were determined by finding a rectangular plate with the same area as the four inch diameter pedestal and by assuming a 45 degree diffusion angle for the force through the loading plate (see Fig. 3.99b).



$$P = \frac{2}{(h/4 - a/4)} [T_1(d_1 - a_0) + T_3(d_3 - a_0) + P_{lat}(d_2 - a_0)]$$

Figure 3.99a Strut-and-Tie Model with Lateral Post-Tensioning

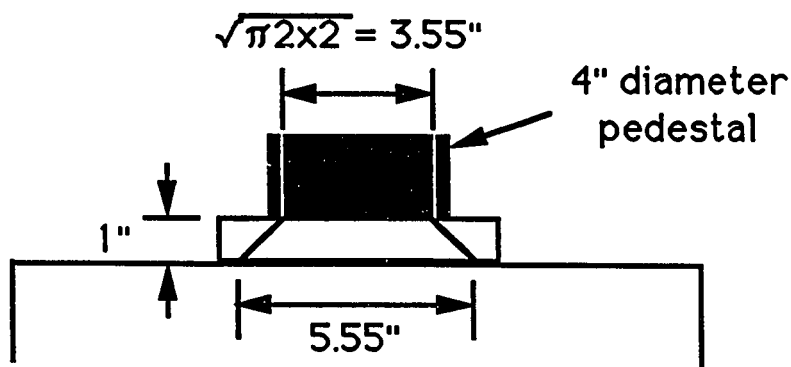


Figure 3.99b Specimen B8 Plate Width Modification for Loading

Table 3.17 STM Predictions for Bearing, Node Compression and Tension Tie Failure

| Specimen | Bursting Tension (kips) | Reinforcement Centroid (in) | Ao (in) | A1 (in) | Tension Tie STM Capacity (kips) | f'c (ksi) | Bearing Capacity (kips) | Node Compression Limit (C3)* (kips) |
|----------|----------------------------|--------------------------------|------------|------------|------------------------------------|--------------|----------------------------|--|
| A1 | 73.9 | 12.00 | 3.00 | 3.00 | 222 | 3.36 | 340 | 276 |
| A2 | 79.8 | 11.00 | 3.00 | 3.00 | 213 | 3.36 | 340 | 276 |
| A3 | 106.8 | 18.50 | 3.00 | 3.00 | 552 | 3.36 | 340 | 276 |
| A4 | 106.80 | 17.50 | 3.00 | 3.00 | 516 | 3.84 | 544 | 427 |
| B1 | 50.80 | 8.63 | 1.63 | 1.63 | 299 | 5.38 | 602 | 289 |
| B2 | 29.36 | 13.44 | 1.63 | 1.63 | 292 | 5.38 | 602 | 289 |
| B3 | 39.60 | 10.50 | 1.63 | 1.63 | 296 | 5.38 | 602 | 289 |
| B4 | 42.56 | 9.34 | 1.63 | 1.63 | 277 | 5.38 | 602 | 289 |
| B5 | 0 | N/A | 1.63 | 1.63 | 0 | 5.32 | 599 | 289 |
| B6 | 42.56 | 9.14 | 1.63 | 1.63 | 269 | 5.32 | 218 | 79 |
| B7 | 42.56 | 9.14 | 1.63 | 1.63 | 269 | 5.32 | 599 | 289 |
| B8 | 42.56 | 9.14 | 1.39 | 1.39 | 253 | 5.32 | 567 | 210 |
| C1 | 52.80 | 15.00 | 1.63 | 1.63 | 192 | 5.19 | 439 | 201 |
| TPT1 | 26.20 | 11.50 | 1.63 | 1.63 | 180 | 4.95 | 484 | 192 |
| TPT2 | 38.09 | 11.19 | 1.63 | 1.63 | 253 | 4.95 | 484 | 192 |
| TPT3 | 55.12 | 8.08 | 1.63 | 1.63 | 247 | 5.15 | 492 | 194 |
| TPT4 | 49.80 | 8.42 | 1.63 | 1.63 | 235 | 4.95 | 484 | 192 |

*Node Compression Limit must be greater than bursting reinforcement tension capacity

Table 3.17 shows the STM prediction results for the concentric anchorage zone series assuming that the tension ties control and that the full yield strength of all the bursting reinforcement is developed. Since Specimen B5 had zero bursting reinforcement, the STM predicts zero capacity. Table 3.17 also shows the predicted failure loads for a bearing failure and a nodal compression failure. Specimen A4 has a much higher bearing capacity than the other "A" series specimens because of the transverse post-tensioning which was treated as an equivalent spiral applying confinement ($0.625 \text{ ksi} = A_s f_y / s d$). The nodal compression limit value (C_3) should be compared with the total bursting force on the left side of the table rather than with the axial capacity. All the specimens have nodal compression limit values (C_3) much greater than the magnitude of total tension bursting force. Table 3.18 shows the predicted anchorage capacity when it is controlled by

Table 3.18a STM Node-Strut Interface Capacity

| Specimen | Alpha (degrees) | Strut Width (in) | Strut Thickness (in) | Confined Width (in) | Confined Allowable (ksi) | Unconfined Allowable (ksi) | Predicted Capacity (kips) |
|----------|--------------------|------------------------|----------------------------|---------------------------|--------------------------------|----------------------------------|---------------------------------|
| A1 | 33.65 | 8.32 | 6.00 | 0.00 | N/A | 2.35 | 195 |
| A2 | 36.84 | 8.40 | 6.00 | 0.00 | N/A | 2.35 | 190 |
| A3 | 21.15 | 7.76 | 6.00 | 0.00 | N/A | 2.35 | 204 |
| A4 | 22.49 | 7.84 | 6.00 | 2.61 | 5.19 | 2.69 | 306 |
| B1 | 18.77 | 4.12 | 7.22 | 3.28 | 14.61 | 4.70 | 646 |
| B2 | 11.39 | 3.83 | 7.30 | 3.16 | 14.55 | 4.65 | 636 |
| B3 | 15.05 | 3.98 | 7.26 | 3.21 | 14.58 | 4.67 | 642 |
| B4 | 17.10 | 4.06 | 7.24 | 3.25 | 14.59 | 4.69 | 645 |
| B5 | 0.00 | 3.25 | 7.40 | 3.10 | 14.44 | 4.53 | 599 |
| B6 | 17.57 | 4.08 | 7.23 | N/A | N/A | 4.63 | 261 |
| B7 | 17.57 | 4.08 | 7.23 | 3.25 | 14.54 | 4.63 | 642 |
| B8 | 18.68 | 3.52 | 6.40 | 3.27 | 15.14 | 5.24 | 605 |
| C1 | 28.81 | 4.41 | 7.11 | 3.99 | 10.24 | 4.34 | 528 |
| TPT1 | 16.23 | 4.03 | 7.25 | 3.69 | 10.39 | 4.78 | 550 |
| TPT2 | 16.03 | 4.02 | 7.25 | 3.69 | 10.38 | 4.78 | 550 |
| TPT3 | 24.05 | 4.29 | 7.16 | 3.88 | 10.64 | 5.04 | 564 |
| TPT4 | 21.59 | 4.22 | 7.19 | 3.81 | 10.43 | 4.82 | 554 |

Table 3.18b STM Local Zone-General Zone Capacity

| Specimen | Depth of Confinement (in) | Alpha (degrees) | Strut Width (in) | Strut Thickness (in) | Unconfined Allowable (ksi) | Predicted Capacity (kips) |
|----------|---------------------------------|--------------------|------------------------|----------------------------|----------------------------------|---------------------------------|
| A1 | | | | | | |
| A2 | | | | | | |
| A3 | | | | | | |
| A4 | 4(9.82) | 22.49 | 10.76 | 6.00 | 2.69 | 321 |
| B1 | 9.75 | 18.77 | 8.31 | 8.84 | 3.84 | 533 |
| B2 | 9.75 | 11.39 | 6.39 | 9.00 | 3.77 | 425 |
| B3 | 9.75 | 15.05 | 7.36 | 9.00 | 3.77 | 482 |
| B4 | 9.75 | 17.10 | 7.88 | 9.00 | 3.77 | 511 |
| B5 | 9.75 | 0.00 | 3.25 | 9.00 | 3.72 | 218 |
| B6 | | | | | | |
| B7 | 9.75 | 17.57 | 8.00 | 9.00 | 3.72 | 511 |
| B8 | 9.75 | 13.68 | 7.99 | 9.00 | 3.72 | 507 |
| C1 | 9.50 | 28.81 | 10.44 | 8.14 | 3.79 | 565 |
| TPT1 | 7.75 | 16.23 | 6.54 | 8.89 | 3.90 | 436 |
| TPT2 | 7.75 | 16.03 | 6.51 | 8.90 | 3.90 | 434 |
| TPT3 | 7.75 | 24.05 | 7.96 | 8.64 | 4.17 | 524 |
| TPT4 | 7.75 | 21.59 | 7.53 | 8.73 | 3.97 | 485 |

the compression struts at the node-strut interface (Table 3.18a) and by the local zone-general zone interface (Table 3.18b). The depth of the confinement for Specimen A4 is shown as 4(9.82) inches. Four inches was the depth of the confining transverse post-tensioning force, while 9.82 inches was the depth of the strut along the specimen centerline when the last portion of the strut width became unconfined ($9.82 - 10.76 \sin(22.49) = 4$ inches).

Table 3.19 STM Prediction Summary

| Specimen | Tension Tie (kips) | Bearing (kips) | Node-Strut Interface (kips) | L.Z.-G.Z. Interface (kips) | Controlling Load (kips) | Ultimate Test (kips) | Test/Predicted |
|---|--------------------|----------------|-----------------------------|----------------------------|-------------------------|----------------------|----------------|
| A1 | 222 | 340 | <u>195</u> | - | 195 | 298 | 1.52 |
| A2 | 213 | 340 | <u>190</u> | - | 190 | 275 | 1.45 |
| A3 | 552 | 340 | <u>204</u> | - | 204 | 265 | 1.30 |
| A4 | 516 | 544 | <u>306</u> | 321 | 306 | 437 | 1.43 |
| B1 | <u>299</u> | 602 | 646 | 533 | 299 | 366 | 1.22 |
| B2 | <u>292</u> | 602 | 636 | 425 | 292 | 290 | 0.99 |
| B3 | <u>296</u> | 602 | 642 | 482 | 296 | 331 | 1.12 |
| B4 | <u>277</u> | 602 | 645 | 511 | 277 | 337 | 1.22 |
| B5 | - | 599 | 599 | <u>218</u> | 218 | 212 | 0.97 |
| B6 | 269 | <u>218</u> | 261 | - | 218 | 297 | 1.36 |
| B7 | <u>269</u> | 599 | 642 | 511 | 269 | 296 | 1.10 |
| B8 | <u>252</u> | 567 | 605 | 507 | 252 | 276 | 1.09 |
| C1 | <u>192</u> | 439 | 528 | 565 | 192 | 370 | 1.93 |
| TPT1 | <u>180</u> | 484 | 550 | 436 | 180 | 310 | 1.72 |
| TPT2 | <u>253</u> | 484 | 550 | 434 | 253 | 300 | 1.19 |
| TPT3 | <u>247</u> | 492 | 564 | 524 | 247 | 370 | 1.50 |
| TPT4 | <u>235</u> | 484 | 554 | 485 | 235 | 332 | 1.41 |
| Note: Node Compression was found to not to control in Table 3.17. | | | | | | Average | 1.32 |
| | | | | | | Standard Deviation | 0.25 |
| | | | | | | Coef. of Variance | 0.19 |

Table 3.19 is a summary of the predicted loads for all the failure modes for the concentric anchorage specimens. The minimum or governing load predicted for each specimen is underlined. The tension tie was predicted as the controlling failure mode for all of the tests except Specimens A1, A2, A3, A4, B5 and B6. Specimen B5 is shown as a compression failure because the theoretical STM tie failure (0 kips) is not reasonable due to the large concrete tension contribution. Specimen B6 had all of the tension tie reinforcement yield prior to

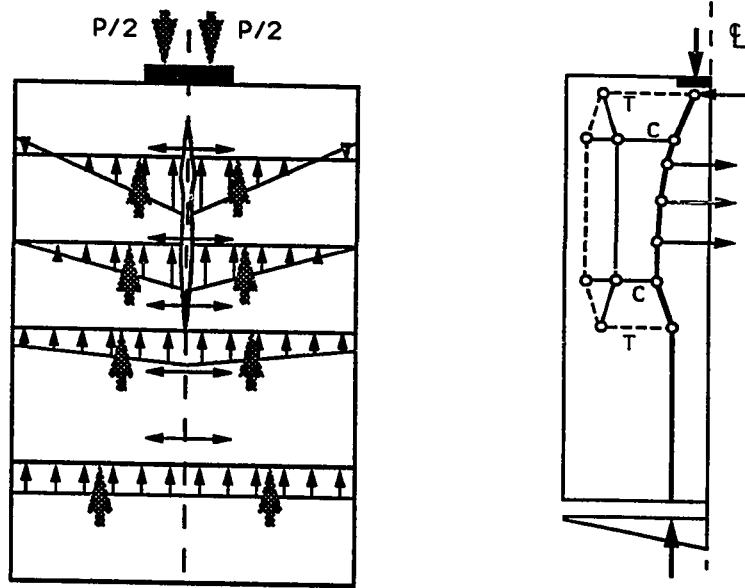
failure but did show considerably less post-maximum load ductility than Specimen B4 (see Fig. 3.41) possibly due to the local zone weakness. Note that the test-to-predicted ratio for this specimen is the highest of all of the Series "B" specimens. The compression failure predictions for the "A" series specimen are confirmed by the experimental results. The maximum bursting reinforcement strains measured in Specimens A1, A2, and A3 were below 70 percent of their yield value. The STM is supposedly a lower bound model. It predicts a conservative load for all the tests except Specimens B2 and B5, which are respectively only one and three percent unconservative. On the average, the model is 32 percent conservative with a coefficient of variance of 19 percent. This is quite acceptable for this type of application for a design model.

3.4.4 Capacity beyond the Basic STM. The conventional way to use the STM is to use experience or an elastic stress distribution to locate the compression struts, to neglect any concrete tension capacity, and to provide reinforcement to carry all of the tensile bursting forces. It is obvious that the tension capacity of concrete largely resists the bursting forces before the concrete cracks and plays an important role after cracking begins. This behavior is reflected in the measured bursting reinforcement strains (measured with strain gages) which remain very small until after first cracking. The role that the tension capacity of concrete may play at loads near ultimate and the reason why some of the concentric anchorage zone specimens can reach loads significantly above the predictions of the basic STM are addressed in this subsection. Models will be developed which more closely model the plastic behavior of the specimens near their ultimate load. The next subsection will go through a development of the plastic behavior of the concentric anchorage specimens through the use of a beam on an elastic foundation analysis.

3.4.4.1 Development of Beam-Columns. As the anchorage zone begins to crack, the stress distribution can deviate significantly from

the elastic distribution. As the crack propagates down the section, the anchorage zone begins to act as two separate beam-columns tied together by the bursting reinforcement, the local zone confining reinforcement, and the uncracked concrete at the base of the section (see Fig. 3.100a). The stress distributions shown at various locations in the sections in Fig. 3.100a are crude estimates of the stresses in the direction of the tendon. Near the top of the specimen they indicate tension stresses along the fiber farthest away from the tendon axis. The possibility of these exterior tension forces was suggested by the appearance of horizontal cracks on the transverse face at or near the ultimate load in Specimen TPT1 and in many of the other concentric anchorage specimens. Figure 3.64 is a picture of Specimen TPT1 at the ultimate load. Once the specimen is split along the centerline, the height to depth ratio for half of a specimen is 24/8 or three for the "B" series, 4.67 for the "TPT" series, and four for Specimen C1. These height to depth ratios are large enough to allow the development of secondary internal forces as shown in Fig. 3.100b which suggest the development of tension forces along the extreme fiber. The base support conditions would not allow tension to develop at the specimen base, but a nonuniform reaction distribution could occur signaling the presence of an eccentricity and hence a bending moment as shown in Fig. 3.100b. The nonuniform reaction at the base causes the centroid of the compression strut to shift toward the tendon axis from its location in the basic STM.

If the specimen is cut in half along the tendon line, the specimen can be modelled as a beam-column on an elastic foundation (see Fig. 3.101). This method was first suggested by Lenschow and Sozen [95]. They split the specimen along a reference plane parallel to the tendon axis and introduced fictitious springs to model the concrete (see Chapter 2 for more detail). Using a truss/frame program, a beam-column on an elastic foundation analysis was performed which varied the crack length to study its effect on the bursting force distribution



a) Stress Distribution

b) Strut-and-Tie Model

Figure 3.100 Basic Beam-Column Stresses

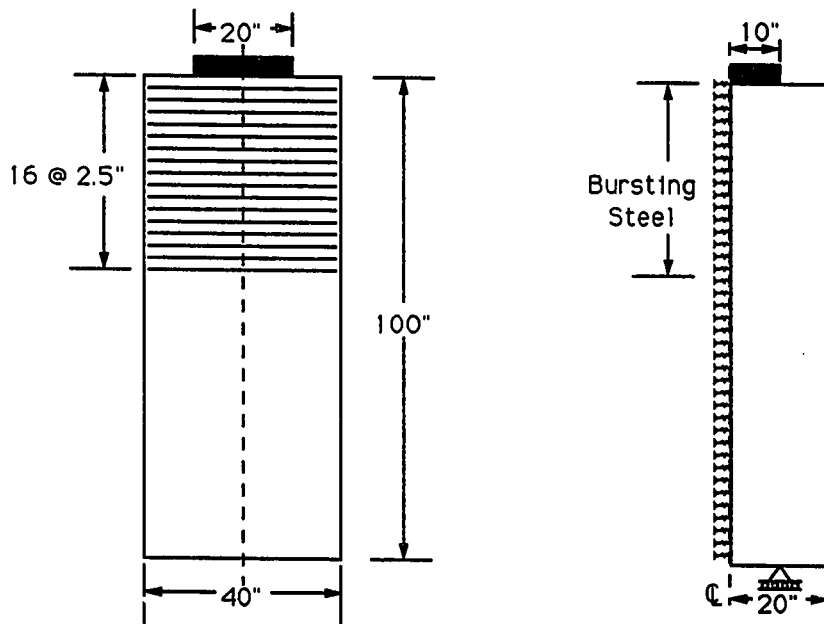


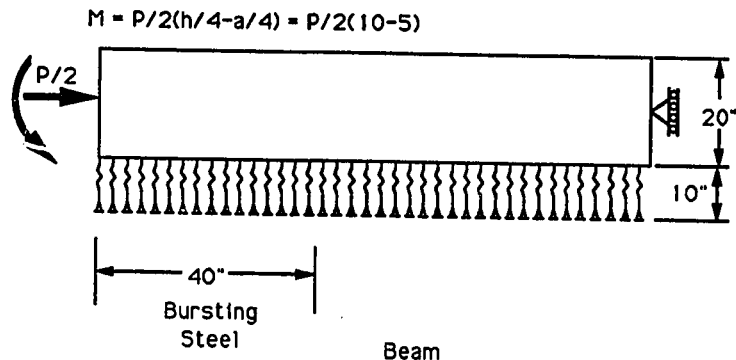
Figure 3.101 Beam-Column on an Elastic Foundation

(force in the springs) and on the moment and shear in the beam. The difficulty comes in selecting the appropriate stiffnesses for the springs. The parameters used for the beam are given in Fig. 3.102. The length of the springs were set at ten inches, the distance from the centerline to the midpoint of the beam-column section. Three spring stiffnesses were used in the analysis: uncracked concrete ($A = 25 \text{ in}^2$, $E = 4,300 \text{ ksi}$), cracked concrete with reinforcement ($A = 25 \text{ in}^2$, $E = 1,340 \text{ ksi}$), and cracked concrete with no reinforcement ($A = 0.001 \text{ in}^2$, $E = 1 \text{ ksi}$). In the determination of the cracked stiffness, a crack width of 0.015 inches was assumed for the portion of the reinforcement not bonded to the concrete. The concrete that was effective in the cracked state was determined by assuming that the tension force from the reinforcement spreads at 45 degrees from the reinforcing bar (see Fig. 3.102).

Figure 3.103 shows the bursting force values in the springs as the length of the crack along the foundation (specimen centerline) increases. The uncracked concrete curve indicated a peak tension force of 3.17 kips. If the force is distributed over the concrete area ($2.5 \times 10 = 25 \text{ in}^2$) between springs, the peak bursting stress would be 0.127 ksi. The peak stress determined from Guyon's curves is 0.110 ksi, which is a 15 percent difference. This seems reasonable given the coarseness of the assumptions made. Another check made on the uncracked concrete curve was the total bursting tension force. A summation of all the springs in tension yields a total bursting force of 25.4 kips with a load of 200 kips applied on the entire specimen (100 kips per beam-column). This compares very well with Guyon's value of 25 kips for the bursting force.

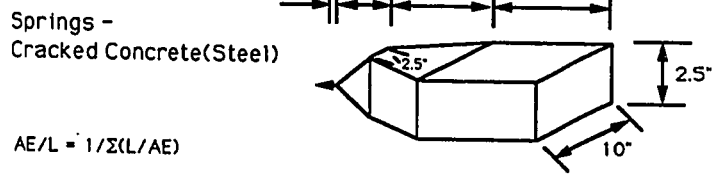
When the specimen is assumed to be cracked from 10 to 20 inches and from 0 to 30 inches, the force carried by the cracked concrete region drops but the strain in the reinforcing bar increases because the AE value of the springs change from 108,000 kips for the uncracked section to 33,500 kips. The total bursting force carried by the

concrete remains high. In Fig. 3.103b, the crack length is assumed to extend beyond the reinforcement, so there is a zone that carries no bursting force. The force in the reinforcement increased, and the amount carried in concrete tension decreased. Figure 3.104 shows the shear diagrams, while Fig. 3.105 shows the bending moment diagrams for the beam-columns with varying crack lengths. These curves show that there are large bending moments in the beam and that, for this particular geometry, positive moments occur deep in the section.



| | |
|---------------------------------|---------------------------------|
| Springs - Uncracked Concrete | Beam |
| $A = 10(2.5) = 25 \text{ in}^2$ | $t = 10 \text{ in}$ |
| $E = 4300 \text{ ksi}$ | $A = 20(10) = 200 \text{ in}^2$ |
| | $I = 6667 \text{ in}^4$ |
| | $E = 4300 \text{ ksi}$ |

Springs - Cracked Concrete (No Steel)
 $A = 0.001 \text{ in}^2$
 $E = 1 \text{ ksi}$



$AE/L = 1/\Sigma(L/AE)$

$$AE/L = \frac{1}{\frac{0.015}{29000(0.05)} + \frac{5}{4300(2.5(10))} + \frac{(5 - 1.25)}{4300((2.5)(10 + 2.5)/2)} + \frac{1.25}{4300((2.5/2)(2.5/2)}}$$

$AE/L = 3348 \text{ k in}^2$ if $A = 25 \text{ in}^2$ and $L = 10 \text{ in}$, then $E = 1339 \text{ ksi}$

Figure 3.102 Parameters for Beam-Column on an Elastic Foundation

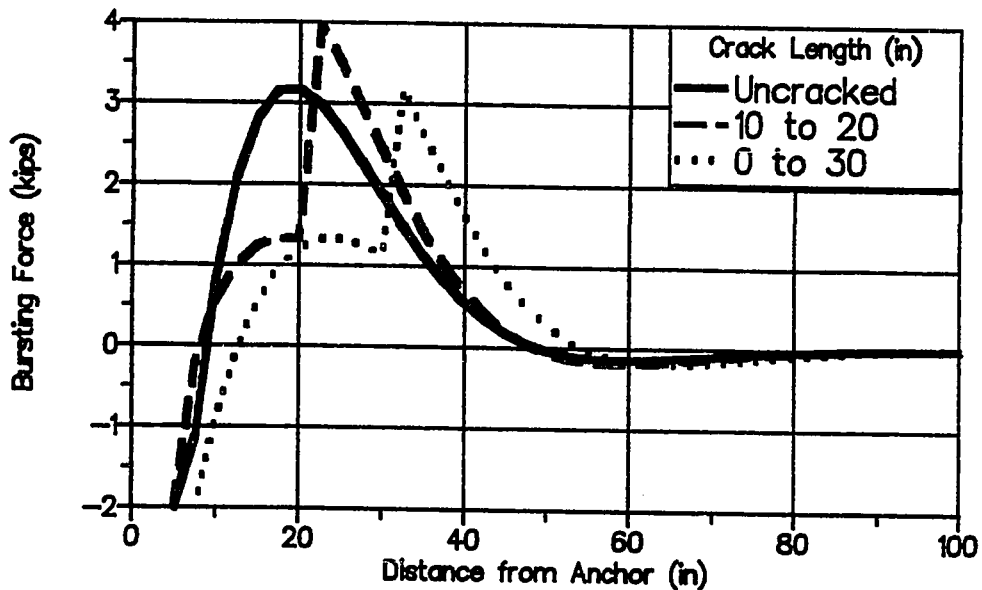


Figure 3.103a Force in Springs for Short Crack Lengths

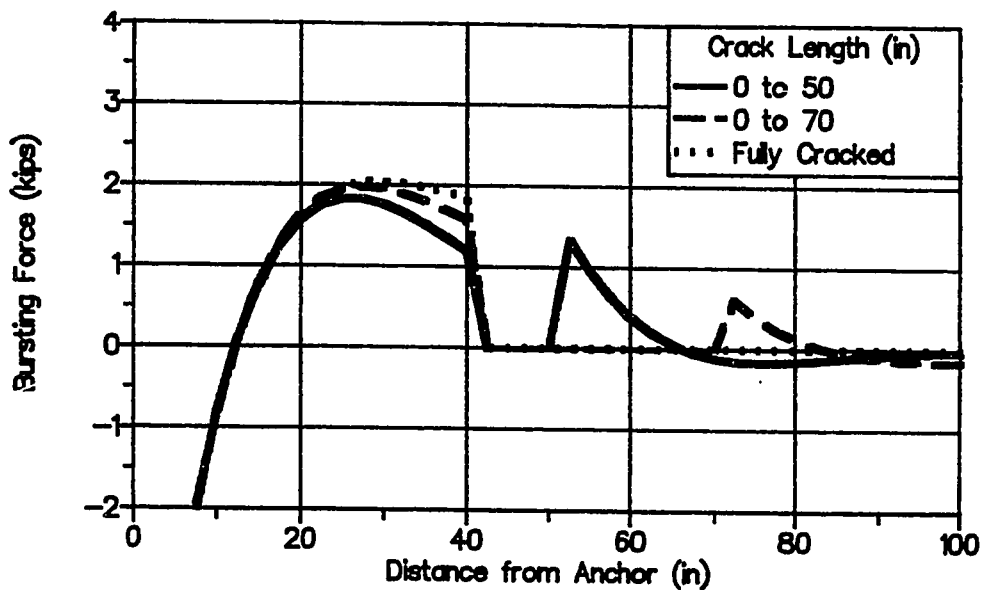


Figure 3.103b Force in Springs for Long Crack Lengths

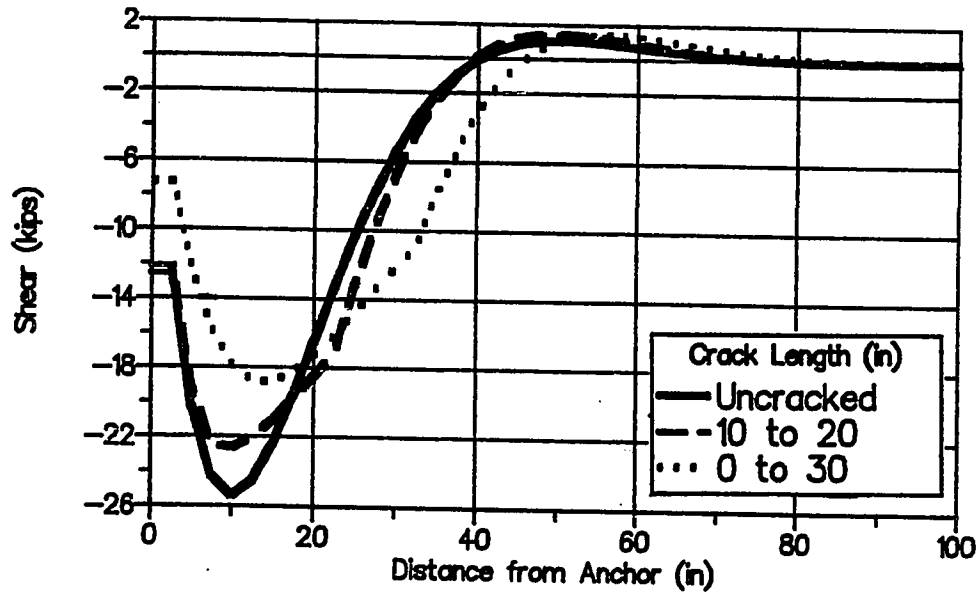


Figure 3.104a Shear Diagrams for Short Crack Lengths

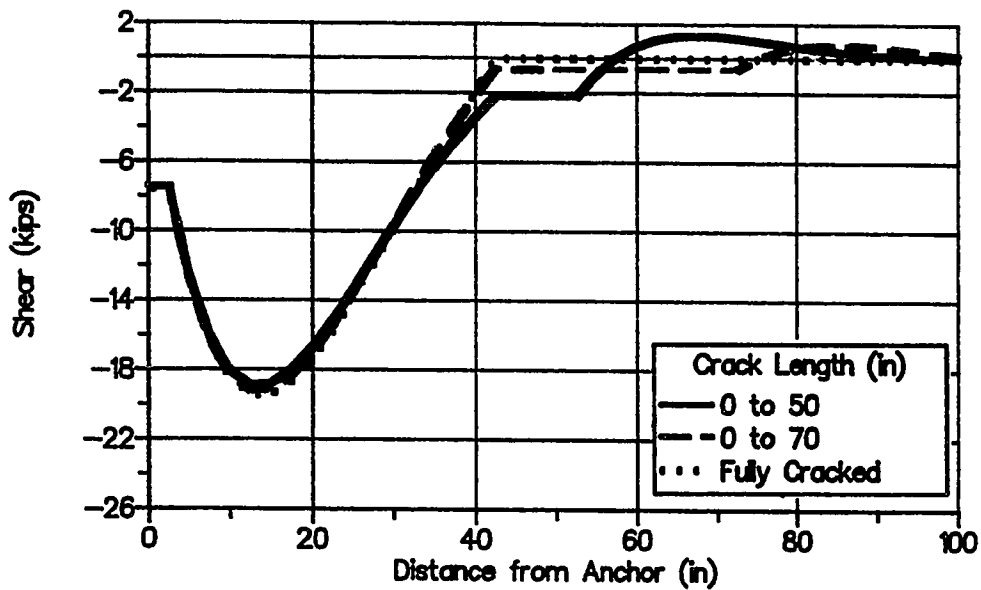


Figure 3.104b Shear Diagrams for Long Crack Lengths

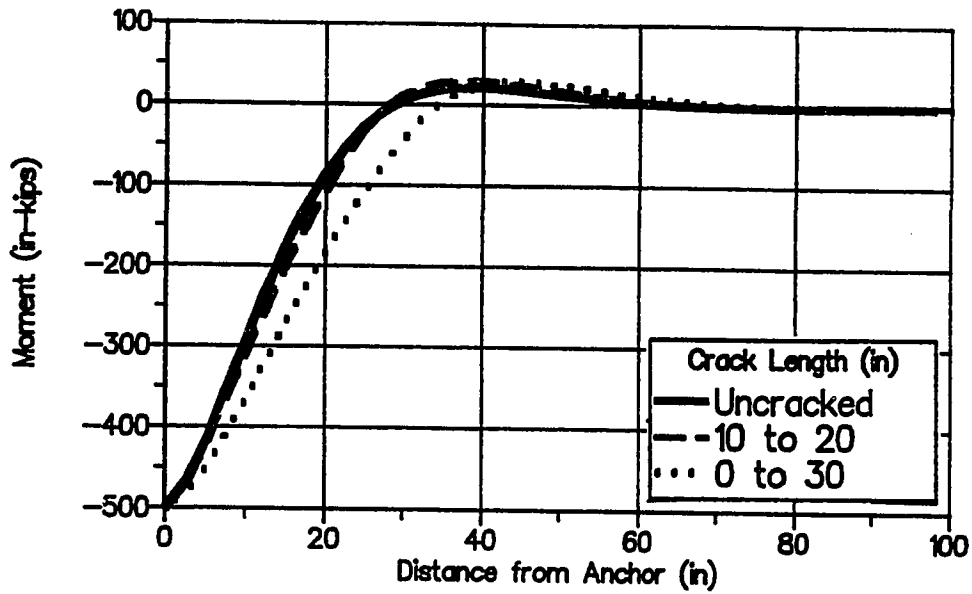


Figure 3.105a Moment Diagrams for Short Crack Lengths

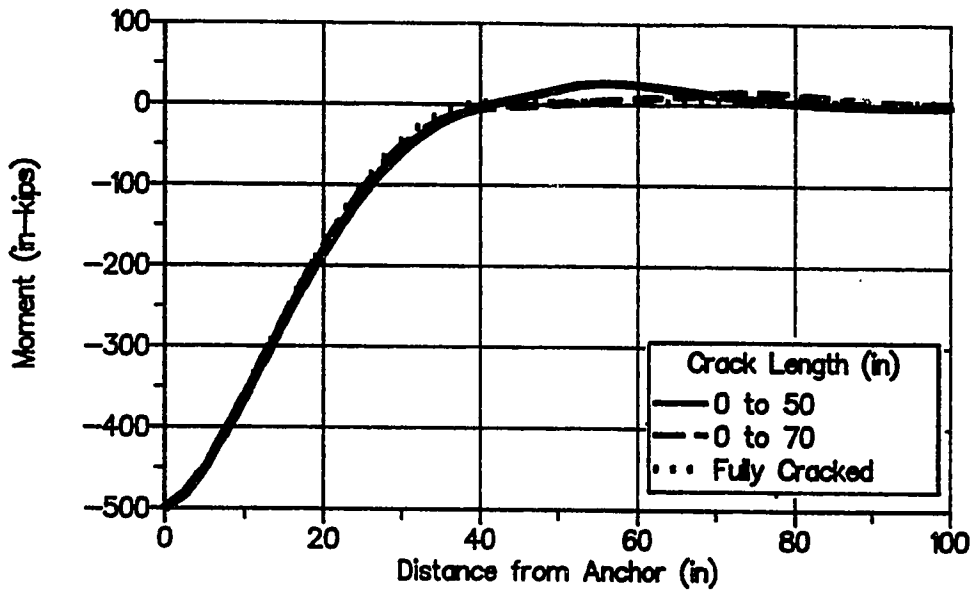


Figure 3.105b Moment Diagram for Long Crack Lengths

These elastic analyses are accurate for the specimens until the bursting reinforcement begins to yield. Therefore, to use this method to model the specimen behavior when the bursting reinforcement begins to yield, the springs representing the reinforcement must be limited to a particular force. The springs were replaced with 1-kip loads (see Fig. 3.106). Figure 3.107 shows the bursting force diagram for four cases: 1) the beam is uncracked, 2) the beam cracked from 0 to 50 inches ahead of the loading surface with no redistribution of the force in the bursting reinforcement, 3) the beam cracked from 0 to 50 inches when the force in each bar was restricted to 1 kip, and 4) the beam was fully cracked with the bar force restricted to one kip. The lines for cases 3 and 4 overlap between 0 and 40 inches at one kip. The yielding of the bars causes significant changes in forces within the beam. Figure 3.108 shows the beam-column moment diagram for the four cases. When the specimen is uncracked, the moment in the beam becomes positive around 30 inches from the plate. When the specimen cracks, the moment diagram is shifted but maintains the same shape. When the reinforcement yields, the moment diagram changes significantly in order to carry the load. If the specimen cracks to the base, the load is partially carried by a base moment of 175 in-kips.

$$M = P/2(h/4 - a/4) = P/2(10 - 5)$$

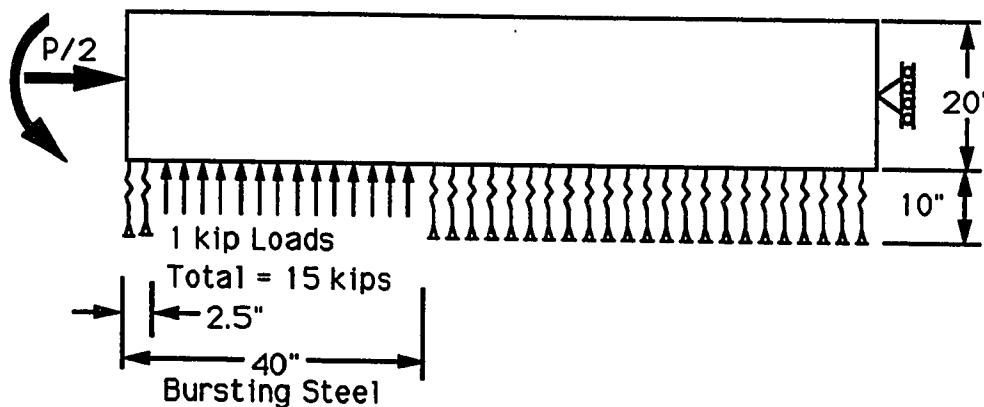


Figure 3.106 Elastic Foundation including Inelastic Effects

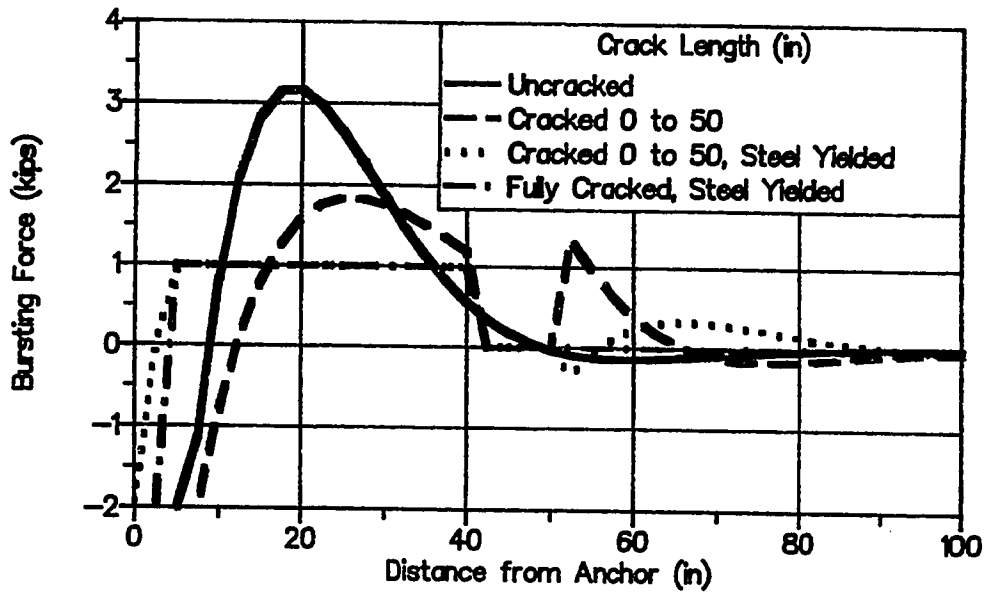


Figure 3.107 Bursting Force Distribution including Inelastic Effects

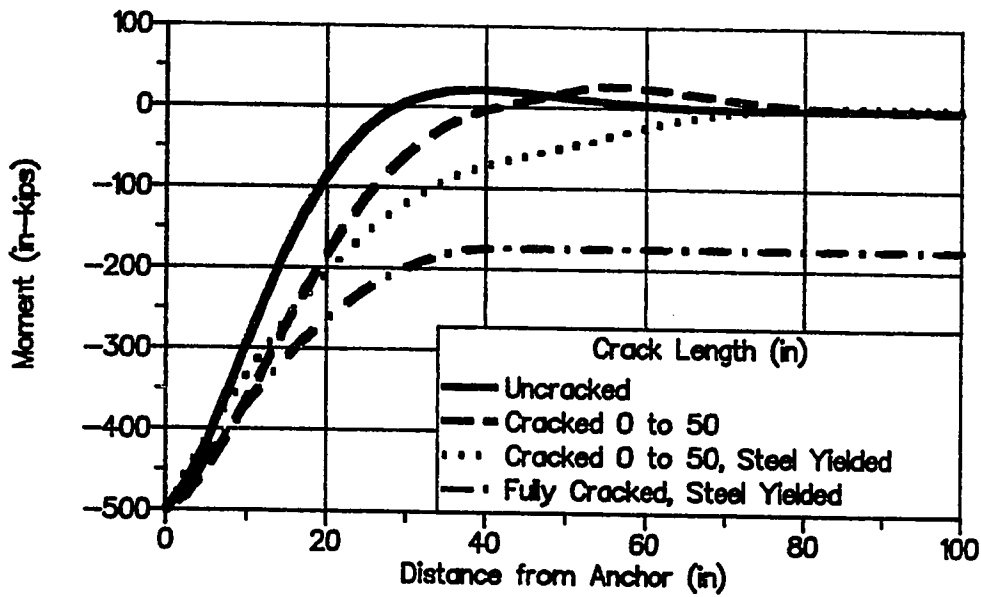


Figure 3.108 Moment Diagrams including Inelastic Effects

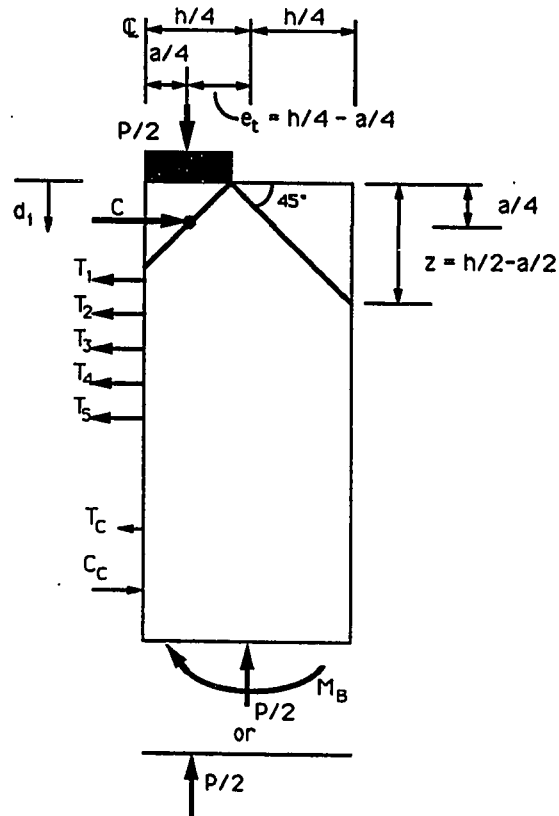


Figure 3.109 Free Body Diagram for Beam-Column

The last case described shows some of the reasons which probably enabled most of the concentric anchorage specimens to reach loads higher than those predicted by the basic STM. The STM, as typically implemented, includes the plastic behavior of the bursting ties by allowing the placement of the bursting reinforcement along the tendon path with a centroid not necessarily at the elastic bursting force centroid. Typically, the location of the compression struts on a section located a distance equal to the height of the section ahead of the loading surface is assumed to be at the elastic centroids (the quarter points of the section height) since it assumes a uniform stress distribution. Figure 3.109 shows the free-body diagram for the specimen cut along the section centerline. At the base of the free-

body diagram, an axial load and bending moment combination is shown instead of a centrally located load which would correspond to a uniform distribution. This was analytically predicted in the case of the fully cracked beam on an elastic foundation (see Fig. 3.108), where there was a base moment of 175 in-kips. The effect of such a moment is to shift the compression strut closer to the centerline of the section. As the strut moves toward the centerline of the section, the compression stresses increase as the diffusion angle of the strut decreases. Many of the specimens developed extensive cracking ahead of the bearing surface near the ultimate load. In addition, the magnitude of the tensile forces on the extreme fiber, parallel and farthest away from the tendon path, continued to increase near the top of the specimen. The failure of many of the concentric anchorage specimens was preceded by horizontal cracking on the transverse face.

The development of compression cracking ahead of the bearing plate and the horizontal cracking on the extreme fiber lead to the following methods for modelling the ultimate behavior of the concentric anchorage specimens: modified strut-and-tie model of Sections 3.4.4.2 and combined stress analysis of Section 3.4.4.3.

The modified STM is identical to the basic STM with the exception that the plastic behavior of the section is taken into account not only with the location of the bursting ties but also with the location of the compression struts at the base of the section. This is accomplished by allowing the movement of the centroids of the compression struts toward the tendon axis thereby increasing the axial capacity based on the tension ties and decreasing the axial capacity based on the compression struts. The predicted failure load corresponds to the condition where the axial capacity computed based on the tension ties governing is the same magnitude as that computed based on the compression strut governing.

The alternate or combined stress analysis procedure theorizes that the cracking of the extreme fiber causes a sudden shift in the

stress distribution. The shift causes an increase in the compression stresses near the specimen centerline which causes a compression failure. Therefore, the key to this analysis is to determine the load that causes cracking on the extreme fiber.

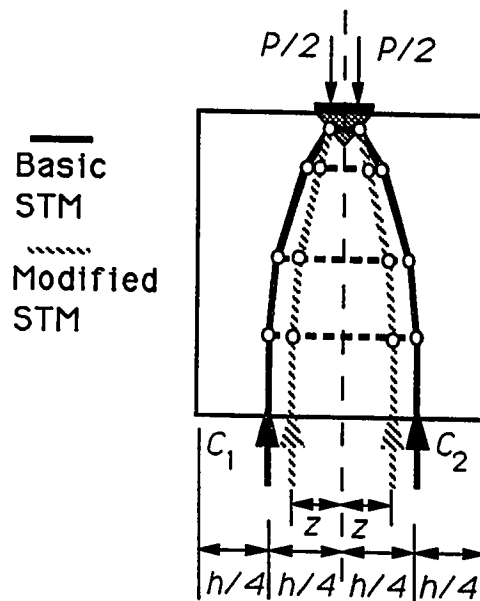


Figure 3.110 Modified Strut-and-Tie Model

3.4.4.2 Modified Strut-and-Tie Model Ultimate Load Prediction.

The modified STM approach is an iteration process. By moving the compression struts toward the tendon axis, the tension tie capacity of the STM increases and the compression strut capacity decreases since the width of the strut is being reduced (see Fig. 3.110). In the concentric test series, when computations are made using the basic STM all of the tests in the "B", "C", and "TPT" series have a tension tie capacity significantly below the strut capacity. Therefore, for these specimens, moving the struts inward will predict a higher ultimate load. The following example calculations will help to explain the method. The example is for Specimen B1 and correlates the tension tie

capacity with the compression strut capacity at the local zone-general zone interface.

- 1) Given: Plate Size = 6.5" x 6.5" (a x b)
 Specimen Thickness (t) = 9 inches
 Depth of Section (h) = 16 inches
 $f'_c = 5.38$ ksi
 Spiral = #4 ($f_y = 80.3$ ksi) smooth bar,
 $d_c = 7$ inches, $s = 1.25$ inches, and $l_c = 9.75$ inches
 Bursting Reinforcement: #4 ties at 7 3/8 inches and 9 7/8 inches with $F_y = 12.7$ kips/bar (two legs of a closed hoop at each level)

Iteration 1)

Determination of Ultimate Load assuming Tension Ties Control with base strut located at the quarter points, $z = h/4$

$$P = 2 \sum [T_i(d_i - a/4)] / (z - a/4) \text{ where } i \text{ is the number of the reinforcement layer}$$

$$P = 2[12.7 \cdot 2 \cdot (7.375 - 6.5/4) + 12.7 \cdot 2 \cdot (9.875 - 6.5/4)] / (16/4 - 6.5/4) \\ = 711 / (16/4 - 6.5/4) = \underline{299 \text{ kips}}$$

Strut Capacity at Interface between the Local Zone and the General Zone (Base of the Spiral)

$$\tan(\alpha) = (z - a/4) / (d_{\text{centroid}} - a/4)$$

where d_{centroid} = the distance from the loading surface to the centroid of the bursting reinforcement

$$\tan(\alpha) = (16/4 - 6.5/4) / (8.625 - 6.5/4) \\ \alpha = 18.8 \text{ degrees}$$

The width of the strut is conservatively estimated in accordance with Fig. 3.97a.

$$w_{s2} = a/2 \cdot \cos(\alpha) + (2l_c - a/2) \sin(\alpha) \\ = 6.5/2 \cdot \cos(18.8) + (2 \cdot 9.75 - 6.5/2) \cdot \sin(18.8) \\ = 8.31 \text{ inches} \leq 16/2 / \cos(18.8) = 8.45 \text{ inches}$$

$$t_s = 6.5 + (9 - 6.5) \cdot (9.75 - 8.31 / 2 \cdot \sin(18.8)) / 9 \\ = 8.84 \text{ inches}$$

$$A_{s,t} = 8.84 \cdot 8.31 = 73.4 \text{ in}^2$$

$$A = t \cdot (w_{s2} \cdot t / t_e) = 9 \cdot (8.31 \cdot 9 / 8.84) = 76.1 \text{ in}^2$$

$$\sigma_s = 0.7 \cdot 5.38 \sqrt{76.1 / 73.4} + 0 = 3.90 \text{ ksi}$$

$$P_s = 2 \cdot [3.90 \cdot 73.4] \cdot \cos(18.8) = \underline{542} \text{ kips} \gg \text{ This is greater than the load predicted by the tension ties (299 kips). Therefore, select a location for the strut closer than } h/4 \text{ or 4 inches.}$$

Iteration 2) Let $z = 3.5$ inches

Determination of Ultimate Load assuming Tension Ties Control with base strut located at $z = 3.5$

$$P = 711 / (3.5 - 6.5/4) = \underline{379} \text{ kips}$$

Strut Capacity at Interface between the Local Zone and the General Zone (Base of the Spiral)

$$\tan(\alpha) = (z - a/4) / (d_{cent} - a/4)$$

$$\begin{aligned} \tan(\alpha) &= (3.5 - 6.5/4) / (8.625 - 6.5/4) \\ \alpha &= 15.0 \text{ degrees} \end{aligned}$$

$$\begin{aligned} w_{s2} &= a/2 \cdot \cos(\alpha) + (2l_c - a/2) \sin(\alpha) \\ &= 6.5/2 \cdot \cos(15.0) + (2 \cdot 9.75 - 6.5/2) \cdot \sin(15.0) \\ &= 7.35 \text{ inches} \leq 3.5 \cdot 2 / \cos(15.0) = 7.25 \text{ inches} \gg \end{aligned}$$

The strut width, w_{s2} , must be checked to be sure that its width at the base of the spiral is not greater than the base strut width. Therefore, $w_{s2} = 7.25$ inches.

$$\begin{aligned} t_e &= 6.5 + (9 - 6.5) \cdot (9.75 - 7.25 / 2 \cdot \sin(15.0)) / 9 \\ &= 8.95 \text{ inches} \end{aligned}$$

$$A_{st} = 8.95 \cdot 7.25 = 64.9 \text{ in}^2$$

$$A = t \cdot (w_{s2} \cdot t / t_e) = 9 \cdot (7.25 \cdot 9 / 8.95) = 65.6 \text{ in}^2$$

$$A/A_{st} = 65.6 / 64.9 = 1.01 \approx 1$$

$$\sigma_s = 0.7 \cdot 5.38 \sqrt{1} + 0 = 3.77 \text{ ksi}$$

$$P_s = 2 \cdot [3.77 \cdot 65.6] \cdot \cos(15.0) = \underline{478} \text{ kips} \gg \text{ This is greater than the load predicted by the tension ties (379 kips). Therefore, select a location for the strut closer than 3.5 inches.}$$

Iteration 3) Let $z = 3.25$ inches

Determination of Ultimate Load assuming Tension Ties Control with base strut located at $z = 3.25$

$$P = 711 / (3.25 - 6.5/4) = \underline{438 \text{ kips}}$$

Strut Capacity at Interface between the Local Zone and the General Zone (Base of the Spiral)

$$\text{atan}(\alpha) = (z - a/4) / (d_{\text{cent}} - a/4)$$

$$\begin{aligned} \text{atan}(\alpha) &= (3.25 - 6.5/4) / (8.625 - 6.5/4) \\ \alpha &= 13.0 \text{ degrees} \end{aligned}$$

$$\begin{aligned} w_{s2} &= a/2 \cdot \cos(\alpha) + (2l_c - a/2) \sin(\alpha) \\ &= 6.5/2 \cdot \cos(13.0) + (2 \cdot 9.75 - 6.5/2) \cdot \sin(13.0) \\ &= 6.82 \text{ inches} \leq 3.25 \cdot 2 / \cos(13.0) = 6.67 \text{ inches} \end{aligned}$$

Therefore, $w_{s2} = 6.67$ inches

$$\begin{aligned} t_e &= 6.5 + (9 - 6.5) \cdot (9.75 - 6.67/2 \cdot \sin(13.0)) / 9 \\ &= 9.00 \text{ inches} \end{aligned}$$

$$A = A_{st} = 9.00 \cdot 6.67 = 60.0 \text{ in}^2$$

$$A/A_{st} = 1$$

$$\sigma_s = 0.7 \cdot 5.38 \sqrt{1} + 0 = 3.77 \text{ ksi}$$

$P_s = 2 \cdot [3.77 \cdot 60.0] \cdot \cos(13.0) = \underline{441 \text{ kips}}$ >> This is very close to the tension tie capacity of 438 kips. Therefore, the predicted capacity would be 438 kips.

The modified STM can be time-consuming when calculated by hand, but it is very easily implemented in a spreadsheet where the iterating can be done automatically. By using the modified STM, the engineer is more closely modelling the full potential plastic behavior of the section. For design, the engineer would use the same iteration process at the node-strut interface. The lowest predicted capacity between the node-strut interface and the local zone-general zone interface would govern the design. The bearing capacity and node compression limit

must also be checked in the same way that they were for the basic STM. Tables 3.20 and 3.21 show the results of the modified STM. Since the method is very dependent on compression capacity, the coefficient of variance is 27 percent, which is typical for a compression analysis. The average of the test-to-predicted ratio is very close to one. In the test specimens, the amount of compression cracking and the high strains in the bursting reinforcement seem to indicate a failure where the compression strut and tension tie fail at the same load. The high standard deviation can be explained by the reliability of the compression equations. The tension capacity of reinforcing steel is well-known, but the prediction equation of Roberts has a coefficient of variance of 15 percent with the best curve predicting a compression capacity in plain concrete of $0.7f'_c$. Several of the specimen predictions are unconservative by over 20 percent. This is just outside one standard deviation as determined by Roberts. The "A" series raised the average and the coefficient of variance. Without the "A" series the average is 0.86 with a coefficient of variance of 19 percent.

In addition, these specimens had long spirals. The effectiveness of the spirals may diminish with the length. Table 3.22 shows the results from the modified STM if the depth of the unconfined concrete is assumed to be one plate width away from the loading surface and has a compressive strength of $0.7f'_c$. This would be a good assumption if the designer did not know the length of the spiral. The model reduces the unconservatism to a maximum of ten percent. The model also has a lower coefficient of variance, 16 percent. The "A" series specimens are unaffected by the spiral modification. Without the "A" series, the average is 1.04 and the coefficient of variance is 11 percent.

The modified STM enables a slightly more accurate prediction of the test load than the basic STM. The effect of the plastic action is the extension of the general zone past the Saint Vénant zone (a depth of the section away from the loading surface) through the lengthening

Table 3.20a Modified STM Node-Strut Interface Capacity

| Specimen | Alpha (degrees) | Strut Width (in) | Strut Thickness (in) | Confined Width (in) | Confined Allowable (ksi) | Unconfined Allowable (ksi) | Predicted Capacity (kips) |
|----------|--------------------|------------------------|----------------------------|---------------------------|--------------------------------|----------------------------------|---------------------------------|
| A1 | 14.15 | 7.28 | 6.00 | 0.00 | N/A | 2.35 | 199 |
| A2 | 22.10 | 7.82 | 6.00 | 0.00 | N/A | 2.35 | 204 |
| A3 | 30.45 | 8.21 | 6.00 | 0.00 | N/A | 2.35 | 200 |
| A4 | 29.20 | 8.16 | 6.00 | 4.06 | 5.19 | 2.69 | 336 |
| B1 | 9.15 | 3.73 | 7.32 | 3.14 | 14.54 | 4.63 | 631 |
| B2 | 5.41 | 3.54 | 7.36 | 3.12 | 14.52 | 4.61 | 620 |
| B3 | 7.25 | 3.63 | 7.34 | 3.13 | 14.53 | 4.62 | 626 |
| B4 | 7.74 | 3.66 | 7.33 | 3.13 | 14.53 | 4.62 | 627 |
| B5 | 0.00 | 3.25 | 7.40 | 3.10 | 14.44 | 4.53 | 599 |
| B6 | 18.08 | 4.10 | 7.23 | N/A | N/A | 4.64 | 261 |
| B7 | 7.77 | 3.66 | 7.33 | 3.13 | 14.47 | 4.57 | 624 |
| B8 | 8.22 | 3.14 | 6.53 | 3.13 | 15.04 | 5.13 | 590 |
| C1 | 11.46 | 3.83 | 7.30 | 3.57 | 10.13 | 4.23 | 521 |
| TPT1 | 5.68 | 3.56 | 7.35 | 3.56 | 10.32 | 4.71 | 527 |
| TPT2 | 7.77 | 3.66 | 7.33 | 3.58 | 10.33 | 4.73 | 533 |
| TPT3 | 11.30 | 3.82 | 7.30 | 3.61 | 10.54 | 4.94 | 552 |
| TPT4 | 9.80 | 3.76 | 7.31 | 3.60 | 10.34 | 4.74 | 538 |

Table 3.20b Modified STM Local Zone-General Zone Interface Capacity

| Specimen | Depth of Confinement (in) | Alpha (degrees) | Strut Width (in) | Strut Thickness (in) | Unconfined Allowable (ksi) | Predicted Capacity (kips) |
|----------------------|---------------------------------|--------------------|------------------------|----------------------------|----------------------------------|---------------------------------|
| A1 A2 A3 A4 | 4(9.82) | 29.30 | 11.91 | 6.00 | 2.69 | 335 |
| B1 | 9.75 | 13.01 | 6.65 | 9.00 | 3.77 | 440 |
| B2 | 9.75 | 8.77 | 5.69 | 9.00 | 3.77 | 381 |
| B3 | 9.75 | 10.83 | 6.25 | 9.00 | 3.77 | 416 |
| B4 | 9.75 | 11.25 | 6.44 | 9.00 | 3.77 | 429 |
| B5 | 9.75 | 0.00 | 3.25 | 9.00 | 3.72 | 218 |
| B6 | 9.75 | | | 9.00 | | |
| B7 | 9.75 | 11.43 | 6.42 | 9.00 | 3.72 | 421 |
| B8 | 9.75 | 11.89 | 6.17 | 9.00 | 3.72 | 405 |
| C1 | 9.50 | 14.14 | 7.00 | 8.50 | 3.63 | 419 |
| TPT1 | 7.75 | 8.61 | 5.05 | 9.08 | 3.82 | 346 |
| TPT2 | 7.75 | 10.95 | 5.52 | 9.03 | 3.84 | 376 |
| TPT3 | 7.75 | 14.32 | 6.18 | 8.94 | 4.03 | 432 |
| TPT4 | 7.75 | 13.06 | 5.93 | 8.98 | 3.86 | 401 |

Table 3.21 Modified STM Prediction Summary

| Specimen | Bearing (kips) | Node-Strut Interface (kips) | L.Z.-G.Z. Interface (kips) | Controlling Load (kips) | Ultimate Test (kips) | Test/ Predicted |
|--|-------------------|-----------------------------------|----------------------------------|-------------------------------|--|----------------------|
| A1 | 340 | 199 | - | 199 | 298 | 1.49 |
| A2 | 340 | <u>204</u> | - | 204 | 275 | 1.35 |
| A3 | 340 | <u>200</u> | - | 200 | 265 | 1.33 |
| A4 | 544 | 336 | <u>335</u> | 335 | 437 | 1.30 |
| B1 | 602 | 631 | <u>440</u> | 440 | 366 | 0.83 |
| B2 | 602 | 620 | <u>381</u> | 381 | 290 | 0.76 |
| B3 | 602 | 626 | <u>416</u> | 416 | 331 | 0.80 |
| B4 | 602 | 627 | <u>429</u> | 429 | 337 | 0.79 |
| B5 | 599 | 599 | <u>218</u> | 218 | 212 | 0.97 |
| B6 | <u>218</u> | 261 | - | 218 | 297 | 1.36 |
| B7 | 599 | 624 | <u>421</u> | 421 | 296 | 0.70 |
| B8 | 567 | 590 | <u>405</u> | 405 | 276 | 0.68 |
| C1 | 439 | 521 | <u>419</u> | 419 | 370 | 0.88 |
| TPT1 | 484 | 527 | <u>346</u> | 346 | 310 | 0.90 |
| TPT2 | 484 | 533 | <u>376</u> | 376 | 300 | 0.80 |
| TPT3 | 492 | 552 | <u>432</u> | 432 | 370 | 0.86 |
| TPT4 | 484 | 538 | <u>401</u> | 401 | 332 | 0.83 |
| Note: Node Compression was found to not control in Table 3.17. | | | | | Average Standard Deviation Coef. of Variance | 0.98 0.26 0.27 |

Table 3.22 Modified STM Prediction Summary using One Plate Length Spirals

| Specimen | Bearing (kips) | Node-Strut Interface (kips) | L.Z.-G.Z. Interface (kips) | Controlling Load (kips) | Ultimate Test (kips) | Test/ Predicted |
|--|-------------------|-----------------------------------|----------------------------------|-------------------------------|--|----------------------|
| A1 | 340 | 199 | - | 199 | 298 | 1.49 |
| A2 | 340 | <u>204</u> | - | 204 | 275 | 1.35 |
| A3 | 340 | <u>200</u> | - | 200 | 265 | 1.33 |
| A4 | 544 | 336 | <u>335</u> | 335 | 437 | 1.30 |
| B1 | 602 | 631 | <u>343</u> | 343 | 366 | 1.07 |
| B2 | 602 | 620 | <u>305</u> | 305 | 290 | 0.95 |
| B3 | 602 | 626 | <u>326</u> | 326 | 331 | 1.02 |
| B4 | 602 | 627 | <u>330</u> | 330 | 337 | 1.02 |
| B5 | 599 | 599 | <u>201</u> | 201 | 212 | 1.05 |
| B6 | <u>218</u> | 261 | - | 218 | 297 | 1.36 |
| B7 | 599 | 624 | <u>327</u> | 327 | 296 | 0.90 |
| B8 | 567 | 590 | <u>303</u> | 303 | 276 | 0.91 |
| C1 | 439 | 521 | <u>328</u> | 328 | 370 | 1.13 |
| TPT1 | 484 | 527 | <u>290</u> | 290 | 310 | 1.07 |
| TPT2 | 484 | 533 | <u>311</u> | 311 | 300 | 0.96 |
| TPT3 | 492 | 552 | <u>351</u> | 351 | 370 | 1.05 |
| TPT4 | 484 | 538 | <u>328</u> | 328 | 332 | 1.01 |
| Note: Node Compression was found to not control in Table 3.17. | | | | | Average Standard Deviation Coef. of Variance | 1.12 0.17 0.16 |

of the bursting cracks. The propagation of the cracks allows the further development of the bending moments in the beam-column sections and the flattening of the strut angles. The flattening of the strut angles increases the effectiveness of the bursting reinforcement but also increases the compression stress through a reduction in the strut size. This behavior can occur in typical girder anchorage zones. The boundary conditions of the test specimens were such that a bending moment could occur at the base of the specimen. A typical girder would most likely be substantially longer than the specimens; and, therefore, a uniform distribution would eventually occur.

3.4.4.3 Combined Stress Analysis for Ultimate Load Prediction.

The stress distribution near the anchorage device is very nonlinear, and the compression stresses along the specimen centerline are very high. Since the combined stress analysis relies on the prediction of the first cracking load for the extreme fiber, a model must be used to estimate these tension stresses. One possibility is using the combined stress theory ($P/A \pm Mc/I$). To determine the location closest to the loading surface when a simple combined stress theory could be used to estimate the stress distribution is difficult. A 45-degree line from the corner of the bearing plate to the section edge (see Fig. 3.109) determines a depth where it was assumed that a combined stress analysis would give a reasonable answer for the tension stress on the extreme fiber. The following calculations are those necessary to determine the load for Specimen B1 (see Figs. 3.17 and 3.109) which, according to a combined stress analysis, will cause cracking on the extreme fiber.

$$-f_t = P/A - M/S \quad \gg \quad -f_{sp} = P/A - M_{cr}/S$$

where f_{sp} is the split cylinder strength
 f_t is the tensile stress on the extreme fiber
 P is the load applied to the beam-column, in the case of concentric anchorage, half the total load
 A is the cross-sectional area of the beam-column
 M is the moment about the centerline of the beam-column

M_{cr} is the cracking moment
 S is the section modulus of the beam-column

$$M_{cr} = (P/A + f_{sp}) \cdot S \quad \text{and} \quad M_z = P/2 \cdot e_t - C_3 \cdot (z - a/4)$$

where $A = 9 \cdot 16 = 144 \text{ in}^2$ $e_t = 16/4 - 6.5/4 = 2.375$ inches

$$f_{sp} = 0.464 \text{ ksi} \quad C_3 = 4 \cdot 12.7 = 50.8 \text{ kips}$$

$$S = 1/6 \cdot 9 \cdot 8^2 = 96 \text{ in}^3 \quad z = 16/2 - 6.5/2 = 4.75 \text{ inches}$$

therefore if $M_{cr} = M_z$ then

$$(P/144 + 0.464) \cdot 96 = P/2 \cdot 2.375 - 50.8 \cdot (4.75 - 1.625)$$

$$0.52P = 203 \text{ kips} \rightarrow \underline{P = 390 \text{ kips}}$$

If the distance to any bar is less than "z" then the tensile strength of each bar times its distance from the "z" plane must be added to the value of M_z . In addition to checking the extreme fiber, which is checking the tension side of the combined stress analysis, compression checks must be done similar to those done for the STM. The procedures used in the previous subsections are still applicable except when calculating the initial angle of the compression strut. The location of the strut is no longer at the quarter point of the section (as was seen in the modified STM). Therefore, the path of the strut must be determined by using equilibrium at the secondary node. The strut angle near the node for Specimen B1 is calculated as follows.

$$\text{atan}(\alpha) = C_3/(P/2) = (4 \cdot 12.7)/(390/2) = 14.6 \text{ degrees}$$

Table 3.23 shows the compression strut interface capacities, while Table 3.24 is the summary of the failure predictions for the concentric anchorage specimens using the combined stress analysis. Included in Table 3.24 are the extreme fiber tension capacity, bearing capacity, node-strut interface compression capacity, and the local zone-general zone compression capacity. The node compression limit check must also be conducted, but is not included in the table because in previous subsections it was clearly proven not to control. The combined stress analysis results agree with tests results more closely than with the basic STM. However, there are several unconservative

Table 3.23a Combined Stress Node-Strut Interface Capacity

| Specimen | Alpha (degrees) | Strut Width (in) | Strut Thickness (in) | Confined Width (in) | Confined Allowable (ksi) | Unconfined Allowable (ksi) | Predicted Capacity (kips) |
|----------|--------------------|------------------------|----------------------------|---------------------------|--------------------------------|----------------------------------|---------------------------------|
| A1 | 17.87 | 7.55 | 6.00 | 0.00 | N/A | 2.35 | 203 |
| A2 | 19.79 | 7.68 | 6.00 | 0.00 | N/A | 2.35 | 204 |
| A3 | 14.46 | 7.31 | 6.00 | 0.00 | N/A | 2.35 | 200 |
| A4 | 19.14 | 7.64 | 6.00 | 1.54 | 5.19 | 2.69 | 276 |
| B1 | 14.64 | 3.97 | 7.26 | 3.21 | 14.58 | 4.67 | 642 |
| B2 | 12.24 | 3.87 | 7.29 | 3.17 | 14.56 | 4.65 | 637 |
| B3 | 13.52 | 3.92 | 7.28 | 3.19 | 14.57 | 4.66 | 640 |
| B4 | 14.19 | 3.95 | 7.27 | 3.20 | 14.57 | 4.67 | 641 |
| B5 | 0.00 | 3.25 | 7.40 | 3.10 | 14.44 | 4.53 | 599 |
| B6 | 14.65 | 3.97 | 7.26 | N/A | N/A | 4.61 | 257 |
| B7 | 14.69 | 3.97 | 7.26 | 3.21 | 14.52 | 4.61 | 638 |
| B8 | 16.69 | 3.45 | 6.42 | 3.24 | 15.12 | 5.21 | 603 |
| C1 | 16.08 | 4.02 | 7.25 | 3.64 | 10.16 | 4.26 | 528 |
| TPT1 | 10.16 | 3.77 | 7.31 | 3.60 | 10.34 | 4.74 | 539 |
| TPT2 | 13.49 | 3.92 | 7.28 | 3.65 | 10.37 | 4.77 | 546 |
| TPT3 | 15.96 | 4.02 | 7.25 | 3.69 | 10.58 | 4.97 | 560 |
| TPT4 | 15.20 | 3.99 | 7.26 | 3.67 | 10.38 | 4.78 | 548 |

Table 3.23b Combined Stress Local Zone-General Zone Interface Capacity

| Specimen | Depth of Confinement (in) | Alpha (degrees) | Strut Width (in) | Strut Thickness (in) | Unconfined Allowable (ksi) | Predicted Capacity (kips) |
|----------------------|---------------------------------|--------------------|------------------------|----------------------------|----------------------------------|---------------------------------|
| A1 A2 A3 A4 | 4(9.82) | 19.14 | 10.14 | 6.00 | 2.69 | 309 |
| B1 | 9.75 | 14.64 | 7.25 | 9.00 | 3.77 | 476 |
| B2 | 9.75 | 12.24 | 6.62 | 9.00 | 3.77 | 439 |
| B3 | 9.75 | 13.52 | 6.96 | 9.00 | 3.77 | 459 |
| B4 | 9.75 | 14.19 | 7.13 | 9.00 | 3.77 | 469 |
| B5 | 9.75 | 0.00 | 3.25 | 9.00 | 3.72 | 218 |
| B6 | | | | | | |
| B7 | 9.75 | 14.69 | 7.27 | 9.00 | 3.72 | 471 |
| B8 | 9.75 | 16.69 | 7.46 | 9.00 | 3.72 | 479 |
| C1 | 9.50 | 16.08 | 7.49 | 8.50 | 3.63 | 444 |
| TPT1 | 7.75 | 10.16 | 5.36 | 9.05 | 3.83 | 366 |
| TPT2 | 7.75 | 13.49 | 6.02 | 8.97 | 3.87 | 406 |
| TPT3 | 7.75 | 15.96 | 6.49 | 8.90 | 4.05 | 450 |
| TPT4 | 7.75 | 15.20 | 6.35 | 8.92 | 3.89 | 425 |

Table 3.24 Combined Stress Prediction Summary

| Specimen | Combined Stress (kips) | Bearing (kips) | Node-Strut Interface (kips) | L.Z.-G.Z. Interface (kips) | Controlling Load (kips) | Ultimate Test (kips) | Test/Predicted |
|---|------------------------|----------------|-----------------------------|----------------------------|-------------------------|--|----------------------|
| A1 | 461 | 340 | <u>203</u> | - | 203 | 298 | 1.47 |
| A2 | 440 | 340 | <u>206</u> | - | 204 | 275 | 1.35 |
| A3 | 839 | 340 | <u>200</u> | - | 200 | 265 | 1.33 |
| A4 | 617 | 544 | <u>276</u> | 309 | 276 | 437 | 1.58 |
| B1 | <u>390</u> | 602 | 642 | 476 | 390 | 366 | 0.94 |
| B2 | <u>262</u> | 602 | 637 | 439 | 262 | 290 | 1.11 |
| B3 | <u>313</u> | 602 | 640 | 459 | 313 | 331 | 1.06 |
| B4 | <u>336</u> | 602 | 641 | 469 | 336 | 337 | 1.00 |
| B5 | <u>153</u> | 599 | 599 | 218 | 153 | 212 | 1.39 |
| B6 | <u>327</u> | 218 | 257 | - | 218 | 297 | 1.36 |
| B7 | <u>327</u> | <u>599</u> | 638 | 471 | 327 | 296 | 0.90 |
| B8 | <u>281</u> | 567 | 603 | 479 | 281 | 276 | 0.98 |
| C1 | <u>342</u> | 439 | 528 | 444 | 342 | 370 | 1.08 |
| TPT1 | <u>227</u> | 484 | 539 | 366 | 227 | 310 | 1.37 |
| TPT2 | <u>302</u> | 484 | 546 | 406 | 302 | 300 | 0.99 |
| TPT3 | <u>386</u> | 492 | 560 | 450 | 386 | 370 | 0.96 |
| TPT4 | <u>341</u> | 484 | 548 | 425 | 341 | 332 | 0.97 |
| Note: Node Compression was found to not to control in Table 3.17. Calculation for B-C Analysis is identical to STM. | | | | | | Average Standard Deviation Coef. of Variance | 1.17 0.21 0.18 |

results. The most unconservative result is for Specimen B7 with a test-to-predicted ratio of 0.9. The basic STM had a test-to-predicted ratio of 1.32 with a coefficient of variance of 0.17, while the combined stress analysis test-to-predicted ratio is 1.17 with a coefficient of variance equal to 0.18.

The application of the combined stress analysis would be difficult in an actual girder application because of the more complex stress state and the possibility of cracks existing due to other effects such as creep, shrinkage, or overall girder flexural bending. However, the model does show that, if an engineer is designing for a given load, the combined effect of the amount of reinforcement and the depth of the reinforcement has an effect on the behavior of the section. The farther ahead of the loading surface that the reinforcement is placed in order to carry a larger axial load, the higher the moment will be within the beam-column. This high moment

will cause an increase in the compression stresses near the tendon axis and additional cracking. There is a concern related to the effectiveness of reinforcement when the reinforcement is placed deeper into the section. A determination of the maximum depth at which reinforcement should be placed was not one of the explicit objectives of this program. Therefore, until additional research is conducted, reinforcement should be placed within 1 to 1.5 times the width of the section from the loading surface.

3.4.4.4 *Concrete Tensile Contribution to Axial Load Capacity.*

In the test description section, it was discussed how some of the specimens reached higher loads because there was still significant uncracked concrete across the section centerline. The specimens that had sharp peaks in the load-displacement curves at ultimate were observed to be partially uncracked until the ultimate load. Due to the uncertainty of the concrete cracking behavior along the specimen centerline, uncracked concrete along the load axis is not included in the previously discussed models. In Table 3.25, the prediction models are compared with the peak fully cracked load. This is not a cracking load prediction but a comparison of the ultimate load models with the load carried by the test specimens after all the concrete contribution has been removed. In several of the specimens, the maximum ultimate load corresponds with the full removal of any uncracked concrete along the tendon axis. Since the concrete capacity was removed, the load dropped. The specimens were reloaded and were able to reach another peak load, which was less than the ultimate load, without any tensile concrete contribution along the tendon axis. The table includes the predictions using the basic STM, the modified STM, and the combined stress analysis. Specimen B5 is not included, because at the peak load, there was still concrete tensile capacity along the load axis. Since there was no general zone reinforcement when the concrete became uncracked along the load axis, the load dropped to 25 kips. There was no bursting reinforcement to hold the specimen together. The beam-

columns separated from each other, and the local zone failed. The "A" series specimens and Specimen B6 are not included in the statistical analysis at the bottom of the table. They were controlled by a compression and not a tension failure according to the basic STM. Therefore, the concrete contribution along the tendon axis would not effect the ultimate load. The combined stress analysis and the modified STM have very low standard deviations and mean values very close to one. The models are unconservative for several of the specimens. There is a slight improvement with the basic STM. This shows that a certain portion of the inaccuracies of the models was caused by the additional capacity due to the tension concrete which was not included in the models.

Table 3.25 Prediction Summary for Ultimate Load Methods Compared with Peak Fully Crack Load

| Specimen | Test Ultimate (kips) | Peak Fully Cracked Load (kips) | Conventional STM | | Modified STM | | Combined Stress Analysis | |
|---|-------------------------|-----------------------------------|--------------------------|-----------------------------------|--------------------------|-----------------------------------|--------------------------|-----------------------------------|
| | | | Predicted Load (kips) | Fully Cracked Load/ Prediction | Predicted Load (kips) | Fully Cracked Load/ Prediction | Predicted Load (kips) | Fully Cracked Load/ Prediction |
| A1 | 298 | 298 | 195 | 1.53 | 199 | 1.50 | 203 | 1.47 |
| A2 | 275 | 275 | 190 | 1.45 | 204 | 1.35 | 204 | 1.35 |
| A3 | 265 | 265 | 204 | 1.30 | 200 | 1.33 | 200 | 1.33 |
| A4 | 437 | 437 | 306 | 1.43 | 335 | 1.30 | 276 | 1.58 |
| B1 | 366 | 365 | 299 | 1.22 | 343 | 1.06 | 390 | 0.94 |
| B2 | 290 | 280 | 292 | 0.96 | 305 | 0.92 | 262 | 1.07 |
| B3 | 331 | 313 | 296 | 1.06 | 326 | 0.96 | 313 | 1.00 |
| B4 | 337 | 337 | 277 | 1.22 | 330 | 1.02 | 336 | 1.00 |
| B5 | 212 | N/A | 218 | | 201 | | 153 | |
| B6 | 297 | 297 | 218 | 1.36 | 218 | 1.36 | 218 | 1.36 |
| B7 | 296 | 296 | 269 | 1.10 | 327 | 0.91 | 327 | 0.91 |
| B8 | 276 | 273 | 252 | 1.08 | 303 | 0.90 | 281 | 0.97 |
| C1 | 370 | 345 | 192 | 1.80 | 328 | 1.05 | 342 | 1.01 |
| TPT1 | 310 | 240 | 180 | 1.33 | 290 | 0.83 | 227 | 1.06 |
| TPT2 | 300 | 300 | 253 | 1.19 | 311 | 0.96 | 302 | 0.99 |
| TPT3 | 370 | 370 | 247 | 1.50 | 351 | 1.05 | 366 | 0.96 |
| TPT4 | 332 | 326 | 235 | 1.39 | 328 | 0.99 | 341 | 0.96 |
| All Concentric Tests | | | Average | 1.31 | | 1.09 | | 1.12 |
| | | | Stand. Dev. | 0.21 | | 0.20 | | 0.21 |
| | | | Coef. Var. | 0.16 | | 0.18 | | 0.19 |
| Specimen Controlled by Tension Tie or Beam-Column Failure | | | Average | 1.26 | | 0.97 | | 0.99 |
| | | | Stand. Dev. | 0.23 | | 0.07 | | 0.05 |
| | | | Coef. Var. | 0.18 | | 0.07 | | 0.05 |

For most of the specimens, the concrete tensile strength across the specimen centerline carried a significant portion of the tie force until they were very close to the ultimate load. Figure 3.111 shows the transfer of the bursting force from the concrete to the bursting reinforcement for Specimen B1. At early load stages, the bursting reinforcement contributes little to the total load. When cracking begins to occur, the transfer of force also occurs. For the case of Specimen B1, the concrete contribution stayed constant until the very end, when the specimen cracked completely through the specimen.

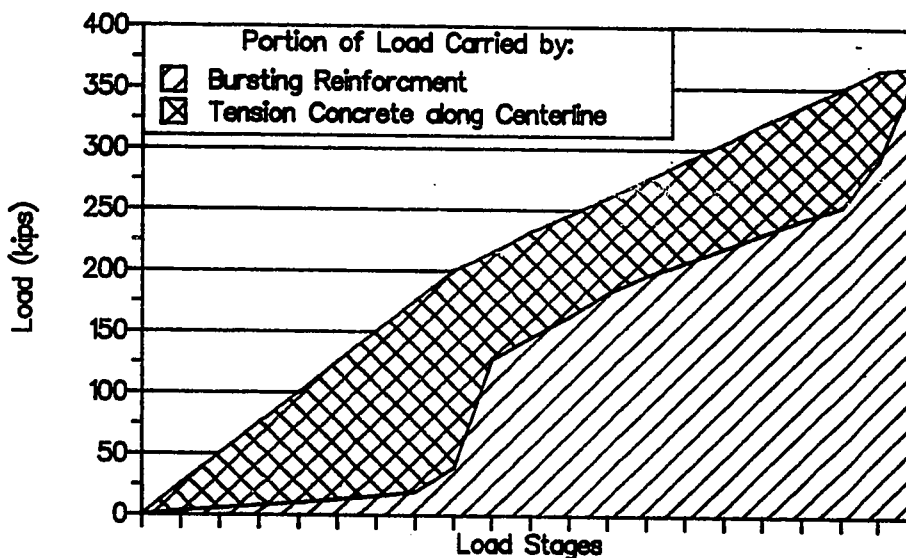


Figure 3.111 Tension Concrete versus Reinforcement Contribution

3.4.5 Current Methods for Ultimate Load Prediction. Table 3.26 shows the calculations found in the survey discussed in Chapter 2 to be the most common for determining the capacity of anchorage zones. Currently, the bearing capacity is checked and the bursting reinforcement is designed using Guyon's equation.

$$P = 4T/(1-a/h)$$

A closer look at Guyon's equation, indicates a format very similar to the STM. By rearranging the equation, the following equation can be

seen.

$$P = 2T(0.5h)/(h/4-a/4)$$

This is exactly the same equation for a basic STM constructed for a section with the centroid of the bursting reinforcement at $0.5h$ from the secondary node in the local zone. Therefore, if a designer used Guyon's equation and placed the bursting reinforcement closer than $0.5h + 0.25a$ from the loading surface, their prediction would be unconservative according to the STM. What has allowed designs with reinforcement close to the loading surface to reach their design load is probably the beam-column action (plastic behavior). Table 3.26 shows that the current method would be conservative for the "B", "C" and "TPT" series. The "A" series is unconservative because these specimens failed in the compression strut. Current design practice does not check compressive stresses except bearing stresses immediately ahead of the bearing plate.

Table 3.26 Current Design Procedure Ultimate Load Prediction

| Specimen | Bursting Reinforcement (in ²) | Predicted Load (kips) | Bearing Capacity (kips) | Controlling Load (kips) | Ultimate Load (kips) | Peak/Predicted |
|--|---|-----------------------|-------------------------|-------------------------|----------------------|----------------------|
| A1 | 73.9 | 443 | <u>340</u> | 340 | 298 | 0.88 |
| A2 | 79.8 | 479 | <u>340</u> | 340 | 275 | 0.81 |
| A3 | 106.8 | 641 | <u>340</u> | 340 | 265 | 0.78 |
| A4 | 106.8 | 641 | <u>544</u> | 544 | 437 | 0.80 |
| B1 | 50.8 | <u>342</u> | 639 | 342 | 366 | 1.07 |
| B2 | 29.4 | 198 | 639 | 198 | 290 | 1.46 |
| B3 | 39.6 | <u>267</u> | 639 | 267 | 331 | 1.24 |
| B4 | 42.6 | <u>287</u> | 639 | 287 | 337 | 1.17 |
| B5 | 0 | <u>0</u> | 636 | 0 | 212 | |
| B6 | 42.6 | <u>287</u> | <u>218</u> | 218 | 297 | 1.36 |
| B7 | 42.6 | <u>287</u> | <u>636</u> | 287 | 296 | 1.03 |
| B8 | 42.6 | <u>261</u> | 464 | 261 | 276 | 1.06 |
| C1 | 52.8 | <u>258</u> | 450 | 258 | 370 | 1.44 |
| TPT1 | 26.2 | <u>164</u> | 462 | 164 | 310 | 1.89 |
| TPT2 | 38.1 | <u>239</u> | 462 | 239 | 300 | 1.26 |
| TPT3 | 55.1 | <u>345</u> | 471 | 345 | 370 | 1.07 |
| TPT4 | 49.8 | <u>312</u> | 462 | 312 | 332 | 1.06 |
| Average Standard Deviation Coef. of Variance | | | | | | 1.15 0.28 0.25 |

3.5 Concentric Anchorage Zone Conclusions

1) The STM is a lower-bound model based on the theory of plasticity. It should be a conservative estimate of the ultimate strength of the specimens. It was found to be a conservative way of estimating the ultimate strength of the specimens. The average of the test-to-predicted ratio was 1.32 with a coefficient of variance equal to 0.19. Two specimens (B2 and B5) were very slightly unconservative (one to three percent). Specimen B5 had zero bursting reinforcement and was only three percent unconservative according to the compression check. In a typical design situation the predicted capacity would have been zero because there was zero bursting reinforcement. Specimen B2 was only one percent unconservative, possibly because of the extreme depth of effective reinforcement. Care should be taken not to place effective reinforcement too far from the loading surface. Until further research is conducted, reinforcement should be distributed over a length from the loading surface to 1.5 times the width of the section. Excessive cracking is necessary near the loading surface to mobilize reinforcement placed far from the loading surface. When using the STM, it is important to check all the possible failure modes: nodes, tension ties, and compression struts.

2) The local zone node can be represented with a triangle that has a height equal to half the plate width. The local nodes (secondary nodes) of the STM should be assumed to be at 1/4 of the plate width from the specimen centerline and the same distance ahead of the loaded surface.

3) A determination of the compression strut and bearing capacity can be done using the equation developed by Roberts.

$$P_{b,s} = 0.7f'_c\sqrt{A/A_g}A_b + k \cdot f_y \cdot A_s / (s \cdot d) \cdot (1-s/d_c)^2 \cdot A_{core} \leq 3f'_c \cdot A_b$$

where A - the effective area, which is the maximum area of the supporting surface that is geometrically similar to the loaded area and concentric with it

A_b - the bearing or strut area

A_{core} - the area confined by the local confining reinforcement

- A_g - gross area of the bearing plate
- A_s - the area of the confining reinforcement with the spacing "s"
- d_s - the diameter of the spiral or the width of the ties
- f_c - the concrete compressive strength at the time of stressing
- f_y - the yield strength of the confining reinforcement
- k - 4 for spirals or active confinement and 2 for ties
- s - the pitch of the spiral or the spacing of the ties

4) The width of the compression strut may be taken to be two times the distance from the specimen centerline to the strut axis. The stress distribution across the strut is assumed to be uniform unless a portion of the strut is confined. The confined portion of the strut may utilize the additional concrete strength available from the confining reinforcement. The strut width should be checked to ensure that it does not extend outside the cross section and that it does not overlap another strut.

5) Compression strut capacity must be checked at the node-strut interface, at the local zone-general zone interface, at changes in the section thickness, and between the secondary nodes in the local zone. If test results verifying the adequacy of the anchorage device and corresponding reinforcement are provided, the engineer needs to check only the strut capacity at the local zone-general zone interface, where the local zone confining reinforcement changes, and at locations where the section thickness changes.

6) The combined stress analysis and the modified STM are ways to more accurately model the ultimate behavior of the specimens. Both methods model the plastic behavior of the specimens by allowing the compression struts to move toward the specimen tendon axis to increase the tension bursting tie prediction. When compared with the test results, the combined stress analysis had an average of the test-to-predicted ratio of 1.17 with a coefficient of variance of 0.18. The modified STM matches the compression capacity and the bursting tension tie capacity. It had an average of test-to-predicted ratio of 0.98

with a coefficient of variance of 0.27. However, a number of the specimens had very unconservative results. It is uncertain whether this unconservatism is due to the method or to the spiral length. When the local zone-general zone interface is checked at a distance from the loading surface of one plate width, the model results are much less unconservative. For the modified STM, the average of the results changed to 1.04 with a coefficient of variance of 0.11. Therefore, caution should be used when utilizing long spirals to increase the local zone-general zone interface capacity. Both methods depend on the extension of the general zone past the depth of the member to increase the specimen capacity. If additional cracking and an extension of the general zone are satisfactory, the modified STM could be used in design. Since large amounts of cracking are typically not acceptable, the modified STM is not recommended for design.

7) The use of the combined stress analysis in typical girder applications is much more complicated than the STM. When checking the critical moment, the stress distribution in the girder must be used (dead load and live load stress distribution). In addition a reduced tensile strength of concrete of $4.2\sqrt{F'_c}$ should be used to ensure a conservative prediction of the beam-column cracking moment. To benefit from the additional capacity prediction of the combined stress analysis, additional cracking must be allowed near the loading surface. The combined stress analysis worked well for the simple concentric tests. If an engineer is to use a fully plastic method (allowing the extension of the general zone), the modified STM is much more adaptable and rational.

8) Most of the specimens were able to reach higher loads than the STM prediction due, in part, to the contribution of concrete bursting tension capacity across the tendon axis. Once the tendon axis crack propagated to the base, this concrete contribution was lost. None of the prediction methods discussed in this chapter take into account this concrete contribution. If the predictions of the models are compared

with the peak load of the specimens when they are completely cracked along the tendon axis, the average and coefficient of variance improve. For the basic STM, the average of the test fully cracked ultimate loads divided by the results of the prediction model is 1.26 with a coefficient of variance of 0.18 for the specimen that were controlled by the tension tie capacity. The combined stress analysis average was 0.99 with a coefficient of variance of 0.05. The modified STM had an average of 0.97 with a coefficient of variance of 0.07. These statistical results only include specimens which failed in tension according to the basic STM.

9) Spalling stresses did not cause cracking in any of the concentric anchorage zone specimens.

10) The cracking load is difficult to predict accurately. The best models match the maximum elastic analysis bursting stress with the triaxial tensile strength of the concrete. This method can yield some unconservative results. Use of $4.2\sqrt{F'_c}$ for the concrete tensile capacity and the inside diameter of the duct to obtain an effective thickness of the concrete ensures conservative results for the cracking load prediction in the specimens tested.

11) A general trend in the cracking load is that the lowest cracking load relative to the bearing capacity of the local zone concrete occurs at an a/h of 0.5.

CHAPTER 4
ECCENTRIC ANCHORAGES WITH STRAIGHT TENDONS

4.1 Introduction

When the load axis of a post-tensioned anchorage zone does not pass through the centroid of the cross section, the anchorage zone is eccentric with respect to the section centroid. In Chapter 3, concentric anchorages were discussed in detail. Concentric anchorages allowed the convenient definition of many variables for that simple condition. In actual post-tensioned structures, concentric anchorages occur in only a small percentage of the total number of anchorage zones. The next step in complexity is the eccentric anchorage zone. The amount of eccentricity can change the stress pattern and stress level significantly. Eccentric anchorage zones can be divided into two groups: those located inside the section kern and those located outside the section kern. The kern is the greatest eccentricity of the resultant post-tensioning force for which the elastic stress on the outer fiber farthest from the load axis is zero when computed by ordinary mechanics procedures using a combined stress analysis ($P/A \pm Mc/I$) at the end of the diffusion zone (general zone). If a single anchorage is placed outside the kern, tension stresses are computed on the opposite outside fiber. If a single anchorage is placed inside the kern, then the computed stresses on the opposite outside fiber are compressive.

Figure 4.1 shows the calculated elastic stress distributions for a rectangular section with the anchorage located at the kern, $e/h = 1/6$ (Fig. 4.1a), and outside the kern, $e/h = 1/3$ (Fig. 4.1b). The forces and stresses in the bursting region are caused primarily by the spreading of the forces from the anchorage plate into the section. The tensile forces and stresses in the longitudinal edge tension region are created when the resultant post-tensioning force is located outside the kern of the section. Along the loaded surface, spalling forces and

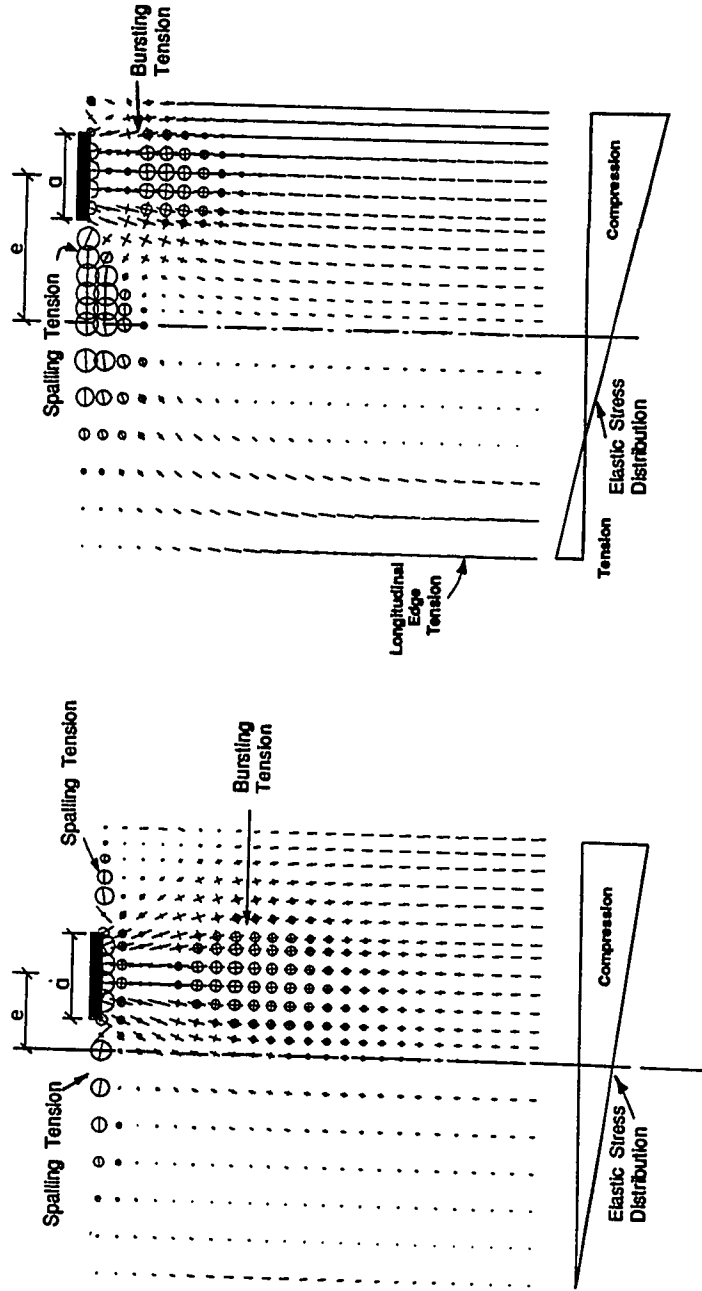


Figure 4.1 Eccentric Anchorage Elastic Stress Distribution

stresses are caused by equilibrium conditions with the longitudinal edge tension force and the bursting force, and compatibility conditions between the concrete and the bearing plate.

Seven eccentric specimens were tested. Two had the anchorage zone located at the kern, while five had resultant load axis locations outside the kern. This chapter describes the test setups and results in detail for the eccentric anchorage test series. The test results are analyzed from both a first crack and an ultimate load standpoint.

4.2 Test Program

The objective of the eccentric anchorage test series was to add the variable of eccentricity to the investigation and to study its effect on the cracking behavior and ultimate load. The test procedure for the eccentric anchorage specimen series was generally identical to the concentric anchorage test series (see Sec. 3.2.1). The testing machine used and the support conditions varied from the concentric test series as will be discussed in the following subsections.

4.2.1 Specimens with Load Point At the Kern. The two specimens that were loaded inside the kern are shown in detail in Figs. 4.2 (Specimen E1) and 4.3 (Specimen E5). Both specimens were loaded in the universal testing machine through a 10-inch diameter spherical loading head. Both specimens were leveled at the base with metal shims and then hydrostone was poured around the base to provide full and uniform support at the base of the specimen. Both specimens were supported at the base and at mid height in the transverse direction to prevent any transverse movement (see Fig. 4.4). The supports consisted of metal frames bolted to the floor which held in place a steel plate welded on the end of a threaded rod. Two teflon sheets were placed between the metal plate and the concrete surface to allow lateral movement of the specimen. The plates were held lightly against the concrete surface by threaded rods connected to the support frames. Table 4.1 gives the material information for Specimens E1 and E5.

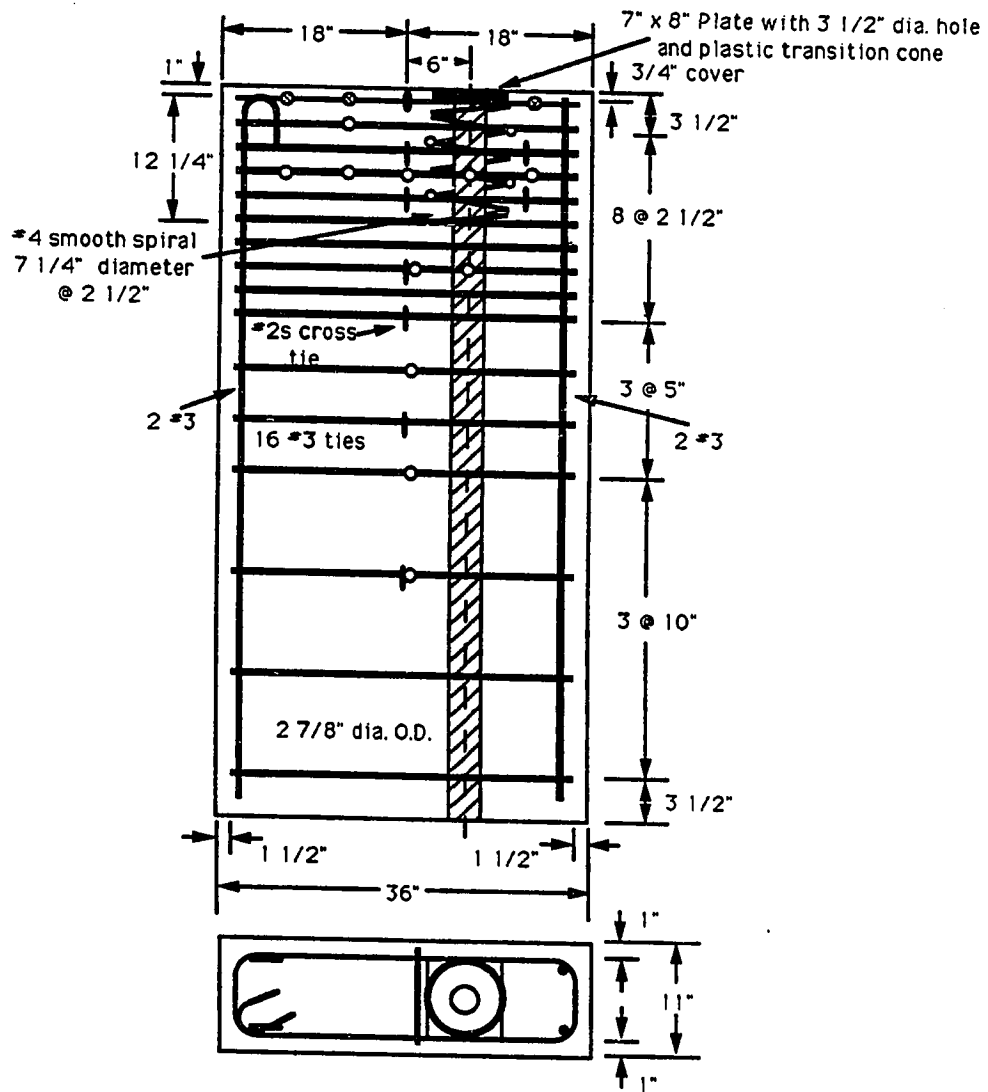


Figure 4.2 Specimen E1 Details

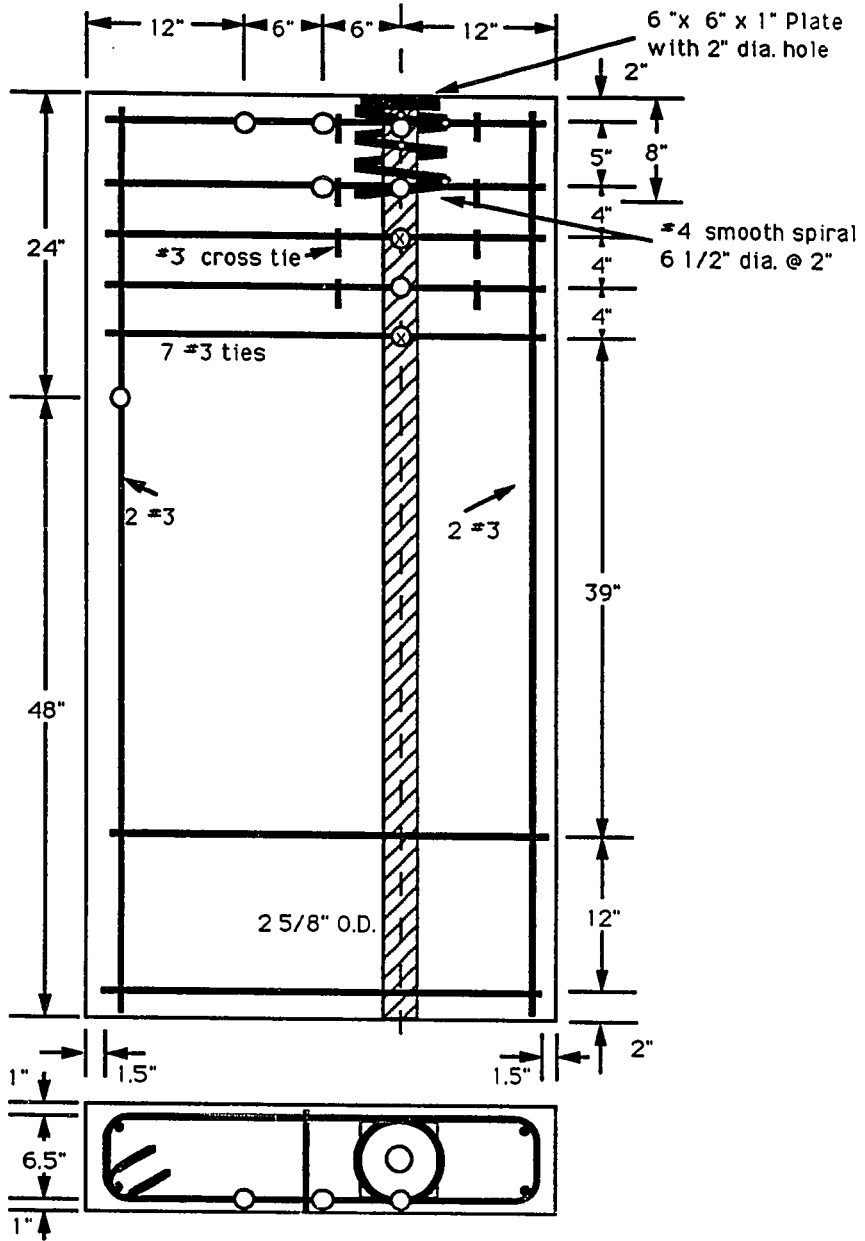


Figure 4.3 Specimen E5 Details



Figure 4.4 Transverse Braces for Eccentric Specimens

Table 4.1 Material Information for Specimens E1 and E5

| Specimen | Concrete | | E (ksi) | #3 Reinforcing Bar | | |
|----------|-------------------|-----------------|--------------|--------------------|----------------|-------------------------------|
| | f_{sp} (psi) | f'_c (psi) | | F_y (kips) | f_y (ksi) | Yield Strain (microstrain) |
| E1 | 428 | 5450 | 28700 | 7.34 | 66.7 | 2320 |
| E5 | 459 | 5710 | 28700 | 7.34 | 66.7 | 2320 |

Specimen E1 was heavily reinforced (see Fig. 4.2) with #3 Grade 60 reinforcing bar ties distributed from 3/4 inch to 68 1/2 inches from the loaded surface. If all the reinforcement along tendon axis was effective, the total tension bursting resistance force would be 234.9 kips with a centroid of 24.9 inches measured from the loading surface. The anchorage device was a flat plate anchor that was 7 x 8 x 1 inches with the 7-inch dimension oriented in the lateral direction. The plate was loaded over its full width. The local zone was confined with a #4 smooth spiral. The spiral had a diameter of 7 1/4 inches and a pitch of 2 1/2 inches. The spiral had a yield stress of 80.3 ksi and a modulus of elasticity of 26,900 ksi. The first and last half turns were tied to the adjacent turn for development. Cross ties, #2s bar ($F_y = 3.57$ kips, $E = 28,900$ ksi) were included to carry the bursting forces caused by the transverse spreading of the forces.

The first crack occurred at a load of 345 kips and was located on the west side of the specimen along the tendon axis. The first crack was noted on the east side along the tendon path at 375 kips. The tendon axis cracks continued to propagate along the tendon until they reached a depth of 33 inches from the loading surface (see Fig. 4.5). At 390 kips, a diagonal crack opened on the east side of the specimen that started at the anchorage plate 2 1/2 inches from the tendon axis on the short side of the specimen with an angle of approximately ten degrees. The diagonal crack propagated to a point 5 inches from the outer transverse face and 22 inches from the loaded surface. The peak load was 475 kips. This occurred in conjunction with a bulging of the concrete on the west side of the specimen (see Fig. 4.6). The cracks caused by the bulging started at the corners of the anchorage plate and propagated on the loaded surface until they reached the lateral face. After the peak load, the load decreased to 420 kips, but the specimens were reloaded to 471 kips as shown in the load-displacement curve, Fig. 4.7. As load was reapplied the portion

of concrete ahead of the anchor continued to spall away from the specimen.



Figure 4.5 Bursting Cracks for Specimen E1

Figure 4.8 shows the strain data for two gages on the bursting reinforcement along the tendon axis. Problems occurred with additional gages along the tendon axis, but the known strains and a knowledge of the cracking pattern allow a reasonable estimate of the strain pattern. Because the bars at 8 1/2 inches were close to yielding and there were large deformations near the plate, it was assumed that the reinforcing bars at 3/4, 3 1/2 and 6 inches from the anchor plate yielded. A

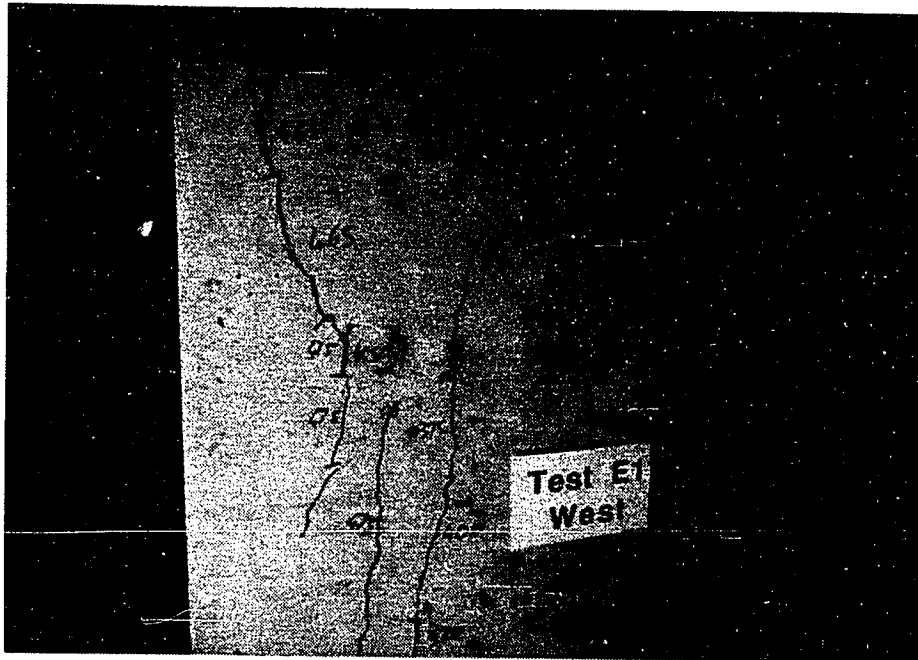


Figure 4.6 Spalling of Specimen E1 at Ultimate

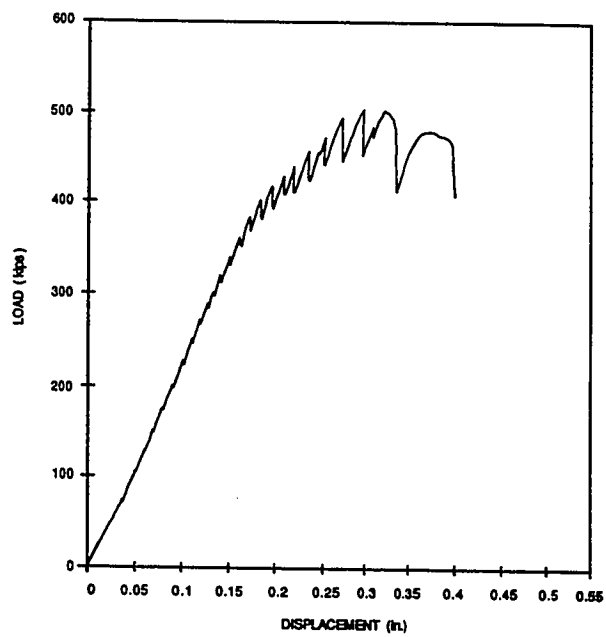


Figure 4.7 Load-Displacement Curve, Specimen E1

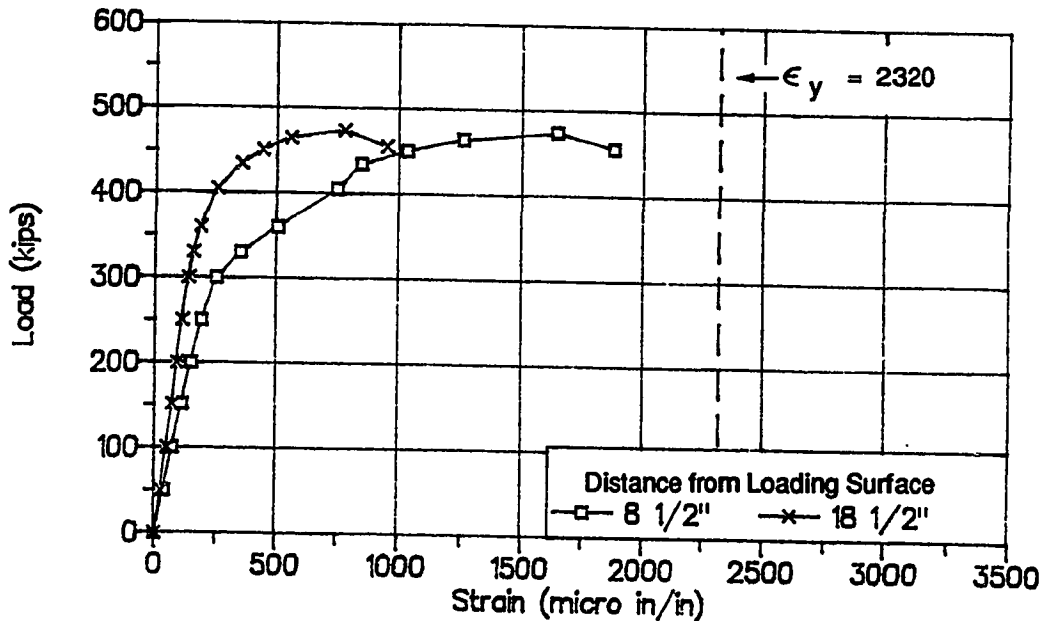


Figure 4.8 Bursting Reinforcement Strain Data, Specimen E1

linear approximation was used to estimate the strains between the data points at 8 1/2 and 18 1/2 inches. Since the concrete crack near the tendon ended at 33 inches, the strain at the first bar beyond the crack (33 1/2 inches) was assumed to have a strain of 200 microstrain. (From the concentric series, it was determined that 250 microstrain in the reinforcement was the approximate value at which the first crack was typically seen in the concrete.) Since this bar is located slightly beyond the known crack location, the strain in the bar was assumed to be slightly below the cracking strain. The bars at 48 1/2, 58 1/2 and 68 1/2 inches were assumed to have zero strain since the concrete crack was arrested at 15 1/2 inches above the closest of the two bars. Figure 4.9 shows the estimates for the bursting strains at the peak load of 475 kips and the reload to 471 kips. Table 4.2 is a summary of the first cracking and peak loads for Specimens E1 and E5. Two values are listed for the first cracking load because the first cracking loads were different for each lateral face of the specimen.

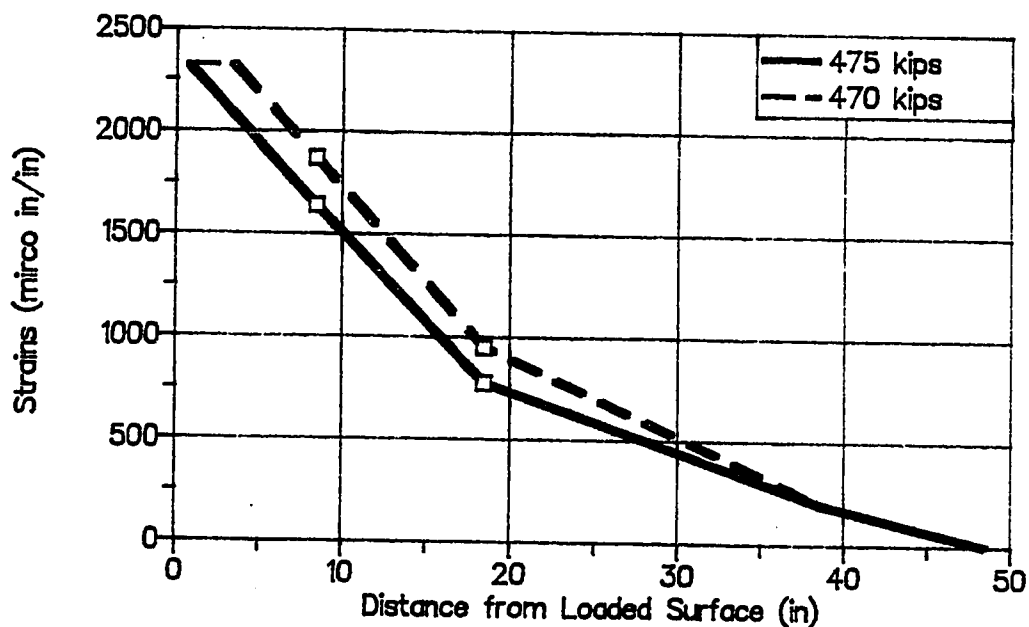


Figure 4.9 Bursting Reinforcement Strain Distribution near Ultimate, Specimen E1

Table 4.2 Load Summary for Specimens E1 and E5

| Specimen | First Crack (kips) | | Peak Load (kips) | 2nd Hump (kips) |
|----------|--------------------|-----|------------------|-----------------|
| | 345 | 375 | | |
| E1 | 345 | 375 | 475 | 471 |
| E5 | 215 | 250 | 332 | 315 |

Specimen E5 was loaded similarly to Specimen E1 with the anchorage device at an e/h of $1/6$, the location of the kern. Specimen E5 had a thinner section and much less bursting reinforcement than Specimen E1. The total bursting reinforcement tension capacity was 73.4 kips with a centroid of 10.8 inches from the anchorage plate, if

the bursting reinforcement at 58 and 70 inches from the anchor were neglected. This reinforcement was neglected because cracks did not propagate far enough down into the section to mobilize the reinforcement. The bursting tension capacity was significantly less than the 234.9 kips in Specimen E1. The local zone confinement consisted of a #4 smooth spiral with a diameter of 6 1/2 inches and a pitch of 2 inches. The spiral material was the same as described for Specimen E1. Number three cross ties were furnished on each side of the spiral to a depth of 15 inches ahead of the anchor. The anchorage device was a 6 x 6 x 1-inch flat plate.

The first cracking load for Specimen E5 occurred at 215 kips on the west side. The first crack was not seen on the east side until 250 kips. Both cracks occurred along the tendon path. The cracks propagated very deeply into the specimen and, by the failure load of 332 kips had reached 46 inches from the loaded surface. At 315 kips, cracks formed on the corners of the loading plate and propagated onto the lateral face. At the ultimate load, a horizontal crack formed on the transverse face at 4 1/2 (seen in Fig. 4.10) and 8 inches from the loaded surface. Crack measurements were taken on the main tendon axis crack and are shown in Fig. 4.11. Cracks remained small until 300 kips. The specimen was loaded to 330 kips and the load decreased suddenly to 285 kips (see Fig. 4.12). The specimen was reloaded to 332 kips, and a gradual loss in strength occurred as the displacement increased.

Figure 4.13 shows the bursting strain data. All the bursting reinforcement considered effective yielded or was close to the yield strain at the ultimate load. Figure 4.14 shows the bursting force per reinforcement layer as calculated from the bursting strains and expressed as a percentage of the axial load. Fully plastic behavior was exhibited by the bursting reinforcement with the bursting force almost evenly distributed between the four reinforcement layers.

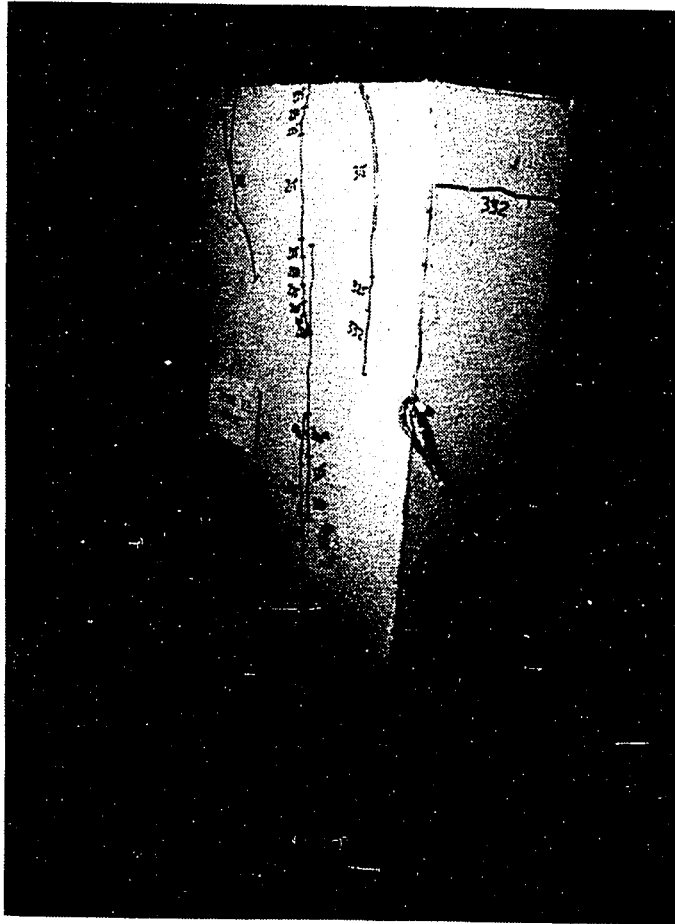


Figure 4.10 Cracking Pattern at Ultimate, Specimen E5

4.2.2 Specimens with Load Point Outside the Kern. When the load is placed outside the kern, tension stresses are created on the outer fiber farthest away from the load axis. Five specimens were tested with the load axis outside the kern. Three specimens (E2, E3, and E4) had the load axis at an e/h of $1/3$, and two specimens (E6 and M5) had the load axis at an e/h of $1/4$. A universal testing machine with a 10-inch spherical head was used to load Specimens E2, E3, E4, and E6; while a 1,200-kip horizontal testing machine (see Fig. 4.15) with a fixed loading head was used to load Specimen M5. Specimens E2, E3, and

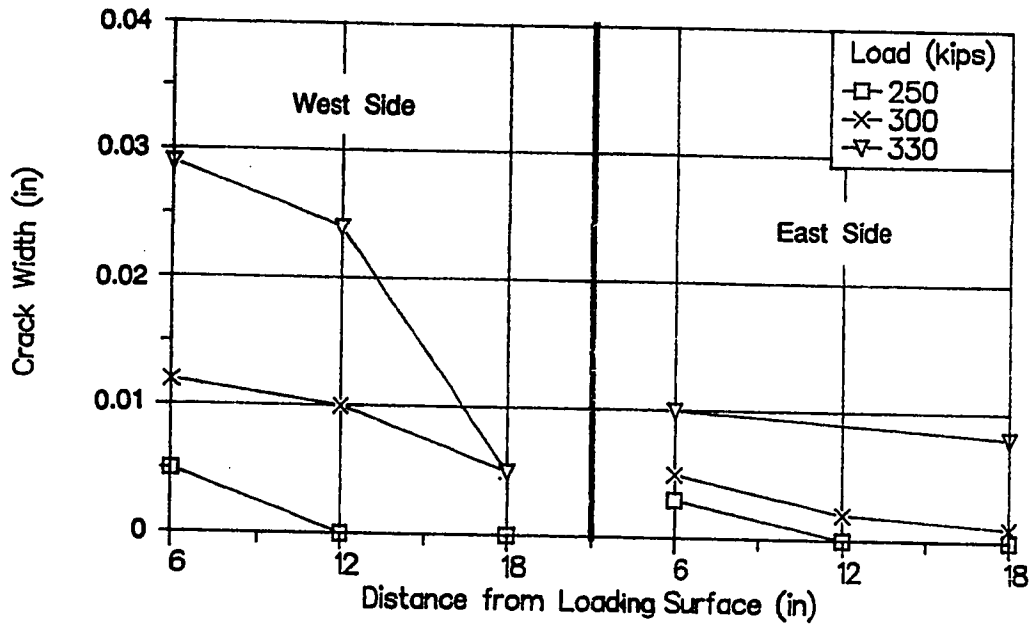


Figure 4.11 Bursting Crack Widths, Specimen E5

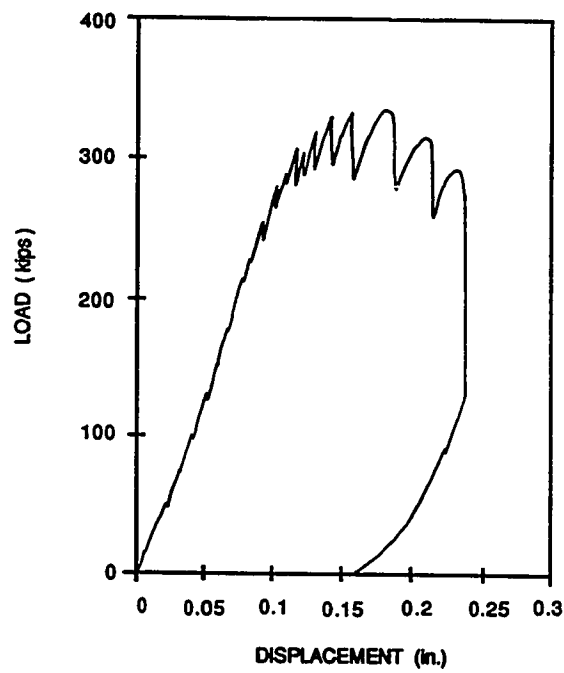


Figure 4.12 Load-Displacement Curve, Specimen E5

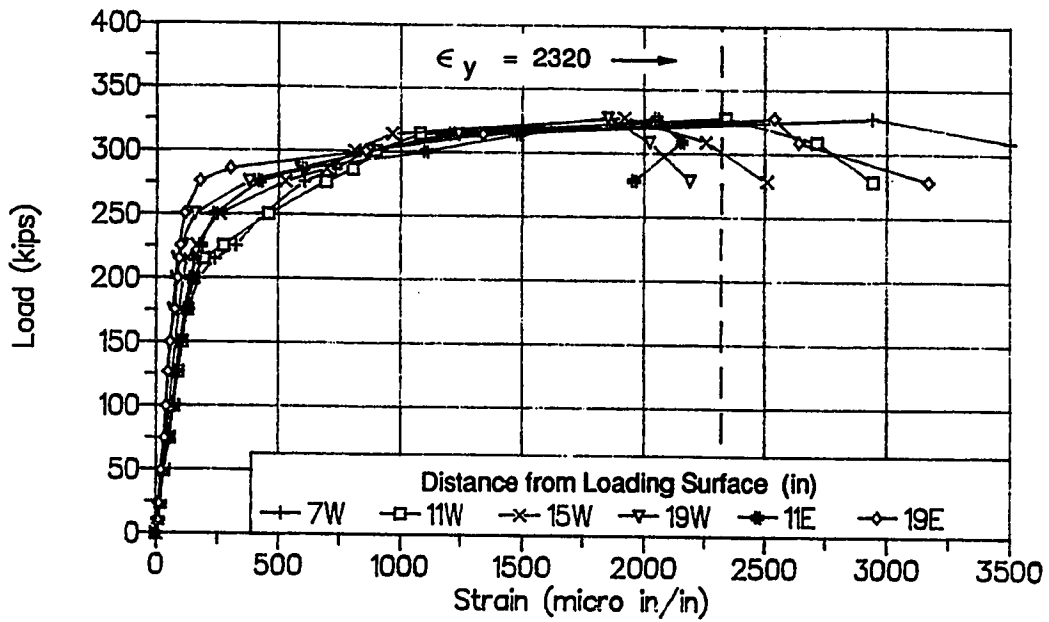


Figure 4.13 Bursting Reinforcement Strain Data, Specimen E5

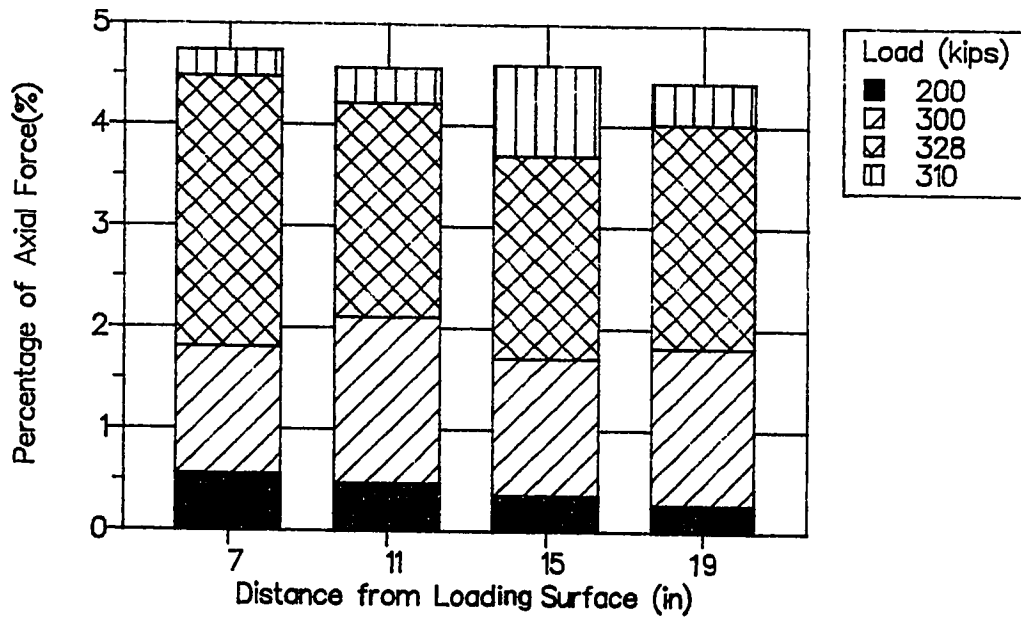


Figure 4.14 Bursting Force as a Percentage of Axial Load, Specimen E5

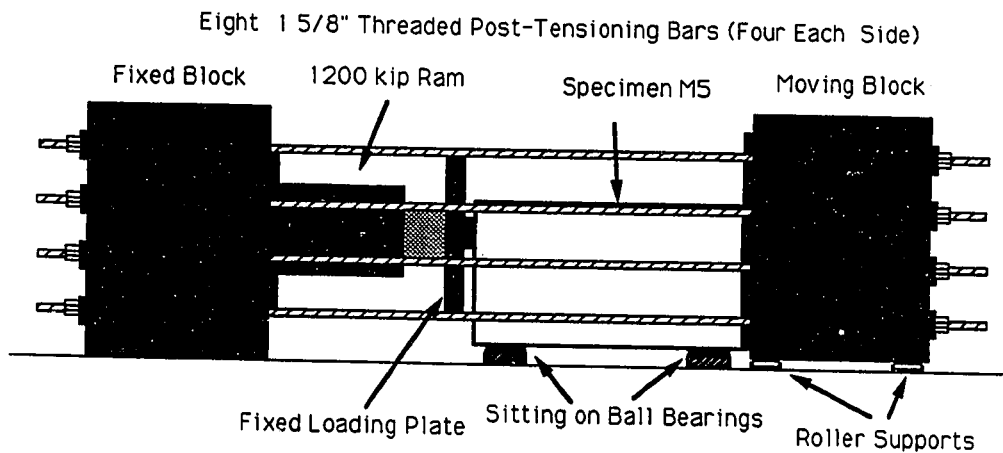


Figure 4.15 1200 kips Horizontal Test Machine

E4 were used to examine the effects of longitudinal edge tension stresses and spalling stresses shown in Fig. 4.1b.

Specimen E2 was the control specimen (see Fig. 4.16). The specimen was heavily reinforced with #3 and #4 Grade 60 reinforcing bars (see Table 4.3). The bursting reinforcement layers started at 3/4 inch from the loading surface and extended down to 68 1/2 inches. The total tension bursting capacity was 248 kips with a centroid of 23.0 inches from the loading surface. The specimen was reinforced for the spalling forces with five #4 bars, three of which are continuous with the outer longitudinal edge tension reinforcement. The outer longitudinal edge tension reinforcement consisted of five #4 bars. The total tension capacity of the spalling reinforcement and the longitudinal edge tension reinforcement as 68.5 kips. Number 2s cross ties were used in addition to a #4 smooth spiral with a 7 1/4-inch diameter and a 2 1/2-inch pitch (see Specimen E1 for its material properties) to carry transverse bursting forces. At the base of the specimen, the section was altered to prevent uplift of the specimen (see Fig. 4.17). The kern of the base section is outside the load axis; so, theoretically, there are no tension stresses on the extreme fiber.

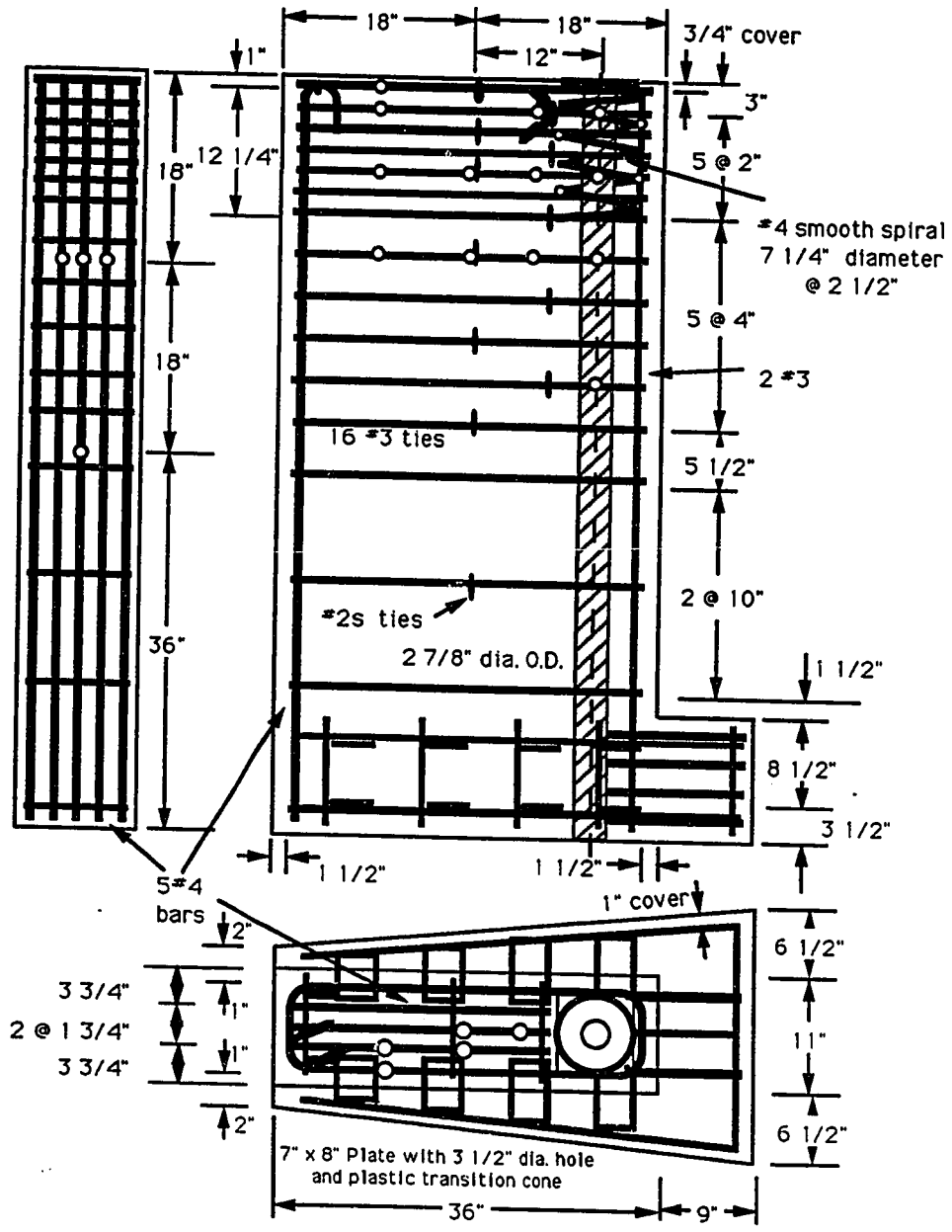


Figure 4.16 Specimen E2 Details

Table 4.3 Material Information for Specimens E2, E3, E4, E6 and M5

| Specimen | Concrete | | Reinforcing Bar | | | | |
|------------|-------------------|-----------------|-----------------|--------------|-----------------|----------------|-------------------------------|
| | f_{sp} (psi) | f'_c (psi) | Bar Size | E (ksi) | F_y (kips) | f_y (ksi) | Yield Strain (microstrain) |
| E2, E3, E4 | - | - | #3 | 28700 | 7.34 | 66.7 | 2320 |
| | | | #4 | 27000 | 13.70 | 68.5 | 2540 |
| E2 | 460 | 5950 | - | - | - | - | - |
| E3 | 492 | 6130 | - | - | - | - | - |
| E4 | 475 | 5690 | - | - | - | - | - |
| E6 | 443 | 5650 | #2m* | 27600 | 2.20 | 44.9 | 1640 |
| | | | #3 | 28700 | 7.34 | 66.7 | 2320 |
| M5 | 393 | 4670 | #2s* | 28900 | 3.57 | 75.1 | 2600 |
| | | | #3 | 27500 | 6.60 | 60.0 | 2200 |

* #2m $A_s = 0.049 \text{ in}^2$

* #2s $A_s = 0.0475 \text{ in}^2$

Figure 4.18 shows the load-displacement curve for Specimen E2. The change in stiffness at 150 kips is difficult to explain since the first crack along the tendon path was seen at 265 kips on the east side and not until 315 kips on the west side. An examination of the strain data, bursting (see Fig. 4.19), spalling (see Fig. 4.20), and longitudinal edge tension (see Fig. 4.21) shows a slight change in strains at 150 kips. The cracking patterns were extensive in Specimen E2 with cracking occurring on all of the exposed concrete surfaces. Figure 4.22 shows the southeast corner of the specimen which is underneath the loading plate. The cracks on the east face show the spreading of the bursting forces from the loading plate. The crack shown propagating toward the south face came to within 1 inch of the exterior surface before the specimen failed. The bursting cracks extended to a depth of 28 inches from the loaded surface. Since the

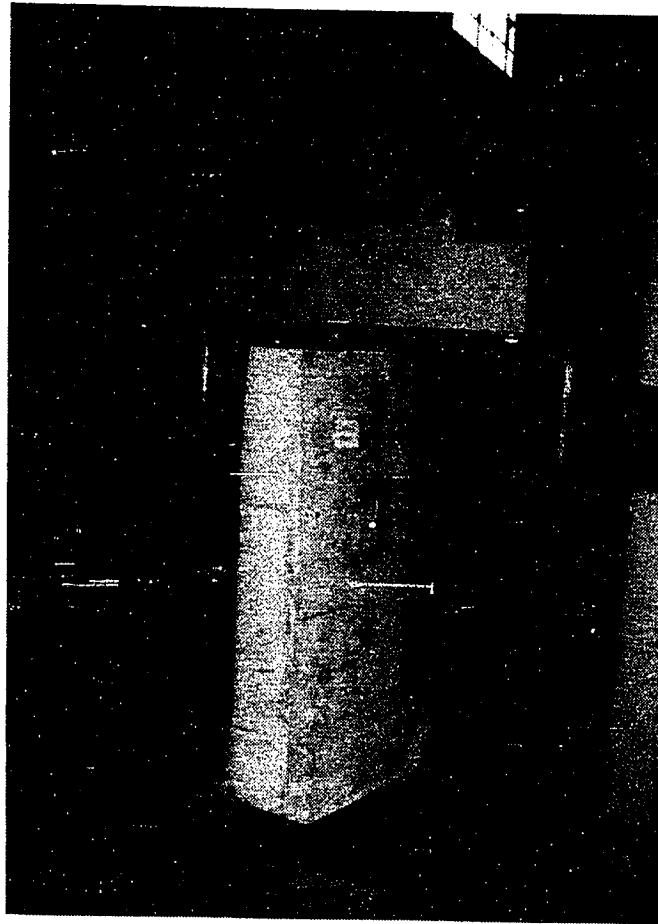


Figure 4.17 Specimen E2 Base Modification

anchorage plate was only 6 inches from the south surface, the concrete capacity was not enough to carry the transverse bursting force. The transverse spreading of forces caused vertical and diagonal cracking on the south face. Cracking also occurred in the spalling region (see Fig. 4.23). The first crack on the loaded surface occurred at 360 kips. The cracks extended over the full thickness of the section but only extended 2 inches into the specimen. From the strain gages the maximum spalling force was 12.9 kips at an applied load of 500 kips.

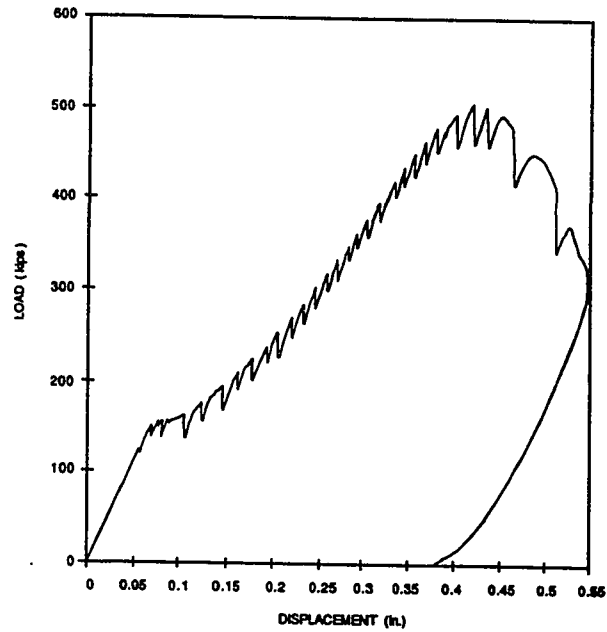


Figure 4.18 Load-Displacement Curve, Specimen E2

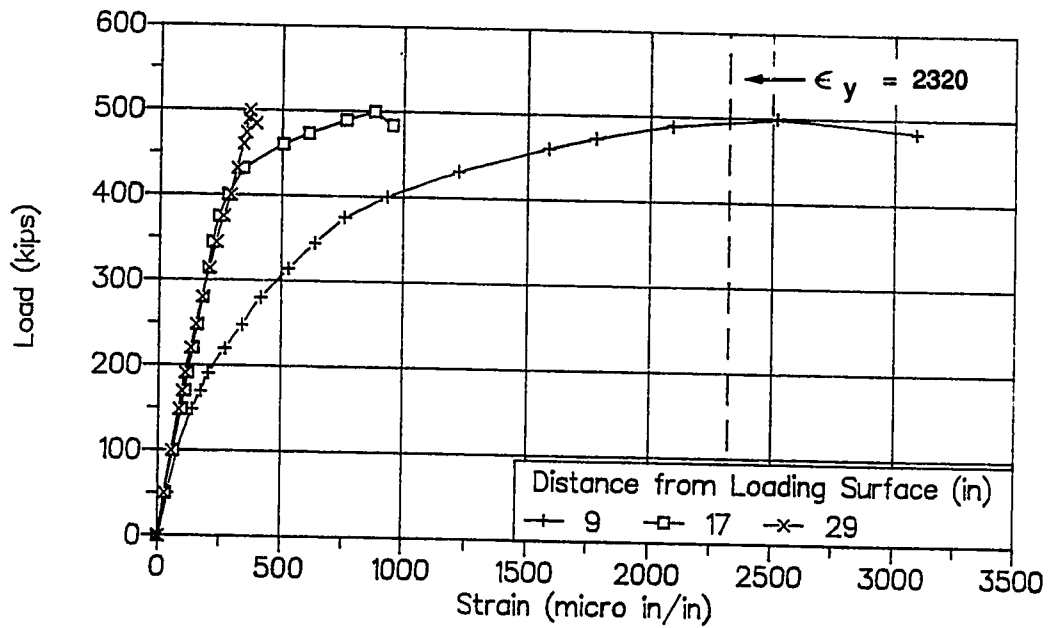


Figure 4.19 Bursting Reinforcement Strain Data, Specimen E2

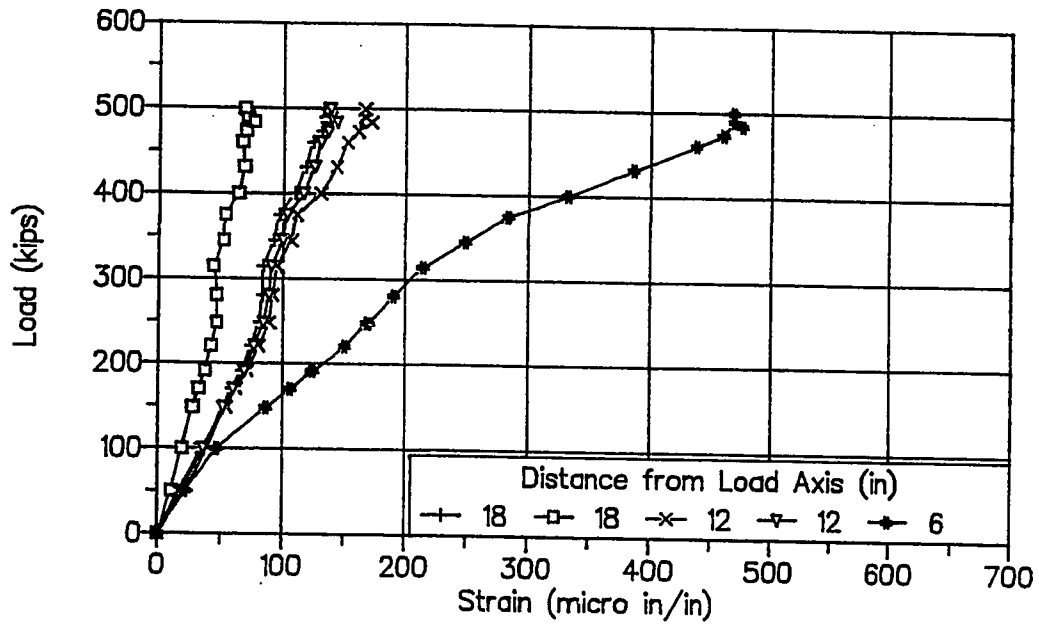


Figure 4.20 Spalling Reinforcement Strains, Specimen E2

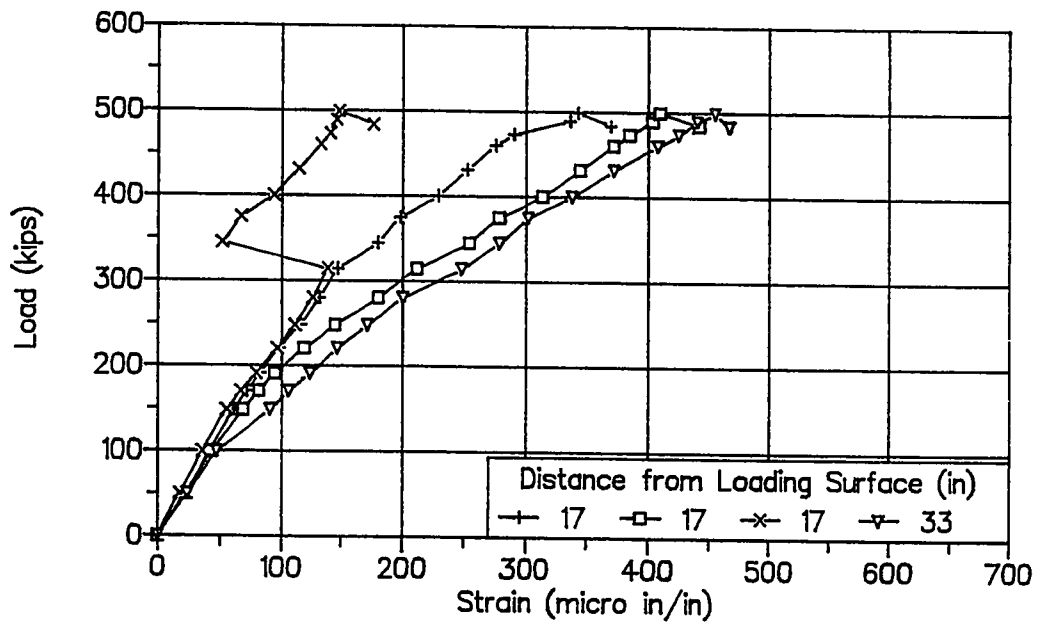


Figure 4.21 Longitudinal Edge Tension Strains, Specimen E2

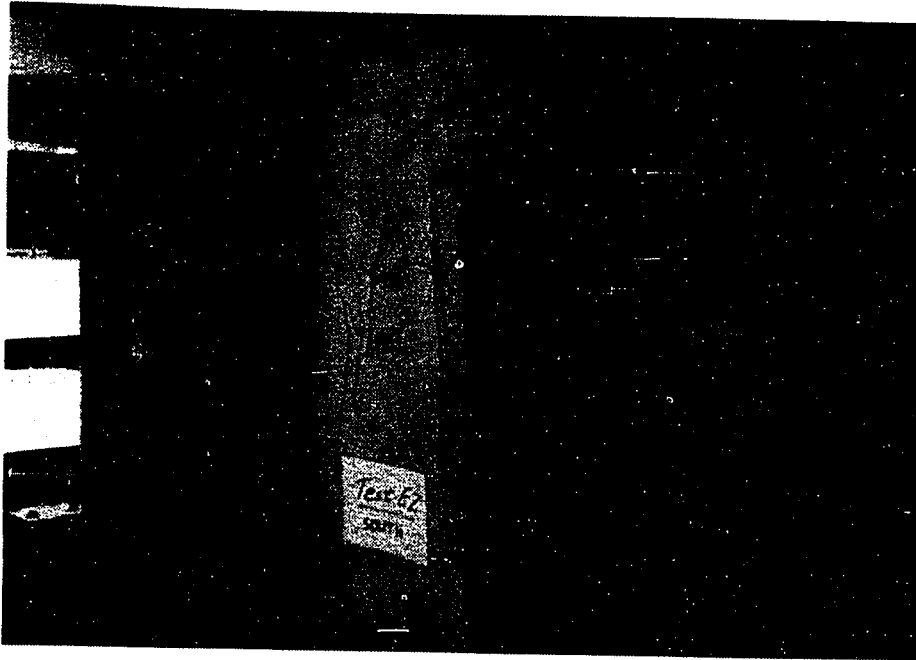


Figure 4.22 Bursting Crack Patterns, Specimen E2

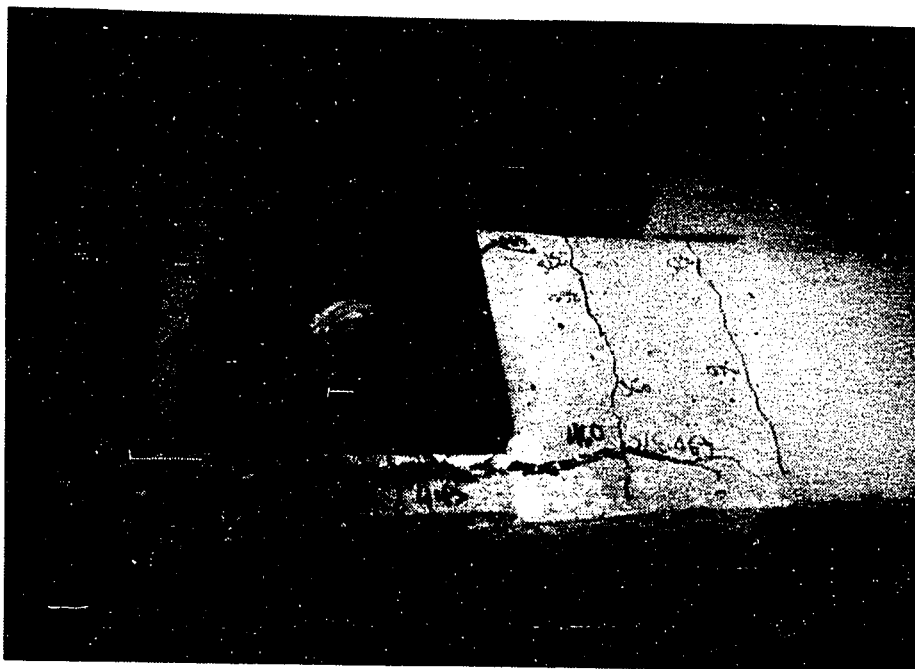


Figure 4.23 Spalling Cracks, Specimen E2

A crack formed at 250 kips on the longitudinal edge tension face (north face, see Fig. 4.24). Longitudinal edge tension cracks extended onto the west and east faces for a maximum of 10 inches. The elastic analysis (see Fig. 4.16) indicates that the longitudinal edge tension force should be 12.5 percent of the axial load. The maximum longitudinal edge tension force determined from the reinforcement strains was 10.5 kips at an axial load of 500 kips (2.1 percent). This was well below the 12.5 percent that was calculated.

During reloading after the ultimate load, most of the concrete outside the reinforcing bars and immediately ahead of the anchor spalled off (see Fig. 4.25). As with Specimen E1, the bursting strain data along the tendon axis was not provided for all the bars. A linear extrapolation was done between the known bursting strain values with the bar at 38 1/2 inches from the bearing plate being assumed to be at zero strain. Figure 4.26 shows the bursting strain approximation for load stages near or at ultimate. Table 4.4 is a summary of the first crack and ultimate loads for the specimens with the load axis outside the kern.

Table 4.4 Load Summary for Specimen E2, E3, E4, E6 and M5

| Specimen (e/h) | Bursting First Crack (kips) | | Peak Load (kips) | 2nd Hump (kips) |
|-------------------|--------------------------------|-----|---------------------|--------------------|
| E2(1/3) | 265 | 315 | 500 | 498 |
| E3(1/3) | 300 | | 522 | 515 |
| E4(1/3) | 250 | 290 | 500 | 500 |
| E6(1/4) | 225 | | 348 | 340 |
| M5(1/4) | 400 | | 677 | 668 |

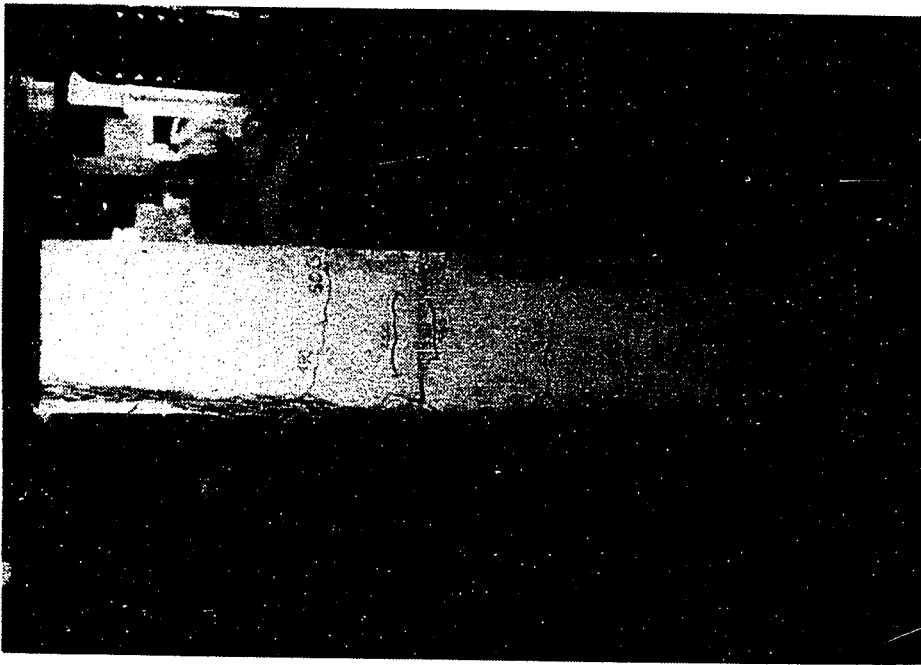


Figure 4.24 Longitudinal Edge Tension Cracks

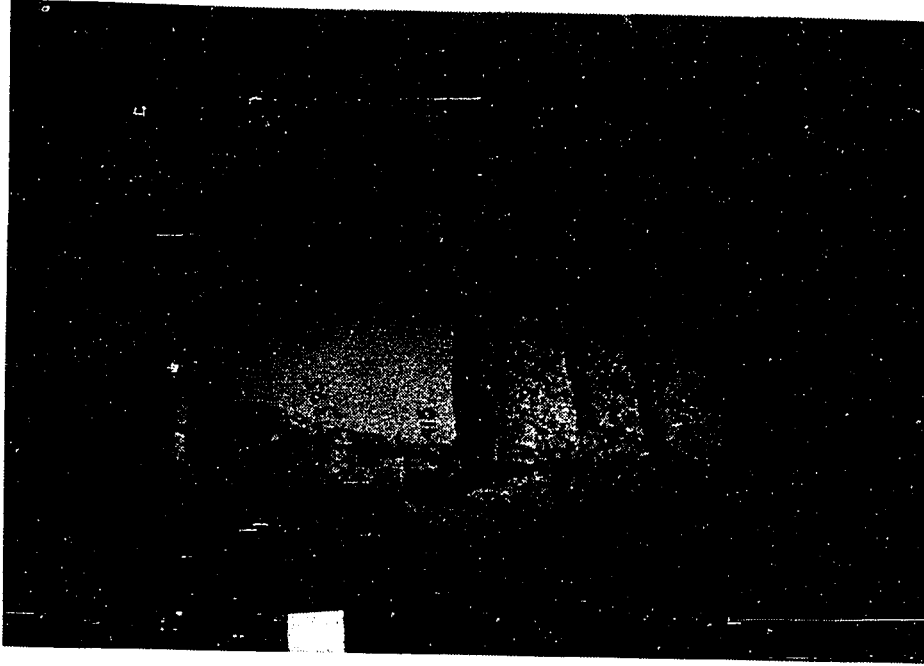


Figure 4.25 Specimen E2 at Ultimate

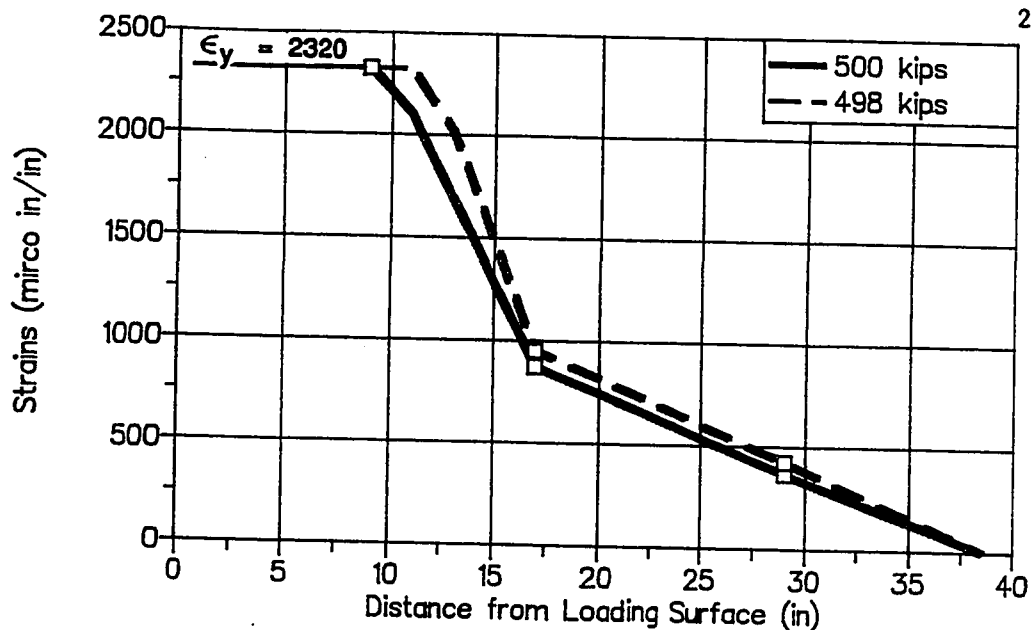


Figure 4.26 Bursting Reinforcement Strain Distribution at Ultimate, Specimen E2

Specimen E3 was reinforced with the same bursting, spalling, and longitudinal edge tension reinforcement as Specimen E2 (see Fig. 4.27). Specimen E3 was different because thin plastic sheets ($t = 0.0040$ inches) were placed in the concrete in the regions of longitudinal edge tension and spalling force to eliminate any tension concrete contribution. The plastic sheets were located at the specimen centerline in the loaded surface region and 23 inches from the loading surface in the longitudinal edge tension region. The base section was modified from the configuration used in Specimen E2 to a cross section that was easier to cast. The base section modification moved the kern outside the load axis at the base to prevent uplift.

Figure 4.28 shows the load-displacement curve for Specimen E3. The curve was very linear until the load approached the ultimate load. The specimen load reached an ultimate load of 522 kips. The load then decreased to 460 kips before it was reloaded to 515 kips where the displacement began to increase rapidly. The first cracking load on the

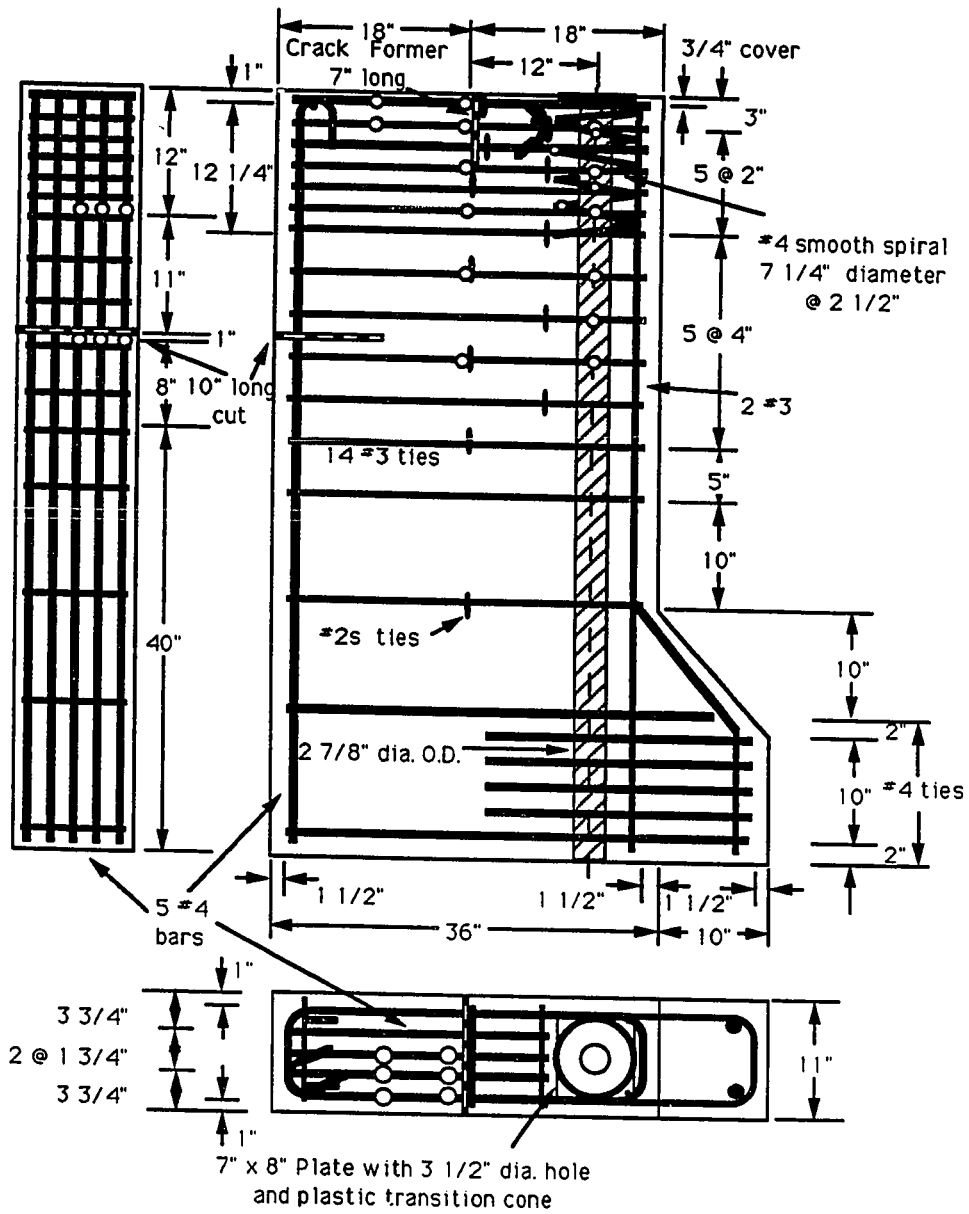


Figure 4.27 Specimen E3 Details

bursting faces occurred at 300 kips for the lateral surfaces (the major axis) and 400 kips on the transverse bursting surfaces. The cracking patterns were very similar to those of Specimen E2. On the loaded surface and the longitudinal edge tension surface, the cracks were initially restricted to the location of the crack formers. On the loaded surface, a crack eventually opened between the crack former and the edge of the plate. On the longitudinal edge tension surface, additional cracks opened both above and below the crack former. The strain data from the spalling region (see Fig. 4.29) and from the longitudinal edge tension force region (see Fig. 4.30) show significant strain increases from the beginning of the test. This indicates that the reinforcement was carrying most of the load and that there was negligible concrete tension contribution. The spalling strain data given in Fig. 4.29 is for several locations. The location is based on a coordinate system with the first term being the distance from the load axis and the second term being the distance from the loaded

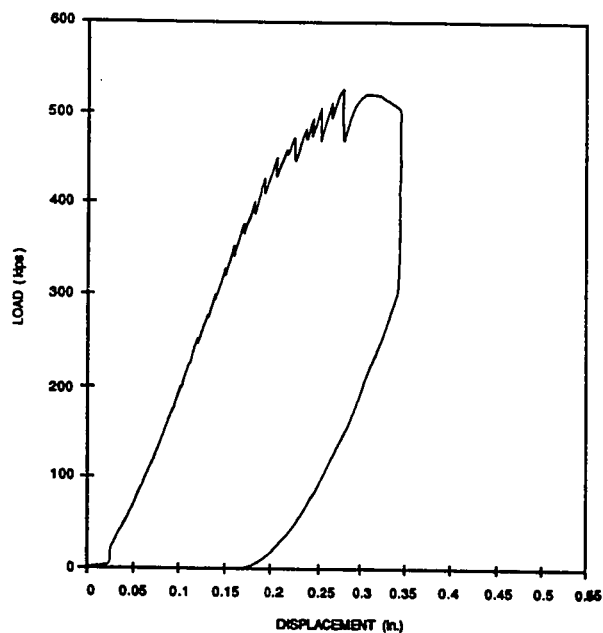


Figure 4.28 Load-Displacement Curve, Specimen E3

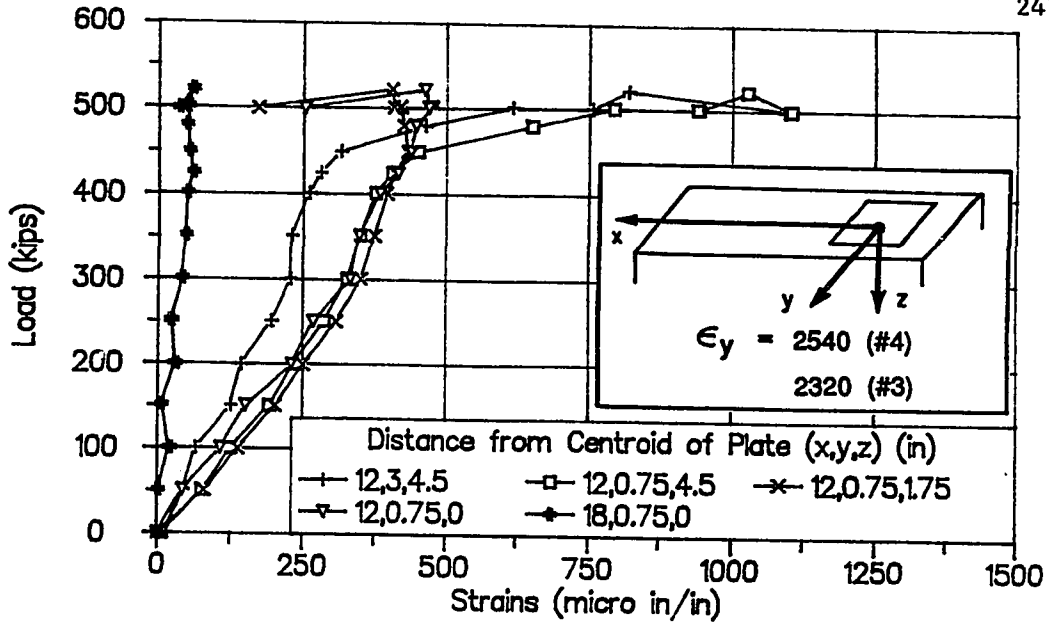


Figure 4.29 Spalling Strains, Specimen E3

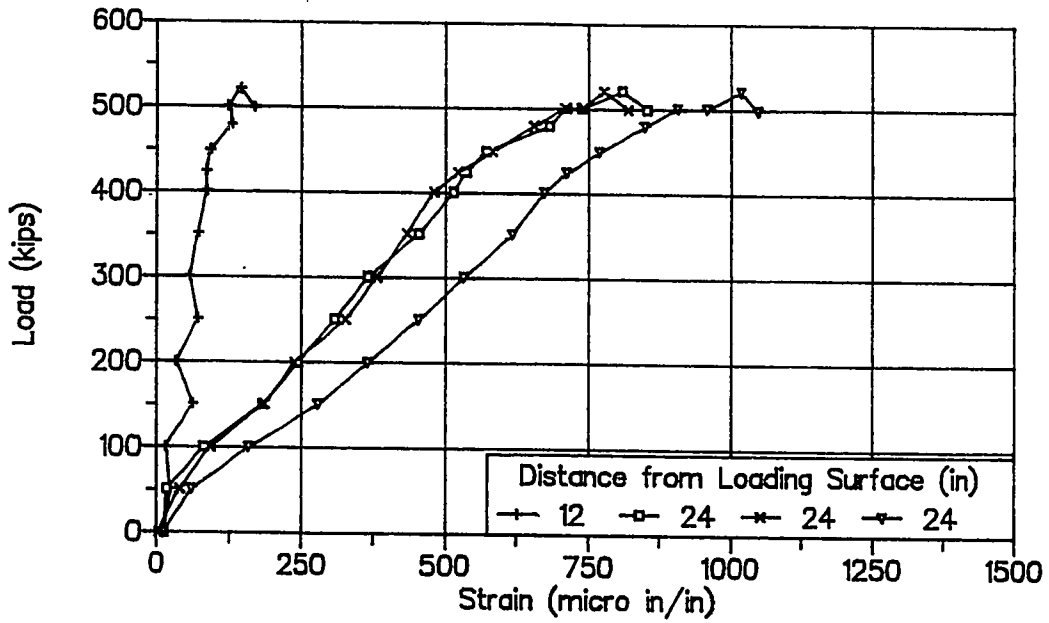


Figure 4.30 Longitudinal Edge Tension Strains, Specimen E3

surface in the direction of the tendon. In the spalling region, two additional gages were at (18, 0.75) that gave identical responses to the one gage shown in Fig. 4.29. This was also true for the longitudinal edge tension gages at 12 inches where there were two gages that recorded results identical to the one reported in Fig. 4.30. Figure 4.31 shows the percentage of the total spalling force and longitudinal edge tension force with respect to axial load. The recorded values were very close together but far below the 12.5 percent predicted by a combined stress analysis ($P/A \pm Mc/I$) for the longitudinal edge tension forces.

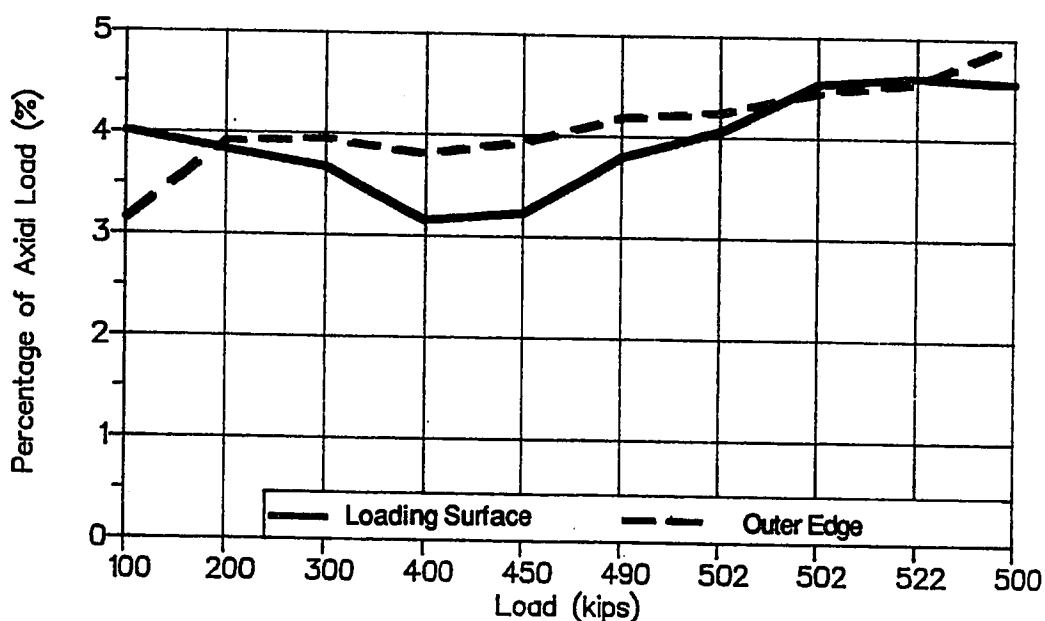


Figure 4.31 Comparison of Spalling and Longitudinal Edge Tension Reinforcement Strains, Specimen E3

Figure 4.32 shows the bursting strain data. Strain gages were located on every other bursting reinforcement bar, and a linear extrapolation was used between known points. Bars within 12 inches of the surface yielded. Bursting cracks started near the tendon duct and then moved toward the closest transverse face as the load increased

and the cracks extended. Cracks also formed from the loaded surface toward the transverse face most distant from the tendon axis, but they were not as wide nor did they propagate as deeply into the section. The maximum bursting crack increased in width from 0.007 inches at 350 kips, to 0.009 inches at 400 kips, to 0.016 inches at 459 kips, and to 0.04 inches at 500 kips. At ultimate, the concrete ahead of the anchorage plate bulged out and could be removed by hand.

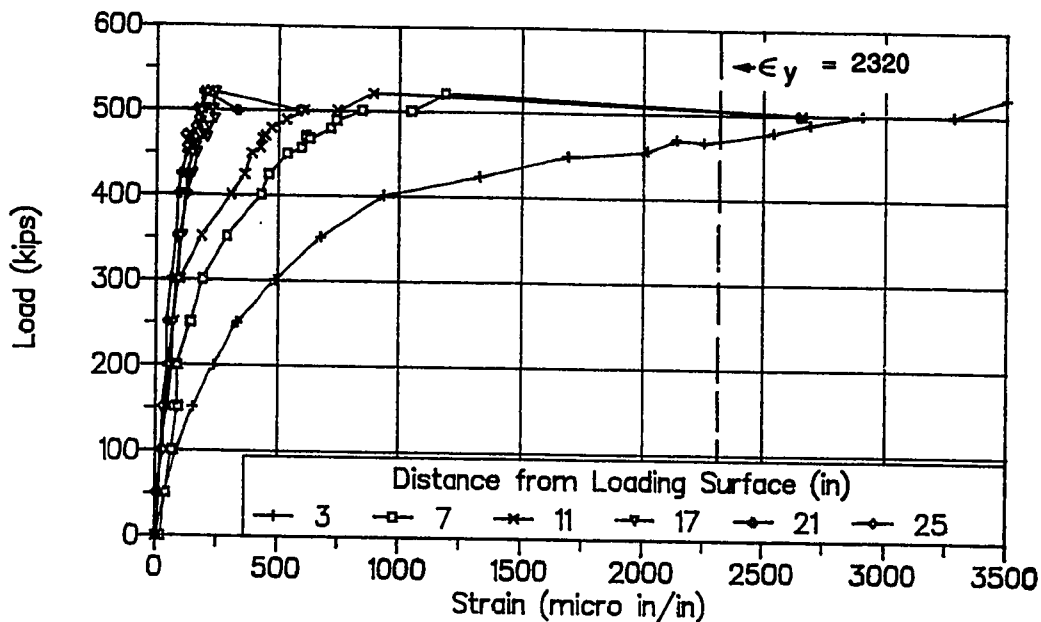


Figure 4.32 Bursting Reinforcement Strain Data, Specimen E3

Specimen E4 examined the effects of removing most of the longitudinal edge tension and spalling reinforcement. The specimen had essentially the same bursting steel as Specimens E2 and E3 with the exception of the #4 bar located 3/4 inch from the loaded surface (see Fig. 4.33). Spalling reinforcement in Specimen E4 consisted of only two #3 bars located 3 inches from the loaded surface. Only two #3 bars were in the longitudinal edge tension region. Both regions had five #4 bars in Specimens E2 and E3.

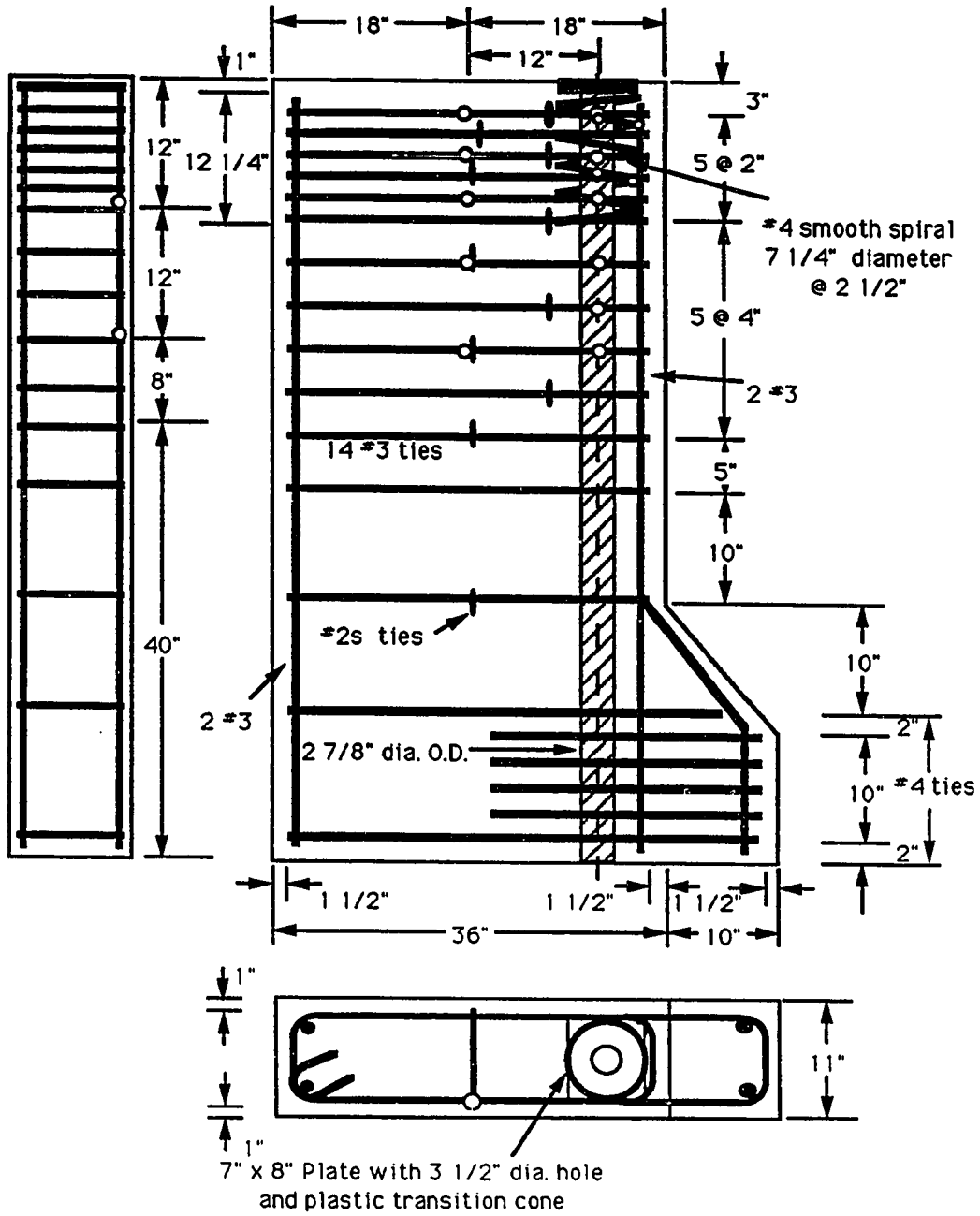


Figure 4.33 Specimen E4 Details

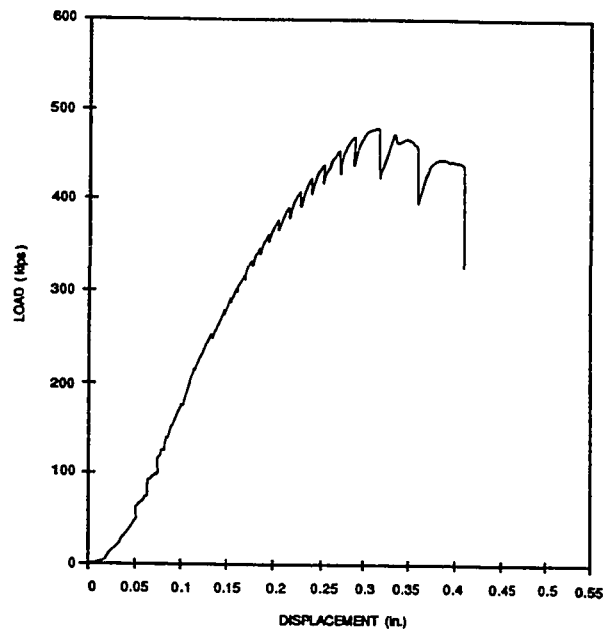


Figure 4.34 Load-Displacement Curve, Specimen E4

Figure 4.34 shows the load-displacement curve for Specimen E4. The curve is very similar to that of Specimen E3. The first cracks in Specimen E4 occurred on the loaded surface and the longitudinal edge tension surface at 225 kips. The first bursting crack occurred along the load path at 250 kips on the west side and 290 kips on the east. The cracking patterns were similar to those of Specimens E2 and E3 except that the cracks in the loaded surface and longitudinal edge tension regions were much longer. Figure 4.35 is a photograph of Specimen E4 at ultimate. The spalling crack extended 6 inches into the lateral face compared with 2 inches in Specimen E2, while the longitudinal edge tension crack was 15 inches long on the lateral face compared with 10 inches in Specimen E2. The bursting cracks show the spreading of forces away from the bearing surface towards the south side and the north side. Cracks had also formed on the south face due to the transverse spreading of the force and propagated down to a depth of 36 inches from the loading surface. The ultimate load of the

specimen was 500 kips. After reaching a load of 500 kips, the load decreased to 450 kips but was reloaded to 500 kips when the specimen failed. Failure was the same as in Specimens E2 and E3 with the concrete bulging out on one side (see Fig. 4.36). When the load was reapplied after the peak load, the displacement increased significantly as the plate was pushed into the concrete.

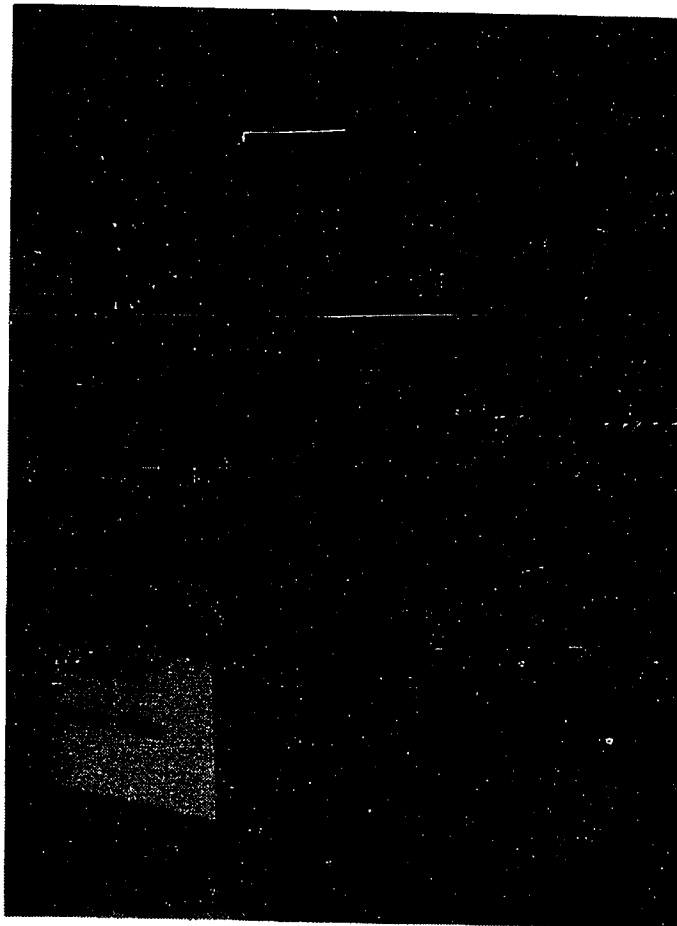


Figure 4.35 Specimen E4 Crack Patterns

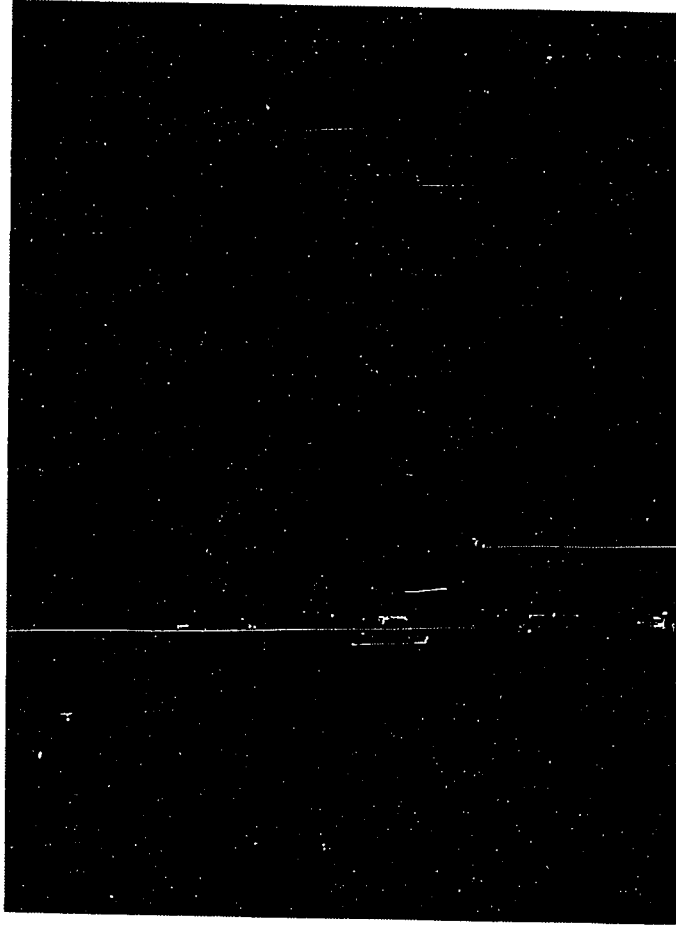


Figure 4.36 Specimen E4 Bulging Concrete Near Anchorage Plate

Figure 4.37 shows the bursting steel strain data. Bars within 11 inches of the loaded surface yielded. Figure 4.38 shows the bursting strain distribution near ultimate. Most of the bursting reinforcement was not utilized. Figure 4.39 gives the strain information for the #3 bars in the longitudinal edge tension region, and Fig. 4.40 gives the strain information along the centerline of the specimen for the bars below the loaded surface region. Even though the total areas of longitudinal edge tension and spalling reinforcement in Specimen E4 were greatly reduced from those in Specimens E2 and E3,

yielding or large strains in the corresponding reinforcement did not occur. Spalling cracking in Specimen E4 allowed the mobilization of more reinforcement along the centerline axis by propagating much deeper than in Specimens E2 and E3. Figure 4.41 shows the crack size for four of the concrete surfaces of the specimen. West and east are the lateral bursting surfaces, while south is the transverse face near the anchor. The north side is the longitudinal edge tension surface. None of the crack widths exceeded 0.015 inches.

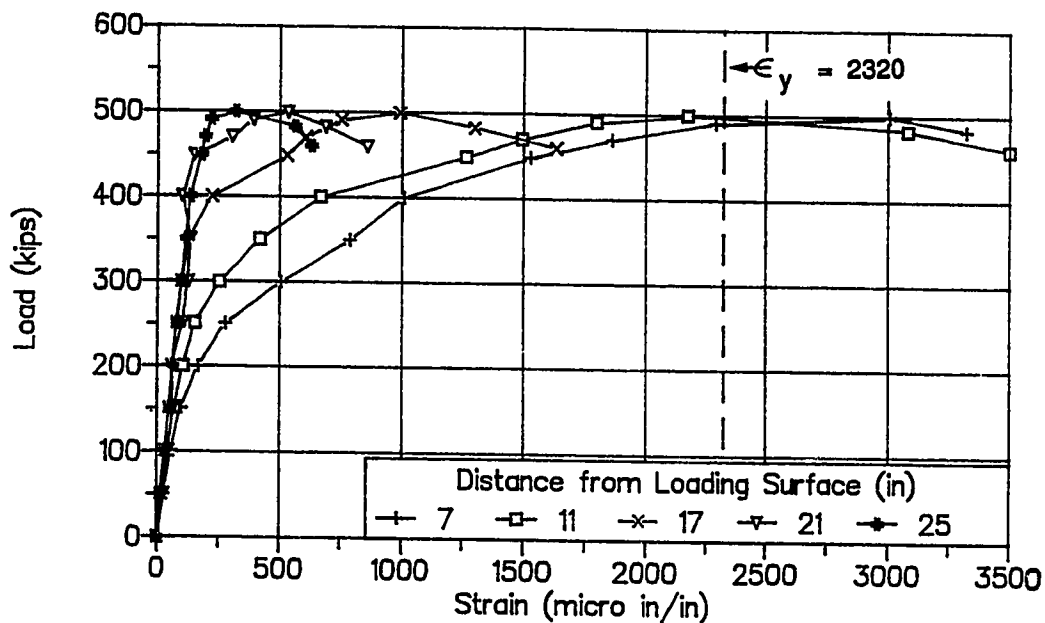


Figure 4.37 Bursting Reinforcement Strain Data, Specimen E4

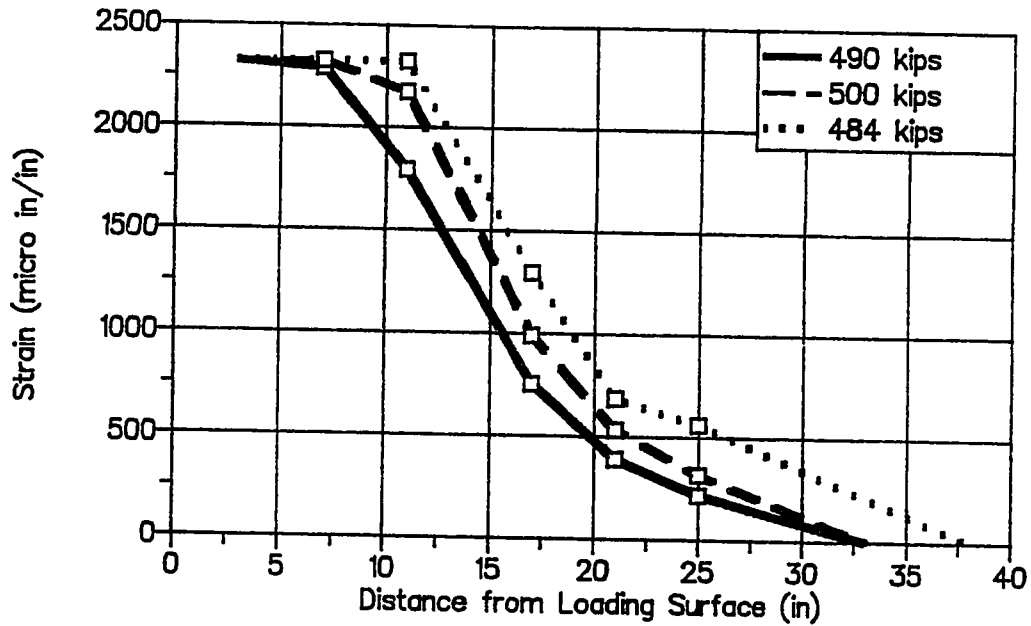


Figure 4.38 Bursting Reinforcement Strain Distribution, Specimen E4

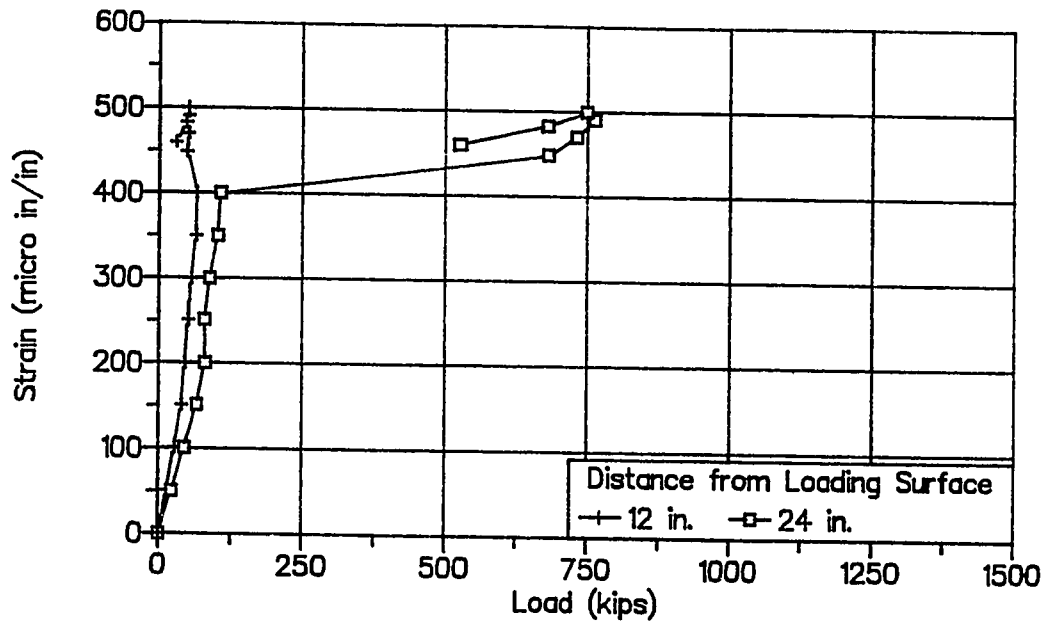


Figure 4.39 Longitudinal Edge Tension Strains, Specimen E4

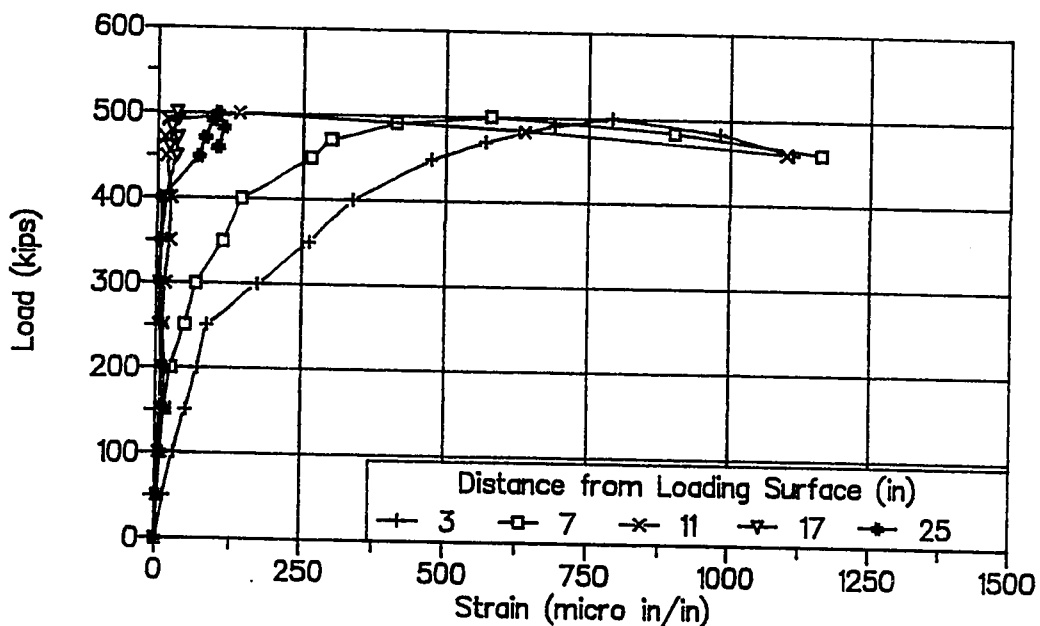


Figure 4.40 Specimen E4 Centerline Reinforcement Strains

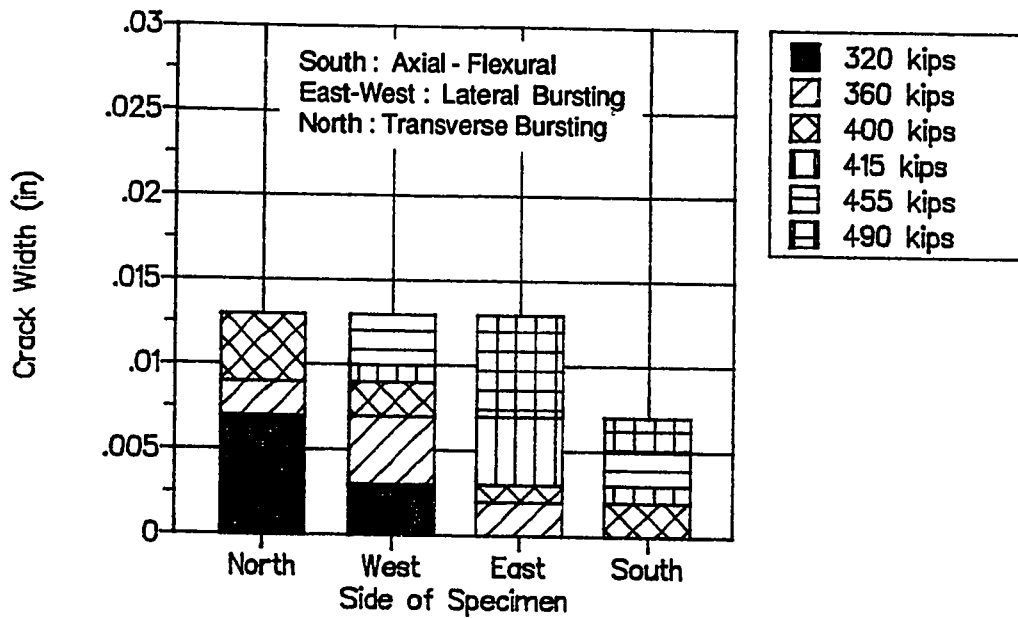


Figure 4.41 Crack Widths, Specimen E4

Specimen E6 had the load axis at an e/h of $1/4$ (see Fig. 4.42). Specimen E6 had a #3 smooth spiral with a yield stress of 73.6 ksi and a modulus of elasticity of 25,400 ksi for local zone reinforcement. The specimen was thinner than Specimens E2, E3, and E4 and had significantly less bursting steel. The total tension capacity of the bursting steel was 36.7 kips at a centroid of 13.9 inches from the loading surface when the bottom two bars far from the loading surface are neglected. The specimen had two #3 bars in the longitudinal edge tension region and four #2m bars in the spalling region. The load-displacement curve is shown in Fig. 4.43. The specimen reached a peak load of 345 kips; the load decreased but the specimen was able to be reloaded to 348 kips. The specimen was reloaded again but was only able to reach 340 kips.

The first bursting crack occurred at 225 kips along the tendon path. The first spalling crack occurred at 300 kips and extended 10 inches in the direction of the tendon path. The first longitudinal edge tension crack occurred at 345 kips. Figure 4.44 shows the crack pattern at the ultimate load stage. The main bursting crack started at the load axis and then moved away from the axis at approximately a ten-degree angle. The crack became parallel with the tendon axis about 18 inches away from the loading plate and 6 inches from the load axis. There was also a diagonal crack that started $3\frac{1}{2}$ inches away from the load axis and propagated onto the transverse face. The maximum bursting crack size was 0.004 inches at 250 kips, 0.009 inches at 300 kips, and 0.037 inches at 345 kips.

Figure 4.45 shows the bursting strain data, while Fig. 4.46 shows the spalling strain data. At the ultimate load the bursting reinforcement within 12 inches of the plate was yielded. Spalling reinforcement did not yield. Gages at 9 inches away from the center of the plate on the spalling reinforcement did reach 50 percent of yield. The failure was characterized by a separation of the concrete

from the main body of the specimen below the anchorage device on the west side.

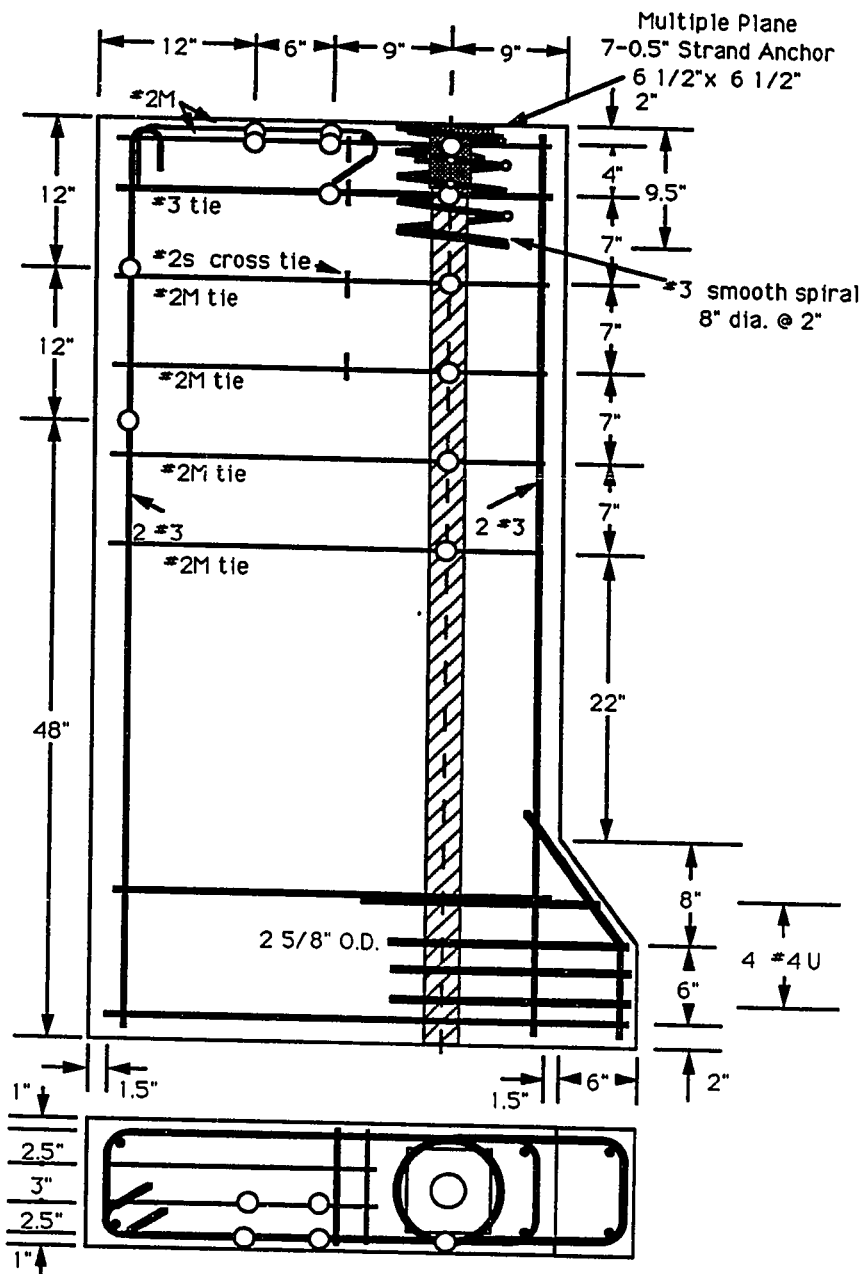


Figure 4.42 Specimen E6 Details

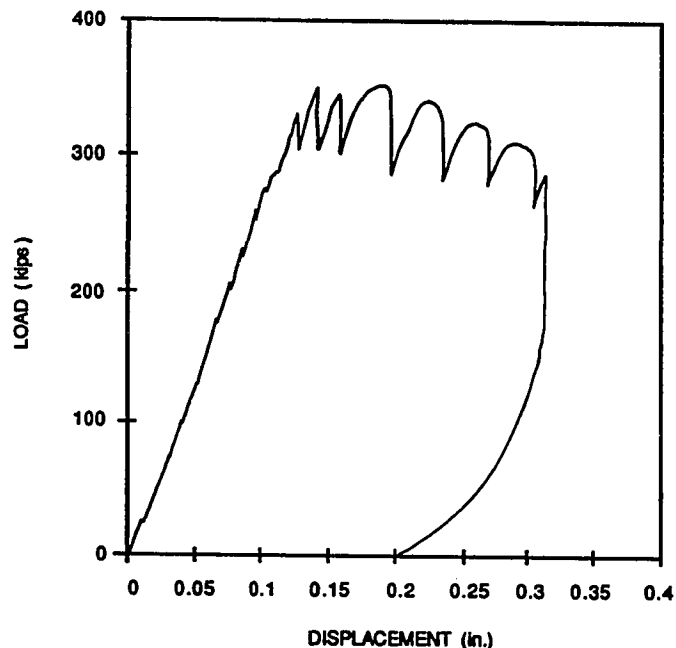


Figure 4.43 Load-Displacement Curve, Specimen E6

Specimen M5 had an e/h of $1/4$ and had two anchorage devices located at the same eccentricity (see Fig. 4.47). The specimen was originally considered to be a multiple anchorage specimen but displayed behavior better described in the eccentric specimen section. The bursting steel consisted of six #2s ties with a total tensile capacity of 39.4 kips and a centroid located 15.25 inches from the loading surface. The spalling and longitudinal edge tension reinforcement were two #2s and two #3 bars. The local zone was designed as two separate anchors, and then they were tied together with additional reinforcement. Each anchor had a #4 smooth spiral with a 7-inch diameter and a 2-inch pitch (see Specimen E1 for material properties). The two spirals were then held together with two #2s U's and six #3 U's, four on each side. The 1,200-kip testing machine was not equipped with a spherical loading head, so hydrostone was poured between the anchor plates and the stiff loading head to ensure even loading.

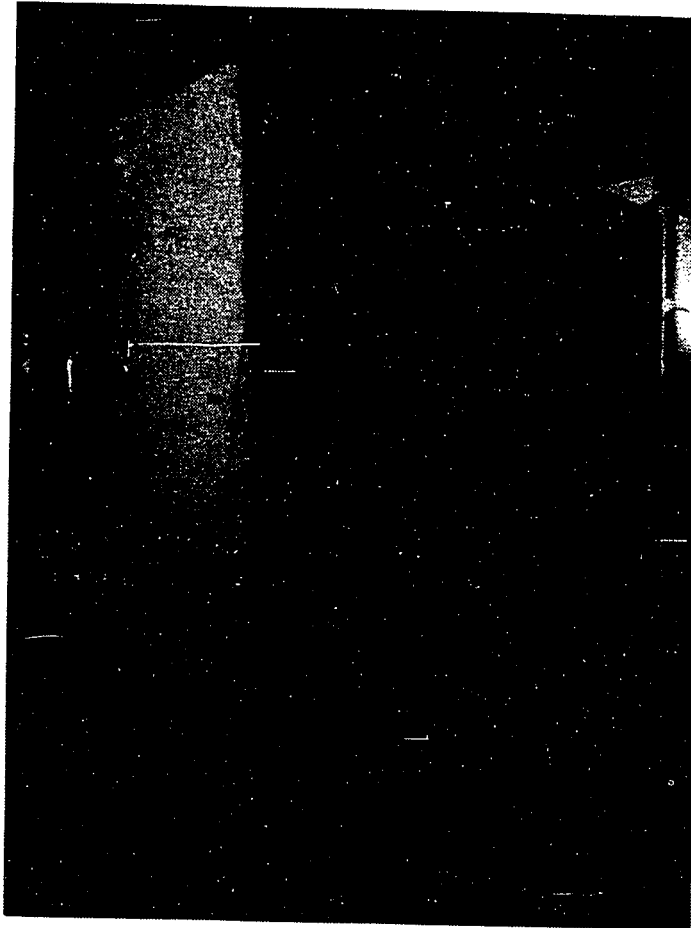


Figure 4.44 Crack Patterns at Ultimate, Specimen E6

The first bursting crack occurred at 400 kips on both sides of the specimen. The cracking pattern spread out from the anchors with the main central crack extending to a depth of 40 inches from the loading plate. At 650 kips, a horizontal crack partially opened across the transverse surface nearest the tendon axis, 6 inches from the loaded surface. At the failure load of 677 kips, the horizontal crack went completely across the transverse surface and the anchorages were

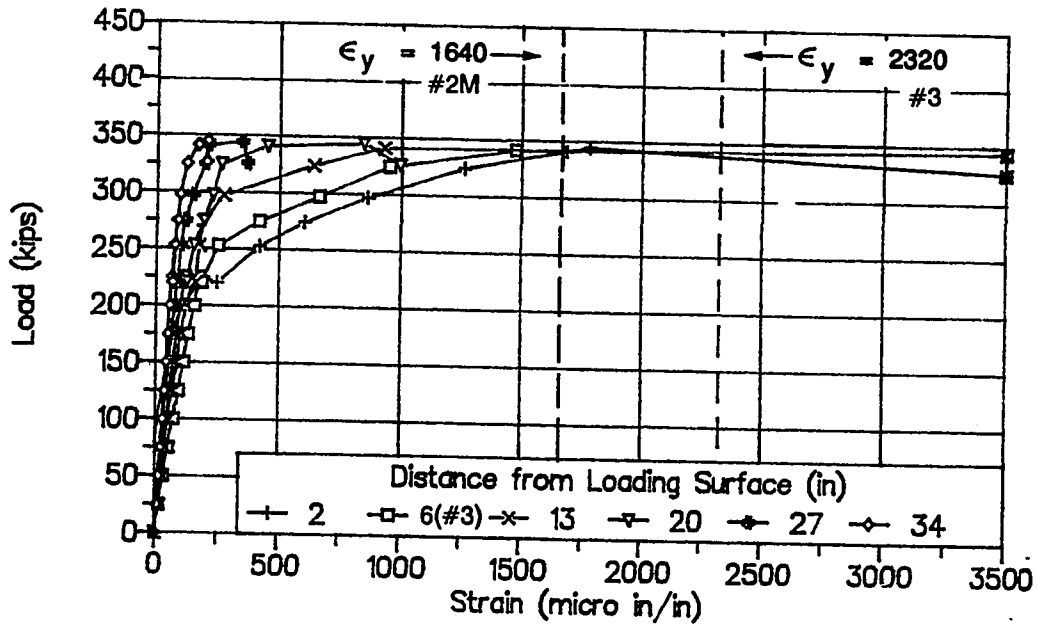


Figure 4.45 Bursting Reinforcement Strain Data, Specimen E6

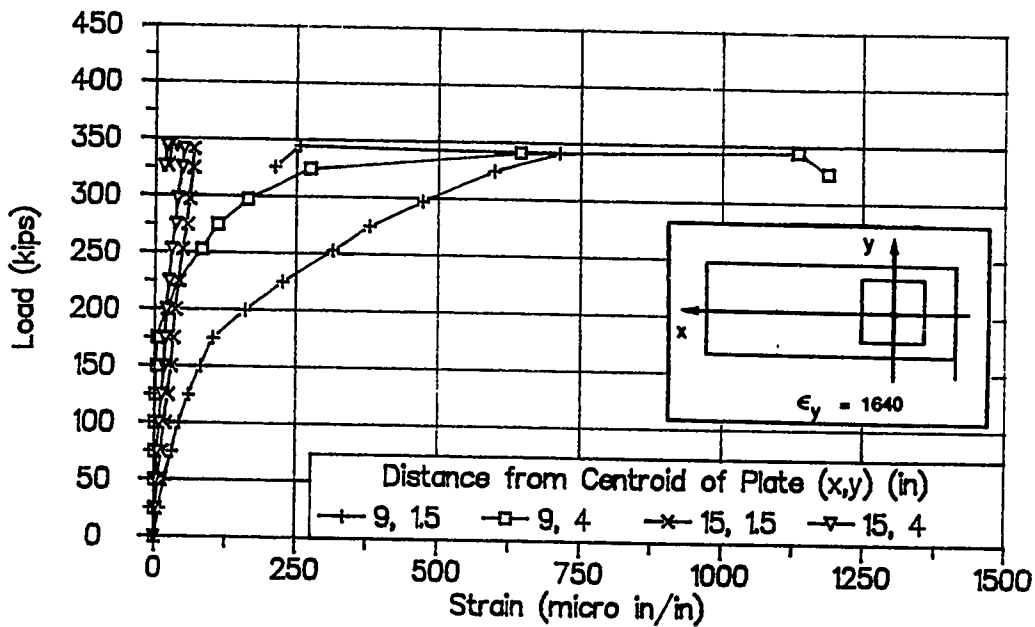


Figure 4.46 Spalling Reinforcement Strain Data, Specimen E6

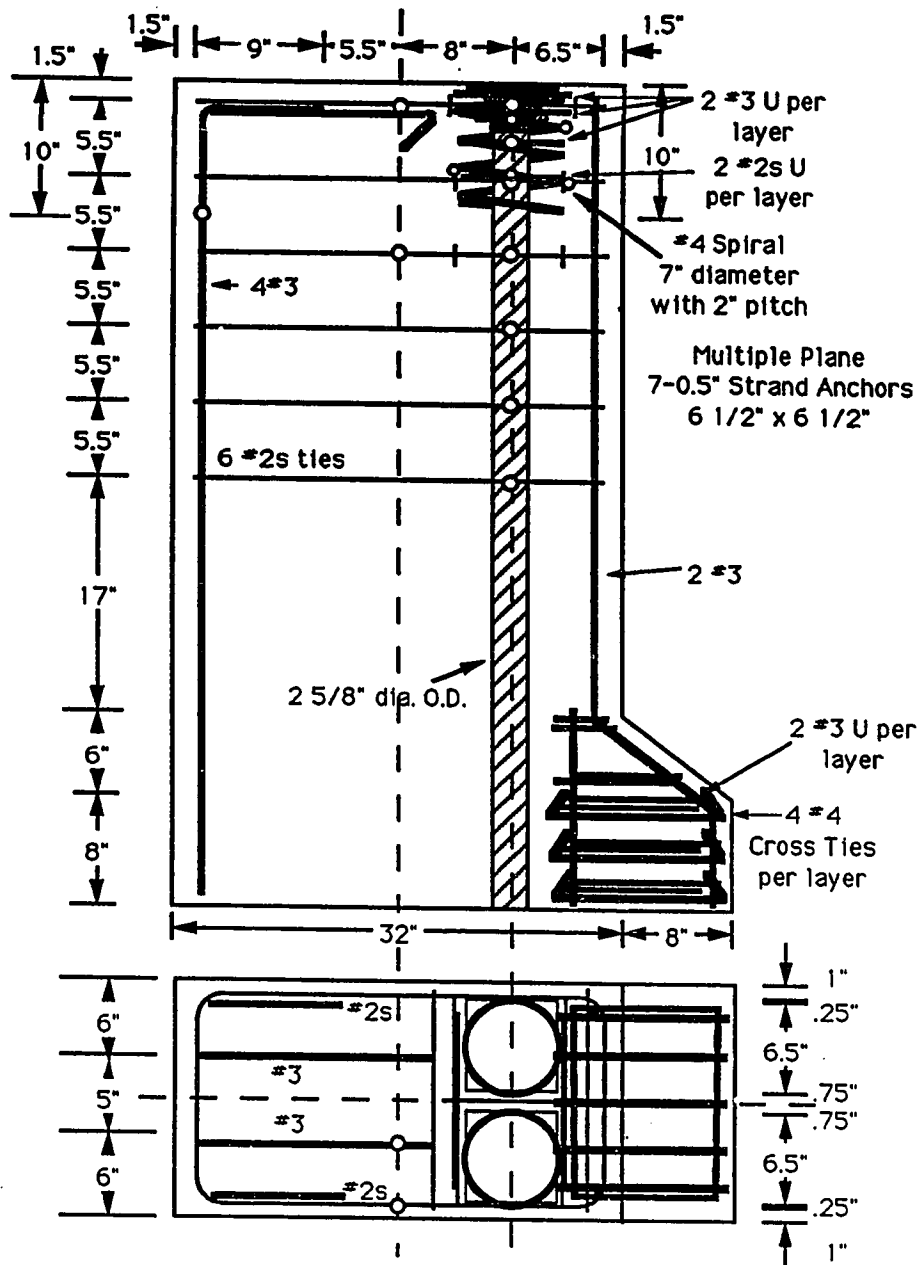


Figure 4.47 Specimen M5 Detail

driven into the specimen by the hydraulic ram pressure. Figure 4.48 shows the load-displacement curve for the specimen. The displacement was determined by subtracting the movable block displacement from the movement of the hydraulic ram piston. At failure, the ram piston is driven into the specimen until the specimen can carry the load applied by the hydraulic rams. The load decreased to 175 kips before stabilizing.

Figure 4.49 shows the crack distribution after ultimate. The push on the anchorages propagated the diagonal crack to a depth of 42 inches from the loading surface. Figure 4.50 shows the bursting strain information for the gages along the load axis. All of the bursting steel yielded. Figure 4.51 shows the spalling strains. The maximum spalling strain converted into a force which was only 0.78 percent of the axial load. No spalling cracks were seen during the test, but the strain indicates that a spalling crack probably occurred near a total

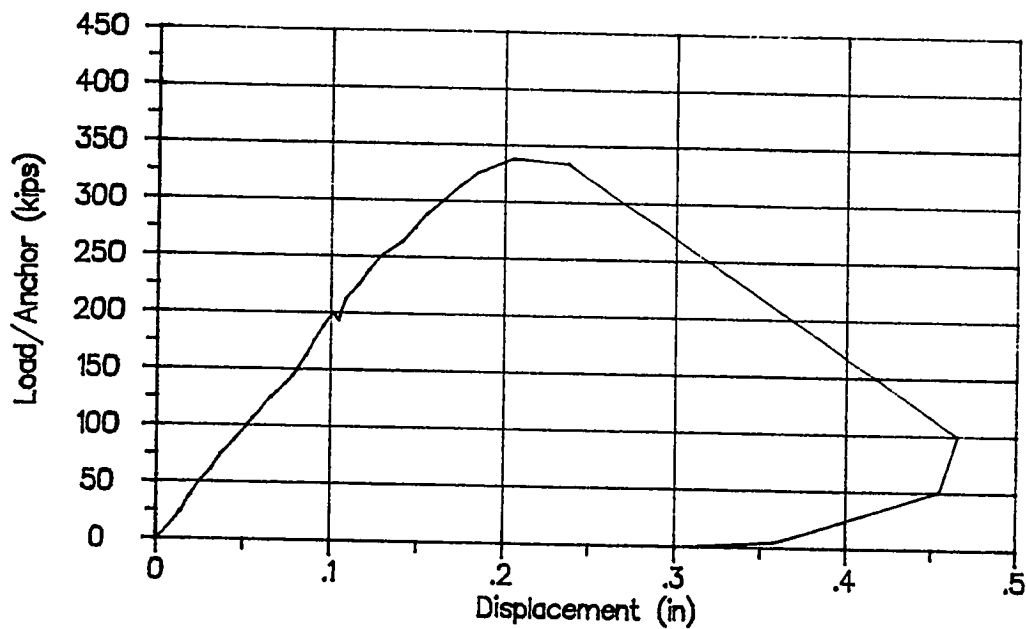


Figure 4.48 Load-Displacement Curve, Specimen M5

load of 500 kips since the reinforcement strains were above 250 microstrain. No longitudinal edge tension cracks were observed. The two anchors acted as one large anchor since they were tied together and were in close proximity to each other. No negative effects due to the two anchor groups were observed. At failure, both anchors were still tied together, effectively acting as one larger anchor.

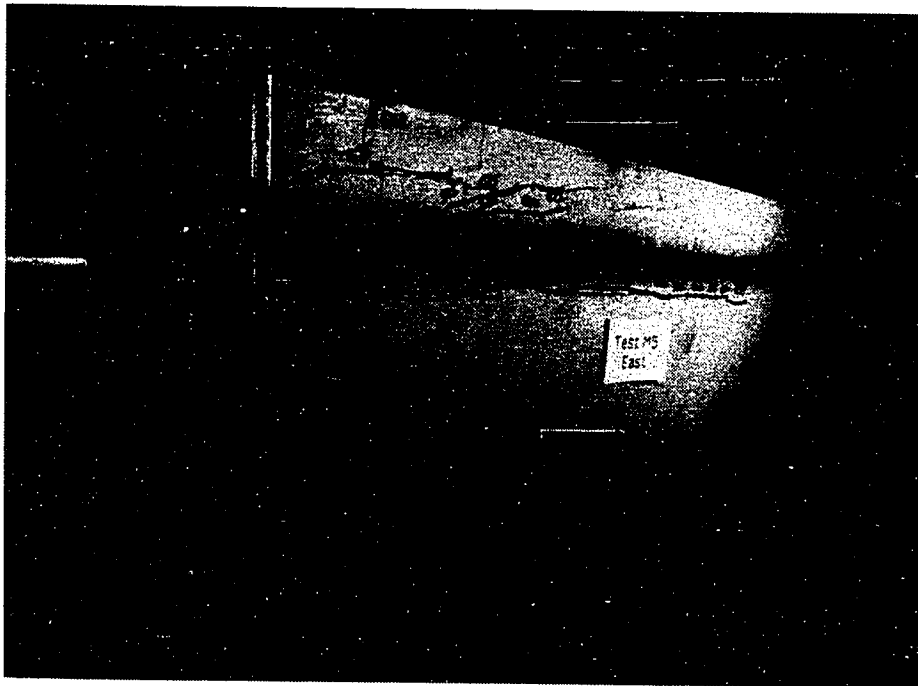


Figure 4.49 Crack Pattern at Ultimate, Specimen M5

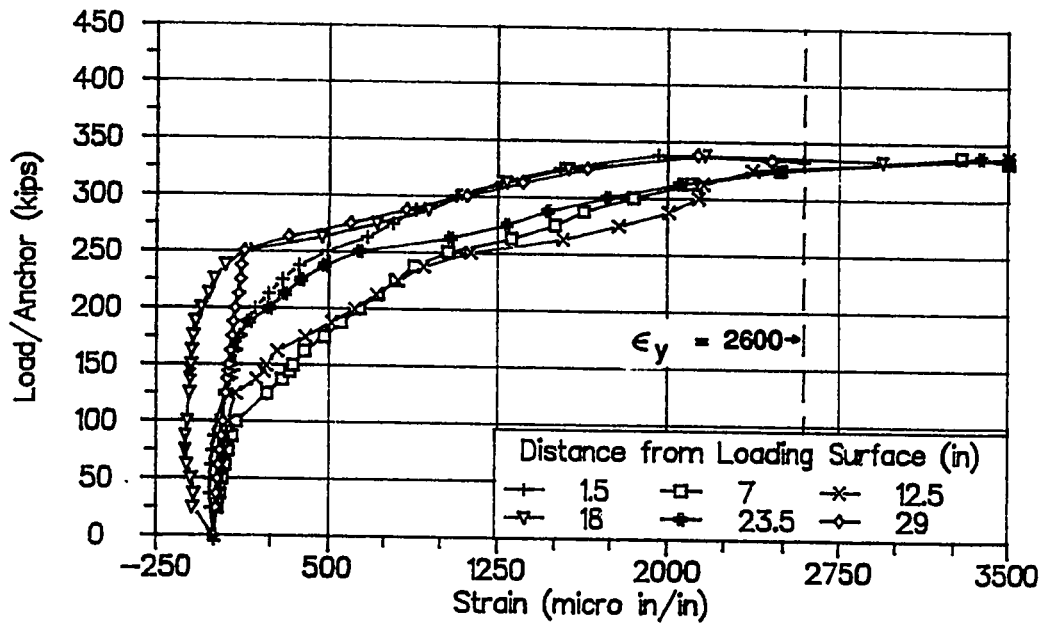


Figure 4.50 Bursting Reinforcement Strains, Specimen M5

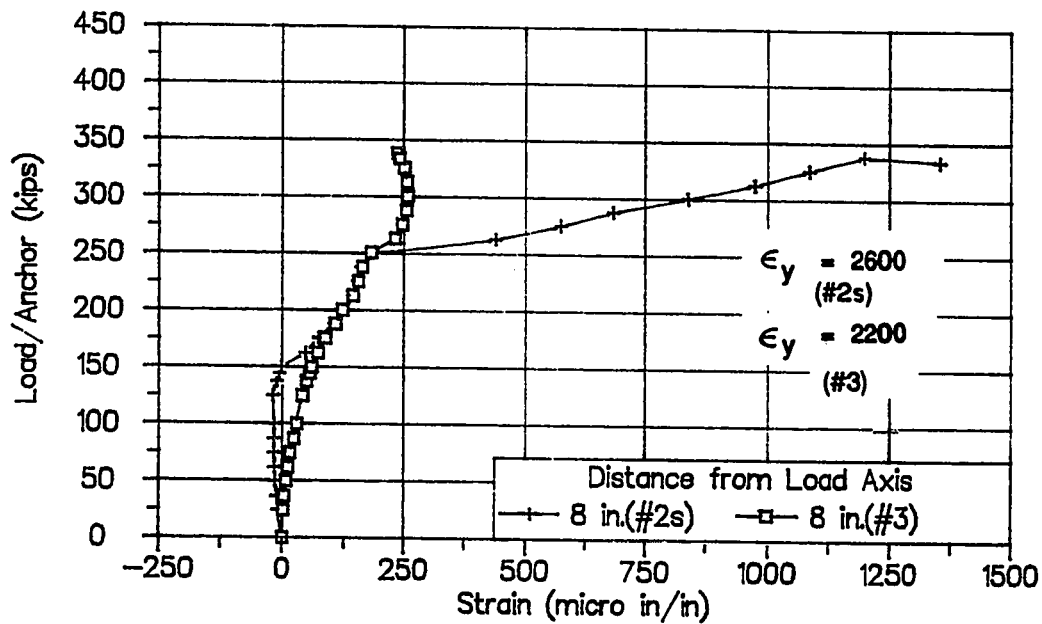


Figure 4.51 Spalling Reinforcement Strains, Specimen M5

4.3 Prediction of the First Cracking Load using Elastic Analysis Models

For serviceability purposes, the prediction of the first cracking load can be important. In the concentric anchorage chapter, cracking load prediction models were discussed in detail (Section 3.3). The models used to predict the cracking load in eccentric anchorage specimens will be extensions of those discussed in Section 3.3. In eccentric anchorage zones, there are three regions (see Fig. 4.1) within the general zone where cracking can occur: bursting (along the tendon axis), spalling (along the loading surface due to compatibility conditions with the anchorage device, eccentric anchor effects and multiple anchor effects), and longitudinal edge tension (along the outermost face of the specimen where tensile stresses may be set up due to the combined flexural and axial load effects). The cracking load in each of these regions was determined by matching the best estimate of the actual concrete tensile strength with the elastically computed maximum tensile stress. The maximum tensile stress for the bursting region can be determined from finite element analysis and elasticity based models (Guyon's curves [70]). For the longitudinal edge tension region, finite element analysis and combined stress theory can be used, while, for the spalling region only, finite elements will give an accurate representation. Table 4.5 is a summary of the observed cracking loads for the eccentric specimen series.

4.3.1 Longitudinal Edge Tension and Spalling Cracking. For anchorage zones at large eccentricities (e/h greater than $1/6$ for rectangular sections), tension stresses are indicated by elastic analysis in the longitudinal edge tension and spalling regions (see Fig. 4.1b). When the eccentricity of the anchorage zone is inside the kern (less than an e/h of $1/6$ for rectangular sections), the behavior of the anchorage zone is close to that of a concentric anchorage zone. When eccentricities are small, cracking in the longitudinal edge tension and spalling region will not occur unless caused by creep, shrinkage, or other beam loads. The finite element analysis of the

spalling region indicates that there are very high stresses near the loaded surface. These high stresses can be seen in Fig. 4.1. These stresses are artificially high in the finite element analysis due to boundary conditions which do not occur in the actual section.

Table 4.5 Cracking Loads for Eccentric Specimens

| Specimen (e/h) | Bursting (kips) | Longitudinal Edge Tension (kips) | Spalling (kips) |
|-----------------------|--------------------|--|--------------------|
| E1 (1/6) | 345 | None | None |
| E5 (1/6) | 215 | None | None |
| E2 (1/3) | 265 | 250 | 360 |
| E3 (1/3) | 250 | Crack Formers | Crack Formers |
| E4 (1/3) | 250 | 225 | 225 |
| E6 (1/4) | 225 | 345 | 300 |
| M5 (1/4) | 400 | None | None |

The maximum tensile stress on the outermost fiber away from the load axis may be calculated by either a combined stress analysis or a finite element analysis to determine the longitudinal edge tension cracking load. The first longitudinal edge tension cracking load is determined to be the one which causes a tensile stress on the outer fiber equal to the split cylinder strength (since there are no appreciable compressive stresses in the orthogonal direction, this is the best estimate of the actual tensile strength). Table 4.6 shows the results of this analysis. The longitudinal edge tension stress is non dimensionalized with respect to the average axial stress at the base of the specimen ($\sigma_o = P/th$). The analysis was conservative in

all applicable cases. For Specimens E1 and E5, the elastic analysis indicated zero stress and no cracks were observed. In Specimen E3, crack formers were placed in the concrete, so a crack comparison is not applicable. In Specimen M5, no cracks formed in the longitudinal edge tension region before the ultimate load. When split cylinder data is not available, $6\sqrt{F'_c}$ may be used as a rough estimate for the tensile strength of concrete. When using $6\sqrt{F'_c}$ for the tensile strength conservative results are also achieved for the three specimens with longitudinal edge tension cracks.

Table 4.6 Longitudinal Edge Tension Cracking Load Prediction

| Specimen | Split Cylinder (psi) | Longitudinal Edge Tension Stress/ σ_o | Predicted Cracking Load (kips) | Test Cracking Load (kips) | Test/Predicted |
|-------------------|----------------------|--|--------------------------------|---------------------------|----------------|
| E1 | 428 | 0 | Infinite | No Crack | No Crack |
| E5 | 459 | 0 | Infinite | No Crack | No Crack |
| E2 | 460 | 1.00 | 182 | 250 | 1.37 |
| E3 | 492 | 1.00 | 195 | N/A | N/A |
| E4 | 475 | 1.00 | 188 | 225 | 1.20 |
| E6 | 443 | 0.50 | 319 | 345 | 1.08 |
| M5 | 393 | 0.50 | 428 | No Crack | No Crack |
| $\sigma_o = P/ht$ | | | Average | | 1.22 |
| | | | Standard Deviation | | 0.12 |
| | | | Coef. of Variance | | 0.10 |

The tensile spalling stresses near the loading surface are difficult to determine because of the high stress gradient and the high computed stresses near the edge. The forces and stresses in the region are caused both by compatibility requirements between the anchorage device and the concrete and by equilibrium conditions involving with the longitudinal edge tension and bursting forces. Specimens E2 and E4 should have the same spalling cracking loads since the specimens are essentially the same. Their observed bursting and longitudinal edge

tension cracking loads are very similar, but they have very different observed spalling cracking loads. The prediction of spalling cracking load and spalling stresses requires a more complex analysis than combined stress theory. Table 4.7 shows the peak spalling stress and corresponding cracking loads as determined by a two-dimensional finite element analysis conducted by Burdet [25] except for Specimen M5 in which a three-dimensional analysis was used. Two peak values are given. The first value listed for each specimen is the normalized maximum tensile stress on the loaded surface, while the second value is the normalized maximum tensile stress at a depth of 1 1/2 inches below the loaded surface. Using the stress on the loaded surface is very conservative, while utilizing the stresses slightly below the surface yields a good average value but some unconservative values. Unfortunately, the standard deviation is quite high for both cases and this calculation must be termed as relatively unsatisfactory. Fortunately, it is of little importance in actual design.

Table 4.7 Spalling Crack Load Prediction

| Specimen | Split Cylinder (psi) | Spalling Stress/ σ_o | Predicted Cracking (kips) | Test Cracking Load(kips) | Test/Predicted |
|----------|----------------------|-----------------------------|---------------------------|--------------------------|----------------|
| E1 | 428 | 0.616 | 275 | No Crack | |
| E5 | 459 | 0.163 0.736 0.204 | 1037 191 689 | No Crack | |
| E2 | 460 | 1.626 0.779 | 112 234 | 360 | 3.21 1.54 |
| E3 | 492 | 1.626 0.779 | 120 250 | N/A | N/A N/A |
| E4 | 475 | 1.626 0.779 | 116 242 | 225 | 1.95 0.93 |
| E6 | 443 | 0.736 0.338 | 217 472 | 300 | 1.38 0.64 |
| M5 | 393 | 1.748 0.741 | 122 288 | No Crack | |
| | | On Surface - | | Average | 2.18 |
| | | | | Standard Deviation | 0.77 |
| | | | | Coef. of Variance | 0.35 |
| | | 1 1/2" Below Surface - | | Average | 1.04 |
| | | | | Standard Deviation | 0.38 |
| | | | | Coef. of Variance | 0.36 |

$$\sigma_o = P/ht$$

4.3.2 Bursting Crack Prediction. The methods used to determine the first bursting crack load along the tendon axis for eccentric specimens are the same as those for the concentric specimens. The peak tension stress value must be determined from an elastic analysis for the bursting zone ahead of the plate. The load that causes this peak tension stress to reach the effective tension capacity of the concrete is the first cracking load. The parameters that must be considered are the section geometry, anchorage size and location, and concrete tensile strength. The concrete tensile strength can be determined by a split cylinder test and then, if desired, modified to consider the lateral compression stress effects from the high compression loads and to consider the transverse bursting stresses at the location of the peak lateral load (see Section 3.3). The elastic computed stresses used in this section were determined from the two-dimensional finite element results provided by Burdet [25]. The stress results from the two-dimensional analysis must be divided by the section thickness to convert the two-dimensional results into three-dimensional results. The section thickness can be modified to take into account the effect of a post-tensioning duct. Burdet compared three-dimensional analysis results by assuming a hole in the center of the section with the basic two-dimensional analysis results (see Fig. 3.82). Good correlation was found with the three-dimensional analysis when the two-dimensional analysis results were divided by an effective thickness equal to the section thickness minus the duct diameter. In Chapter 3, four effective section thicknesses were examined: the full section thickness, the section thickness minus the outside diameter of the duct, a transformed section thickness, and the section thickness minus inside diameter of the duct. The transformed section thickness analysis provided the best results. For eccentric anchor specimens, four first cracking models were examined which systematically alter two parameters: the effective tensile strength (f_t) and the effective section thickness (t_e).

- 1) f_t = unmodified split cylinder strength
 t_o = full section thickness
- 2) f_t = unmodified split cylinder strength
 t_o = section thickness - duct outside diameter
- 3) f_t = split cylinder strength modified for triaxial effects
 t_o = section thickness - duct outside diameter
- 4) f_t = split cylinder strength modified for triaxial effects
 t_o = transformed thickness

Table 4.8 is a summary of the results from the first two models. The peak stress value used in the calculation of the first cracking load is non-dimensionalized by the average axial stress at the base of the specimen ($\sigma_o = P/th$). When the peak bursting stress from the two-dimensional analysis is divided by the full section thickness and matched to the split cylinder strength, quite unconservative results (average = 0.73) are determined. In the second model the peak stress from the two-dimensional analysis is divided by an effective thickness equal to the section thickness minus outside diameter of the duct (see Table 4.9). This stress is then matched to the split cylinder test data. The average of the test-to-predicted ratios is very good (average = 1.01) for the eccentric test series, and the coefficient of variance is 12 percent (see Table 4.8).

Table 4.8 Bursting Crack Load Prediction with Split Cylinder Strength and Full Duct Reduction

| Specimen | Split Cylinder (psi) | First Cracking Load (kips) | Thickness (in) | Full Section Thickness | | | Removing Full Duct Width | | | |
|-------------------|-------------------------|-------------------------------|-------------------|----------------------------|-------------------------------|----------------|--------------------------|----------------------------|-------------------------------|----------------|
| | | | | Peak Stress $/\sigma_o$ | Predicted Cracking Load(kips) | Test/Predicted | Effective Thickness (in) | Peak Stress $/\sigma_o$ | Predicted Cracking Load(kips) | Test/Predicted |
| E1 | 428 | 345 | 11 | 0.366 | 463 | 0.74 | 8.13 | 0.495 | 342 | 1.01 |
| E5 | 459 | 215 | 8.5 | 0.399 | 352 | 0.61 | 5.88 | 0.577 | 243 | 0.88 |
| E2 | 460 | 265 | 11 | 0.502 | 363 | 0.73 | 8.13 | 0.679 | 268 | 0.99 |
| E3 | 492 | 300 | 11 | 0.502 | 388 | 0.77 | 8.13 | 0.679 | 287 | 1.05 |
| E4 | 475 | 250 | 11 | 0.502 | 375 | 0.67 | 8.13 | 0.679 | 277 | 0.90 |
| E6 | 443 | 225 | 10 | 0.493 | 324 | 0.70 | 7.38 | 0.668 | 239 | 0.94 |
| M5 | 393 | 400 | 17 | 0.474 | 451 | 0.89 | 11.75 | 0.685 | 312 | 1.28 |
| $\sigma_o = P/ht$ | | | | Average | | 0.73 | | | | 1.01 |
| | | | | Standard Deviation | | 0.08 | | | | 0.12 |
| | | | | Coef. of Variance | | 0.11 | | | | 0.12 |

Table 4.9 Post-Tensioning Duct Dimensions

| Specimen | Outer Diameter (in) | Inside Diameter (in) | Thickness (in) |
|----------------|---------------------|----------------------|----------------|
| E1, E2, E3, E4 | 2 7/8 | 2 5/8 | 1/32 |
| E5, E6, M5 | 2 5/8 | 2 3/8 | 1/32 |

The third model incorporates the reductions in the tensile strength in the specimen due to the triaxial state of stress. The state of compressive stress in the split cylinder is low in comparison to that in the anchorage zone specimen. The compressive stresses in the anchorage zone at the peak lateral stress location can be three times higher than those in the split cylinder. In addition, there are also transverse bursting stresses that further reduce the effective tensile strength of the concrete. The reduction in the tensile strength is determined from a model developed by Ottosen [125] and is discussed in detail in Section 3.3. The model incorporates the loss in the effective section thickness by subtracting the full duct diameter from the thickness. The model has a mean of 1.09, and, therefore, is nine percent conservative (see Table 4.10) with two very slightly unconservative test predictions.

The first bursting crack prediction shown in Table 4.11 includes the reduction in tensile strength due to the consideration of the triaxial stress state and the effective thickness of the section based on a transformed section (described in Fig. 3.83). The transformed thickness is equal to the section thickness minus the inside diameter of the duct plus two times the duct thickness times E_s/E_c . The average of the test-to-predicted ratios is 1.02 with a coefficient of variation of 13 percent. The model represents the behavior of the eccentric anchorage zone specimen somewhat more accurately than the previous model did but is not conservative for five of the seven specimens.

Table 4.10 Bursting Crack Load Prediction with Effective Tensile Strength and Full Duct Reduction

| Specimen | Peak Stress/ σ_o | Transverse Stress (psi) | Compression Stress (psi) | Reduced Tensile Strength (psi) | Change in Tensile Strength (psi) | Predicted Cracking Load (kips) | First Cracking Load (kips) | Test/ Predicted |
|----------|----------------------------|----------------------------|-----------------------------|-----------------------------------|-------------------------------------|-----------------------------------|-------------------------------|--------------------|
| E1 | 0.495 | 32 | 1062 | 417 | -11 | 333 | 345 | 1.03 |
| E5 | 0.577 | 0 | 1812 | 418 | -41 | 222 | 215 | 0.97 |
| E2 | 0.679 | 224 | 1486 | 430 | -30 | 251 | 265 | 1.06 |
| E3 | 0.679 | 238 | 1580 | 457 | -35 | 266 | 300 | 1.13 |
| E4 | 0.679 | 228 | 1514 | 438 | -37 | 255 | 250 | 0.98 |
| E6 | 0.668 | 119 | 1843 | 397 | -46 | 214 | 225 | 1.05 |
| M5 | 0.685 | 88 | 1565 | 349 | -44 | 277 | 400 | 1.44 |
| | | | | | | | Average | 1.09 |
| | | | | | | | Standard Deviation | 0.15 |
| | | | | | | | Coef. of Variance | 0.14 |

$$\sigma_o = P/ht$$

Table 4.11 Bursting Crack Load Prediction with Effective Concrete Tensile Strength and Transformed Section

| Specimen | Effective Thickness (in) | Peak Stress/ σ_o | Transverse Stress (psi) | Compression Stress (psi) | Reduced Tensile Strength (psi) | Change in Tensile Strength (psi) | Predicted Cracking Load (kips) | First Cracking Load (kips) | Test/ Predicted |
|----------|-----------------------------|----------------------------|----------------------------|-----------------------------|-----------------------------------|-------------------------------------|-----------------------------------|-------------------------------|--------------------|
| E1 | 8.81 | 0.457 | 32 | 1143 | 414 | -14 | 359 | 345 | 0.96 |
| E5 | 6.56 | 0.517 | 0 | 1981 | 409 | -50 | 242 | 215 | 0.89 |
| E2 | 8.81 | 0.627 | 239 | 1588 | 424 | -36 | 268 | 265 | 0.99 |
| E3 | 8.81 | 0.627 | 254 | 1686 | 450 | -42 | 284 | 300 | 1.05 |
| E4 | 8.81 | 0.627 | 243 | 1614 | 431 | -44 | 272 | 250 | 0.92 |
| E6 | 8.06 | 0.612 | 127 | 1972 | 389 | -54 | 229 | 225 | 0.98 |
| M5 | 13.22 | 0.609 | 96 | 1712 | 339 | -54 | 303 | 400 | 1.32 |
| | | | | | | | Average | 1.02 | |
| | | | | | | | Standard Deviation | 0.13 | |
| | | | | | | | Coef. of Variance | 0.13 | |

$$\sigma_o = P/ht$$

Because of this lack of conservatism, it is not any better than just using the full split cylinder and the full thickness reduction due to the post-tensioning duct.

The concentric series established the need for including the triaxial effects on the tensile strength of concrete. Many of the concentric specimens did not have post-tensioning ducts. When the computed peak stress was matched to the split cylinder results, the cracking load was 25 percent unconservative. When the tensile strength was reduced due to the triaxial effects, the predictions were all within ten percent of the test values. Therefore, the accuracy of the second model (with split cylinder strength and full duct width reduction) could not be relied upon to be consistent. Using the triaxial effects with a reduction in the cross section is more consistent with the behavior.

The triaxial analysis is time-consuming and is not always conservative. Table 4.12 shows the results for a conservative simplified model which assumes the effective tensile strength to be equal to $4.2\sqrt{F'_c}$ and reduces the concrete section width by the inside diameter of the duct. The model does yield conservative results (average = 1.39) but can be very conservative (Note Specimen M5). For the concentric series, $4.2\sqrt{F'_c}$ was determined to be an accurate tensile concrete capacity. The concentric series had losses due to the triaxial effect of around 20 percent with some tests being as high as 30 percent ($0.7 \cdot 6\sqrt{F'_c} = 4.2\sqrt{F'_c}$). The loss in concrete tensile capacity due to a consideration of the triaxial effects in the eccentric specimens was around 10 percent with some as high as 15 percent. Therefore, for these eccentric tests the reduction in the approximate concrete tensile strength would not be as high, approximately $0.8 \cdot 6\sqrt{F'_c}$ ($4.8\sqrt{F'_c}$). This would reduce the conservatism.

Guyon developed a symmetrical prism concept (see Fig. 4.52) for adapting the concentric anchorage zone bursting stress curves to be applicable to eccentric anchorage zones (see Fig. 3.77). Instead of

Table 4.12 Bursting Crack Prediction Load with Conservative Concrete Tensile Strength

| Specimen | Effective Thickness (in) | f'c (psi) | 4.2√f'c (psi) | Peak Stress /σ _o | Predicted Cracking Load(kips) | Cracking Load (kips) | Test/ Predicted |
|-------------------|--------------------------|-----------|---------------|-----------------------------|-------------------------------|----------------------|-----------------|
| E1 | 8.38 | 5450 | 310 | 0.480 | 256 | 345 | 1.35 |
| E5 | 6.13 | 5710 | 317 | 0.554 | 175 | 215 | 1.23 |
| E2 | 8.38 | 5950 | 324 | 0.659 | 195 | 265 | 1.36 |
| E3 | 8.38 | 6130 | 329 | 0.659 | 198 | 300 | 1.52 |
| E4 | 8.38 | 5690 | 317 | 0.659 | 190 | 250 | 1.31 |
| E6 | 7.63 | 5650 | 316 | 0.646 | 176 | 225 | 1.28 |
| M5 | 12.25 | 4670 | 287 | 0.657 | 238 | 400 | 1.68 |
| $\sigma_o = P/ht$ | | | | | | Average | 1.39 |
| | | | | | | Standard Deviation | 0.15 |
| | | | | | | Coef. of Variance | 0.11 |

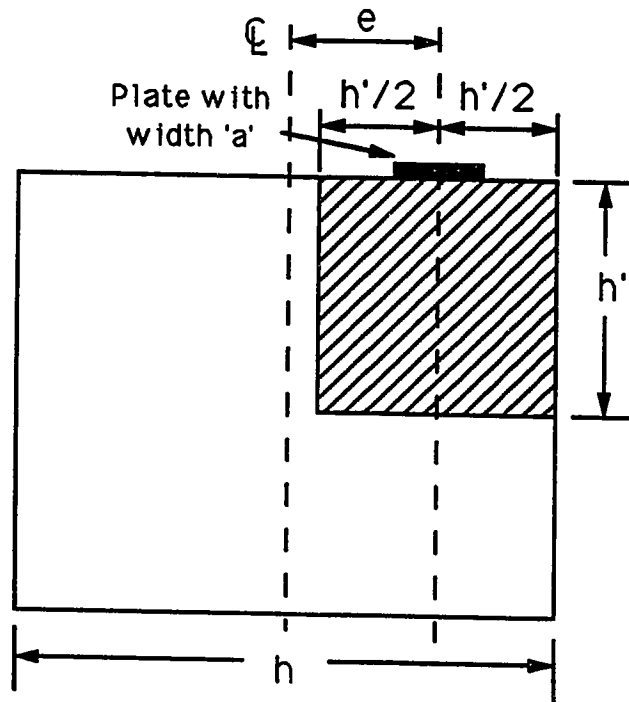


Figure 4.52 Guyon's Symmetrical Prism

a stress distribution depending on a/h , the ratio of a/h' is used. Table 4.13 compares the two-dimensional finite element analysis stress results with the peak stress results of the symmetrical prism. Guyon's symmetrical prism predicted stresses were found to be conservative values for the finite element stresses for the several cases investigated. The stresses shown are based on a 100-kip load. If a quick conservative result is needed, one could determine the peak stress using Guyon's symmetrical prism, use a reduced section thickness utilizing the inside diameter of the duct, and match the peak stress to an assumed effective tensile strength of the concrete allowing for triaxial effects ($4.2\sqrt{f'_c}$) (see Table 4.13).

Table 4.13 Guyon's Symmetrical Prism First Bursting Crack Prediction

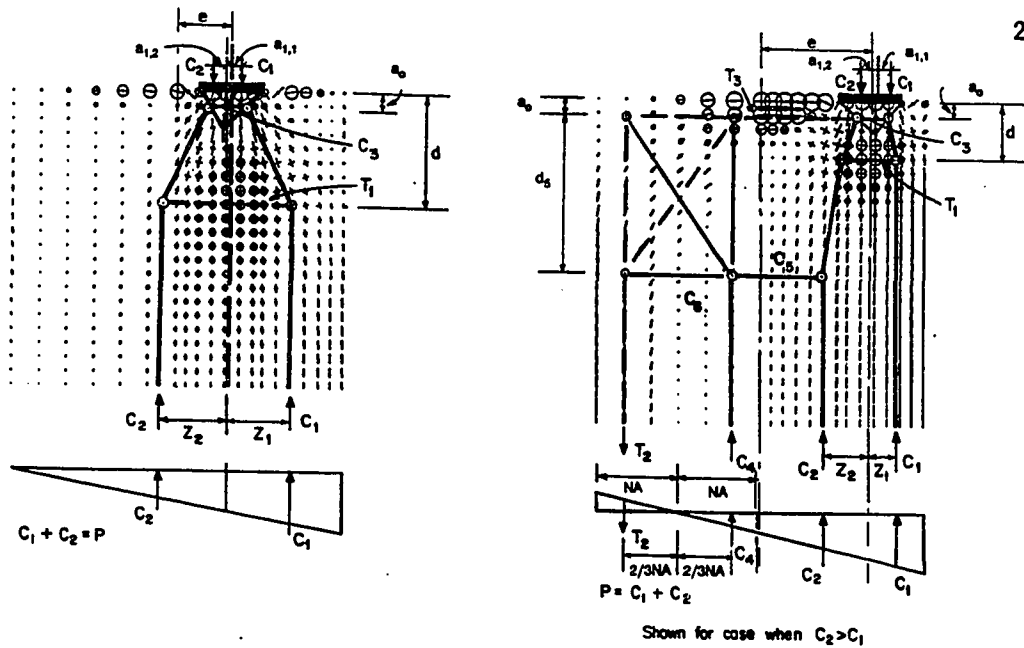
| Specimen | FEM Peak Stress (ksi) | Guyon's Peak Stress (ksi) | Guyon / FEM | $4.2\sqrt{f'_c}$ (ksi) | Predicted Cracking Load(kips) | Cracking Load (kips) | Test/ Predicted |
|--------------------|-----------------------|---------------------------|-------------|------------------------|-------------------------------|----------------------|-----------------|
| E1 | 0.092 | 0.118 | 1.28 | 0.310 | 256 | 345 | 1.35 |
| E5 | 0.130 | 0.163 | 1.25 | 0.317 | 176 | 215 | 1.22 |
| E2 | 0.127 | 0.139 | 1.10 | 0.324 | 195 | 265 | 1.36 |
| E3 | 0.127 | 0.139 | 1.10 | 0.329 | 198 | 300 | 1.52 |
| E4 | 0.127 | 0.139 | 1.10 | 0.317 | 190 | 250 | 1.31 |
| E6 | 0.137 | 0.157 | 1.15 | 0.316 | 160 | 225 | 1.41 |
| M5 | 0.087 | 0.097 | 1.11 | 0.287 | 238 | 400 | 1.68 |
| Average | | | 1.15 | | | | 1.41 |
| Standard Deviation | | | 0.07 | | | | 0.14 |
| Coef. of Variance | | | 0.06 | | | | 0.10 |

* Stresses are for 100 kip Load

4.4 Strut-and-Tie Model Prediction of the Ultimate Load

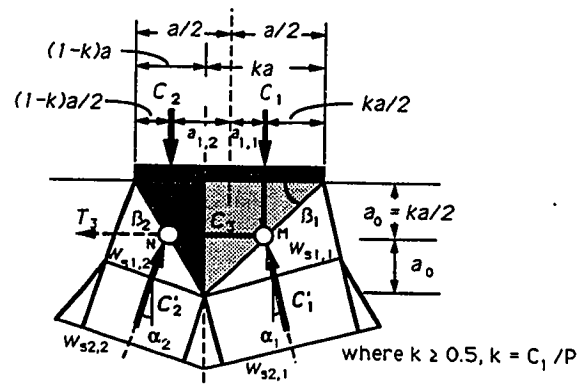
The power of the strut-and-tie model (STM) in design is its adaptability to many different geometries and loading configurations. The following subsections expand the STM development presented in the previous chapter for the concentric anchorage zones in order to predict the ultimate loads of the eccentric anchorage zone specimens. The first subsection describes the changes required in the STM from the concentric to the eccentric anchorage zone application. In the second subsection, the basic STM is used to predict the ultimate load which includes the checking of the tension ties, nodes and compression struts; while, in the third subsection, the modified STM is used. The fourth subsection examines current methods for ultimate load prediction.

4.4.1 Components of the Strut-and-Tie Model. Figure 4.53 shows the elastic stress distribution and possible STM's for the anchorages located inside the kern (see Fig. 4.53a) and outside the kern (see Fig. 4.53b). For anchorage forces within the kern (see Fig. 4.53a), the division of the load between the base compression struts (C_1 and C_2) is determined from the location of the tendon axis. Equilibrium determines the location and magnitude of C_1 and can be based on the elastic or $P/A \pm Pec/I$ stress distribution from the tendon path to the nearest outside edge. The magnitude of C_1 and C_2 are found by integrating the stress distribution. Compression strut C_2 is equal to the total axial load minus C_1 . At the loaded surface, the axial force is also divided into forces equal to C_1 and C_2 . The location of the struts on the anchorage device is determined by assuming a uniform stress distribution across the portion of the anchorage device which is loaded. As the forces, C_1 and C_2 , spread away from the anchorage device, the bursting force (T_1) is needed to satisfy equilibrium. The paths of C_1 and C_2 are determined from the location of the centroid of the bursting tie reinforcement at an assumed depth "d".



a) Inside the Kern ($e/h = 1/6$) b) Outside the Kern ($e/h = 1/3$)
 Figure 4.53 Strut-and-Tie Models for Eccentric Anchors $e/h = 1/6$

The local zone node shape is necessary when calculating the bursting tension capacity and the compressive capacity. The local zone node shape is also used to estimate the line of application of the spalling tension force T_3 (see Fig. 4.53b) which will be discussed in the following pages. The eccentric anchorage local zone node geometry varies from that of the node used for the concentric anchorage zone. The node for eccentric anchorages is unsymmetric because the values of compression struts C'_1 and C'_2 typically are not equal nor are C_1 and C_2 (see Fig. 4.54). Figure 4.54 shows the basic node for unequal compression struts. The lateral location of the peak of the node can be determined from the ratio of C'_1 to C'_2 or from the ratio of C_1 to C_2 . It is easier to use C_1 and C_2 since they are determined directly from the assumed stress distribution at the end of the general zone (see Fig. 4.53). Therefore, unless C_1 and C_2 are equal the peak of the node will not be located along the centerline of the loading plate.



$$\begin{aligned}
 C_1 &= kP & C_2 &= (1-k)P \\
 a_{1,1} &= a/2 - ka/2 & a_{1,2} &= a/2 - (1-k)a/2 \\
 \beta_1 &= 45^\circ & \beta_2 &= \text{atan}[k/(1-k)] \\
 \tan(\alpha_1) &= (C_3 + T_3)/[(1-k)P] & \tan(\alpha_2) &= C_3/(kP) \\
 w_{s1,1} &= ka/\cos(45) \cdot \cos(\beta_1 - \alpha_1) & w_{s1,2} &= (1-k)a/\cos(\beta) \cdot \cos(\beta_2 - \alpha_2) \\
 w_{s2,1} &= w_{s1,1} + 2 \cdot (l_c - 2a_0) \cdot \sin(\alpha_1) & w_{s2,2} &= w_{s1,2} + 2 \cdot (l_c - 2a_0) \cdot \sin(\alpha_2)
 \end{aligned}$$

Figure 4.54 Eccentric Local Zone Node

The assumed depth of the node, $2a_0$, is equal to the width of the portion of the plate carrying the larger of C_1 or C_2 . This assumes a 45-degree angle from the corner of the plate to the peak of the node on the side of the plate carrying the larger strut. The opposite side of the node is defined by the line which connects the node peak with the opposite corner of the plate. When C_1 or C_2 are zero, the node is assumed to be as depicted in Fig. 4.55a. This is unlikely but is the extreme of an anchorage located very close to a exterior boundary in the plane being considered. If two anchorage plates are very close to each other (see Fig. 4.55b), the magnitude of the force in the struts closest to the other anchorage plate must be very close to zero or zero. Therefore, the shape of the node looks identical to the one determined if the two anchorage plates were treated as one large plate

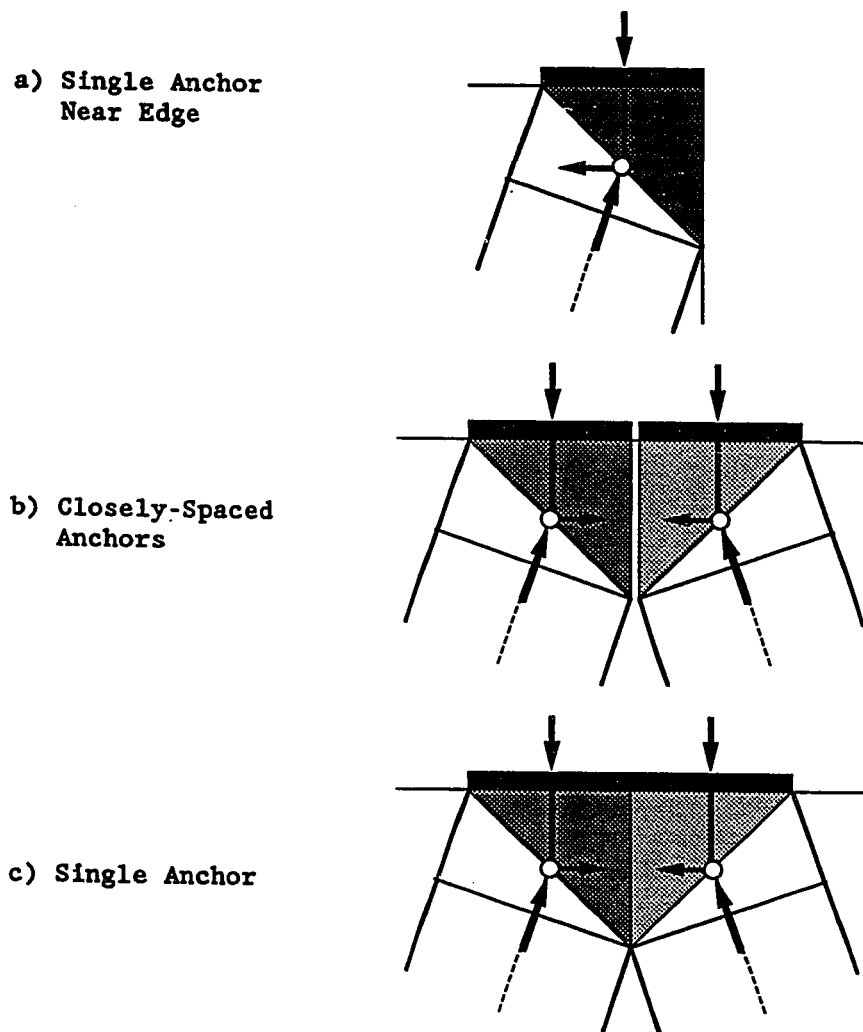


Figure 4.55 Verification of the Eccentric Node for Closely Spaced Anchors

(see Fig. 4.55c). The secondary nodes (pts. "M" and "N", Fig. 4.54) that are used as work points to determine the points of the application for the compression struts and tension ties are located at the

midheight of the node and at the centroid of each division of the anchorage plate.

In the eccentric local zone node, the peak of the node is not necessarily along the load axis (tendon axis). To be consistent, the location of the peak of the node should correspond with the division line of C_1 and C_2 . To match the location of the node peak with the division line, an iterative process is required that involves assuming a new division line for the forces C_1 and C_2 and then determining the location of the peak of the node. This process continues until the location of the peak of the node and the general zone division line between C_1 and C_2 are the same. In most eccentric anchorage cases, this process is unnecessary because the values of C_1 and C_2 are quite similar and therefore, the difference between the location of the peak of the node and the division line is small. If the difference between C_1 and C_2 is more than ten percent the iterative process may be necessary. This method will be shown in more detail in the Chapter 5.

For anchorage forces outside the kern (see Fig. 4.53b), tension forces occur on the far outer longitudinal edge fibers that are modelled in the STM with a tension tie (T_2). Compression strut C_1 is found by the integration of the stress distribution at the end of the anchorage general zone from the tendon axis to the closest longitudinal edge. Compression strut C_2 is equal to the total applied axial load (P) minus C_1 . Compression strut C_4 has the same magnitude of force as tension tie T_2 which is determined by integration of the tensile stresses. Compression strut C_4 and tension tie T_2 are used to determine the spalling tension force, T_3 . Figure 4.56 shows the portion of the STM and the calculation method used to determine the spalling tension force T_3 . The elastic stress trajectories indicated a flow of the compressive strut C_4 toward the longitudinal edge tension force and a flow of the longitudinal edge tension force toward the anchorage device. The STM models the flow pattern for both the compression and tension forces. The compression force (C_5) is necessary to meet the

equilibrium requirements of T_2 , T_3 , and C_4 . C_5 is carried by concrete; and, therefore, its location is not explicitly known. The location assumed for C_5 has a direct effect on the magnitude of the spalling tension force, T_3 . The deeper C_5 is placed in the section, the lower its magnitude and, therefore, the lower the calculated value of T_3 .

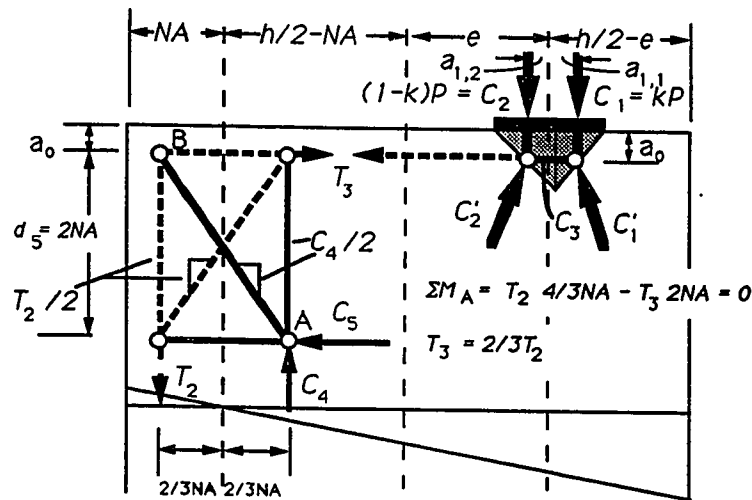
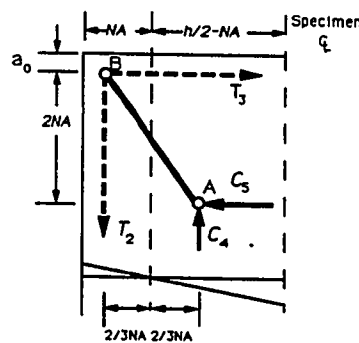
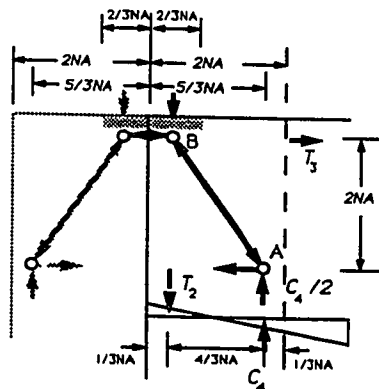


Figure 4.56 Spalling Force STM

To determine a reasonable estimate of the depth of C_5 , the components of the STM representing the spalling forces were examined individually. Figure 4.57a shows a somewhat equivalent concentric anchorage model illustrating the compression strut between nodes "A" and "B" in Fig. 4.56 with the effective direction of the forces at the nodes. For example, in Fig. 4.56 at node "A", vertical compression forces exist on both sides of the node. They are modelled in Fig. 4.57a by a single compressive force ($C_4/2$). Similarly the two horizontal compression forces at node "A" in Fig. 4.56 are modelled by the net resultant in Fig. 4.57a. The configuration of forces and struts in Fig. 4.57a, just described, is identical to a concentric anchor STM divided along the centerline. To show this more clearly, the phantom side of the concentric anchorage zone is shown by dotted

lines in Fig. 4.57a. It is a reasonable assumption in a concentric anchorage zone that the centroid of the bursting force would be located at the midpoint of the general zone, and therefore, be located at a distance from the loading surface of $h/2$. The equivalent concentric anchor zone shown in Fig. 4.57a would therefore have the same section dimensions as a section with a height, h , of $4NA$ and an anchor width, a , of $4/3NA$. If the height of a concentric anchorage zone is $4NA$, then the approximate location of the elastic centroid of the bursting forces is $h/2$ or $2NA$ from the load point. Therefore, an approximation of the depth of C_5 is $2NA$. Using these dimensions, the STM predicts a spalling tension force, T_3 , equal to two-thirds of the longitudinal edge tension force, T_2 . Figure 4.57b shows a STM for the spalling region that is statically equivalent to the one shown in Figs. 4.56 and 4.57a. The model in Fig. 4.57b yields the same magnitude for the spalling force T_3 . The model in Fig. 4.57b helps to stress the importance of continuing the spalling reinforcement to the corner of the section and verifying that the spalling force can be transferred to the longitudinal edge tension reinforcement.



$$\sum M_A = T_2 \cdot 4/3NA - T_3 \cdot 2NA = 0$$

$$T_3 = 2/3T_2$$

a) Concentric Model

b) Simplified Model

Figure 4.57 Equivalent Concentric STM for Spalling Force

Figure 4.58 compares the STM calculated value of the spalling force with the results from a two-dimensional elastic finite element analysis. The STM results which correspond to two-thirds of the longitudinal edge tension force are unconservative for e/h values less than 0.28 when compared to the finite element analysis. This is not surprising because the completely equilibrium based STM does not reflect the compatibility effects which are very important in respect to the spalling stresses and which are satisfied in the finite element analysis. A suggested design model is shown in Fig. 4.58 which adds two percent of the total axial force to two-thirds of the longitudinal edge tension force (which is the STM solution) to account for the compatibility forces that occur near the anchorage device in the concrete. This model yields conservative answers for all the values of e/h shown. Also shown is an approximation which proposes that the spalling force, T_3 , be taken to be equal to the longitudinal edge tension force, T_2 . If this model includes a minimum value for the spalling force estimate of two percent of the axial load, it does a

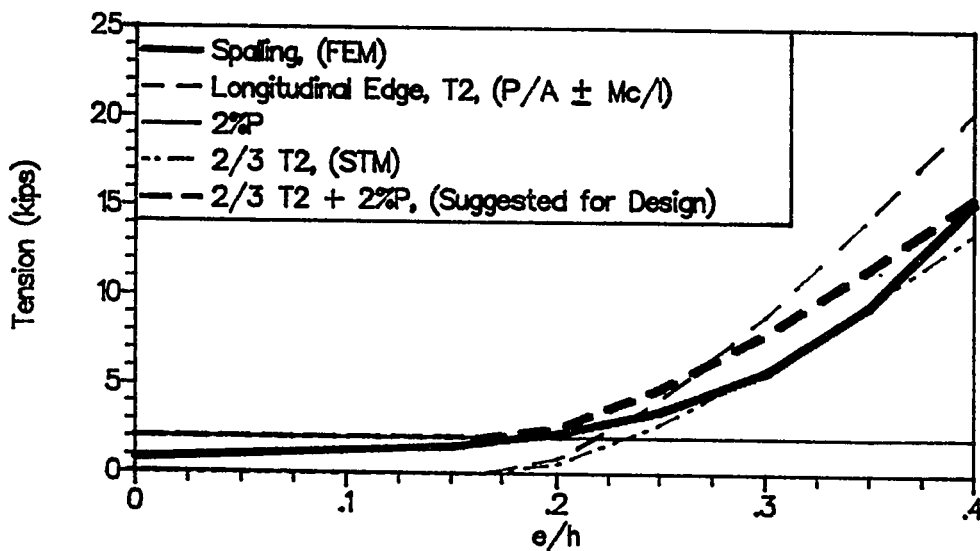


Figure 4.58 Spalling Tension Prediction Models Compared with Finite Element Results

fair job of approximating the elastic results except near an e/h of 0.2 where it is slightly unconservative. The finite element results shown are for a specimen with an a/h equal to 0.1. Burdet [25] compared the magnitude of the spalling tension force as a function of the size of the bearing plate and noted little effect in practical ranges. Therefore, the finite element analysis curve shown in Fig. 4.58 is generally applicable to other a/h ratios. Therefore, for single anchor eccentric systems the best estimate for the spalling force is to use two-thirds of the longitudinal edge tension force plus two percent of the total axial force. This is also the STM result plus two percent of the axial load. This equation will be compared with the experimental results in the next subsection.

Figure 4.59 shows the equations for determining the tension tie capacity with the STM. The first step in the STM process is to assume a force distribution at the far end of the anchorage general zone. In Fig. 4.59 the $P/A \pm Pec/I$ elastic stress distribution is shown. The stress distribution is used to determine the magnitudes and locations of T_2 , C_1 , C_2 , and C_4 . Once the magnitudes of C_1 and C_2 are known, the dimension of the local zone node can be determined. All of the parameters are now known or can be assumed except the location and capacity of the bursting tension ties. By utilizing Equation 2 in Fig. 4.59, the axial capacity can be determined for various bursting reinforcement magnitudes and locations. Equation 1 in Fig. 4.59 can be used to determine the relationship between the tension longitudinal edge tension force and the spalling force. The equations are based on STM principles. As mentioned previously, Equation 1 adds two percent times the axial load to the longitudinal edge tension force to supplement the spalling force to reflect compatibility.

The procedure that must be used to check strut and node capacities after the design of the tension tie reinforcement in the eccentric anchorage zones is the same as that used in Chapter 3 for the concentric anchorage zones. The four checks are as follows:

- 1) Determine local zone bearing capacity ahead of the loading surface including confinement effects
- 2) Determine node compression capacity perpendicular to the tendon path and centered on the secondary nodes
- 3) Determine compressive strut capacity at the local zone node-strut interface
- 4) Determine strut compressive capacity at the local-zone general zone interface and/or when the section thickness changes

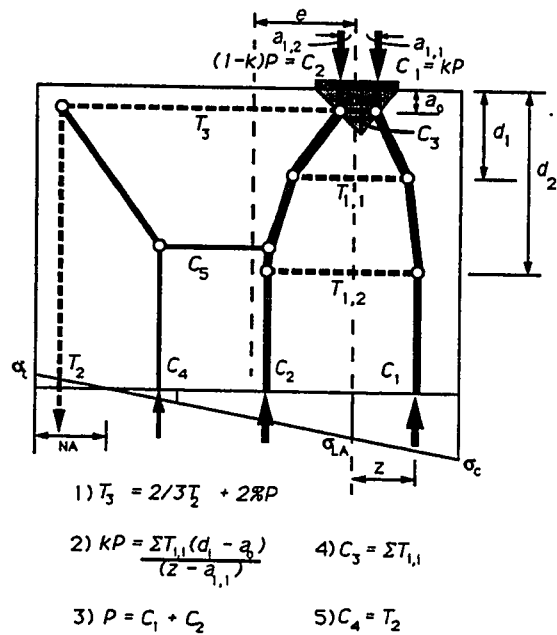


Figure 4.59 Eccentric Strut-and-Tie Model

The width of the compression struts are determined the same way as for concentric anchorage zones except that the struts are not the same width on each side of the load axis. To minimize a repetition of the information presented for the concentric anchorage zones in Section 3.4.1, little detail is given for the specifics of all the parameters that must be determined to check the compression struts and nodes. The

items that differ between the concentric model and the eccentric model are the shape of the local zone node, the width of struts, and the dispersion angles of the struts which are different for each side of the node.

The value of alpha, α , (the dispersion angle of the compression struts) differs on each side of the node. Since the dispersion angle and the width of the plate contributing to the strut are different on both sides of the node, the strut widths also vary. Figure 4.57 shows the equations for determining the strut width at the node-strut interface and at the local zone-general zone interface.

In the following subsection, the eccentric anchorage specimens are checked for compression capacity and the ultimate load predictions for all the eccentric test specimens are compared with the test results.

4.4.2 Basic Strut-and-Tie Model (STM) Prediction of the Ultimate Load. The basic STM assumes that there is no concrete tension contribution to the bursting tie forces and that the locations of the centroids and magnitudes of the compression struts at the far end of the general zone are based on the elastic stress distribution. This subsection uses the STM to check the eccentric anchorage zone specimen compression failure and tension tie failure capacities. The following calculations demonstrate the design and the checks necessary for the bursting reinforcement, the local zone, and the compression struts for Specimen M5 (see Fig.4.47). In the design and analysis, load factors and ϕ factors of unity are used for comparison with a test conducted under laboratory conditions. The calculations are made independent of the measured test ultimate load. This is the same procedure that would be used by an engineer who knew only the specimen dimensions, concrete strength, reinforcement layout, and anchorage size.

The calculations are divided into six parts. First, all of the given information is shown. Then the ultimate load is predicted for the known reinforcement distribution while assuming the tension ties

control. Any contribution of the spiral as a bursting tension tie is neglected.

- 1) Given: Plate Size = 2 each of 6.5 x 6.5 inches ($a \times b$) Multiple Plane Anchors
 Eccentricity (e) = 8 inches
 Height of Section (h) = 32 inches
 Section thickness (t) = 17 inches
 Duct Diameter = 2 5/8 inches
 $f'_c = 4.670$ ksi
 Spiral = #4 ($f_y = 80.3$ ksi) smooth bar,
 $d_c = 7$ inches, $s = 2$ inches and $l_c = 10$ inches
 Bursting Reinforcement: #2s ties at 1-1/2, 7, 12-1/2, 18, 23-1/2, and 29 inches with $F_y = 3.57$ kips/bar and each tie layer having two effective legs
 Longitudinal Edge Tension Reinforcement 4 - #3 bars with $F_y = 6.60$ kips/bar
 Spalling Reinforcement 2 #2s and 2 #3 with F_y same as for bursting and longitudinal edge tension reinforcement

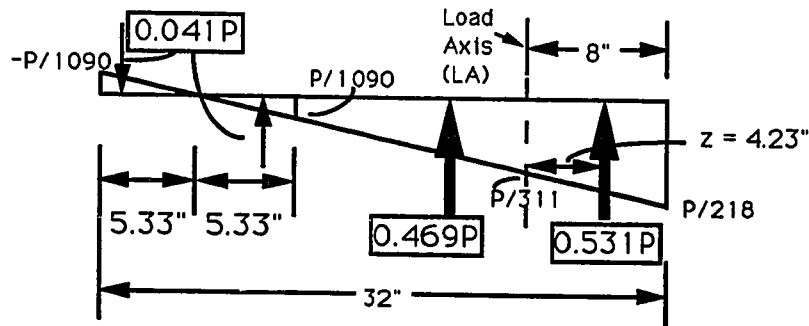


Figure 4.60 Specimen M5 Elastic Stress Distribution at End of General Zone

2) Determination of Ultimate Load assuming Tension Ties Control

Assume elastic distribution at the end of the general zone at 32 inches from the loaded surface (see Fig. 4.60) determined from a $P/A \pm Pec/I$ analysis. P for tension tie calculation is the total load on both plates.

$$A = 17 \cdot 32 = 544 \text{ in}^2$$

$$I = 1/12 \cdot 17 \cdot 32^3 = 46400 \text{ in}^4$$

$$\sigma_t = P/544 - P \cdot 8 \cdot 16/46400 = -P/1090$$

$$\sigma_c = P/544 + P \cdot 8 \cdot 16/46400 = P/218$$

$$NA = (P/1090)/[(P/218 + P/1090)/32] = 5.33 \text{ inches}$$

$$T_2 = \sigma_c \cdot NA \cdot t/2 = P/1090 \cdot 5.33 \cdot 17/2 = P/24.0$$

$$C_1 = (\sigma_c + \sigma_{LA}) \cdot (h/2 - e) \cdot t/2$$

$$\sigma_{LA} = P/544 + P \cdot 8 \cdot 8/46400 = P/311$$

$$C_1 = (P/218 + P/311) \cdot 8 \cdot 17/2 = P/1.884 = 0.531 \cdot P$$

$$z = [\sigma_{LA} \cdot (h/2 - e)^2/2 + (\sigma_c - \sigma_{LA}) \cdot (h/2 - e)^2/2 \cdot 2/3] \cdot t/C_1$$

$$= [P/311 \cdot 8^2/2 + (P/218 - P/311) \cdot 8^2/3] \cdot 17/(0.531 \cdot P) = 4.23 \text{ inches}$$

Node Geometry - short side

$$a_1 = 6.5/2 - 0.531 \cdot 6.5/2 = 1.52 \text{ inches}$$

$$a_0 = 0.531 \cdot 6.5/2 = 1.73 \text{ inches}$$

Bursting Reinforcement Axial Load Capacity

$$C_1 = \Sigma T_{11} \cdot (d_1 - a_0)/(z - a_1)$$

$$0.531 \cdot P = (2 \cdot 3.57) \cdot [(7-1.73) + (12.5-1.73) + (18-1.73) + (23.5-1.73) + (29-1.73)]/(4.23-1.52)$$

$$P = \underline{403 \text{ kips}}$$

Longitudinal edge tension Reinforcement Axial Load Capacity

$$T_2 = P/24.0 = 7.34 \cdot 4 = 29.4 \text{ kips}$$

$$P = 24.0 \cdot 29.4 = \underline{705 \text{ kips}}$$

Spalling Reinforcement

$$T_3 = 2/3 \cdot T_2 + 0.02 \cdot P = 2/3 \cdot P/24.0 + 0.02 \cdot P = 0.0478 \cdot P$$

$$T_3 = 3.57 \cdot 2 + 6.60 \cdot 2 = 20.3 \text{ kips}$$

$$P = 20.3/0.0478 = \underline{426 \text{ kips}}$$

Bursting Reinforcement Controls P = 403 kips

Therefore, the capacity of the anchorage zone for both anchors when the tension reinforcement controls (bursting, spalling, or longitudinal edge tension) is 403 kips. The following four compression checks will be compared against the tension tie load prediction. The first compression capacity check is immediately ahead of the bearing surface (see Fig. 3.93a). Then, the strut capacity between the secondary nodes is checked (see Figs. 3.93b and 4.57). The final two checks verify the capacity at the local zone node-strut interface (see Fig. 4.57) and at

the interface between the local zone and the general zone. For the compression strut checks, the spiral in the local zone is assumed to confine an equivalent square area concentric with the spiral.

3) Bearing Capacity Immediately Ahead of the Anchorage Device

Gross Bearing Area per anchorage device (A_g) -

$$6.5 \cdot 6.5 = 42.3 \text{ in}^2$$

Effective Area per anchorage device (A) = $8.0 \cdot 8.0 = 64.0 \text{ in}^2$

where 8 inches is equal to two times the edge distance.

Net Bearing Area per anchorage device (A_b) -

$$A_g - \pi \cdot 2.625 \cdot 2.625 / 4 = 36.9 \text{ in}^2$$

Confined Core Area (A_{core}) = $\pi \cdot 7^2 / 4 = 38.5 \text{ in}^2$

$$P_b \leq 0.7 \cdot 4.67 \sqrt{64.0 / 42.3} \cdot 36.9 +$$

$$4 \cdot (80.3 \cdot 0.2 \cdot 2) / (2 \cdot 7) \cdot (1 - 2/7)^2 \cdot 38.5$$

$$\leq 329 \text{ kips/anchor} = \underline{657 \text{ kips}} \text{ including both anchors} \gg \text{ tension tie capacity will still control (403 kips)}$$

4) Force Between Secondary Nodes

Node Area = $2a_o \cdot b = 2 \cdot 1.73 \cdot 6.5 = 22.5 \text{ in}^2$

Capacity of Concrete between Secondary Nodes if Controlled by Capacity of Confinement Perpendicular to Load Path

$$P_s \leq 0.7 \cdot 4.67 \sqrt{1} \cdot 22.5 +$$

$$4 \cdot (80.3 \cdot 0.2 \cdot 2) / (2 \cdot 7) \cdot (1 - 2/7)^2 \cdot 22.5$$

$$= 179 \text{ kips/anchor} = \underline{358 \text{ kips}} \text{ including both anchors}$$

Capacity of Concrete between Secondary Nodes if Controlled by Capacity of Confinement Parallel to Load Path

$$P_s \leq 0.7 \cdot 4.67 \sqrt{1} \cdot 22.5 + 4 \cdot (403 / (2 \cdot 6.5 \cdot 6.5)) \cdot 22.5$$

$$= 503 \text{ kips/anchor} = \underline{1007 \text{ kips}} \text{ including both anchors}$$

General Confinement Restriction

$$P_s \leq 3f'_c \cdot A_{co} = 3 \cdot 4.67 \cdot 22.5 = 315 \text{ kips/anchor} = \underline{630 \text{ kips}}$$

including both anchors

Therefore, the maximum compression capacity of the concrete between the secondary nodes is 358 kips.

$$P_s \geq C_3 \text{ ??}$$

where C_3 = Total Bursting Reinforcement Tension Force
 $= 5 \cdot 3.57 \cdot 2 = 35.7$ kips $\ll 358$ kips \gg Therefore, the
 strut between the secondary nodes will not control
 with the given reinforcement pattern.

5) Strut Capacity on the Node-Strut Interface

The strut capacity must be checked on each side of the load axis, struts C_1 and C_2 . Calculations shown are for the strut beneath one anchor. Therefore, the specimen is split into two portions for modelling purposes. The width of each of these sections is $17/2$ or 8.5 inches.

Determine Strut Angles (α_1 and α_2):

Short Side: $\text{atan}(\alpha_1) = C_3/C_1$

$$\text{atan}(\alpha_1) = 35.7 / (0.531 \cdot 403)$$

$$\alpha_1 = 9.45 \text{ degrees}$$

Long Side: $\text{atan}(\alpha_2) = (C_3 + T_3)/C_2$: T_3 is consistent with
 the bursting reinforcement STM analysis.

$$\text{atan}(\alpha_2) = (35.7 + 11.23) / ((1 - 0.531) \cdot 403)$$

$$\alpha_2 = 13.9 \text{ degrees}$$

Determine Width of Confined Area:

$d_c = \sqrt{\pi \cdot 7 \cdot 7 / 4} = 6.2$ inches; therefore, the distance from
 the specimen centerline to the confined boundary is 3.1
 inches.

Short Side Strut C_1

Determine the Width of the Strut:

$$w_{s1} = 0.531 \cdot 6.5 \cdot \cos(45 - 9.45) / \cos(45) = 3.98 \text{ inches}$$

$$t_s = 6.5 + (8.5 - 6.5) \cdot (3.46 - 3.98 / 2 \cdot \sin(9.45)) / 8.5$$

$$= 7.24 \text{ inches}$$

Determine Maximum Compressive Strut Stress:

$$\text{Effective Area (A)} = 8.5 \cdot (3.98 \cdot 8.5 / 7.24) = 39.6 \text{ in}^2$$

$$\text{Strut Area (A}_b\text{)} = 3.98 \cdot 7.24 = 28.7 \text{ in}^2$$

$$\text{Confined Width} = 3.1 + (0.531 - 0.5) \cdot 6.5 = 3.3 \text{ inches}$$

Note: The confined width of the strut is modified because the centerline of the node is not identical to the spiral axis. In the transverse direction,

the confined width is still 6.2 inches.

$$\text{Area Confined} = 6.2 \cdot (3.3 / \cos(9.45)) = 20.8 \text{ in}^2$$

$$\text{Area Unconfined} = 28.7 - 20.8 = 7.9 \text{ in}^2$$

Maximum Stress in the Confined Zone

$$\begin{aligned} \sigma_s &= 0.7 \cdot 4.67 \sqrt{39.6/28.7} + \\ &\quad 4 \cdot (80.3 \cdot 0.2 \cdot 2) / (2.7) \cdot (1-2/7)^2 \\ &= 8.52 \text{ ksi} \end{aligned}$$

Maximum Stress in the Unconfined Zone

$$\sigma_s = 0.7 \cdot 4.67 \sqrt{39.6/28.7} + 0 = 3.84 \text{ ksi}$$

Maximum Axial Load

$$P_s = [8.52 \cdot 20.8 + 3.84 \cdot 7.9] / 0.531 \cdot \cos(9.45)$$

$$= 386 \text{ kips/anchor} = \underline{771} \text{ kips including both anchors} \gg$$

Therefore, tension ties still control (403 kips)

Long Side Strut C_2

$$C_2 = (1 - 0.531) \cdot P = 0.469 \cdot P$$

$$\alpha_2 = 13.9 \text{ degrees}$$

Node Geometry

$$a_1 = 6.5/2 - 0.469 \cdot 6.5/2 = 1.73 \text{ inches}$$

$$a_o = 0.531 \cdot 6.5/2 = 1.73 \text{ inches}$$

$$\text{atan}(\beta) = 1.73 \cdot 2 / (0.469 \cdot 6.5) = 48.6 \text{ degrees}$$

$$w_{s1} = 0.469 \cdot 6.5 \cdot \cos(48.6 - 13.9) / \cos(48.6) = 3.79 \text{ inches}$$

$$t_o = 6.5 + (8.5 - 6.5) \cdot (1.73 \cdot 2 - 3.79 / 2 \cdot \sin(13.9)) / 8.5$$

$$= 7.21 \text{ inches}$$

Determine Maximum Compressive Strut Stress

$$\text{Effective Area (A)} = 8.5 \cdot (3.79 \cdot 8.5 / 7.21) = 38.0 \text{ in}^2$$

$$\text{Strut Area (A}_b) = 3.79 \cdot 7.21 = 27.3 \text{ in}^2$$

$$\text{Confined Width} = 3.1 + (0.469 - 0.5) \cdot 6.5 = 2.9 \text{ inches}$$

$$\text{Area Confined} = 6.2 \cdot (2.9 / \cos(13.9)) = 18.5 \text{ in}^2$$

$$\text{Area Unconfined} = 27.3 - 18.5 = 8.8 \text{ in}^2$$

Maximum Stress in the Confined Zone

$$\begin{aligned} \sigma_s &= 0.7 \cdot 4.67 \sqrt{38.0/27.3} + \\ &\quad 4 \cdot (80.3 \cdot 0.2 \cdot 2) / (2.7) \cdot (1-2/7)^2 = 8.54 \text{ ksi} \end{aligned}$$

Maximum Stress in the Unconfined Zone

$$\sigma_s = 0.7 \cdot 4.67 \sqrt{38.0/27.3} + 0 = 3.85 \text{ ksi}$$

Maximum Axial Load

$$P_s = [8.54 \cdot 18.5 + 3.85 \cdot 8.8] / 0.469 \cdot \cos(13.9)$$

$$= 397 \text{ kips/anchor} = \underline{794} \text{ kips including both anchors}$$

>> Greater than Tension Tie, 403 kips.

6) Strut Capacity at Interface between Local Zone and the General Zone
(Base of the Spiral), unconfined concrete

Note: The calculations shown are for the strut beneath one anchor. Therefore, the specimen is split into two portions for modelling purposes. The width of each of these sections is 17/2 or 8.5 inches.

Short Side Strut C₁

$$\alpha_1 = 9.45 \text{ degrees}$$

$$w_{s2} = w_{s1} + 2 \cdot (l_c - a_o \cdot 2) \cdot \sin(\alpha)$$

$$= 3.98 + 2 \cdot (10.0 - 1.73 \cdot 2) \cdot \sin(9.45) = 6.13 \text{ inches}$$

$$t_o = 6.5 + (8.5 - 6.5) \cdot (10.0 - 6.13 / 2 \cdot \sin(9.45)) / 8.5$$

$$= 8.73 \text{ inches} \geq 8.5 \text{ inches} \implies t_o = 8.5 \text{ inches}$$

$$\text{Strut Area} = 6.13 \cdot 8.5 = 52.1 \text{ in}^2$$

$$\text{Assume } A/A_b = 1$$

$$\sigma_s = 0.7 \cdot 4.67 \sqrt{1} + 0 = 3.27 \text{ ksi}$$

$$P_s = [3.27 \cdot 52.1] / 0.531 \cdot \cos(9.45)$$

$$= 317 \text{ kips/anchor} = \underline{633} \text{ kips including both anchors} \gg$$

Therefore, tension ties still control (403 kips).

Long Side Strut C₂

$$\alpha_2 = 13.9 \text{ degrees}$$

$$w_{s2} = 3.79 + 2 \cdot (10.0 - 1.73 \cdot 2) \cdot \sin(13.9) = 6.93 \text{ inches}$$

$$t_o = 6.5 + (8.5 - 6.5) \cdot (10.0 - 6.93 / 2 \cdot \sin(13.9)) / 8.5$$

$$= 8.66 \text{ inches} \geq 8.5 \text{ inches} \implies t_o = 8.5 \text{ inches}$$

$$\text{Strut Area} = 6.93 \cdot 8.5 = 58.9 \text{ in}^2$$

$$\text{Assume } A/A_b = 1$$

$$\sigma_c = 0.7 \cdot 4.67 / (1) + 0 = 3.27 \text{ ksi}$$

$$P_c = [3.27 \cdot 58.9] / 0.469 \cdot \cos(13.9)$$

$$= 399 \text{ kips/anchor} = \underline{797} \text{ kips including both anchors}$$

>> Therefore, tension ties still control (403 kips).

Table 4.14 Node Parameters for Elastic Stress Distribution at the End of the General Zone

| Specimen | Short Side | | | Long Side | | |
|----------|------------|------------|------------|-----------|------------|------------|
| | % | Ao (in) | A1 (in) | % | Ao (in) | A1 (in) |
| E1 | 0.56 | 1.94 | 1.56 | 0.44 | 1.94 | 1.94 |
| E5 | 0.56 | 1.67 | 1.33 | 0.44 | 1.67 | 1.67 |
| E2 | 0.44 | 1.94 | 1.94 | 0.56 | 1.94 | 1.56 |
| E3 | 0.44 | 1.94 | 1.94 | 0.56 | 1.94 | 1.56 |
| E4 | 0.44 | 1.94 | 1.94 | 0.56 | 1.94 | 1.56 |
| E6 | 0.53 | 1.73 | 1.52 | 0.47 | 1.73 | 1.73 |
| M5 | 0.53 | 1.73 | 1.52 | 0.47 | 1.73 | 1.73 |

Table 4.14 shows the basic node information assuming a linear distribution of stresses at the end of the general zone for all the eccentric specimens. Table 4.15 shows the axial load capacity for the basic STM assuming that the bursting tie capacity controls and checks the nodal compression capacity (C_3). Assuming that the bursting ties control, the capacity is given for two cases: 1) assuming all the bursting reinforcement outside the node zone has yielded and 2) assuming that only reinforcement outside the node zone and within a general zone limited to the depth of the section contributes to the axial load capacity. All of the specimens except Specimen M5 had bursting reinforcement located beyond the extent of the general zone. In order to develop these bars fully, extremely large deformations would need to occur in the general zone portion of the specimen. The strain measurements from the bursting reinforcement indicated very small strains at a depth of 40 inches from the top in Specimens E1, E2, E3, and E4. Specimens E5 and E6 each had two ties at the bottom of the

specimen that would require very large general zone deformations to mobilize them.

The predicted ultimate loads shown in Table 4.15 are very high for Specimens E1 to E4. The magnitude of the bursting force from the STM calculation in Specimen E1 ($e/h = 1/6$) is much greater than that in Specimens E2, E3, and E4 ($e/h = 1/3$) for a given load. Therefore, Specimen E1 has a much smaller capacity than Specimens E2, E3, and E4 even though they all have the same bursting tension capacity. Large area of bursting reinforcement was used in Specimens E1, E2, E3, and E4 to explore compression failure capacities since such failures can be critical in many situations. Strut compression capacity is checked later in this subsection. The nodal compression capacity shown on the right side of Table 4.15 should be compared with and should exceed the total bursting reinforcement. For all the eccentric specimens, the nodal compression capacity did not control. The nodal capacity is calculated using Robert's equation (see Section 3.4).

Table 4.15 STM Prediction Assuming Bursting Ties Control and Node Compression Check

| Specimen | All Bursting Reinforcement Effective | | | Only Bursting Reinforcement within General Zone | | | Nodal Compression Force C3 (kips) |
|----------|--------------------------------------|------------------------|-------------------------|---|------------------------|-------------------------|-----------------------------------|
| | Bursting Tension (kips) | Bursting Centroid (in) | STM-Tie Capacity (kips) | Bursting Tension (kips) | Bursting Centroid (in) | STM-Tie Capacity (kips) | |
| E1 | 220.20 | 26.50 | 2010 | 161.48 | 16.68 | 884 | 213 |
| E5 | 102.76 | 26.00 | 888 | 73.40 | 10.80 | 238 | 175 |
| E2 | 220.20 | 25.80 | 10000 | 161.48 | 15.73 | 4240 | 224 |
| E3 | 220.20 | 25.80 | 10000 | 161.48 | 15.73 | 4240 | 228 |
| E4 | 220.20 | 25.80 | 10000 | 161.48 | 15.73 | 4240 | 219 |
| E6 | 66.04 | 36.63 | 1340 | 36.68 | 13.92 | 259 | 140 |
| M5 | 35.70 | 18.00 | 403 | 35.70 | 18.00 | 403 | 357 |

Table 4.16 STM Prediction assuming Longitudinal Edge Tension or Spalling Ties Control

| Specimen | Test Ultimate (kips) | Longitudinal Edge | | | Spalling | | |
|----------|-------------------------|----------------------------|---------------|----------|----------------------------|---------------|----------|
| | | Tension Capacity (kips) | STM (kips) | Test/STM | Tension Capacity (kips) | STM (kips) | Test/STM |
| E1 | 475 | 14.68 | N/A | N/A | 14.68 | 734 | 0.65 |
| E5 | 332 | 14.68 | N/A | N/A | 14.68 | 734 | 0.45 |
| E2 | 500 | 68.50 | 548 | 0.91 | 83.18 | 805 | 0.62 |
| E3 | 522 | 68.50 | 548 | 0.95 | 83.18 | 805 | 0.65 |
| E4 | 500 | 14.68 | 117 | 4.26 | 14.68 | 142 | 3.52 |
| E6 | 348 | 14.68 | 352 | 0.99 | 8.80 | 184 | 1.89 |
| M5 | 677 | 26.40 | 634 | 1.07 | 20.34 | 426 | 1.59 |

For eccentric anchorage zones, the capacity of the longitudinal edge tension and the spalling regions must be checked (see Table 4.16). The load axes for Specimens E1 and E5 are located at the kern, so there are no longitudinal edge tension forces. However, there are spalling forces. Specimens E2, E3, and E4 were designed very conservatively in the bursting region but not in the longitudinal edge tension and spalling regions. The longitudinal edge tension reinforcement must be distributed in the longitudinal edge tension region to be effective. The spalling reinforcement must be distributed along the loaded surface within the height of the local zone node. Specimen E4 had the same reinforcement pattern as Specimen E2 except Specimen E4 had significantly less reinforcement in the longitudinal edge tension and spalling regions. Specimen E4 was able to reach loads four times higher than predicted by longitudinal edge tension or spalling criteria. The measured strains in these areas were far below the yield values. This seems to indicate, that after cracking in these regions, the force flow changed significantly.

In the specimens in which the anchorage zone was located outside the kern, the base cross section was modified to shift the load axis

inside the kern at the base. This prevented uplift while allowing the longitudinal edge tension forces to develop. Once the bursting cracks form and the specimen begins to act as two beam-columns (see Fig. 4.61), the uplift of the section must be reexamined. Figure 4.62 shows the shifting of the calculated kern location. The location of the kern depends on the cross section that is considered within the specimen. In the uncracked specimen at the top of the specimen, the load axis is outside the kern line. At the bottom of the specimen, using the modified section, the load axis is inside the kern line. When the specimen cracks and begins to act as two beam-columns, the modification of the section becomes ineffective in shifting the kern on the long side of the specimen. The long side of the specimen is now a rectangular section with the load axis outside the kern. Therefore, the section can lift up and the magnitudes of the longitudinal edge tension and spalling tension forces are reduced. In the typical girder application, even though the beam-column forms, the longitudinal edge tension forces remain because of overall beam equilibrium. It is important to realize that the specimens in this test series more accurately represent the spreading of forces in the bursting region than match the full longitudinal edge tension force and spalling tension force because of the boundary conditions. Therefore, even though the tests indicated that spalling and longitudinal edge tension forces were not critical, until further research is conducted on full beam specimens it would be prudent to provide the full calculated reinforcement. The spalling tension, T_3 , is taken to be two-thirds times the tension longitudinal edge tension force plus two percent of the axial load. The beam-column effects will be examined in more detail in the next subsection as it relates to the tie capacity of the STM.

Table 4.17 shows the capacity at the node-strut interface (short side, a, and long side, b). The short side of the specimen controls over the long side for all specimens. Table 4.18 is the check of

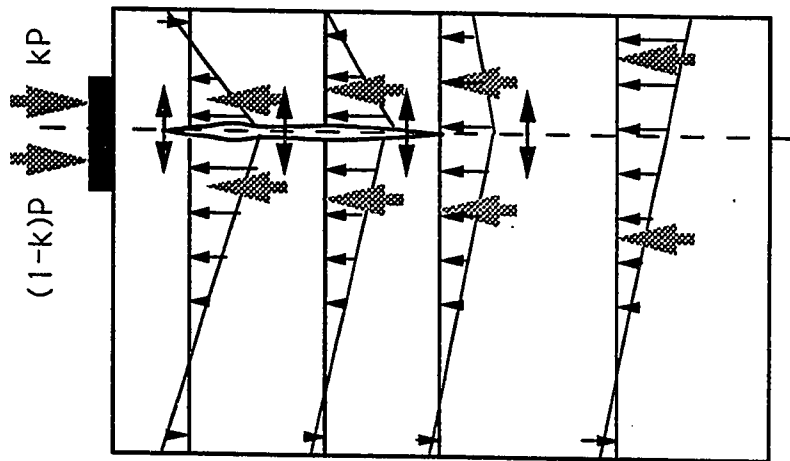


Figure 4.61 Beam Bending in Eccentric Anchorage Specimens

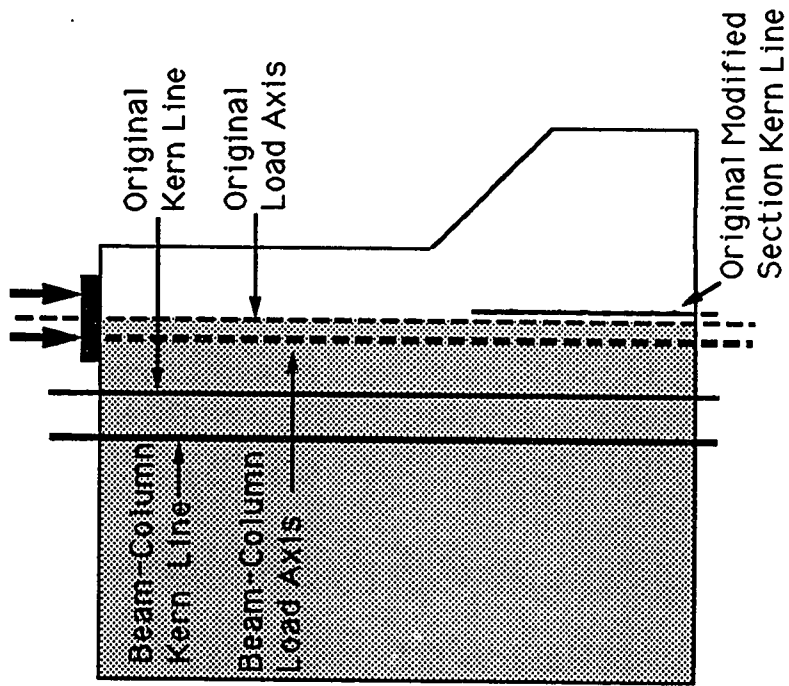


Figure 4.62 Location of the Kern Comparison

Table 4.17a STM Node-Strut Interface Capacity for Short Side

| Specimen | Alpha (degrees) | Strut Width (in) | Strut Thickness (in) | Confined Width (in) | Confined Allowable (ksi) | Unconfined Allowable (ksi) | Predicted Capacity (kips) |
|----------|--------------------|------------------------|----------------------------|---------------------------|--------------------------------|----------------------------------|---------------------------------|
| E1 | 18.20 | 4.91 | 8.85 | 3.60 | 7.78 | 4.74 | 479 |
| E5 | 29.04 | 4.53 | 6.66 | 3.21 | 9.84 | 5.10 | 400 |
| E2 | 4.90 | 3.43 | 9.02 | 2.82 | 8.12 | 5.08 | 477 |
| E3 | 4.90 | 3.43 | 9.02 | 2.82 | 8.28 | 5.23 | 487 |
| E4 | 4.90 | 3.43 | 9.02 | 2.82 | 7.90 | 4.86 | 461 |
| E6 | 14.91 | 4.23 | 7.52 | 3.75 | 7.54 | 5.26 | 418 |
| M5 | 9.45 | 3.98 | 7.24 | 3.31 | 8.52 | 3.84 | 771 |

Table 4.17b STM Node-Strut Interface Capacity for Long Side

| Specimen | Alpha (degrees) | Strut Width (in) | Strut Thickness (in) | Confined Width (in) | Confined Allowable (ksi) | Unconfined Allowable (ksi) | Predicted Capacity (kips) |
|----------|--------------------|------------------------|----------------------------|---------------------------|--------------------------------|----------------------------------|---------------------------------|
| E1 | 22.35 | 4.36 | 8.83 | 3.05 | 7.79 | 4.75 | 505 |
| E5 | 34.76 | 4.09 | 6.64 | 3.10 | 9.85 | 5.12 | 413 |
| E2 | 12.33 | 4.63 | 8.93 | 3.69 | 8.18 | 5.13 | 500 |
| E3 | 12.33 | 4.63 | 8.93 | 3.69 | 8.33 | 5.29 | 511 |
| E4 | 12.33 | 4.63 | 8.93 | 3.69 | 7.95 | 4.91 | 484 |
| E6 | 19.90 | 4.04 | 7.47 | 3.55 | 7.57 | 5.29 | 436 |
| M5 | 13.94 | 3.79 | 7.21 | 2.98 | 8.53 | 3.85 | 795 |

the capacity at the local zone-general zone interface (short side, a and long side, b). Table 4.19 is a summary of the failure modes that were checked including the bearing capacity. The table indicates that bearing limits were reached by four of the seven specimens. Some additional bearing capacity above that which was provided by the spiral could have been supplied by the portion of the bursting reinforcement which was located close to the loading surface since the bursting reinforcement was so excessive in Specimens E1, E2, E3, and E4. Even by including this additional confinement capacity, the same specimens were predicted to fail in bearing but were much less conservative. These compression type failure predictions agree with the experimental observations. All of the specimens except Specimens E5 and M5 failed before all the general zone bursting reinforcement yielded. Half of

Table 4.18a STM Local Zone-General Zone Interface Capacity for Short Side

| Specimen | Depth of Confinement (in) | Alpha (degrees) | Strut Width (in) | Strut Thickness (in) | Unconfined Allowable (ksi) | Predicted Capacity (kips) |
|----------|---------------------------|-----------------|------------------|----------------------|----------------------------|---------------------------|
| E1 | 13.25 | 18.20 | 10.76 | 11.00 | 3.82 | 772 |
| E5 | 8.00 | 29.04 | 9.06 | 7.71 | 4.41 | 485 |
| E2 | 13.25 | 4.90 | 5.03 | 11.00 | 4.17 | 517 |
| E3 | 13.25 | 4.90 | 5.03 | 11.00 | 4.29 | 532 |
| E4 | 13.25 | 4.90 | 5.03 | 11.00 | 3.98 | 494 |
| E6 | 9.50 | 14.91 | 7.34 | 9.49 | 4.17 | 527 |
| M5 | 10.00 | 9.45 | 6.13 | 8.50 | 3.27 | 631 |

Table 4.18b STM Local Zone-General Zone Interface Capacity for Long Side

| Specimen | Depth of Confinement (in) | Alpha (degrees) | Strut Width (in) | Strut Thickness (in) | Unconfined Allowable (ksi) | Predicted Capacity (kips) |
|----------|---------------------------|-----------------|------------------|----------------------|----------------------------|---------------------------|
| E1 | 13.25 | 22.35 | 11.47 | 11.00 | 3.82 | 1002 |
| E5 | 8.00 | 34.76 | 9.41 | 7.56 | 4.49 | 591 |
| E2 | 13.25 | 12.33 | 8.63 | 11.00 | 4.17 | 695 |
| E3 | 13.25 | 12.33 | 8.63 | 11.00 | 4.29 | 716 |
| E4 | 13.25 | 12.33 | 8.63 | 11.00 | 3.99 | 665 |
| E6 | 9.50 | 19.90 | 8.15 | 9.34 | 4.23 | 647 |
| M5 | 10.00 | 13.94 | 6.94 | 8.50 | 3.27 | 799 |

Table 4.19 Basic STM Prediction Summary

| Specimen | Tension Tie | Bearing Spiral Only | Bearing Ties Included | Node-Strut Interface | | L.Z.-G.Z. Interface | | Controlling Load | Ultimate Load | Test/Prediction |
|--------------------------|-------------|---------------------|-----------------------|----------------------|------|---------------------|------|------------------|--------------------|-----------------|
| | | | | Short | Long | Short | Long | | | |
| E1 | 884 | 369 | 404 | 479 | 505 | 772 | 1002 | 404 | 475 | 1.17 |
| E5 | <u>238</u> | 343 | <u>343</u> | 400 | 413 | 485 | 591 | 238 | 332 | 1.39 |
| E2 | 4240 | 391 | <u>445</u> | 477 | 500 | 517 | 695 | 445 | 500 | 1.12 |
| E3 | 4240 | 399 | <u>453</u> | 487 | 511 | 532 | 716 | 453 | 522 | 1.15 |
| E4 | 4240 | 380 | <u>434</u> | 461 | 484 | 494 | 665 | 434 | 500 | 1.15 |
| E6 | 259 | 339 | <u>339</u> | 418 | 436 | 527 | 647 | 259 | 348 | 1.34 |
| M5 | <u>403</u> | 657 | 657 | 771 | 795 | 631 | 799 | 403 | 677 | 1.68 |
| Note: All Forces in kips | | | | | | | | | Average | 1.29 |
| | | | | | | | | | Standard Deviation | 0.19 |
| | | | | | | | | | Coef. of Variance | 0.15 |

the bursting reinforcement yielded in Specimen E6. The bearing capacity controls for Specimens E1, E2, E3, and E4. Specimens E5, E6, and M5 were controlled by the bursting tie capacity. The STM and bearing stress predictions are quite conservative with a test-to-predicted ratio for the ultimate load of 1.29 and a 15 percent coefficient of variance. Even though these conditions controlled the design, the average of the test-to-predicted ratios would be 0.99 with a coefficient of variance of 0.11, if the lowest load from the node-strut interface and the local zone-general zone interface were used for the controlling load. This indicates that a substantial reserve was available in the tension and bearing type predicted failure loads. All of the eccentric specimens had extensive cracking in and around the local zone. None of the eccentric specimens cracked to the base of the specimen; so, the low values for the STM tie predictions for Specimens E5, E6, and M5 compared to the test results could be explained by additional concrete tensile capacity across the tendon axis.

4.4.3 Modified Strut-and-Tie Model (STM) Prediction of the Ultimate Load. The use of the basic STM described in the previous subsection conservatively predicts the ultimate load. In Chapter 3, Concentric Anchorage Zones, two models were discussed that help to explain how the specimens were behaving and why they were able to sustain higher loads than predicted. As with concentric anchorage zones, the specimen can be modelled as two beam-columns once cracks begin to form along the tendon axis as shown in Fig. 4.61. Because of the boundary conditions of the specimens, the compression struts of the STM are able to shift toward the tendon axis, which permits higher axial loads. The modified STM will be used to model this behavior in the eccentric specimens. As discussed in Chapter 3, the modified STM method matches the axial load as determined from the capacity of the bursting ties assuming a plastic stress distribution with that determined from the compression strut capacities.

Table 4.20a Modified STM Node-Strut Interface Capacity for Short Side

| Specimen | Alpha (degrees) | Strut Width (in) | Strut Thickness (in) | Confined Width (in) | Confined Allowable (ksi) | Unconfined Allowable (ksi) | Predicted Capacity (kips) |
|----------|--------------------|------------------------|----------------------------|---------------------------|--------------------------------|----------------------------------|---------------------------------|
| E1 | 31.70 | 5.35 | 8.68 | 3.60 | 7.88 | 4.84 | 471 |
| E5 | 18.18 | 4.21 | 6.79 | 3.21 | 9.74 | 5.01 | 402 |
| E2 | 34.47 | 4.77 | 8.69 | 2.82 | 8.31 | 5.27 | 529 |
| E3 | 33.77 | 4.75 | 8.70 | 2.82 | 8.47 | 5.42 | 543 |
| E4 | 35.55 | 4.79 | 8.68 | 2.82 | 8.09 | 5.05 | 509 |
| E6 | 9.04 | 3.96 | 7.60 | 3.75 | 8.07 | 5.20 | 434 |
| M5 | 5.10 | 3.75 | 7.27 | 3.31 | 8.50 | 3.82 | 752 |

Table 4.20b Modified STM Node-Strut Interface Capacity for Long Side

| Specimen | Alpha (degrees) | Strut Width (in) | Strut Thickness (in) | Confined Width (in) | Confined Allowable (ksi) | Unconfined Allowable (ksi) | Predicted Capacity (kips) |
|----------|--------------------|------------------------|----------------------------|---------------------------|--------------------------------|----------------------------------|---------------------------------|
| E1 | 36.60 | 4.82 | 8.67 | 3.52 | 7.88 | 4.84 | 489 |
| E5 | 21.49 | 3.70 | 6.78 | 2.74 | 9.74 | 5.01 | 420 |
| E2 | 29.86 | 5.31 | 8.70 | 4.15 | 8.31 | 5.27 | 506 |
| E3 | 29.25 | 5.29 | 8.71 | 4.13 | 8.46 | 5.42 | 519 |
| E4 | 30.77 | 5.33 | 8.69 | 4.19 | 8.09 | 5.05 | 488 |
| E6 | 10.66 | 3.63 | 7.59 | 3.40 | 7.48 | 5.21 | 416 |
| M5 | 5.75 | 3.37 | 7.27 | 2.91 | 8.50 | 3.82 | 757 |

Tables 4.20 and 4.21 show the results of the modified STM at the node-strut interface and at the local zone-general zone interface respectively. Table 4.22 shows the controlling load. Table 4.22 also includes the bearing capacity. Since the test series was dominated by bearing type failures, it is difficult to verify the method. The limits on capacities due to the longitudinal edge tension or spalling modes were neglected because the behavior of the specimens showed these areas not to be critical. The solution is less conservative than the basic STM model. As with the basic STM solution, the failure solution is dominated by bearing failures which raises the conservatism over the node-strut interface and local zone-general zone interface interactions. If the bearing prediction is neglected, the test-to-

predicted ratio average becomes 0.99 with a coefficient of variance equal to 0.12.

Table 4.21a Modified STM Local Zone-General Zone Interface Capacity for Short Side

| Specimen | Depth of Confinement (in) | Alpha (degrees) | Strut Width (in) | Strut Thickness (in) | Unconfined Allowable (ksi) | Predicted Capacity (kips) |
|----------|---------------------------|-----------------|------------------|----------------------|----------------------------|---------------------------|
| E1 | 13.25 | 19.85 | 11.33 | 11.00 | 3.82 | 805 |
| E5 | 8.00 | 17.84 | 7.05 | 8.04 | 4.23 | 411 |
| E2 | 13.25 | 30.43 | 6.96 | 11.00 | 4.17 | 619 |
| E3 | 13.25 | 29.69 | 6.91 | 11.00 | 4.29 | 637 |
| E4 | 13.25 | 31.56 | 7.04 | 11.00 | 3.98 | 591 |
| E6 | 9.50 | 9.09 | 5.87 | 9.66 | 4.09 | 431 |
| M5 | 10.00 | 6.83 | 5.40 | 8.50 | 3.27 | 560 |

Table 4.21a Modified STM Local Zone-General Zone Interface Capacity for Long Side

| Specimen | Depth of Confinement (in) | Alpha (degrees) | Strut Width (in) | Strut Thickness (in) | Unconfined Allowable (ksi) | Predicted Capacity (kips) |
|----------|---------------------------|-----------------|------------------|----------------------|----------------------------|---------------------------|
| E1 | 13.25 | 20.68 | 10.90 | 11.00 | 3.82 | 963 |
| E5 | 8.00 | 18.99 | 6.64 | 8.04 | 4.23 | 480 |
| E2 | 13.25 | 18.77 | 10.96 | 11.00 | 4.17 | 856 |
| E3 | 13.25 | 18.42 | 10.83 | 11.00 | 4.29 | 873 |
| E4 | 13.25 | 19.30 | 11.14 | 11.00 | 3.99 | 830 |
| E6 | 9.50 | 9.57 | 5.58 | 9.66 | 4.09 | 465 |
| M5 | 10.00 | 7.24 | 5.10 | 8.50 | 3.27 | 600 |

4.4.4 Current Methods for Prediction of the Ultimate Load. The most common method currently used for determining the capacity of the anchorage zone is Guyon's symmetrical prism which was discussed in Chapter 2. Table 4.23 shows the predicted capacity and a comparison with test results when the symmetrical prism method (see Fig. 4.52) is

Table 4.22 Modified STM Prediction Summary

| Specimen | Bearing Spiral Only | Bearing Ties Included | Node-Strut Interface | | L.Z.-G.Z. Interface | | Controlling Load | Ultimate Load | Test/ Prediction |
|--------------------------|---------------------------|-----------------------------|-------------------------|------|------------------------|------|---------------------|--------------------|---------------------|
| | | | Short | Long | Short | Long | | | |
| E1 | 369 | <u>404</u> | 471 | 489 | 805 | 963 | 404 | 475 | 1.18 |
| E5 | 343 | <u>343</u> | 402 | 420 | 411 | 480 | 343 | 332 | 0.97 |
| E2 | 391 | <u>445</u> | 529 | 506 | 619 | 856 | 445 | 500 | 1.12 |
| E3 | 399 | <u>453</u> | 543 | 519 | 637 | 873 | 453 | 522 | 1.15 |
| E4 | 380 | <u>434</u> | 509 | 488 | 591 | 830 | 434 | 500 | 1.15 |
| E6 | 339 | <u>339</u> | 434 | 416 | 431 | 465 | 339 | 348 | 1.03 |
| M5 | 657 | <u>657</u> | 752 | 757 | <u>560</u> | 600 | 560 | 677 | 1.21 |
| Note: All Forces in kips | | | | | | | | Average | 1.12 |
| | | | | | | | | Standard Deviation | 0.08 |
| | | | | | | | | Coef. of Variance | 0.07 |

utilized. In addition to determining the bursting reinforcement by the symmetrical prism method, the spalling reinforcement is typically designed for four percent of the axial load. The bearing capacity is checked by conservative bearing capacity formulas, and the longitudinal edge tension reinforcement is designed from edge tension forces determined by a conventional combined stress ($P/A \pm Pec/I$) theory. As with Table 4.19 for the STM, longitudinal edge tension and spalling failure criteria have been neglected. If the bearing check is included, all of the eccentric specimens are essentially conservative (Specimen E5, 0.97). Specimens E6 and M5 are extremely conservative. They are the only two specimen predictions controlled by the symmetrical prism tension tie value. A comparison with Table 4.19 for these two specimens indicates that the STM is a substantially better predictor than the symmetrical prism method for eccentric anchorages. It is also of substantial concern that the symmetrical prism prediction of the bursting tension capacity for Specimen E5 was unconservative when compared to the experimental test and especially when compared to the STM tension tie prediction. Strain readings indicated that the tension tie reinforcement yielded in Specimen E5. The STM, including the checks of the compression strut, tension ties, and bearing stress in the nodes, is much more accurate than the current methods. In the cases

of Specimens E6 and M5, bursting reinforcement was placed deep in the section that was not utilized by the symmetrical prism. If bursting reinforcement was placed very close to the loading surface, the symmetrical prism could be unconservative because the symmetrical prism is assuming the bursting reinforcement to be at a depth of approximately $0.5h'$.

Table 4.23 Guyon's Symmetric Prism Prediction Method

| Specimen | Bursting Tension using the Symmetrical Prism | a (in) | h' (in) | Tension Tie Prediction (kips) | Bearing Prediction (kips) | Controlling Load (kips) | Test Ultimate (kips) | Test/Prediction |
|----------|--|--------|---------|-------------------------------|---------------------------|-------------------------|----------------------|-----------------|
| E1 | 146.80 | 7.00 | 24.00 | 829 | <u>369</u> | 369 | 475 | 1.29 |
| E5 | 73.40 | 6.00 | 24.00 | 391 | <u>343</u> | 343 | 332 | 0.97 |
| E2 | 100.80 | 7.00 | 12.00 | 968 | <u>391</u> | 391 | 500 | 1.28 |
| E3 | 100.80 | 7.00 | 12.00 | 968 | <u>399</u> | 399 | 522 | 1.31 |
| E4 | 73.40 | 7.00 | 12.00 | 705 | <u>380</u> | 380 | 500 | 1.32 |
| E6 | 23.48 | 6.50 | 18.00 | <u>147</u> | 339 | 147 | 348 | 2.37 |
| M5 | 21.42 | 6.50 | 16.00 | <u>144</u> | 657 | 144 | 677 | 4.69 |
| | | | | | | | Average | 1.89 |
| | | | | | | | Standard Deviation | 1.21 |
| | | | | | | | Coef. of Variance | 0.64 |

4.5 Conclusions for Eccentric Anchorage Zones

1) The use of the basic STM is a conservative but reasonable way to design eccentric anchorage zones. The average of the test ultimate compared to the predicted capacity of the seven eccentric tests was 1.29 with a coefficient of variance of 0.15. It is very important to check all the components of the STM: compression strut stresses, node stresses, and tie strengths. Caution should be exercised when counting on bursting reinforcement at depths where the slope of the strut boundary between the secondary local zone node and the furthest effective layer of reinforcement is less than six degrees. The

furthest bar in Specimen M5 had an angle of 6.1 degrees, and the specimen performed well. However, when reinforcement is placed deep in the section, the local cracking in the section closest to the loading surface may be excessive and the reinforcement may not be fully developed.

2) All of the specimens eventually failed in compression because the force paths were able to adjust to allow higher axial capacity than that predicted by the yielding of the bursting ties. Therefore, the most critical check of the actual failure becomes the compression checks.

3) The modified STM, which allows the compression struts to move in toward the tendon axis until the compression strut failure load and the bursting tension tie failure load match, modelled the specimens slightly more accurately than the basic STM (test-to-predicted ratio average of 1.12). The coefficient of variance was 0.07. As with the basic STM, the prediction was dominated by the bearing capacity of the specimens. If the bearing capacity equation is neglected, the test-to-predicted ratio average becomes 0.99 with a coefficient of variance equal to 0.12. The bearing capacity should not be neglected in design. What it does show is that if there is excess strength in one area (bursting reinforcement), the reinforcement can be used to increase the strength of the weaker area (bearing capacity) but only if the bursting reinforcement is in the bearing area and gives effective reinforcement.

4) The particular test specimens used probably did not accurately model the longitudinal edge tension and the spalling tension force effects because some uplift could occur at the base of the specimens with the load axis outside the kern. The specimens were very adaptable in carrying the spalling and the longitudinal edge tension that were created. The cracks in the spalling region were much longer in the cases of Specimens E4 and E6 because of the lack of spalling reinforcement. The cracks propagated until sufficient capacity was found. A good conservative approximation of the eccentric anchor

induced spalling forces caused by equilibrium and compatibility conditions seems to be two-thirds of the longitudinal edge tension force plus two percent of the axial load.

5) Using Guyon's symmetrical prism equations and the conventional bearing stress equations is an inconsistent and sometimes unconservative method of ultimate load design.

6) The initial cracking load is most accurately predicted by reducing the split cylinder strength to account for the triaxial effects and decreasing the section thickness by considering the duct hole with the transformed section. A conservative approach is to use $4.2\sqrt{F'_c}$ as the concrete tensile strength and the thickness of the section minus the inside diameter of the duct as the effective section thickness.

7) The use of Guyon's stress curves and the symmetrical prism is a very conservative approach for peak bursting stress predictions in determining the cracking load.

8) When effectively tied together, a pair of closely spaced anchors can act as a single larger anchor.

CHAPTER 5
MULTIPLE ANCHORAGE SPECIMENS WITH STRAIGHT TENDONS

5.1 Introduction

To develop the necessary level of post-tensioning force in a girder, it is often essential to use multiple anchorages. Chapters 3 and 4 examined single anchorages with straight tendons. Beams with multiple anchorages can have the resultant of the forces either along the centroidal axis of the specimen or eccentric to it. Five multiple anchorage specimens were tested with their resultant force axis along the centroidal axis, while three had the resultant eccentric to the centroidal axis. The objectives of testing multiple anchorage specimens were to determine if the behavior varied from that of single anchors, and to verify if models developed for single anchorages would apply.

5.2 Test Program

The test results for each of the multiple anchorage specimens are described in detail in the following subsections. The specimen descriptions are divided into two groups: Specimens with Concentric Force Axis and Specimens with Eccentric Force Axis. A crack history is given for each specimen along with strain gage data from the tension reinforcement. The test procedure was identical to that of the concentric test series (see Sec. 3.2.1), but the testing machine and the support conditions varied and will be discussed.

5.2.1 Specimens with Concentric Load Axis. The resultant load axis was concentric because the anchorages were symmetrical about the specimen centerline and were loaded simultaneously. Four specimens examined the effect of spacing between the anchors (see Figs. 5.1 to 5.4) and one studied the effects of tightly grouping four anchorages (see Fig. 5.5). In Specimen M1, the anchorages were very close together with a spacing between the anchorages of only 2 inches. In Specimens M2 and M4, the spacing between the anchorages was increased

to a plate width, 6 inches. Specimen M3 had anchorages placed outside the quarter points of the section. There were four anchorages in Specimens M6, closely spaced and concentric about the centroid of the section. Figure 5.6 shows the elastic principal stress trajectories [25] for Specimens M1, M2, and M3. The elastic stress trajectories of Specimen M1 (see Fig. 5.6a) are very similar to those of a concentric anchorage having a large bursting tension area along the specimen centerline and spalling tension stresses, induced by compatibility, along the outer edges of the loaded surface. The size of the circles represents the magnitude of the stress vector. The scale is purposely distorted to emphasize the tensile stresses. The scale is such that, for equal stresses of compression and tension, the circle diameter would be five times smaller for the compression values than for the tension values. The elastic stress trajectories of Specimens M2 and M4 (see Fig. 5.6b) indicate the large bursting tension stresses along the centerline of the section as in the concentric specimens, but the independent behavior of the anchorages is becoming somewhat more pronounced. The stress patterns for Specimen M3 (see Fig. 5.6c) are completely different than the specimens just described. In Specimen M3, a large spalling tension force exists along the loading face between the anchorages in addition to two independent bursting tension regions ahead of the anchors.

Specimen M1 was loaded in the 600-kip universal testing machine. Because of the distance between the anchorages, a large loading beam (see Fig. 5.7) was used to apply the loads to the anchorages. The specimen was placed in the testing machine on top of two pieces of 1/32-inch teflon. The specimen was centered underneath the loading beam and leveled with metal shims at the base. Once leveled and centered, hydrostone was poured beneath the specimen and on top of the teflon surface to provide a uniform bearing surface. The specimen was supported transversely by the same frames used for the eccentric

specimens and Specimen C1. The material information for Specimens M1, M2, M3, M4, and M6 is shown in Table 5.1.

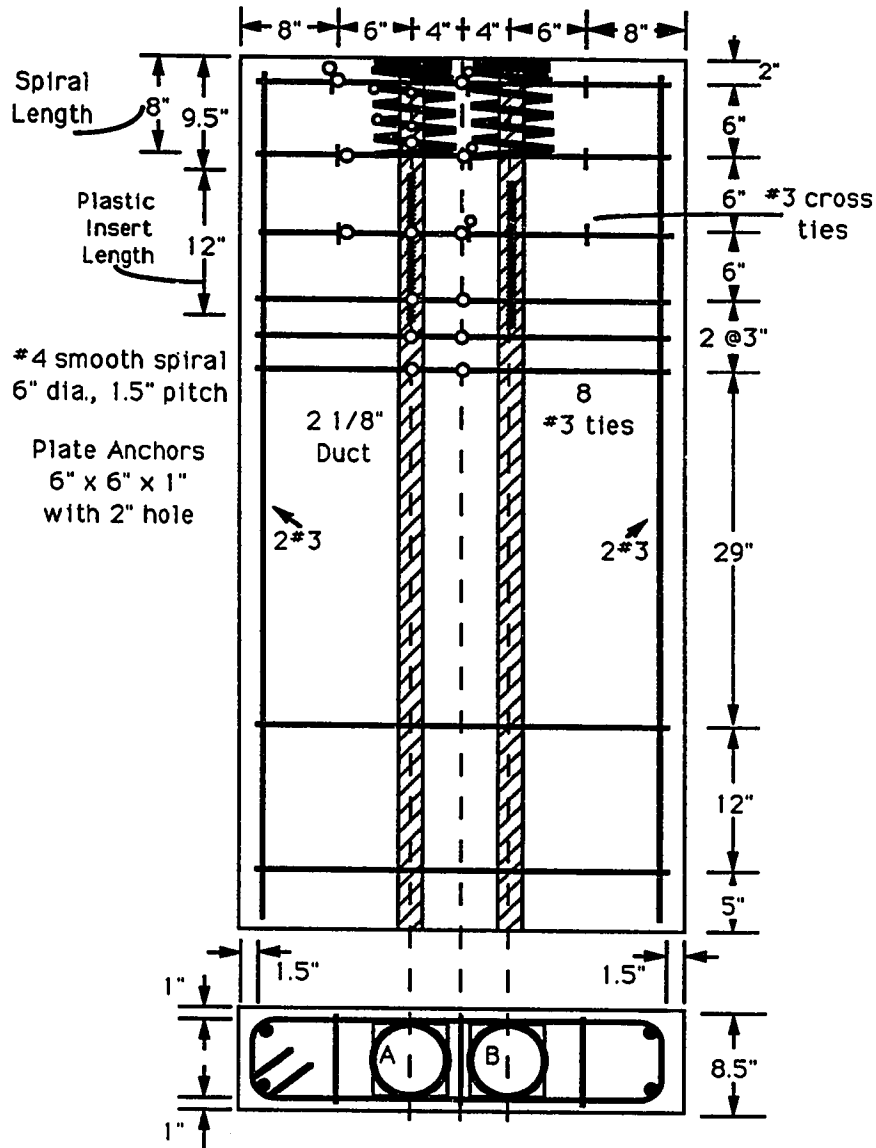


Figure 5.1 Specimen M1 Detail

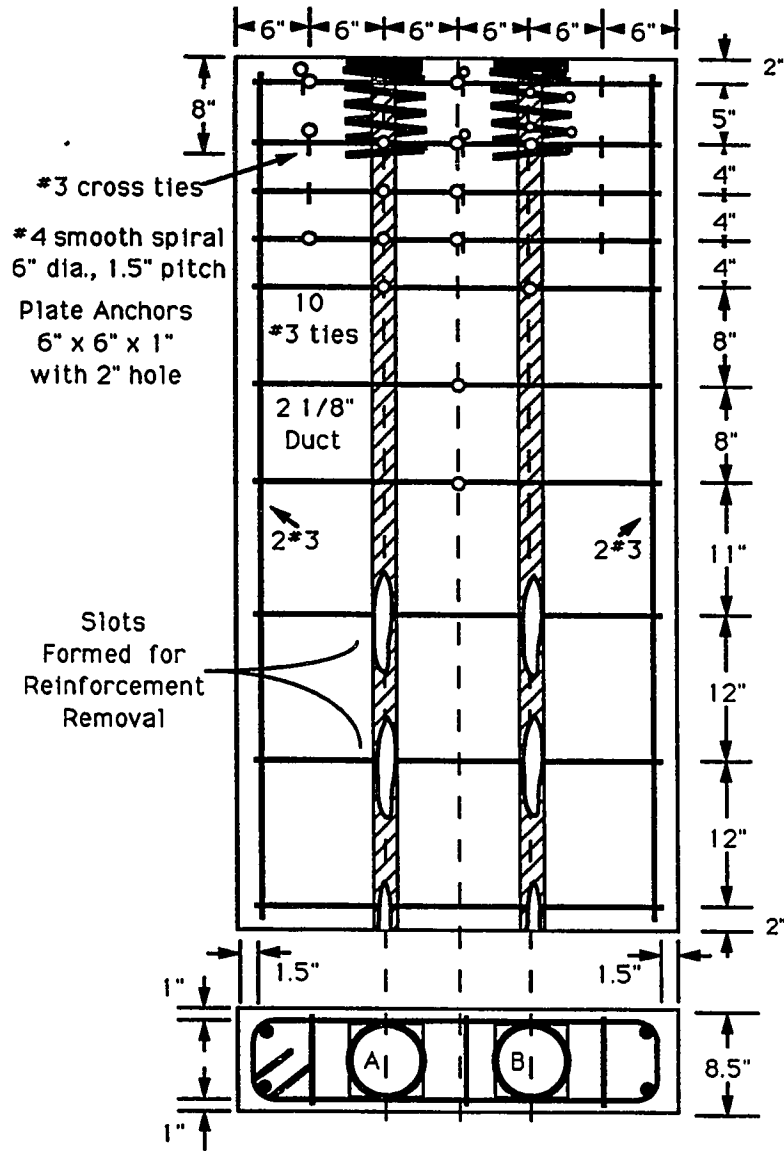


Figure 5.2 Specimen M2 Detail

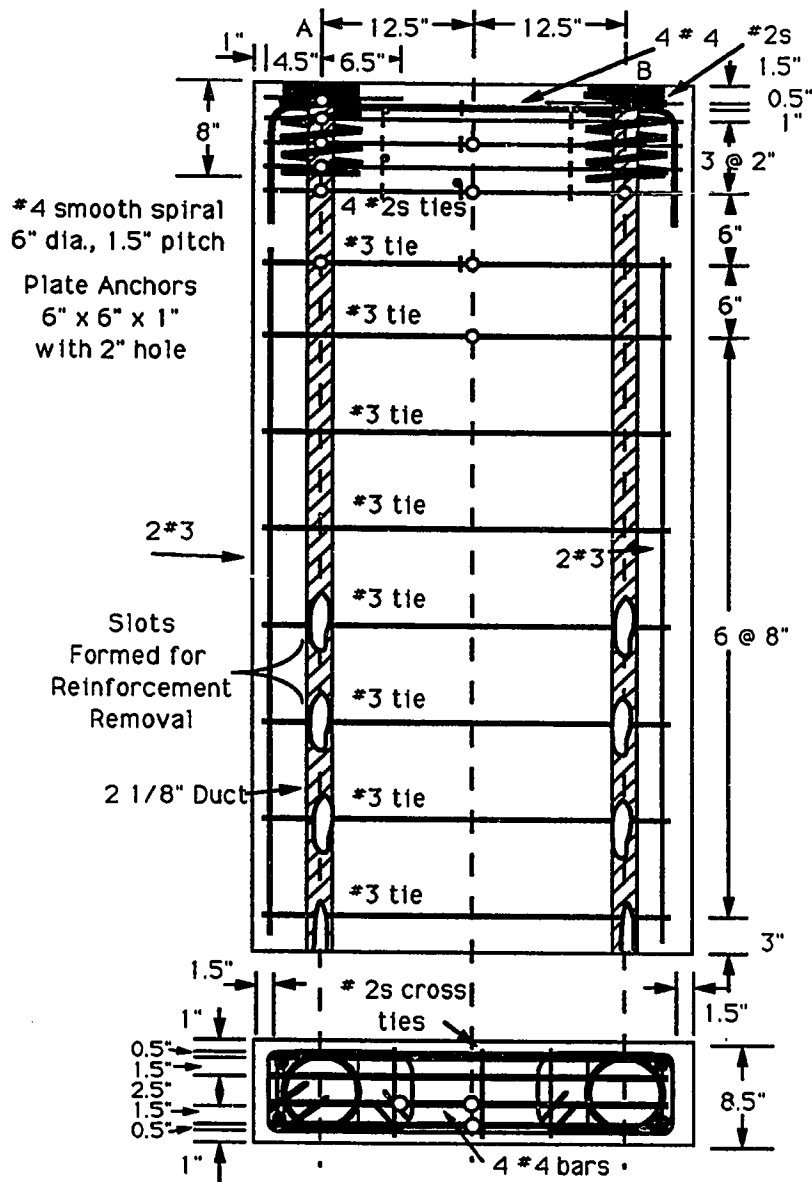


Figure 5.3 Specimen M3 Detail

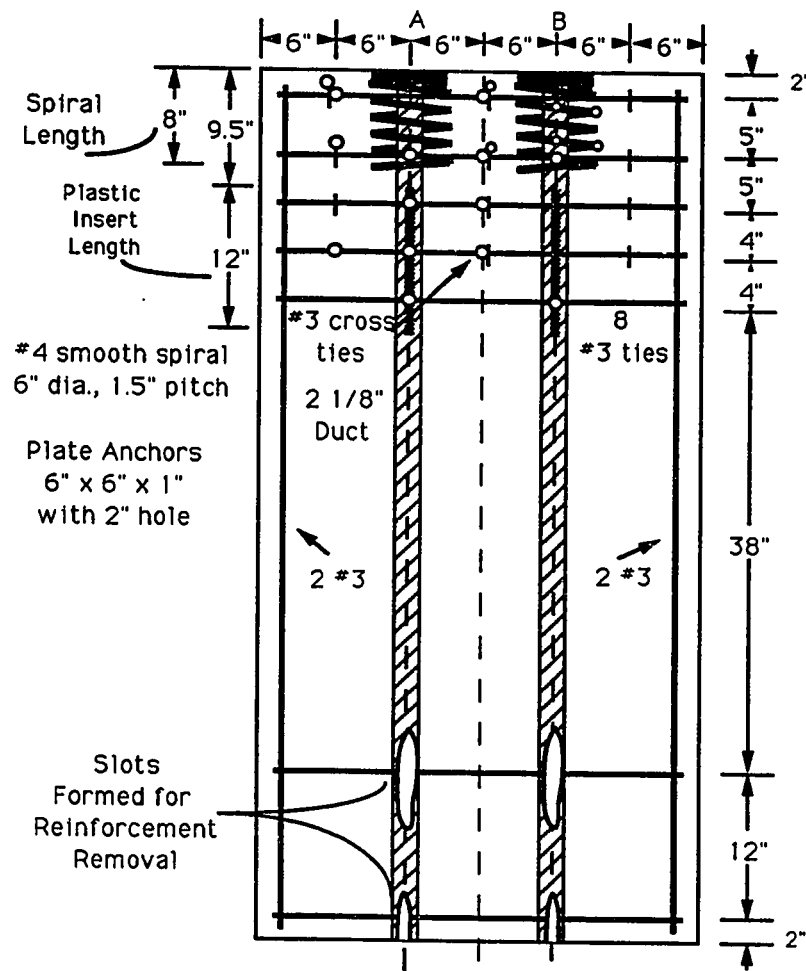


Figure 5.4 Specimen M4 Detail

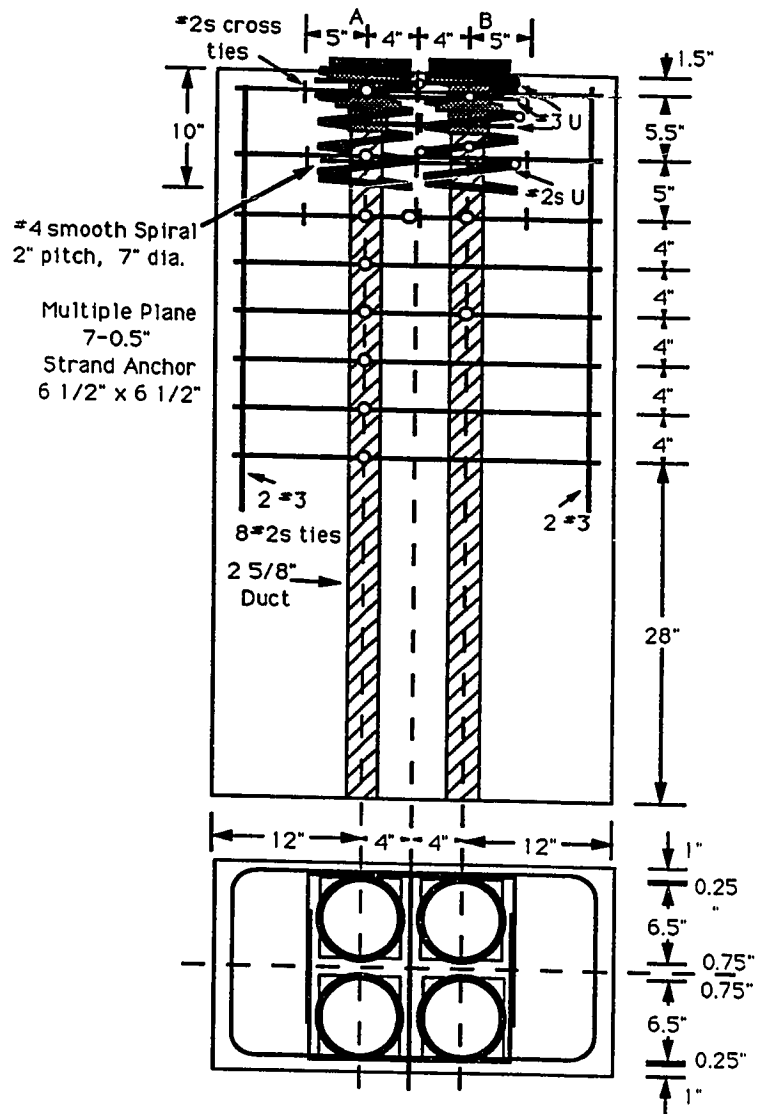
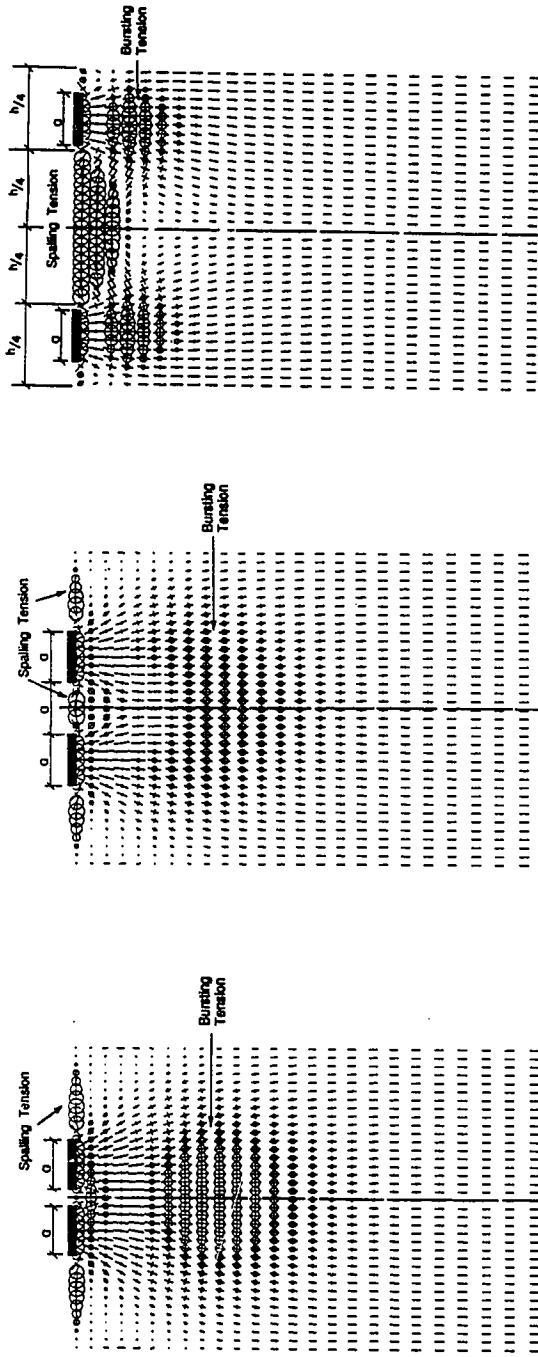


Figure 5.5 Specimen M6 Detail



a) Specimen M1

b) Specimen M2

c) Specimen M3

Figure 5.6 Principal Stresses for Specimens M1, M2 and M3

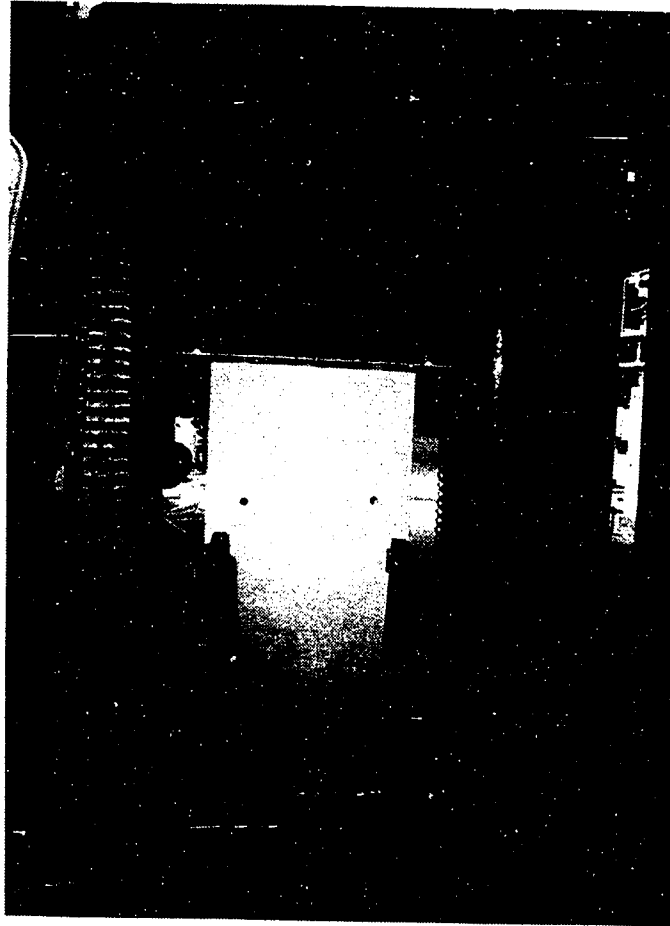


Figure 5.7 Loading Beam

Specimen M1 was reinforced with #3 ties in the general zone. Including all of the bursting reinforcement along the tendon path (except the first layer which would be in a compression stress zone) places the bursting resisting force centroid at 29.7 inches from the loading surface with a total tension capacity of 92.4 kips. In the local zone, each anchor had a #4 smooth spiral with a 6-inch diameter and a 1 1/2-inch pitch. The yield strength of the spiral was 80.3 ksi.

The modulus of elasticity was 26,900 ksi. Number 3 cross ties were placed on either side of the spiral to assist in the carrying of the transverse spreading of forces. Crack formers were placed along the tendon ducts because of concerns, at the time of casting, that the concrete tensile strength contribution across the tendon duct would increase the load capacity to the degree that the specimen could not be failed with the available testing equipment. This was later found to be an improper approach and is discussed in section 5.4. The only effect of the crack formers was to alter the first cracking load.

Table 5.1 Material Information for Specimens M1, M2, M3, M4 and M6

| Specimen | Concrete | | Reinforcing Bar | | | | |
|-----------------------|-------------------|-----------------|------------------|-------------------------|-----------------------|----------------------|-------------------------------|
| | f_{sp} (psi) | f'_c (psi) | Bar Size | E (ksi) | F_y (kips) | f_y (ksi) | Yield Strain (microstrain) |
| M1, M2, M3 M4 & M6 | - | - | #2s* #3 #4 | 28900 27500 27900 | 3.57 6.60 12.70 | 75.1 60.0 63.5 | 2600 2200 2270 |
| M1 | 441 | 5940 | | | | | |
| M2 M2P** | 497 500 | 5330 5730 | | | | | |
| M3 M3P** | 497 500 | 5330 5730 | | | | | |
| M4 M4P** | 441 511 | 5570 6620 | | | | | |
| M6 | 415 | 4750 | | | | | |

* #2s $A_s = 0.0475 \text{ in}^2$

** the suffix P indicates a retest of the specimen at a later date

The load-displacement curve for Specimen M1 is shown in Fig. 5.8. The specimen exhibited extremely linear behavior until very close to the ultimate load. The load was recorded as the total load applied to both anchorages. For comparison purposes with single anchorage tests, the cracking loads and ultimate loads are given for each anchorage while assuming equal distribution. Because of the crack formers, a determination of a first cracking load in the bursting region is not possible. Cracks formed along both tendon paths. Cracks first formed outside the crack formers at 150 kips per anchorage ahead of anchorage "B", the west anchorage. At 225 kips, the first crack away from the tendon path opened ahead of anchorage "A". It was a diagonal crack extending from the bearing plate toward the transverse face. As the load approached 300 kips, the loss in applied force after each load stage began to increase. The anchorages were loaded to approximately 300 kips four times before failure occurred after which the load per anchorage dropped to 210 kips (see Fig. 5.8). The peak load per anchorage was 304 kips.

Figure 5.9 shows the extensive cracking pattern at ultimate. The load written next to the cracks on the specimen in Fig. 5.9 was the total applied load when the crack occurred. The main load axis cracks extended deep into the section. On one side, it propagated to within 6 inches of the bottom of the specimen. On the other side, it stopped at 23 inches from the bottom. Several large diagonal cracks formed in the top half of the specimen. As the specimen was being reloaded for the second time after the attainment of the peak load, horizontal cracks formed on the transverse faces. In addition, spalling of concrete occurred near the end of the bursting reinforcement at a depth of 25 inches from the loading surface. The maximum measured crack size was 0.014 inches at 6 inches from the loading surface. Table 5.2 is a load summary for Specimen M1, M2, M3, M4, and M6.

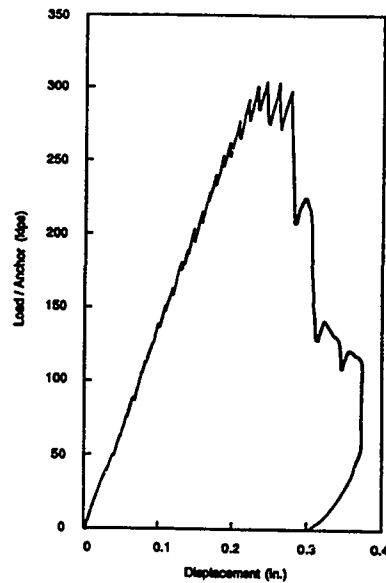


Figure 5.8 Load-Displacement Curve, Specimen M1

Table 5.2 Load Summary for Specimen M1, M2, M3, M4 and M6

| Specimen | First Crack (kips)** | | | | Peak Load** (kips) | | |
|------------|------------------------------|------------|----------|-----|--------------------|------|-------------------|
| | Bursting | | Spalling | | | | |
| | Anchor "A" | Anchor "B" | | | | | |
| M1 | Crack Formers | | | | None | | 304 |
| M2 M2P* | 225 | 250 | 213 | 238 | 265 | None | No Failure 401 |
| M3 M3P* | 113 | 188 | 150 | 200 | 88 | 75 | No Failure 364 |
| M4 M4P* | Crack Former Crack Former | | | | None None | | No Failure 411 |
| M6 | 244 | 244 | 244 | 231 | None | | 300 |

* The suffix P indicates a retest of the specimen at a later date

** All loads expressed per anchorage

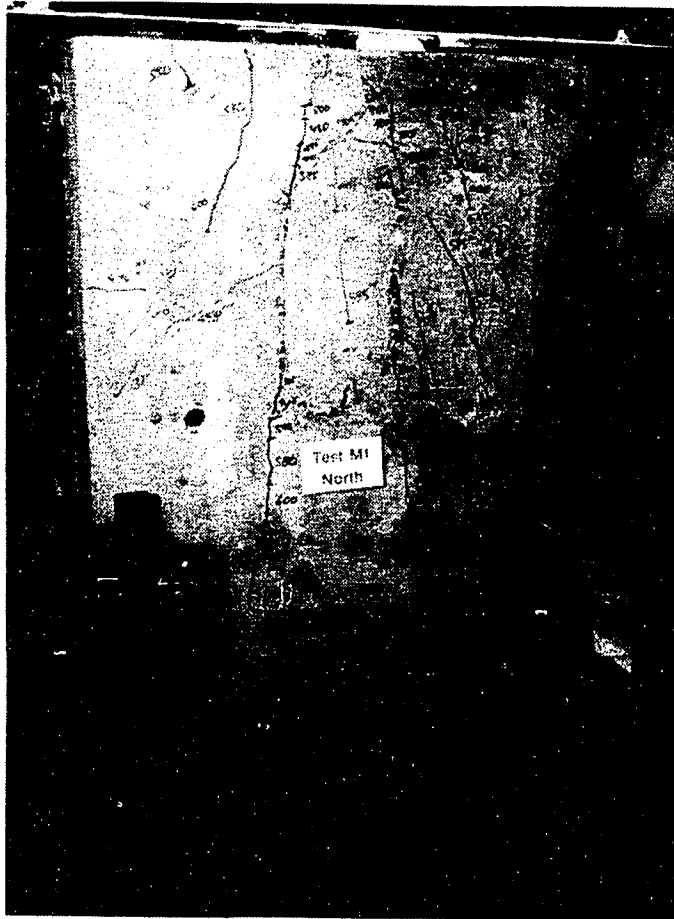


Figure 5.9 Specimen M1 Crack Pattern at Ultimate

Strain gages were placed on the bursting reinforcement along the load axis ahead of anchorage "A" (see Fig. 5.10) and along the specimen centerline (see Fig. 5.11). Because of the crack formers along the load axis, strains in the bursting reinforcement increase faster than in the single anchorage specimens. Figure 5.12 shows the bursting strain distribution along the load axis of anchorage "A" for various load stages. After the peak load, all the gages indicated a yielding of the bursting reinforcement except the last bar (26 inches), which was close to yielding, and the bar at 8 inches from the loading

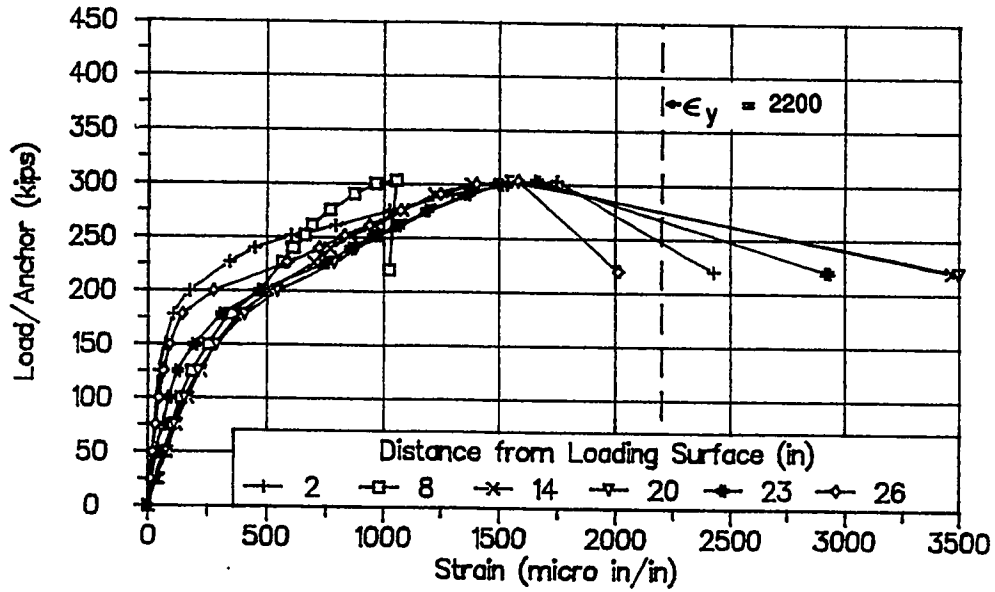


Figure 5.10 Bursting Reinforcement Strain Data, Specimen M1

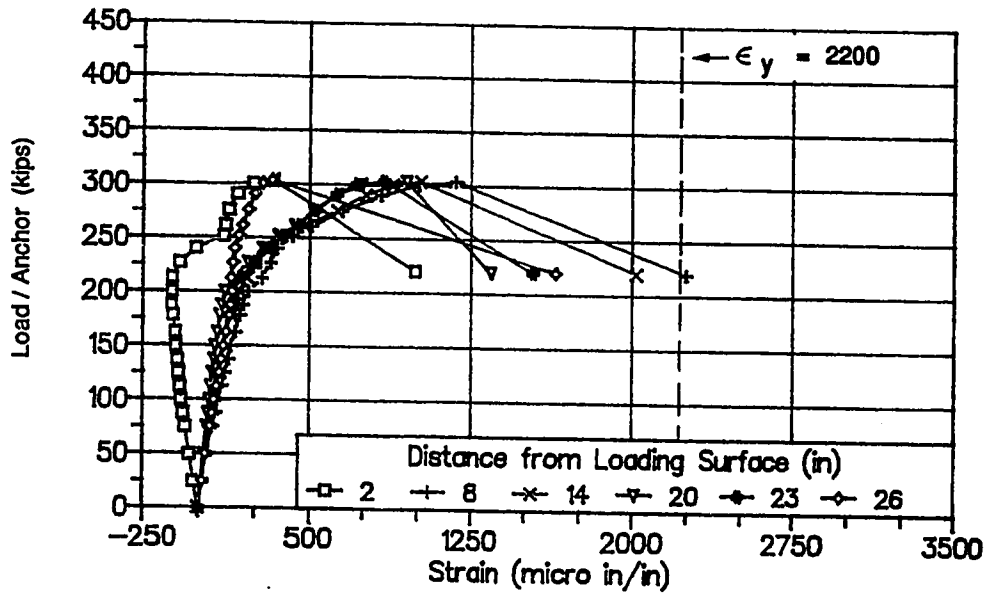


Figure 5.11 Centerline Reinforcement Strain Data, Specimen M1

surface. The bar at 8 inches from the loading surface was very close to the end of the spiral where there was a high concentration of reinforcement. Since the concrete along the specimen centerline was mostly uncracked, the strains in bursting reinforcement at the centerline shown in Fig 5.11 were lower than those along the load axis shown in Fig. 5.10. The elastic analysis shown in Fig. 5.6 indicates that the bursting force along the centerline should have been higher than those along the load axis. This discrepancy indicates how significant the concrete tensile contribution can be when the section remains uncracked. Figure 5.13 shows that the spiral strains ahead of anchorage "A" were low except for the measurement of a gage oriented in the transverse direction of the spiral near the loading surface.

Specimens M2 and M4 had the clear spacing between the anchorages equal to one plate width (see Figs. 5.2 and 5.4). Specimen M2 had #3 tie reinforcement distributed over the entire length of the specimen. This bursting reinforcement had a total tension capacity of 118.8 kips and a centroid located at 32.0 inches from the loading surface. The same local reinforcement and transverse bursting reinforcement were used as in Specimen M1. The boundary conditions were the same as in Specimen M1.

Specimen M2 was initially loaded in the 600 kip universal testing machine with the loading beam. The load-displacement curve (see Fig. 5.14) shows the linear behavior of the specimen up to 300 kips per anchor, the maximum load of the testing machine. To determine if the specimen was close to failure, the specimen was unloaded and then the load was applied back to 300 kips. Slight changes were seen in the value of the bursting strains and the crack pattern but not enough to indicate that specimen failure would soon occur. The specimen was unloaded and placed in storage until the completion of the 1,200-kip horizontal testing machine (see Fig. 4.15).

In a retest using the 1,200-kip testing machine, the specimen was then loaded to failure. Figure 5.15 shows the load-displacement curve

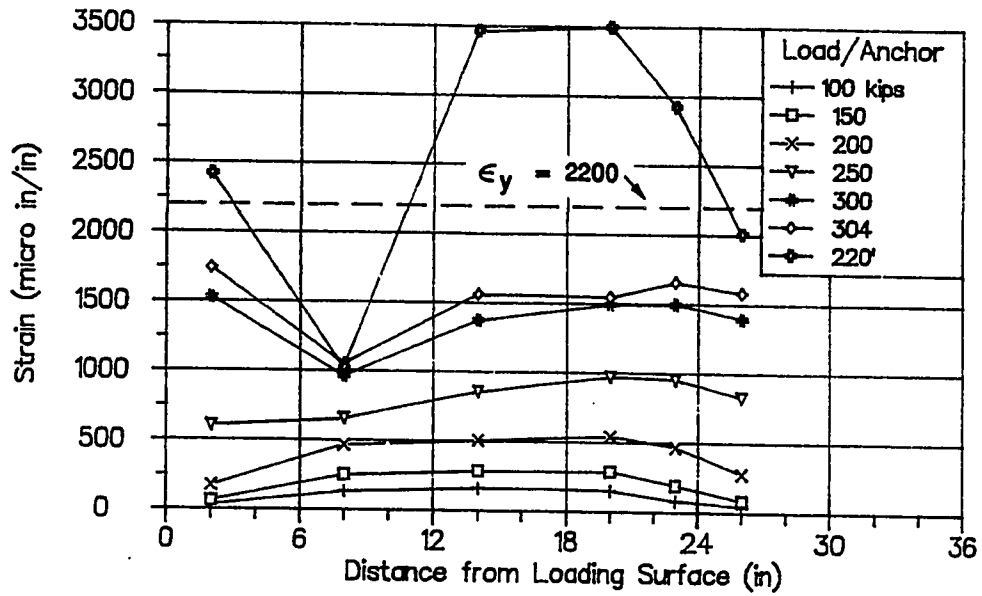


Figure 5.12 Bursting Reinforcement Strain Distribution along the Load Axis of Anchorage "A", Specimen M1

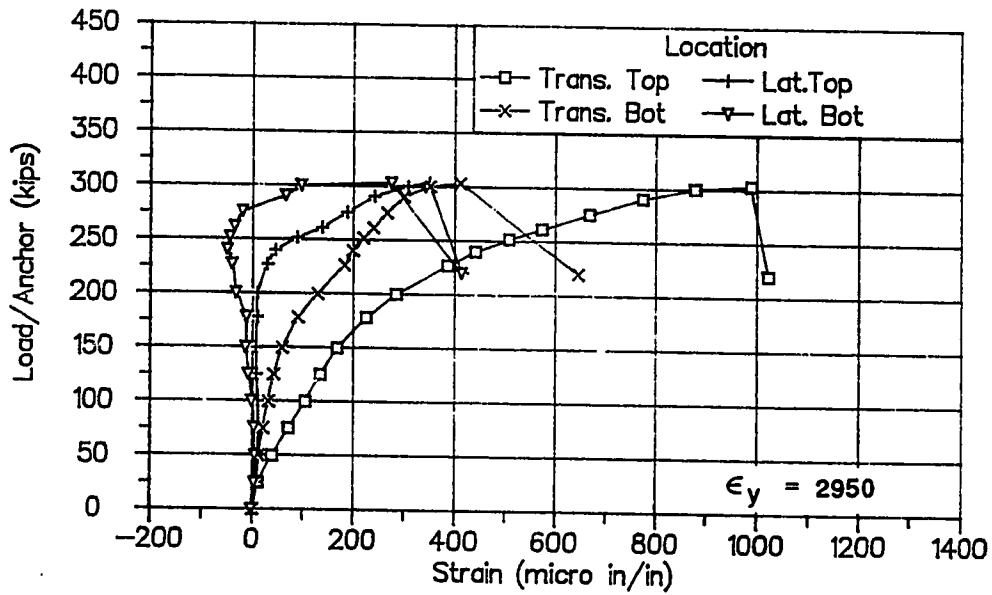


Figure 5.13 Spiral Strain Data, Specimen M1

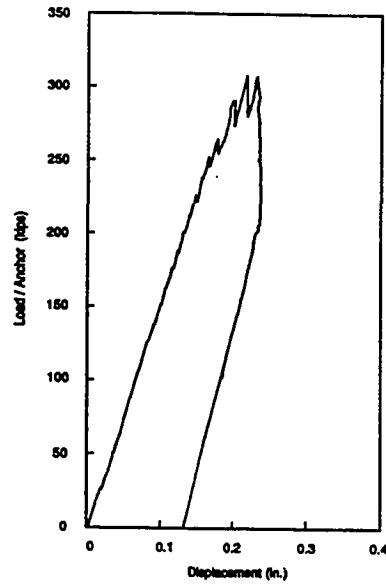


Figure 5.14 Load-Displacement Curve, First Test, Specimen M2

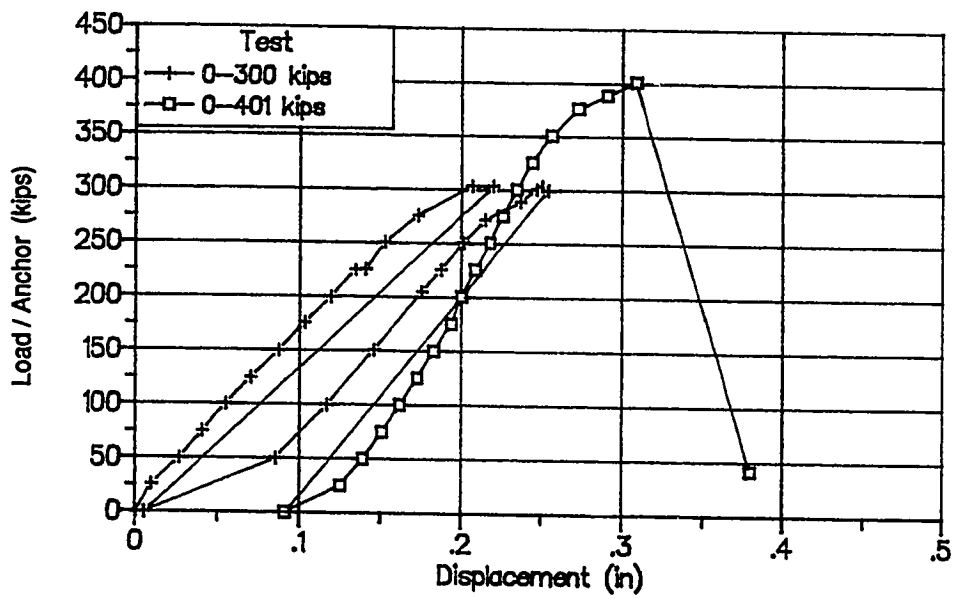


Figure 5.15 Load-Displacement Curve, Test 1 and 2, Specimen M2

for the entire test. The displacement for the test conducted in the 1,200-kip machine is the piston displacement minus the moving-block displacement. The displacement from the retest is shown in the plot as originating at the final displacement of the first test at the zero-kip load.

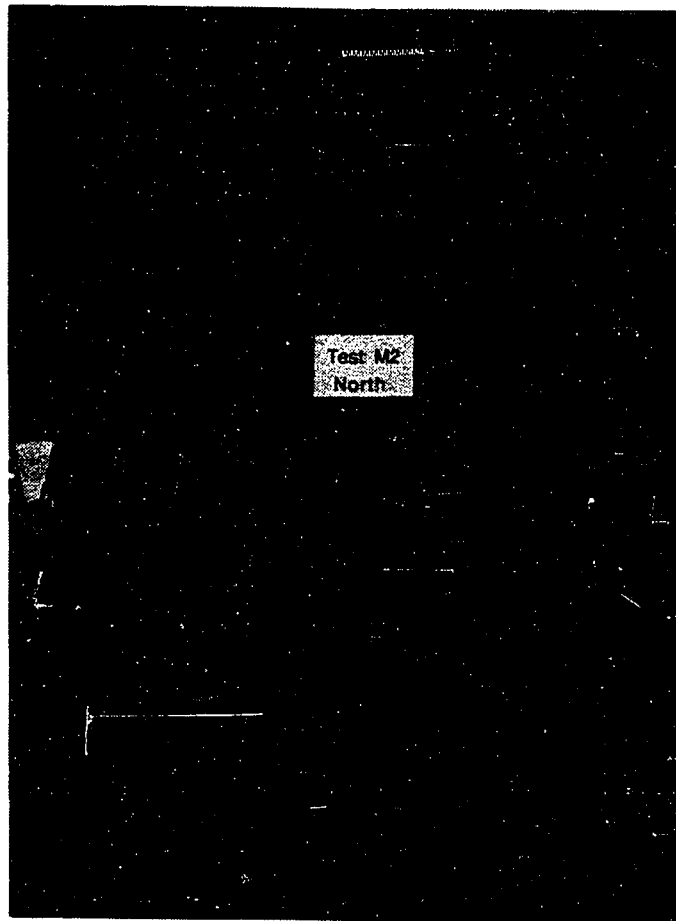


Figure 5.16 Crack Pattern at Conclusion of Test 1 Specimen M2

The first crack in Specimen M2 was at 213 kips per anchor along the west tendon axis ahead of anchorage "A". Figure 5.16 shows the cracking pattern at 300 kips. The cracks indicate a spreading of the forces away from the anchorage plates. By 250 kips, cracks had

appeared ahead of both anchorages on both sides of the specimen. A small spalling crack opened on the loading surface between the anchorage plates at 275 kips. Initial crack sizes were 0.001 to 0.003 inches. By 300 kips per anchor, the maximum crack size had grown to 0.007 inches. Figure 5.17 shows the bursting strain data for the gages ahead of anchorage "A". The strains increased significantly between 250 and 300 kips per anchor. This corresponds with the increased cracking in the bursting regions. During the unloading and reloading of the specimen, only the gage closest to the anchorage increased significantly in strain. None of the bursting reinforcement yielded.

Before the retesting of Specimen M2 in the 1,200-kip machine, an improved prediction model was used to determine the ultimate load of Specimen M2. The model determined that if the reinforcement at 46, 58 and 70 inches were effective in carrying the lateral spreading of the forces, the specimen would not fail in the general zone but in the local zone because of excessive tension tie capacity. Because of concern about the effectiveness of the bursting reinforcement deep in the section, the reinforcing bars at 46, 58, and 70 inches from the loading surface were cut. This was done by removing a 2-inch wide strip of concrete to expose the bars. The bars were then cut with a grinder. An expansive 5,000-psi cement sand mix was used to fill the concrete voids. This reduced the bursting tension capacity to 79.2 kips and shifted the centroid to 19.0 inches from the loading surface. Figure 5.18 shows the patches at the base of the specimen and the bracing system. The bracing system used steel plates with teflon sheets between the plate and the concrete to allow the specimen to move laterally but not transversely.

When the specimen was tested in the 1,200-kip machine, all the strain gages were recorded from a new zero mark. To combine the two tests, the strains at the beginning of the second test were assumed to be the same as the reading taken at the conclusion of the first test when the applied load was zero. Figure 5.19a shows the load axis

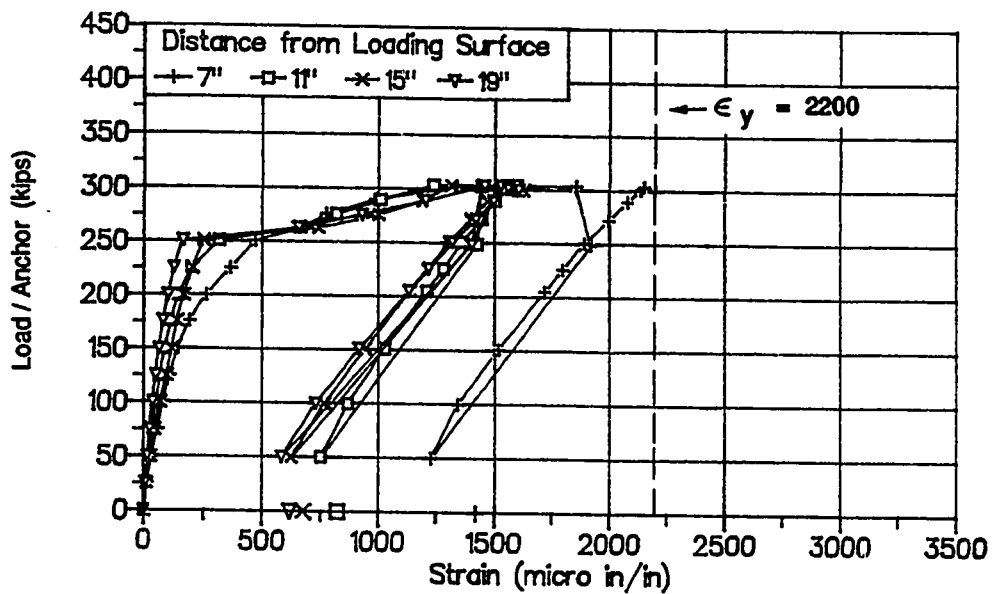


Figure 5.17 Bursting Reinforcement Strain Data for Test 1, Specimen M2

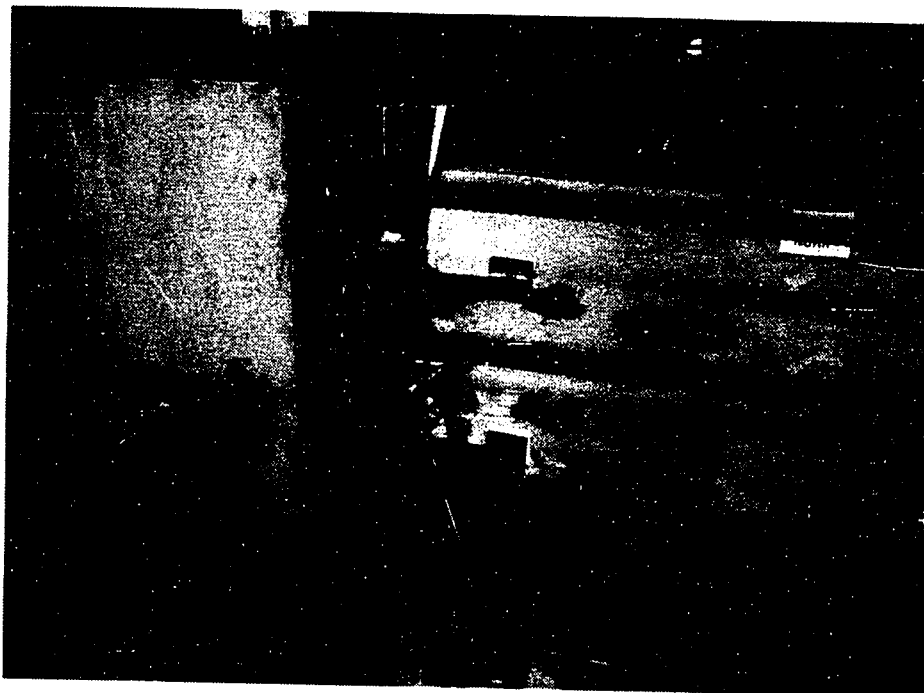


Figure 5.18 Bracing Detail and Reinforcement Removal for Specimen M2

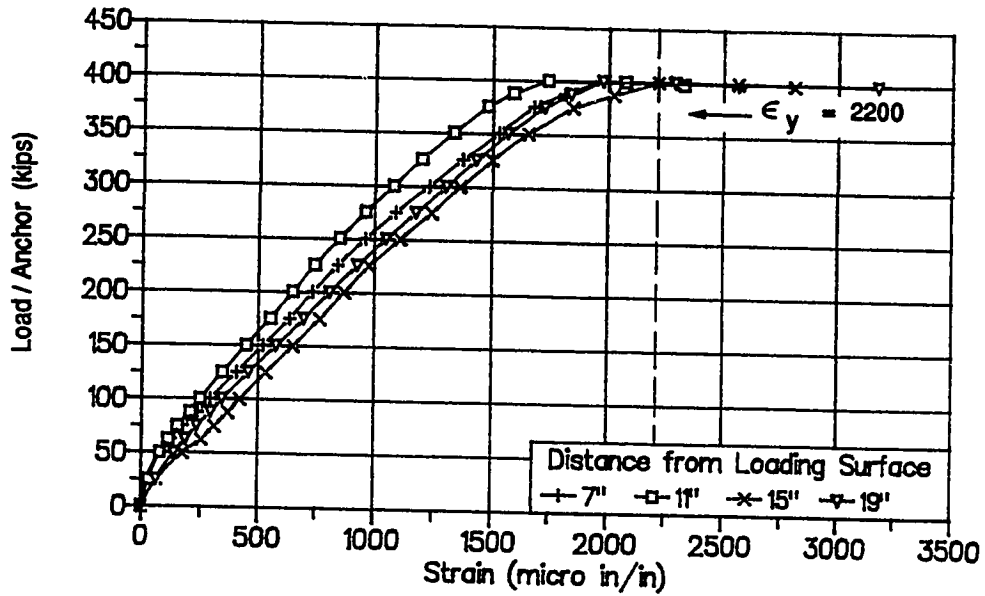


Figure 5.19a Bursting Reinforcement Strain Data, Test 2, Specimen M2

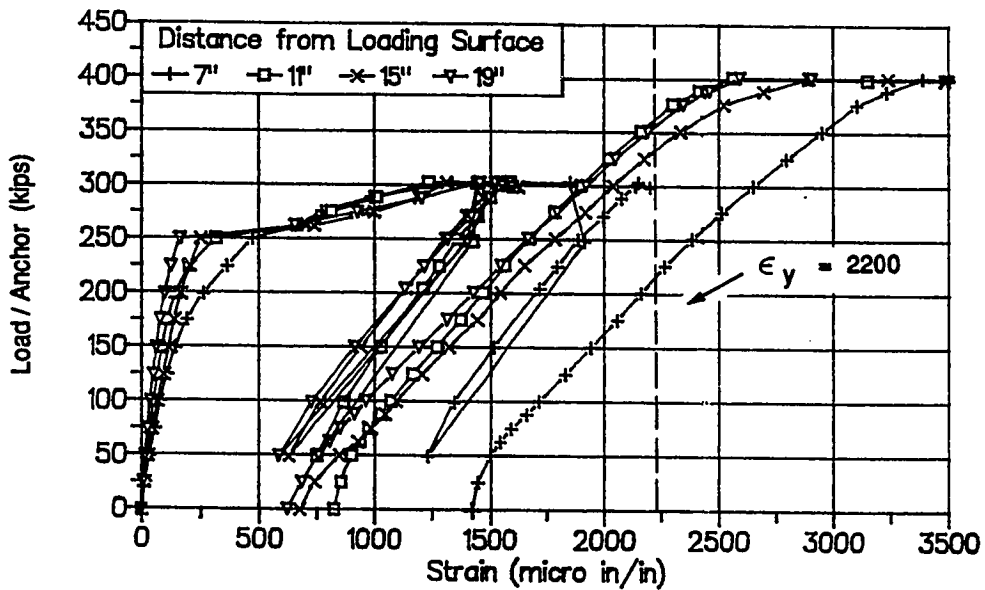


Figure 5.19b Bursting Reinforcement Strain Data, Test 1 and 2, Specimen M2

bursting strain data ahead of anchorage "A" for the retest in the 1,200-kip machine. Figure 5.19b is the same data incorporated with the data from the first test. The figure indicates that all of the bursting reinforcement within 19 inches of the loading surface yielded. The ultimate load was 401 kips per anchor, but the specimen was loaded twice to approximately 400 kips per anchor before the failure occurred. Figure 5.20 shows the cracking pattern at ultimate. There was slight crack propagation from the previous test. The deepest load axis crack was to 46 inches below the loading surface. At the failure load the loading plates were pushed approximately 1 inch into the specimen. Extensive spalling occurred in the local zone region on both sides of the specimen.

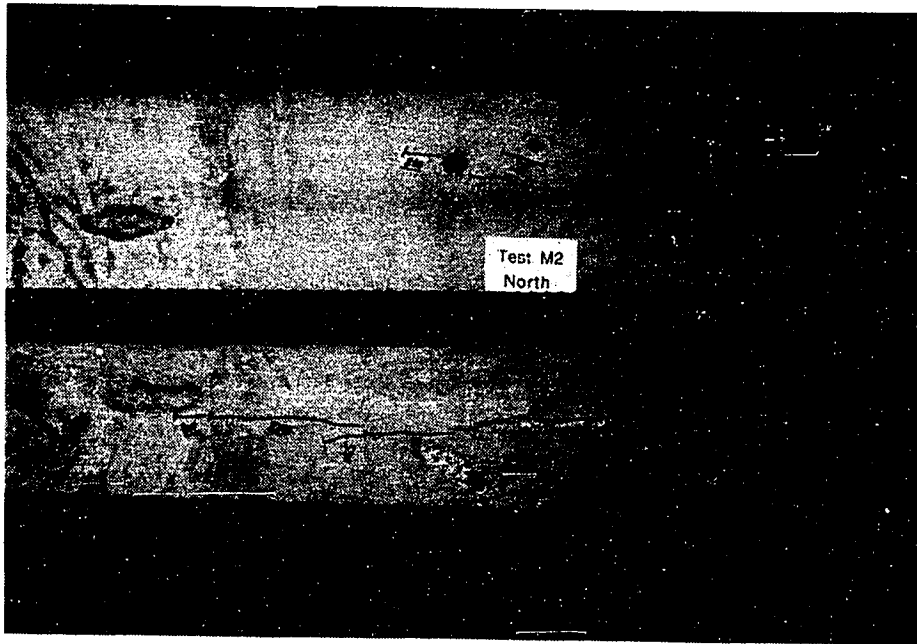


Figure 5.20 Ultimate Load Crack Pattern, Specimen M2

Specimen M4 was the companion to Specimen M2. Specimen M4 had the same anchorage configuration as Specimen M2. To reduce the ultimate capacity, two mid height bars in the bursting region were

omitted and crack formers were placed from a depth of 9 1/2 to 21 1/2 inches from the loading surface along the tendon paths. The specimen was initially tested in the 600-kip universal testing machine. The strength of the specimen exceeded the capacity of the machine. As with Specimen M2, the conclusion of the test was conducted in the 1,200-kip testing machine. When initially tested, the total bursting reinforcement capacity was 79.2 kips with a centroid of 26.1 inches. Before being retested in the 1,200-kip testing machine, the bottom two ties were cut on both sides of specimen as described for Specimen M2. This reduced the bursting reinforcement tensile capacity to 52.8 kips with a centroid of 13.8 inches.

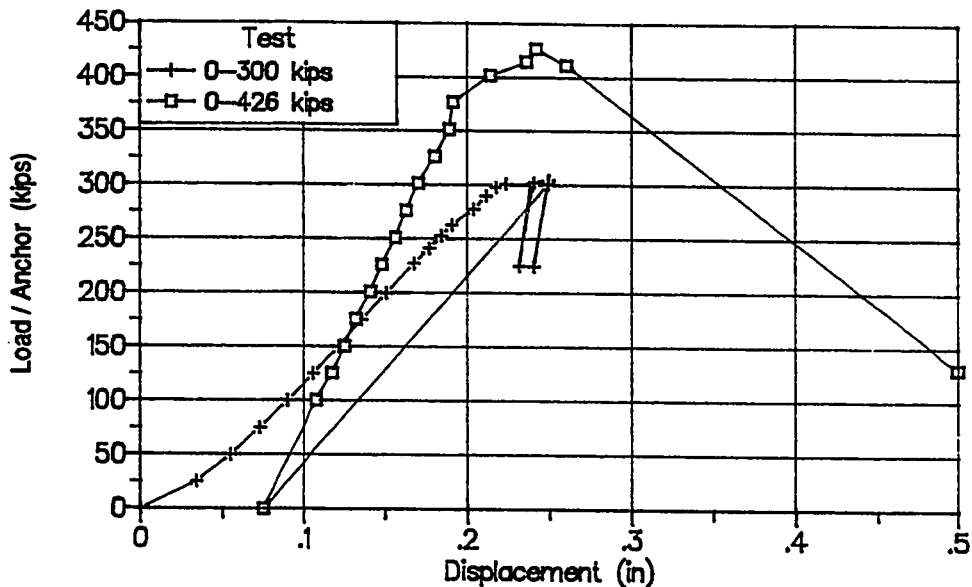


Figure 5.21 Load-Displacement Curve, Specimen M4

Figure 5.21 shows the combined load-displacement diagram from both tests. Since crack formers were used, there is no bursting first crack load. The first observed crack was along the tendon path at 125 kips per anchorage. It was located along the west tendon path beneath anchorage "B". A crack was not observed ahead of anchorage "A" until 263 kips. Figure 5.22 shows the difference between the cracking

patterns beneath each anchor at the conclusion of the first test when the maximum load was 303 kips per anchor. At the conclusion of the test, the maximum measured crack width ahead of anchorage "B" was 0.008 inches in the bursting region where reinforcement was provided and 0.031 inches where reinforcement was not provided.



Figure 5.22 Crack Pattern at Conclusion of Test 1, Specimen M4

The specimen was then loaded to ultimate in the 1,200-kip testing machine. The cracking pattern shown in Fig. 5.23 indicates a very uniform cracking pattern for the two anchors. The tendon path crack under anchorage "B" extended to within 12 inches of the base at the

ultimate load of 852 kips (426 kips per anchor). While the crack was propagating to the base, compression failure occurred underneath both anchors as shown by the spalling of concrete in Fig. 5.23. At the ultimate, load cracks formed on the transverse face at 8 inches from the loading surface. Figure 5.24a shows the strain data along the west load axis ahead of anchorage "A". Strains were very small during the first test. At the ultimate load, all the bars had yielded except those at 12 inches from the loading surface. Figure 5.24b shows the bursting strain data along the west load axis ahead of anchorage "B". During the first test, the bar at 16 inches from the plate had yielded. Measured spiral strains before the final compression failure were less than 650 microstrain.

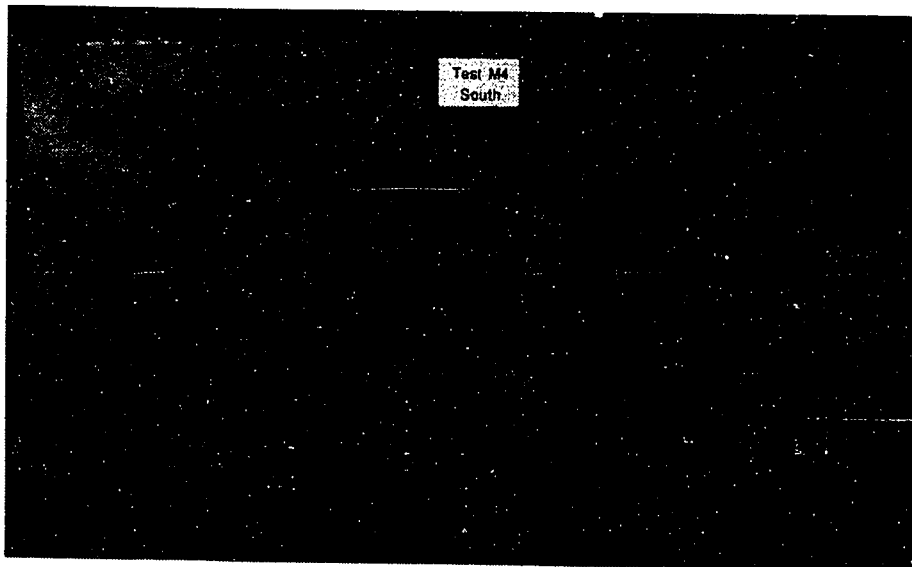


Figure 5.23 Crack Pattern at Ultimate, Specimen M4

Specimen M3 (see Fig. 5.3) had anchors placed symmetrically about the specimen centerline but outside the quarter points of the specimen. Since the anchors were outside the quarter points, it was necessary to place four #4 bars between the anchors as a tension tie to carry the spalling tension force along the loading surface. The crack caused by

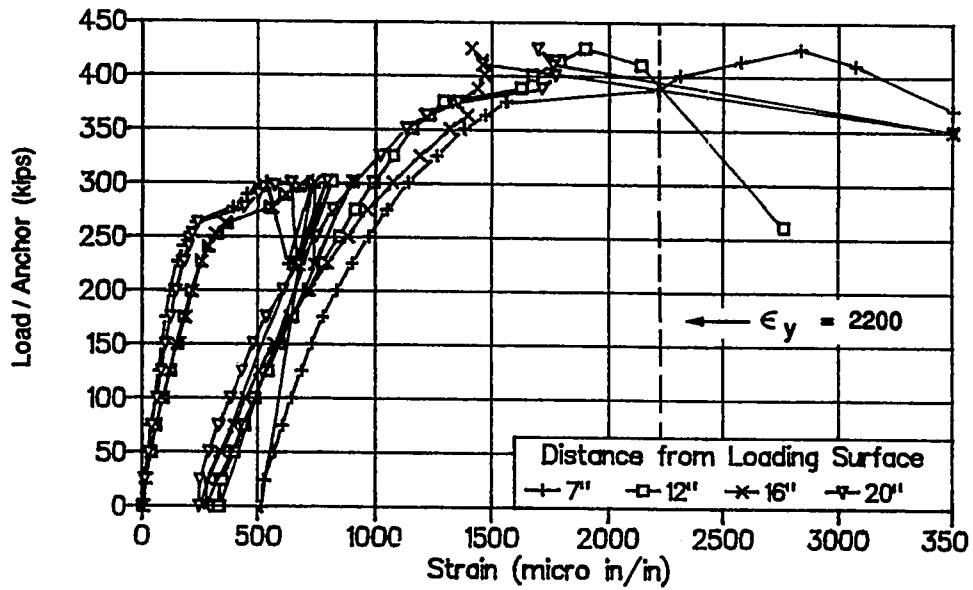


Figure 5.24a Bursting Reinforcement Strain Data along Load Axis of Anchorage "A", Specimen M4

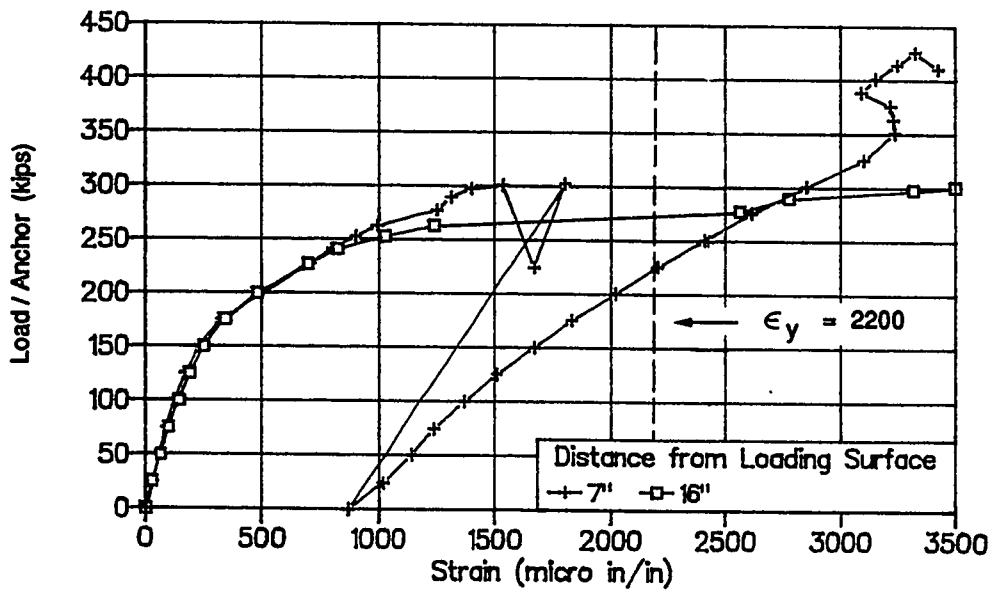


Figure 5.24b Bursting Reinforcement Strain Data along Load Axis of Anchorage "B", Specimen M4

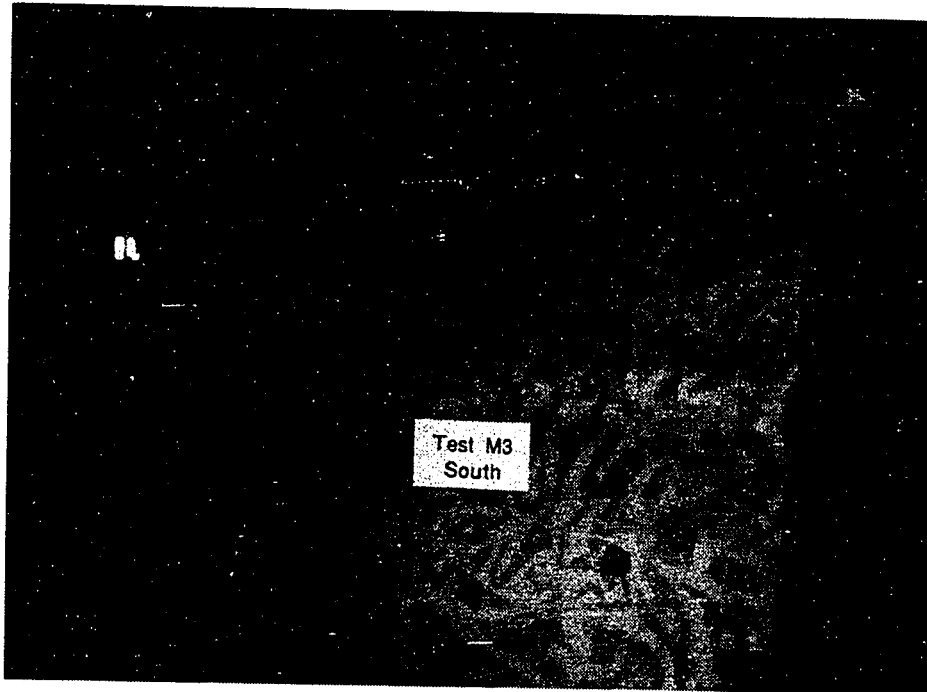


Figure 5.25 Crack Patterns at the Conclusion of Test 1, Specimen M3

the spalling tension force can be seen at the loaded surface along the centerline of the section in Fig. 5.25. The spalling crack was first seen at 75 kips per anchor and, by 300 kips per anchor, had extended into the lateral surface for 6 inches. Figure 5.25 shows the cracking pattern at the conclusion of the initial test in the 600-kip testing machine. Bursting cracks that formed ahead of the anchorages near the transverse faces were nearly vertical. Bursting cracks that were inclined toward the interior of the specimen had an angle of about five degrees from vertical. The first bursting crack did not occur until 113 kips per anchor ahead of anchorage "A". The specimen strength was once again greater than the capacity of the 600-kip testing machine. Because of the distance between the anchors, the 1,200-kip machine used for the retests of Specimens M2 and M4 could not be used. The large spacing did allow the use of post-tensioning rams and tendons to load the specimen.

Figure 5.26 is a schematic of the retest setup for Specimen M3.

Twelve tendons were placed through each tendon duct. The specimen was mounted on a load floor in the laboratory. The holes through the slab and the tunnel underneath the slab allowed the anchoring of the tendons. The rams were loaded simultaneously and evenly with two hydraulic pumps. The testing floor is 32 inches thick. This allows the dispersion of forces from the dead-end anchorage in the tunnel to occur before entering the base of the specimen. Figure 5.27 shows the load history for the specimen. During the first portion of the test the load was applied by the testing machine. In the second portion, the double ram system was used. The magnitude of the ram loads stayed very close until the concrete under the west ram (anchorage "A") failed at 364 kips. Figure 5.28 shows the final crack pattern. The spalling crack on the loaded surface propagated 10 inches into the specimen. The large interior bursting diagonal cracks propagated 20 inches from the loading surface and to within 10 inches of each other. On the transverse faces, extensive cracking occurred because of the closeness of the anchorages to the transverse surface. The final failure was a compression failure with concrete spalling and bulging ahead of the anchorage plate.

The bursting strain measurements along the load axis (see Fig. 5.29) indicated that all the bars within 15 inches of the loading surface yielding. Strain measurements along the specimen centerline indicated that reinforcement at 2 and 5 inches from the loading surface was highly effective in controlling the spalling force (see Fig. 5.30). Figure 5.31 shows the strain gage data for some of the reinforcement, four #4 and four #2s bars, effective in carrying the spalling force. All of the bars were close to yielding at the ultimate load. Gages were located on two of the #4 bars at the centerline [(0"(x), 2.75"(y), 2"(z)) and (0", 1.25", 2")] where x is the distance from the centerline, y is the distance from the centroid of the cross section, and z is the distance from the loading surface. The four #2s bars were located in two layers at 3 and 5 inches from the loading surface. The

gage at (6", 1.25", 2") was 3.5 inches from the edge of the plate and indicated the consistency of the force between the plates.

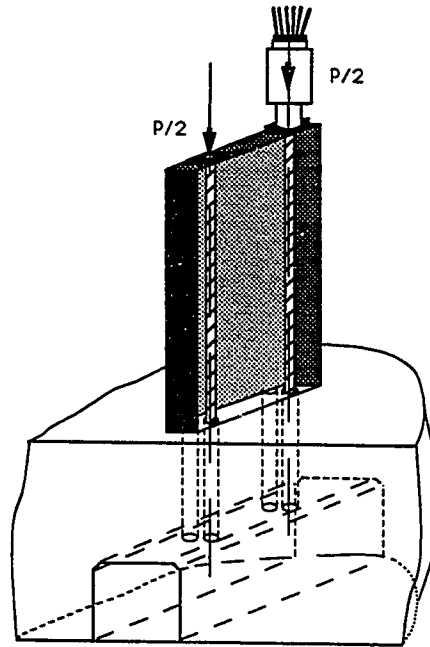


Figure 5.26 Specimen M3 Test Setup, Test 2

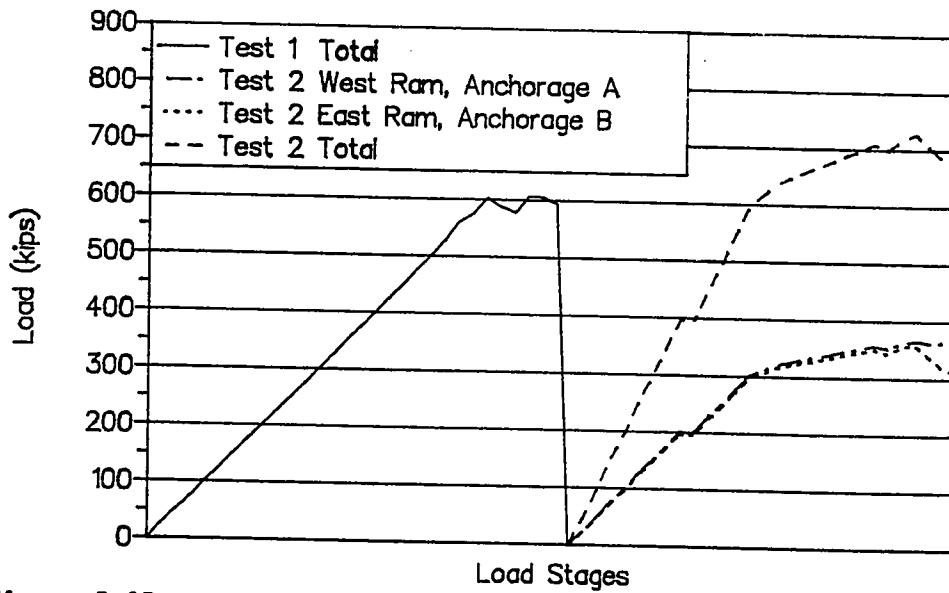


Figure 5.27 Load History Specimen M3

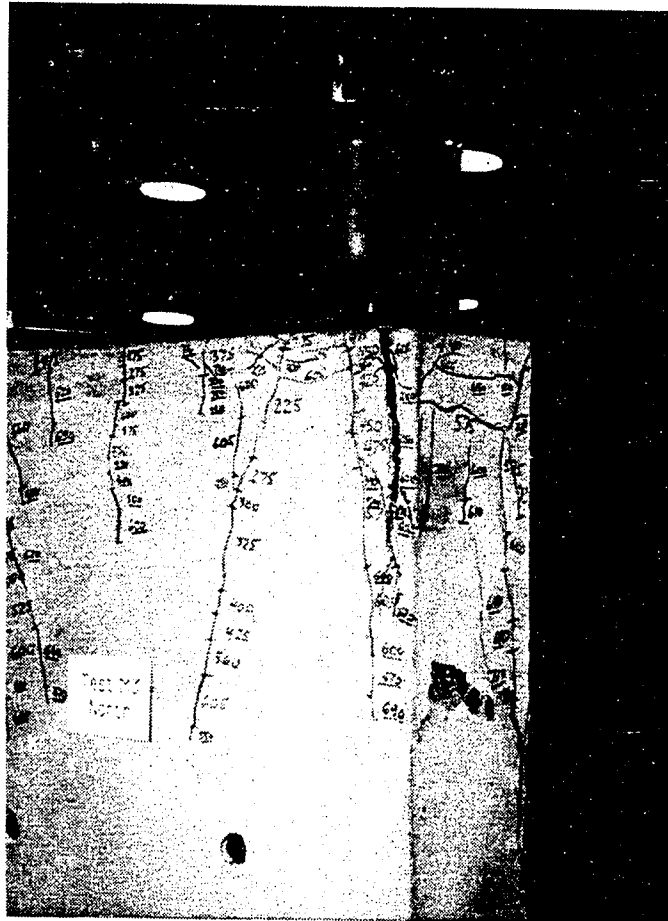


Figure 5.28 Cracking Pattern at Ultimate, Specimen M3

Specimen M6 was similar to Specimen M1 (see Fig. 5.5 and Fig. 5.1) with a very small lateral spacing, 1.5 inches, between the anchorage plates, but the section thickness was increased to permit four anchorages. The specimen was loaded in the 1,200-kip testing machine. The bursting reinforcement consisted of eight #2s ties with a total tension capacity of 50.0 kips and a centroid of 19.9 inches from the loading surface. A combination of 'U' bars and spirals was used for the local zone reinforcement. The spirals were the smooth #4 bar with 7-inch diameter and a 2-inch pitch. Number 3 and #2s 'U' bars

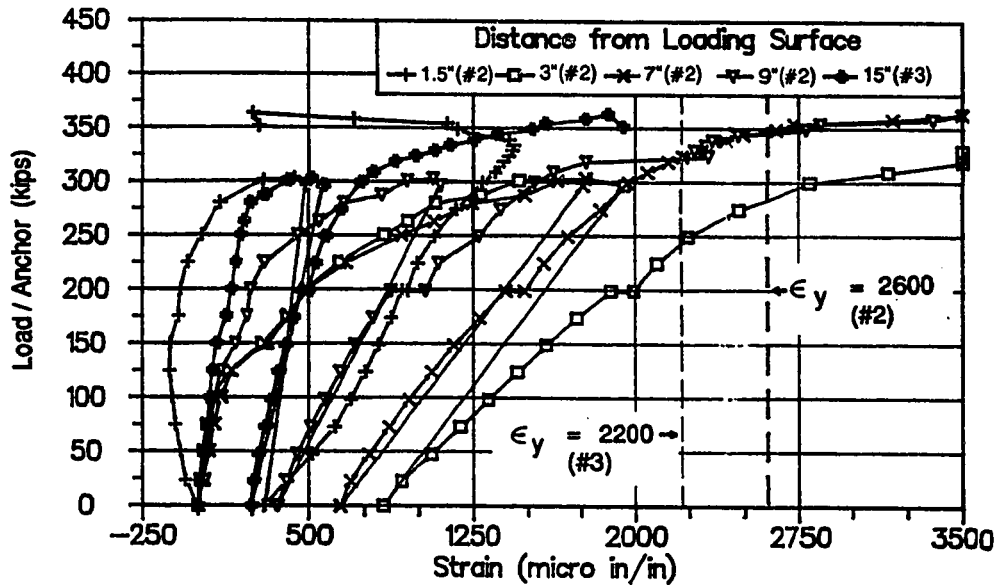


Figure 5.29 Bursting Reinforcement Strain Data, Specimen M3

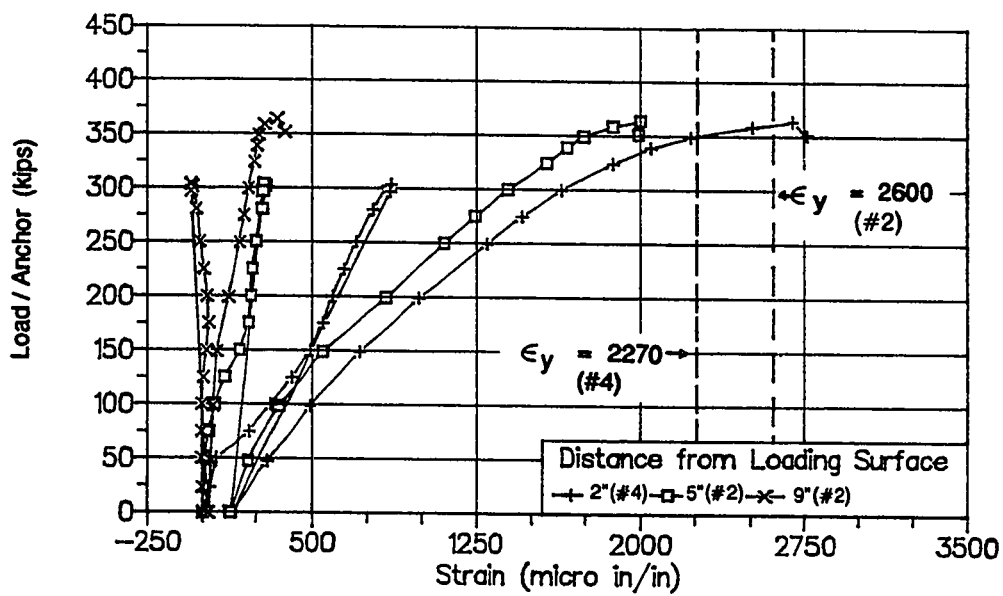


Figure 5.30 Centerline Reinforcement Strains, Specimen M3

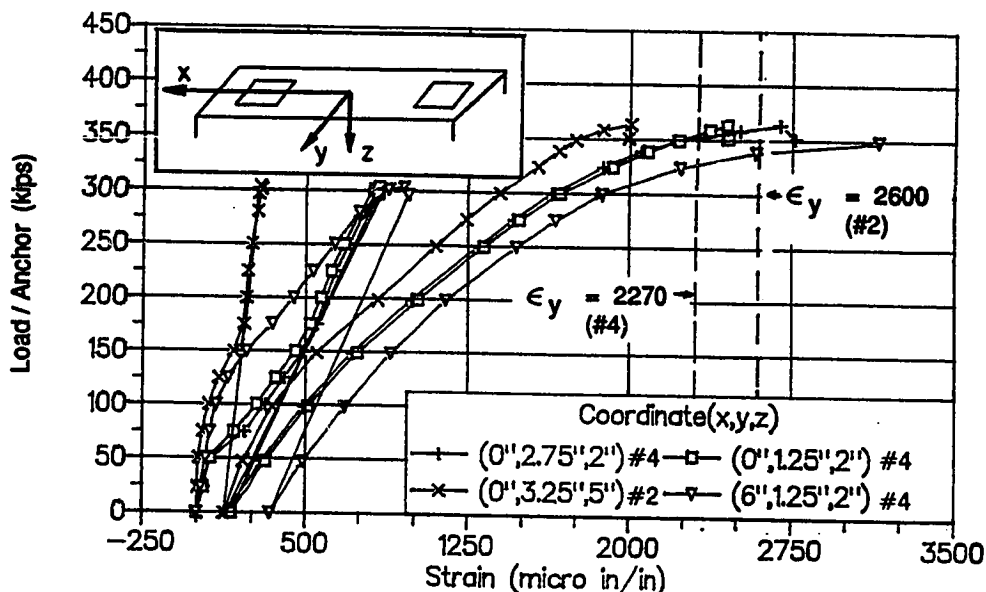


Figure 5.31 Spalling Tension Strain Data, Specimen M3

were used to join the four individual local zones by tying the four anchors together as well as providing auxiliary reinforcement because of the closeness of the anchorages to the surface.

Figure 5.32 shows the load-displacement curve for the specimen. The displacement was determined by subtracting the displacement of the movable block from the displacement of the ram piston. The load shown is the total load applied by the ram to the specimen divided by four for the number of anchors. The first crack was at 231 kips per anchor along the tendon path ahead of the "B" anchorages. At 244 kips per anchor cracks had formed ahead of all four anchors. The crack propagated to the base ahead of the two "B" anchorages. The loading was continued to 300 kips per anchor where the specimen exploded (see Figs. 5.33 and 5.34). Not only did concrete spall near the anchorage plates but also all along the tendon axes and at the base of the specimen. A horizontal crack formed on the transverse face at the ultimate load (see Fig. 5.34).

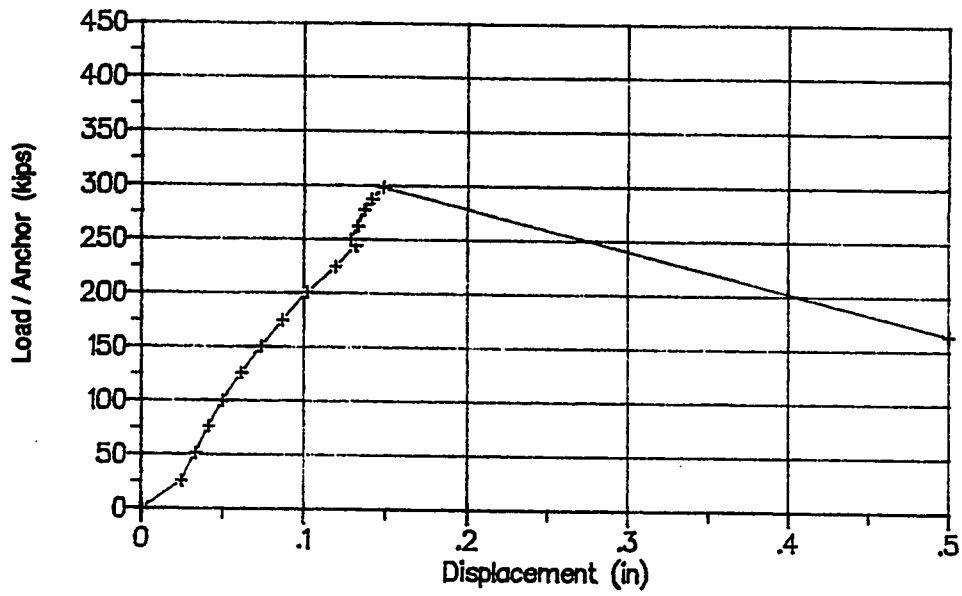


Figure 5.32 Load-Displacement Curve, Specimen M6

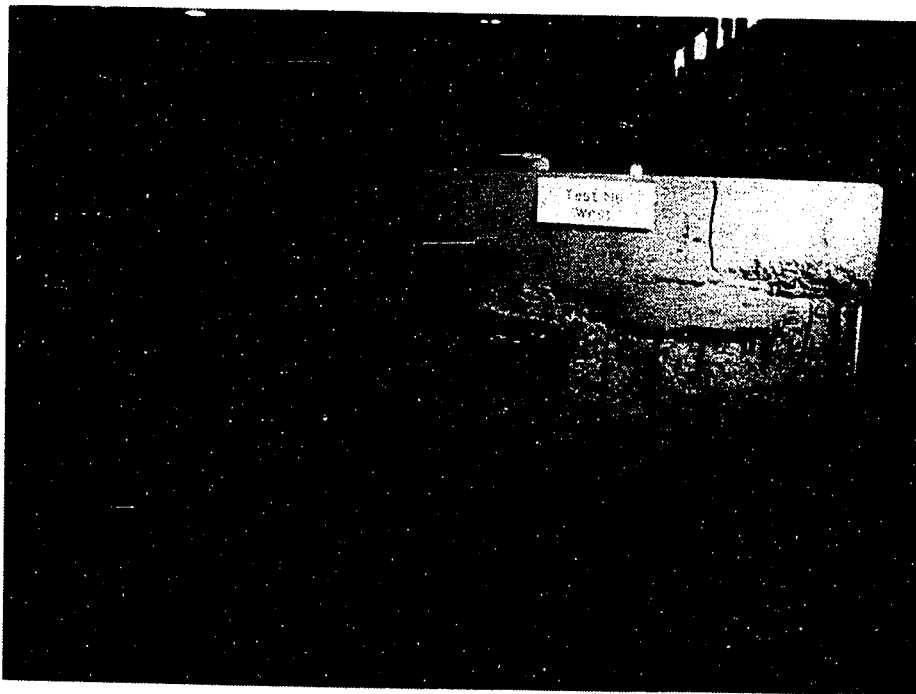


Figure 5.33 Cracking Pattern at Ultimate, West Side, Specimen M6

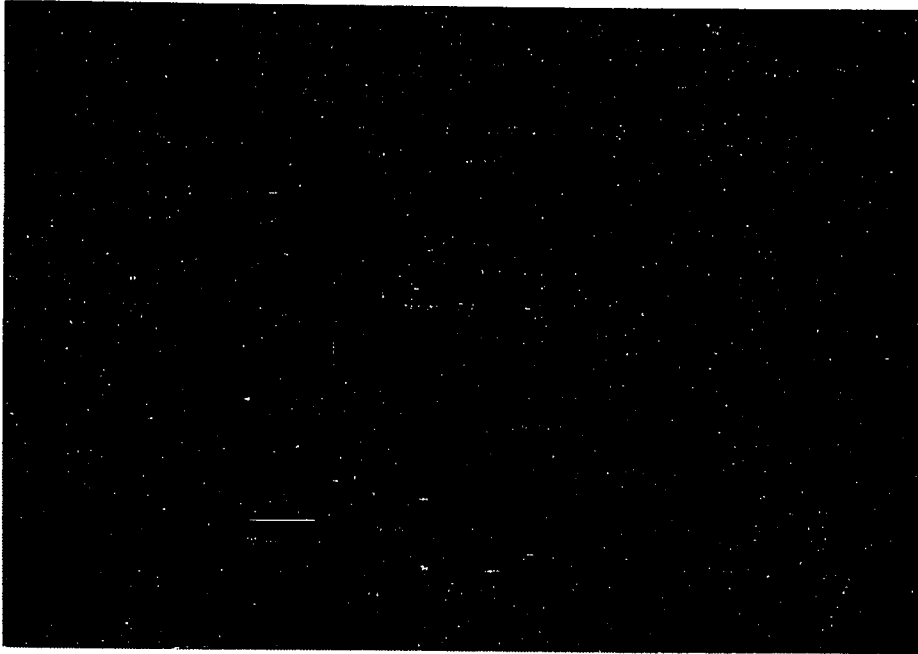


Figure 5.34 Cracking Pattern at Ultimate, East Side, Specimen M6

Figure 5.35 shows the bursting reinforcement strain data along the load axis ahead of anchorage "A". When the specimen cracked at 244 kips per anchor, the strains in the bursting reinforcement increased significantly. By 300 kips, all the bursting reinforcement had yielded except for the two bars closest to the loaded surface. All of the spiral strains were below 410 microstrain at the load stage before failure.

5.2.2 Specimens with Eccentric Load Axis. Three multiple anchorage specimens were tested which did not have the resultant load axis along the centroidal axis of the specimen. Specimen M5 was discussed previously in Chapter 4. It had two anchors located at an e/h of $1/4$. Specimen ME1 (see Fig. 5.36) had a rectangular section with one anchorage "A" located at -4 inches from the specimen centerline and the other anchorage "B" located at +12 inches. Since the anchorages were loaded simultaneously, this placed the specimen

resultant load axis at +4 inches. During the casting process, the duct at -4 inches floated upward 7/8 inches in the section, at 5 1/2 inches below the loading surface, which is just below the anchorage device. A drill bit was used to widen the passage to allow the tendon to pass through the duct. It was necessary to widen the duct down to 18 inches below the loading surface. The effect of this widening was to reduce the effective concrete width from 7 3/8 to 6 1/2 inches and to reduce the duct cover on one side of the specimen from 3 11/16 to 2 13/16 inches at the end of the anchorage device. The second specimen, Specimen F1, was a "T" section with two anchors (see Fig. 5.37). The centroid of the section was at 21.3 inches from the bottom of the web, while the resultant load axis was at 26 inches. The two anchors were loaded simultaneously and located at 22 inches, "A", and 30 inches, "B", from the bottom of the web. Bursting regions exist in both the web and the flange. Table 5.3 shows the material information for Specimens ME1 and F1.

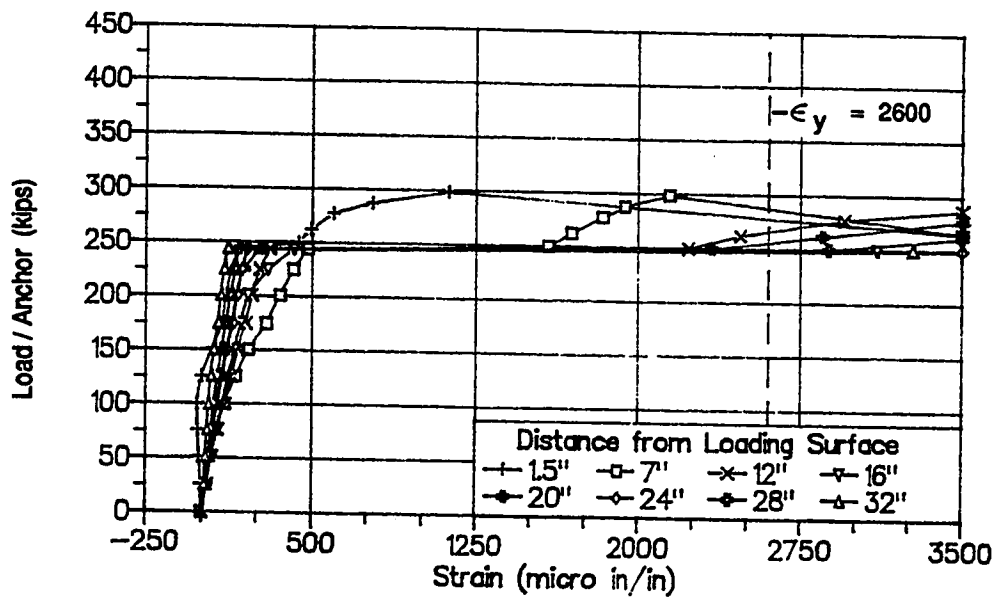


Figure 5.35 Bursting Reinforcement Strain Data, Specimen M6

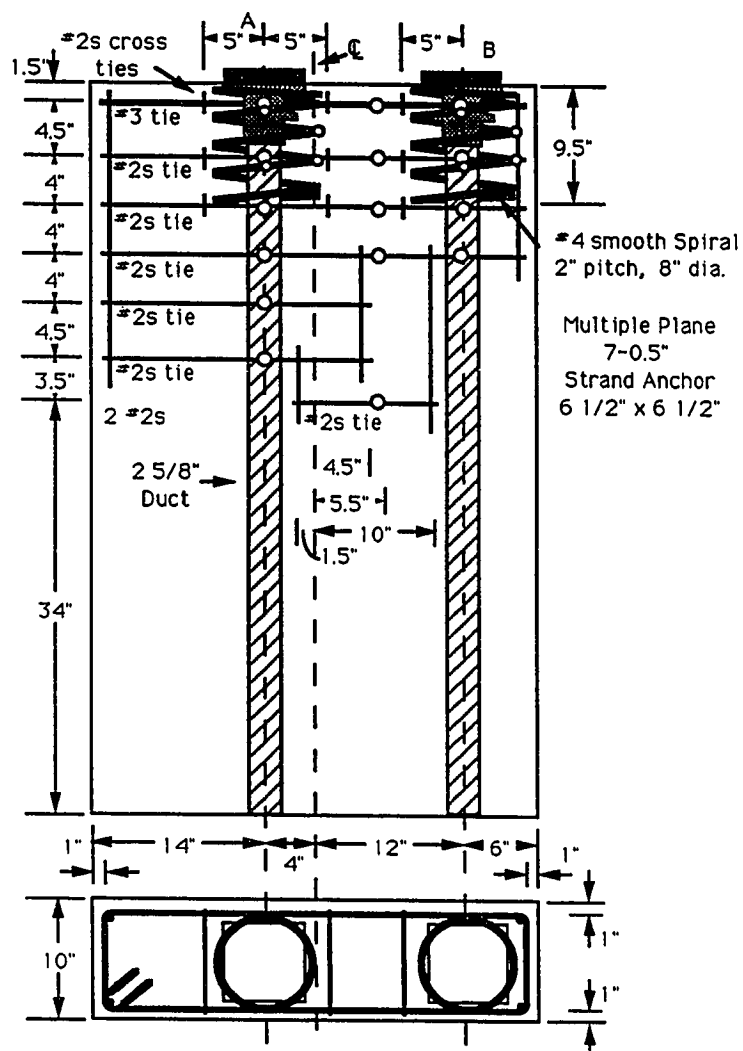


Figure 5.36 Specimen ME1 Detail

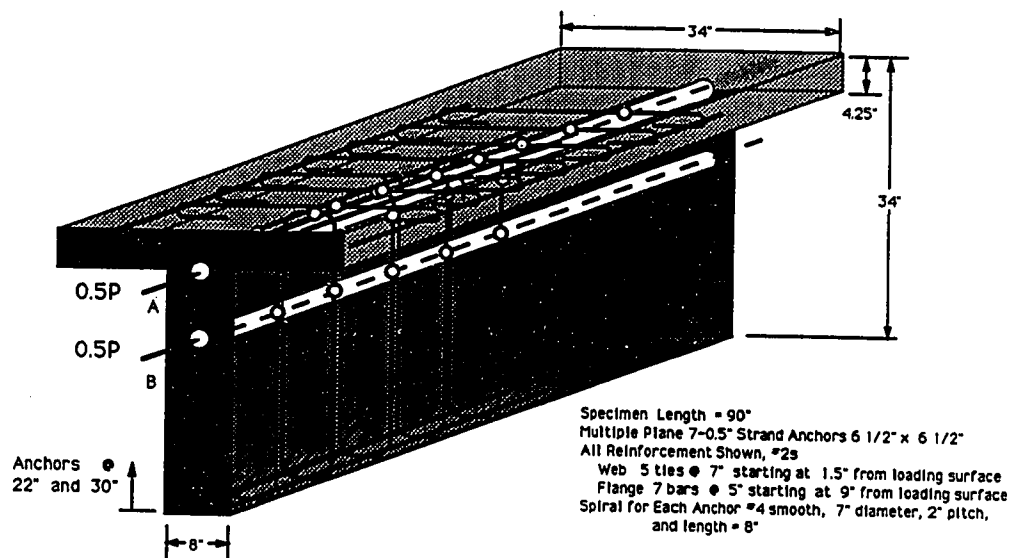


Figure 5.37 Specimen F1 Detail

Table 5.3 Material Information for Specimens ME1 and F1

| Specimen | Concrete | | Reinforcing Bar | | | | |
|-------------|-------------------|-----------------|-----------------|--------------|-----------------|----------------|-------------------------------|
| | f_{sp} (psi) | f'_c (psi) | Bar Size | E (ksi) | F_y (kips) | f_y (ksi) | Yield Strain (microstrain) |
| ME1 & F1 | - | - | #2s* | 28900 | 3.57 | 75.1 | 2600 |
| | | | #3 | 27500 | 6.60 | 60.0 | 2200 |
| ME1 | 571 | 6210 | | | | | |
| F1 | 316 | 4540 | | | | | |

* #2s $A_s = 0.0475 \text{ in}^2$

Specimen ME1 was loaded in the same way as Specimen M3. The load was applied with 12 strands in each tendon duct and 200-ton rams (see Fig. 5.38). The tendons were anchored in a tunnel 32 inches below the base of the specimen. Ahead of anchorage "A" the total bursting reinforcement capacity was 35.7 kips with a centroid at 14.1 inches

from the loading surface. Ahead of anchorage "B", the total bursting reinforcement capacity was 21.4 kips with a centroid of 10.0 inches. The first crack noted was a spalling crack along the loading surface between the anchors and ahead of anchorage "A" (see Fig. 5.39) at 175 kips per anchor. This was the side of the specimen with reduced cover over the tendon duct. Table 5.4 is a summary of the first cracking loads and the ultimate loads for Specimen ME1 and F1. The first crack ahead of anchorage "B" occurred at 210 kips. Cracks occurred on the transverse face at 300 kips near anchorage "B" due to the transverse

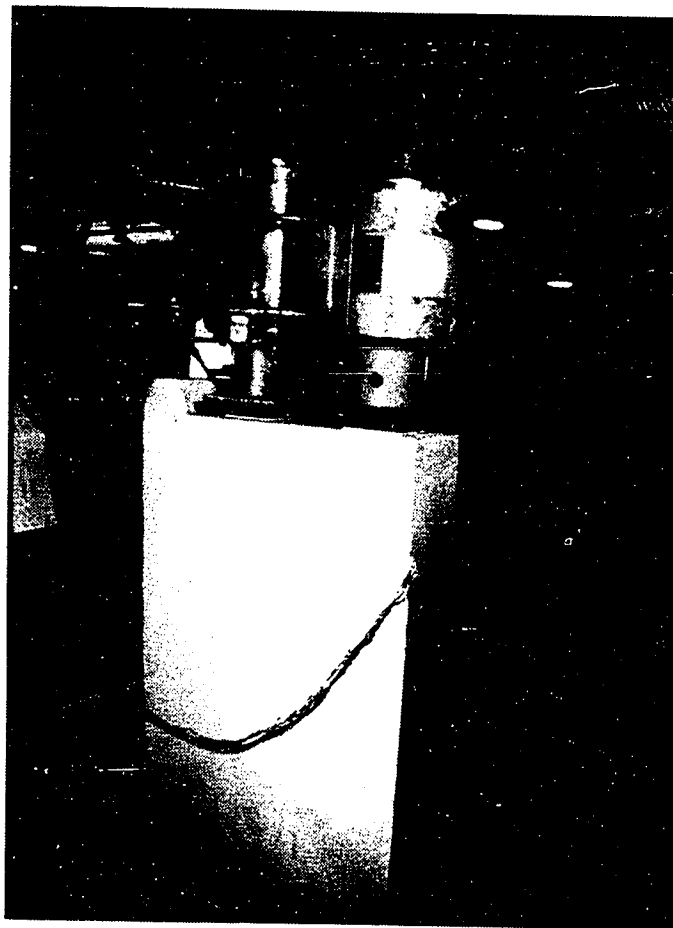


Figure 5.38 Test Setup Specimen ME1



Figure 5.39 Spalling Force Cracking, Specimen ME1

spreading of forces (see Fig. 5.40). Cracks ahead of anchorage "A" propagated to the base at 350 kips per anchor, while the cracks near anchorage "B" were still small. While marking the cracks at 350 kips, an internal cracking of concrete could be heard. The failure of the specimen occurred at 350 kips, and concrete spalled ahead of anchorage "A" (see Fig.5.41). The anchorage "A" load dropped to 107 kips, and cracks opened on the transverse face closest to anchorage "A". The load on anchorage "B" dropped slightly to 340 kips.

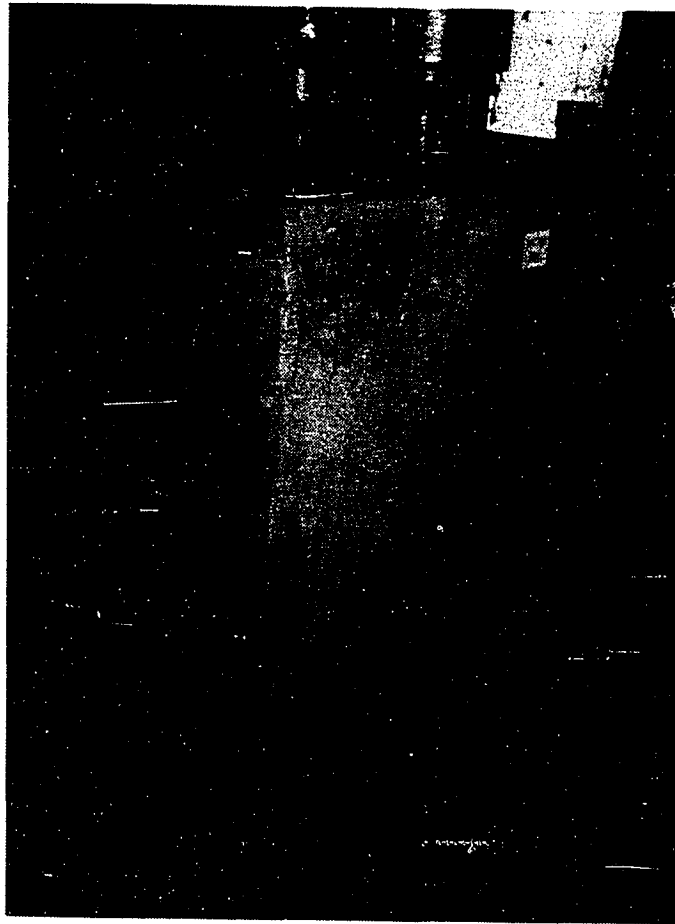


Figure 5.40 Transverse Cracking at Ultimate, Specimen ME1

Table 5.4 Load Summary for Specimen ME1 and F1

| Specimen | First Crack (kips)** | | | | Peak** Load (kips) | |
|----------|----------------------|------------|------------|-----|--------------------------|-----|
| | Bursting Web | | Anchor "B" | | | |
| | Anchor "A" | Anchor "B" | | | | |
| ME1 | 175 | 275 | 210 | 260 | 175 Spalling | 350 |
| F1 | 145 | 175 | None | | 265 Flange | 248 |

* Cracking loads for each side of the specimen

** All loads expressed per anchorage

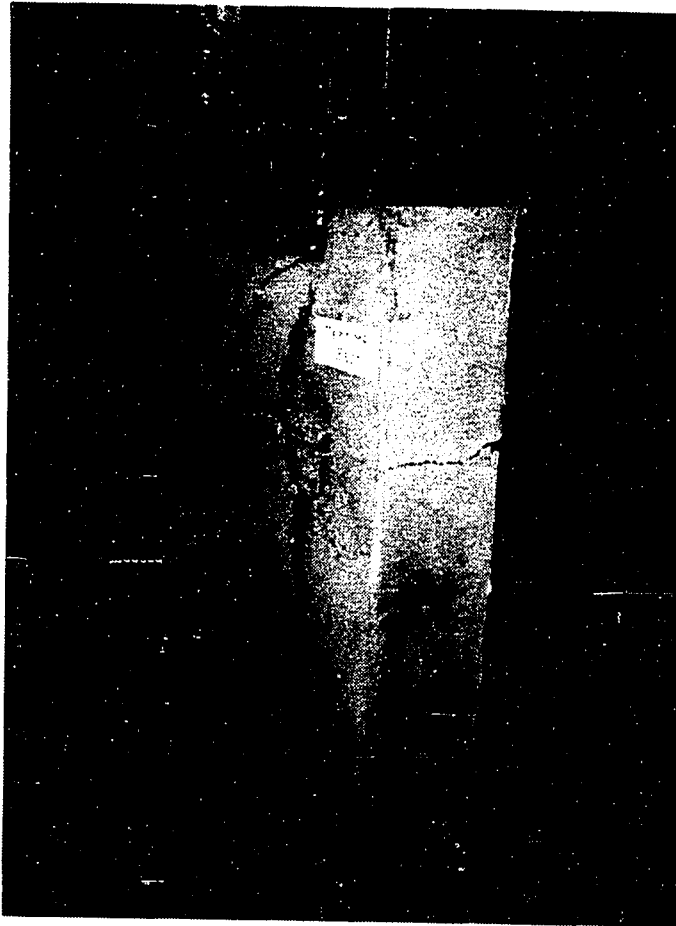


Figure 5.41 Spalling Ahead of Anchorage "A", Specimen ME1

The bursting strains underneath anchorage "A" are shown in Fig. 5.42. At the ultimate load of 350 kips per anchorage, most of the reinforcement was close to yielding. After the specimen cracked to the base, all the reinforcement along the anchorage "A" tendon axis had yielded. Strains along the anchorage "B" tendon axis were smaller and, at the ultimate load, none of the reinforcement had yielded (see Fig. 5.43). The gages on the bars resisting the spalling force between the anchors showed small strains except for the gage at 1 1/2 inches below the loading surface (see Fig. 5.44). The maximum spalling strain

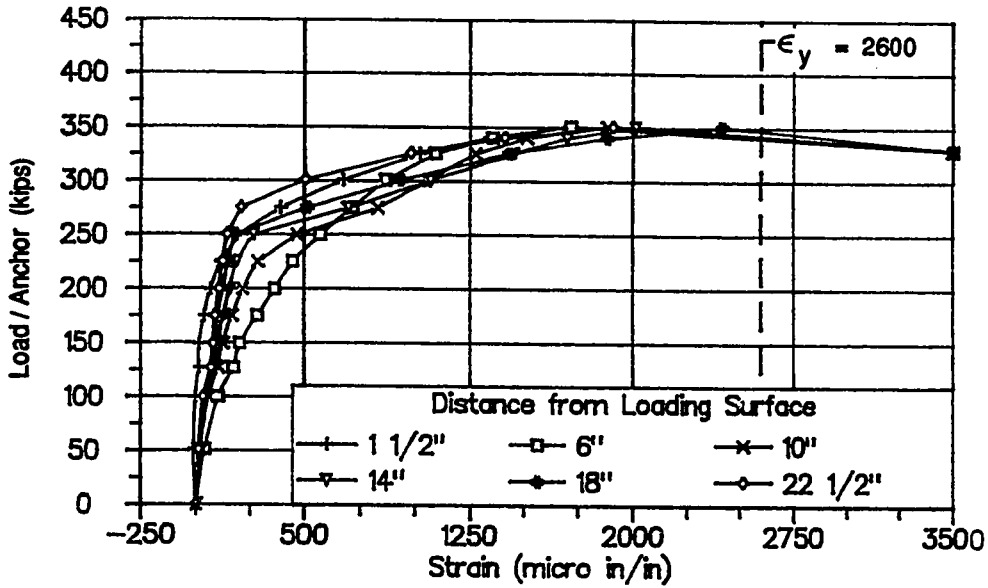


Figure 5.42 Bursting Reinforcement Strain Data along Load Axis of Anchorage "A", Specimen ME1

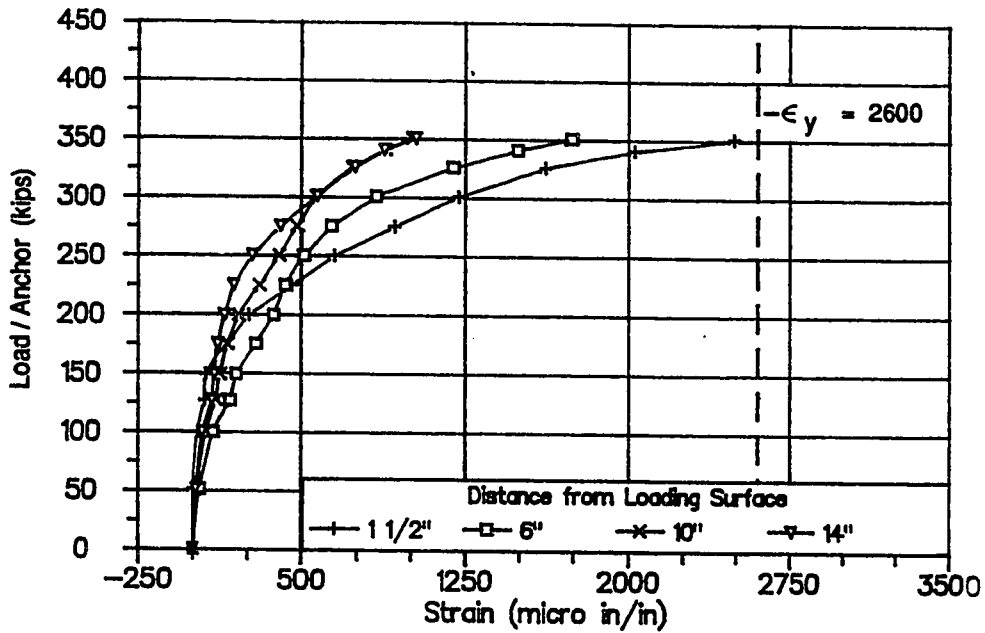


Figure 5.43 Bursting Reinforcement Strain Data along Load Axis of Anchorage "B", Specimen ME1

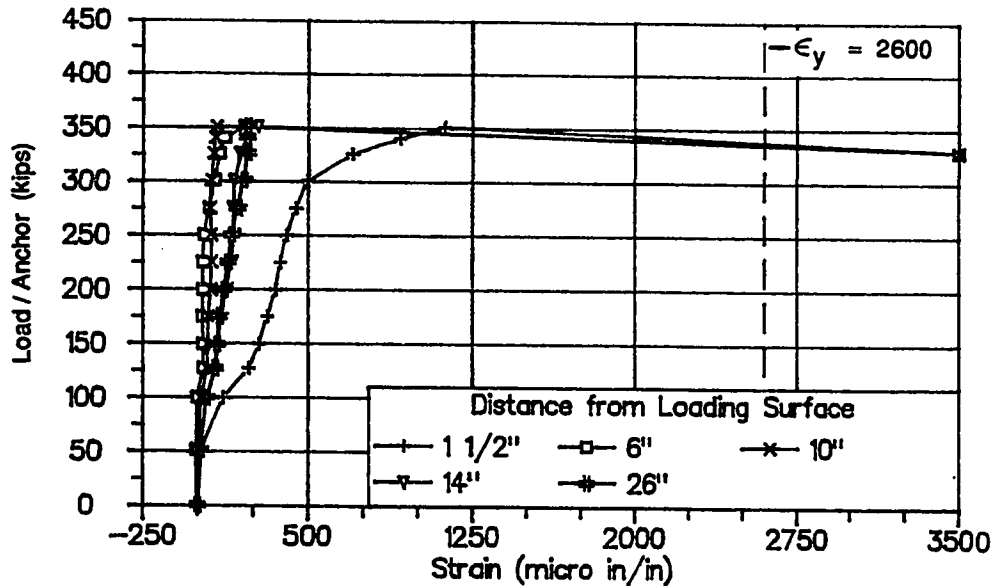


Figure 5.44 Spalling Reinforcement Strain Data, Specimen ME1

reached 1010 microstrain before failure occurred at 350 kips per anchor. The spalling force resisted by the reinforcement was 6.11 kips at an axial load of 350 kips per anchor or 0.87 percent of the total load (700 kips). The largest spiral strain ahead of the anchorage "A" was 340 microstrain. Ahead of anchorage "B", the largest spiral strain was 190 microstrain except for a gage oriented in the transverse direction near the transverse surface which reached 730 microstrain.

Since there was still reserve capacity in anchorage "B" after the failure, it was decided to retest anchorage "B" without load on anchorage "A". The load applied to anchorage "B" was dropped to 200 kips, and the load applied to anchorage "A" was removed. The load was then increased on anchorage "B" until it failed at 350 kips. When the bursting crack ahead of anchorage "B" shot to the base at 350 kips, the bursting reinforcement yielded and then the specimen below anchorage "B" exploded (see Fig. 5.45). This demonstrates the importance of distributing reinforcement along the entire length of the general zone

to prevent catastrophic failures. For the design load, the bursting reinforcement near the anchorage was all that was needed. Since there was no reinforcement across the duct below 14 inches from the anchor, there was nothing to stop the crack from widening when it propagated to the base; therefore, the specimen exploded.



Figure 5.45 Cracking Pattern at Ultimate Load of Test 2, Specimen ME1 (Only Anchorage "B" Loaded)

Specimen F1 (see Fig. 5.37) was the only specimen tested which did not have a rectangular cross section. The specimen was loaded with simultaneous load being applied to the two loading plates. According

to the elastic analysis, 54 percent of the total load would be resisted by the flange. Closed reinforcing ties were used in the web, and single tie bars with 180 degree hooks were used in the flange. The flange bursting reinforcement had a tension capacity of 25.0 kips and a centroid of 24 inches from the loading surface. The web bursting reinforcement had a tension capacity of 28.6 kips and a centroid of 19.0 inches from the loading surface. The first three ties in the web were closed hoops that extended into the flange (see Fig. 5.46). The last two ties were open ended in the flange and anchored with 135 degree hooks. In addition to gages on the bursting reinforcement along each tendon path, concrete gages were placed on the surface of the flange (see Fig. 5.46) to study the compressive stress distribution. The specimen was tested against a concrete reaction wall and placed on roller supports (see Fig. 5.47). There was not enough room to put the jacking rams on the same end of the specimen, because the anchorages were only 8 inches apart. Therefore, the live end for tendon "A" was on the specimen end, and the live end for tendon "B" was against the reaction wall as shown in Fig. 5.47b. Additional plates were placed between the wedge plate and the anchorage plate to ensure a uniform distribution on the anchorage plates.

Figure 5.48 shows the load-displacement curves for both anchorages "A" and "B". Anchorage "B" shows a larger displacement because all of its load was carried by the thin flange member which is half as thick as the web. The first flange crack occurred at the flange-web interface at 145 kips per anchor (see Fig. 5.49). The first crack occurred in the flange at 265 kips. The crack in the flange propagated from the center of the plate toward the 4.25-inch thick portion of the flange (see Fig. 5.50). The concrete gages nearest the centerline of the flange were 3 inches from the centerline. The distance from the centerline to the edge of the web was 4 inches. The second line of concrete gages in Fig. 5.50 were 8 1/2 inches from the centerline. At 248 kips per anchor, the flange crack propagated to the

end of the specimen. As measurements were being taken, an internal cracking of concrete could be heard. The concrete near the anchorage plate then exploded. Concrete flew up into the air and came back down on the specimen (see Fig. 5.51). At the conclusion of the test students in the laboratory reported hearing two explosions at the time of failure. The order of failure was that the flange crack propagated to the base of the specimen, then a compression failure occurred ahead of anchorage "B", which was quickly followed by a compression failure ahead of anchorage "A" (see Fig. 5.52). No bursting cracks had been seen in front of anchorage "B" before the failure load. The crack marked in Fig. 5.52 ahead of the anchorage occurred during the failure load. Extensive cracking was observed in the flange near the outside edge of the flange and perpendicular to the tendon path (see Fig. 5.52).

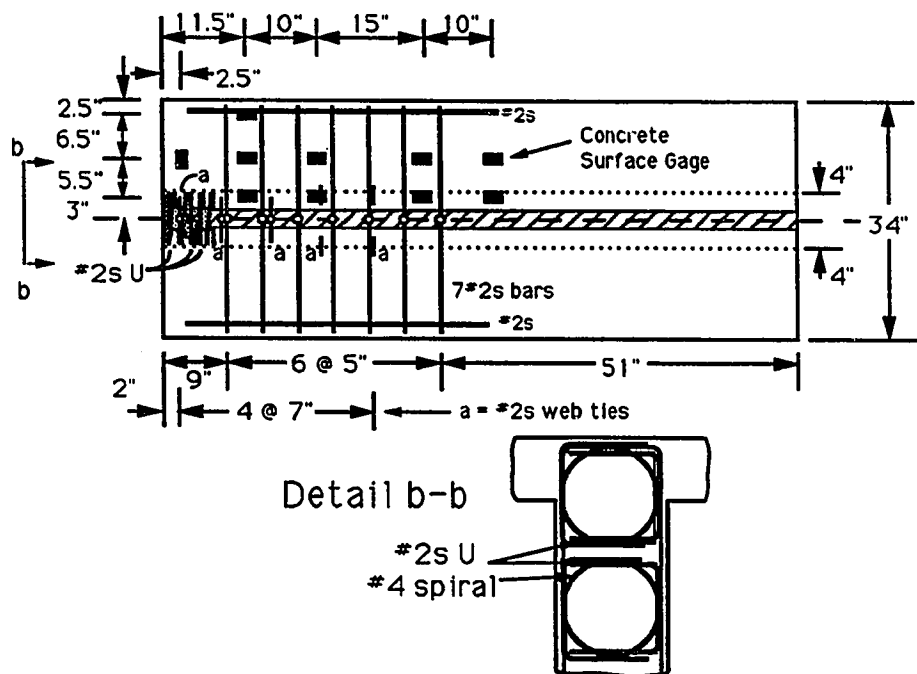
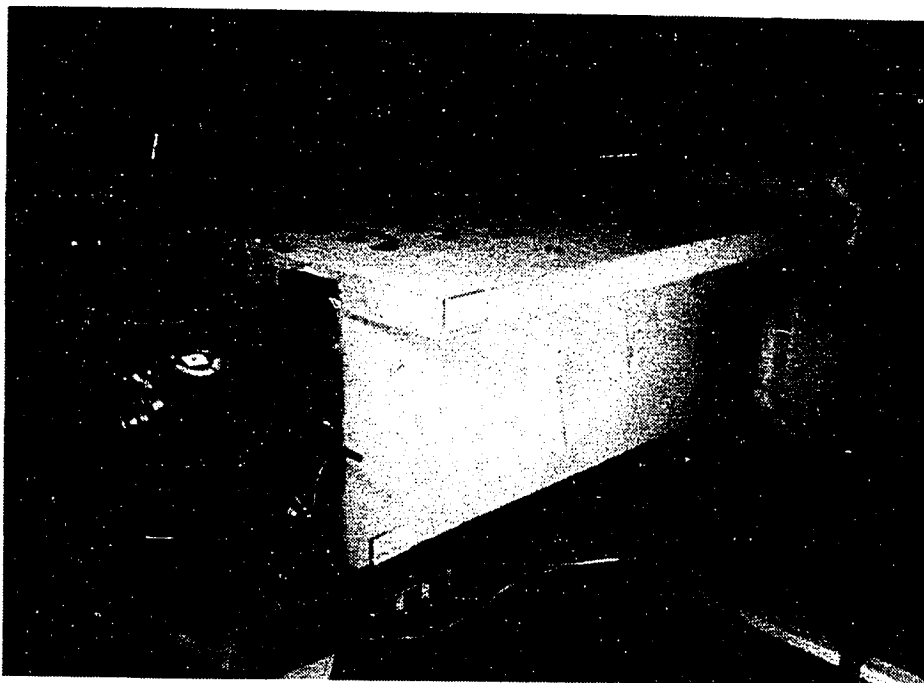
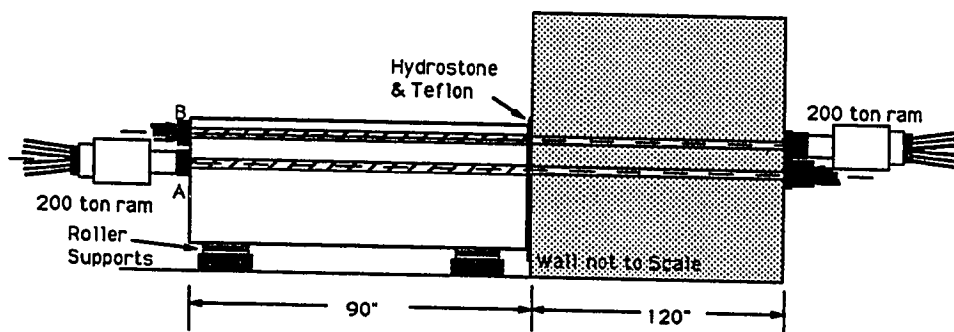


Figure 5.46 Flange Reinforcement and Locations of Concrete Gages, Specimen F1



a) Specimen Photo



b) Test Setup Schematic

Figure 5.47 Test Setup for Specimen F1

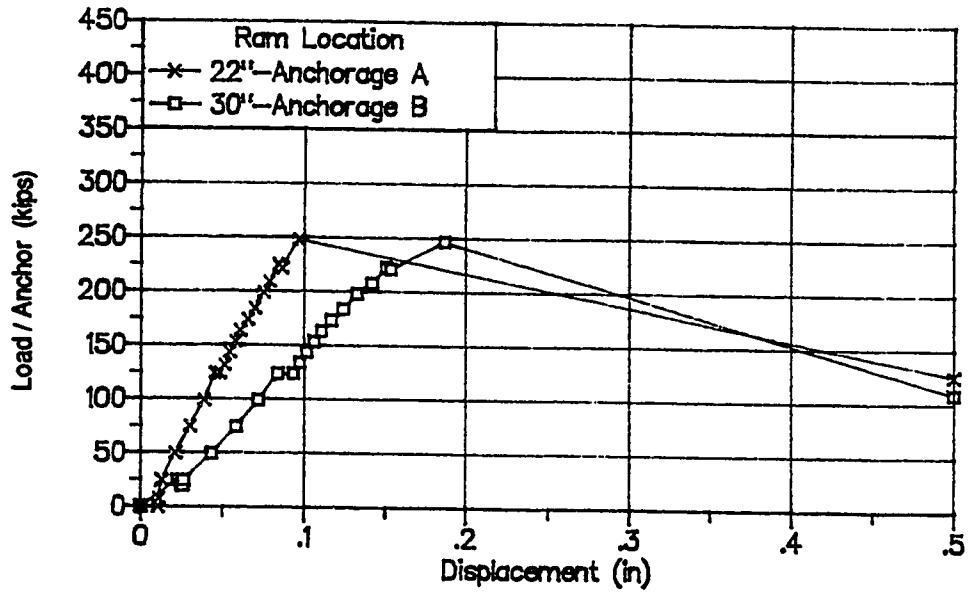


Figure 5.48 Load-Displacement Curve, Specimen F1

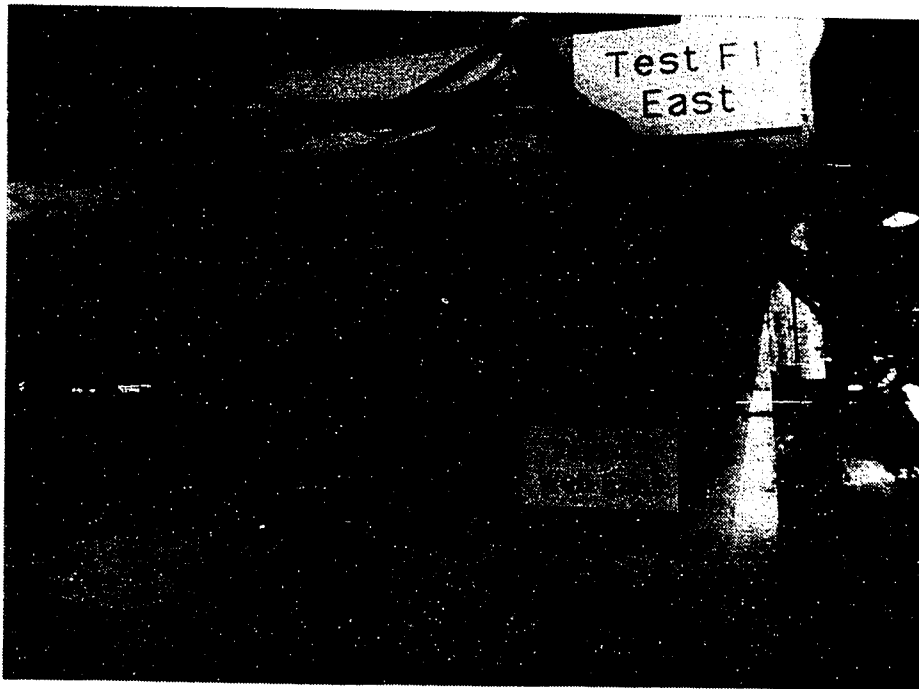


Figure 5.49 Cracking along Flange-Web Interface, Specimen F1

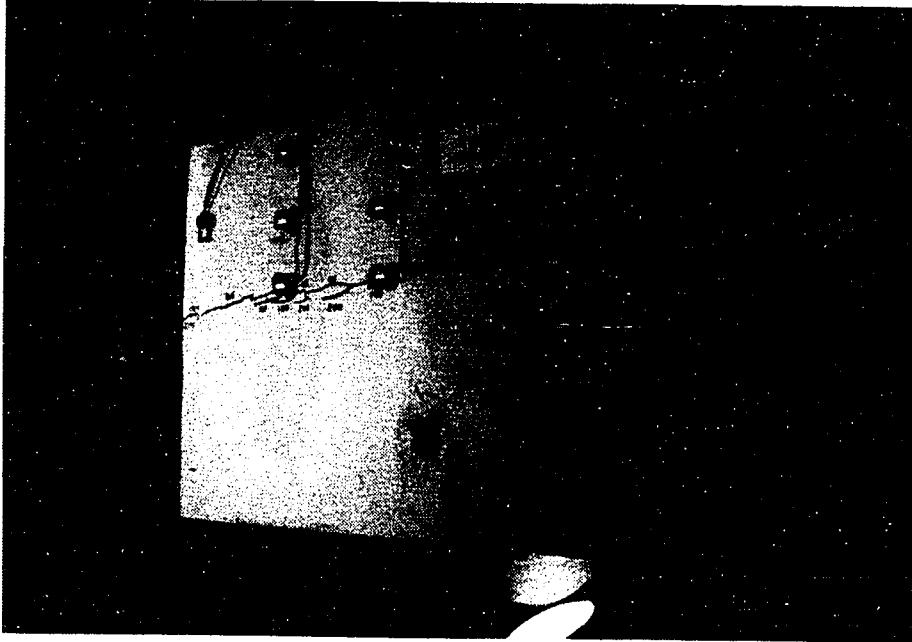


Figure 5.50 Flange Cracking, Specimen F1

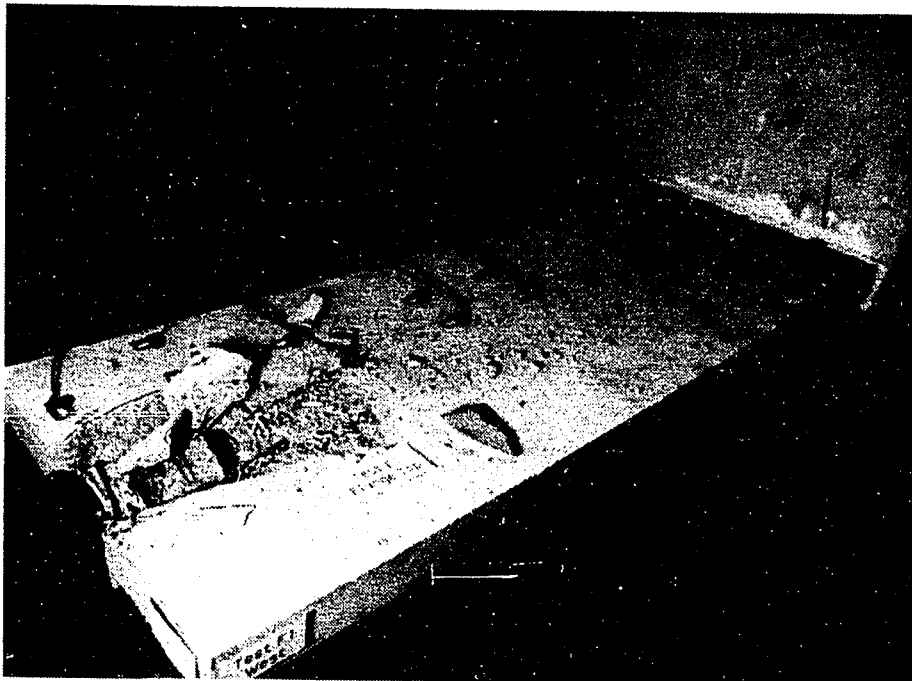


Figure 5.51 Top of Flange after Specimen Failure, Specimen F1

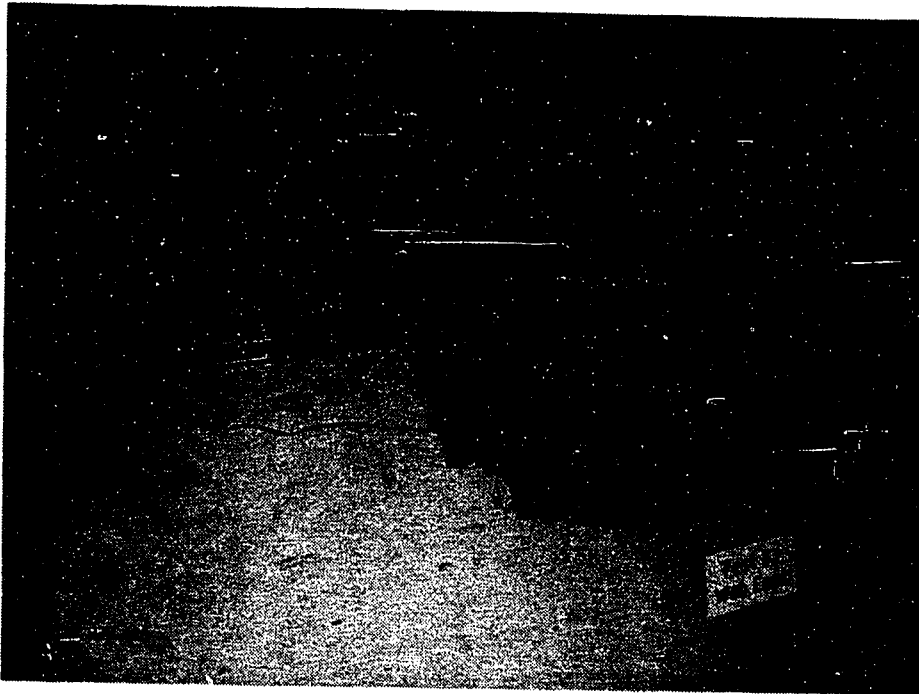


Figure 5.52 Anchorage "A" Failure and Flange Bottom Face Cracking, Specimen F1

Figure 5.53 shows the bursting strain data for the flange reinforcement. Some of the strains were approaching yield when the crack propagated to the base. When all of the concrete tension contribution was lost, the reinforcing strains increased significantly. Figure 5.54 shows the strain data for the web bursting reinforcement. The bursting strains near anchorage "A" were low until the failure; the bursting strains near anchorage "B" were much larger. The strains in bursting reinforcement ahead of anchorage "B" began to increase more rapidly after the flange-web cracks occurred. Figures 5.55 and 5.56 show the concrete strain gage readings at 3 inches and 8 1/2 inches from the specimen centerline. The strains increased steadily until the cracks became very long at 225 kips per anchor. The readings from gages at 8 1/2 inches from the centerline and 11 1/2 inches from the loading surface did not increase as fast as the other gages because the compression forces did not spread out to a large enough degree to cause

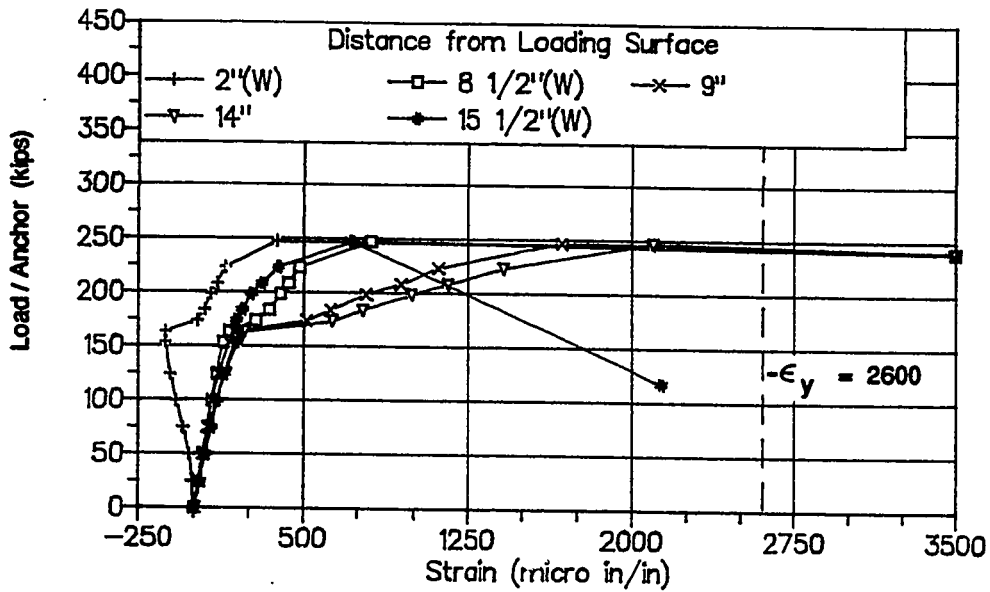


Figure 5.53a Flange Reinforcement Bursting Strains, Near Anchorage "B", Specimen F1

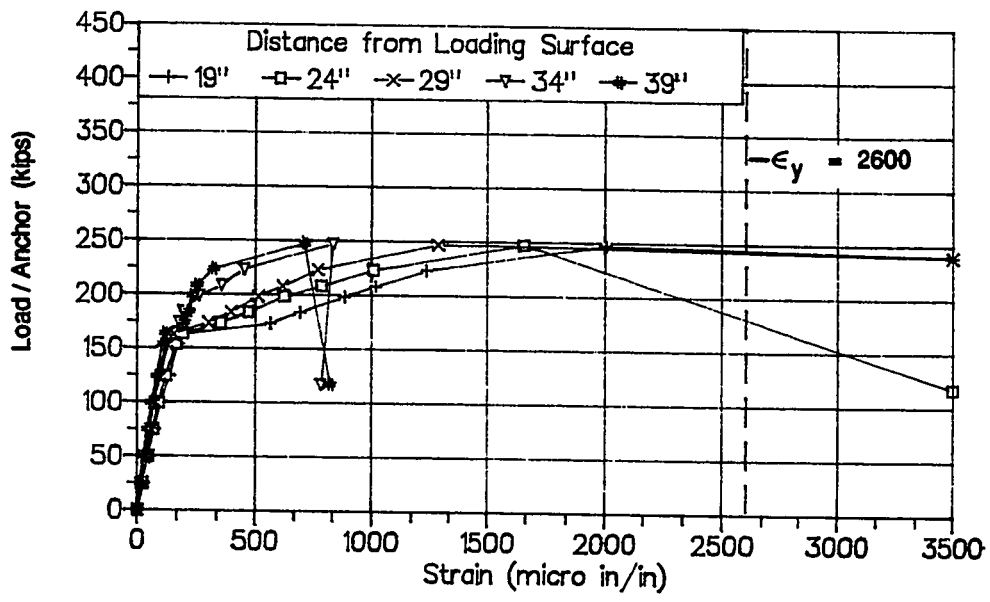


Figure 5.53b Flange Reinforcement Bursting Strains, Distant from Anchorage "B", Specimen F1

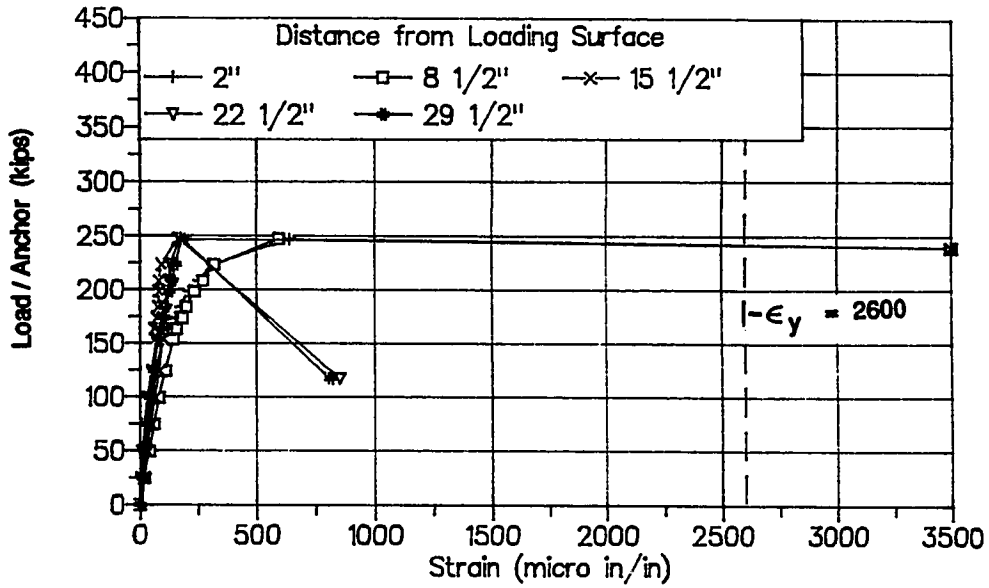


Figure 5.54a Web Reinforcement Bursting Strains, Ahead of Anchorage "A", Specimen F1

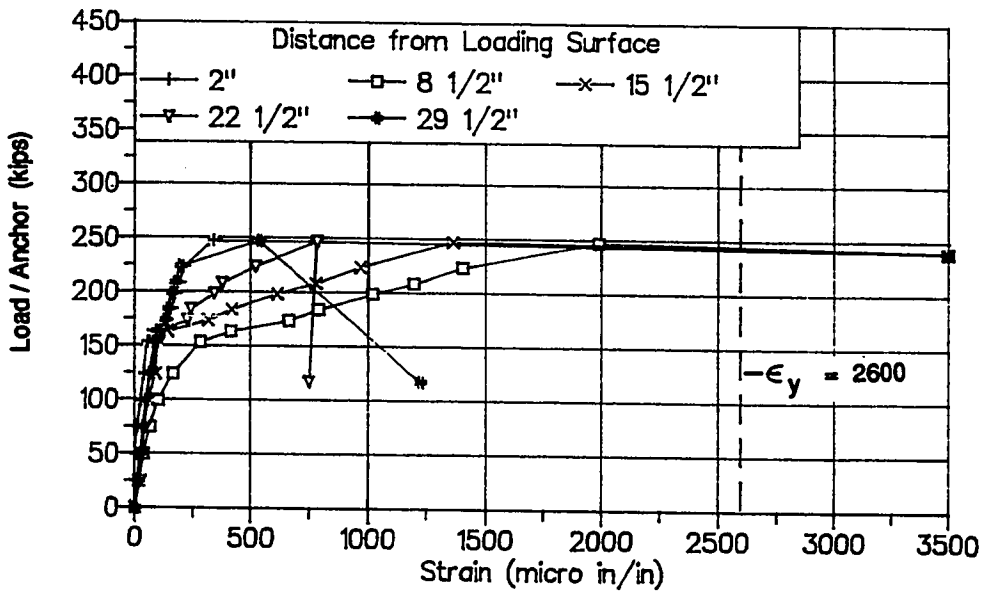


Figure 5.54b Web Reinforcement Bursting Strains, Ahead of Anchorage "B", Specimen F1

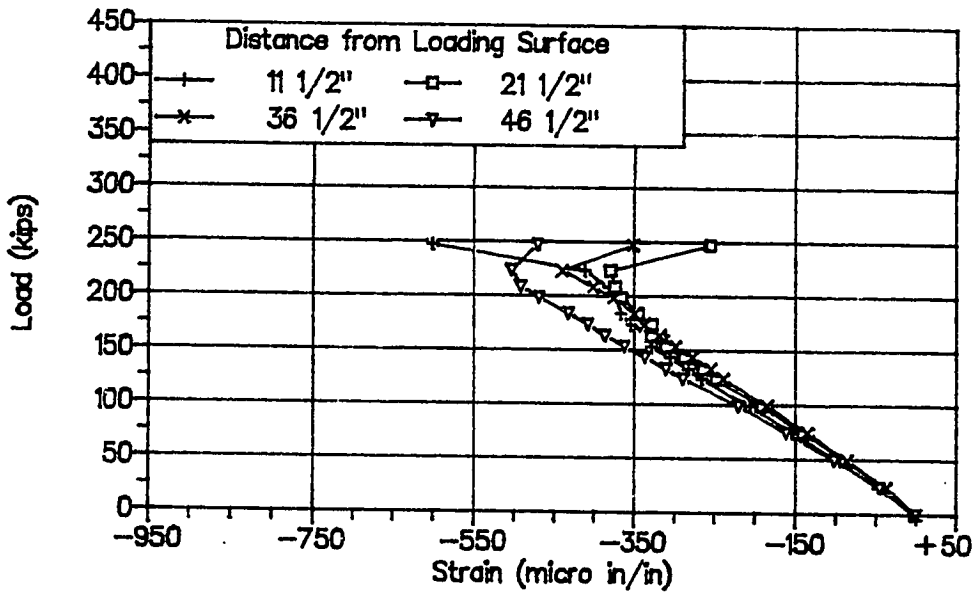


Figure 5.55 Flange Concrete Strains 3-1/2 inches from Flange Centerline, Specimen F1

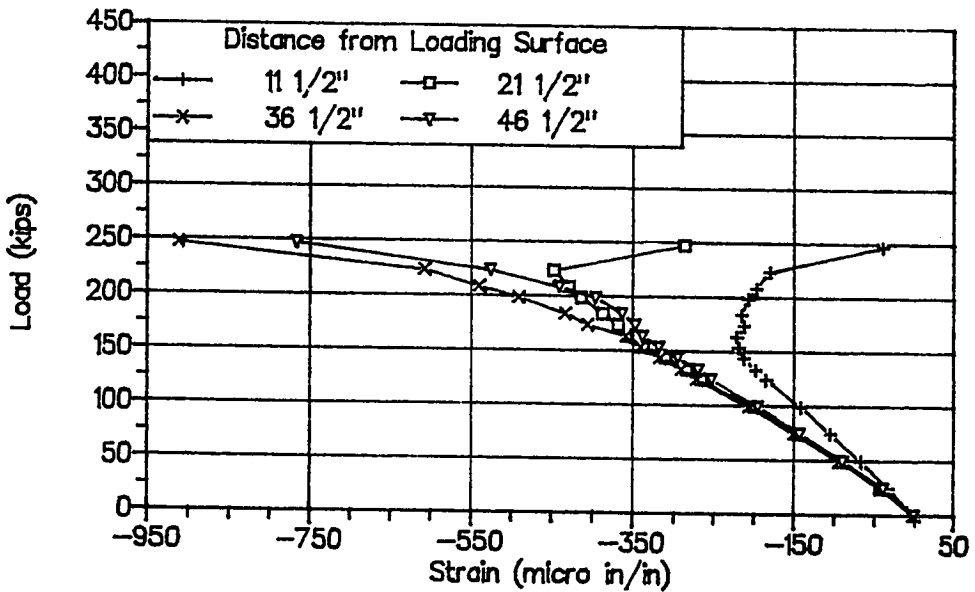


Figure 5.56 Flange Concrete Strains at 8-1/2 inches from Flange Centerline, Specimen F1

large compressive strains at those locations. After the concrete cracked, the strain gages indicated that the stress distribution across the section changed. This was noted especially near the outside edges in the loading surface region in the flange and near the longitudinal edge region at 11 1/2 inches from the loading surface (see Fig. 5.57). The gages showed a reversal in the direction of the strain increments. The longitudinal edge strain gage actually indicated very small tension values. In the test, this was observed by the extensive cracking on the outside edge (see Fig. 5.52). All spiral strains at anchorage "A" were below 560 microstrain. The spiral strains at anchorage "B" were much higher since the spiral was closer to the surface. The maximum strains were 1,200 microstrain at ultimate.

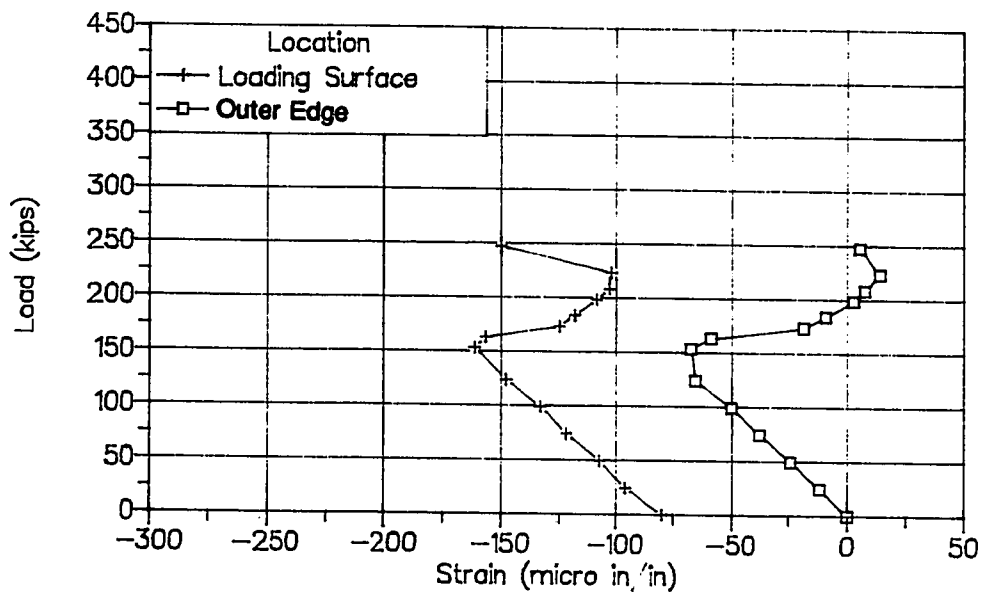


Figure 5.57 Edge Strains in the Flange, Specimen F1

5.3 Prediction of the First Cracking Load using Elastic Analysis Models

As stated in previous chapters, the prediction of the first cracking load can be important under certain design circumstances. In multiple anchorage sections, cracking due to anchorage zone effects can occur in three areas just as it can in the eccentric single anchorage specimens. The areas are the bursting zone (along the tendon axis), the spalling zone (along the loading surface due to compatibility conditions with the anchorage device, eccentric anchor effects and multiple anchor effects), and the longitudinal edge tension zone (along the outermost face of the specimens where tensile stresses may develop due to combined flexural and axial effects). The longitudinal edge tension zone only becomes critical in the anchorage zone when the resultant of all of the tendon forces is outside the kern of the section. As with the crack predictions for concentric and eccentric single anchorages, the cracking load will be determined by matching the best estimate of the actual concrete tensile strength with the elastically computed maximum tensile stress. The maximum tensile stress can be determined from finite element analysis, elasticity based models, and/or combined stress theory.

Eight multiple anchorage specimens with straight tendons were tested. One specimen with extremely closely spaced multiple anchorages (Specimen M5) was examined previously in the eccentric specimen chapter because it behaved very similarly to a single anchorage eccentric specimen. Of the seven remaining specimens, five provide bursting first crack information while all provide spalling first crack information (see Tables 5.2 and 5.4). Specimens M1 and M4 were precracked in the bursting zone with the expectation of reducing the ultimate load and, therefore, do not provide bursting first crack information. The precracking was achieved by placing thin plastic sheets along the tendon axis. Specimens M1 to M6 vary the spacing between anchorages, but their resultant force was along the centerline of the specimen. Specimen ME1 had two anchorages placed so that the

resultant force was at an e/h of 0.11. Specimen F1 investigated the three dimensional effects of a flange with two anchorages. The following subsections will first investigate longitudinal edge tension and spalling cracking and then investigate bursting cracking.

5.3.1 Longitudinal Edge Tension and Spalling Cracking. Since none of the multiple anchorage specimens had the resultant of the tendon force outside the kern, longitudinal edge tension cracking did not occur until extensive cracking had formed in the bursting region and the specimen was near its ultimate load.

Specimens M1 to M4 examined the effects of the spacing between anchorages on the behavior of anchorage zones. The distance between the anchorages was increased varied: 2 inches in Specimen M1, 6 inches in Specimens M2 and M4, and 19 inches in Specimen M3. As the distance between the anchorages increased, the magnitudes of the spalling force and stress between the anchorages also increased. No spalling cracking was observed in Specimens M1 and M4. A small 2-inch spalling crack formed in Specimen M2, while a spalling crack 10 inches long formed along the centerline in Specimen M3. In Specimen M3, the spalling cracking occurred (75 kips per anchor) before the first bursting crack (113 kips per anchor). Spalling cracks also occurred in Specimen ME1. The first spalling crack in Specimen ME1 occurred at the same load stage as the first bursting crack (175 kips per anchor). Therefore, if the distance between the anchorages becomes large enough, the first concrete crack will occur in the spalling zone.

The spalling tension stresses that induce the spalling cracking are difficult to determine because of the high stress gradients and the high stresses predicted near the loading surface. Table 5.5 shows the spalling tensile stresses determined from a finite element analysis conducted by Burdet [25]. The stress values are given for two locations: on the loading surface and at the first node location away from the loading surface. These stresses are matched with the split cylinder data for each specimen to determine the cracking load.

Table 5.5a Spalling Crack Prediction with Stress on Loaded Surface

| Specimen | Split Cylinder (psi) | Thickness (in) | Test Cracking Load (kips) | Stress on Loaded Surface | | |
|----------|-------------------------|-------------------|------------------------------|---------------------------------|--------------------------------|----------------|
| | | | | Peak Tension Stress/ σ_c | Predicted Cracking Load (kips) | Test/Predicted |
| M1 | 441 | 8.5 | None | None | None | - |
| M2 | 497 | 8.5 | 265 | 0.63 | 120 | 2.20 |
| M3 | 497 | 8.5 | 75 | 1.13 | 67 | 1.12 |
| M4 | 441 | 8.5 | None | 0.63 | 107 | - |
| M6 | 415 | 17 | None | None | None | - |
| ME1 | 571 | 10 | 175 | 1.04 | 99 | 1.77 |
| F1 | 316 | 8 | None | None | None | - |

$$\sigma_c = P/ht$$

Table 5.5b Spalling Crack Prediction with First Node Line

| Specimen | Split Cylinder (psi) | Thickness (in) | Test Cracking Load (kips) | Stress at First Node Line from Loaded Surface | | | |
|----------|-------------------------|-------------------|------------------------------|---|---------------------------------|--------------------------------|----------------|
| | | | | Distance from Loaded Surface (in) | Peak Tension Stress/ σ_c | Predicted Cracking Load (kips) | Test/Predicted |
| M1 | 441 | 8.5 | None | 1.72 | None | None | - |
| M2 | 497 | 8.5 | 265 | 1.72 | None | None | Infinite |
| M3 | 497 | 8.5 | 75 | 1.72 | 0.70 | 109 | 0.69 |
| M4 | 441 | 8.5 | None | 1.72 | None | None | - |
| M6 | 415 | 17 | None | 1.69 | None | None | - |
| ME1 | 571 | 10 | 175 | 1.69 | 0.19 | 537 | 0.33 |
| F1 | 316 | 8 | None | 1.91 | None | None | - |

The compression stresses in the longitudinal edge tension and spalling regions are small. Therefore, the biaxial and triaxial effects used to modify the split cylinder data (discussed in previous chapters and modelled by Ottosen) are very small and do not affect the split cylinder data. For the specimens where the anchorages are very close (Specimens M1 and M6), the finite element analysis indicates no tension stresses near the loading surface between the anchors. The analysis for Specimens M2 and M4 indicated tension stresses on the surface. At the first inner node, located 2 inches from the surface, the stresses

parallel to the surface were compressive. Specimens M3 and ME1 had significant tension stresses parallel to the loading surface. None of the predictions are very accurate. Using the stress on the loading surface as determined from the finite element analysis does produce conservative results. In the experimental program, it was found that the spalling crack width remained small as long as reinforcement was placed across the crack path. Therefore, the prediction of the cracking load is probably not critical for most applications.

5.3.2 Bursting Crack Prediction. The first bursting crack load is typically the crack prediction of most interest to the designer. The reader is referred to Sections 3.3.2 and 4.3.2 for more details on the models that are used to predict the first bursting crack load. As with the eccentric specimens, four cracking models were examined that systematically altered two parameters: effective tensile strength (f_t) and effective section thickness (t_e).

- 1) f_t = unmodified split cylinder strength
 t_e = full section thickness
- 2) f_t = unmodified split cylinder strength
 t_e = section thickness - duct outside diameter
- 3) f_t = split cylinder strength modified for triaxial effects
 t_e = section thickness - duct outside diameter
- 4) f_t = split cylinder strength modified for triaxial effects
 t_e = transformed thickness

Table 5.6 is a summary of the results from the first two models, while Table 5.7 is a summary of the tendon duct information. The peak stress in Table 5.6 is normalized using to the average compression stresses across the section. The tendon duct ahead of anchorage "A" in Specimen ME1 shifted during the casting process and, therefore, caused a lower first crack load. The results of Specimen ME1A are not included in the average of any of the first crack analyses. Neglecting the duct effects in analysis produces very unconservative results. By including the effects of the duct, the average of the test-to-predicted

ratios is closer to one. The results for Specimens M2, M3, ME1B, and F1B (the anchor closest to the flange in Specimen F1) are still very unconservative even when including the duct effect. The coefficient of variance is very large for both models. Specimens M1 and M4 are not shown because they are the specimens that were precracked along the tendon path. The next two models will include the reduction in tensile strength due to the triaxial stress effects.

Table 5.6 Bursting Crack Prediction using Split Cylinder Data

a) Full Section Thickness

| Specimen | Split Cylinder (psi) | First Cracking Load (kips) | Thickness (in) | Full Section Thickness | | |
|--|----------------------|----------------------------|----------------|--------------------------|--------------------------------|-----------------|
| | | | | Peak Stress / σ_o | Predicted Cracking Load (kips) | Test/ Predicted |
| M2 | 497 | 213 | 8.5 | 0.335 | 454 | 0.47 |
| M3 | 497 | 113 | 8.5 | 0.712 | 214 | 0.53 |
| M6 | 415 | 244 | 8.5 | 0.845 | 267 | 0.91 |
| ME1A | 571 | 175 | 10 | 0.351 | 585 | 0.30* |
| ME1B | 571 | 260 | 10 | 0.548 | 375 | 0.69 |
| F1A | 316 | none | 8 | 0.362 | 334 | No Crack |
| F1Bw | 316 | 145 | 8 | 0.451 | 268 | 0.54 |
| F1Bf | 316 | 165 | 4.25 | 0.603 | 201 | 0.82 |
| * Duct Shifted Note: Thickness for M6 is per anchor. $\sigma_o = P/ht$ | | | | Average | 0.66 | |
| | | | | Standard Deviation | 0.16 | |
| | | | | Coef. of Variance | 0.25 | |

b) Removing Full Duct Width

| Specimen | Split Cylinder (psi) | First Cracking Load (kips) | Thickness (in) | Removing Full Duct Width | | | |
|---|----------------------|----------------------------|----------------|--------------------------|--------------------------|--------------------------------|-----------------|
| | | | | Effective Thickness (in) | Peak Stress / σ_o | Predicted Cracking Load (kips) | Test/ Predicted |
| M2 | 497 | 213 | 8.5 | 6.38 | 0.447 | 341 | 0.62 |
| M3 | 497 | 113 | 8.5 | 6.38 | 0.949 | 160 | 0.70 |
| M6 | 415 | 244 | 8.5 | 5.88 | 1.223 | 185 | 1.32 |
| ME1A | 571 | 175 | 10 | 7.38 | 0.476 | 431 | 0.41* |
| ME1B | 571 | 260 | 10 | 7.38 | 0.743 | 277 | 0.94 |
| F1A | 316 | none | 8 | 5.38 | 0.539 | 224 | No Crack |
| F1Bw | 316 | 145 | 8 | 5.38 | 0.671 | 180 | 0.80 |
| F1Bf | 316 | 165 | 4.25 | 2.69 | 0.953 | 127 | 1.30 |
| * Duct Shifted Note: Thickness for M6 is per anchor. | | | | Average | 0.95 | | |
| | | | | Standard Deviation | 0.27 | | |
| | | | | Coef. of Variance | 0.29 | | |

Table 5.7 Duct Information for Multiple Anchorage Series

| Specimen | Outer Diameter (in) | Inside Diameter (in) | Thickness (in) |
|----------------|---------------------|----------------------|----------------|
| M1, M2, M3, M4 | 2 1/8 | 2 | 1/32 |
| M6, ME1, F1 | 2 5/8 | 2 3/8 | 1/32 |

The first crack analysis shown in Table 5.8 reduces the concrete thickness by the outside diameter of the duct and reduces the concrete tensile strength from the split cylinder strength to include the triaxial stress effects. The overall model is conservative, but there are still three specimens that are unconservative. Using the transformed thickness of the section (see Table 5.9), the average of the test-to-predicted ratios is one, but the coefficient of variance is still very large. One possible explanation of why the experimental cracking loads are lower than the predicted loads could be the thickness of the specimens. For Specimens M1 to M4, there was only 3.2 inches of concrete over the duct and only 2.6 inches of cover over the duct in Specimen F1. This cover may not be sufficient to smooth out stress concentrations due to the post-tensioning duct or flaws in the concrete.

Table 5.10 gives the results of the lower bound prediction method developed in Chapter 3. The thickness of the concrete is equal to the section thickness minus the inside diameter of the duct. The tensile strength of the concrete is reduced to $4.2\sqrt{f'_c}$ from $6\sqrt{f'_c}$ to include the tensile capacity reduction due to triaxial stress state effects. The model is slightly unconservative for Specimen M2 and 14 percent unconservative for Specimen F1 anchorage "B". The finite element mesh

Table 5.8 Bursting Crack Prediction with Reduced Tensile Strength and Modified Section Thickness

| Specimen | Peak Stress / σ_o | Transverse Stress (psi) | Compression Stress (psi) | Reduced Tensile Strength (psi) | Change in Tensile Strength (psi) | Predicted Cracking Load (kips) | First Cracking Load (kips) | Test/Predicted | | |
|----------------|--------------------------|-------------------------|--------------------------|--------------------------------|----------------------------------|--------------------------------|----------------------------|----------------|--------------------|------|
| M2 | 0.447 | 0 | 2286 | 413 | -84 | 283 | 213 | 0.75 | | |
| M3 | 0.949 | 178 | 1692 | 444 | -53 | 143 | 113 | 0.79 | | |
| M6 | 1.223 | 0 | 1679 | 367 | -48 | 163 | 244 | 1.50 | | |
| ME1A | 0.476 | 264 | 2762 | 433 | -138 | 327 | 175 | 0.53* | | |
| ME1B | 0.743 | 355 | 2368 | 446 | -125 | 216 | 260 | 1.20 | | |
| F1A | 0.539 | 0 | 1846 | 273 | -43 | 194 | none | No Crack | | |
| F1Bw | 0.671 | 0 | 1589 | 283 | -33 | 161 | 145 | 0.90 | | |
| F1Bf | 0.953 | 0 | 1533 | 286 | -30 | 115 | 165 | 1.44 | | |
| * Duct Shifted | | | | | | | $\sigma_o = P/ht$ | | Average | 1.10 |
| | | | | | | | | | Standard Deviation | 0.30 |
| | | | | | | | | | Coef. of Variance | 0.27 |

Table 5.9 Bursting Crack Prediction with Reduced Tensile Strength and Transformed Section

| Specimen | Effective Thickness (in) | Peak Stress / σ_o | Transverse Stress (psi) | Compression Stress (psi) | Reduced Tensile Strength (psi) | Change in Tensile Strength (psi) | Predicted Cracking Load (kips) | First Cracking Load (kips) | Test/Predicted | |
|---------------------------------------|--------------------------|--------------------------|-------------------------|--------------------------|--------------------------------|----------------------------------|--------------------------------|----------------------------|--------------------|------|
| M2 | 6.93 | 0.411 | 0 | 2465 | 399 | -98 | 297 | 213 | 0.71 | |
| M3 | 6.93 | 0.872 | 193 | 1838 | 439 | -58 | 154 | 113 | 0.73 | |
| M6 | 13.22 | 0.544 | 0 | 1828 | 358 | -57 | 178 | 244 | 1.37 | |
| ME1A | 8.11 | 0.433 | 276 | 2886 | 414 | -157 | 342 | 175 | 0.51* | |
| ME1B | 8.11 | 0.676 | 239 | 2466 | 425 | -146 | 225 | 260 | 1.16 | |
| F1A | 6.11 | 0.474 | 0 | 2005 | 263 | -53 | 210 | none | No Crack | |
| F1Bw | 6.11 | 0.590 | 0 | 1747 | 276 | -40 | 177 | 145 | 0.82 | |
| F1Bf | 3.05 | 0.839 | 0 | 1146 | 300 | -16 | 136 | 165 | 1.22 | |
| * Duct Shifted | | | | | | | $\sigma_o = P/ht$ | | Average | 1.00 |
| Note: Thickness for M6 is per Anchor. | | | | | | | | | Standard Deviation | 0.26 |
| | | | | | | | | | Coef. of Variance | 0.26 |

Table 5.10 Bursting Crack Prediction with Conservative Tensile Strength Approximation

| Specimen | Effective Thickness (in) | f'c (psi) | $4.2\sqrt{f'c}$ (psi) | Peak Stress / σ_o | Predicted Cracking Load(kips) | Cracking Load (kips) | Test/ Predicted |
|----------|--------------------------|-----------|-----------------------|--------------------------|-------------------------------|----------------------|-----------------|
| M2 | 6.50 | 5330 | 307 | 0.438 | 214 | 213 | 0.99 |
| M3 | 6.50 | 5330 | 307 | 0.931 | 101 | 113 | 1.12 |
| M6 | 6.13 | 4750 | 289 | 1.173 | 134 | 244 | 1.82 |
| ME1A | 7.63 | 6210 | 331 | 0.461 | 259 | 175 | 0.68* |
| ME1B | 7.63 | 6210 | 331 | 0.719 | 166 | 260 | 1.57 |
| F1A | 5.63 | 4540 | 283 | 0.515 | 210 | none | No Crack |
| F1Bw | 5.63 | 4540 | 283 | 0.641 | 169 | 145 | 0.86 |
| F1Bf | 2.81 | 4540 | 283 | 0.911 | 119 | 165 | 1.39 |
| | | | | | | Average | 1.29 |
| | | | | | | Standard Deviation | 0.33 |
| | | | | | | Coef. of Variance | 0.26 |

* Duct Shifted

Note: Thickness for M6 is per Anchor.

$$\sigma_o = P/ht$$

used to determine the maximum stress ahead of Specimen F1 was made of shell elements and was fairly coarse near the intersection of the web and the flange. Specimen ME1 anchorage "A" shows sensitivity to tendon ducts shifting. The duct shifted 7/8 inches during casting and had to be drilled out to allow the passage of the tendon. This reduced the cross-sectional area of the section from the anchor. This type of effect is very difficult to incorporate into an analysis unless a large factor of safety is used. In a typical girder, there could be additional forces that must also be incorporated into the analysis. As the complexity of the anchorage zone increases a large safety factor must be used in order to ensure that no cracking occurs.

If the anchorage zone is in an area where the other forces besides the post-tensioning force are small, Guyon's symmetrical prism method for determining the maximum bursting stress can be used. Table 5.11a gives a comparison between the results of the symmetrical prism and the finite element analysis. The size of the interior symmetrical prism is governed by the space between the anchorages, while the size of the exterior symmetrical prism is governed by the distance between

Figure 5.11a Peak Bursting Stress Prediction using the Symmetrical Prism

| Specimen | FEM Peak Stress (ksi) | Interior Symmetrical Prism | | | Exterior Symmetrical Prism | | | Conventional Sym. Prism Sym. Prism/FEM |
|--|-----------------------|----------------------------|-------------------|-----------------|--|-------------------|-----------------|--|
| | | a/h | Peak Stress (ksi) | Sym. Prism /FEM | a/h | Peak Stress (ksi) | Sym. Prism /FEM | |
| M2 | 0.11 | 0.50 | 0.22 | 2.02 | 0.25 | 0.16 | 1.49 | 2.02 |
| M3 | 0.23 | 0.24 | 0.16 | 0.68 | 0.55 | 0.22 | 0.93 | 0.93 |
| M6 | 0.16 | 0.81 | 0.13 | 0.82 | 0.23 | 0.14 | 0.92 | 0.82 |
| ME1A | 0.10 | 0.41 | 0.17 | 1.69 | 0.23 | 0.12 | 1.25 | 1.69 |
| ME1B | 0.15 | 0.41 | 0.17 | 1.08 | 0.54 | 0.17 | 1.12 | 1.12 |
| F1A | 0.09 | 0.81 | 0.14 | 1.43 | 0.81 | 0.14 | 1.43 | 1.43 |
| F1Bw | 0.12 | 0.81 | 0.14 | 1.15 | 0.15 | 0.11 | 0.92 | 1.15 |
| F1Bf | 0.16 | 0.19 | 0.25 | 1.59 | 0.19 | 0.25 | 1.59 | 1.59 |
| Note: Peak Stresses are for 100 kips per anchor. | | | | 1.31 | Average Standard Deviation Coef. of Variance | | 1.21 | 1.34 |
| | | | | 0.42 | | | 0.26 | 0.38 |
| | | | | 0.32 | | | 0.21 | 0.29 |

Table 5.11b Bursting Crack Prediction using the Symmetrical Prism

| Specimen | Effective Thickness (in) | f'c (psi) | $4.2\sqrt{f'c}$ (psi) | Peak Stress / σ_o | Predicted Cracking Load(kips) | Cracking load (kips) | Test/ Predicted |
|---|--------------------------|-----------|-----------------------|--------------------------|--|----------------------|-----------------|
| M2 | 6.50 | 5330 | 307 | 0.883 | 106 | 213 | 2.00 |
| M3 | 6.50 | 5330 | 307 | 0.866 | 108 | 113 | 1.04 |
| M6 | 6.13 | 4750 | 289 | 0.542 | 164 | 244 | 1.49 |
| ME1A | 7.63 | 6210 | 331 | 0.780 | 153 | 175 | 1.15* |
| ME1B | 7.63 | 6210 | 331 | 0.803 | 148 | 260 | 1.75 |
| F1A | 5.63 | 4540 | 283 | 0.737 | 147 | none | No Crack |
| F1Bw | 5.63 | 4540 | 283 | 0.737 | 147 | 145 | 0.99 |
| F1Bf | 2.81 | 4540 | 283 | 1.447 | 75 | 165 | 2.21 |
| * Duct Shifted Note: Thickness for M6 is per Anchor. | | | | $\sigma_o = P/ht$ | Average Standard Deviation Coef. of Variance | | 1.58 |
| | | | | | | | 0.46 |
| | | | | | | | 0.29 |

the anchorage and the edge of the specimen. In the conventional symmetrical prism method, the prism with the largest a/h ratio is the one that is used. When compared to the finite element analysis, the conventional symmetrical prism conservatively predicts the bursting stress except in Specimens M3 and M6. The crack predictions from the

conventional symmetrical prism compared to the test results are shown in Table 5.11b. The analysis uses a specimen thickness equal to the section thickness minus the inside diameter of the duct. The analysis is only slightly unconservative for the anchor closest to the flange in Specimen F1 (0.99).

All of the first crack models had high coefficients of variance, and some had unconservative results. Therefore, if cracking is critical, it is very important to use a high factor of safety to ensure no cracking.

5.4 Strut-and-Tie Model Prediction of the Ultimate Load

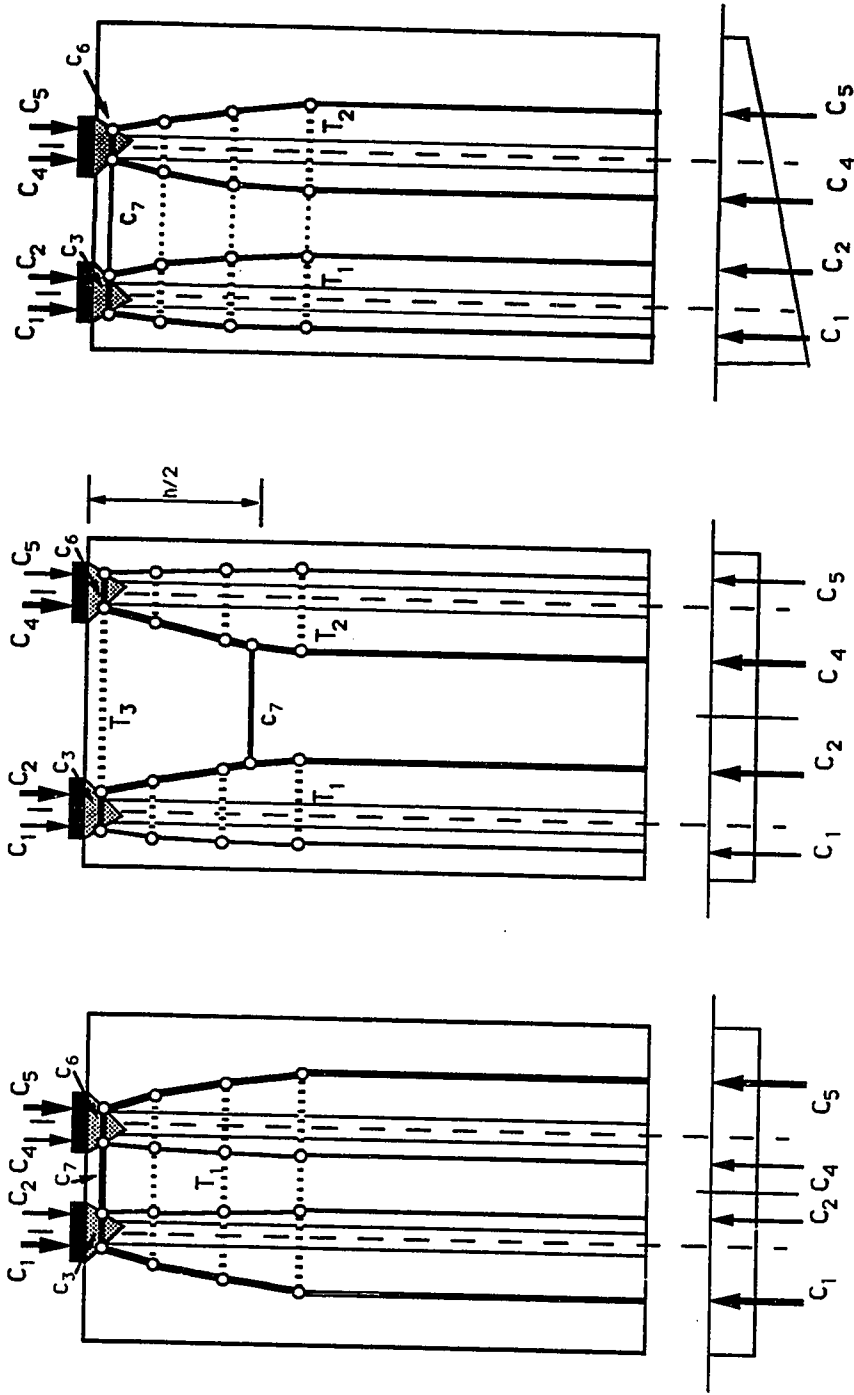
In Chapter 3, the basis was developed for the use of strut-and-tie models (STM's) in post-tensioned applications with concentric anchors. In Chapter 4, the complexity of the problem was increased by placing the anchorage at an eccentricity. It was found that, for both applications, the basic STM with an assumed linear stress distribution at the end of the general zone was conservative as long as all the failure modes were checked. It was also determined that, for the specimens tested, a more accurate prediction of the test results could be found by assuming a more plastic stress distribution at the end of the general zone thereby allowing the struts to be centered more toward the tendon axis. The ultimate load was determined by an iterative process to determine the load which would produce both a tension failure in the ties and a compression failure in the struts. In this section, the principles developed in Chapters 3 and 4 will be applied to the specimens with multiple anchorages.

The particular details for using the STM are not discussed in this chapter except where differences from the methods used in previous chapters occur. More detail may be found in Sections 3.4 and 4.4. The first subsection discusses the aspects of the STM unique to multiple anchorages. The second subsection shows the results from the basic STM, while the third subsection shows the results from the modified STM used for determining the ultimate load of the specimens. The last

subsection compares the results with the current methods for determining the ultimate capacity for multiple anchorage specimens.

5.4.1 Strut-and-Tie Model Prediction. In Figs. 5.58 and 5.59, the basic STM's that will be used in this subsection are shown. Figure 5.58a shows the STM when the anchorages are close together, while Fig. 5.58b shows two anchorages which are far enough apart to cause a spalling tension force to form along the loaded surface. In Fig. 5.58c, the STM is shown for a multiple anchorage specimen with a resultant eccentricity. In the cases of a "T" section or other sections with flanges, the spreading of forces occurs both in the web and in the flange (see Fig. 5.59). As the force from the web (C_2) enters the flange, it then spreads into the flange. When a structure is not planar or of constant width, the three-dimensional effects must be considered. Where these three-dimensional effects appear significant, they can be approximated with the use of a two or more two-dimensional STM. However, the interaction of the models must be considered, and the model loadings and results must be consistent.

When multiple anchors are widely spaced (see Fig. 5.58b), a spalling force, T_3 , forms between the anchorages. Figure 5.60 shows the elastic analysis results for the magnitude of the spalling force as a function of the spacing between the anchorages. The results given in Fig. 5.60 are for a two-anchor system equally spaced on either side of the section centerline. The section had a height of 36 inches and two plates 5 inches wide. Each plate was loaded with 100 kips. The spalling force, according to the finite element analysis, had a tension value for the anchorage spacings greater than $0.2h$. The finite element analysis was conducted by Burdet [25]. The STM only predicts tension forces when the spacing of the anchorages exceeds $0.5h$. The STM does not include the compatibility effects that are included in the finite element analysis results. When tension forces occurred in the spalling zone between the anchors, the stress distribution computed by the finite element analysis midway between the two anchors and parallel to



a) Closely Spaced b) Widely Spaced c) Eccentric

Figure 5.58 Strut-and-Tie Models for Multiple Anchorage Sections

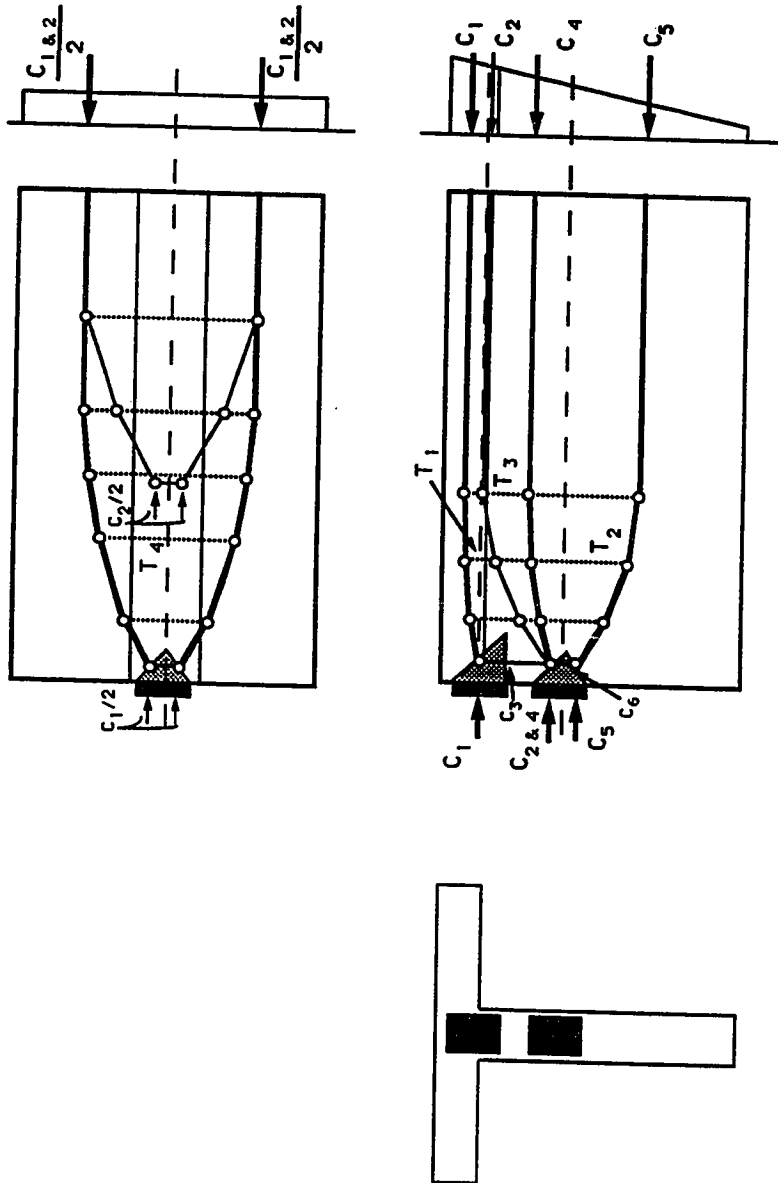


Figure 5.59 Multiple Anchorage Section with a Flange

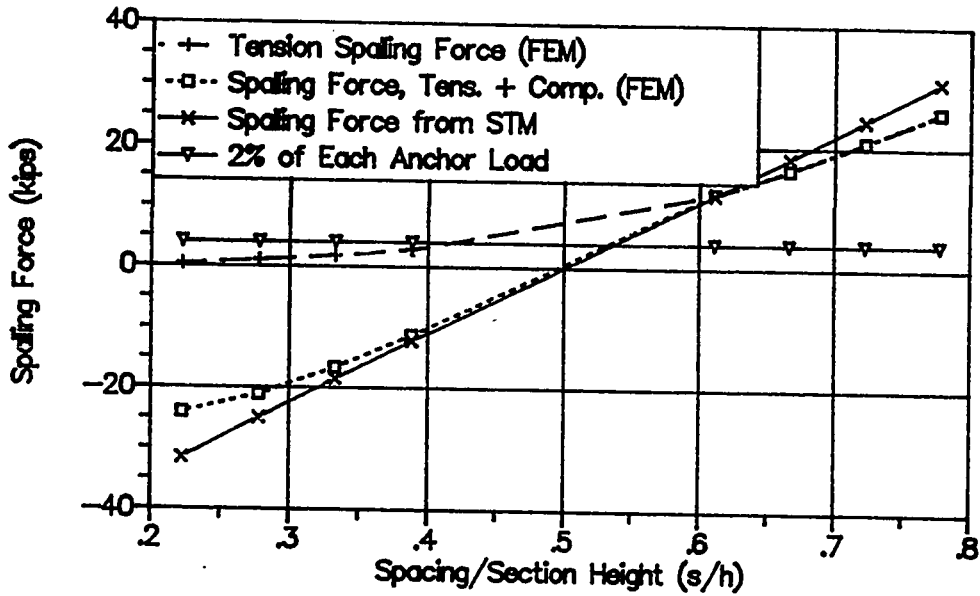


Figure 5.60a Spalling Force Results from STM and Finite Elements

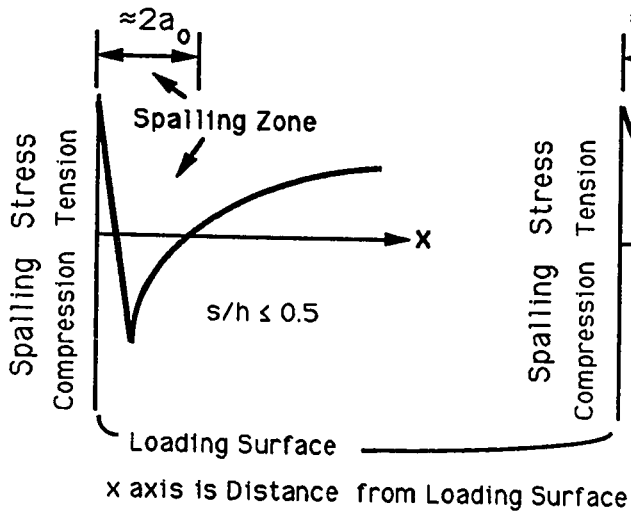


Figure 5.60b Spalling Stress Distribution for Closely Spaced Anchorages

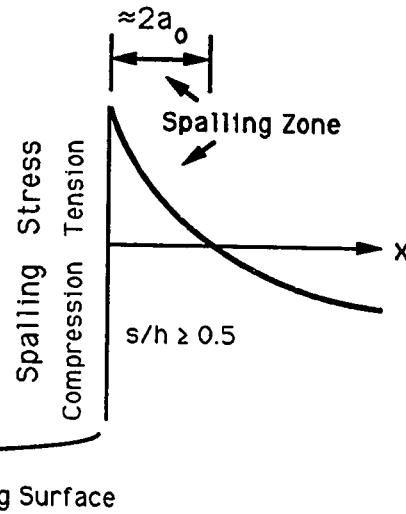
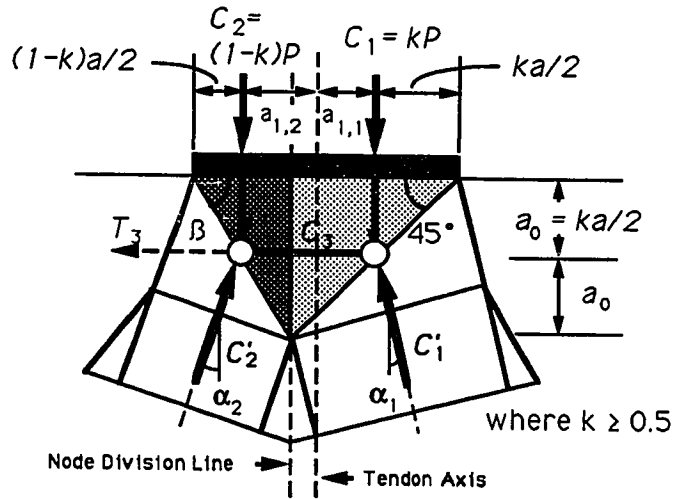


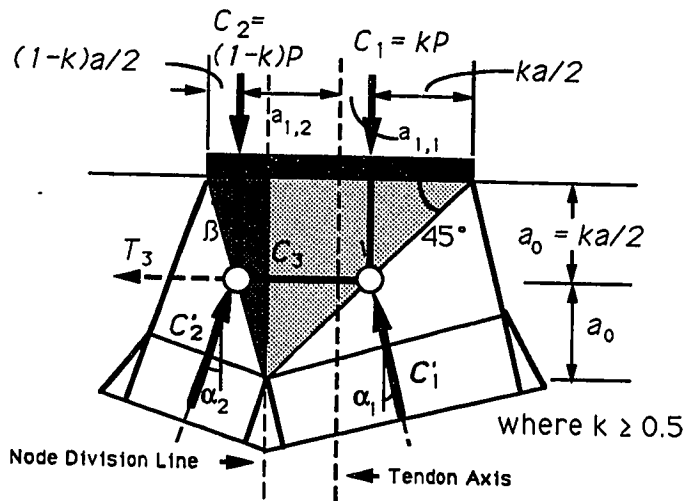
Figure 5.60c Spalling Stress Distribution for Widely Spaced Anchorages

the loading surface was in the forms shown in Figs. 5.60b and 5.60c. For closely spaced anchors (see Fig. 5.60b), the spalling zone consisted of a short tension zone followed by a compression zone. For widely spaced anchors (see Fig. 5.60c), the entire spalling zone was in tension. For $s/h \leq 0.5$, Fig. 5.60a shows a tension force formed near the loading surface but the overall spalling region was in net compression. For $s/h \geq 0.5$, the overall spalling region was in net tension. The depth of the spalling zone was approximately equal to the depth of the local zone node. The STM results follow the net spalling values very closely. The STM in Fig. 5.60a assumed a distance from the loading surface to the compression strut (C , in Fig. 5.58b) of $h/2$ for cases where $s/h \geq 0.5$. If s/h was less than 0.5, the distance was still assumed to be $h/2$ but it was the distance from the loading surface to a tension tie. This STM does not model the very short tension zone near the loading surface. Therefore, the STM models the net force in the spalling zone. In order to provide some reinforcement for the localized tension, it is recommended that minimum spalling force reinforcement be provided to resist a force equal to two percent of the loads applied to each anchor (shown in Fig. 5.60a) when the STM requires less than that amount.

For the eccentric anchorage specimens investigated in Chapter 4, the load applied to each anchorage was divided into two compression struts. The compression forces were almost evenly divided (50/50). The maximum difference between two compression struts was 56 percent to 44 percent. All the concentric specimens had an equal division between the two compression struts. Figure 5.61a shows a local zone node when the magnitudes of the compression struts are close to being equal. Since the division line of the struts in the node and the tendon path are very close together, the difference may be ignored. In the STM's shown and discussed so far, the division of compression strut forces was based on the location of the forces on each side of the tendon path. If the anchorages are symmetrical about the



a) Even Distribution of Force



b) Distribution Heavily Toward One Strut

Figure 5.61 Multiple Anchorage Node

centerline of the specimen, the other compression forces are then divided into forces on each side of the specimen centerline (see struts C_2 and C_4 in Figs. 5.58a and 5.58b). Equilibrium determines the location and magnitude of the compression struts at the end of the general zone. It is usually based on the elastic or $P/A \pm Mc/I$ stress distribution. The magnitude of the struts is determined from integrating the assumed stress distribution over the cross-sectional areas.

Figure 5.61b shows a local zone node when the magnitudes of the compression struts are very different, 25 percent to 75 percent. A large discrepancy between the strut magnitudes becomes much more common in multiple anchorages. In fact, it can affect the results (as will be seen in the next subsection). When the difference between the two struts is more than ten percent of the axial load, the division line for determining the resultant forces should be shifted from the tendon axis to the location where the division line of the node and the division line for the strut are identical.

5.4.2 Basic Strut-and-Tie Model Prediction of the Ultimate Load.

In this subsection the STM's shown in Figs. 5.58 and 5.59 will be used to model the multiple anchorage specimens. The specimens will first be modelled without adjusting the division of the compression struts to account for the local zone node difference. Then the specimens will be modelled by modifying the compression strut magnitude so that the division line for the strut and the division line of the node correspond. As with the concentric and eccentric specimens, all specimens will be checked for:

- 1) Tie capacity (spalling, bursting, and longitudinal edge),
- 2) Local zone bearing capacity,
- 3) Node compression capacity,
- 4) Compression strut capacity at the node-strut interface, and
- 5) Compression strut capacity at the local zone-general zone interface.

Specimens M2, M3, and M4 were able to reach loads higher than those initially expected and exceeded the capacity of the testing machine initially used (600-kip universal). Therefore, after the initial test, some reinforcement was cut and the specimens were tested again in testing equipment with a higher capacity. The second test is shown in the tables with the specimen designation plus a P (M2P, M3P and M4P). Details about the reinforcement and the test equipment are given in Section 5.2.

Table 5.12 Node and Strut Data for Non-Adjusted STM's

| Specimen | a0 | | a1 | | Division of Load | |
|----------|-----------|-----------|-----------|-----------|------------------|------|
| | Ext. (in) | Int. (in) | Ext. (in) | Int. (in) | Ext. | Int. |
| M1 | 2.33 | 2.33 | 0.67 | 2.33 | 0.78 | 0.22 |
| M2 | 2.00 | 2.00 | 1.00 | 2.00 | 0.67 | 0.33 |
| M2P | 2.00 | 2.00 | 1.00 | 2.00 | 0.67 | 0.33 |
| M3 | 2.08 | 2.08 | 2.08 | 0.92 | 0.31 | 0.69 |
| M3P | 2.08 | 2.08 | 2.08 | 0.92 | 0.31 | 0.69 |
| M4 | 2.00 | 2.00 | 1.00 | 2.00 | 0.67 | 0.33 |
| M4P | 2.00 | 2.00 | 1.00 | 2.00 | 0.67 | 0.33 |
| M6 | 2.44 | 2.44 | 0.81 | 2.44 | 0.75 | 0.25 |
| ME1A | 1.75 | 1.75 | 1.75 | 1.50 | 0.46 | 0.54 |
| ME1B | 1.69 | 1.69 | 1.56 | 1.69 | 0.52 | 0.48 |
| F1A | 1.72 | 1.72 | 1.53 | 1.72 | 0.53 | 0.47 |
| F1Bw | 3.25 | N/A | 0.00 | N/A | 1.00 | N/A |
| F1Bf | 1.63 | 1.63 | 1.63 | 1.63 | 0.50 | 0.50 |

Table 5.12 shows the strut percentage and node shape for the multiple anchorage specimens when no node adjustment had been done. Table 5.13 reports the predicted capacity given by the basic STM for the specimens assuming that the tension ties control and using the tendon path as the division line for the load. Two capacities are shown, each depending on what transverse reinforcement is assumed to be effective. Several of the specimens had reinforcement very deep in the section which would require very large deformations to be effective. Therefore, as with the eccentric specimens, reinforcement

Table 5.13a STM Prediction assuming Tension Ties Control and All Bursting Reinforcement Effective

| Specimen | Bursting Tension (kips) | Centroid (in) | All Bursting Reinforcement | | | % of Tension Capacity Utilized | |
|----------|-------------------------|---------------|----------------------------------|----------------------------------|----------------------------------|--------------------------------|-----------------|
| | | | STM-Tie Exterior Capacity (kips) | STM-Tie Interior Capacity (kips) | STM-Tie Combined Capacity (kips) | Across Load Axis | Between Anchors |
| M1 | 92.4 | 29.7 | 514 | 34155 | <u>506</u> | 98.5 | 100.0 |
| M2 | 118.8 | 32.0 | 1069 | 10692 | <u>1069</u> | 100.0 | 90.0 |
| M2P | 79.2 | 19.0 | 404 | 4039 | <u>404</u> | 100.0 | 90.0 |
| M3* | 134.2 | 33.7 | 20853 | 1426 | <u>296</u> | 1.4 | 100.0 |
| M3P* | 81.4 | 18.7 | 6619 | 644 | <u>296</u> | 4.5 | 100.0 |
| M4 | 79.2 | 30.5 | 677 | 6772 | <u>677</u> | 100.0 | 90.0 |
| M4P | 52.8 | 13.8 | 186 | 1861 | <u>186</u> | 100.0 | 90.0 |
| M6 | 50.0 | 19.9 | 112 | 3980 | <u>109</u> | 97.3 | 100.0 |
| ME1A | 35.7 | 14.1 | 226 | 233 | <u>226</u> | 100.0 | 3.0 |
| ME1B | 21.4 | 10.0 | 247 | 228 | <u>228</u> | 100.0 | 7.5 |
| F1A | 28.6 | 19.0 | 141 | 347 | <u>141</u> | 100.0 | 61.5 |
| F1Bw | 28.6 | 19.0 | 216 | N/A | <u>133</u> | 61.5 | 61.5 |
| F1Bf | 25.0 | 24.0 | 141 | 141 | <u>141</u> | 100.0 | N/A |

* Spalling Reinforcement
65 kips, Corresponding Compression Force at d = 18 inches

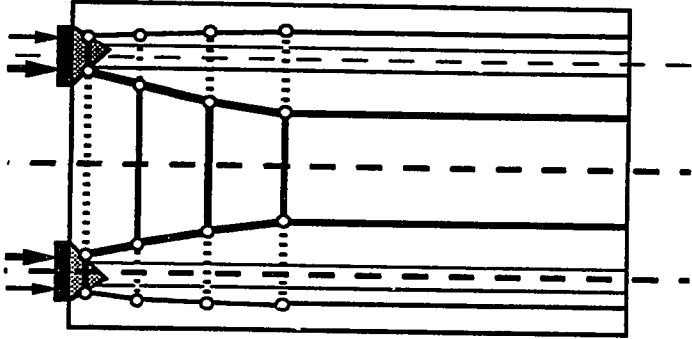
Table 5.13b STM Prediction assuming Tension Ties Control and Only Bursting Reinforcement with 36 inches of Loading Surface Effective

| Specimen | Bursting Tension (kips) | Centroid (in) | Bursting Reinforcement within 36 inches | | | % of Tension Capacity Utilized | |
|----------|-------------------------|---------------|---|----------------------------------|----------------------------------|--------------------------------|-----------------|
| | | | STM-Tie Exterior Capacity (kips) | STM-Tie Interior Capacity (kips) | STM-Tie Combined Capacity (kips) | Across Load Axis | Between Anchors |
| M1 | 66.0 | 17.2 | 199 | 13246 | <u>196</u> | 98.5 | 100.0 |
| M2 | 79.2 | 19.0 | 404 | 4039 | <u>404</u> | 100.0 | 90.0 |
| M2P | 79.2 | 19.0 | 404 | 4039 | <u>404</u> | 100.0 | 90.0 |
| M3* | 68.2 | 15.1 | 4356 | 519 | <u>296</u> | 6.8 | 100.0 |
| M3P* | 68.2 | 15.1 | 4356 | 519 | <u>296</u> | 6.8 | 100.0 |
| M4 | 52.8 | 13.8 | 186 | 1861 | <u>186</u> | 100.0 | 90.0 |
| M4P | 52.8 | 13.8 | 186 | 1861 | <u>186</u> | 100.0 | 90.0 |
| M6 | 50.0 | 19.9 | 112 | 3980 | <u>109</u> | 97.3 | 100.0 |
| ME1A | 35.7 | 14.1 | 226 | 233 | <u>226</u> | 100.0 | 3.0 |
| ME1B | 21.4 | 10.0 | 247 | 228 | <u>228</u> | 100.0 | 7.5 |
| F1A | 28.6 | 19.0 | 141 | 347 | <u>141</u> | 100.0 | 61.5 |
| F1Bw | 28.6 | 19.0 | 216 | N/A | <u>133</u> | 61.5 | 61.5 |
| F1Bf | 25.0 | 24.0 | 141 | 141 | <u>141</u> | 100.0 | N/A |

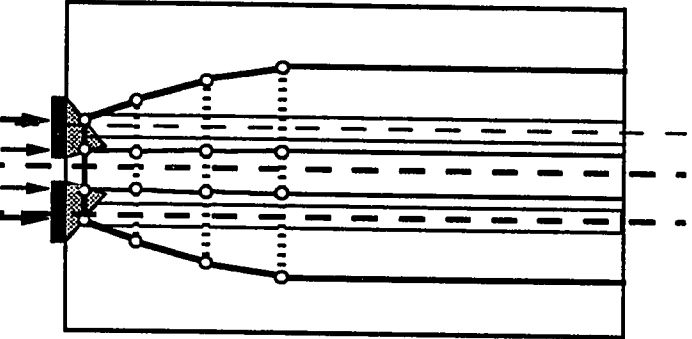
* Spalling Reinforcement
65 kips, Corresponding Compression Force at d = 18 inches

located at a depth beyond 36 inches (h) from the loading surface was neglected in the capacity prediction (see Table 5.13b). In Specimens M2, M3, and M4, there was reinforcement deep in the section but much of this reinforcement was removed for the retest. For Specimens M1 to M6, only one load prediction is given for each test and each reinforcement pattern. For Specimens ME1 and F1, loads are given for each anchor. Since Specimens M1 to M6 have symmetrical anchors, there is no need to check each anchor since they are identical. In Specimens ME1 and F1, the geometry of the section near each anchor is different and must, therefore, be examined.

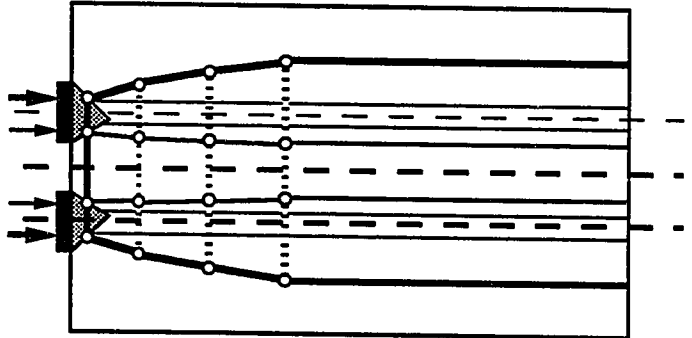
The tension tie STM capacity is given for three cases: exterior, interior, and combined. Utilizing the tendon axis to divide the specimen, a summation of moments about one of the secondary local zone nodes yields the STM capacity assuming the ties control. If the forces in the free-body diagram to the exterior side of the tendon axis are the only ones considered, the exterior STM tie capacity is found. For this calculation, the bursting ties are assumed to be fully yielded. The same procedure is used for the interior STM tie capacity calculation except only forces on the interior side of the tendon axis are considered. Because of the interaction between the anchorages, the capacities predicted by the two models can be very different. In order to have a consistent STM for the entire section, the two models must be considered together. For this to occur, a portion of the reinforcement will not yield according to the STM (see Fig. 5.62). In Fig. 5.62a, the anchors are very closely spaced and, according to the STM, the reinforcement along the centerline of the section yields but the reinforcement along the load axis is slightly below yield. In Fig. 5.62b, the reinforcement along the load axis yields while the centerline reinforcement does not. The last case, Fig. 5.62c, demonstrates that, when the anchors are distant from each other, the reinforcement along the specimen centerline (spalling reinforcement) can become critical. This was the case for Specimen M3. Excessive



a) Centerline Controls



b) Load Axis Controls



c) Spalling Controls

Figure 5.62 Variation of Bursting Tension

reinforcement was provided for the exterior portion of the STM; and, therefore, the centerline (spalling) reinforcement became critical. In Table 5.13, the percentages of the tension capacity that is used along the tendon axis and at the specimen centerline for the combined STM tie capacity is shown. In Specimen M3, which has a large difference between the exterior and interior STM tie capacity, the combined STM has a very small portion of the load axis tension capacity (less than ten percent of T_1 or T_2) utilized because the centerline reinforcement controls the design (spalling reinforcement, T_3). An examination of the strain data for Specimen M3 shows that the load axis (bursting) reinforcement yielded. This discrepancy between the predicted STM and the test measurements indicates a redistribution of forces to obtain a higher capacity. For Specimens M1, M3, and M6, the centerline reinforcement controls the tension tie prediction. In Specimen M3, the reinforcement considered effective in carrying the spalling force was located within the height of the node from the loading surface ($2 \cdot a_o = 2 \cdot 2.08 = 4.16$ inches).

Table 5.14 shows the computed bearing capacity for each anchor as well as the computed node compression force and capacity. The force C_3 is equal to the total bursting force available in the bursting reinforcement along the tendon path. The node compression capacity does not control for any of the specimens. Tables 5.15 and 5.16 show the node-strut interface capacity and the local zone-general zone interface capacity for both the exterior and interior struts. The interior struts are closest to the specimen centerline or the adjacent anchor. The negative strut angles indicate that the line of action of the struts point toward the tendon axis from the secondary node. Table 5.17 is a summary of the predicted loads for each of the failure modes. Node compression is not shown because it was checked and found not to govern (see Table 5.14). The basic STM is extremely conservative with an average ratio of 1.84 and a coefficient of variance of 24 percent. There were no initial test ultimate loads determined for Specimens M2,

Table 5.14 Bearing and Node Capacity if No Node Adjustment Conducted

| Specimen | f' _c (ksi) | Bearing Capacity (kips) | Node C3 Capacity (kips) | Compression Forces C3 Capacity (kips) | C3/ Capacity |
|----------|--------------------------|-------------------------------|----------------------------------|--|-----------------|
| M1 | 5.94 | 418 | 66.00 | 341 | 0.19 |
| M2 | 5.73 | 411 | 79.20 | 289 | 0.27 |
| M2P | 5.73 | 411 | 79.20 | 289 | 0.27 |
| M3 | 5.73 | 411 | 68.20 | 301 | 0.23 |
| M3P | 5.73 | 411 | 68.20 | 301 | 0.23 |
| M4 | 6.62 | 440 | 52.80 | 304 | 0.17 |
| M4P | 6.62 | 440 | 52.80 | 304 | 0.17 |
| M6 | 4.75 | 331 | 50.00 | 254 | 0.20 |
| ME1A | 6.21 | 473 | 35.70 | 202 | 0.18 |
| ME1B | 6.21 | 473 | 21.42 | 194 | 0.11 |
| F1A | 4.54 | 324 | 28.60 | 177 | 0.16 |
| F1Bw | 4.54 | 324 | 28.60 | 332 | 0.09 |
| F1Bf | 4.54 | 324 | 24.99 | 83 | 0.30 |

M3, and M4 because of the limited testing machine capacity. Tension tie capacity controls Specimens M4P, M6, ME1, and F1. The local zone-general zone interface controls Specimens M1, M2P and M3P. The percentage of the anchor load carried by the interior and exterior struts in Specimens M1 to M6 is very different (more than ten percent). Therefore, by using the tendon axis to divide the axial load, inaccuracies could occur in the capacity prediction.

Since the division of the load between struts for each anchor is not within ten percent of being equal for Specimens M1 to M6, a shifting of the assumed load division line away from the tendon axis to better match the nodal division is necessary for an accurate analysis. Table 5.18 shows the readjusted division of the strut loads to coincide with the node division. For example, in Specimen M1 the original division of the load between the exterior and interior strut produced by integrating stresses on each side of the tendon axis was 78 percent and 22 percent respectively. When the strut division line is adjusted to coincide with the node division, the values of the division of the load become 92 percent and 8 percent. Table 5.19 gives

Table 5.15 Node-Strut Interface Capacity if No Node Adjustment Conducted

a) Exterior Strut

| Specimen | Alpha (degrees) | Strut Width (in) | Strut Thickness (in) | Confined Width (in) | Confined Allowable (ksi) | Unconfined Allowable (ksi) | Predicted Capacity (kips) |
|----------|-----------------|------------------|----------------------|---------------------|--------------------------|----------------------------|---------------------------|
| M1 | 23.07 | 6.12 | 7.02 | 4.70 | 13.06 | 5.03 | 493 |
| M2 | 16.39 | 4.97 | 6.97 | 3.81 | 12.92 | 4.89 | 478 |
| M2P | 16.39 | 4.97 | 6.97 | 3.81 | 12.92 | 4.89 | 478 |
| M3 | 2.93 | 2.04 | 7.21 | 1.49 | 12.76 | 4.73 | 436 |
| M3P | 2.93 | 2.04 | 7.21 | 1.49 | 12.76 | 4.73 | 436 |
| M4 | 22.96 | 5.24 | 6.88 | 3.97 | 13.76 | 5.73 | 520 |
| M4P | 22.96 | 5.24 | 6.88 | 3.97 | 13.76 | 5.73 | 520 |
| M6 | 16.54 | 6.06 | 7.44 | 4.93 | 8.48 | 3.80 | 402 |
| ME1A | 18.88 | 3.97 | 7.50 | 3.48 | 10.31 | 5.79 | 583 |
| ME1B | 10.27 | 3.92 | 7.56 | 3.73 | 10.27 | 5.75 | 550 |
| F1A | 20.93 | 4.46 | 7.00 | 3.54 | 8.31 | 3.63 | 380 |
| F1Bw | 7.53 | 7.30 | 7.63 | 6.41 | 8.01 | 3.33 | 368 |
| F1Bf | 17.08 | 4.06 | 3.87 | 3.24 | 8.17 | 3.49 | 285 |

b) Interior Strut

| Specimen | Alpha (degrees) | Strut Width (in) | Strut Thickness (in) | Confined Width (in) | Confined Allowable (ksi) | Unconfined Allowable (ksi) | Predicted Capacity (kips) |
|----------|-----------------|------------------|----------------------|---------------------|--------------------------|----------------------------|---------------------------|
| M1 | -1.28 | 1.23 | 7.38 | .99 | 12.82 | 4.79 | 386 |
| M2 | 3.37 | 2.23 | 7.16 | 1.66 | 12.79 | 4.76 | 440 |
| M2P | 3.37 | 2.23 | 7.16 | 1.66 | 12.79 | 4.76 | 440 |
| M3 | 20.28 | 5.35 | 6.95 | 3.83 | 12.93 | 4.90 | 467 |
| M3P | 20.28 | 5.35 | 6.95 | 3.83 | 12.93 | 4.90 | 467 |
| M4 | 4.84 | 2.33 | 7.15 | 1.66 | 13.54 | 5.51 | 486 |
| M4P | 4.84 | 2.33 | 7.15 | 1.66 | 13.54 | 5.51 | 486 |
| M6 | -1.44 | 1.50 | 7.65 | 1.48 | 8.38 | 3.69 | 341 |
| ME1A | 15.83 | 4.33 | 7.52 | 3.80 | 10.30 | 5.78 | 553 |
| ME1B | 10.23 | 3.68 | 7.57 | 3.42 | 10.26 | 5.75 | 551 |
| F1A | 9.93 | 3.59 | 7.09 | 2.89 | 8.27 | 3.59 | 369 |
| F1Bw | N/A | N/A | N/A | N/A | N/A | N/A | N/A |
| F1Bf | 17.08 | 4.06 | 3.87 | 3.10 | 8.17 | 3.49 | 277 |

Table 5.16 Local Zone-General Zone Interface Capacity with No Node Adjustment Conducted

a) Exterior Strut

| Specimen | Depth of Confinement (in) | Alpha (degrees) | Strut Width (in) | Strut Thickness (in) | Unconfined Allowable (ksi) | Predicted Capacity (kips) |
|----------|---------------------------|-----------------|------------------|----------------------|----------------------------|---------------------------|
| M1 | 8.00 | 23.07 | 8.74 | 7.85 | 4.50 | 365 |
| M2 | 8.00 | 16.39 | 7.22 | 8.05 | 4.23 | 354 |
| M2P | 8.00 | 16.39 | 7.22 | 8.05 | 4.23 | 354 |
| M3 | 8.00 | 2.93 | 2.44 | 8.33 | 4.09 | 271 |
| M3P | 8.00 | 2.93 | 2.44 | 8.33 | 4.09 | 271 |
| M4 | 8.00 | 22.96 | 8.36 | 7.87 | 5.00 | 455 |
| M4P | 8.00 | 22.96 | 8.36 | 7.87 | 5.00 | 455 |
| M6 | 10.00 | 16.54 | 8.98 | 8.55 | 3.30 | 324 |
| ME1A | 9.50 | 18.88 | 7.85 | 9.38 | 4.63 | 701 |
| ME1B | 9.50 | 10.27 | 6.10 | 9.63 | 4.51 | 503 |
| F1A | 8.00 | 20.93 | 7.71 | 7.74 | 3.28 | 344 |
| F18w | 8.00 | 7.53 | 7.69 | 7.91 | 3.18 | 268 |
| F18f | 8.00 | 17.08 | 6.85 | 4.25 | 3.18 | 257 |

b) Interior Strut

| Specimen | Depth of Confinement (in) | Alpha (degrees) | Strut Width (in) | Strut Thickness (in) | Unconfined Allowable (ksi) | Predicted Capacity (kips) |
|----------|---------------------------|-----------------|------------------|----------------------|----------------------------|---------------------------|
| M1 | 8.00 | -1.28 | 1.08 | 8.36 | 4.23 | 172 |
| M2 | 8.00 | 3.37 | 2.70 | 8.33 | 4.09 | 276 |
| M2P | 8.00 | 3.37 | 2.70 | 8.33 | 4.09 | 276 |
| M3 | 8.00 | 20.28 | 8.01 | 7.94 | 4.29 | 369 |
| M3P | 8.00 | 20.28 | 8.01 | 7.94 | 4.29 | 369 |
| M4 | 8.00 | 4.84 | 3.01 | 8.32 | 4.74 | 354 |
| M4P | 8.00 | 4.84 | 3.01 | 8.32 | 4.74 | 354 |
| M6 | 10.00 | -1.44 | 1.25 | 8.86 | 3.19 | 141 |
| ME1A | 9.50 | 15.83 | 7.60 | 9.46 | 4.59 | 590 |
| ME1B | 9.50 | 10.23 | 5.86 | 9.64 | 4.51 | 520 |
| F1A | 8.00 | 9.93 | 5.16 | 7.92 | 3.21 | 276 |
| F18w | N/A | N/A | N/A | N/A | N/A | N/A |
| F18f | 8.00 | 17.08 | 6.85 | 4.25 | 3.18 | 257 |

Table 5.17 STM Prediction Summary with No Node Adjustment Conducted

| Specimen | Tension Tie (kips) | Bearing (kips) | Node-Strut Interface | | L.Z.-G.Z. Interface | | Controlling Load (kips) | Ultimate Test (kips) | Test/Predicted |
|--|--------------------|----------------|----------------------|-----------------|---------------------|-----------------|-------------------------|----------------------|----------------|
| | | | Exterior (kips) | Interior (kips) | Exterior (kips) | Interior (kips) | | | |
| M1 | 196 | 418 | 493 | 386 | 365 | 172 | 172 | 304 | 1.77 |
| M2 | 404 | 411 | 478 | 440 | 354 | 276 | 276 | N/A | N/A |
| M2P | 404 | 411 | 478 | 440 | 354 | 276 | 276 | 401 | 1.45 |
| M3 | 296 | 411 | 436 | 467 | 271 | 369 | 271 | N/A | N/A |
| M3P | 296 | 411 | 436 | 467 | 271 | 369 | 271 | 364 | 1.34 |
| M4 | 186 | 440 | 520 | 486 | 455 | 354 | 186 | N/A | N/A |
| M4P | 186 | 440 | 520 | 486 | 455 | 354 | 186 | 411 | 2.21 |
| M6 | 109 | 331 | 402 | 341 | 324 | 141 | 109 | 300 | 2.75 |
| ME1A | 226 | 473 | 583 | 553 | 701 | 590 | 226 | 350 | 1.55* |
| ME1B | 228 | 473 | 550 | 551 | 503 | 520 | 228 | 350 | 1.54 |
| F1A | 141 | 324 | 380 | 369 | 344 | 276 | 141 | 248 | 1.76* |
| F1Bw | 133 | 324 | 368 | N/A | 268 | N/A | 133 | 248 | 1.86* |
| F1Bf | 141 | 324 | 285 | 277 | 257 | 257 | 141 | 248 | 1.76 |
| Note: Node Compression was found to not control in Table 5.14 Loads are per anchor * Other Anchor for that Specimen Controls | | | | | | | | Average | 1.83 |
| | | | | | | | | Standard Deviation | 0.46 |
| | | | | | | | | Coef. of Variance | 0.25 |

Table 5.18 Node and Strut Data for Adjusted STM's

| Specimen | a0 | | a1 | | Division of Load | |
|----------|------|------|------|------|------------------|------|
| | Ext. | Int. | Ext. | Int. | Ext. | Int. |
| | (in) | (in) | (in) | (in) | | |
| M1 | 2.75 | 2.75 | 0.25 | 2.75 | 0.92 | 0.08 |
| M2 | 2.25 | 2.25 | 0.75 | 2.25 | 0.75 | 0.25 |
| M2P | 2.25 | 2.25 | 0.75 | 2.25 | 0.75 | 0.25 |
| M3 | 2.38 | 2.38 | 2.38 | 0.63 | 0.21 | 0.79 |
| M3P | 2.38 | 2.38 | 2.38 | 0.63 | 0.21 | 0.79 |
| M4 | 2.25 | 2.25 | 0.75 | 2.25 | 0.75 | 0.25 |
| M4P | 2.25 | 2.25 | 0.75 | 2.25 | 0.75 | 0.25 |
| M6 | 2.99 | 2.99 | 0.26 | 2.99 | 0.92 | 0.08 |
| ME1A | 1.75 | 1.75 | 1.75 | 1.50 | 0.46 | 0.54 |
| ME1B | 1.69 | 1.69 | 1.56 | 1.69 | 0.52 | 0.48 |
| F1A | 1.72 | 1.72 | 1.53 | 1.72 | 0.53 | 0.47 |
| F1Bw | 3.25 | N/A | 0.00 | N/A | 1.00 | N/A |
| F1Bf | 1.63 | 1.63 | 1.63 | 1.63 | 0.50 | 0.50 |

Table 5.19a STM Prediction assuming Tension Ties Control and All Bursting Reinforcement Effective, Node Adjusted

| Specimen | Bursting Tension (kips) | Centroid (in) | All Bursting Reinforcement | | | Change in STM-Tie Capacity (kips)** | % of Tension Capacity Utilized | |
|----------|-------------------------|---------------|----------------------------------|----------------------------------|----------------------------------|-------------------------------------|--------------------------------|-----------------|
| | | | STM-Tie Exterior Capacity (kips) | STM-Tie Interior Capacity (kips) | STM-Tie Combined Capacity (kips) | | Across Load Axis | Between Anchors |
| M1 | 92.4 | 29.7 | 494 | 59796 | 494 | -12 | 100.0 | 99.2 |
| M2 | 118.8 | 32.0 | 1047 | 9425 | 1047 | -22 | 100.0 | 88.9 |
| M2P | 79.2 | 19.0 | 393 | 3538 | 393 | -11 | 100.0 | 88.9 |
| M3* | 134.2 | 33.7 | 16162 | 1390 | 291 | -5 | 1.8 | 100.0 |
| M3P* | 81.4 | 18.7 | 5086 | 623 | 290 | -6 | 8.7 | 100.0 |
| M4 | 79.2 | 30.5 | 1038 | 5966 | 663 | -14 | 100.0 | 88.9 |
| M4P | 52.8 | 13.8 | 180 | 1619 | 180 | -6 | 100.0 | 88.9 |
| M6 | 50.0 | 19.9 | 105 | 14235 | 104 | -5 | 100.0 | 99.3 |
| ME1A | 35.7 | 14.1 | 226 | 233 | 226 | 0 | 100.0 | 3.0 |
| ME1B | 21.4 | 10.0 | 247 | 228 | 228 | 0 | 100.0 | 7.5 |
| F1A | 28.6 | 19.0 | 141 | 347 | 141 | 0 | 100.0 | 61.5 |
| F1Bw | 28.6 | 19.0 | 216 | N/A | 133 | 0 | 61.5 | 61.5 |
| F1Bf | 25.0 | 24.0 | 141 | 141 | 141 | 0 | 100.0 | N/A |

* Spalling Reinforcement

- 65 kips, Corresponding Compression Force at $d = 18$ inches

** The difference between the STM-Tie Combined Capacity in this table and Table 5.13. Negative reflects Table 5.13 value is larger.

Table 5.19b STM Prediction assuming Tension Ties Control and Only Bursting Reinforcement with 36 inches of Loading Surface Effective, Node Adjusted

| Specimen | Bursting Tension (kips) | Centroid (in) | Bursting Reinforcement within 36 inches | | | Change in STM-Tie Capacity (kips)** | % of Tension Capacity Utilized | |
|----------|-------------------------|---------------|---|----------------------------------|----------------------------------|-------------------------------------|--------------------------------|-----------------|
| | | | STM-Tie Exterior Capacity (kips) | STM-Tie Interior Capacity (kips) | STM-Tie Combined Capacity (kips) | | Across Load Axis | Between Anchors |
| M1 | 66.0 | 17.2 | 189 | 22889 | 189 | -7 | 100.0 | 99.2 |
| M2 | 79.2 | 19.0 | 393 | 3538 | 393 | -11 | 100.0 | 88.9 |
| M2P | 79.2 | 19.0 | 393 | 3538 | 393 | -11 | 100.0 | 88.9 |
| M3* | 68.2 | 15.1 | 3331 | 501 | 290 | -6 | 8.7 | 100.0 |
| M3P* | 68.2 | 15.1 | 3331 | 501 | 290 | -6 | 8.7 | 100.0 |
| M4 | 52.8 | 13.8 | 180 | 1619 | 180 | -6 | 100.0 | 88.9 |
| M4P | 52.8 | 13.8 | 180 | 1619 | 180 | -6 | 100.0 | 88.9 |
| M6 | 50.0 | 19.9 | 105 | 0 | 104 | -5 | 100.0 | 99.3 |
| ME1A | 35.7 | 14.1 | 226 | 233 | 226 | 0 | 100.0 | 3.0 |
| ME1B | 21.4 | 10.0 | 247 | 228 | 228 | 0 | 100.0 | 7.5 |
| F1A | 28.6 | 19.0 | 141 | 347 | 141 | 0 | 100.0 | 61.5 |
| F1Bw | 28.6 | 19.0 | 216 | N/A | 133 | 0 | 61.5 | 61.5 |
| F1Bf | 25.0 | 24.0 | 141 | 141 | 141 | 0 | 100.0 | N/A |

* Spalling Reinforcement

- 65 kips, Corresponding Compression Force at $d = 18$ inches

** The difference between the STM-Tie Combined Capacity in this table and Table 5.13. Negative reflects Table 5.13 value is larger.

the predicted STM capacities when assuming that the tension ties control. Table 5.19a assumes that all bursting reinforcement is effective. The models in Table 5.19b assume that only reinforcement within h equal to 36 inches from the loading surface is effective. The centerline reinforcement (spalling tension tie) controls the STM tension tie design for only Specimen M3. The difference between the STM tie results with no node adjustment is very small (see Tables 5.13 and 5.19). The bearing capacity and the recomputed node compression capacities are shown in Fig. 5.20. The bearing capacity is not affected by the shifting of the load division line, and the node compression capacity is only slightly effected. The major difference is seen in the node-strut interface and local zone-general zone interface capacity (see Tables 5.21 and 5.22). The maximum change is 197 kips in Specimen M1. Table 5.23 is a summary of the predicted results. The average of the test-to-predicted ratios is still very conservative at 1.81 with a coefficient of variance of 0.30.

Table 5.20 Bearing and Node Capacity with Node Adjustment Conducted

| Specimen | f'c (ksi) | Bearing Capacity (kips) | Node Compression Forces | | |
|----------|--------------|-------------------------------|-------------------------|--------------------|-----------------|
| | | | C3 (kips) | Capacity (kips) | C3/ Capacity |
| M1 | 5.94 | 418 | 66.00 | 404 | 0.16 |
| M2 | 5.73 | 411 | 79.20 | 325 | 0.24 |
| M2P | 5.73 | 411 | 79.20 | 325 | 0.24 |
| M3 | 5.73 | 411 | 68.20 | 343 | 0.20 |
| M3P | 5.73 | 411 | 68.20 | 343 | 0.20 |
| M4 | 6.62 | 440 | 52.80 | 342 | 0.15 |
| M4P | 6.62 | 440 | 52.80 | 342 | 0.15 |
| M6 | 4.75 | 331 | 50.00 | 311 | 0.16 |
| ME1A | 6.21 | 473 | 35.70 | 202 | 0.18 |
| ME1B | 6.21 | 473 | 21.42 | 194 | 0.11 |
| F1A | 4.54 | 324 | 28.60 | 177 | 0.16 |
| F1Bw | 4.54 | 324 | 28.60 | 332 | 0.09 |
| F1Bf | 4.54 | N/A | 24.99 | 83 | 0.30 |

Table 5.21 Node-Strut Interface Capacity with Node Adjustment Conducted

a) Exterior Strut

| Specimen | Alpha (degrees) | Strut Width (in) | Strut Thickness (in) | Confined Width (in) | Confined Allowable (ksi) | Unconfined Allowable (ksi) | Predicted Capacity (kips) | Change in Capacity* |
|----------|-----------------|------------------|----------------------|---------------------|--------------------------|----------------------------|---------------------------|---------------------|
| M1 | 20.89 | 7.13 | 7.25 | 5.54 | 12.90 | 4.87 | 496 | 3 |
| M2 | 15.04 | 5.51 | 7.11 | 4.31 | 12.82 | 4.79 | 479 | 1 |
| M2P | 15.04 | 5.51 | 7.11 | 4.31 | 12.82 | 4.79 | 479 | 1 |
| M3 | 5.61 | 1.71 | 7.37 | 0.91 | 12.65 | 4.62 | 464 | 28 |
| M3P | 5.61 | 1.71 | 7.37 | 0.91 | 12.65 | 4.62 | 464 | 28 |
| M4 | 21.29 | 5.83 | 7.01 | 4.46 | 13.65 | 5.62 | 522 | 2 |
| M4P | 21.29 | 5.83 | 7.01 | 4.46 | 13.65 | 5.62 | 522 | 2 |
| M6 | 14.50 | 7.29 | 7.69 | 6.02 | 8.36 | 3.67 | 401 | -1 |
| ME1A | 18.88 | 3.97 | 7.50 | 3.48 | 10.31 | 5.79 | 583 | 0 |
| ME1B | 10.27 | 3.92 | 7.56 | 3.73 | 10.27 | 5.75 | 550 | 0 |
| F1A | 20.93 | 4.46 | 7.00 | 3.54 | 8.31 | 3.63 | 380 | 0 |
| F1Bw | 7.53 | 7.30 | 7.63 | 6.41 | 8.01 | 3.33 | 368 | 0 |
| F1Bf | 17.08 | 4.06 | 3.87 | 3.24 | 8.17 | 3.49 | 285 | 0 |

* Change in Strut Capacity from Table 5.15a

b) Interior Strut

| Specimen | Alpha (degrees) | Strut Width (in) | Strut Thickness (in) | Confined Width (in) | Confined Allowable (ksi) | Unconfined Allowable (ksi) | Predicted Capacity (kips) | Change in Capacity* |
|----------|-----------------|------------------|----------------------|---------------------|--------------------------|----------------------------|---------------------------|---------------------|
| M1 | 1.94 | .67 | 7.62 | 0.14 | 12.67 | 4.64 | 368 | -18 |
| M2 | 5.12 | 1.90 | 7.30 | 1.16 | 12.70 | 4.67 | 455 | 15 |
| M2P | 5.12 | 1.90 | 7.30 | 1.16 | 12.70 | 4.67 | 455 | 15 |
| M3 | 18.57 | 6.02 | 7.12 | 4.41 | 12.82 | 4.79 | 471 | 4 |
| M3P | 18.57 | 6.02 | 7.12 | 4.41 | 12.82 | 4.79 | 471 | 4 |
| M4 | 7.40 | 2.07 | 7.28 | 1.16 | 13.44 | 5.41 | 519 | 33 |
| M4P | 7.40 | 2.07 | 7.28 | 1.16 | 13.44 | 5.41 | 519 | 33 |
| M6 | 1.28 | .65 | 7.91 | 0.37 | 8.26 | 3.58 | 366 | 25 |
| ME1A | 15.83 | 4.33 | 7.52 | 3.80 | 10.30 | 5.78 | 553 | 0 |
| ME1B | 10.23 | 3.68 | 7.57 | 3.42 | 10.26 | 5.75 | 551 | 0 |
| F1A | 9.93 | 3.59 | 7.09 | 2.89 | 8.27 | 3.59 | 369 | 0 |
| F1Bw | N/A | N/A | N/A | N/A | N/A | N/A | N/A | 0 |
| F1Bf | 17.08 | 4.06 | 3.87 | 3.10 | 8.17 | 3.49 | 277 | 0 |

* Change in Strut Capacity from Table 5.15b

Table 5.22 Local Zone-General Zone Interface Capacity with Node Adjustment Conducted

a) Exterior Strut

| Specimen | Depth of Confinement (in) | Alpha (degrees) | Strut Width (in) | Strut Thickness (in) | Unconfined Allowable (ksi) | Predicted Capacity (kips) | Change in Capacity* (kips) |
|----------|---------------------------|-----------------|------------------|----------------------|----------------------------|---------------------------|----------------------------|
| M1 | 8.00 | 20.89 | 8.89 | 7.89 | 4.48 | 319 | -46 |
| M2 | 8.00 | 15.04 | 7.33 | 8.07 | 4.22 | 322 | -32 |
| M2P | 8.00 | 15.04 | 7.33 | 8.07 | 4.22 | 322 | -32 |
| M3 | 8.00 | 5.61 | 2.34 | 8.32 | 4.10 | 382 | 111 |
| M3P | 8.00 | 5.61 | 2.34 | 8.32 | 4.10 | 382 | 111 |
| M4 | 8.00 | 21.29 | 8.37 | 7.91 | 4.98 | 409 | -46 |
| M4P | 8.00 | 21.29 | 8.37 | 7.91 | 4.98 | 409 | -46 |
| M6 | 10.00 | 14.50 | 9.30 | 8.58 | 3.29 | 277 | -47 |
| ME1A | 9.50 | 18.88 | 7.85 | 9.38 | 4.63 | 701 | 118 |
| ME1B | 9.50 | 10.27 | 6.10 | 9.63 | 4.51 | 503 | -47 |
| F1A | 8.00 | 20.93 | 7.71 | 7.74 | 3.28 | 344 | 0 |
| F1Bw | 8.00 | 7.53 | 7.69 | 7.91 | 3.18 | 268 | 0 |
| F1Bf | 8.00 | 17.08 | 6.85 | 4.25 | 3.18 | 257 | 0 |

* Change in Strut Capacity from Table 5.16a

b) Interior Strut

| Specimen | Depth of Confinement (in) | Alpha (degrees) | Strut Width (in) | Strut Thickness (in) | Unconfined Allowable (ksi) | Predicted Capacity (kips) | Change in Capacity* (kips) |
|----------|---------------------------|-----------------|------------------|----------------------|----------------------------|---------------------------|----------------------------|
| M1 | 8.00 | 1.94 | 0.84 | 8.35 | 4.23 | 369 | 197 |
| M2 | 8.00 | 5.12 | 2.52 | 8.32 | 4.10 | 342 | 66 |
| M2P | 8.00 | 5.12 | 2.52 | 8.32 | 4.10 | 342 | 66 |
| M3 | 8.00 | 18.57 | 8.09 | 7.97 | 4.28 | 330 | -39 |
| M3P | 8.00 | 18.57 | 8.09 | 7.97 | 4.28 | 330 | -39 |
| M4 | 8.00 | 7.40 | 2.97 | 8.30 | 4.75 | 464 | 110 |
| M4P | 8.00 | 7.40 | 2.97 | 8.30 | 4.75 | 464 | 110 |
| M6 | 10.00 | 1.28 | 0.83 | 8.85 | 3.19 | 294 | 153 |
| ME1A | 9.50 | 15.83 | 7.60 | 9.46 | 4.59 | 590 | 0 |
| ME1B | 9.50 | 10.23 | 5.86 | 9.64 | 4.51 | 520 | 0 |
| F1A | 8.00 | 9.93 | 5.16 | 7.92 | 3.21 | 276 | 0 |
| F1Bw | N/A | N/A | N/A | N/A | N/A | N/A | 0 |
| F1Bf | 8.00 | 17.08 | 6.85 | 4.25 | 3.18 | 257 | 0 |

* Change in Strut Capacity from Table 5.16b

Table 5.23 STM Prediction Summary with Node Adjustment Conducted

| Specimen | Tension Tie (kips) | Bearing (kips) | Node-Strut Exterior (kips) | Interface Interior (kips) | L.Z.-G.Z. Exterior (kips) | Interface Interior (kips) | Controlling Load (kips) | Ultimate Test (kips) | Test/Predicted |
|--|--------------------|----------------|----------------------------|---------------------------|---------------------------|---------------------------|-------------------------|----------------------|----------------|
| M1 | 189 | 418 | 496 | 368 | 319 | 369 | 189 | 304 | 1.61 |
| M2 | 393 | 411 | 479 | 455 | 322 | 342 | 322 | N/A | N/A |
| M2P | 393 | 411 | 479 | 455 | 322 | 342 | 322 | 401 | 1.25 |
| M3 | 290 | 411 | 464 | 471 | 382 | 330 | 290 | N/A | N/A |
| M3P | 290 | 411 | 464 | 471 | 382 | 330 | 290 | 364 | 1.26 |
| M4 | 180 | 440 | 522 | 519 | 409 | 464 | 180 | N/A | N/A |
| M4P | 180 | 440 | 522 | 519 | 409 | 464 | 180 | 411 | 2.28 |
| M6 | 104 | 331 | 401 | 366 | 277 | 294 | 104 | 300 | 2.88 |
| ME1A | 226 | 473 | 583 | 553 | 701 | 550 | 226 | 350 | 1.55 |
| ME1B | 228 | 473 | 550 | 551 | 503 | 520 | 228 | 350 | 1.54* |
| F1A | 141 | 324 | 380 | 369 | 344 | 276 | 141 | 248 | 1.76* |
| F1Bw | 133 | 324 | 368 | N/A | 268 | N/A | 133 | 248 | 1.86 |
| F1Bf | 141 | 324 | 285 | 277 | 257 | 257 | 141 | 248 | 1.76* |
| Note: Node Compression was found to not control in Table 5.20 Loads are per anchor * Other Anchor for that Specimen Controls | | | | | | | | Average | 1.81 |
| | | | | | | | | Standard Deviation | 0.55 |
| | | | | | | | | Coef. of Variance | 0.30 |

In the first analysis the tension ties controlled for Specimens M4P, M6, ME1, and F1. In the second analysis, all specimens but Specimen M2 are controlled by the tension ties. At the ultimate load, all of the specimens were extensively cracked in and around the local zones. This indicates that the compression capacities of the local zone-general zone and/or the node-strut interface were also close to their maximum. The low tension tie capacity predictions are causing the high degree of conservatism in the results. If the tension tie results are neglected, the test-to-predicted ratio average drops to 1.01 with a coefficient of variance of 0.14 and all the specimens are controlled by the local zone-general zone interface capacity except Specimen ME1 which is controlled by the bearing. The tension tie capacity limit should not be neglected in design. This interaction of the compression strut and tension ties capacities leads into the next subsection where the modified STM is used to balance the tension tie capacity based on a more plastic distribution of the compressive stresses and the compression strut capacity.

5.4.3 Modified Strut-and-Tie Model Prediction of the Ultimate Load. As was previously shown in the concentric and eccentric

anchorage zone chapters, the compressive stress can be distributed more plastically at the base and the struts can effectively concentrate closer to the tendon axis until compression failure occurs in the struts once the concrete cracks along the tendon axis. The matching of the tension tie capacity and the plastic compression strut capacity is called the modified STM. Tables 5.24 and 5.25 show the compressive capacities of the node-strut interface and the local zone-general zone interface respectively when the strut and tie capacity are matched. Table 5.26 is a summary of the modified STM. The node compression was checked in Table 5.20 and found not to control. The local zone-general zone interface controls for all the specimens. The average of the test-to-predicted ratios is 1.08, and the coefficient of variance for the method is only ten percent. Only one specimen is unconservative, Specimen ME1. The unconservative nature or low ultimate load for Specimen ME1 could have been caused by the shifting of the duct during casting ahead of anchorage "A" as was discussed in Sections 5.2 and 5.3. This could have caused premature failure. The modified STM is much more accurate than the basic STM which has a test-to-predicted ratio average of 1.81 and a coefficient of variance of 0.30. The test specimens allowed the extension of the general zone past the one section depth assumed in the basic STM. The more plastic distribution of forces at the end of the general zone, which is modelled by the modified STM, appears to be occurring and leads to the increased capacity.

5.4.4-Current Method for the Prediction of the Ultimate Load. In current design practice, the symmetrical prism method (see Fig. 4.52) is often utilized in conjunction with a bearing stress check to determine the capacity of the sections with multiple anchorages. The equation for the symmetrical prism is as follows.

$$P = 4T \cdot (1 - a/h')$$

where a is the plate width

h' is the width of the symmetrical prism

P is the force per anchor

T is the bursting reinforcement within the symmetrical prism

Table 5.24 Node-Strut Interface and Tie Capacity with Modified STM's

a) Exterior Strut

| Specimen | Alpha (degrees) | Strut Width (in) | Strut Thickness (in) | Confined Width (in) | Confined Allowable (ksi) | Unconfined Allowable (ksi) | Predicted Capacity (kips) |
|----------|--------------------|------------------------|----------------------------|---------------------------|--------------------------------|----------------------------------|---------------------------------|
| M1 | 8.52 | 6.28 | 7.49 | 5.24 | 12.75 | 4.72 | 479 |
| M2 | 12.53 | 5.37 | 7.15 | 4.26 | 12.80 | 4.77 | 475 |
| M2P | 12.53 | 5.37 | 7.15 | 4.26 | 12.80 | 4.77 | 475 |
| M3 | 26.40 | 3.23 | 7.19 | 1.01 | 12.77 | 4.74 | 660 |
| M3P | 26.40 | 3.23 | 7.19 | 1.01 | 12.77 | 4.74 | 660 |
| M4 | 8.00 | 5.08 | 7.22 | 4.20 | 13.49 | 5.46 | 501 |
| M4P | 8.00 | 5.08 | 7.22 | 4.20 | 13.49 | 5.46 | 501 |
| M6 | 7.94 | 6.75 | 7.80 | 5.89 | 8.31 | 3.62 | 389 |
| ME1A | 8.00 | 3.45 | 7.64 | 3.32 | 10.20 | 5.69 | 551 |
| ME1B | 4.46 | 3.62 | 7.63 | 3.68 | 10.21 | 5.70 | 529 |
| F1A | 8.35 | 3.92 | 7.09 | 3.35 | 8.27 | 3.58 | 366 |
| F1Bw | 2.73 | 6.80 | 7.69 | 6.36 | 7.99 | 3.31 | 357 |
| F1Bf | 10.10 | 3.77 | 3.94 | 3.15 | 8.11 | 3.43 | 280 |

b) Interior Strut

| Specimen | Alpha (degrees) | Strut Width (in) | Strut Thickness (in) | Confined Width (in) | Confined Allowable (ksi) | Unconfined Allowable (ksi) | Predicted Capacity (kips) |
|----------|--------------------|------------------------|----------------------------|---------------------------|--------------------------------|----------------------------------|---------------------------------|
| M1 | 1.16 | 0.59 | 7.62 | 0.14 | 12.67 | 4.64 | 335 |
| M2 | 5.51 | 1.93 | 7.30 | 1.16 | 12.70 | 4.67 | 458 |
| M2P | 5.51 | 1.93 | 7.30 | 1.16 | 12.70 | 4.67 | 458 |
| M3 | 19.70 | 6.08 | 7.10 | 4.41 | 12.83 | 4.80 | 470 |
| M3P | 19.70 | 6.08 | 7.10 | 4.41 | 12.83 | 4.80 | 470 |
| M4 | 2.86 | 1.72 | 7.31 | 1.16 | 13.42 | 5.39 | 469 |
| M4P | 2.86 | 1.72 | 7.31 | 1.16 | 13.42 | 5.39 | 469 |
| M6 | 0.75 | 0.60 | 7.91 | 0.37 | 8.26 | 3.57 | 346 |
| ME1A | 6.69 | 3.89 | 7.65 | 3.80 | 10.20 | 5.68 | 536 |
| ME1B | 4.43 | 3.38 | 7.63 | 3.42 | 10.21 | 5.69 | 531 |
| F1A | 3.97 | 3.27 | 7.13 | 2.89 | 8.25 | 3.57 | 357 |
| F1Bw | N/A | N/A | N/A | N/A | N/A | N/A | N/A |
| F1Bf | 10.20 | 3.77 | 3.94 | 3.10 | 8.11 | 3.43 | 278 |

Table 5.25 Local Zone-General Zone Interface and Tie Capacity with Modified STM's

a) Exterior Strut

| Specimen | Depth of Confinement (in) | Alpha (degrees) | Strut Width (in) | Strut Thickness (in) | Unconfined Allowable (ksi) | Predicted Capacity (kips) |
|----------|---------------------------|-----------------|------------------|----------------------|----------------------------|---------------------------|
| M1 | 8.00 | 13.76 | 7.85 | 8.08 | 4.38 | 293 |
| M2 | 8.00 | 17.46 | 7.74 | 8.01 | 4.26 | 336 |
| M2P | 8.00 | 17.46 | 7.74 | 8.01 | 4.26 | 336 |
| M3 | 8.00 | 21.92 | 5.36 | 8.06 | 4.23 | 815 |
| M3P | 8.00 | 21.92 | 5.36 | 8.06 | 4.23 | 815 |
| M4 | 8.00 | 11.53 | 6.71 | 8.16 | 4.83 | 345 |
| M4P | 8.00 | 11.53 | 6.71 | 8.16 | 4.83 | 345 |
| M6 | 10.00 | 11.73 | 8.70 | 8.64 | 3.27 | 262 |
| ME1A | 9.50 | 8.84 | 5.34 | 9.68 | 4.49 | 498 |
| ME1B | 9.50 | 5.75 | 4.92 | 9.74 | 4.46 | 410 |
| F1A | 8.00 | 11.15 | 5.82 | 7.89 | 3.22 | 273 |
| F1Bw | 8.00 | 4.28 | 7.19 | 7.95 | 3.18 | 227 |
| F1Bf | 8.00 | 12.07 | 5.84 | 4.25 | 3.18 | 234 |

b) Interior Strut

| Specimen | Depth of Confinement (in) | Alpha (degrees) | Strut Width (in) | Strut Thickness (in) | Unconfined Allowable (ksi) | Predicted Capacity (kips) |
|----------|---------------------------|-----------------|------------------|----------------------|----------------------------|---------------------------|
| M1 | 8.00 | 1.24 | 0.71 | 8.35 | 4.23 | 312 |
| M2 | 8.00 | 6.62 | 2.82 | 8.31 | 4.11 | 381 |
| M2P | 8.00 | 6.62 | 2.82 | 8.31 | 4.11 | 381 |
| M3 | 8.00 | 25.39 | 9.12 | 7.78 | 4.38 | 355 |
| M3P | 8.00 | 25.39 | 9.12 | 7.78 | 4.38 | 355 |
| M4 | 8.00 | 3.77 | 2.25 | 8.33 | 4.73 | 354 |
| M4P | 8.00 | 3.77 | 2.25 | 8.33 | 4.73 | 354 |
| M6 | 10.00 | 0.98 | 0.76 | 8.85 | 3.19 | 268 |
| ME1A | 9.50 | 7.97 | 5.62 | 9.69 | 4.49 | 449 |
| ME1B | 9.50 | 5.63 | 4.65 | 9.75 | 4.46 | 418 |
| F1A | 8.00 | 6.02 | 4.34 | 7.96 | 3.20 | 235 |
| F1Bw | N/A | N/A | N/A | N/A | N/A | N/A |
| F1Bf | 8.00 | 12.07 | 5.84 | 4.25 | 3.18 | 234 |

Table 5.26 Modified STM Prediction Summary

| Specimen (kips) | Bearing (kips) | Node-Strut Exterior (kips) | Interface Interior (kips) | L.Z.-G.Z. Exterior (kips) | Interface Interior (kips) | Controlling Load (kips) | Ultimate Test (kips) | Test/ Predicted |
|---|-------------------|----------------------------------|---------------------------------|---------------------------------|---------------------------------|-------------------------------|----------------------------|--------------------|
| M1 | 418 | 479 | 335 | 293 | 312 | 293 | 304 | 1.04 |
| M2 | 411 | 475 | 458 | <u>336</u> | 381 | 336 | N/A | N/A |
| M2P | 411 | 475 | 458 | <u>336</u> | 381 | 336 | 401 | 1.19 |
| M3 | 411 | 660 | 470 | 815 | 355 | 355 | N/A | N/A |
| M3P | 411 | 660 | 470 | 815 | <u>355</u> | 355 | 364 | 1.03 |
| M4 | 440 | 501 | 469 | 345 | 354 | 345 | N/A | N/A |
| M4P | 440 | 501 | 469 | <u>345</u> | 354 | 345 | 411 | 1.19 |
| M6 | 331 | 389 | 346 | <u>262</u> | 268 | 262 | 300 | 1.15 |
| ME1A | 473 | 551 | 536 | 498 | <u>449</u> | 449 | 350 | 0.78* |
| ME1B | 473 | 529 | 531 | 410 | <u>418</u> | 410 | 350 | 0.85 |
| F1A | 324 | 366 | 357 | <u>273</u> | <u>235</u> | 235 | 248 | 1.06* |
| F1Bw | 324 | 357 | N/A | 227 | N/A | 227 | 248 | 1.09 |
| F1Bf | 324 | 280 | 278 | <u>234</u> | <u>234</u> | 234 | 248 | 1.06* |
| Note: Node Compression was found to not control in Table 5.20, Loads are per anchor | | | | | | | Average | 1.08 |
| * Other Anchor for that Specimen Controls | | | | | | | Standard Deviation | 0.11 |
| | | | | | | | Coef. of Variance | 0.10 |

Table 5.27 shows the results of such an analysis which models each anchor as an individual anchor. The results are conservative for all the specimens except Specimen M1 which, interestingly, was the only specimen in which bearing stress was predicted to have controlled. The average of the test-to-predicted ratios is 1.33 with a coefficient of variance of 0.26. Table 5.28 shows the symmetrical prism results when the anchors that are located within one plate width of each other are modelled as a single anchor. The predictions produce a test-to-predicted ratio much closer to one, 1.08 and a coefficient of variance of 0.23. However, all of the specimens (Specimens M1, M2, M4, and M6) modelled as a single anchor have unconservative predictions. The current design method, though not as rational as the STM, produces results that are, overall, slightly more accurate for these test results than the basic STM but more unconservative in isolated cases. The modified STM is still the most accurate model for the test specimens.

Table 5.27 Symmetrical Prism Results Modelling Each Anchor Separately

| Specimen | Bursting Tension using the Symmetrical Prism | a (in) | h' (in) | Tension Tie Prediction (kips) | Bearing Prediction (kips) | Controlling Load (kips) | Test Ultimate (kips) | Test/Prediction |
|----------|--|--------|---------|-------------------------------|---------------------------|-------------------------|----------------------|-----------------|
| M1 | 26.40 | 6.00 | 8.00 | 422 | <u>418</u> | 418 | 304 | 0.73 |
| M2 & M2P | 39.60 | 6.00 | 12.00 | <u>317</u> | 411 | 317 | 401 | 1.27 |
| M3 & M3P | 35.70 | 6.00 | 11.00 | <u>314</u> | 411 | 314 | 364 | 1.16 |
| M4 & M4P | 39.60 | 6.00 | 12.00 | <u>317</u> | 440 | 317 | 411 | 1.30 |
| M6 | 7.14 | 6.50 | 8.00 | <u>152</u> | 331 | 152 | 300 | 1.97 |
| ME1A | 41.76 | 6.50 | 20.00 | 267 | 473 | 247 | 350 | 1.41* |
| ME1B | 27.48 | 6.50 | 12.00 | <u>240</u> | 373 | 240 | 350 | 1.46 |
| F1A | 14.28 | 6.50 | 8.00 | <u>305</u> | 324 | 305 | 248 | 0.81* |
| F1Bw | 14.28 | 6.50 | 8.00 | <u>305</u> | 324 | 305 | 248 | 0.81* |
| F1Bf | 35.70 | 6.50 | 34.00 | <u>177</u> | 324 | 177 | 248 | 1.40 |
| | | | | | | | Average | 1.33 |
| | | | | | | | Standard Deviation | 0.34 |
| | | | | | | | Coef. of Variance | 0.26 |

* Other Anchor for that Specimen Controls

Table 5.28 Symmetrical Prism Results Modelling Closely Spaced Anchor as One Anchor

| Specimen | Bursting Tension using the Symmetrical Prism | a (in) | h' (in) | Tension Tie Prediction (kips) | Bearing Prediction (kips) | Controlling Load (kips) | Test Ultimate (kips) | Test/Prediction |
|------------|--|--------|---------|-------------------------------|---------------------------|-------------------------|----------------------|-----------------|
| M1 | 66.00 | 14.00 | 36.00 | 432 | <u>418</u> | 418 | 304 | 0.73 |
| M2 & M2P | 79.20 | 18.00 | 36.00 | 634 | <u>411</u> | 411 | 401 | 0.98 |
| M3 & M3P** | N/A | N/A | N/A | N/A | N/A | N/A | 364 | 1.16 |
| M4 & M4P | 52.80 | 18.00 | 26.00 | 686 | 440 | 440 | 411 | 0.93 |
| M6 | 50.00 | 14.50 | 32.00 | 366 | <u>331</u> | 331 | 300 | 0.91 |
| ME1A** | N/A | N/A | N/A | N/A | N/A | N/A | 350 | 1.41* |
| ME1B** | N/A | N/A | N/A | N/A | N/A | N/A | 350 | 1.46 |
| F1A** | N/A | N/A | N/A | N/A | N/A | N/A | 248 | 0.81* |
| F1Bw** | N/A | N/A | N/A | N/A | N/A | N/A | 248 | 0.81* |
| F1Bf** | N/A | N/A | N/A | N/A | N/A | N/A | 248 | 1.40 |
| | | | | | | | Average | 1.08 |
| | | | | | | | Standard Deviation | 0.25 |
| | | | | | | | Coef. of Variance | 0.23 |

* Other Anchor for that Specimen Controls

** More than a plate width apart, too far to be modelled as one plate

5.5 Conclusions for Multiple Anchorage Zones

1) The use of the basic STM is a conservative method for the design of multiple anchorage zones. The conservatism of the method is due mainly to the low tension tie capacity prediction because the location of the compression struts is assumed to be at the centroid of the linear stress profile. The average of the test-to-predicted ratios was 1.81. It is important to check both tension tie capacity and compression strut capacity. When determining the dimensions of the local zone node, it is important that the division line of the node struts and the general zone be the same in the cases where the difference between the struts is more than ten percent.

2) All of the specimens eventually failed in compression because the force paths were able to adjust to allow a higher axial capacity than that predicted when the compression struts were assumed to be located according to the elastic combined stress distribution at a depth of section, h , away from the loading surface.

3) The modified STM, which assumes a more plastic stress distribution, allows the compression struts to shift toward the tendon axis until the compression strut failure load and the tension tie failure load are the same and is much more accurate than the basic STM. The average of the test-to-predicted ratios is 1.08 with a coefficient of variance of ten percent. When the general zone extends past the depth of the section, additional cracking must occur in the general zone.

4) Guyon's symmetrical prism method was less conservative than the basic STM for the multiple anchorage specimens tested with an average ratio of 1.33. Specimen M1 was the only specimen which was unconservative, but it was very unconservative with a test-to-predicted ratio of 0.73. For several of the specimens, a significant amount of bursting reinforcement was located outside the symmetrical prism and was, therefore, not included in the symmetrical prism analysis. Even though this reinforcement outside the symmetrical prism was not

included in the analysis, the reinforcement was utilized by the spreading forces in the actual specimen. Therefore, these specimens could have had conservative ultimate load predictions because of this extra reinforcement not included in the model as opposed to the conservatism of the actual model.

5) When anchorages are spaced sufficiently far apart, tension spalling forces develop between the anchorages. These forces can become very large. In the case of Specimen M3, the spalling tension tie controlled the design. The maximum depth of the effective spalling reinforcement should be taken as the depth of the local zone node. In test M3P in which not enough reinforcement was placed in the spalling zone, the spalling force was able to find additional resistance by cracking further into the section. The spalling crack can become quite large unless sufficient reinforcement is provided. Reinforcement within the spalling zone should not be less than two percent of the axial load of the adjacent anchors; such requirements are not necessarily indicated by the STM. This reinforcement is necessary in order to carry the surface tension that can occur with closely spaced anchors. Spalling reinforcement should be tied back through the anchorages to connect the two anchorages.

6) When anchorage zones are placed in flanged sections or in other sections with substantially different axes, multiple STM's must be used. In the case of a "T" section, the forces can spread through the web and then into the flange.

7) The first crack analysis for the multiple anchorage specimens was not very accurate. When using the transformed thickness of the section and including the triaxial stress effects, the average of the test-to-predicted ratios was 1.00 with a coefficient of variance 0.26. Guyon's symmetrical prism was unconservative for two tests when compared with the finite element analysis. Using the symmetrical prism in conjunction with a lower bound strength approximation of $4.2\sqrt{F'_c}$ produces answers which are essentially all conservative. Only Specimen

F1 was unconservative with a test-to-predicted ratio of 0.99.

CHAPTER 6
SPECIMENS WITH INCLINED ANCHORAGES AND CURVED TENDONS

6.1 Introduction

In order to economically resist the forces induced by dead load and live load on a girder or other post-tensioned structures, curved tendons which result in inclined anchorages are often used. By using an initial inclination in the tendon, a large shear force is induced at the end of the girder. If the tendon is curved, then the external shear is reduced by the "load balancing" due to the deviation of the tendon. This large upward force is helpful in cases where there is a large shear in the anchorage vicinity. When curved tendons are utilized, the tendon can be placed where it is most needed.

Five specimens were tested with anchorage inclination and tendon curvature. Table 6.1 shows the variables investigated and the basic material properties for the five specimens. Specimens I1 and I3 were loaded along the centroidal axis of the section ($e = 0$ inches). Specimens I2, I4 and ME2 had eccentricities other than zero. Specimens I2 and I4 investigated the effect of different amounts of tie-back reinforcement. The anchorage for these two specimens was placed at an e/h of $1/4$ (ratio of eccentricity to the depth of the section). Tie-back reinforcement is the reinforcement placed around the duct so that, when a crack forms along the tendon path, a portion of the radial compression force due to the tendon curvature can be resisted by tension on the opposite side of the tendon. Specimen ME2 was a multiple anchorage specimen with anchorages at +12 inches and -4 inches from the specimen centerline.

6.2 Test Program

All of the curved tendon specimens were tested utilizing tendons, hydraulic rams, and the tunnel slab as shown in Fig. 6.1. This was necessary because of the inclination of the anchorage device and in order to accurately model the forces induced by the tendon curvature.

Table 6.1 Material Information for Specimens I1, I2, I3, I4 and ME2

| Specimen | Reinforcing Bar | | | | | |
|----------------------|-------------------------|-----------------------|-------------------|-------------------------|----------------------------|---------------------------|
| | Bar Size | E (ksi) | F_y (kips) | f_y (ksi) | Yield Strain (microstrain) | |
| I1, I2, I3, I4 & ME2 | #2s* | 28900 | 3.57 | 75.1 | 2600 | |
| | #3 | 27500 | 6.60 | 60.0 | 2200 | |
| | #4 | 27900 | 12.70 | 63.5 | 2270 | |
| | Concrete f_{sp} (psi) | Concrete f'_c (psi) | Eccentricity (in) | Initial Angle (degrees) | Tendon Radius (in) | Tieback Reinforcement (%) |
| I1 | 358 | 5720 | 0 | 20 | 131 | 24.2 |
| I2 | 423 | 6410 | 9 | 20 | 131 | 34.6 |
| I3 | 348 | 4510 | 9 | 10.3 | 239 | 53.0 |
| I4 | 393 | 6170 | 9 | 20 | 131 | 0 |
| ME2 | 491 | 6730 | | | | |
| Tendon A | | | -4 | 15 | 170 | 29.3 |
| Tendon B | | | +12 | 20 | 131 | 36.1 |

* #2s $A_s = 0.0475 \text{ in}^2$

All of the tendons were designed to be perpendicular to the specimen base at the top of the tunnel slab in order for there to be no base shear. In addition, each specimen had a straight portion of tendon extending from the loading surface of the anchorage device for the initial 12 inches. During the casting of the concrete the post-tensioning duct was held in place by bar chairs underneath, wooden plugs in the straight portions, and tensioned piano wire. At several locations along the curved portion of the duct, piano wire was attached to the duct, placed through the side of the form work, and then was tied to an adjustable screw. This screw was used to pull the duct into the desired location. All the specimens used multiple plane seven 1/2-inch strand anchorages which were loaded with 12 1/2-inch strands

and a post-tensioning ram. The excess number of strands permitted an ultimate load testing of the anchorages. The pressure in the ram was measured using electronic pressure transducers. All of the specimens were mounted on 1/32-inch thick teflon sheets laid on top of the test slab. Since one of the specimens, Specimen I1, had a tendon location at the base outside of the kern, a modified base was used on all of the "I" series specimens to make the series as uniform as possible. The spiral reinforcement for all the specimens was a smooth #4 spiral with an 8-inch diameter, a 2-inch pitch and a 9 1/2-inch length. The spiral had a yield stress of 80.3 ksi, a modulus of elasticity of 27,200 ksi, and a yield strain of 3,030 microstrains. The same test procedure was used as described in Chapter 3 for concentric anchorages. The specimens were not tested in numerical order. Changes were made in later specimens because of the initial results. Therefore, the specimens will be described in detail in the order in which they were tested: I4, I2, I3, I1, and ME2.

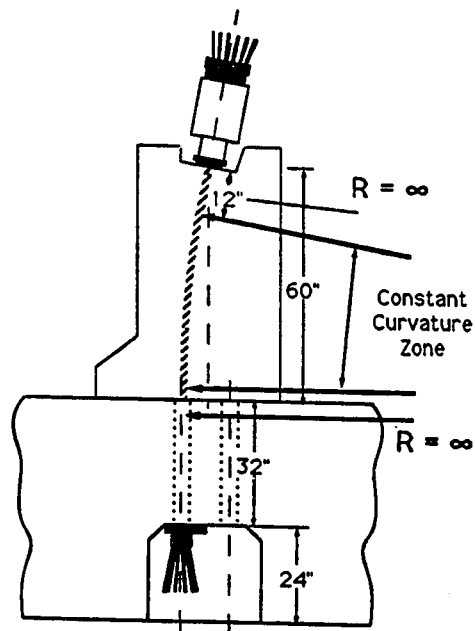


Figure 6.1 Schematic of Test Setup, "I" Series

Specimen I4 (see Fig. 6.2) was an eccentric anchorage specimen with an anchorage inclination of 20 degrees and a radius of curvature of 131 inches. The specimen had no tie-back reinforcement along the tendon path but did have #3 bursting tie reinforcement with a centroid located 14.5 inches from the loading surface, (measured parallel to the specimen axis) and a total tension capacity of 52.8 kips. The base of the specimen was reinforced with a combination of #4 and #3 ties. One #3 tie and two #4 ties crossed the tendon duct. The general material information for Specimen I4 is given in Table 6.1.

The specimen was loaded to 300 kips with no visible signs of cracks. A leak then developed in one of the hydraulic hoses. The load was reduced to 24 kips to replace the hose. The loading was then continued, and the first crack was detected at 350 kips on both sides of the specimen (see Table 6.2). The cracking loads are listed separately for both sides of the specimen. The crack was seen to be propagating as recordings were being taken. The crack extended from the loading surface to 40 inches below the loading surface. The initial crack was perpendicular to the loading surface and was extremely straight. The crack width at 8 inches from the loading surface was 0.006 inches, while the width was 0.008 inches at 28 inches from the loading surface. At 380 kips, these crack widths increased to 0.009 inches and 0.011 inches respectively. When the load was 390 kips, the crack propagated to the base of the specimen. By 420 kips, the crack sizes had increased to 0.02 and 0.015 inches respectively (see Fig. 6-3). This load was also the maximum tendon load which was desirable from a safety standpoint, $0.85F_{pu}$ for the 12 strands. F_{pu} is the guaranteed minimum ultimate strength of the tendon. The specimen was unloaded to 90 kips, loaded back to 420 kips, and then cycled a second time. The load history for the specimen is shown in Fig. 6.4. Strains in the bursting reinforcement increased slightly but not enough to cause failure. The higher than expected capacity was attributed to the transverse force contribution of the reinforcement that crossed the

tendon duct at the base of the specimen. The load and the concrete cover above the reinforcement were removed, and these bars were cut along the tendon axis. This concluded what will be referred to as Test 1.

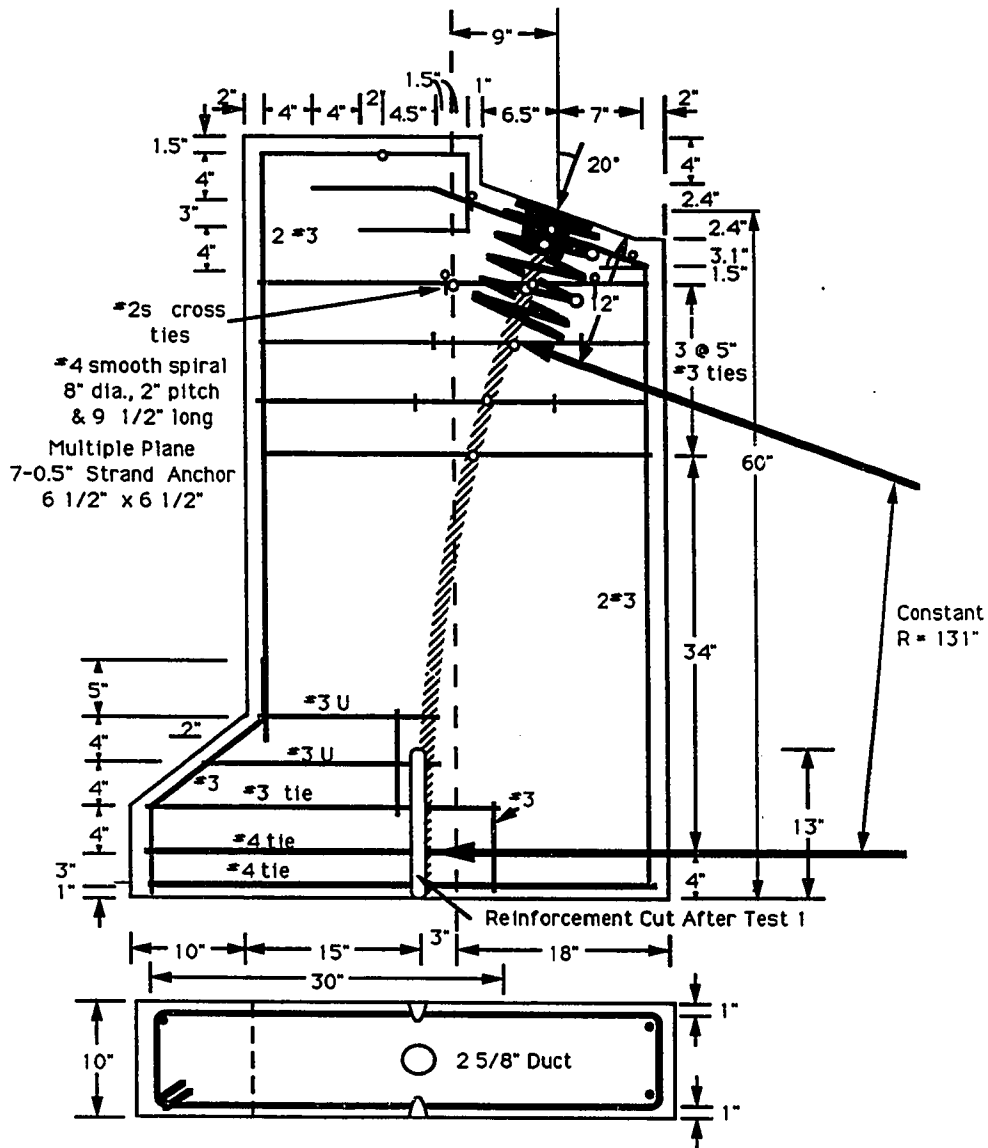


Figure 6.2 Specimen I4 Detail

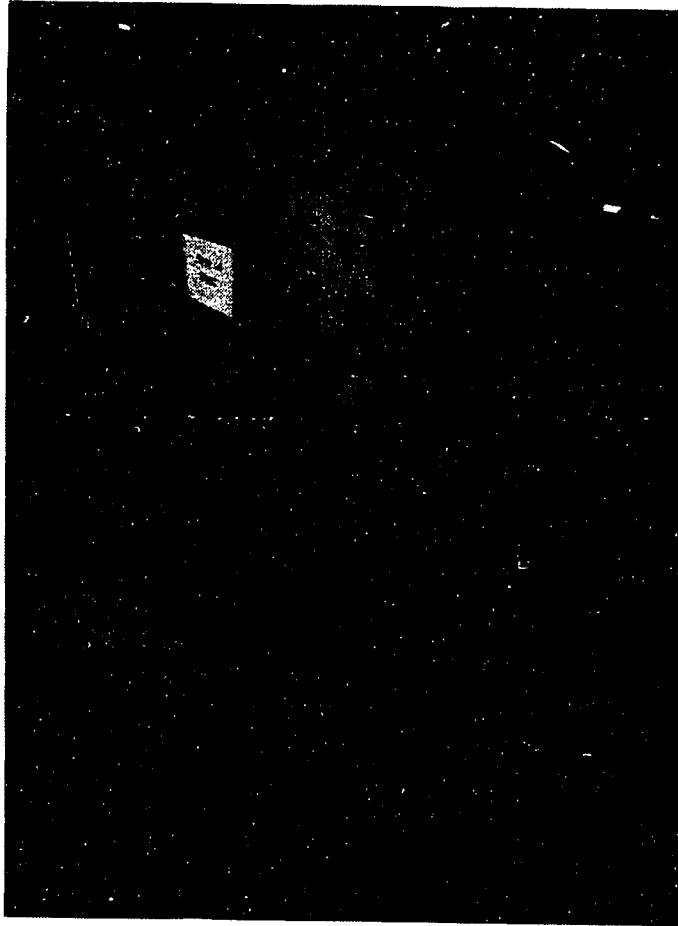


Figure 6.3 Specimen I4 at Conclusion of First Test, 420 kips

Table 6.2 Load Summary for Specimen I1, I2, I3, I4 and ME2

| Specimen | First Bursting Crack (kips) | | Peak Load (kips) | | | |
|----------|--------------------------------|--------|---------------------|-----|----------|----------|
| | Side A | Side B | A | B | | |
| I1 | 250 | 250 | 423 | | | |
| I2 | 325 | 340 | 437 | | | |
| I3 | 250 | 290 | 375 | | | |
| I4 | 350 | 350 | 420 | | | |
| ME2 | Anchorage A 240 | 265 | Anchorage B 240 | 275 | A 370 | B 366 |

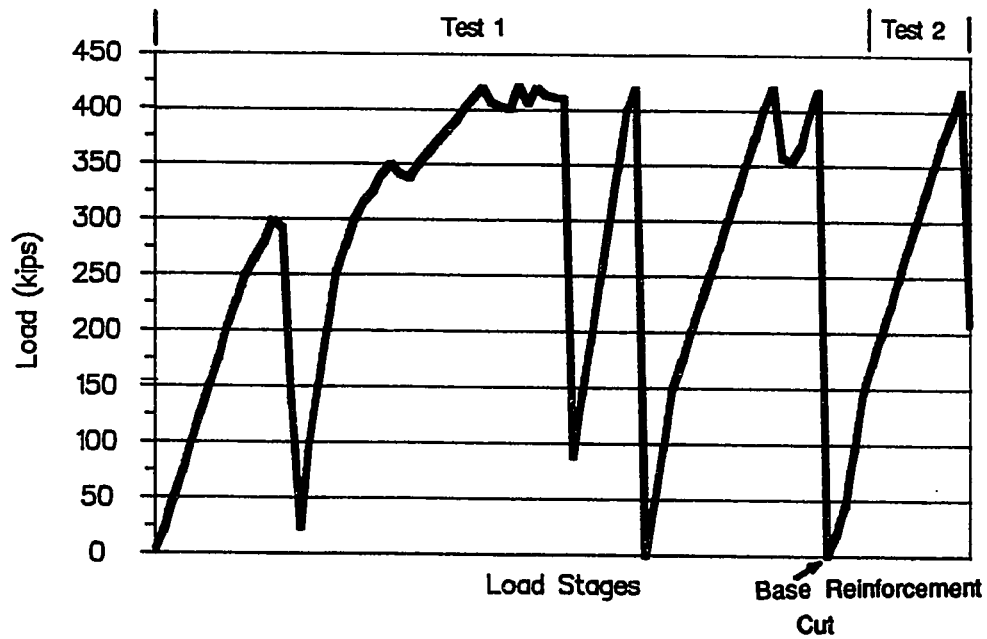


Figure 6.4 Load-History for Specimen I4

Once the base reinforcement was cut, the specimen was reloaded. Figure 6.5 shows the bursting strain data (some of the unloading cycles are removed for clarity). The strains in the bursting reinforcement increased very slowly during Test 1 until the concrete cracked at 350 kips. At the conclusion of the first test the bursting reinforcement at 12, 17, and 22 inches from the loading surface had yielded. In the early stages of Test 2, the bursting strains did not change significantly but the crack size increased. When the load reached 400 kips, the crack at 8 inches from the loading surface was 0.03 inches wide, and the crack at 28 inches from the loading surface was 0.055 inches wide; internal concrete cracking was becoming very noticeable. When the load reached 420 kips, the rate of internal cracking began to accelerate. No additional load was added. The main tendon crack grew for about four minutes until the specimen exploded. Since the lowest complete reinforcing bar crossing the tendon duct was at 22 inches from the loading surface, the specimen split into two parts at the base and light was clearly visible through the crack coming from the opposite side (see Fig. 6.6). Figure 6.6a shows the east side of the specimen with most of the top concrete still intact. Figure 6.6b shows the massive amounts of spalled concrete on the west side of the specimen. The black object near the Test I4 sign is a felt-tip pen. The duct completely separated from the concrete. The bearing plate was pushed into the specimen approximately 1 inch and the load dropped to 208 kips. The spiral strains near the top of the spiral were large near the end of the test with the transverse strains near 1500 microstrain until failure when the spiral yielded (see Fig. 6.7).

Specimen I2 had the same geometry as Specimen I4, but the reinforcement was altered (see Fig. 6.8). The amount of bursting reinforcement across the full depth of the specimen was reduced to a total tension capacity of 35.7 kips with a centroid located at 14 inches ahead of the loading surface. Tie-back reinforcement across the tendon duct consisted of six #3 ties (see Fig. 6.9) spaced 8 inches

apart along the curved portion of the tendon.

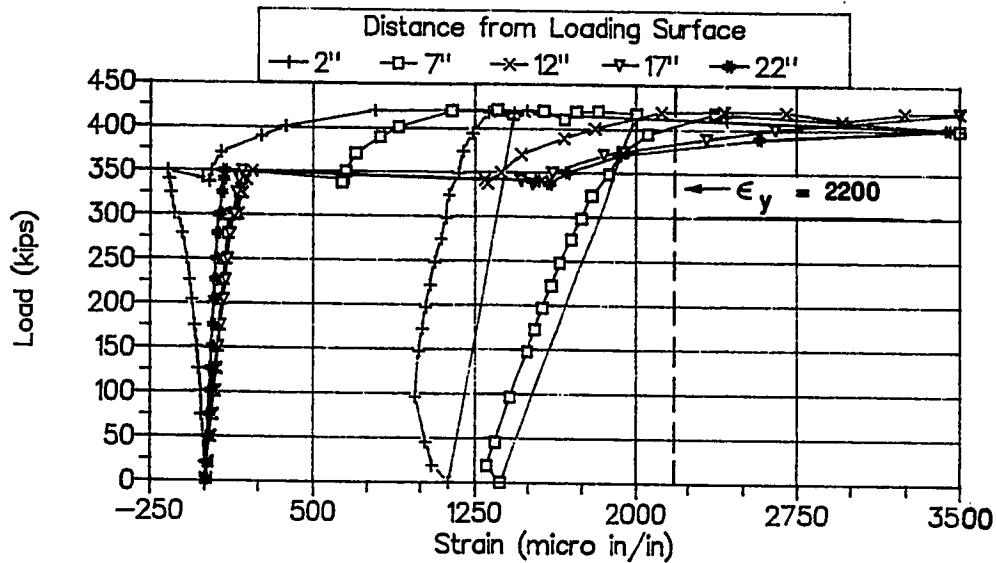
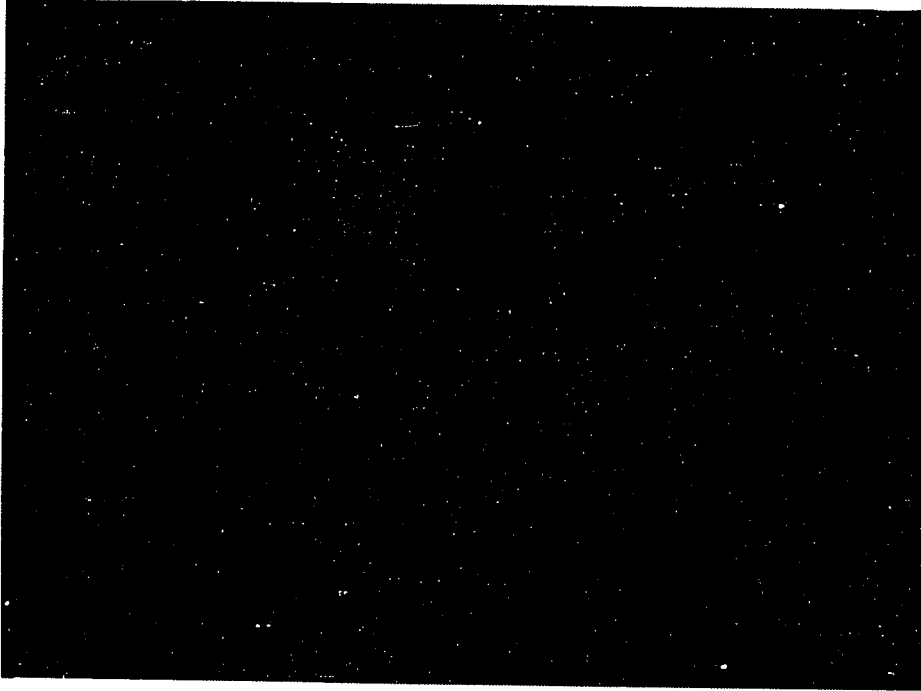


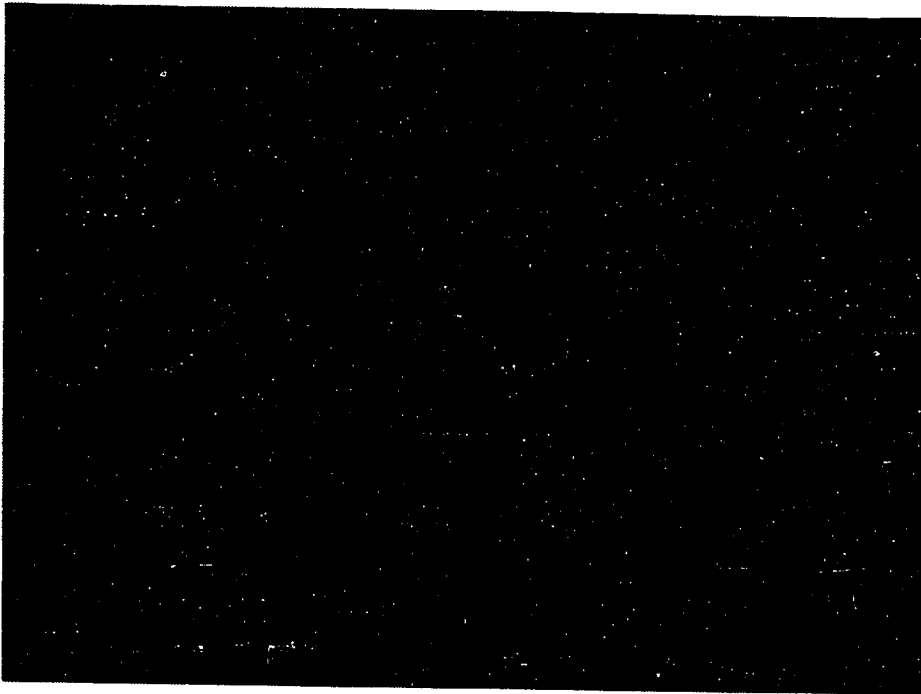
Figure 6.5 Bursting Reinforcement Strain Data, Specimen I4

The initial behavior of Specimen I2 was very similar to that of Specimen I4. The first crack occurred at 325 kips on the west side and at 340 kips on the east side. The cracks were long, extending from the loading surface to a depth of 35 inches from the loading surface. At 400 kips, the crack width at 10 inches from the loading surface was 0.012 inches and was 0.006 inches at 28 inches from the loading surface. By 420 kips, the cracks had only extended slightly (see Fig. 6.10). Therefore, as with Specimen I4, the load was reduced to 25 kips and the reinforcement over the duct at the base of the specimen was removed (see Fig. 6.10). When the base reinforcement was cut, so were the two bottom tie-back bars. Therefore, the number of tie-back ties was reduced to four.



b) East Side

410



a) West Side

Figure 6.6 Crack Patterns at Ultimate, Specimen I4

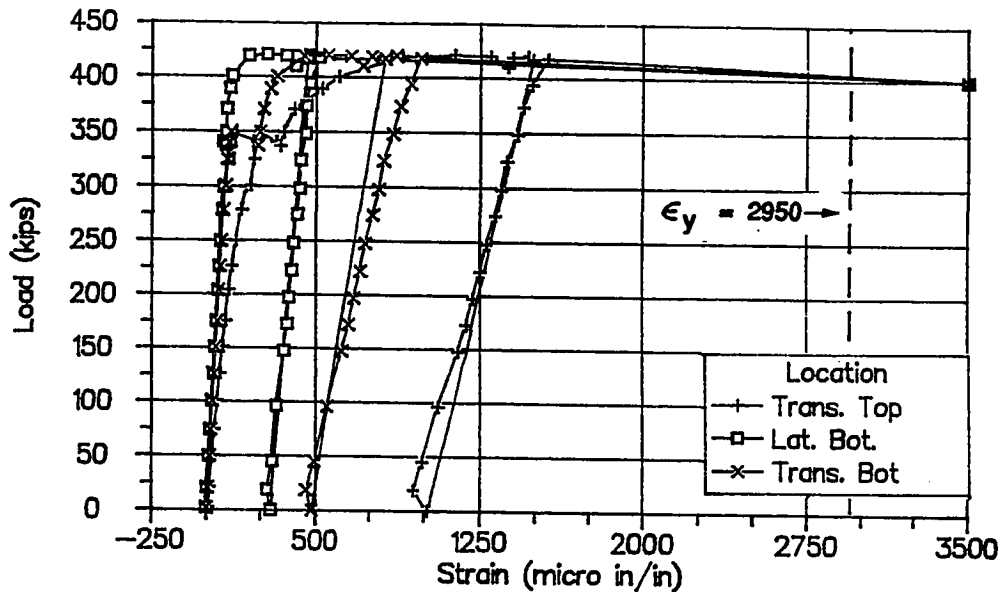


Figure 6.7 Spiral Strain Data, Specimen I4

Figure 6.11 shows the load history for Specimen I2. The bursting strains for Specimen I2 are shown in Fig. 6.12. The bursting strains increased significantly when the specimen cracked at 340 kips. During the loading after the removal of the base reinforcement, strain gages on the two ties closest to the anchor indicated very small increases in strain until 340 kips. The ties at 10, 14, 18, and 22 inches were very close to yielding by 340 kips. At 340 kips, a diagonal crack propagated from the anchorage device to the edge of the specimen at 16 inches above the base (see Fig. 6.13). This caused a change in the stress distribution as seen by the jumps in the bursting strain readings of the gages at 10, 14, and 18 inches from the loading surface. By 410 kips, the diagonal crack was 0.04 inches wide. At 437 kips (see Fig. 6.13), transverse cracks opened on the transverse face nearest the anchorage device. The load decreased to less than 420 kips. While being reloaded, the specimen exploded at 425 kips (see Fig. 6.14). Figure 6.15 shows that the tie-back reinforcement closest

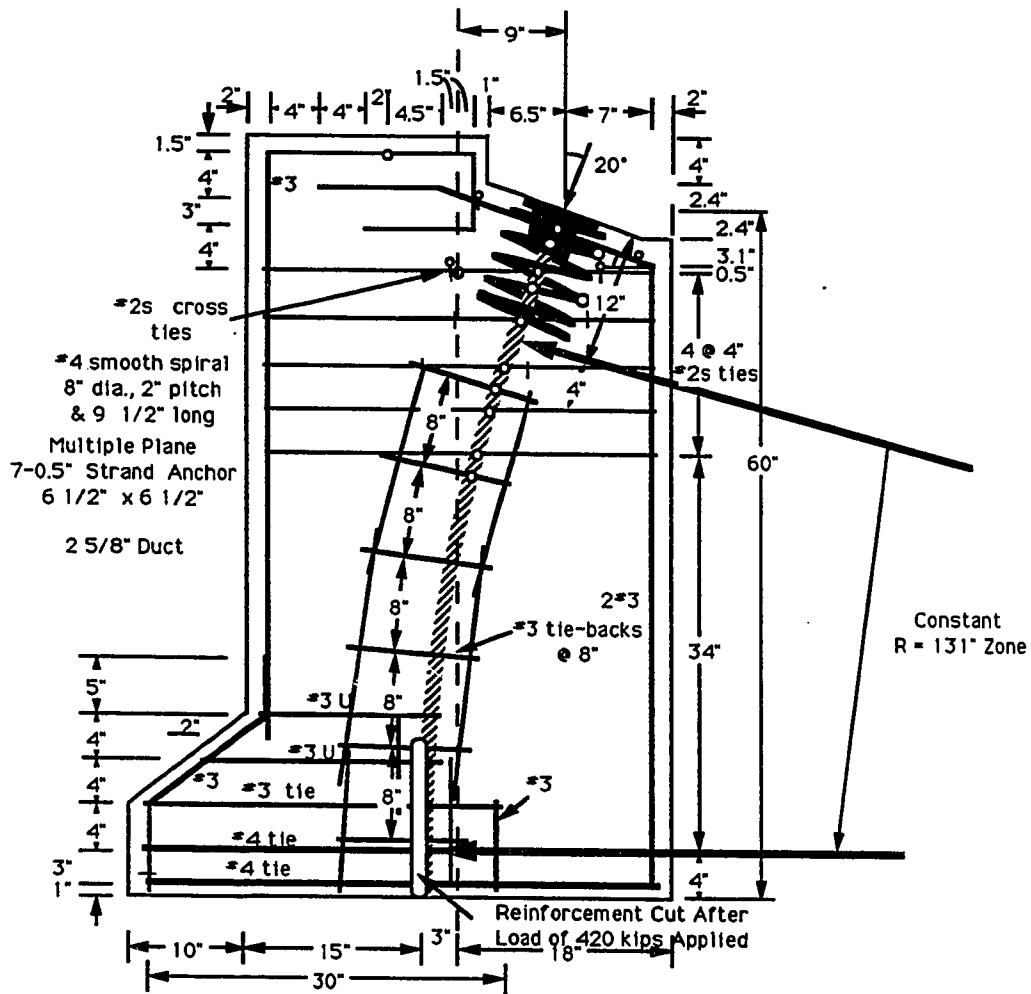


Figure 6.8 Specimen I2 Detail

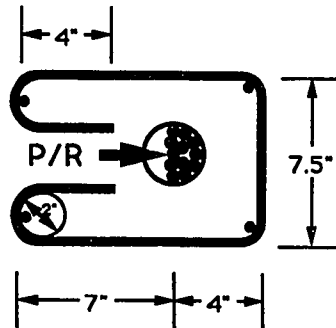


Figure 6.9 Tie-Back Detail

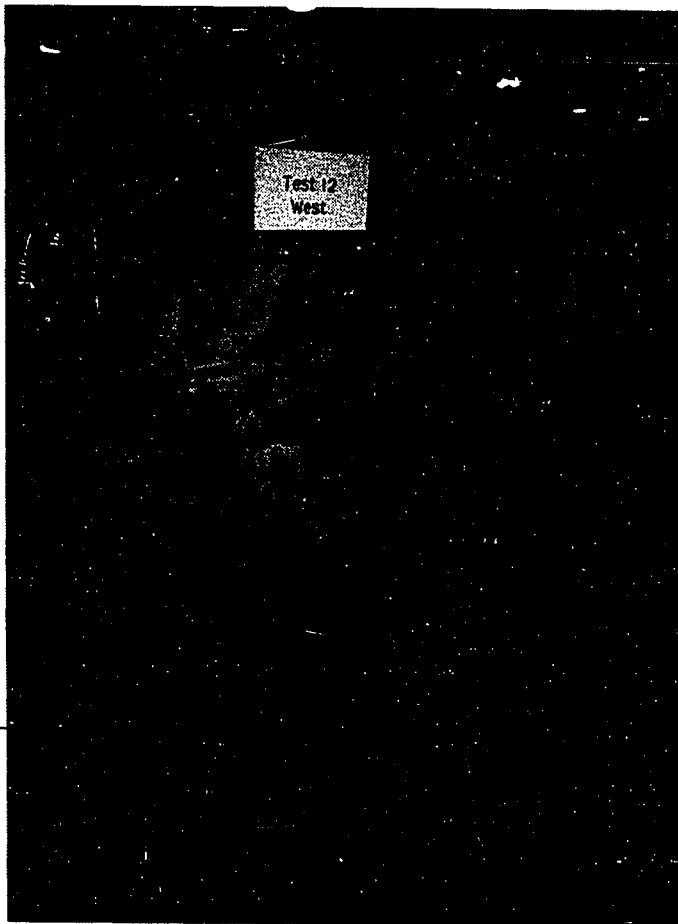


Figure 6.10 Crack Pattern at Conclusion of Test 1, Specimen I2

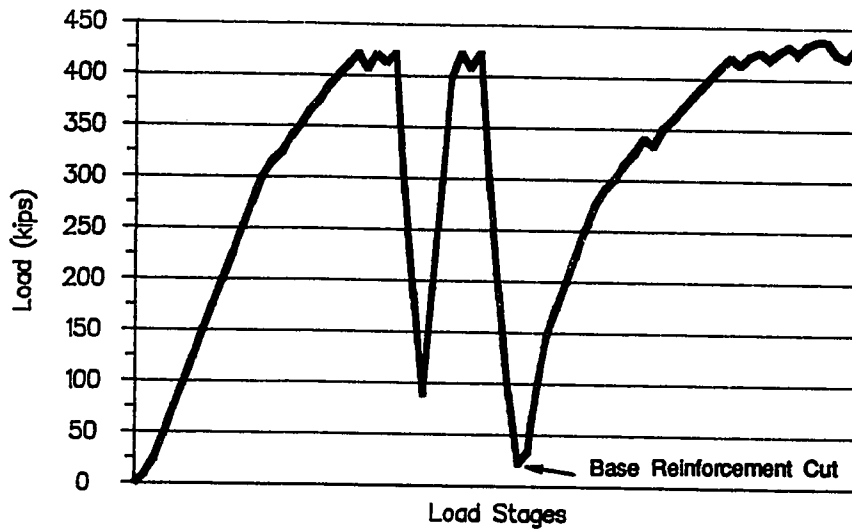


Figure 6.11 Load-History for Specimen I2

to the base of the specimen had yielded by the conclusion of the test. Tie-back reinforcement nearest the anchorage device had not yielded. Figure 6.16 shows that most of the spiral strains at the top of the spiral had begun to increase toward the end of the test and some yielded post failure. Several horizontal cracks opened on the transverse face near the anchorage device. The cracks were located at 8, 16, 22, and 31 inches ahead of the centroid of the loading surface.

Specimen I3 was the most basic of the inclined tendon specimens (see Fig. 6.17). The anchorage device was located on the centerline of the specimen. The tendon exits the base of the specimen within the kern. Specimen I3 had the smallest angle of inclination, ten degrees, and the largest radius of curvature, 239 inches. The specimen had six closed ties extending across the full width of the specimen with a total bursting tension capacity of 35.7 kips and a centroid of 14 inches from the loading surface. The supplementary tie-back reinforcement consisted of five #2s ties at a 9-inch spacing. The base reinforcement was not extended over the duct to prevent any of the problems experienced in Specimens I2 and I4.

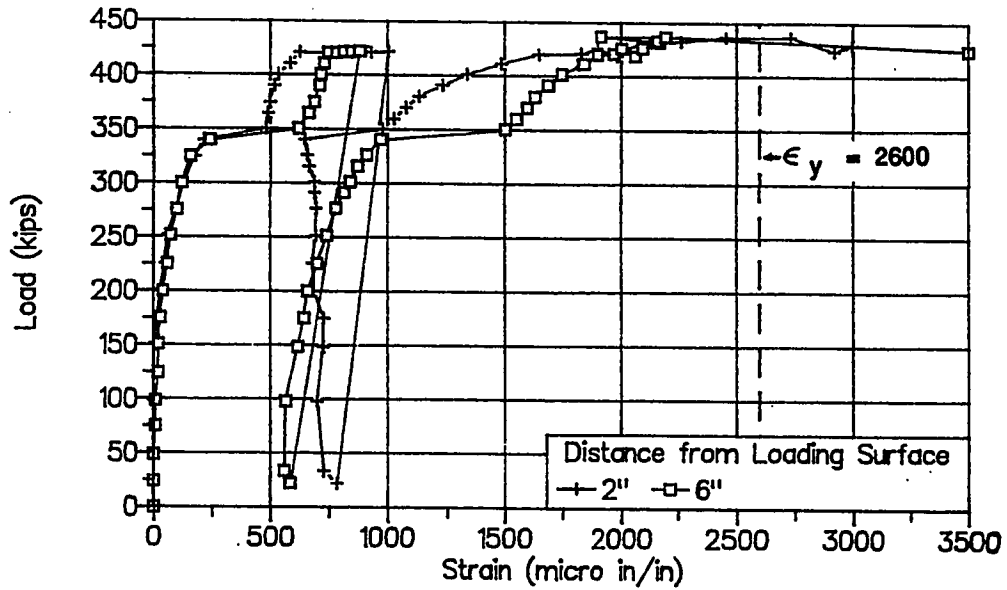


Figure 6.12a Bursting Reinforcement Strain Data, Close to Loading Surface, Specimen I2

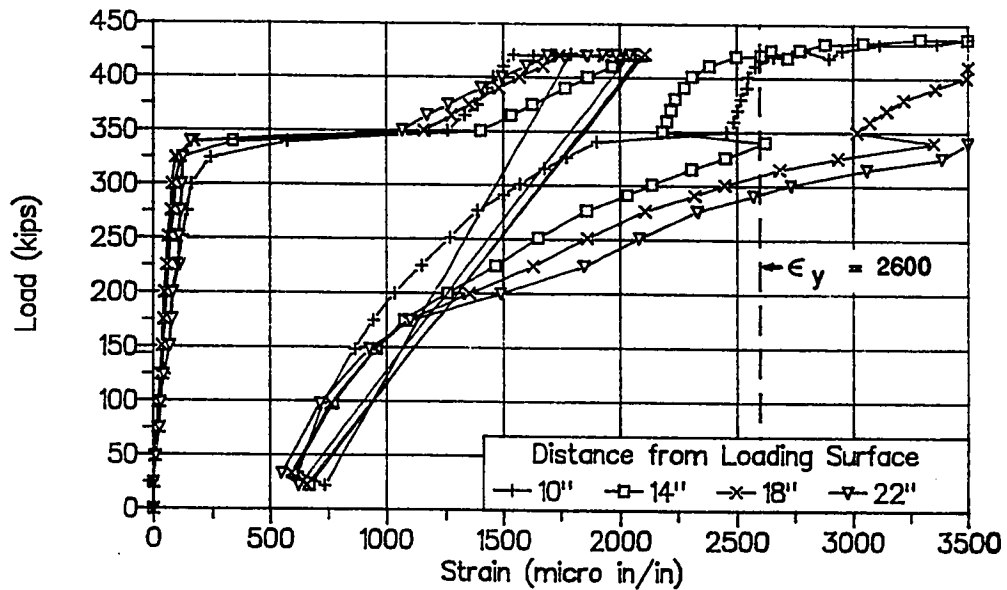
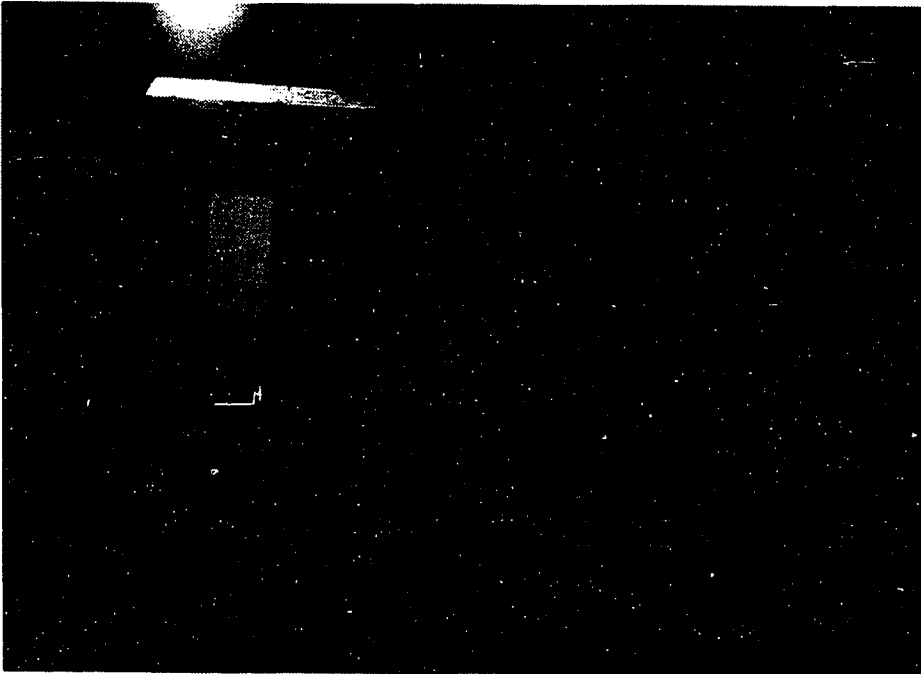


Figure 6.12b Bursting Reinforcement Strain Data, Bars Distant from Loading Surface, Specimen I2



**Figure 6.13 Crack Pattern for Specimen I2,
One Load Stage Before the Ultimate Load**



**Figure 6.14 Crack Pattern for Specimen I2,
After the Ultimate Load**

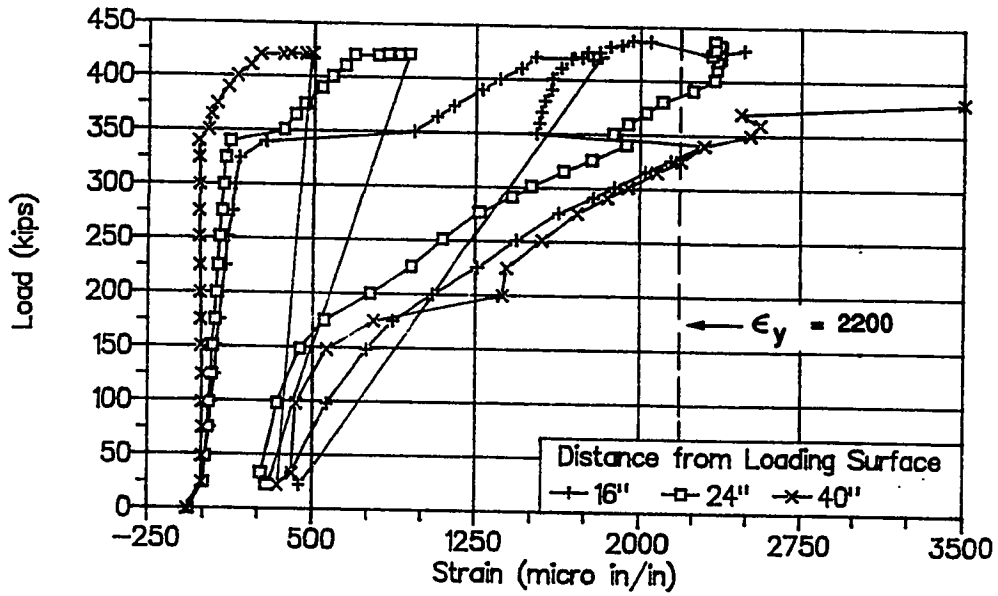


Figure 6.15 Tie-Back Reinforcement Strains, Specimen I2

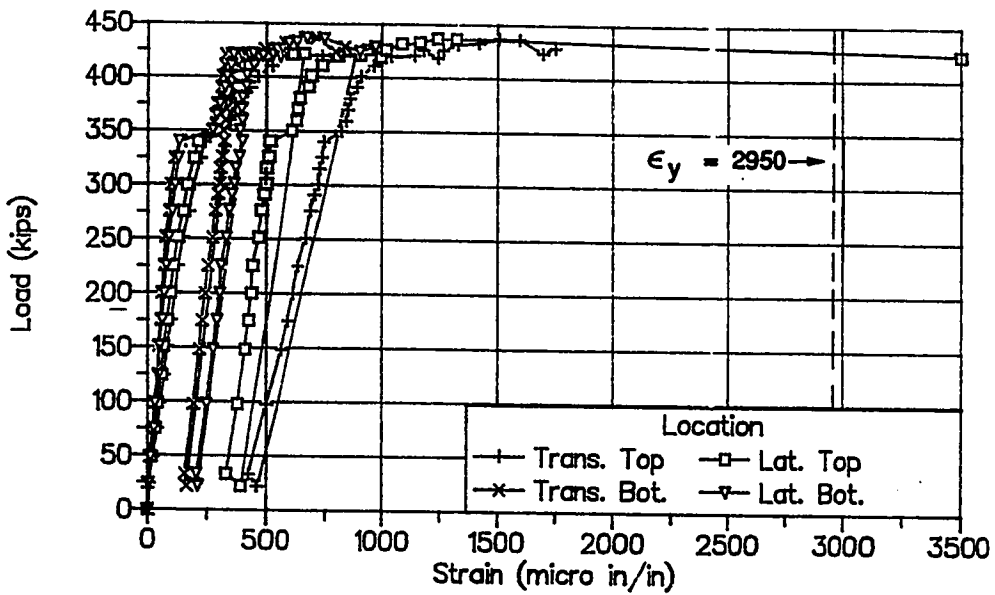


Figure 6.16 Spiral Strain Data, Specimen I2

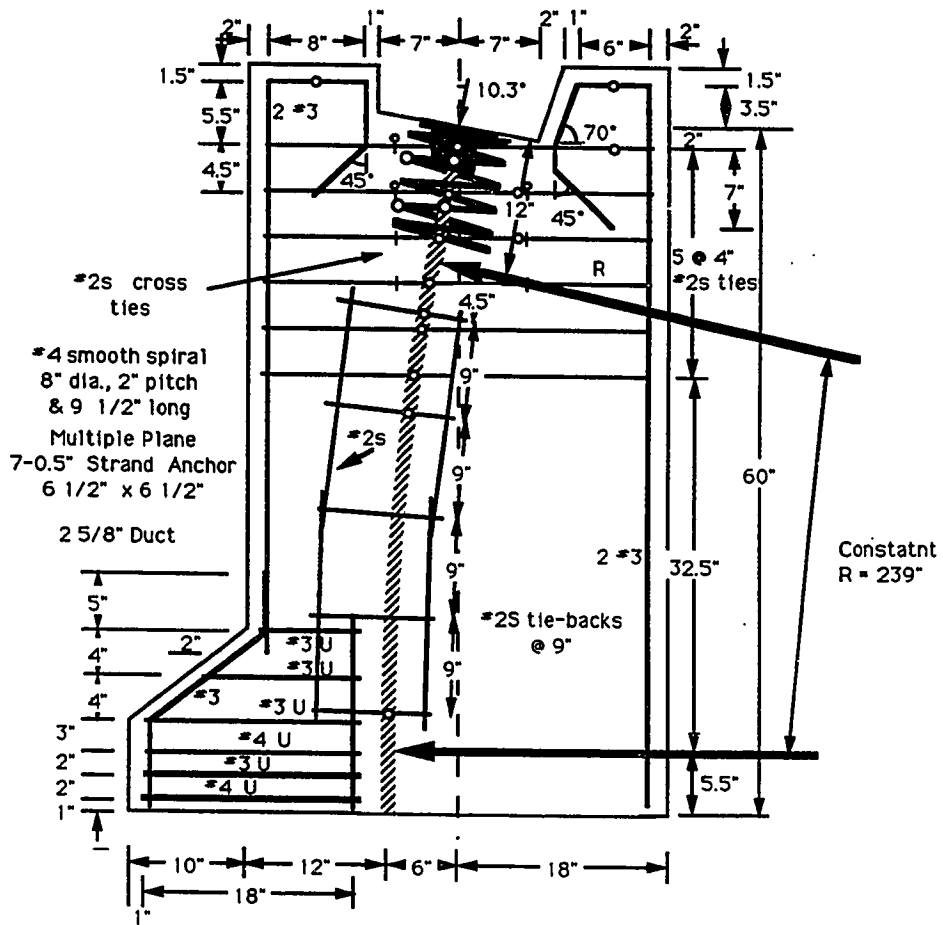


Figure 6.17 Specimen I3 Detail

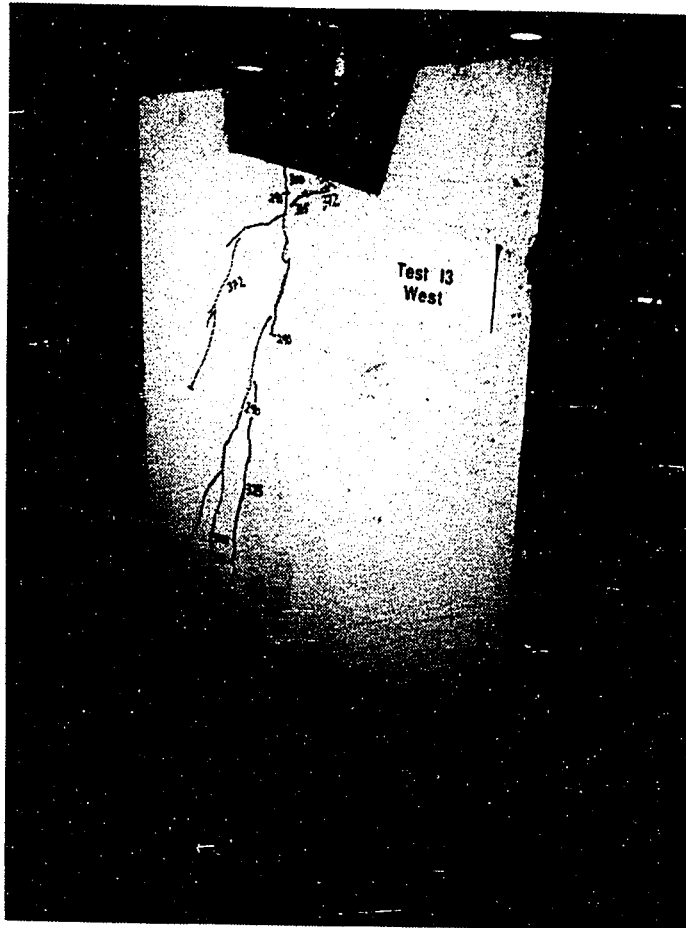
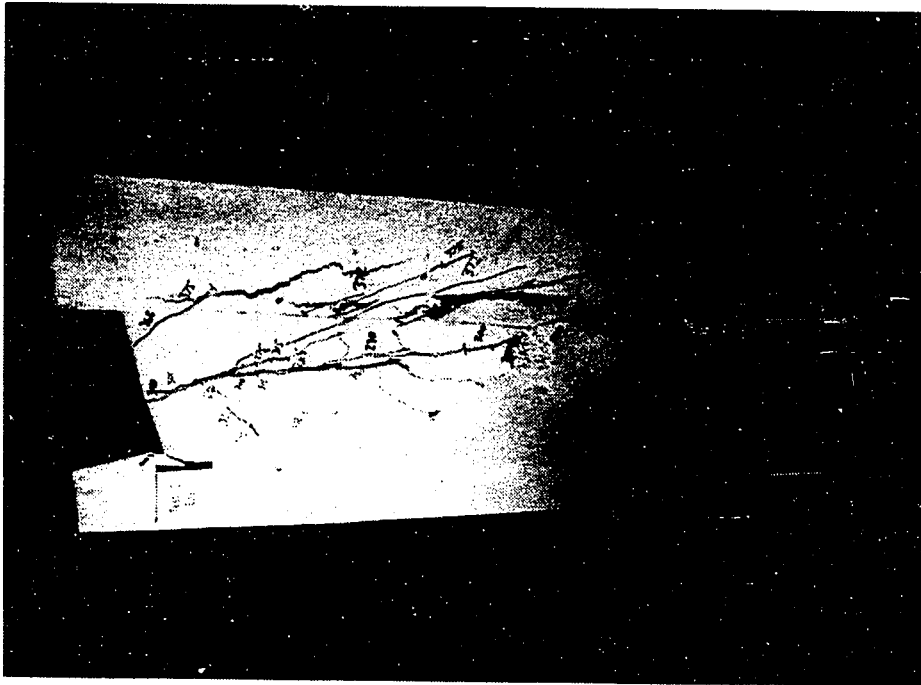
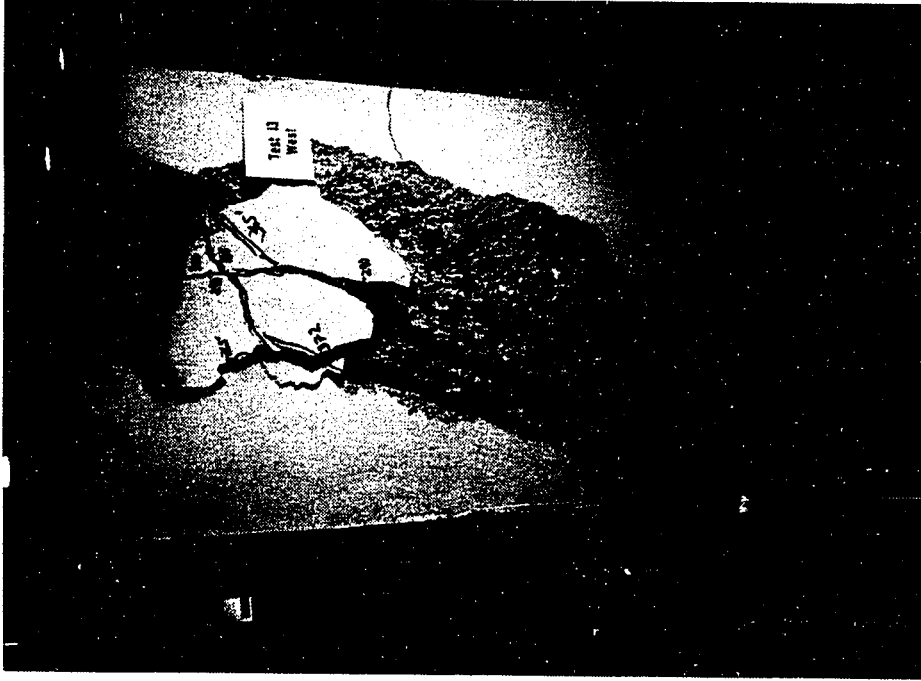


Figure 6.18 Crack Pattern Before Ultimate, Specimen I3

The first crack occurred at the boundary between the basic specimen section and the thickened base at 150 kips. The first bursting crack occurred at 250 kips on the east side and not until 290 kips on the west side. By 350 kips, the crack widths were only 0.012 inches at 5 inches from the loading surface and 0.007 inches at 22 inches from the loading surface. At 372 kips, a diagonal crack grew outward from the anchorage device and another crack extended off the tendon path toward the corner of the specimen (see Fig. 6.18). At 375 kips the specimen failed (see Fig. 6.19). On the east side of the



a) East Side



b) West Side

Figure 6.19 Crack Pattern at Ultimate, Specimen I3

specimen, the concrete was contained and the failure was not as explosive as with Specimens I2 and I4. Cracks formed on the transverse face farthest away from the tendon path, 15 inches below the loading surface. On the west side of the specimen, concrete spalled off over half the specimen. The final crack width was 0.075 inches.

The bursting strains for Specimen I3 showed very uniform behavior (see Fig. 6.20). When the specimen became cracked on both sides of the specimen at 290 kips, bursting strains increased rapidly. All of the strains increased uniformly until failure at 375 kips. The tie-back strains (see Fig. 6.21) near the anchor yielded. The ties toward the base started out with high strains, probably because of the influence of the cracks at the section change. The lowest layer of tie-back reinforcement had not yielded at the conclusion of the test. Spiral strains were high toward the top of the spiral, as was seen in Specimens I2 and I4. The top portion of the spiral in the transverse direction yielded (see Fig. 6.22).

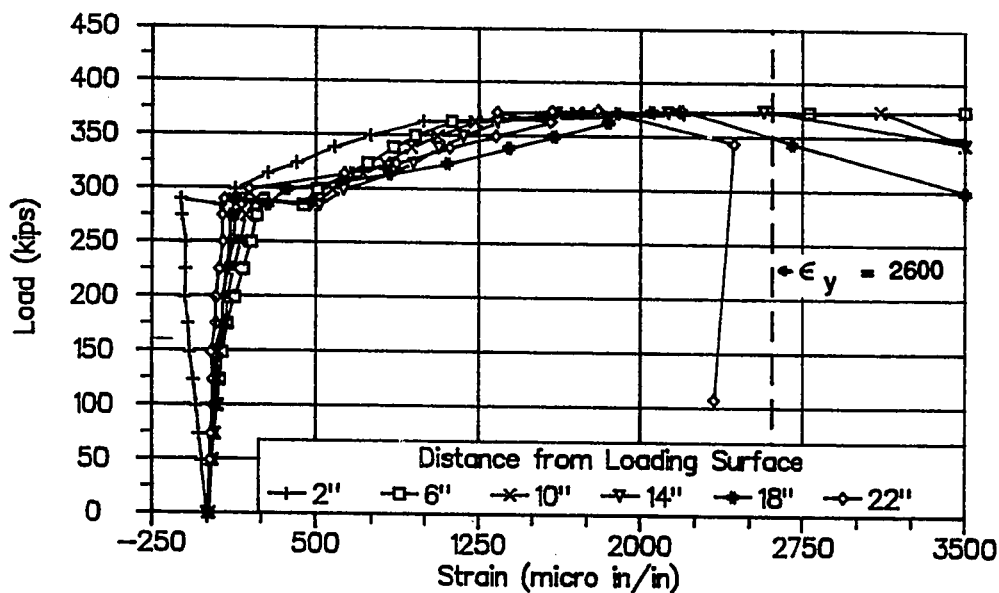


Figure 6.20 Bursting Reinforcement Strain Data, Specimen I3

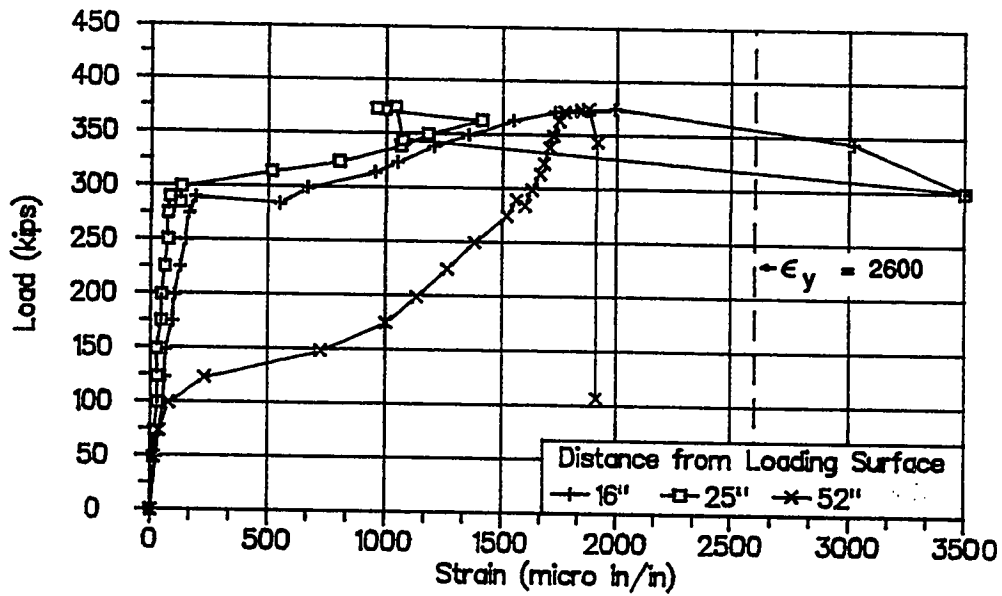


Figure 6.21 Tie-Back Reinforcement Strain Data, Specimen I3

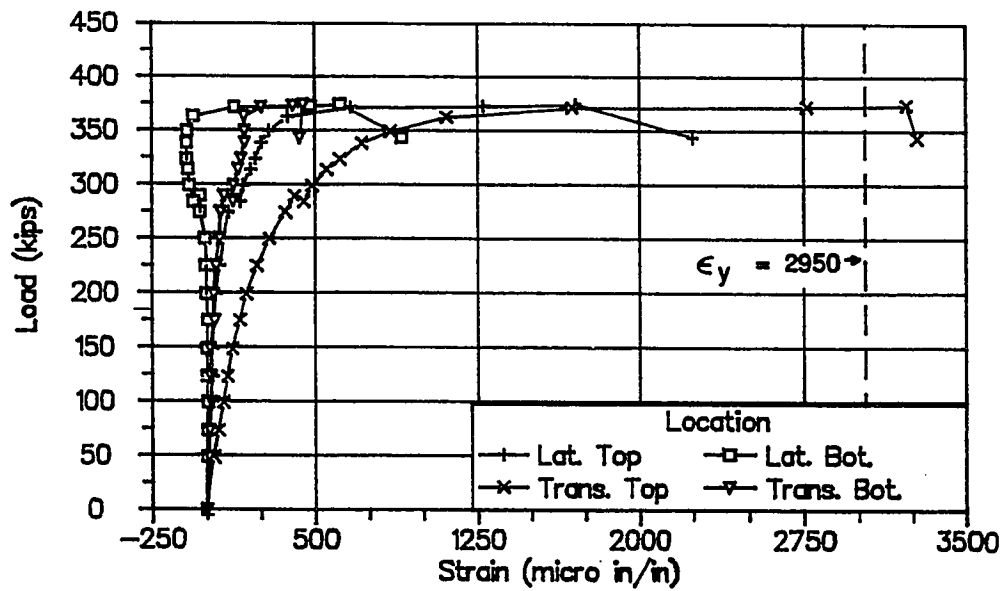


Figure 6.22 Spiral Strain Data, Specimen I3

Specimen I1 had the anchorage device located on the section centerline, as in Specimen I3 (see Fig. 6.23). Specimen I1 had a larger anchorage inclination, 20 degrees and a smaller radius of curvature, 131 inches, than Specimen I3. The radius of curvature and anchorage inclination are the same as those used in Specimens I2 and I4. Because of the large initial angle, the tendon exits the specimen outside the kern of the original section but inside the kern of the modified section. The closed ties anchored fully across the specimen had a total bursting tension capacity of 35.7 kips with a centroid of 14 inches. Supplementary tie-back reinforcement consisted of five #2s ties spaced at 8 inches apart. Since the bottom of the specimen has a resultant force outside of the kern, longitudinal edge tension reinforcement was needed along the surface farthest away from the tendon axis. This reinforcement consisted of four #4 bars.

The first crack occurred at the boundary between the basic specimen section and the thickened base at 50 kips. The first bursting crack along the tendon duct for Specimen I1 occurred at 250 kips on both sides of the specimen. The first crack was extremely straight and followed the initial projection of the load to a point 32 inches ahead of the loading surface. Figure 6.24 shows the jump in the bursting strains at the first tendon path cracking load. The bursting strains increased steadily until failure at 423 kips. The maximum measured crack size at 300 kips was 0.006 inches. At 350 kips, the maximum measured crack size was 0.014 inches; and, by 400 kips, it was 0.032 inches. Figure 6.25a shows the crack pattern at ultimate. At the ultimate load horizontal cracks formed on the transverse face (closest to the tendon) at 10 inches below the centroid of the loading surface. The concrete on the lateral face bulged out from the anchor (see Fig. 6.25b). The anchorage at the conclusion of the test had been pushed approximately 1 inch into the specimen (see Fig. 6.25b). The surface of the anchorage was initially level with the concrete.

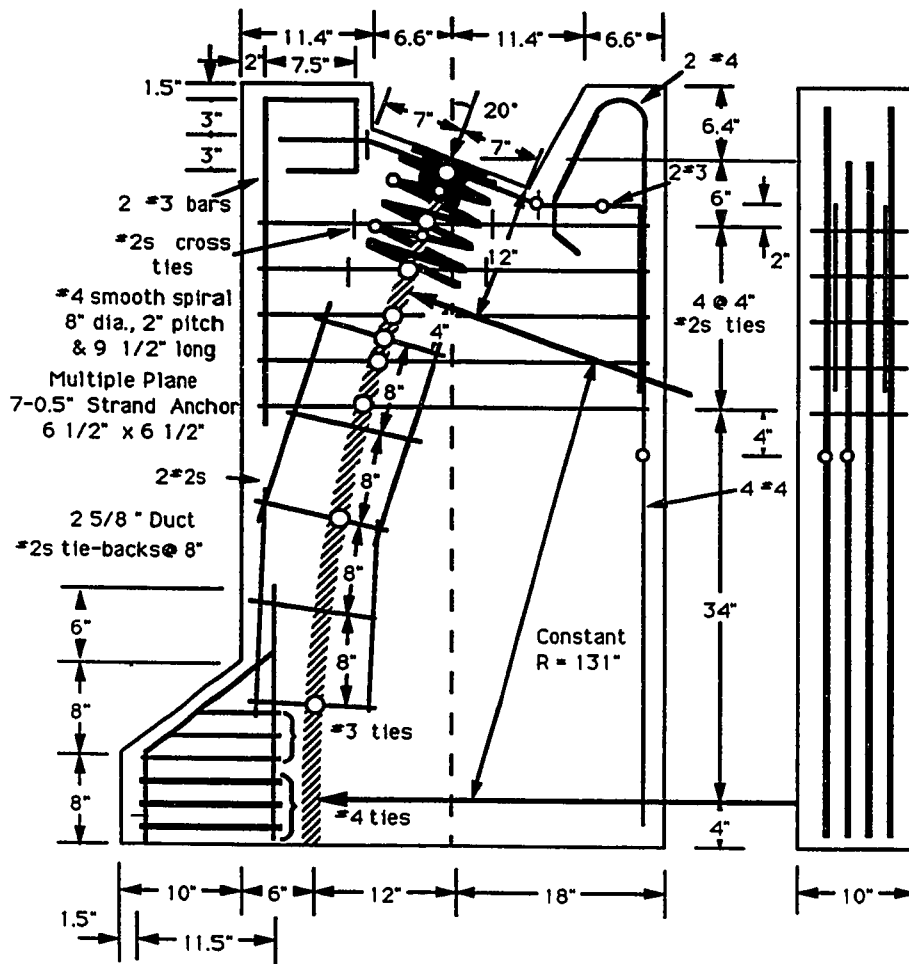


Figure 6.23 Specimen I1 Detail

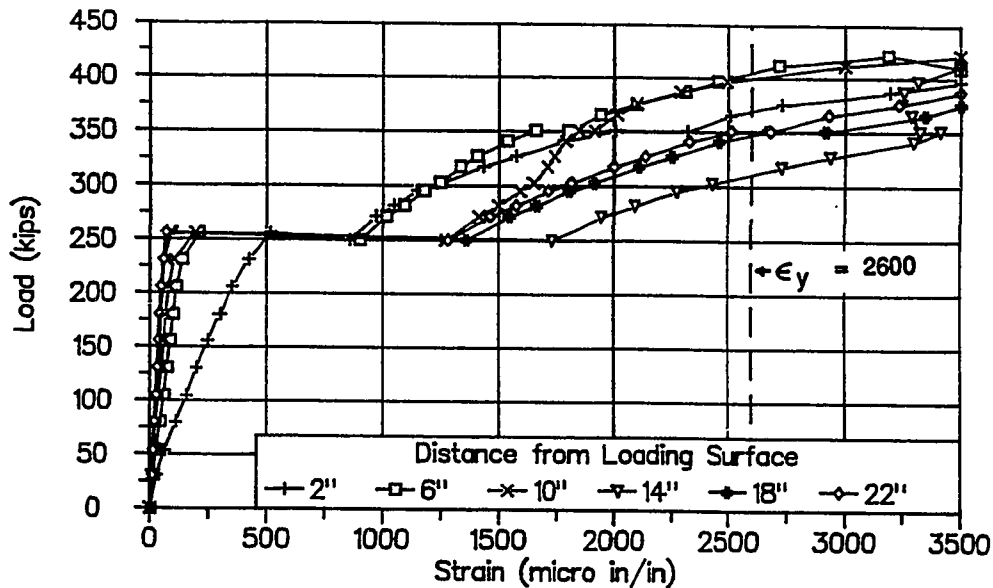
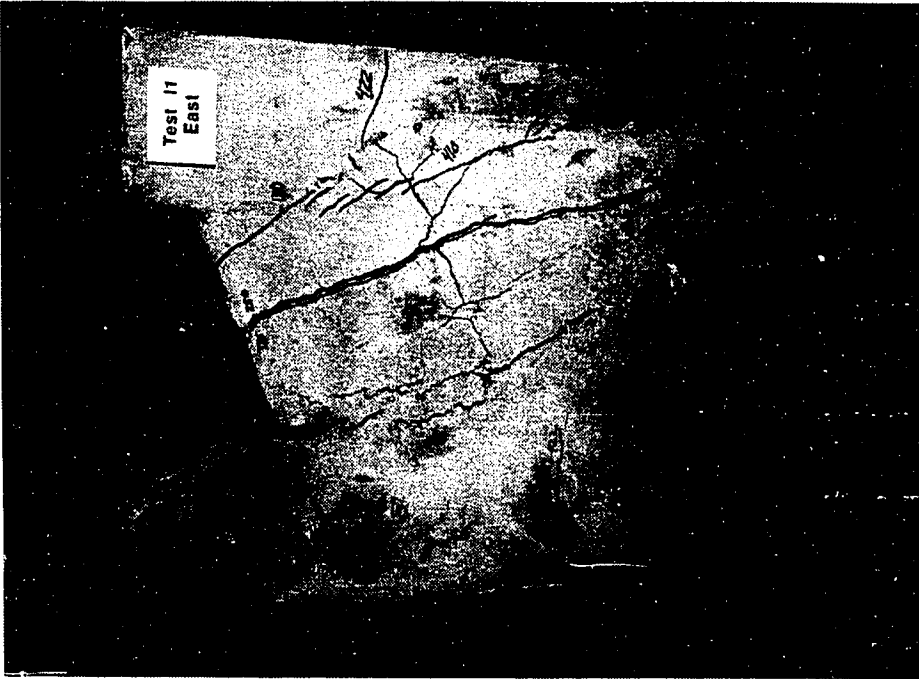
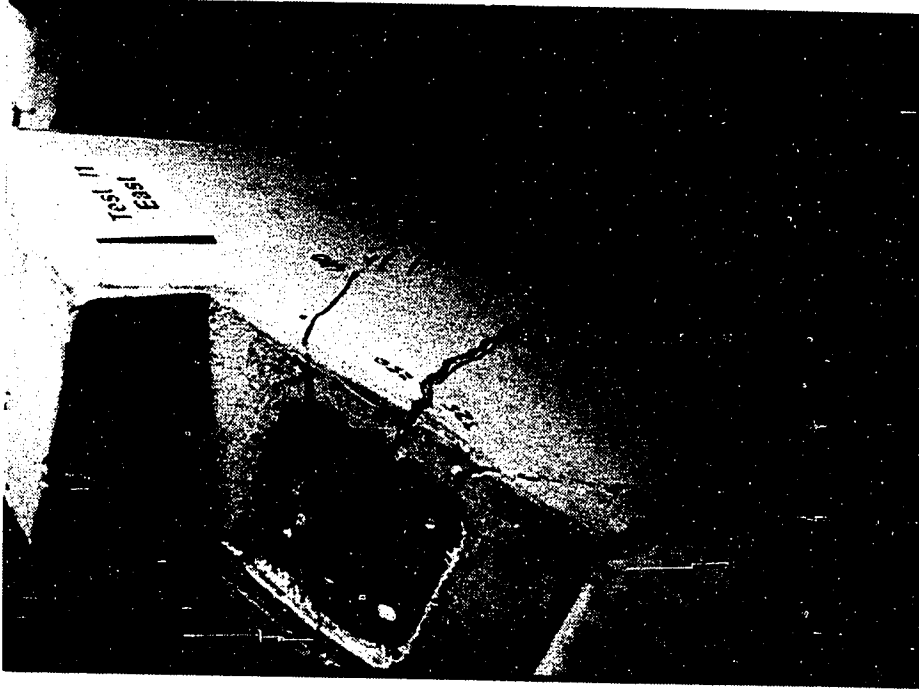


Figure 6.24 Bursting Reinforcement Strain Data, Specimen I1

Figure 6.26 shows the strain results from the gages on the longitudinal edge tension reinforcement located near the outside edge and along the loading surface. The gages on the outer fiber indicated very small strains, but the concrete on that face did not crack until the specimen failed. The total force in the reinforcement located near the outside edge was 6.63 kips at the ultimate load. The strains along the loading surface were much higher, but there were only two #3 bars. The maximum strain at ultimate was 1500 microstrain indicating a total force for both bars of 9.1 kips, 2.1 percent of the tendon load. The strain data for the tie-back reinforcement and the spiral are given in Figs. 6.27 and 6.28 respectively. The tie-back reinforcement, near the base, yielded well in advance of the ultimate load due to the changes in section dimensions and the base crack. The tie-back ties near the middle of the specimen yielded in advance of the ultimate load, while the tie-back ties nearest the anchorage yielded at the ultimate load. The spiral strains were small until after the ultimate load.



a) Lateral Face



b) Loading Surface

Figure 6.25 Crack Patterns at Ultimate, Specimen I1

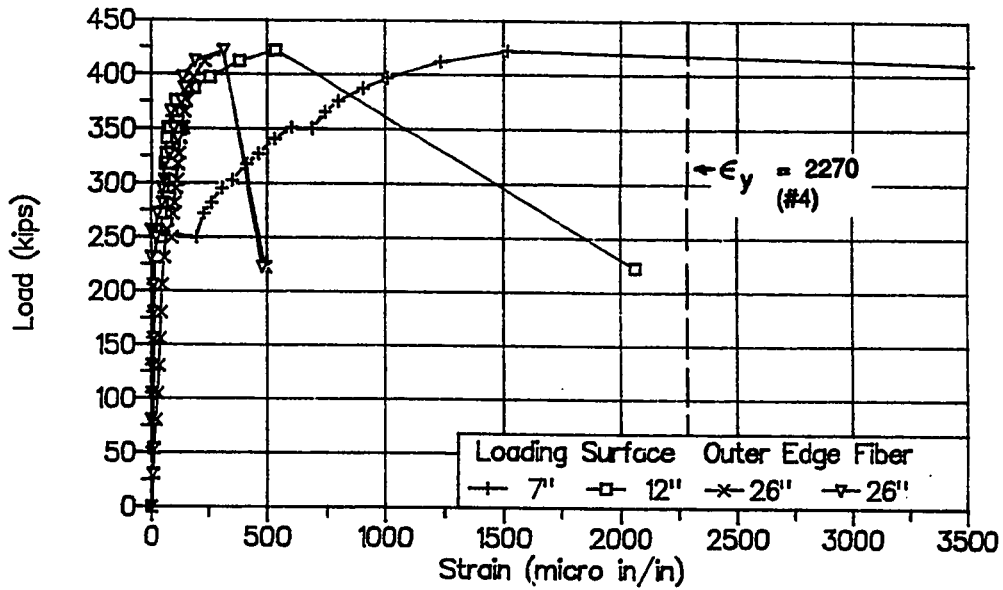


Figure 6.26 Longitudinal Edge Tension Strain Data, Specimen I1

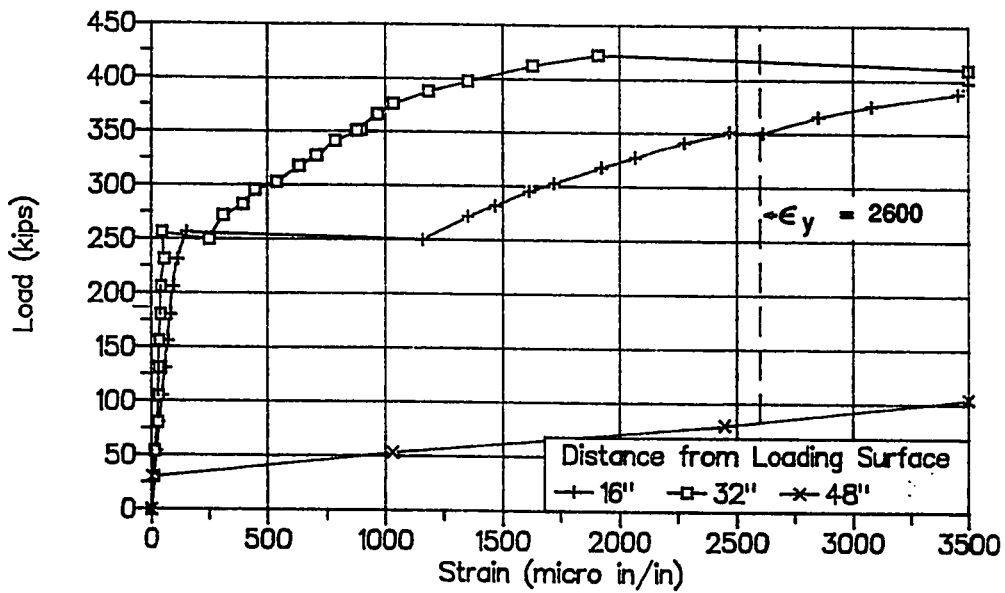


Figure 6.27 Tie-Back Reinforcement Strains, Specimen I1

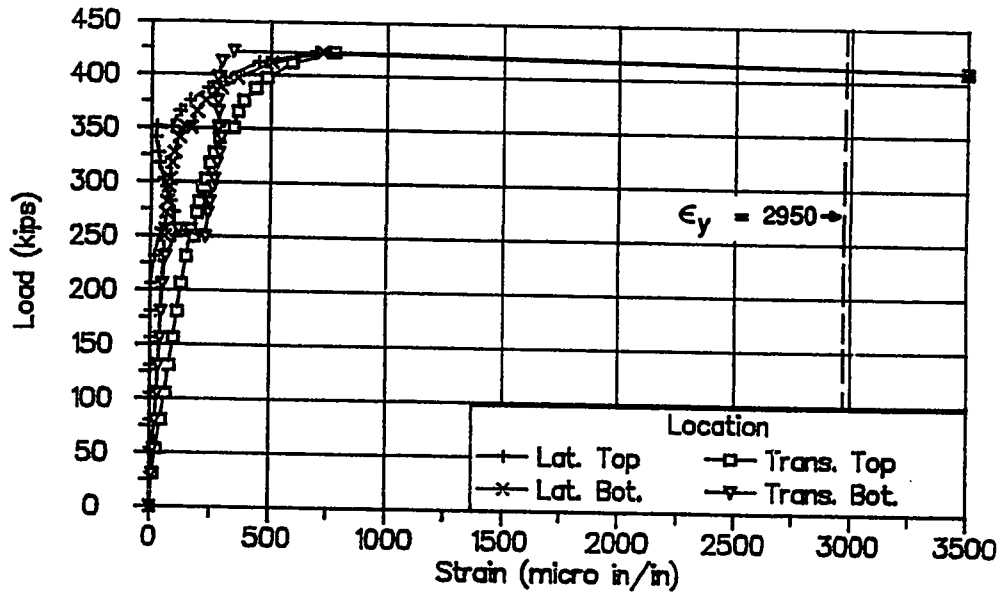


Figure 6.28 Spiral Strain Data, Specimen I1 .

Specimen ME2 was the only specimen that combined multiple anchorages with anchorage inclinations and tendon curvatures (see Fig. 6.29). Specimen ME1 had the same anchorage locations as ME2. However, the anchorage inclination in Specimen ME1 was zero, and there was no tendon curvature. Anchorage "A" was located at -4 inches from the specimen centerline. It had an anchorage inclination of 15 degrees and a tendon radius of curvature of 170 inches. Anchorage "B" was located at +12 inches from the specimen centerline, had an initial inclination of 20 degrees, and had a tendon radius of curvature of 131 inches. Both anchorages were loaded simultaneously, so the resultant centroid was at +4 inches. Anchorage "A" had a primary bursting reinforcement capacity of 35.7 kips with a centroid located at 14 inches from the loading surface. Anchorage "B" had a primary bursting reinforcement capacity of 42.8 kips with a centroidal distance of 16 inches. Tendon "A" had tie-back reinforcement consisting of four #2s ties at 11 inches, while tendon "B" had six #2s ties spaced 7 inches apart.

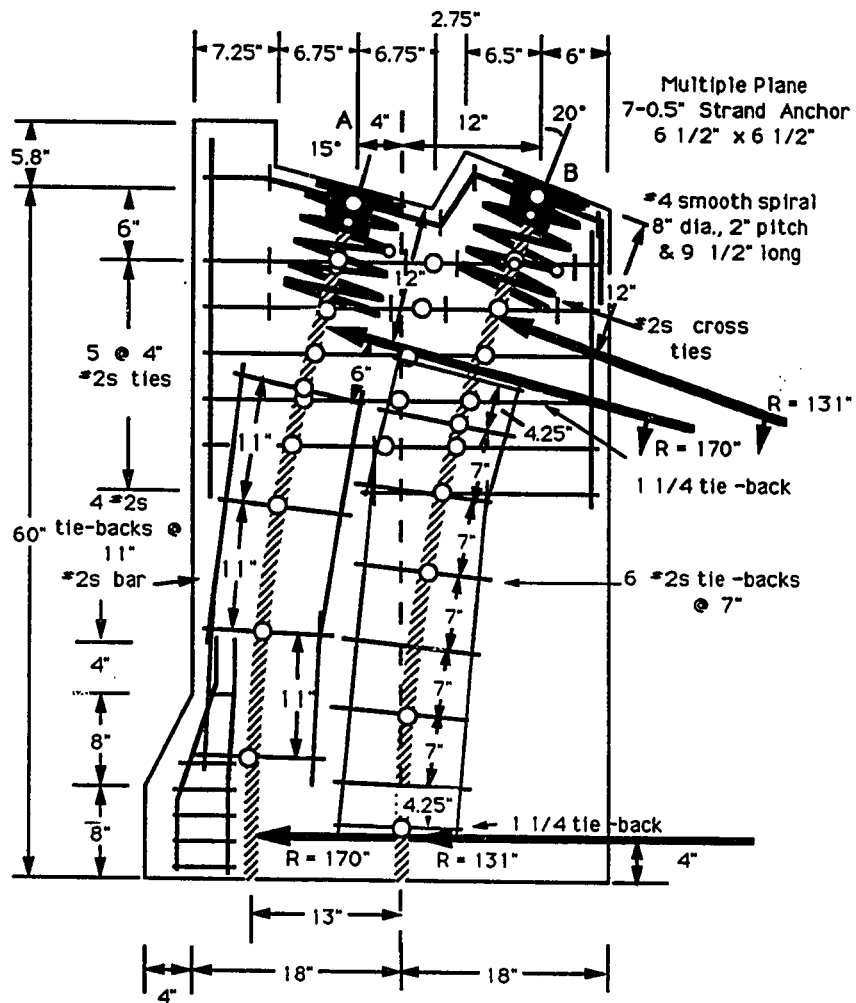


Figure 6.29 Specimen ME2 Detail

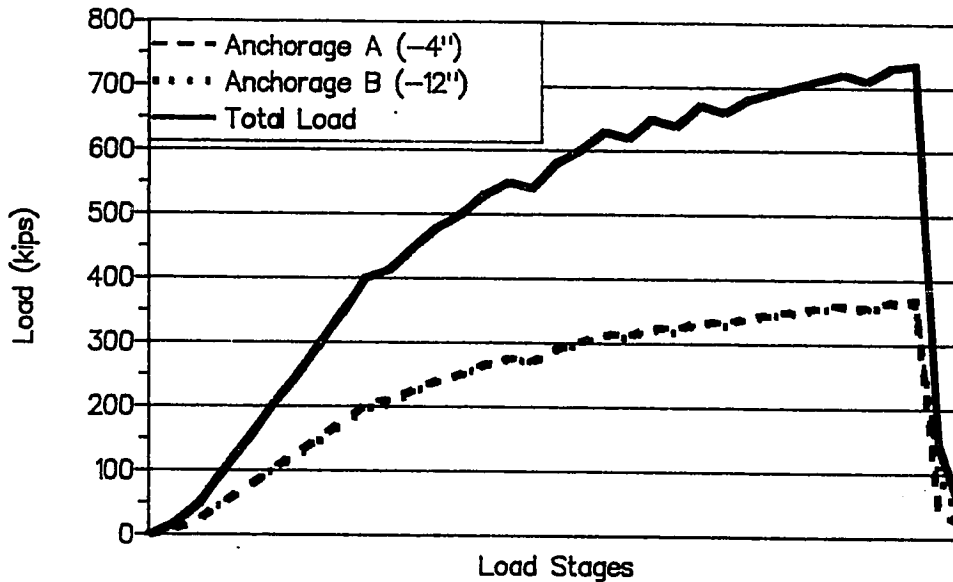
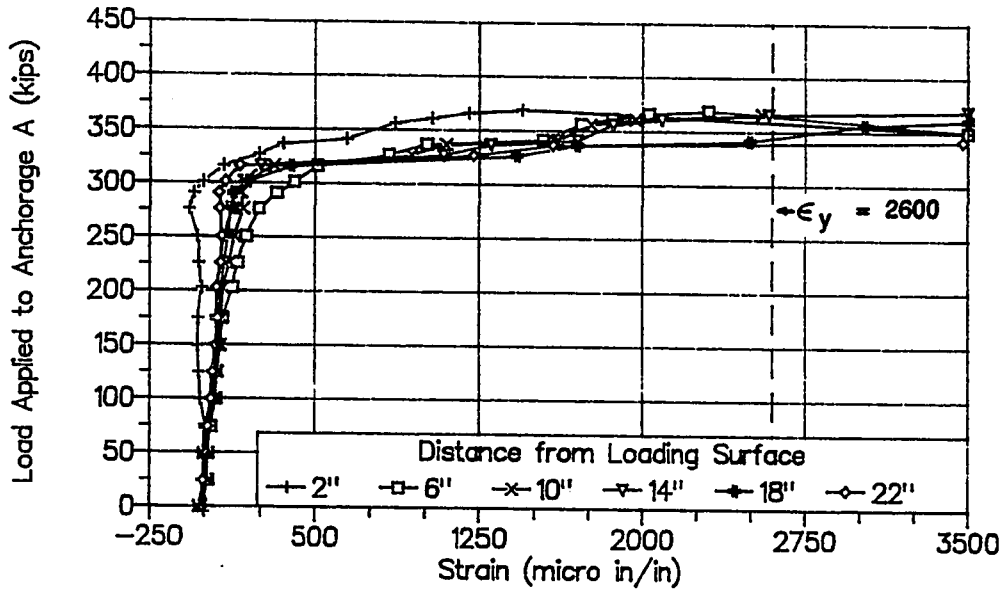
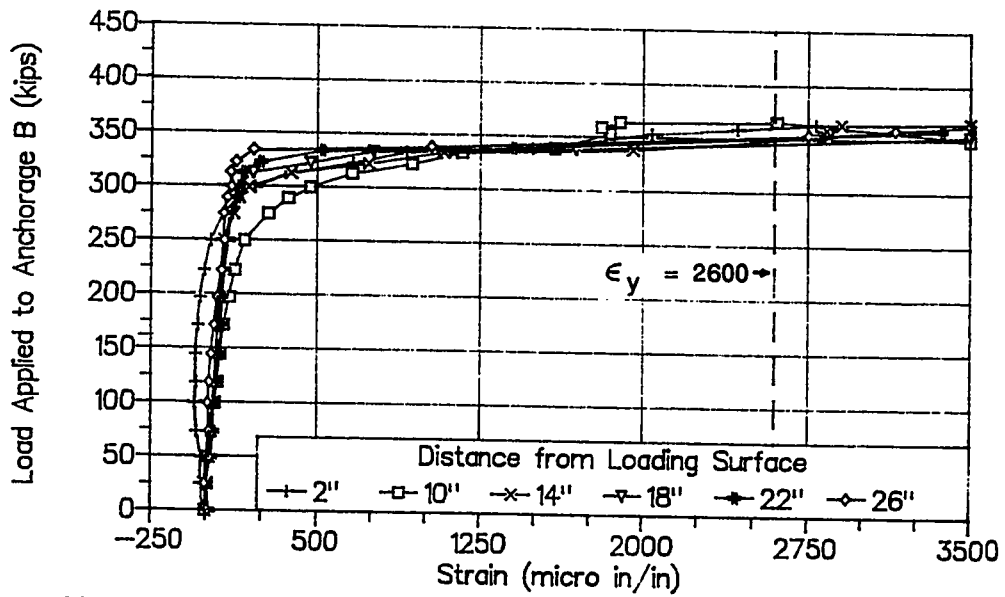


Figure 6.30 Load-History Specimen ME2

Figure 6.30 shows the load history for both anchorages. All load references are to the load per anchor. The two loads were almost identical until failure. The first crack occurred at 75 kips at the boundary between the basic specimen section and the widened section. The first bursting cracks occurred ahead of both anchorages at 240 kips. The cracks were very small until 290 kips. The bursting strains began to increase significantly after 310 kips (see Fig. 6.31a) under anchorage "A" but not until 330 kips for anchorage "B" (see Fig. 6.31b). Figure 6.32 shows the cracking pattern at 365 kips. The crack ahead of anchorage "A" connected into the base crack at 335 kips. At 340 kips the crack ahead of anchorage "B" propagated to the base. A spalling crack opened at 335 kips about midway between anchorages "A" and "B" in the multiple anchor force region, corresponding with an increase in the strain readings on bars in this region (see Fig. 6.33). The specimen failed with 370 kips load on anchorage "A" and with 366 kips load on anchorage "B". Extensive cracking occurred on the south



a) Ahead of Anchorage "A"



b) Ahead of Anchorage B

Figure 6.31 Bursting Reinforcement Strain Data, Specimen ME2

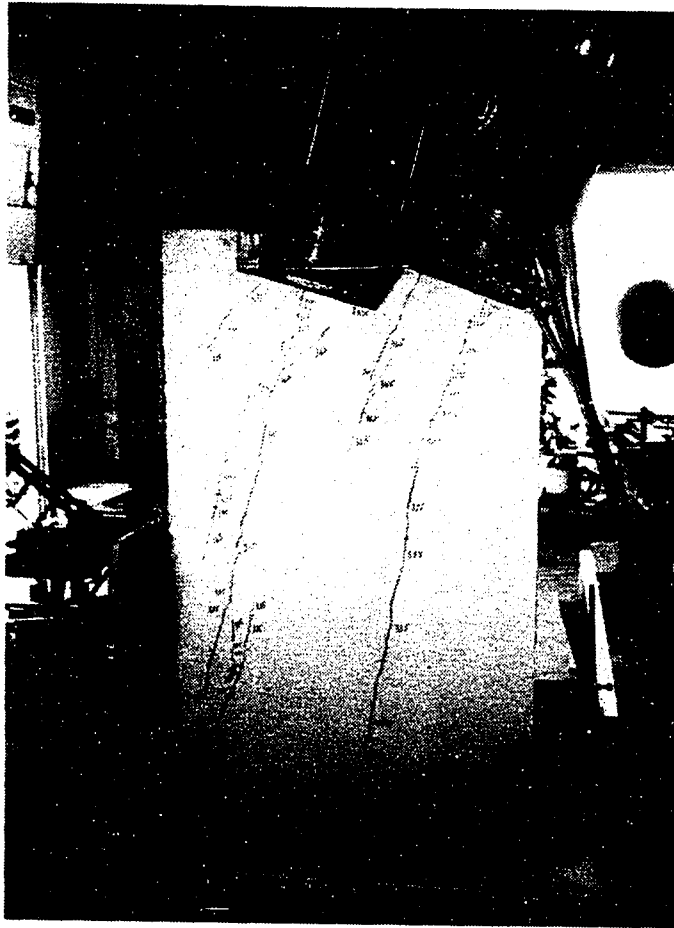


Figure 6.32 Crack Pattern before Ultimate Load, 365 kips/anchor

face (see Fig. 6.34a). At the ultimate load horizontal cracks formed on the transverse face ahead of anchorage "B". The failure on the west side was much more explosive with concrete being thrown away from the anchorage (see Fig. 6.34b). Figure 6.35 shows that the concrete within the spiral was still completely confined and acted as a plug. At the ultimate load this confined concrete plug was thrust into the specimen. Figure 6.36 shows the tie-back reinforcement strains for both anchorages. Both indicated very small increases in strain until after

300 kips, at which point the concrete began to crack. As with Specimen II, the strain for the tie-back reinforcement increased very quickly for the tie at 50 inches because of the early cracking between the basic specimen and the thickened section.

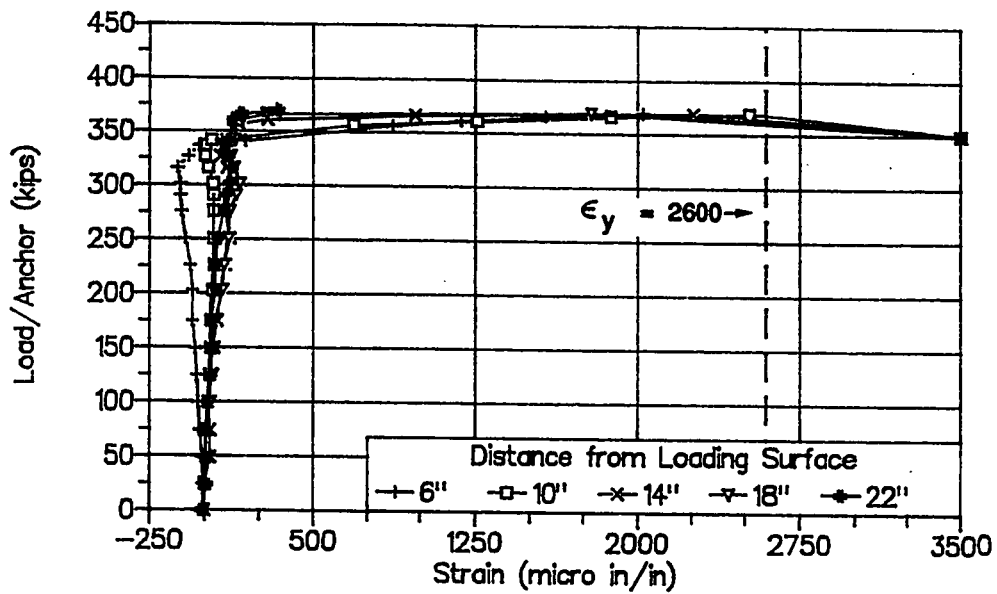
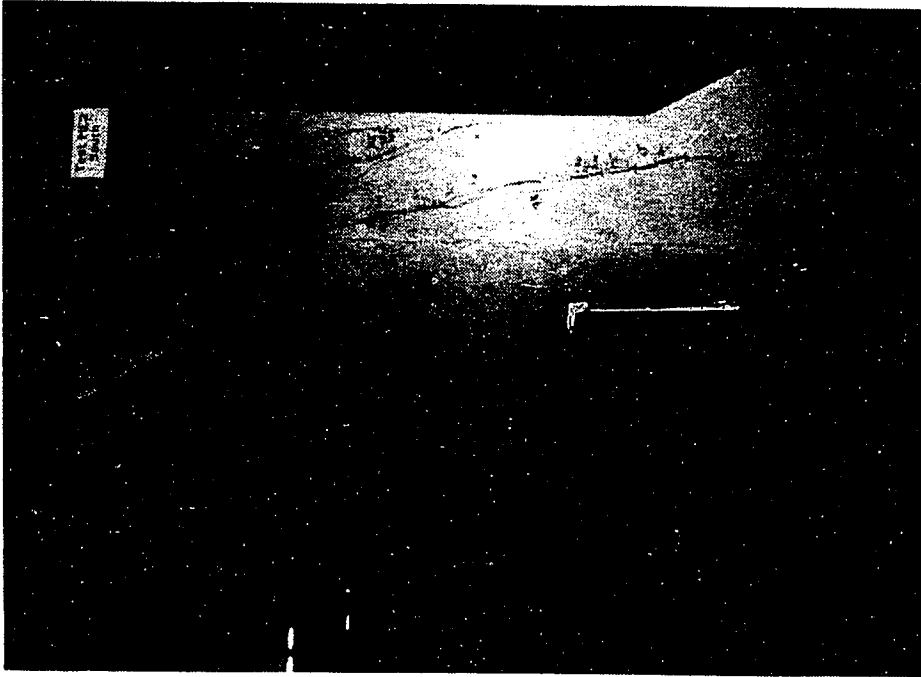


Figure 6.33 Spalling Reinforcement Strain Data between Anchors "A" & "B"



a) South Side



b) North Side

Figure 6.34 Crack Pattern at Ultimate, Specimen ME2

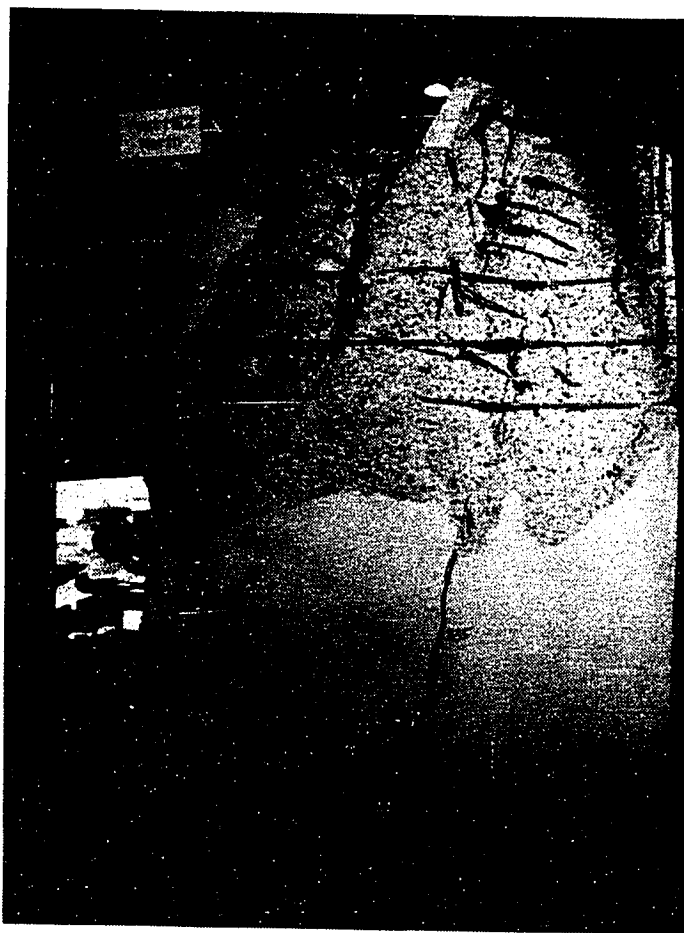
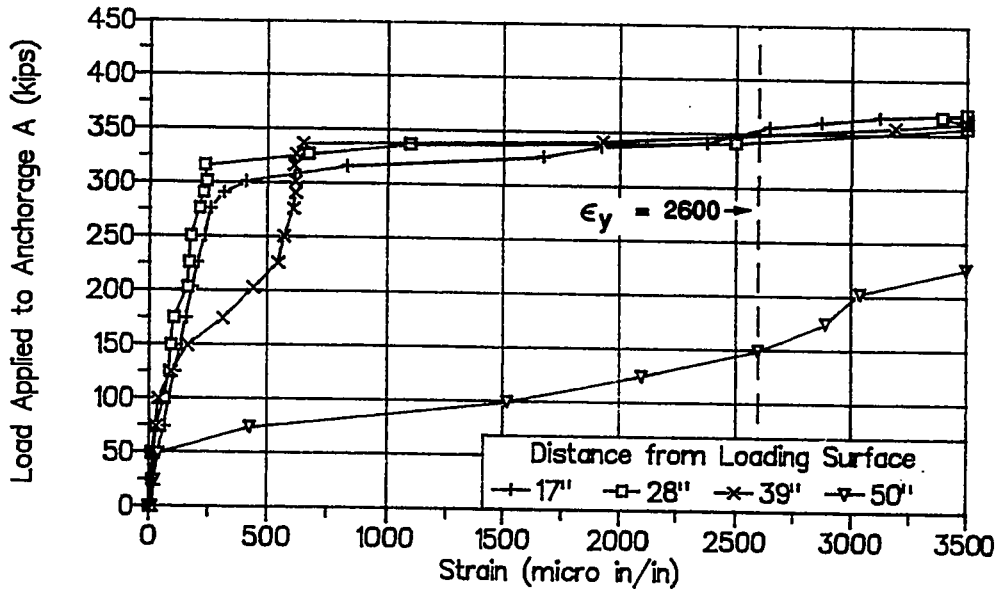
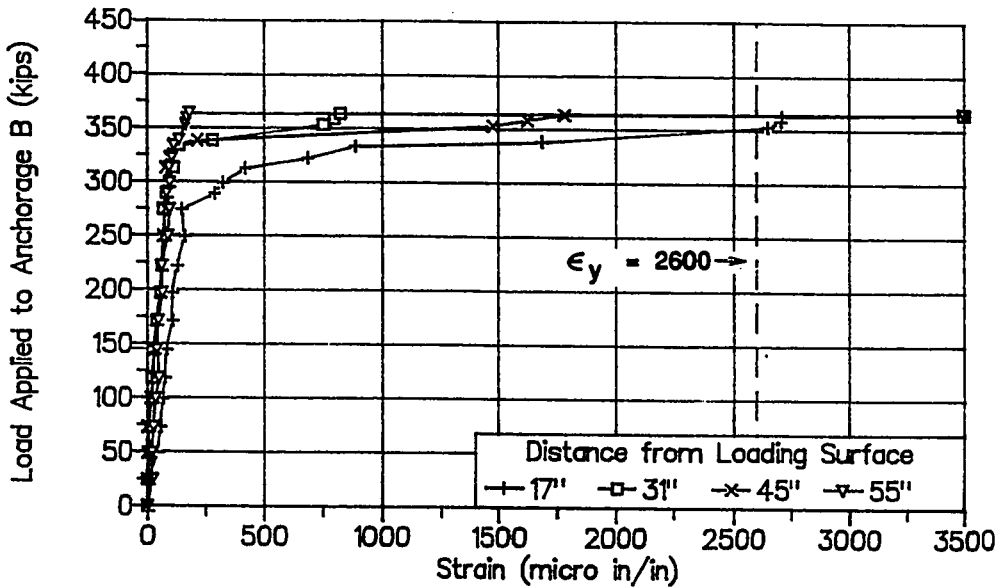


Figure 6.35—Local Zone Close-up at Failure, Specimen ME2



a) Ahead of Anchorage "A"



b) Ahead of Anchorage "B"

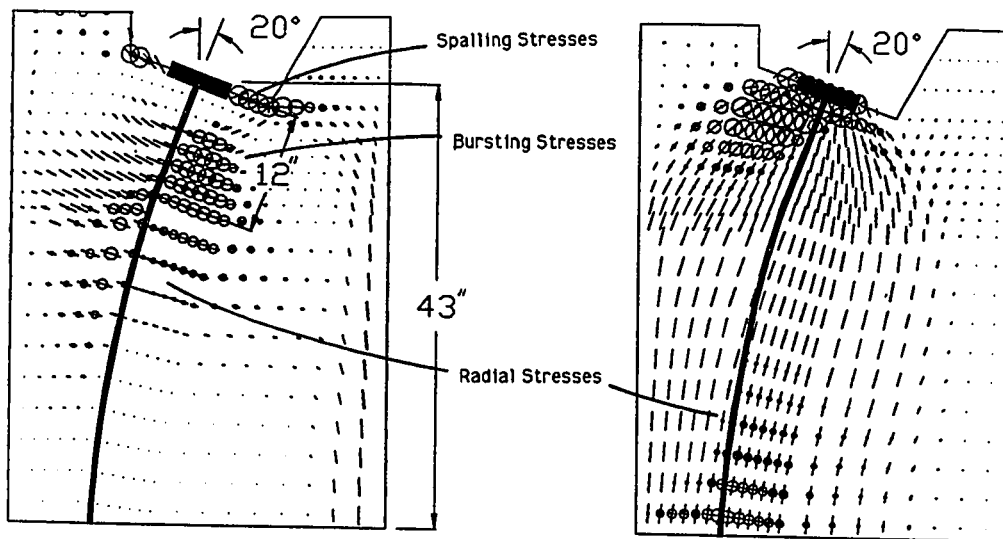
Figure 6.36 Tie-Back Reinforcement Strain Data, Specimen ME2

6.3 Prediction of the First Cracking Load using Elastic Analysis Models

As stated in previous chapters, the determination of the first cracking load can be critical for some design situations in aggressive exposures. In the case where the anchorage has an initial inclination and the tendon has a curvature, the stress state near the anchorage can become very complicated. Figure 6.37 shows the elastic stress distribution for Specimen 11 as determined from a finite element analysis conducted by Burdet [25]. Figure 6.37a shows the tension principal stresses. The circles represent the magnitude of the two-dimensional principal stress while the lines represent the direction. The maximum circle, before reducing, was 0.5 inches which represented a tensile stress of 1.5 ksi for a 100 kips load. Figure 6.37b show the compression principal stresses. The maximum circle, before reducing, was 0.5 inches which represented a compression stress of 3 ksi for a 100 kips load. For the straight tendon specimens seen in previous chapters, there were bursting stress fields that were essentially similar on either side of the tendon axis. Because of the lateral force component caused by the inclined anchorage, the bursting region has higher tension stresses to the right of the tendon path (see Fig. 6.37) very close to the anchorage. The tendon curvature begins 12 inches ahead of the loading surface. The radial tension stresses were increased to the left of the tendon path and decreased to the right because of the radial forces caused by the tendon curvature. As the bursting stresses diminished, the transverse stresses to the right of the tendon path became compressive. The only cracking observed at the service loads in the inclined tendon series were bursting cracks ahead of the anchorage device. The first bursting crack loads can be predicted by matching the peak stress (determined from the elastic finite element analysis [25]) to an estimate of the tensile strength of the concrete. Four models will be used to predict the first bursting crack load. The models systematically alter two parameters: effective tensile strength (f_t) and effective section thickness (t_e).

These are the same parameters that were examined in Chapters 3, 4, and 5. The following models were examined.

- 1) f_t - unmodified split cylinder strength
 t_c - full section thickness
- 2) f_t - unmodified split cylinder strength
 t_c - section thickness - duct outside diameter
- 3) f_t - split cylinder strength modified for triaxial effects
 t_c - section thickness - duct outside diameter
- 4) f_t - split cylinder strength modified for triaxial effects
 t_c - transformed thickness



a) Tension Stresses

b) Compressive Stresses

Figure 6.37 Elastic Stress Distribution for Specimen I1

Table 6.3 shows the results from the first two models. The models used the split cylinder strength to estimate the tensile strength of the concrete. In the first analysis, the reduction in the effective concrete thickness due to the post-tensioning duct is not considered. This models yields unconservative results for all of the specimens and has a very high coefficient of variance. In the second analysis, the effect of the duct is taken into account by reducing the effective concrete thickness by the outside diameter of the duct. This raises the average of the ratio test-to-predicted of the first bursting crack load to 0.98. The coefficient of variance is still 20 percent. Specimen I2 and both bursting crack predictions for Specimen ME2 are unconservative.

Table 6.3 First Bursting Crack Prediction using Split Cylinder Data for Concrete Tensile Strength

| Specimen | Split Cylinder (psi) | First Cracking Load (kips) | Thickness (in) | Full Section Thickness | | | Removing | | Full Duct Width | |
|----------|----------------------|----------------------------|----------------|--------------------------|--------------------------------|----------------|--------------------------|--------------------------|--------------------------------|----------------|
| | | | | Peak Stress / σ_c | Predicted Cracking Load (kips) | Test/Predicted | Effective Thickness (in) | Peak Stress / σ_c | Predicted Cracking Load (kips) | Test/Predicted |
| 11 | 358 | 250 | 10 | 0.486 | 265 | 0.94 | 7.38 | 0.659 | 196 | 1.28 |
| 12 | 423 | 325 | 10 | 0.321 | 475 | 0.68 | 7.38 | 0.435 | 350 | 0.93 |
| 13 | 348 | 250 | 10 | 0.394 | 318 | 0.79 | 7.38 | 0.535 | 234 | 1.07 |
| 14 | 393 | 350 | 10 | 0.321 | 441 | 0.79 | 7.38 | 0.435 | 325 | 1.08 |
| ME2A | 491 | 240 | 10 | 0.483 | 366 | 0.66 | 7.38 | 0.655 | 270 | 0.89 |
| ME2B | 491 | 240 | 10 | 0.356 | 497 | 0.48 | 7.38 | 0.483 | 366 | 0.66 |
| | | | | Average | | 0.72 | | | 0.98 | |
| | | | | Standard Deviation | | 0.14 | | | 0.19 | |
| | | | | Coef. of Variance | | 0.20 | | | 0.20 | |

$$\sigma_c = P/ht$$

In addition to the bursting zone tensile stresses in the strong axis principle plane caused by the lateral spreading of the post-tensioning force, there are also very high compressive stresses and stresses caused by the transverse spreading of the post-tensioning force in the weak axis plane. These conditions induce a triaxial stress state. As discussed in Chapter 3, the presence of the triaxial stress state can cause a reduction in the tensile strength from the value determined from the split cylinder test. Tables 6.4 and 6.5 show the results of models that include the reduction in tensile strength due to the triaxial stress state described in Section 3.3. For all of the specimens except Specimen ME2 anchorage "B", the peak lateral bursting stresses occurred farther ahead of the loading surface than 10 inches. It was assumed that the transverse distribution of the force in the weak axis, thin plane, was completed within the thickness of the section (10 inches). Therefore, the stress in the transverse direction was taken to be zero for all the anchorage zones except anchorage "B" of Specimen ME2. In Table 6.4, the peak stress determined from the finite element analysis is modified to include the reduction in thickness caused by the duct. The effective thickness is taken to be the specimen thickness minus the outside diameter of the duct. The average result for specimens with inclined anchorages and tendon curvatures is conservative. By including the triaxial effects, the coefficient of variance dropped slightly to 17 percent. However, the first crack predictions for Specimen ME2 are still unconservative. In Table 6.5 the transformed section thickness is utilized when determining the peak stress from the finite element analysis. By incorporating the transformed thickness and the triaxial effects, the average of the test-to-predicted ratios close to one. However, it is slightly unconservative. The first bursting cracking loads are unconservatively predicted for both Specimens ME2 and I2.

Table 6.4 First Bursting Crack Prediction including Triaxial Effect and Thickness Reduction

| Specimen | First Cracking Load (kips) | Peak Stress / σ_o | Transverse Stress (psi) | Compression Stress (psi) | Reduced Tensile Strength (psi) | Change in Tensile Strength (psi) | Predicted Cracking Load (kips) | Test/ Predicted | |
|-------------------|----------------------------|--------------------------|-------------------------|--------------------------|--------------------------------|----------------------------------|--------------------------------|--------------------|------|
| 11 | 250 | 0.659 | 0 | 1249 | 346 | -12 | 189 | 1.32 | |
| 12 | 325 | 0.435 | 0 | 2025 | 389 | -34 | 322 | 1.01 | |
| 13 | 250 | 0.535 | 0 | 1360 | 321 | -27 | 216 | 1.16 | |
| 14 | 350 | 0.435 | 0 | 1895 | 364 | -29 | 301 | 1.16 | |
| ME2A | 240 | 0.655 | 0 | 1761 | 463 | -28 | 254 | 0.94 | |
| ME2B | 240 | 0.483 | 257 | 2224 | 431 | -60 | 321 | 0.75 | |
| $\sigma_o = P/ht$ | | | | | | | | Average | 1.06 |
| | | | | | | | | Standard Deviation | 0.18 |
| | | | | | | | | Coef. of Variance | 0.17 |

Table 6.5 First Bursting Crack Predicting including Triaxial Effect and Transformed Section

| Specimen | First Cracking Load (kips) | Effective Thickness (in) | Peak Stress / σ_o | Transverse Stress (psi) | Compression Stress (psi) | Reduced Tensile Strength (psi) | Change in Tensile Strength (psi) | Predicted Cracking Load (kips) | Test/ Predicted |
|-------------------|----------------------------|--------------------------|--------------------------|-------------------------|--------------------------|--------------------------------|----------------------------------|--------------------------------|-----------------|
| 11 | 250 | 8.06 | 0.603 | 0 | 1357 | 344 | -14 | 205 | 1.22 |
| 12 | 325 | 8.06 | 0.398 | 0 | 2180 | 383 | -40 | 347 | 0.94 |
| 13 | 250 | 8.06 | 0.489 | 0 | 1464 | 316 | -32 | 233 | 1.07 |
| 14 | 350 | 8.06 | 0.398 | 0 | 2043 | 359 | -34 | 325 | 1.08 |
| ME2A | 240 | 8.06 | 0.599 | 0 | 1904 | 458 | -33 | 275 | 0.87 |
| ME2B | 240 | 8.06 | 0.442 | 273 | 2369 | 420 | -71 | 342 | 0.70 |
| $\sigma_o = P/ht$ | | | | | | | | Average | 0.98 |
| | | | | | | | | Standard Deviation | 0.17 |
| | | | | | | | | Coef. of Variance | 0.17 |

The results are similar to those found for eccentric and multiple anchorage specimens. Models incorporating the triaxial effects and the duct effects were slightly more accurate than simpler models which ignore the triaxial effects on the concrete tensile strength. However, all the methods contained some unconservative results as compared to the test results. The combination of complex stress states, elastic analysis procedures, and the problems in determining an accurate prediction for the specimen tensile strength cause the prediction of the first bursting crack to be difficult and not always accurate. Table 6.6 shows a first bursting crack analysis which uses a conservative approximation for the tensile strength of the concrete, $4.2\sqrt{F'_c}$, which is based on the compressive strength and which uses an effective thickness determined by reducing the specimen thickness by the inside diameter of the duct. The equation $4.2\sqrt{F'_c}$ for the tensile strength was developed in Chapter 3 by assuming a 30 percent reduction in the split cylinder strength due to triaxial effects. An established equation for approximating the split cylinder strength from the compressive strength is $6\sqrt{F'_c}$; Reducing the split strength by 30 percent determines the value of $4.2\sqrt{F'_c}$. All the first crack predictions on this basis are conservative except the bursting crack ahead of anchorage "B" in Specimen ME2. Utilizing this approximation for the tensile strength and reducing the specimen thickness by the inside diameter of the tendon duct yielded the smallest coefficient of variance, 13 percent, of any of the methods discussed in this chapter.

Since it is inconvenient in many applications to use a finite element analysis, a correlation was attempted between the peak stresses determined from Guyon's symmetrical prism and the finite element results. Table 6.7a shows the results from this investigation. The short side of the anchorage zone is the side with the largest a/h ratio and is the side used with the conventional symmetrical prism method. The overall comparison with the finite element results is conservative; but Specimens I1 and I3 are unconservative when compared to the finite

element analysis. Table 6.7b shows the prediction of the first cracking load using the symmetrical prism method for the peak stress value, an effective thickness of the specimen's thickness minus the inside duct diameter, and $4.2\sqrt{F'_c}$ for the concrete tensile strength. The model has a very high coefficient of variance but is conservative for all specimens.

Table 6.6 First Bursting Crack Prediction using Tensile Strength Approximation, $4.2\sqrt{F'_c}$

| Specimen | First Cracking Load (kips) | Effective Thickness (in) | f'_c (psi) | $4.2\sqrt{F'_c}$ (psi) | Peak Stress / σ_o | Predicted Cracking Load(kips) | Test/ Predicted |
|-------------------|----------------------------|--------------------------|--------------|------------------------|--------------------------|-------------------------------|-----------------|
| 11 | 250 | 7.63 | 5720 | 318 | 0.637 | 179 | 1.39 |
| 12 | 325 | 7.63 | 6410 | 336 | 0.421 | 288 | 1.13 |
| 13 | 250 | 7.63 | 4510 | 282 | 0.517 | 196 | 1.27 |
| 14 | 350 | 7.63 | 6170 | 330 | 0.421 | 282 | 1.24 |
| ME2A | 240 | 7.63 | 6732 | 345 | 0.634 | 196 | 1.23 |
| ME2B | 240 | 7.63 | 6732 | 345 | 0.467 | 266 | 0.90 |
| $\sigma_o = P/ht$ | | | | | | Average | 1.19 |
| | | | | | | Standard Deviation | 0.15 |
| | | | | | | Coef. of Variance | 0.13 |

In conclusion, the correlation of cracking load of the test results and the model results was not particularly good and all the models using the split cylinder data yielded some unconservative answers. The coefficient of variance of the models using the split cylinder or a modified split cylinder strength for the tensile concrete strength were close to 20 percent. The best model for design was to use a lower bound approximation of the tensile strength based on $4.2\sqrt{F'_c}$ while modifying the section thickness by deducting the inside diameter of the duct. Using Guyon's symmetrical prism method to determine the

peak bursting stress was conservative for the cases investigated when using a lower bound approximation for the concrete tensile strength but did have a large coefficient of variance.

Table 6.7a Finite Element and Guyon's Symmetrical Prism Comparison

| Specimen | FEM Peak Stress (ksi) | Short Side Sym. Prism | | | Long Side Sym. Prism | | | Conventional Sym. Prism /FEM |
|----------|-----------------------|-----------------------|-------------------|-----------------|----------------------------|-------------------|-----------------|------------------------------|
| | | a/h | Peak Stress (ksi) | Sym. Prism /FEM | a/h | Peak Stress (ksi) | Sym. Prism /FEM | |
| 11 | 0.14 | 0.18 | 0.10 | 0.75 | 0.18 | 0.10 | 0.75 | 0.75 |
| 12 | 0.09 | 0.36 | 0.16 | 1.76 | 0.12 | 0.07 | 0.81 | 1.76 |
| 13 | 0.11 | 0.18 | 0.10 | 0.93 | 0.18 | 0.10 | 0.93 | 0.93 |
| 14 | 0.09 | 0.36 | 0.16 | 1.76 | 0.12 | 0.07 | 0.81 | 1.76 |
| ME2A | 0.13 | 0.41 | 0.17 | 1.23 | 0.23 | 0.12 | 0.91 | 1.23 |
| ME2B | 0.10 | 0.54 | 0.17 | 1.72 | 0.41 | 0.17 | 1.67 | 1.72 |
| | | | | 1.36 | Average Standard Deviation | | 0.98 | 1.36 |
| | | | | 0.41 | Coef. of Variance | | 0.31 | 0.41 |
| | | | | 0.30 | | | 0.32 | 0.30 |

Table 6.7b First Bursting Crack Prediction using Guyon's Symmetrical Prism

| Specimen | First Cracking Load (kips) | Effective Thickness (in) | f'c (psi) | $4.2\sqrt{f'c}$ (psi) | Peak Stress / σ_o | Predicted Cracking Load(kips) | Test/ Predicted |
|----------|----------------------------|--------------------------|-----------|-----------------------|--------------------------|-------------------------------|-----------------|
| 11 | 250 | 7.625 | 5720 | 318 | 0.366 | 238 | 1.05 |
| 12 | 325 | 7.625 | 6410 | 336 | 0.566 | 163 | 1.99 |
| 13 | 250 | 7.625 | 4510 | 282 | 0.366 | 211 | 1.18 |
| 14 | 350 | 7.625 | 6170 | 330 | 0.566 | 160 | 2.19 |
| ME2A | 240 | 7.625 | 6732 | 345 | 0.595 | 159 | 1.51 |
| ME2B | 240 | 7.625 | 6732 | 345 | 0.613 | 154 | 1.55 |
| | | | | | | Average | 1.58 |
| | | | | | | Standard Deviation | 0.40 |
| | | | | | | Coef. of Variance | 0.26 |

$$\sigma_o = P/ht$$

6.4 Strut-and-Tie Model to Prediction of the Ultimate Load

The power of the strut-and-tie model (STM) has been demonstrated in previous chapters in which the model was applied to concentric, eccentric, and multiple anchorage zones. Two types of STM's have been utilized. The basic STM locates the centroid of the compression struts at the end of the general zone according to the centroids of the assumed elastic stress distribution. For the basic STM, the end of the general zone is typically assumed to be at a depth of the section away from the loading surface. In the modified STM, the general zone is assumed to extend farther than a depth of the section away from the loading surface, and the centroids of the struts need not be located by the elastic stress distribution but are found from a plastic stress distribution. Since the general zone is extending deeper into the section and the plastic stress distribution is used, the centroids of the compression struts are located closer to the tendon axis. Figure 6.38 shows a comparison of the strut paths for the basic STM and the modified STM for Specimen I3. The figure clearly shows the movement of the compression struts closer to the tendon axis when a more plastic distribution is used to determine the compression strut centroids. The initial angles of the compression struts (see Fig. 6.38, α_1 and α_2) are smaller and the capacity of the STM increases if it is assumed that the tension ties control when using the modified STM. The limit of the movement of the strut centroids toward the tendon axis is the failure of the compression struts in compression. As the struts move closer to the tendon axis, the width of the strut is reduced. The reduction of the strut width increases the compression stresses in the struts and, therefore, reduces the strut capacity. In this section, these same methods will be applied for the specimens which had inclined anchorages and tendons with curvature.

6.4.1 Components of the Strut-and-Tie Model. The use of a tendon with curvature adds another component to the STM, radial forces along the tendon path. These radial forces can be assumed to act as a

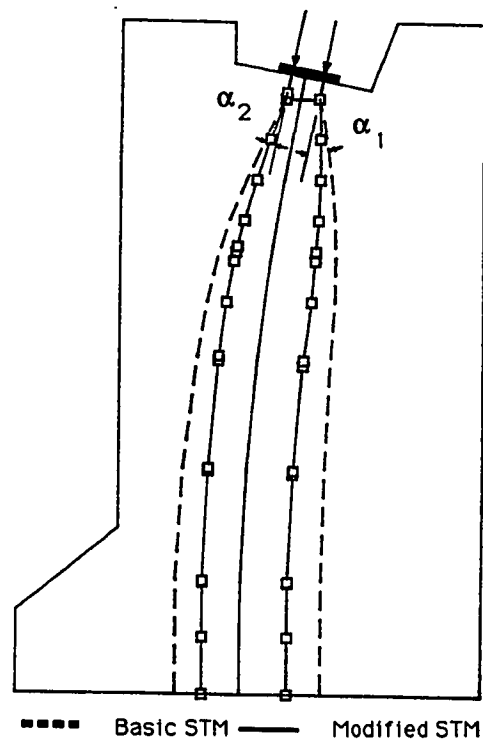
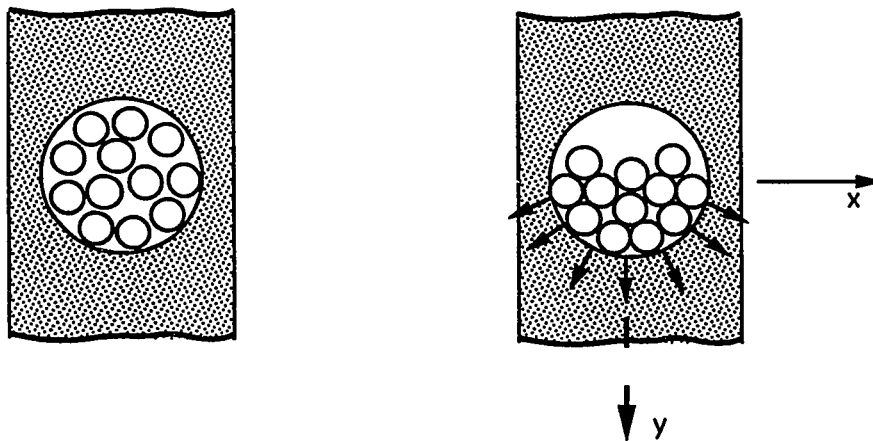


Figure 6.38 Comparison of Strut Paths for Specimen I3

distributed load perpendicular to the tendon path with a value at any point along the curved portion of the tendon which is equal to the tendon load divided by the radius of curvature of the tendon at that point. Since the multistrand tendon in a curved duct is pushing against the sides of the post-tensioning duct, transverse forces are also generated. Figure 6.39a shows the location of the strands within the duct when they are not stressed, while Fig. 6.39b shows the stressed state. The component of the force in the "y" direction is radial force. The components of the force in the positive and negative "x" directions are the transverse forces. The magnitude of these

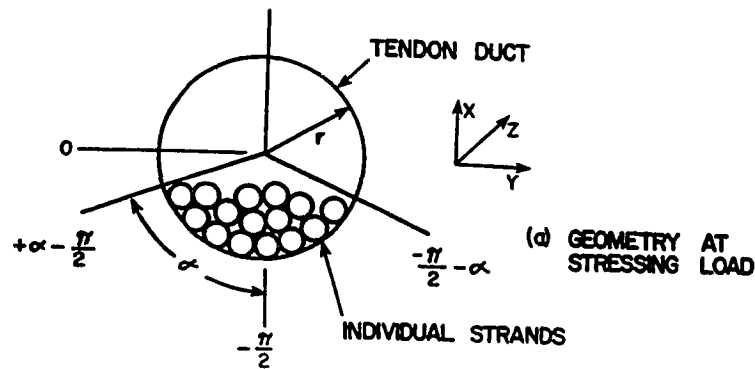
transverse forces are dependent on the configuration of the tendons within the duct (see Fig. 6.40). The tendon duct used in this series had an inside diameter of $2 \frac{3}{8}$ inches. When $12 \frac{1}{2}$ inch-strands were placed in the duct, their total area was 41 percent of the available duct area. Therefore, when the tendon force was applied, the tendon was assumed to occupy half of the duct, α in Fig. 6.40 equal to approximately 90 degrees. According to the report, Design and Construction Specifications for Segmental Concrete Bridges [135], reinforcement must be provided for this transverse force if the value of the shear stress along the transverse plane is greater than $2\sqrt{F'_c}$.



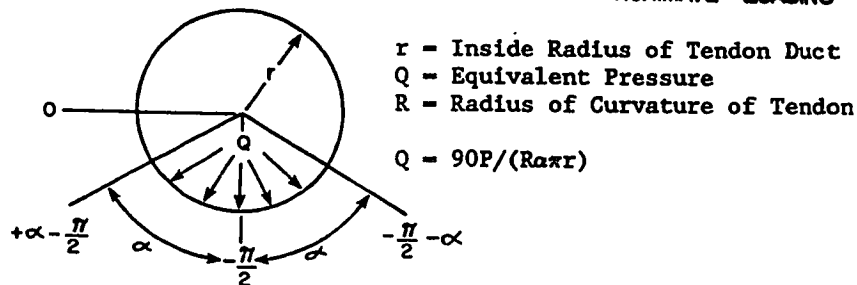
a) Unstressed Tendon

b) Stressed Tendon

Figure 6.39 Multistrand Effect in Curved Tendons [167]



(b) APPROXIMATE LOADING



ARC LENGTH = $2\alpha \cdot \frac{2\pi r}{360} = \frac{\alpha\pi r}{90}$ (α in DEGREES)

(c) EQUILIBRIUM

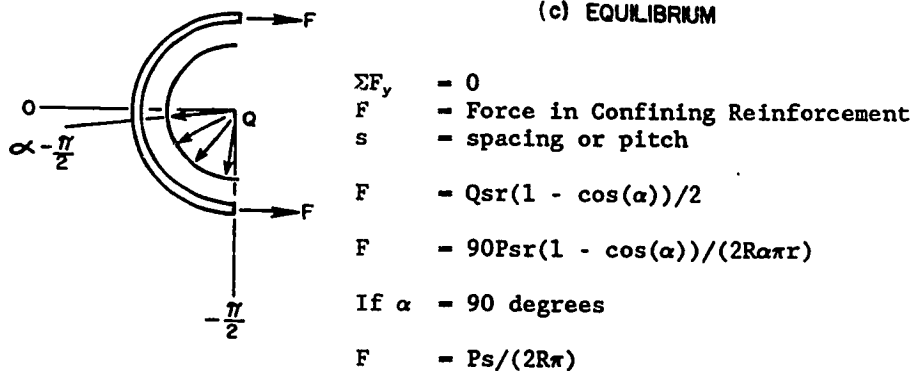


Figure 6.40 Confinement for Multistrand Loading [167]

In addition to providing confining reinforcement in the areas of curved tendon to counter the transverse force, reinforcement must be provided to tie-back or equilibrate the radial forces. According to the elastic analysis, a portion of the radial force is resisted by the compression in the concrete ahead of the duct while the remaining portion of the radial force is resisted by the concrete in tension behind the duct. In actuality, the concrete is very weak in tension and cannot be relied upon to resist high tensile force levels. Cracks will form in zones of high concrete tension. Reinforcement must be provided to carry a large portion of the radial force in tension in order to provide for proper resistance if a crack forms along the tendon path. This reinforcement is in addition to the bursting reinforcement necessary to handle the spreading of the axial force applied to the anchorage device.

For the purpose of this investigation, it was desirable to distinguish between the behavior of the reinforcement utilized for bursting forces and the behavior of the reinforcement utilized for the radial force. Therefore, a short stirrup was used for the radial reinforcement (see Fig. 6.9). In normal practice, a longer stirrup should be used to ensure that the force is fully tied back. The report on segmental bridge construction [135] states that radial reinforcement shall not be spaced farther apart than 12 inches and that closer spacing should be utilized if the tendon radius of curvature is less than 15 feet. The amount of force that must be anchored back in tension to provide a resistance pattern close to the elastic analysis case varies depending on the application and location of the tendon (see Fig. 6.41). If a tendon is placed very close to an exterior surface with radial forces directed toward the center of the section (see Fig. 6.41a), most of the radial forces will be resisted by the compression in the concrete. If the tendon is placed in the middle of the section, the radial force will be evenly distributed between the compression and tension resistances in the elastic state (see Fig.

6.41b). Figure 6.41c shows a case where most of the radial force must be anchored back in tension because the small amount of concrete in compression near the exterior surface cannot equilibrate the force.

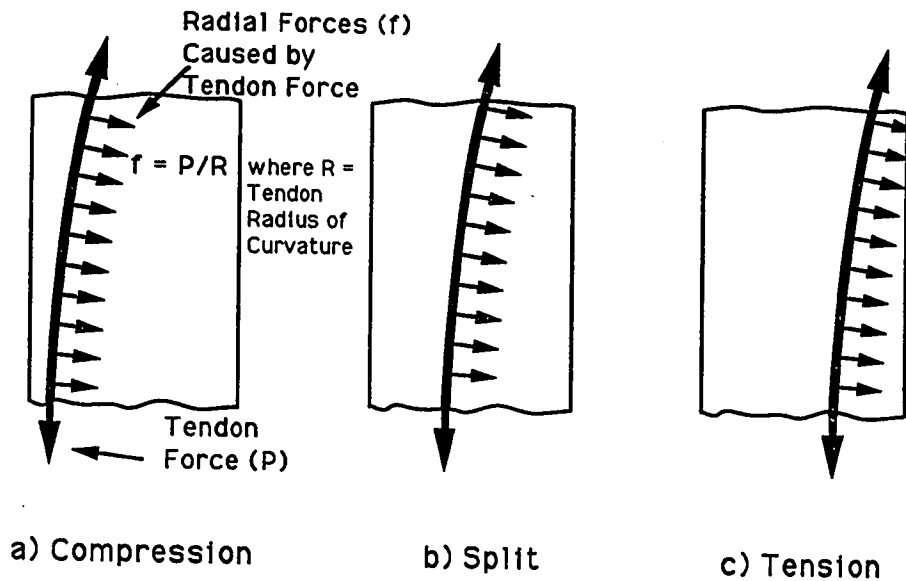


Figure 6.41 Radial Force Distribution between Compression and Tension Resistance

Figure 6.42 shows a STM including the radial forces. The STM uses the tendon path at the end of the general zone to divide the compression force between struts C_1 and C_2 . The radial forces are modelled as forces being applied to the compression struts. The assumed division of the radial force between the compression and tension resistances has a great effect on the resulting STM. Figure 6.43a illustrates a resulting STM, where tie-back reinforcement is furnished to provide tension resistance for the radial forces. Figure 6.43b is a resulting STM when zero tie-back reinforcement is provided. When zero tie-back reinforcement is provided, the left compression strut remains straight until encountering the tension bursting tie

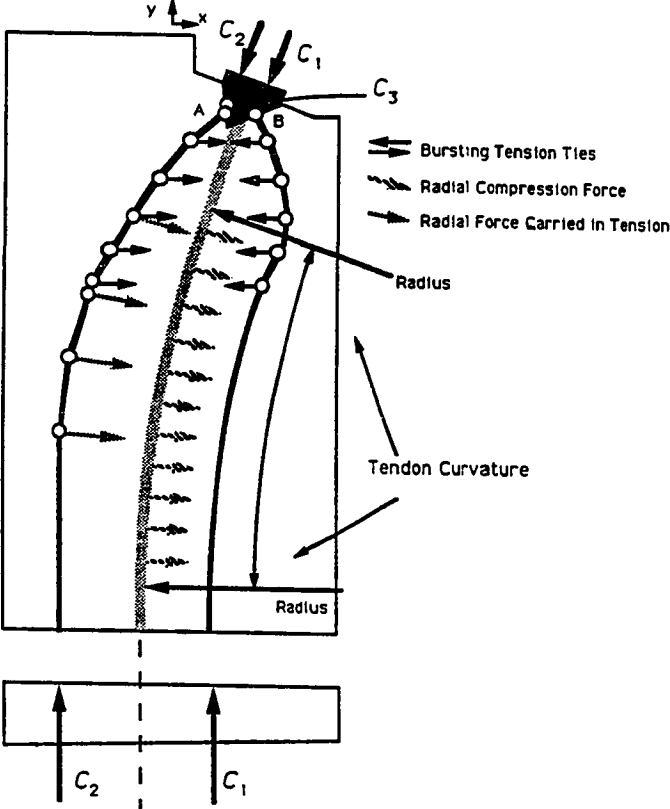
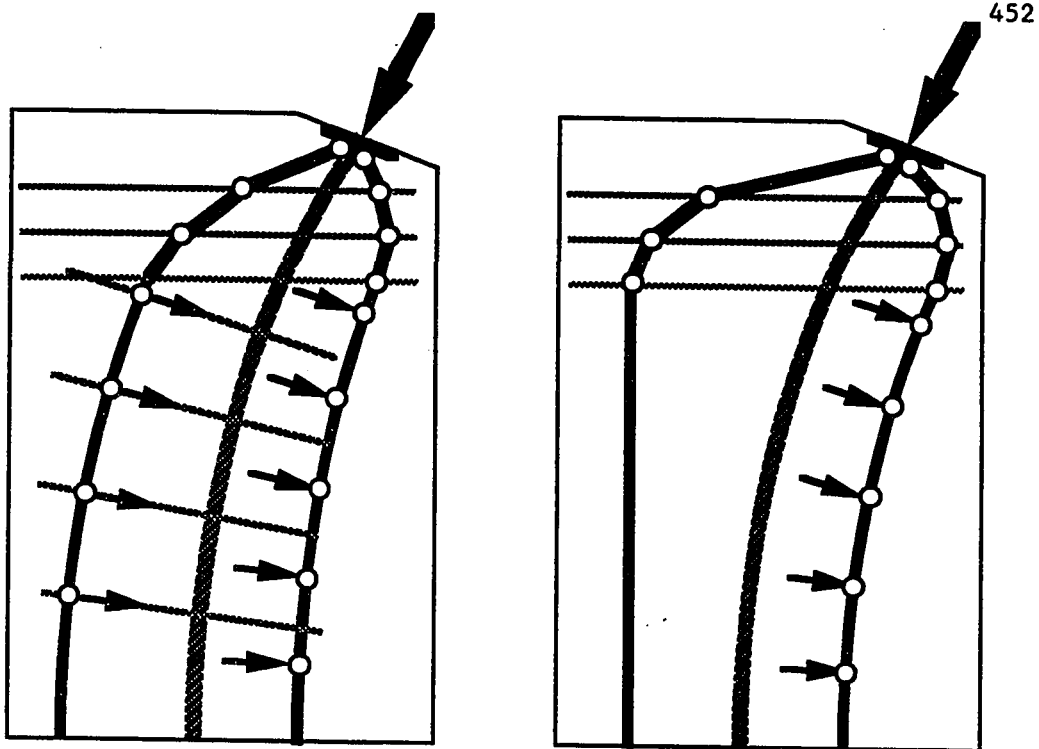


Figure 6.42 STM using the Tendon Path for the Division of Compression Struts

force. Using the STM, the appropriate division of the radial force between the compression and tension resistances can be estimated for the tendon cases shown in Fig. 6.41. For example, in Fig. 6.41a the magnitude of the strut to the left of the tendon path will be very small. Therefore, if this strut is required to carry a large portion of the radial force, the strut will be shifted too far to the right. Figure 6.44a shows a STM with a correctly proportioned radial force distribution, while Figure 6.44b shows a STM where the left compression strut is carrying too much of the radial force. For determining the portion of the radial force which should be shifted to each strut, it

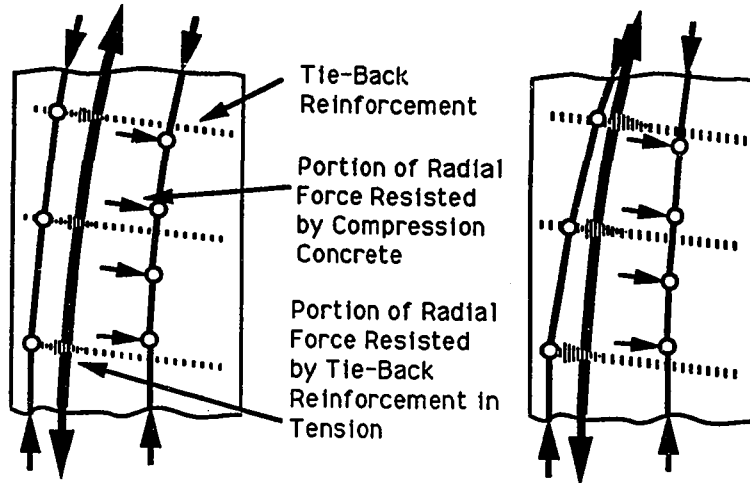


a) Tie-Back Reinforcement

b) Zero Tie-Back Reinforcement

Figure 6.43 Effect of Tie-Back Reinforcement on STM

seems appropriate to use a ratio equal to the magnitudes of the struts. Figure 6.44b shows the strut paths where a larger portion of the radial force is resisted in tension by the radial reinforcement. Table 6.8 shows the calculated percentage of the radial force carried in tension for each specimen with respect to the radial force component of the ultimate load. The magnitude of the radial forces carried in tension is computed by using the full yielding strength of the radial reinforcement. In the tests, all the instrumented radial reinforcement yielded except one tie-back hoop in Specimen I3 which was 52 inches from the loaded surface at the base of the specimen. Also shown in the table is the capacity of the bursting force reinforcement provided, its capacity as a percentage of the applied load, and similar values for the total tension reinforcement compared to the ultimate axial load.



a) Correctly Proportioned STM b) Incorrectly Proportioned STM
 Figure 6.44 Variation in STM Depending on Division of Radial Force

Table 6.8 Percentage of Load Carried in Tension

| Specimen | Ultimate Test Load (kips) | Radial Tension Force (kips) | Percentage of Ultimate Radial Force | Bursting Tension Force (kips) | Percentage of Ultimate Load | Total Tension Capacity as Percentage of Ultimate |
|----------|---------------------------|-----------------------------|-------------------------------------|-------------------------------|-----------------------------|--|
| 11 | 423 | 35.7 | 24.2 | 35.7 | 8.4 | 16.9 |
| 12 | 437 | 52.8 | 34.6 | 35.7 | 8.2 | 20.3 |
| 13 | 375 | 35.7 | 53.0 | 35.7 | 9.5 | 19.0 |
| 14 | 420 | 0 | 0 | 52.8 | 12.6 | 12.6 |
| ME2A | 370 | 28.6 | 29.3 | 35.7 | 9.6 | 17.4 |
| ME2B | 366 | 46.2 | 36.1 | 42.8 | 11.7 | 24.3 |

The local zone nodes for the STM are identical to those used in previous chapters except that they are inclined to match the anchorage device (see Fig. 6.45). The path and magnitude of the compression strut, C_3 , between the two sides of the STM will vary depending on the distribution of the radial forces carried in tension and compression,

the amount of bursting reinforcement, and the percentage of the axial force carried by each side of the STM. When checking the node compression force, the concrete along the plane (plane NR, Fig. 6.45) within the node parallel to the axial force resists the node compression force, as was done in previous chapters. Strut C_3 is not necessarily parallel to the loading surface. Therefore, the location of the secondary node (see Fig. 6.45, node A, A') may not be on the original node boundary, line MN. For the purpose of simplicity, the node will be assumed to stay at point "A". The inaccuracy introduced by this assumption is the distance Δ (see Fig. 6.45). Delta is typically small, and the difference caused in the results is within the accuracy of the model.

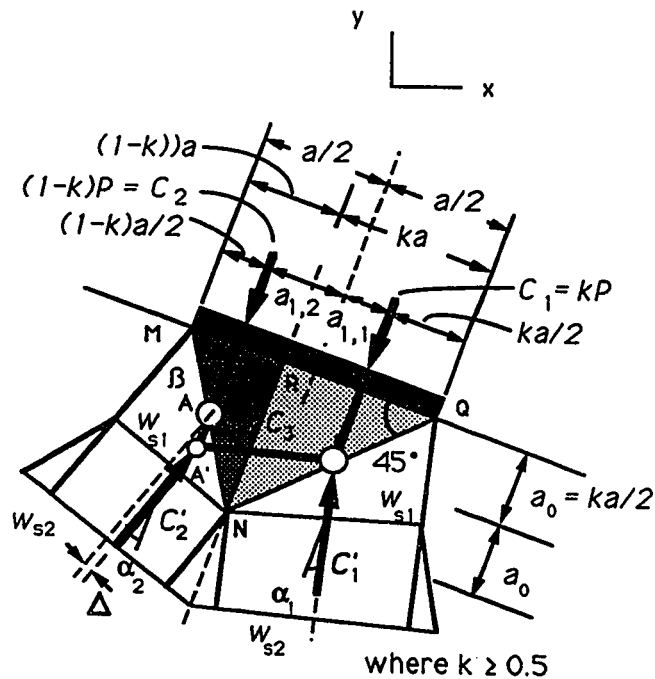


Figure 6.45 Inclined Local Zone Node

6.4.2 Basic Strut-and-Tie Model. This subsection demonstrates the calculations necessary for using the STM for specimens with inclined anchorages and tendon curvatures. All the specimens are checked against the following failure modes:

- 1) Tension tie failure of the bursting reinforcement,
- 2) Bearing failure ahead of the loading surface,
- 3) Compression failure of the local zone node,
- 4) Node-strut interface compression failure, and
- 5) Local zone-general zone interface compression failure.

The calculations shown are for Specimen I2. In carrying out this analysis, load factors and ϕ factors of 1.0 were used because the comparison was being made with a test conducted under laboratory conditions. The design calculations were carried out prior to testing and have been reported here independently of the actual test ultimate load. This is the same procedure that would be used by an engineer in checking an anchorage proposal while knowing only the concrete strength, proposed reinforcement layout, and anchorage size. In design, the engineer should include the proper load factors and ϕ factors.

The calculations are divided into six parts. First, the known physical dimensions and properties are given. Based on the given and proposed properties, the ultimate load is computed with the assumption that the tension ties would control. Any contribution of the spiral to the tension tie forces is neglected when determining the capacity while assuming that the tension ties control. Then four compression checks are compared against the prediction based on the expectation of the tension tie yielding. The first compression capacity check is for failure immediately ahead of the bearing surface. Then, the strut capacity between the secondary nodes is checked. The final two checks verify the capacity at the node-strut interface and at the interface between the local zone and the general zone. For the compression strut checks, the spiral in the local zone is assumed to confine an

equivalent square area concentric with the spiral. The lowest of the five prediction loads is then the predicted capacity.

- 1) Given: Specimen I2 (see Fig. 6.8)
- $t = 10$ inches
 - $h = 36$ inches
 - Plate Size = 6.5 inches x 6.5 inches
 - Tendon Radius of Curvature = 131 inches
 - Duct Outside Diameter = 2.63 inches
 - Initial Anchorage Inclination = 20 degrees from vertical
 - $f'_c = 6.41$ ksi
 - Spiral = #4 ($f_y = 80.3$ ksi) smooth bar,
 - $d_c = 8$ inches, $s = 2$ inches and $l_c = 9.5$ inches
 - Bursting Reinforcement: #2s ties at 6, 10, 14, 18, 22, and 26 inches with $F_y = 3.57$ kips/bar (two legs of the closed hoops at each level), Total Bursting Tension Capacity (T_{burst}) = 35.7 kips with a centroid of 14 inches as measured from the centroid of the loading surface parallel to the axis of the specimen (y direction).
 - Radial Reinforcement: 4 #3 tie back hoops with $F_y = 6.6$ kips/bar (two legs per hoop), Total Force = 52.8 kips acting at centroid of tendon with an average angle of 10 degrees, Located 33.29 inches from the centroid of the loading surface in the y direction and 10.01 inches from the centroid of the loading surface in the x direction.
 - Division of Load assumed according to the Elastic Stress Distribution at the end of the general zone using the tendon axis as the dividing line (see Fig. 6.46).

- 2) Determination of Ultimate Load assuming Tension Ties Control (see Fig. 6.46)

Sum moments about secondary node "B" with specimen cut along tendon axis:

Determine the Location of Secondary Node B (see Fig. 6.45):

- 1) Locate a_0 and a_1 in reference to the local zone node:

$$a_0 = (1 - 0.462) \cdot 6.5 / 2 = 1.75 \text{ inches}$$

$$a_1 = 6.5 / 2 - 0.462 \cdot 6.5 / 2 = 1.75 \text{ inches}$$

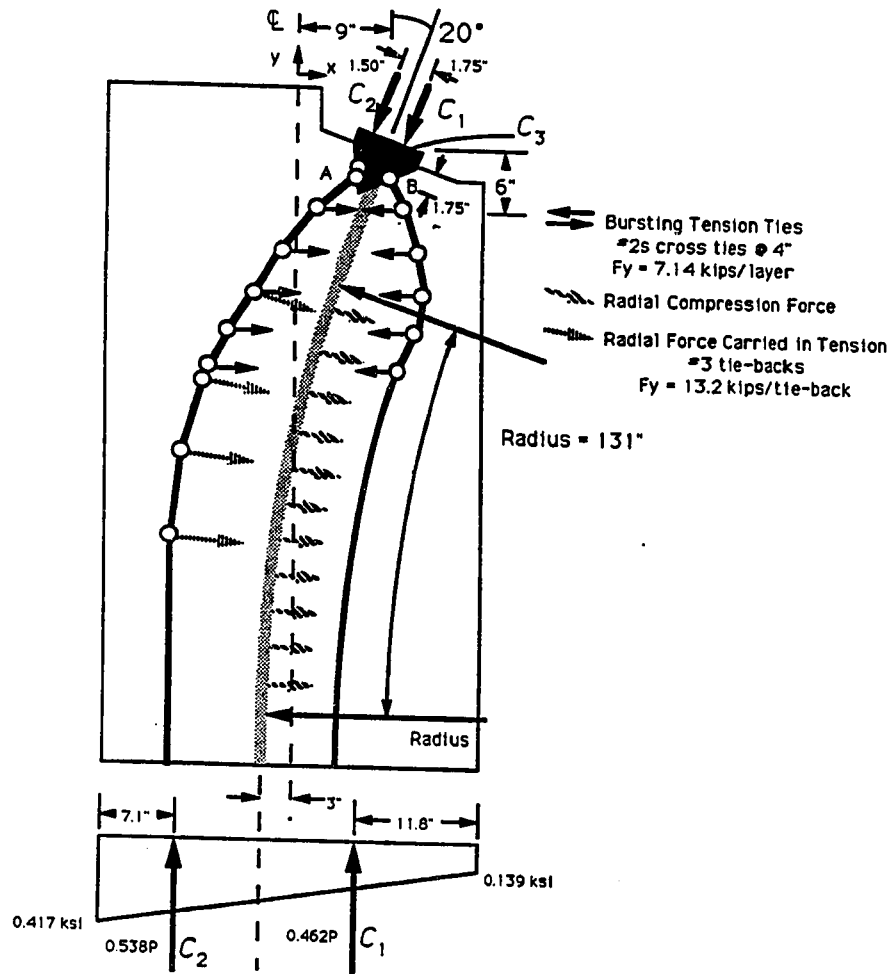


Figure 6.46 STM and Elastic Stress Distribution for Specimen I2

- 2) Translate a_0 and a_1 into x and y coordinates as measured from the centroid of the loading surface.

$$\begin{aligned}
 a_{0y} &= a_0 \cdot \cos(\theta) + a_1 \cdot \sin(\theta) \\
 &= 1.75 \cdot \cos(20) + 1.75 \cdot \sin(20) = 2.24 \text{ inches} \\
 a_{1x} &= a_1 \cdot \cos(\theta) - a_0 \cdot \sin(\theta) \\
 &= 1.75 \cdot \cos(20) - 1.75 \cdot \sin(20) = 1.05 \text{ inches}
 \end{aligned}$$

where θ = Initial Anchorage Inclination

$$\text{Total Radial Force} = P/R \cdot L_{\text{tendon}}$$

$$\begin{aligned} \text{where } L_{\text{tendon}} &= \text{Tendon Length} = \pi \cdot R \cdot \theta / 180 \\ P &= \text{Applied Tendon Force} \\ R &= \text{Tendon Radius} \end{aligned}$$

$$L_{\text{tendon}} = \pi \cdot 131 \cdot 20 / 180 = 45.73 \text{ inches}$$

$$\text{Total Radial Force} = P / 131 \cdot 45.73 = 0.349P$$

$$\begin{aligned} \text{Total Radial Force carried in Compression } (C_{\text{radial}}) \\ = 0.349P - 52.8 \end{aligned}$$

$$\begin{aligned} \Sigma M_B = 0 &= 0.462P \cdot (27 - 24.21 + 1.05) + 35.7 \cdot (14 - 2.24) - \\ &\quad (0.349P - 52.8) \cdot \cos(20/2) \cdot (33.29 - 2.24) - \\ &\quad (0.349P - 52.8) \cdot \sin(20/2) \cdot (10.01 + 1.05) \\ 0 &= -9.57P + 2136 \quad \text{Therefore } P = \underline{223 \text{ kips}} \end{aligned}$$

Therefore, the capacity of the anchorage zone is 223 kips if the tension ties control.

3) Bearing Capacity Immediately Ahead of the Anchorage Device

$$P_b = 0.7f'_c \sqrt{A/A_g} A_b + k \cdot f_y \cdot A_s / (s \cdot d) \cdot (1 - s/d_c)^2 \cdot A_{\text{core}} \leq 3f'_c \cdot A_b$$

- where A - the effective area which is the maximum area of the supporting surface that is geometrically similar to the loaded area and concentric with it;
- A_b - the bearing or strut area (A_{st});
- A_{core} - the area confined by the local confining reinforcement (A_{stc} for struts);
- A_g - the gross area of the bearing plate;
- A_s - the area of the confining reinforcement with the spacing "s";
- d_c - the diameter of the spiral or the width of the ties;
- f'_c - the concrete compressive strength at the time of stressing;
- f_y - the yield strength of the confining reinforcement;
- k - 4 for spirals or active confinement and 2 for ties; and
- s - the pitch of the spiral or the spacing of the ties.

$$A_b = 6.5 \cdot 6.5 - \pi \cdot 2.63^2 / 4 = 36.8 \text{ in}^2$$

$$A_g = 6.5 \cdot 6.5 = 42.3 \text{ in}^2$$

$$A_{\text{core}} = \pi \cdot 8^2 / 4 = 50.3 \text{ in}^2$$

$$\begin{aligned}
 A &= 10.0 \cdot 10.0 = 100.0 \text{ in}^2 \\
 P_b &= 0.7 \cdot 6.41 \sqrt{100.0/42.3} \cdot 36.8 + \\
 &\quad 4 \cdot (80.3 \cdot 0.2 \cdot 2) / (2 \cdot 8) (1 - 2/8)^2 \cdot 50.3 \\
 &= \underline{481 \text{ kips}} \gg \text{tension tie load still controls (299 kips)}
 \end{aligned}$$

4) Force Between Secondary Nodes

$$P_s = 0.7 f'_c \sqrt{I} A_{st} + k \cdot f_y \cdot A_s / (s \cdot d) \cdot (1 - s/d_c)^2 \cdot A_{stc} \leq 3 f'_c \cdot A_{st}$$

where A_{st} = the total strut area

A_{stc} = the area of the strut which is confined

$$A_{st} = A_{stc} = a_o \cdot 2 \cdot b = 1.75 \cdot 2 \cdot 6.5 = 22.8 \text{ in}^2$$

b = plate width in the transverse direction

$$\begin{aligned}
 P_s &= 0.7 \cdot 6.41 \cdot 22.8 + \\
 &\quad 4 \cdot (80.3 \cdot 0.2 \cdot 2) / (2 \cdot 8) (1 - 2/8)^2 \cdot 22.8 \\
 &= \underline{205 \text{ kips}}
 \end{aligned}$$

$$P_s \geq C_3 \text{ ??}$$

where C_3 is determined by summing forces using the tendon path as the dividing line.

$$\begin{aligned}
 \Sigma F_x = 0 &= C_3 \cdot \cos(\beta) - C_2 \cdot \sin(\theta) - T_{burst} + C_{radial} \cdot \cos(\theta/2) \\
 \Sigma F_y = 0 &= C_3 \cdot \sin(\beta) + C_2 \cdot \cos(\theta) - C_2 + C_{radial} \cdot \sin(\theta/2)
 \end{aligned}$$

β is the angle C_3 makes with the x axis

$$\theta = 20 \text{ degrees}$$

$$C_{radial} = 0.349P - 52.8$$

$$C_2 = 0.462P$$

$$T_{burst} = 35.7 \text{ kips}$$

therefore

$$\tan(\beta) = \frac{[0.462P - 0.462P \cdot \cos(20) - C_{radial} \cdot \sin(20/2)]}{[0.462P \cdot \sin(20) + T_{burst} - C_{radial} \cdot \cos(20/2)]}$$

$$C_3 = [0.462P - 0.462P \cdot \cos(20) - C_{radial} \cdot \sin(20/2)] / \sin(\beta)$$

For Controlling Load of 223 kips:

$$C_{radial} = 25.0 \text{ kips}$$

$$\beta = 2.31 \text{ degrees}$$

$$C_3 = 46.7 \text{ kips} \ll 205 \text{ kips}$$

Therefore, node compression does not control and the predicted capacity is 223 kips.

5) Strut Capacity at the Node-Strut Interface

$$P_s = (\text{Confined Concrete Capacity} + \text{Unconfined Concrete Capacity}) \cdot \cos(\alpha) / \text{Percentage of Total Axial Load Carried by the Strut under investigation}$$

$$P_s = (\sigma_{s\text{-confined}} \cdot A_{stc} + \sigma_{s\text{-unconfined}} \cdot A_{stn}) \cdot \cos(\alpha) / \text{Load Percentage}$$

where

$$A_{stc} = \text{confined strut area}$$

$$A_{stn} = A_{st} - A_{stc} = \text{unconfined strut area}$$

$$A_{st} = \text{total strut area}$$

$$\sigma_{s\text{-confined}} = \text{maximum stress in confined concrete}$$

$$\sigma_{s\text{-unconfined}} = \text{maximum stress in unconfined concrete}$$

Must Check Strut Capacity for Each Side of the Node (C_1 and C_2)

Determine Strut Angle (α):

The angle, α , can be determined by assuming that the tension tie load controls and by summing forces at the secondary nodes A and B.

Left Strut (C_1):

$$\Sigma F_x = 0 = C_3 \cdot \cos(\beta) + 0.538P \cdot \sin(20) - F_{\text{strut}} \cdot \sin(\alpha)$$

$$\Sigma F_y = 0 = C_3 \cdot \sin(\beta) - 0.538P \cdot \cos(20) + F_{\text{strut}} \cdot \cos(\alpha)$$

where F is the force in the strut C_1 if the applied load is the load predicted by the tension tie model.

$$0 = 46.7 \cdot \cos(2.31) + 0.538 \cdot 223 \cdot \sin(20) - F_{\text{strut}} \cdot \sin(\alpha)$$

$$0 = 46.7 \cdot \sin(2.31) - 0.538 \cdot 223 \cdot \cos(20) + F_{\text{strut}} \cdot \cos(\alpha)$$

$$\tan(\alpha) = (87.69)/(110.9) \quad \alpha = 38.34 \text{ degrees}$$

This angle is in the global coordinate system; to convert it into the local coordinate system (local zone node), the initial angle of the anchorage must be subtracted from α .

$$\alpha_{\text{local-1}} = 38.34 - 20 = 18.34 \text{ degrees}$$

Right Strut (C_2):

$$\Sigma F_x = 0 = C_3 \cdot \cos(\beta) - 0.462P \cdot \sin(20) - F_{\text{strut}} \cdot \sin(\alpha)$$

$$\Sigma F_y = 0 = C_3 \cdot \sin(\beta) + 0.462P \cdot \cos(20) - F_{\text{strut}} \cdot \cos(\alpha)$$

where F is the force in the strut (C_2) assuming that the applied load is the load predicted by the tension tie model.

$$0 = 46.7 \cdot \cos(2.31) - 0.462 \cdot 223 \cdot \sin(20) - F_{\text{strut}} \cdot \sin(\alpha)$$

$$0 = 46.7 \cdot \sin(2.31) + 0.462 \cdot 223 \cdot \cos(20) - F_{\text{strut}} \cdot \cos(\alpha)$$

$$\tan(\alpha) = (11.43)/(98.70) \quad \alpha = 6.37 \text{ degrees}$$

This angle is in the global coordinate system, to convert into the local coordinate system (local zone node) the initial angle of the anchorage must be added to α .

$$\alpha_{\text{local-2}} = 20 + 6.37 = 26.37 \text{ degrees}$$

Determine the portion of the strut which is confined and unconfined:

Since $2 \cdot a_o = 2 \cdot 1.75 = 3.5$ inches is less than the length of the spiral (9.5 inches), a portion of the node-strut interface is confined concrete.

Determine Equivalent Width of Confined Area

(Since a spiral is round, it is easier to convert spiral into an equivalent square to compare it with rectangular struts. This is especially true when the struts are not symmetrical like they are in eccentric and multiple anchorages.)

$d_c = \sqrt{\pi \cdot 8 \cdot 8 / 4} = 7.08$ inches >> Therefore, the distance from the specimen centerline to the confined boundary is 3.55 inches.

Since the strut forces are not divided evenly, the confined width for strut C_1 is $(3.55 + 7.08 \cdot (0.538 - 0.5)) / \cos(18.34) = 4.00$ inches and the confined width for strut C_2 is $(3.55 + 7.08 \cdot (0.462 - 0.5)) / \cos(26.37) = 3.30$ inches.

Strut C_1 :

Determine the Width and Thickness of the Strut:

$$w_{s1} = a \cdot 0.538 \cdot \cos(45 - \alpha) / \cos(45)$$

$$= 6.5 \cdot 0.538 \cdot \cos(45 - 18.34) / \cos(45) = 4.42 \text{ inches}$$

$$t_s = b + (t - b) \cdot d / t$$

$$d = \text{distance to the centroid of plane } w_{s1} \text{ from the}$$

loading surface perpendicular to the tendon axis

$$= a_o \cdot 2 - w_{s1}/2 \cdot \sin(\alpha) = 1.75 \cdot 2 - 4.42/2 \cdot \sin(18.34)$$

$$= 2.81 \text{ inches}$$

$$t_o = 6.5 + (10 - 6.5) \cdot 2.81/10 = 7.48 \text{ inches}$$

$$A_{st} = w_{s1} \cdot t_o = 4.42 \cdot 7.48 = 33.06 \text{ in}^2$$

$$A_{stc} = 4.00 \cdot 7.08 = 28.32 \text{ in}^2$$

$$A_{stu} = A_{st} - A_{stc} = 33.06 - 28.32 = 4.74 \text{ in}^2$$

Determine Maximum Compressive Strut Stress:

Maximum Stress in the Confined Zone

$$\sigma_s = 0.7f'_c \sqrt{A/A_{st}} + k \cdot f_y \cdot A_s / (s \cdot d) \cdot (1 - s/d_c)^2 \leq 3f'_c$$

A = the effective area which in most cases is restricted by the ratio of the section thickness to the strut thickness

$$A = t \cdot (w_{s1} \cdot t / t_o) = 10 \cdot (4.42 \cdot 10 / 7.48) = 59.09 \text{ in}^2$$

$$\sigma_s = 0.7 \cdot 6.41 \sqrt{59.1/33.1} + 4 \cdot (80.3 \cdot 0.2 \cdot 2) / (2 \cdot 8) \cdot (1 - 2/8)^2$$

$$= 10.51 \text{ ksi}$$

Maximum Stress in the Unconfined Zone

$$\sigma_s = 0.7 \cdot 6.41 \sqrt{59.1/33.1} + 0 = 6.00 \text{ ksi}$$

Maximum Axial Load for Strut C₁:

$$P_s = [10.51 \cdot 28.32 + 6.00 \cdot 4.74] \cdot \cos(18.34) / 0.538 = \underline{576} \text{ kips}$$

This is greater than the load predicted by the tension ties. Therefore, the node-strut interface for strut C₁ does not control.

Strut C₂:

Determine the Width and Thickness of the Strut:

$$w_{s1} = a \cdot 0.462 \cdot \cos(\beta - \alpha) / \cos(\beta)$$

$$\beta = \text{atan}(a_o \cdot 2 / (0.462 \cdot a)) = \text{atan}(1.75 \cdot 2 / (0.462 \cdot 6.5))$$

$$= 49.37 \text{ degrees}$$

$$w_{s1} = 6.5 \cdot 0.462 \cdot \cos(49.37 - 26.37) / \cos(49.37) = 4.24 \text{ inches}$$

$$t_o = b + (t - b) \cdot d/t$$

$$\begin{aligned}
 d &= \text{distance to the centroid of plane } w_{s1} \text{ from the} \\
 &\quad \text{loading surface perpendicular to the tendon axis} \\
 &= a_o \cdot 2 - w_{s1}/2 \cdot \sin(\alpha) = 1.75 \cdot 2 - 4.24/2 \cdot \sin(26.37) \\
 &= 2.56 \text{ inches} \\
 t_o &= 6.5 + (10-6.5) \cdot 2.56/10 = 7.39 \text{ inches} \\
 A_{st} &= w_{s1} \cdot t_o = 4.24 \cdot 7.39 = 31.33 \text{ in}^2 \\
 A_{stc} &= 3.30 \cdot 7.08 = 23.36 \text{ in}^2 \\
 A_{stu} &= A_{st} - A_{stc} = 31.33 - 23.36 = 7.97 \text{ in}^2
 \end{aligned}$$

Determine Maximum Compressive Strut Stress:

Maximum Stress in the Confined Zone

$$\begin{aligned}
 \sigma_s &= 0.7f'_c \sqrt{A/A_{st}} + k \cdot f_y \cdot A_s / (s \cdot d) \cdot (1-s/d_c)^2 \leq 3f'_c \\
 A &= \text{the effective area which in most cases is} \\
 &\quad \text{restricted by the ratio of the section thickness} \\
 &\quad \text{to the strut thickness} \\
 A &= t \cdot (w_{s1} \cdot t / t_o) = 10 \cdot (4.24 \cdot 10 / 7.39) = 57.37 \text{ in}^2 \\
 \sigma_s &= 0.7 \cdot 6.41 \sqrt{57.4/31.3} + \\
 &\quad 4 \cdot (80.3 \cdot 0.2 \cdot 2) / (2 \cdot 8) \cdot (1-2/8)^2 \\
 &= 10.51 \text{ ksi}
 \end{aligned}$$

Maximum Stress in the Unconfined Zone

$$\sigma_s = 0.7 \cdot 6.41 \sqrt{57.4/31.3} + 0 = 6.07 \text{ ksi}$$

Maximum Axial Load for Strut C_1 :

$$P_s = [10.51 \cdot 23.36 + 6.07 \cdot 7.97] \cdot \cos(26.37) / 0.462 = \underline{574} \text{ kips}$$

This is greater than the load predicted by the tension ties. Therefore, the node-strut interface for strut C_2 does not control.

6) Strut Capacity at Interface between the Local Zone and the General Zone (Base of the Spiral)

Strut C_1

$$\begin{aligned}
 w_{s2} &= w_{s1} + 2 \cdot (l_c - a_o \cdot 2) \cdot \sin(\alpha) \\
 &= 4.42 + 2 \cdot (9.5 - 1.75 \cdot 2) \cdot \sin(18.34) = 8.20 \text{ inches} \\
 t_o &= 6.5 + (10-6.5) \cdot (9.5-8.20/2 \cdot \sin(18.34)) / 10 \\
 &= 9.37 \text{ inches} \\
 A_{st} &= 8.20 \cdot 9.37 = 76.8 \text{ in}^2
 \end{aligned}$$

$$A = t \cdot (w_{s2} \cdot t / t_e) = 10 \cdot (8.20 \cdot 10 / 9.37) = 87.5 \text{ in}^2$$

$$\sigma_s = 0.7 \cdot 6.41 \sqrt{87.5 / 76.8} + 0 = 4.79 \text{ ksi}$$

Maximum Axial Load for Strut C₁:

$P_s = 4.79 \cdot 76.8 \cdot \cos(18.34) / 0.538 = \underline{649}$ kips >> This is greater than the load predicted by the tension ties. Therefore, the local zone-general zone interface does not control.

Strut C₂

$$\begin{aligned} w_{s2} &= w_{s1} + 2 \cdot (l_c - a_o \cdot 2) \cdot \sin(\alpha) \\ &= 4.24 + 2 \cdot (9.5 - 1.75 \cdot 2) \cdot \sin(26.37) = 9.58 \text{ inches} \end{aligned}$$

$$\begin{aligned} t_e &= 6.5 + (10 - 6.5) \cdot (9.5 - 9.58 / 2 \cdot \sin(26.37)) / 10 \\ &= 9.08 \text{ inches} \end{aligned}$$

$$A_{st} = 9.58 \cdot 9.08 = 87.0 \text{ in}^2$$

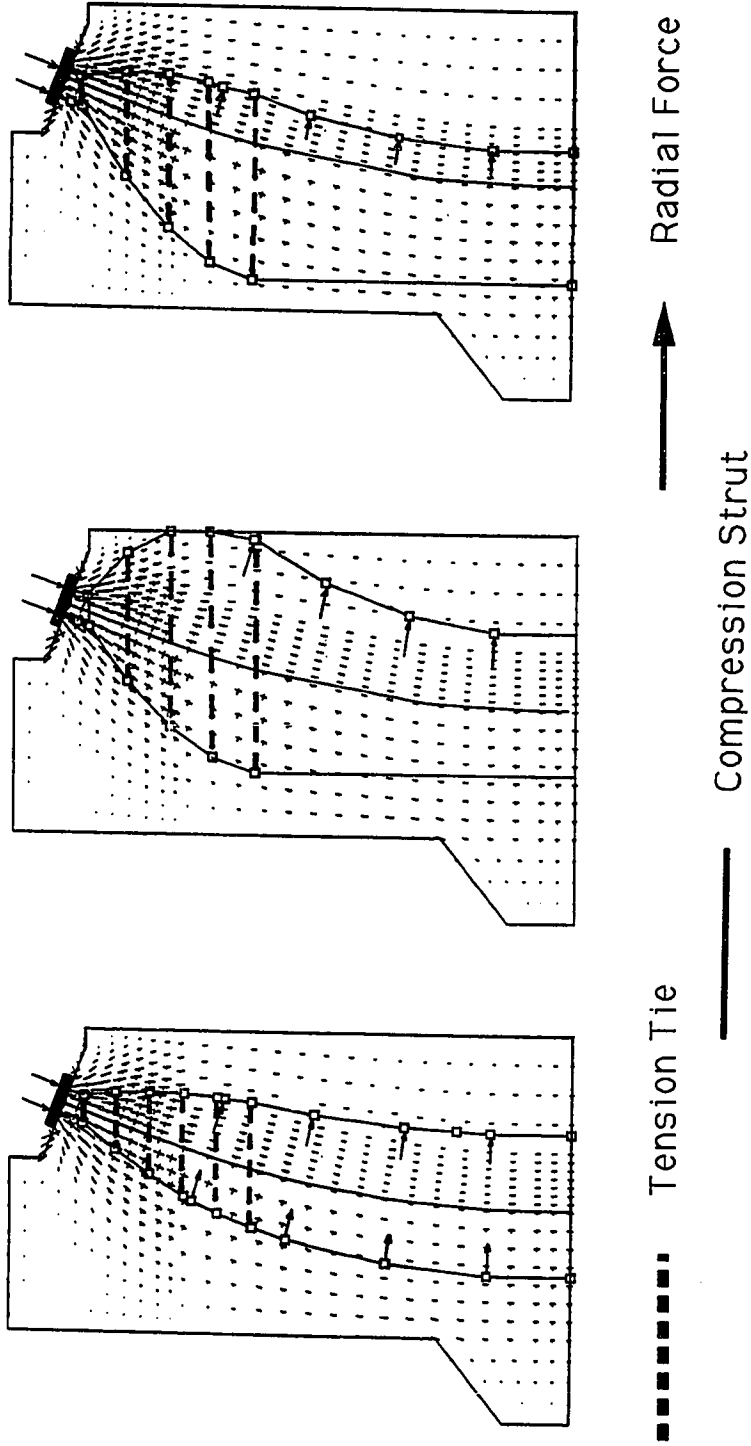
$$A = t \cdot (w_{s2} \cdot t / t_e) = 10 \cdot (9.58 \cdot 10 / 9.08) = 105.5 \text{ in}^2$$

$$\sigma_s = 0.7 \cdot 6.41 \sqrt{105.5 / 87.0} + 0 = 4.94 \text{ ksi}$$

Maximum Axial Load for Strut C₁:

$P_s = 4.94 \cdot 87.0 \cdot \cos(26.37) / 0.462 = \underline{833}$ kips >> This is greater than the load predicted by the tension ties. Therefore, the local zone-general zone interface does not control.

Figure 6.47a shows the path of the compression struts and tension ties for Specimen I2 superimposed on the elastic stress distribution determined by Burdet [25]. The STM was designed to follow the stress distribution closely. In contrast, Specimen I4, with no radial reinforcement, has strut paths that vary significantly from the elastic distribution (see Fig. 6.47b). At the ultimate load Specimen I4 was fully cracked along the tendon path with zero tie-back reinforcement provided. Therefore, a realistic assumption for Specimen I4 is that all the radial force was resisted by the concrete in compression. If the tendon path is used to divide the compression struts, the right hand strut is projected to exit the specimen near the top of the specimen (see Fig. 6.47b). Since this force path differs from the elastic distribution significantly, the force thrust line is used to divide the compression struts (see Figs. 6.47c and 6.48). The point



a) Specimen I2 STM

b) Specimen I4 STM using the Tendon Path

c) Specimen I4 STM using the Thrust Line

Figure 6.47 STM comparison for Specimens I2 and I4

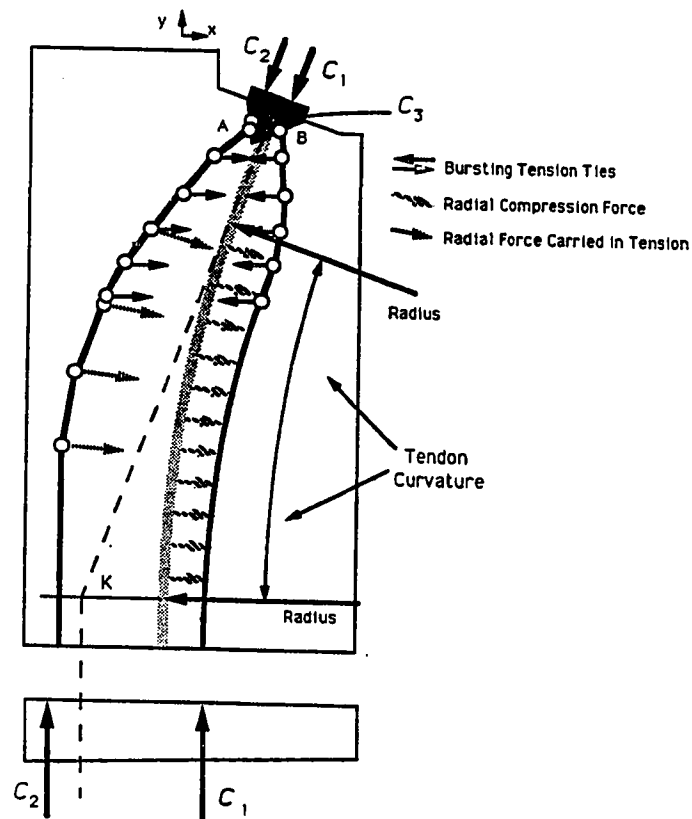


Figure 6.48 STM using the Thrust Line for Compression Strut Division

used to divide the struts (see Fig. 6.48, pt. K) is where the thrust line intersects the plane that corresponds with the end of the tendon curvature. The use of the thrust line and the subsequent result of one strut carrying a majority of the load can be somewhat justified by the observed cracking pattern of Specimen I4. There were very small amounts of cracking away from the tendon path in the actual test. The cracking that did occur away from the tendon path followed very closely the path shown in Fig. 6.48 for the right-hand strut. This model was more realistic under the given reinforcement conditions than dividing the struts using the tendon path for this specimen. The decision on

how to divide the compression forces into individual struts is one which can vary depending on the situation.

Table 6.9 Geometry Summary and STM Capacity assuming Tension Ties Control

| Specimen | Side 1 | | | | Side 2 | | | | Capacity if Tension Tie Controls (kips) |
|-----------|-----------------------------|------|---------------------|---------------------|-----------------------------|------|---------------------|---------------------|---|
| | Location-Base Section Width | % | A _o (in) | A ₁ (in) | Location-Base Section Width | % | A _o (in) | A ₁ (in) | |
| I1 | Left-6" Wide | 0.44 | 1.81 | 1.81 | Right-30" Wide | 0.56 | 1.81 | 1.44 | 281 |
| I2 | Left-15" Wide | 0.54 | 1.75 | 1.50 | Right-21" Wide | 0.46 | 1.75 | 1.75 | 223 |
| I3 | Left-12" Wide | 0.56 | 1.81 | 1.44 | Right-24" Wide | 0.44 | 1.81 | 1.81 | 262 |
| I4-Thrust | Left-15" Wide | 0.26 | 2.41 | 2.41 | Right-21" Wide | 0.74 | 2.41 | 0.84 | 126 |
| I4-Tendon | Left-15" Wide | 0.54 | 1.75 | 1.50 | Right-21" Wide | 0.46 | 1.75 | 1.75 | 68 |
| ME2A | Left-5" Wide | 0.54 | 1.74 | 1.51 | Right-5.12" Wide | 0.46 | 1.74 | 1.74 | 261 |
| ME2B | Right-18" Wide | 0.46 | 1.76 | 1.76 | Left-7.88" Wide | 0.54 | 1.76 | 1.49 | 267 |

Table 6.9 shows the division of the forces for the compression struts and the location of the secondary nodes as measured perpendicular to the initial tendon path (a_1) and to the loading surface (a_0). Also shown in the table are the results for the STM for each specimen when assuming that the tension tie controls and a description of the sides of the specimen that will be used in the compression strut capacity calculations. Because of the unrealistic strut paths seen for Specimen I4 when using the tendon as the division line, the compression checks for Specimen I4 were calculated only for the thrust line division method. It should be noted that using the tendon path would be more conservative than using the thrust line.

The failure of Specimen I4 was very explosive since there was zero radial reinforcement provided along the tendon path. In the previous section, Fig. 6.6 showed Specimen I4 at failure and a 2-inch separation between the duct and the concrete after failure. Radial reinforcement should be placed across the tendon path. Reinforcement is needed to maintain small crack sizes and a stress distribution close to that of the elastic state.

Tables 6.10 to 6.12 show the compression checks and capacities

for the "I" series specimens and Specimen ME2. Table 6.13 is a summary for all the failure modes for the basic STM. The tension tie governed all of these failures according to the basic STM predictions. The model is extremely conservative, with Specimen I4 being the most conservative. The average of the test-to-predicted ratios is 1.93 with a coefficient of variance of 0.38. The conservative average will raise even higher if the tendon division line method is used for Specimen I4. The ratio of the test-to-predicted load for Specimen I4 increases to 6.20 when using the tendon axis for the division of forces. Even if Specimen I4 is neglected in the statistical analysis, the average drops only to 1.58 with a coefficient of variance of 0.14. If the prediction load which assumes that the tension ties control is neglected, the prediction model results are much closer to unity. However, when this is done all the specimen predictions are unconservative. The average test-to-predicted ratio is 0.88 with a coefficient of variance of 0.08.

Table 6.10 Bearing and Node Compression Capacity

| Specimen | f'_c (ksi) | Bearing Capacity (kips) | Node C3 (kips) | Compression Forces Capacity (kips) | C3/ Capacity |
|-----------|-----------------|-------------------------------|----------------------|--|-----------------|
| I1 | 5.72 | 454 | 28.2 | 200 | 0.14 |
| I2 | 6.41 | 481 | 46.7 | 205 | 0.23 |
| I3 | 4.51 | 406 | 45.2 | 180 | 0.25 |
| I4-Thrust | 6.17 | 472 | 41.7 | 277 | 0.15 |
| ME2A | 6.73 | 494 | 27.6 | 209 | 0.13 |
| ME2B | 6.73 | 494 | 38.4 | 211 | 0.18 |

When examining the actual experimental results, it was noted that all of the bursting reinforcement yielded prior to failure and that, at the time of failure, a compression type of failure seemed to occur. This observation, when coupled with the more accurate results obtained

for the straight tendon specimens by using the modified STM, (which assumes a more plastic force distribution at the end of the extended general zone), again suggests that there was a possibility of a modified and improved STM available.

Table 6.11 STM Capacity at Node-Strut Interface

a) Side 1

| Specimen | Alpha (degrees) | Strut Width (in) | Strut Thickness (in) | Confined Width (in) | Confined Allowable (ksi) | Unconfined Allowable (ksi) | Predicted Maximum (kips) |
|-----------|--------------------|------------------------|----------------------------|---------------------------|--------------------------------|----------------------------------|--------------------------------|
| I1 | 10.83 | 3.52 | 7.65 | 3.24 | 9.75 | 5.24 | 541 |
| I2 | 18.34 | 4.42 | 7.48 | 4.00 | 10.51 | 6.00 | 576 |
| I3 | 16.29 | 4.48 | 7.54 | 4.07 | 8.70 | 4.18 | 469 |
| I4-Thrust | 38.33 | 4.31 | 7.72 | 2.52 | 10.11 | 5.59 | 809 |
| ME2A | 10.07 | 4.04 | 7.60 | 3.84 | 10.72 | 6.20 | 575 |
| ME2B | 18.23 | 3.93 | 7.52 | 3.45 | 10.79 | 6.27 | 613 |

b) Side 2

| Specimen | Alpha (degrees) | Strut Width (in) | Strut Thickness (in) | Confined Width (in) | Confined Allowable (ksi) | Unconfined Allowable (ksi) | Predicted Maximum (kips) |
|-----------|--------------------|------------------------|----------------------------|---------------------------|--------------------------------|----------------------------------|--------------------------------|
| I1 | 9.94 | 4.18 | 7.64 | 3.91 | 9.76 | 5.24 | 519 |
| I2 | 26.37 | 4.24 | 7.39 | 3.30 | 10.58 | 6.07 | 574 |
| I3 | 22.21 | 4.04 | 7.50 | 3.18 | 8.73 | 4.21 | 478 |
| I4-Thrust | 26.31 | 6.46 | 7.69 | 5.12 | 10.14 | 5.62 | 535 |
| ME2A | 13.06 | 3.72 | 7.57 | 3.31 | 10.74 | 6.22 | 591 |
| ME2B | 12.87 | 4.22 | 7.57 | 3.81 | 10.74 | 6.23 | 578 |

Table 6.12 STM Capacity at Local Zone-General Zone Interface

a) Side 1

| Specimen | Depth of Confinement (in) | Alpha (degrees) | Strut Width (in) | Strut Thickness (in) | Unconfined Allowable (ksi) | Predicted Maximum (kips) |
|-----------|---------------------------|-----------------|------------------|----------------------|----------------------------|--------------------------|
| 11 | 9.50 | 10.83 | 5.73 | 9.64 | 4.15 | 507 |
| 12 | 9.50 | 18.34 | 8.20 | 9.37 | 4.79 | 649 |
| 13 | 9.50 | 16.29 | 7.78 | 9.44 | 3.34 | 425 |
| 14-Thrust | 9.50 | 38.33 | 10.11 | 8.73 | 4.95 | 1326 |
| ME2A | 9.50 | 10.07 | 6.15 | 9.64 | 4.89 | 531 |
| ME2B | 9.50 | 18.23 | 7.67 | 9.40 | 5.01 | 749 |

b) Side 2

| Specimen | Depth of Confinement (in) | Alpha (degrees) | Strut Width (in) | Strut Thickness (in) | Unconfined Allowable (ksi) | Predicted Maximum (kips) |
|-----------|---------------------------|-----------------|------------------|----------------------|----------------------------|--------------------------|
| 11 | 9.50 | 9.94 | 6.21 | 9.64 | 4.15 | 441 |
| 12 | 9.50 | 26.37 | 9.58 | 9.08 | 4.94 | 834 |
| 13 | 9.50 | 22.21 | 8.49 | 9.26 | 3.41 | 558 |
| 14-Thrust | 9.50 | 26.31 | 10.60 | 9.00 | 4.80 | 554 |
| ME2A | 9.50 | 13.06 | 6.44 | 9.57 | 4.92 | 638 |
| ME2B | 9.50 | 12.87 | 6.88 | 9.56 | 4.93 | 584 |

Table 6.13 Basic STM Capacity Summary

| Specimen | Tension Tie (kips) | Bearing (kips) | Node-Strut Interface | | L.Z.-G.Z. Interface | | Controlling Load (kips) | Ultimate Test (kips) | Test/Predicted |
|---|--------------------|----------------|----------------------|----------|---------------------|----------|-------------------------|----------------------|----------------|
| | | | 1 (kips) | 2 (kips) | 1 (kips) | 2 (kips) | | | |
| 11 | 281 | 454 | 541 | 519 | 507 | 441 | 281 | 423 | 1.51 |
| 12 | 223 | 481 | 576 | 574 | 649 | 834 | 223 | 437 | 1.96 |
| 13 | 262 | 406 | 469 | 478 | 425 | 558 | 262 | 375 | 1.43 |
| 14-Thrust | 126 | 472 | 809 | 535 | 1326 | 554 | 126 | 420 | 3.33 |
| ME2A | 261 | 494 | 575 | 591 | 531 | 638 | 261 | 370 | 1.42 |
| ME2B | 267 | 494 | 613 | 578 | 749 | 584 | 267 | 366 | 1.26* |
| Note: Node Compression was found to not control in Table 6.10 Loads are per anchor | | | | | | | | Average | 1.93 |
| * Other Anchor for that Specimen Controls | | | | | | | | Standard Deviation | 0.73 |
| | | | | | | | | Coef. of Variance | 0.38 |

6.4.3 Modified Strut-and-Tie Model. When calculating capacities for most of the specimens with the basic STM, there is a significant difference between the predicted axial load at tension tie failure and at compression strut failure. As in previous chapters, the modified STM centroidal locations of the struts are closer to the tendon axis with a higher and more concentrated stress distribution. The locations of the strut centroids at the end of the general zone are moved toward the tendon axis until the specimen capacity predicted under the assumption that the tension tie controls and the capacity predicted with the assumption that the different compression struts control are at the same magnitude. Tables 6.14 and 6.15 show the predicted maximum load for each of the compression interfaces. Table 6.9 gives the location of each interface. For Specimen I4, the models are given which utilized 1) the thrust line for division of load and 2) the tendon path. Table 6.16 is a summary of the predicted loads. The bearing capacity is identical to the basic STM. The node compression was found not to control as shown in Table 6.10. This modified STM is, on the average, 13 percent conservative and has a very acceptable coefficient of variance of only eight percent. Specimen ME2 is predicted slightly unconservatively with a test-to-predicted ratio of 0.99. The local zone-general zone interface was found to control the compression failure for all of the specimens while the tension ties were assumed to yield as well.

6.5 Conclusions for Specimens with Inclined Anchorages and Tendon Curvatures

1) The accurate prediction of the first bursting crack load for inclined anchorages with curved tendons was difficult because of the complex stress state along the tendon path. The best model was found to be based on using a conservative value of $4.2\sqrt{F'_c}$ for the tensile strength of concrete while, at the same time, matching that strength with the peak stress determined from a finite element analysis. The two-dimensional finite element analysis was modified to consider the

elevation of the stresses due to the reduction of the cross-sectional area due to the presence of post-tensioning ducts. An effective thickness equal to the section thickness minus the inside duct diameter determined the best results. The average of the test-to-predicted ratios for all the specimens was 1.19 with a coefficient of variance of 13 percent.

Table 6.14 Modified STM Capacity at Node-Strut Interface

a) Side 1

| Specimen | Alpha (degrees) | Strut Width (in) | Strut Thickness (in) | Confined Width (in) | Confined Allowable (ksi) | Unconfined Allowable (ksi) | Predicted Maximum (kips) |
|-----------|--------------------|------------------------|----------------------------|---------------------------|--------------------------------|----------------------------------|--------------------------------|
| 11 | -1.48 | 2.79 | 7.78 | 3.18 | 9.67 | 5.15 | 481 |
| 12 | -1.67 | 3.39 | 7.74 | 3.79 | 10.31 | 5.80 | 509 |
| 13 | 5.84 | 3.96 | 7.69 | 3.93 | 8.62 | 4.10 | 449 |
| I4-Thrust | 0.82 | 1.75 | 8.18 | 1.97 | 9.80 | 5.28 | 537 |
| I4-Tendon | -8.03 | 2.98 | 7.80 | 3.83 | 10.06 | 5.54 | 462 |
| ME2A | -2.01 | 3.36 | 7.74 | 3.79 | 10.60 | 6.09 | 521 |
| ME2B | -2.73 | 2.81 | 7.76 | 3.28 | 10.59 | 6.08 | 517 |

b) Side 2

| Specimen | Alpha (degrees) | Strut Width (in) | Strut Thickness (in) | Confined Width (in) | Confined Allowable (ksi) | Unconfined Allowable (ksi) | Predicted Maximum (kips) |
|-----------|--------------------|------------------------|----------------------------|---------------------------|--------------------------------|----------------------------------|--------------------------------|
| 11 | -1.13 | 3.54 | 7.78 | 3.91 | 9.67 | 5.15 | 480 |
| 12 | -2.17 | 2.87 | 7.74 | 3.30 | 10.31 | 5.79 | 507 |
| 13 | 7.08 | 3.31 | 7.69 | 3.18 | 8.62 | 4.10 | 461 |
| I4-Thrust | 0.65 | 4.87 | 8.18 | 5.12 | 9.80 | 5.28 | 505 |
| I4-Tendon | -9.35 | 2.39 | 7.79 | 3.30 | 10.06 | 5.54 | 446 |
| ME2A | -2.43 | 2.86 | 7.74 | 3.31 | 10.60 | 6.09 | 519 |
| ME2B | -2.12 | 3.39 | 7.75 | 3.81 | 10.59 | 6.08 | 520 |

Table 6.15 Modified STM Capacity at Local Zone-General Zone Interface
a) Side 1

| Specimen | Depth of Confinement (in) | Alpha (degrees) | Strut Width (in) | Strut Thickness (in) | Unconfined Allowable (ksi) | Predicted Maximum (kips) |
|-----------|---------------------------|-----------------|------------------|----------------------|----------------------------|--------------------------|
| 11 | 9.50 | 4.36 | 4.05 | 9.77 | 4.10 | 364 |
| 12 | 9.50 | 4.05 | 4.58 | 9.77 | 4.59 | 381 |
| 13 | 9.50 | 10.08 | 6.25 | 9.63 | 3.28 | 350 |
| 14-Thrust | 9.50 | 4.22 | 2.72 | 9.79 | 4.41 | 453 |
| 14-Tendon | 9.50 | -0.31 | 3.41 | 9.83 | 4.39 | 274 |
| ME2A | 9.50 | 2.88 | 4.26 | 9.79 | 4.81 | 374 |
| ME2B | 9.50 | 3.37 | 3.88 | 9.79 | 4.82 | 399 |

b) Side 2

| Specimen | Depth of Confinement (in) | Alpha (degrees) | Strut Width (in) | Strut Thickness (in) | Unconfined Allowable (ksi) | Predicted Maximum (kips) |
|-----------|---------------------------|-----------------|------------------|----------------------|----------------------------|--------------------------|
| 11 | 9.50 | 4.67 | 4.85 | 9.76 | 4.10 | 349 |
| 12 | 9.50 | 3.99 | 4.07 | 9.78 | 4.59 | 395 |
| 13 | 9.50 | 10.51 | 5.65 | 9.64 | 3.27 | 394 |
| 14-Thrust | 9.50 | 4.43 | 5.90 | 9.75 | 4.43 | 343 |
| 14-Tendon | 9.50 | -0.38 | 2.90 | 9.83 | 4.39 | 271 |
| ME2A | 9.50 | 2.89 | 3.79 | 9.79 | 4.81 | 385 |
| ME2B | 9.50 | 3.56 | 4.47 | 9.78 | 4.82 | 389 |

Table 6.16 Modified STM Capacity Summary

| Specimen (kips) | Bearing (kips) | Node-Strut Interface | | L.Z.-G.Z. Interface | | Controlling Load (kips) | Ultimate Test (kips) | Test/ Predicted |
|--|-------------------|----------------------|-------------|---------------------|-------------|-------------------------------|--|----------------------|
| | | 1 (kips) | 2 (kips) | 1 (kips) | 2 (kips) | | | |
| I1 | 454 | 481 | 480 | 364 | 349 | 349 | 423 | 1.21 |
| I2 | 481 | 509 | 507 | 381 | 395 | 381 | 437 | 1.15 |
| I3 | 406 | 449 | 461 | 350 | 394 | 350 | 375 | 1.07 |
| 14-Thrust | 472 | 537 | 505 | 453 | 343 | 343 | 420 | 1.22 |
| 14-Tendon | 472 | 462 | 446 | 274 | 271 | 271 | 420 | 1.55* |
| ME2A | 494 | 521 | 519 | 374 | 385 | 374 | 370 | 0.99 |
| ME2B | 494 | 517 | 520 | 399 | 389 | 389 | 366 | 0.94** |
| Note: Node Compression was found to not control in Table 6.10, Loads are per anchor * Only used Thrust Line Division for Statistical Correlation ** Other Anchor for that Specimen Controls | | | | | | | Average Standard Deviation Coef. of Variance | 1.13 0.09 0.08 |

2) Utilizing Guyon's symmetrical prism method yielded inconsistent results relative to the finite element analysis. When used to predict the first bursting crack load, the analysis had a large coefficient of variance of 26 percent but was conservative for all specimens.

3) The prediction of the ultimate load with the basic STM was very conservative with an average ratio of test-to-predicted load of 1.93 and a coefficient of variance of 38 percent. According to the model all of the specimens were controlled by the tension tie failure.

4) Utilizing the modified STM produced a much more accurate prediction of the ultimate load and the average test-to-predicted ratio dropped to 1.13 with a coefficient of variance of only eight percent. The model predicted a simultaneous failure of the bursting tension ties and the compression struts at the local zone-general zone interface. The additional capacity predicted by the modified STM over the basic STM is achieved by additional and wider cracking occurring.

5) Tie-back reinforcement along the tendon path is necessary to prevent large cracks and explosive failures. Reinforcement should be provided for both radial and transverse forces.

CHAPTER 7
SUMMARY OF RESULTS AND AASHTO SPECIFICATION PROPOSAL

7.1 Introduction

This chapter summarizes the experimental results and prediction models examined in detail in Chapters 3 through 6. In addition, proposed revisions are presented for the post-tensioned anchorage zone provisions of the AASHTO Bridge Specification [5].

7.2 Experimental Results

The general zone experimental program consisted of 36 specimens: 17 concentric single anchorage specimens, six eccentric single anchorage specimens, eight multiple anchorage specimens and five specimens with tendon curvature and inclined anchorages. These specimens investigated first crack (serviceability) and ultimate strength behavior. The first crack prediction models used elastic analysis, while the ultimate strength prediction models used the strut-and-tie model.

7.2.1 First Crack Prediction. Cracking in the specimens occurred in the spalling zone, longitudinal edge tension zone, and the bursting zone. Spalling and longitudinal edge tension cracking at service stress levels occurred only in specimens with anchorages which had a resultant eccentricity outside the kern. Near the ultimate load of many specimens, longitudinal edge tension cracking occurred due to the combined axial force and bending stresses and the redistribution of forces within the specimens. In all the specimens, spalling cracking occurred as the applied load approached the ultimate load of the specimen. The cracking was around the anchorage device and occurred when the anchor displacement became nonlinear in relation to the applied force. The major focus of the cracking investigation was the first cracking within the bursting zone. For most specimens, the first observed crack was due to bursting stresses along the tendon path or the load axis. This crack would start approximately one to two plate

widths ahead of the loading surface. As the load increased, the crack would propagate toward the loading surface as well as farther along the tendon path. In most of the specimens, the main bursting crack eventually propagated to the specimen base. Cracks also formed parallel to the axis of the compression struts. These cracks would start near the loading surface, then propagate out away from the loading surface.

Accurately predicting the first bursting crack load proved to be difficult. Variables included concrete surface conditions, the prediction of peak elastic bursting stresses, and an accurate determination of the concrete tensile strength of the specimen. Finite element analyses by Burdet [25] determined the peak bursting stress of the specimens. These were mostly two-dimensional elastic analyses. The analyses for Specimens M5 and M6 were three-dimensional finite element analyses. The finite element analysis for Specimen F1 used shell elements for the web and flange. To include the effects of a post-tensioning duct, the peak stress from the two-dimensional analysis was divided by an effective section thickness. The two effective section widths that yielded the best results were a transformed section and a section with a width equal to the total section thickness minus the inside diameter of the post-tensioning duct. After the peak bursting stress was determined, it was matched to the concrete tensile strength to find the cracking load.

The split cylinder test was used to experimentally estimate the concrete tensile strength of the specimens. Due to the high compressive stresses in the anchorage zone, the relationships for the biaxial and the triaxial stress effects developed by Ottosen [125] were used to adjust the measured split cylinder strength in order to represent more accurately the tensile strength of the concrete in the critical regions of the specimen. This was an involved process; therefore, a simplified formula was developed to conservatively estimate the concrete tensile strength. The lower bound estimate of

the concrete tensile strength was taken to be $4.2\sqrt{F'_c}$. This estimate was determined by multiplying $6\sqrt{F'_c}$ by 0.7. The value $6\sqrt{F'_c}$ is a common formula for estimating the concrete tensile strength from the compression cylinder test results. This lower bound approximation represented a 30 percent reduction from the usual split cylinder strength estimate. This is very close to the results of the equation, $1/3 w^{0.5}\sqrt{F'_c}$, used by ACI Committee 209 to estimate concrete tensile strength. In the equation, w is the weight of the concrete (145 lbs./ft³). Substituting w into the equation gives the concrete tensile strength as $4\sqrt{F'_c}$.

The methods for determining the first cracking load were visual observation and the monitoring of strain gage results. Most first cracks occurred when the strain readings from strain gages located on the nearby bursting reinforcement were approximately 250 microstrain. Most cracks had a width of approximately 0.001 inches when they were first noticed. The rough surface conditions could have prevented earlier observation of some of the cracks.

To determine if serviceability would have been a problem for these specimens, the first cracking load can be compared with the nominal peak stressing load of the specimen anchors. The peak stressing load is specified by AASHTO to be 0.9 times the yield strength of the tendon. For stress-relieved strands, the yield strength is approximately $0.85f_{pu}$ where f_{pu} is the maximum tensile strength of the tendon. For low-relaxation strands, the yield strength is approximately $0.9f_{pu}$. The maximum tensile force of a tendon for a particular anchor is often called "GUTS", guaranteed ultimate tensile strength. Therefore, for low-relaxation strand the nominal maximum tension force is 0.81 times "GUTS". ACI 318-89 limits the nominal maximum force to 0.8 times "GUTS". The most commonly used prestressing steel has a f_{pu} equal to 270 ksi. Table 7.1 shows the strand configuration that would be used with the specimen anchorages used in this study. Laboratory technicians fabricated the anchorages for

Table 7.1 Anchorage Size and Tendon Configurations

| Specimens | Anchorage Size and Configuration | Maximum Tension Force - 'Guts' (kips) |
|--|--|---------------------------------------|
| 'A' Series | 6" x 12" flat plate 7 strand 0.5" | 289 |
| 'B' Series | 6.5" x 6.5" flat plate 3 strand 0.6" | 174 |
| 'TPT' Series C1, M5, M6, E6 and 'I' Series | 6.5" x 6.5" Multiplane Anchor 7 strand 0.5" | 289 |
| E1, E2, E3 and E4 | 8" x 7" flat plate 4 strand 0.6" | 232 |
| M1, M2, M3, M4 and E5 | 6" x 6" flat plate 4 strand 0.5" | 165 |

Table 7.2 First Crack Load versus the Maximum Stressing Load

| Specimen | Test First Crack Load (kips) | Anchorage 0.81 x Guts Load (kips) | Test First Crack /0.81xGuts | Specimen | Test First Crack Load (kips) | Anchorage 0.81 x Guts Load (kips) | Test First Crack /0.81xGuts | |
|----------|------------------------------|-----------------------------------|-----------------------------|---------------------|------------------------------|-----------------------------------|-----------------------------|------|
| A1 | 298 | 234 | 1.27 | M1 | Cr. Formers | 134 | 1.59 | |
| A2 | 226 | 234 | 0.96 | M2 | | 213 | | |
| A3 | 250 | 234 | 1.07 | M3 | | 113 | | 0.84 |
| A4 | 300 | 234 | 1.28 | M4 | | 134 | | |
| B1 | 200 | 141 | 1.42 | M5 | | 200 | | 0.85 |
| B2 | 186 | 141 | 1.32 | M6 | | 244 | | 1.04 |
| B3 | 217 | 141 | 1.54 | ME1A | 175 | 234 | 0.76* | |
| B4 | 200 | 141 | 1.42 | ME1B | 260 | 234 | 1.11 | |
| B5 | 170 | 141 | 1.21 | ME2A | 240 | 234 | 1.02 | |
| B6 | 171 | 141 | 1.21 | ME2B | 240 | 234 | 1.02 | |
| B7 | 170 | 141 | 1.21 | F1A F1Bw F1Bf | No Crack | 234 | 0.62 | |
| B8 | 156 | 141 | 1.11 | | | 145 | | 234 |
| C1 | 225 | 234 | 0.96 | | | 165 | | 234 |
| TPT1 | 200 | 234 | 0.85 | I1 | 250 | 234 | 1.07 | |
| TPT2 | 225 | 234 | 0.96 | I2 | 325 | 234 | 1.39 | |
| TPT3 | 270 | 234 | 1.15 | I3 | 250 | 234 | 1.07 | |
| TPT4 | 240 | 234 | 1.02 | I4 | 350 | 234 | 1.49 | |
| E1 | 345 | 188 | 1.83 | | | Average for both Columns | 1.19 | |
| E2 | 265 | 188 | 1.41 | | | | | |
| E3 | 300 | 188 | 1.60 | | | | | |
| E4 | 250 | 188 | 1.33 | | | | | |
| E5 | 215 | 134 | 1.61 | | | | | |
| E6 | 225 | 188 | 1.20 | | | | | |

* Duct Shifted During Casting

the "A" and "B" specimen series; therefore, the tendon configurations are estimates. The other strand configurations are normal ratings for commercial anchors. Table 7.2 shows the relationship between the first surface crack load and the peak nominal stressing load for the particular anchors used in each specimen. 75 percent of the specimens did not crack until above the peak nominal stressing load. Therefore, most of the anchorage configurations should not present a serviceability problem when only the anchorage zone stresses are considered. It is critical to note that the specimens tested provide cracking data for only isolated anchorages. Anchorages located in areas where other forces are influencing the stress distribution, or where there is creep or shrinkage could have significantly different cracking behavior.

Several specimens need additional explanation before discussing the first crack models. Specimens M1 and M4 did not provide first bursting crack data because crack formers existed along the tendon ducts. Anchorage "A" in Specimen ME1 is not included in the statistical analyses because the post-tensioning duct ahead of that anchorage shifted during casting. This is believed to have caused a premature cracking of the specimen. Specimen F1 is included in analyses, but the finite element analysis that modelled the specimen had a crude mesh, especially in the area around the web flange interface. Therefore, the peak stress estimate for Specimen F1 may not be as accurate as those for the other specimens.

Table 7.3, Fig. 7.1, and Fig. 7.2 show the results of a refined model compared with the experimental tests. This prediction model uses the Ottosen reduction in measured split cylinder strength data to find the usable concrete tensile strength and uses the transformed section to modify the finite element analysis to account for the three-dimensional effects. The average of the test-to-predicted ratios is close to one and is slightly conservative. The coefficient of variance is large, but reasonable, for cracking load prediction. Figures 7.1

Table 7.3 First Crack Prediction Summary for Triaxial Model

| Specimen | Predicted First Crack (kips) | Test First Crack (kips) | Test/Prediction | Specimen | Predicted First Crack (kips) | Test First Crack (kips) | Test/Prediction |
|----------|------------------------------|-------------------------|-----------------|--------------------|------------------------------|-------------------------|-----------------|
| A1 | 189 | 298 | 1.57 | M1 | Crack | Formers | |
| A2 | 189 | 226 | 1.19 | M2 | 297 | 213 | 0.71 |
| A3 | 194 | 250 | 1.29 | M3 | 154 | 113 | 0.73 |
| A4 | 207 | 300 | 1.45 | M4 | Crack | Formers | |
| B1 | 201 | 200 | 0.99 | M5 | 152 | 200 | 1.32 |
| B2 | 201 | 186 | 0.92 | M6 | 178 | 244 | 1.37 |
| B3 | 201 | 217 | 1.08 | ME1A | 342 | 175 | 0.51* |
| B4 | 201 | 200 | 0.99 | ME1B | 225 | 260 | 1.16 |
| B5 | 191 | 170 | 0.89 | ME2A | 275 | 240 | 0.87 |
| B6 | 191 | 171 | 0.90 | ME2B | 342 | 240 | 0.70 |
| B7 | 169 | 170 | 1.01 | F1A | 210 | No Crack | No Crack |
| B8 | 158 | 156 | 0.99 | F1Bw | 177 | 145 | 0.82 |
| C1 | 221 | 225 | 1.02 | F1Bf | 136 | 165 | 1.22 |
| TPT1 | 157 | 200 | 1.28 | I1 | 205 | 250 | 1.22 |
| TPT2 | 197 | 225 | 1.14 | I2 | 347 | 325 | 0.94 |
| TPT3 | 237 | 270 | 1.14 | I3 | 233 | 250 | 1.07 |
| TPT4 | 227 | 240 | 1.06 | I4 | 325 | 350 | 1.08 |
| E1 | 359 | 345 | 0.96 | Average | | 1.05 | |
| E2 | 268 | 265 | 0.99 | Standard Deviation | | 0.20 | |
| E3 | 284 | 300 | 1.05 | Coef. of Variance | | 0.19 | |
| E4 | 272 | 250 | 0.92 | | | | |
| E5 | 242 | 215 | 0.89 | | | | |
| E6 | 229 | 225 | 0.98 | | | | |

* Duct Shifted During Casting

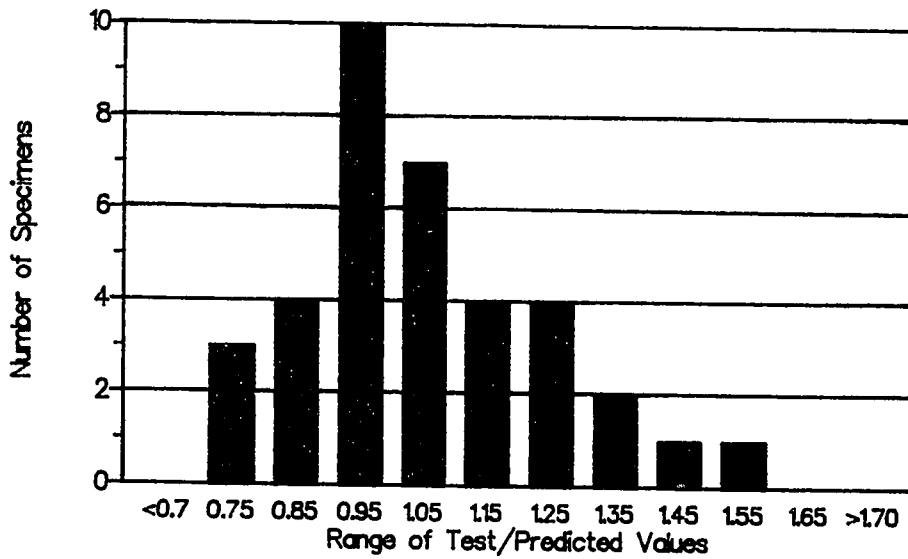


Figure 7.1 Frequency of Occurrence for Triaxial First Crack Model

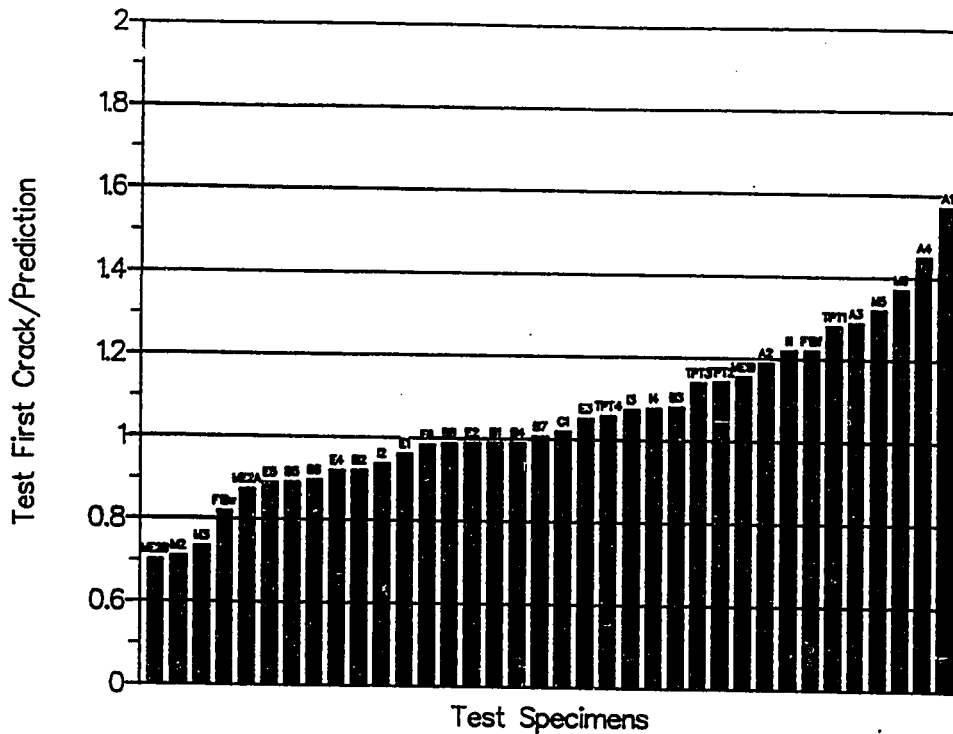


Figure 7.2 Distribution of Results for Triaxial First Crack Prediction

and 7.2 are graphical representations of the results in Table 7.3. Of the 36 measurements of first cracking, 17 of the predictions were unconservative while 19 were conservative. Figure 7.1 shows the frequency of occurrence for different ranges of the test value divided by the prediction. The model determines an adequate average value but would not be appropriate for design because of the large percentage of low values.

Table 7.4, Fig. 7.3 and Fig. 7.4 show the results for the prediction model that uses a lower bound approximation, $4.2\sqrt{F'_c}$, for the concrete tensile strength and uses the section thickness minus the inside diameter of the post-tensioning duct for the effective thickness in adjusting the finite element analysis stresses. The average value of the model is conservative by 28 percent, and the coefficient of variance is even slightly lower than in the Ottosen model discussed previously. Only five of the specimens are unconservative. One is

Table 7.4 First Crack Prediction Summary for Approximate Model

| Specimen | Predicted First Crack (kips) | Test First Crack (kips) | Test/Prediction | Specimen | Predicted First Crack (kips) | Test First Crack (kips) | Test/Prediction |
|----------|------------------------------|-------------------------|-----------------|--------------------|------------------------------|-------------------------|-----------------|
| A1 | 179 | 298 | 1.67 | H1 | Crack | Formers | |
| A2 | 179 | 226 | 1.26 | H2 | 214 | 213 | 1.00 |
| A3 | 182 | 250 | 1.37 | H3 | 101 | 113 | 1.12 |
| A4 | 191 | 300 | 1.57 | H4 | Crack | Formers | |
| B1 | 173 | 200 | 1.15 | H5 | 119 | 200 | 1.68 |
| B2 | 173 | 186 | 1.07 | H6 | 134 | 244 | 1.82 |
| B3 | 173 | 217 | 1.25 | ME1A | 259 | 175 | 0.68* |
| B4 | 173 | 200 | 1.15 | ME1B | 166 | 260 | 1.57 |
| B5 | 172 | 170 | 0.99 | ME2A | 196 | 240 | 1.23 |
| B6 | 172 | 171 | 0.99 | ME2B | 266 | 240 | 0.90 |
| B7 | 135 | 170 | 1.26 | F1A | 210 | No Crack | No Crack |
| B8 | 120 | 156 | 1.30 | F1Bw | 169 | 145 | 0.86 |
| C1 | 181 | 225 | 1.24 | F1Bf | 119 | 165 | 1.39 |
| TPT1 | 131 | 200 | 1.53 | I1 | 179 | 250 | 1.39 |
| TPT2 | 179 | 225 | 1.26 | I2 | 288 | 325 | 1.13 |
| TPT3 | 230 | 270 | 1.18 | I3 | 196 | 250 | 1.27 |
| TPT4 | 216 | 240 | 1.11 | I4 | 282 | 350 | 1.24 |
| E1 | 256 | 345 | 1.35 | Average | | | 1.28 |
| E2 | 195 | 265 | 1.36 | Standard Deviation | | | 0.22 |
| E3 | 198 | 300 | 1.52 | Coef. of Variance | | | 0.17 |
| E4 | 190 | 250 | 1.31 | | | | |
| E5 | 175 | 215 | 1.23 | | | | |
| E6 | 176 | 225 | 1.28 | | | | |

* Duct Shifted During Casting

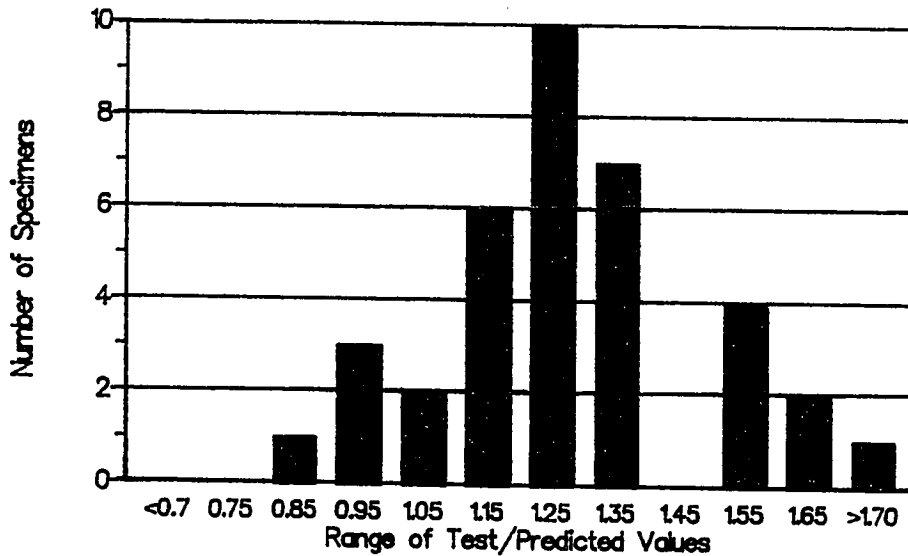


Figure 7.3 Frequency of Occurrence for Approximate First Crack Model

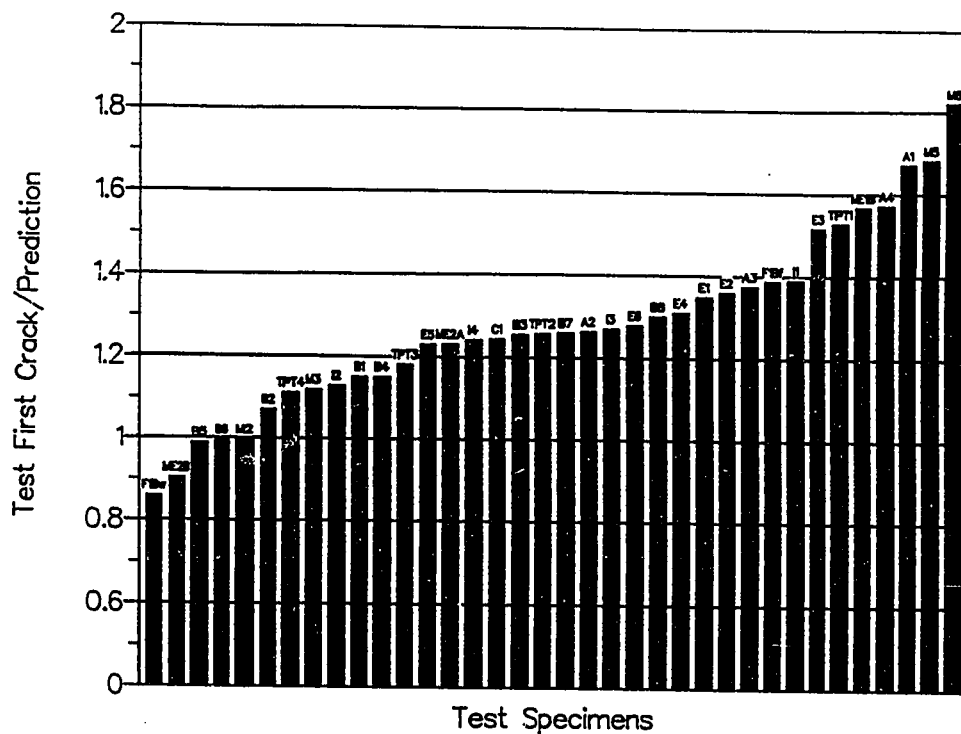


Figure 7.4 Distribution of Results for Approximate First Crack Prediction

anchorage "B" of Specimen F1 at the corner of the web and flange. An accurate peak stress is difficult to predict in this area due to the complex stress state. Three of the unconservative specimens have a ratio of 0.99. Therefore, only anchorage "B" of Specimen ME2 is significantly unconservative (0.9). The approximation presented is a conservative estimate of the bursting cracking load for anchorage zones where the anchorage stresses dominate and where cracking is not influenced by creep or shrinkage. The tests also showed a large amount of post cracking strength. Table 7.5 and Fig. 7.5 show the relationship between the ultimate load and first cracking load. The average for all the specimens was 1.57. Therefore, the observation of cracking does not necessarily indicate an immediate failure. There were only five specimens (15 percent) that had ultimate to first crack ratios of less than 1.25. Three of these specimens were from the "A"

series. In the "A" series, compression stresses were very high at the ultimate and first crack loads.

Table 7.5 Ultimate - First Crack Summary

| Specimen | Test Ultimate Load (kips) | Test First Crack Load (kips) | Ultimate/First Crack | Specimen | Test Ultimate Load (kips) | Test First Crack Load (kips) | Ultimate/First Crack |
|----------|---------------------------|------------------------------|----------------------|----------|---------------------------|--------------------------------|----------------------|
| A1 | 298 | 298 | 1.00 | M1 | 304 | Cr. Formers 213 | 1.88 |
| A2 | 275 | 226 | 1.22 | M2 | 401 | | |
| A3 | 265 | 250 | 1.06 | M3 | 364 | Cr. Formers 200 | 1.69 |
| A4 | 437 | 300 | 1.46 | M4 | 411 | | |
| B1 | 366 | 200 | 1.83 | M5 | 339 | 244 | 1.23 |
| B2 | 290 | 186 | 1.56 | M6 | 300 | | |
| B3 | 331 | 217 | 1.53 | ME1A | 350 | 175 | 2.00* |
| B4 | 337 | 200 | 1.69 | ME1B | 350 | 260 | 1.35 |
| B5 | 212 | 170 | 1.25 | ME2A | 370 | 240 | 1.54 |
| B6 | 297 | 171 | 1.74 | ME2B | 370 | 240 | 1.54 |
| B7 | 296 | 170 | 1.74 | F1A | 248 | No Crack 145 | 1.71 |
| B8 | 276 | 156 | 1.77 | F1Bw | 248 | | |
| C1 | 370 | 225 | 1.64 | F1Bf | 248 | 165 | 1.50 |
| TPT1 | 310 | 200 | 1.55 | I1 | 423 | 250 | 1.69 |
| TPT2 | 300 | 225 | 1.33 | I2 | 437 | 325 | 1.34 |
| TPT3 | 370 | 270 | 1.37 | I3 | 375 | 250 | 1.50 |
| TPT4 | 332 | 240 | 1.38 | I4 | 420 | 350 | 1.20 |
| E1 | 475 | 345 | 1.38 | | | Average for both Columns | 1.57 |
| E2 | 500 | 265 | 1.89 | | | | |
| E3 | 522 | 300 | 1.74 | | | | |
| E4 | 500 | 250 | 2.00 | | | | |
| E5 | 332 | 215 | 1.54 | | | | |
| E6 | 348 | 225 | 1.55 | | | | |

* Duct Shifted During Casting

7.2.3 Ultimate Capacity Prediction. The strut-and-tie model (STM) was effective in predicting the ultimate capacity of the specimens. Five ultimate capacities within the STM must be checked; they are the:

- 1) Tension tie capacity,
- 2) Bearing compression capacity,
- 3) Node compression capacity,
- 4) Node-strut interface compression capacity, and
- 5) Local zone-general zone interface compression capacity.

The basic STM assumes an elastic stress distribution at the end of the general zone assumed to be located a depth of the section away from the loading surface. Other basic assumptions include: the

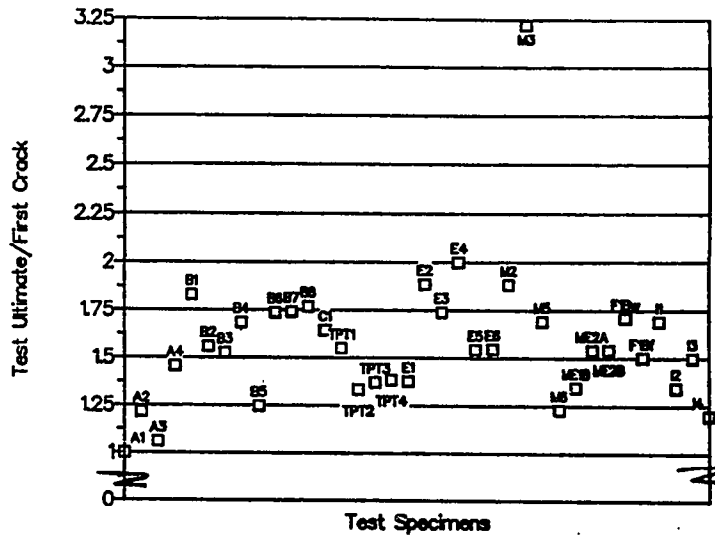


Figure 7.5 Ultimate - First Crack Summary

confining spiral does not contribute to the tension tie capacity; the strut width is equal to twice the distance from the tendon axis to the line of action of the strut; the concrete tension capacity does not contribute to the tension tie capacity; the anchorage zone has sufficient ductility to mobilize the necessary anchorage zone reinforcement; and the compression capacity can be estimated using the equation developed by Roberts [143]. Table 7.6, Fig. 7.6 and Fig. 7.7 are comparisons between the ultimate test loads and the predicted values for the basic STM.

The basic STM is very conservative with a test-to-predicted ratio equal to 1.50 with a coefficient of variance of 0.33. The STM is a lower bound model based on the theory of plasticity. It should be a conservative estimate of the ultimate strength of the specimens. The degree of conservatism and coefficient of variance are very reasonable when examined from the perspective of the CEB survey (see Chapter 2), which showed a range of responses of current design procedures that differed by an order of magnitude of ten. Figures 7.6 and 7.7 show that only two specimens (Specimens B5 and B2) were unconservative, but barely so. They were both within three percent of the ultimate

load. Specimen B5 was reinforced with zero bursting reinforcement, therefore, the tension tie capacity was zero. The specimen reached its ultimate load because of its concrete tension capacity, which the

Table 7.6 Basic STM Results Summary

| Specimen | Failure Mode | Predicted Capacity (kips) | Test Ultimate (kips) | Test/Prediction |
|--|-----------------------|---------------------------|----------------------|-----------------|
| A1 | Node-Strut Interface | 195 | 298 | 1.52 |
| A2 | Node-Strut Interface | 190 | 275 | 1.45 |
| A3 | Node-Strut Interface | 204 | 265 | 1.30 |
| A4 | Node-Strut Interface | 306 | 437 | 1.43 |
| B1 | Tension Tie | 299 | 366 | 1.22 |
| B2 | Tension Tie | 292 | 290 | 0.99 |
| B3 | Tension Tie | 296 | 331 | 1.12 |
| B4 | Tension Tie | 277 | 337 | 1.22 |
| B5* | L.Z. - G.Z. Interface | 218 | 212 | 0.97 |
| B6 | Bearing | 218 | 297 | 1.36 |
| B7 | Tension Tie | 269 | 296 | 1.10 |
| B8 | Tension Tie | 252 | 276 | 1.09 |
| C1 | Tension Tie | 192 | 370 | 1.93 |
| TPT1 | Tension Tie | 180 | 310 | 1.72 |
| TPT2 | Tension Tie | 253 | 300 | 1.19 |
| TPT3 | Tension Tie | 247 | 370 | 1.50 |
| TPT4 | Tension Tie | 235 | 332 | 1.41 |
| E1 | Bearing | 404 | 475 | 1.17 |
| E2 | Bearing | 445 | 500 | 1.12 |
| E3 | Bearing | 453 | 522 | 1.15 |
| E4* | Bearing | 434 | 500 | 1.15 |
| E5 | Tension Tie | 238 | 332 | 1.39 |
| E6 | Tension Tie | 259 | 348 | 1.34 |
| M1 | Tension Tie | 189 | 304 | 1.61 |
| M2 | L.Z. - G.Z. Interface | 322 | 401 | 1.25 |
| M3 | Tension Tie | 290 | 364 | 1.26 |
| M4 | Tension Tie | 180 | 411 | 2.28 |
| M5 | Tension Tie | 202 | 339 | 1.68 |
| M6 | Tension Tie | 104 | 300 | 2.88 |
| ME1 | Tension Tie | 226 | 350 | 1.55 |
| ME2 | Tension Tie | 261 | 370 | 1.42 |
| F1 | Tension Tie | 133 | 248 | 1.86 |
| I1 | Tension Tie | 281 | 423 | 1.51 |
| I2 | Tension Tie | 223 | 437 | 1.96 |
| I3 | Tension Tie | 262 | 375 | 1.43 |
| I4 | Tension Tie | 126 | 420 | 3.33 |
| * Tension Tie Capacity Ignored | | Average | | 1.50 |
| ** Longitudinal Edge Tension and Spalling Capacity Ignored | | Standard Deviation | | 0.49 |
| | | Coef. of Variance | | 0.33 |

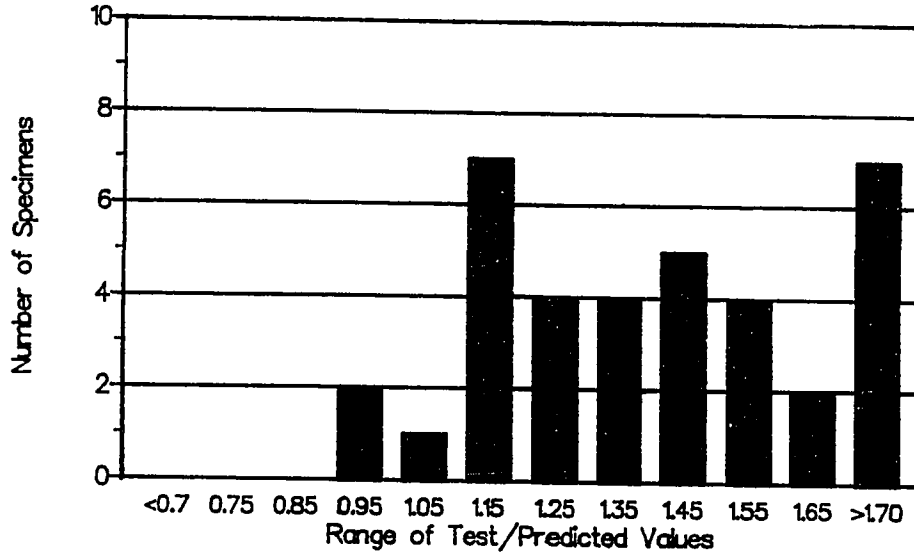


Figure 7.6 Frequency of Occurrence for Basic STM

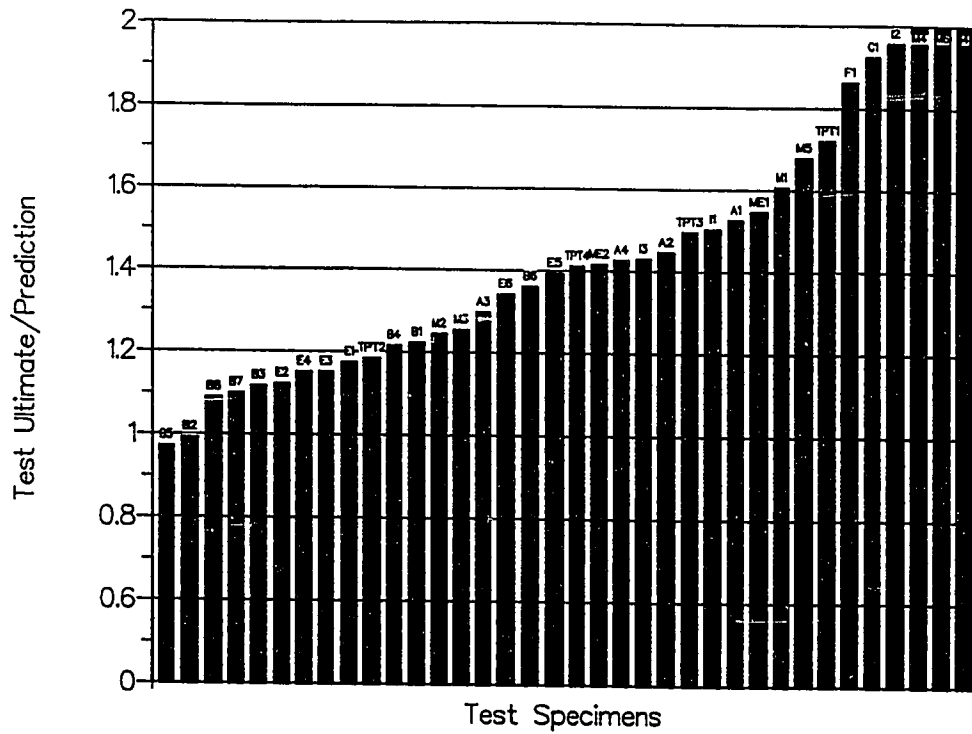


Figure 7.7 Distribution of Results for Basic STM

prediction models neglected. The analysis and design of Specimen B5 using the basic STM would have had an ultimate capacity prediction of zero. Using this of course, the results would have been extremely conservative. Specimen B2 was unconservative possibly because of the distance of the bursting reinforcement centroid from the loading surface ($d_{\text{centroid}}/h = 0.84$). Care should be taken not to place reinforcement which is considered to be effective far from the anchorage device or at locations significantly different from the elastic distribution. The use of reinforcement far from the loading surface requires greater ductility from the anchorage zone in order to permit complete redistribution of paths. Although the best placement of reinforcement was not a specific objective of the research project, it is recommended that all reinforcement should be placed within 1.5 times the width (not thickness) of the section to be considered effective, and that it should have a centroid at approximately 0.5 times the width from the loaded surface to prevent the need for large plastic deformations. If the section is very wide, all reinforcement considered effective should be placed closer than 1 times the section width.

The specimen concrete compressive strength at testing ranged from 3360 psi to 6730 psi. Existing literature, summarized in Reference 19, indicates a reduction in the efficiency of concrete compressive struts with increasing concrete compressive strength. With the increased usage of very high strength concretes and especially in the cases where fully cured concrete is being post-tensioned, designers may desire to utilize compressive strength at time of stressing significantly higher than the 7000 psi range for which this study seems to be adequate. Therefore, additional research is recommended for design of anchorage zone with concrete compressive strengths at the time of stressing greater than 7000 psi.

The basic STM indicated that most specimens would be controlled by the bursting tension tie failure. This agreed with the experimental

results which showed most of the bursting reinforcement to be at or above its yield value at the time of specimen failure. The spalling tension tie between the anchors controlled the design in Specimen M3, although the spalling crack propagated farther into the specimen to mobilize additional reinforcement. Many of the specimens also suggest a large amount of force redistribution by displaying significant cracking in and around the local zone and horizontal cracking on the extreme longitudinal fiber. In a design process, Specimen E4 would have been controlled by the longitudinal edge and spalling tension capacities. These controlling capacities were not included because they would have been artificially low. Specimen E4 had small amounts of longitudinal edge and spalling tension reinforcement. In all of the eccentric specimens with resultant eccentricities outside the kern, the longitudinal edge tension and the subsequent spalling forces along the loading surface were much lower than expected as shown by the strain gage results on the corresponding reinforcement. This is attributed to the concrete tensile capacity, a redistribution of forces, and, possibly, to the specimen configuration. Potentially, a full development of these forces was not possible because the specimen base did not provide tension capacity. Therefore, although the prediction capacities for the longitudinal edge and spalling tension would have controlled the design of Specimen E4, they did not control the failure.

The significant amounts of increased cracking, force redistribution, and high compression stresses observed and calculated for the specimens led to the development of a modified STM. The modified STM, as the name suggests, was the same as the basic STM except it modified the stress distribution at the far end of the general zone to include more plastic behavior of the specimens. Such behavior was observed in the tests by the lengthening of the anchorage zone through increased cracking. This behavior was modelled by shifting the assumed centroids of the struts toward the tendon axis. The modified STM ultimate load predictions were determined by moving

the strut centroids toward the tendon axis until the calculated axial load capacity based on the assumption that the tension ties governed matched the calculated axial load capacity based on the assumption that

Table 7.7 Modified STM Results Summary

| Specimen | Failure Mode | Predicted Capacity (kips) | Test Ultimate (kips) | Test/Prediction |
|----------|-----------------------|---------------------------|----------------------|-----------------|
| A1 | Node-Strut Interface | 199 | 298 | 1.49 |
| A2 | Node-Strut Interface | 204 | 275 | 1.35 |
| A3 | Node-Strut Interface | 200 | 265 | 1.33 |
| A4 | L.Z. - G.Z. Interface | 335 | 437 | 1.30 |
| B1 | L.Z. - G.Z. Interface | 440 | 366 | 0.83 |
| B2 | L.Z. - G.Z. Interface | 381 | 290 | 0.76 |
| B3 | L.Z. - G.Z. Interface | 416 | 331 | 0.80 |
| B4 | L.Z. - G.Z. Interface | 429 | 337 | 0.79 |
| B5 | L.Z. - G.Z. Interface | 218 | 212 | 0.97 |
| B6 | Bearing | 218 | 297 | 1.36 |
| B7 | L.Z. - G.Z. Interface | 421 | 296 | 0.70 |
| B8 | L.Z. - G.Z. Interface | 405 | 276 | 0.68 |
| C1 | L.Z. - G.Z. Interface | 419 | 370 | 0.88 |
| TPT1 | L.Z. - G.Z. Interface | 346 | 310 | 0.90 |
| TPT2 | L.Z. - G.Z. Interface | 376 | 300 | 0.80 |
| TPT3 | L.Z. - G.Z. Interface | 432 | 370 | 0.86 |
| TPT4 | L.Z. - G.Z. Interface | 401 | 332 | 0.83 |
| E1 | Bearing | 404 | 475 | 1.18 |
| E2 | Bearing | 445 | 500 | 1.12 |
| E3 | Bearing | 453 | 522 | 1.15 |
| E4* | Bearing | 434 | 500 | 1.15 |
| E5 | Bearing | 343 | 332 | 0.97 |
| E6 | Bearing | 339 | 348 | 1.03 |
| M1 | L.Z. - G.Z. Interface | 293 | 304 | 1.04 |
| M2 | L.Z. - G.Z. Interface | 336 | 401 | 1.19 |
| M3 | L.Z. - G.Z. Interface | 355 | 364 | 1.03 |
| M4 | L.Z. - G.Z. Interface | 345 | 411 | 1.19 |
| M5 | L.Z. - G.Z. Interface | 280 | 339 | 1.21 |
| M6 | L.Z. - G.Z. Interface | 262 | 300 | 1.15 |
| ME1 | L.Z. - G.Z. Interface | 410 | 350 | 0.85 |
| ME2 | L.Z. - G.Z. Interface | 374 | 370 | 0.99 |
| F1 | L.Z. - G.Z. Interface | 227 | 248 | 1.09 |
| I1 | L.Z. - G.Z. Interface | 349 | 423 | 1.21 |
| I2 | L.Z. - G.Z. Interface | 381 | 437 | 1.15 |
| I3 | L.Z. - G.Z. Interface | 350 | 375 | 1.07 |
| I4 | L.Z. - G.Z. Interface | 343 | 420 | 1.22 |
| | | Average | | 1.04 |
| | | Standard Deviation | | 0.20 |
| | | Coef. of Variance | | 0.19 |

* Longitudinal Edge Tension and Spalling Capacity Ignored

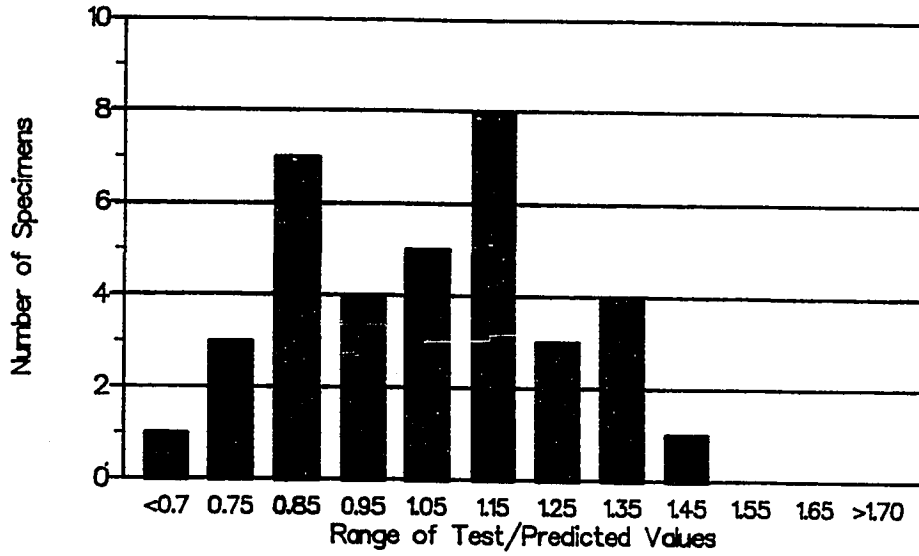


Figure 7.8 Frequency of Occurrence for Modified STM

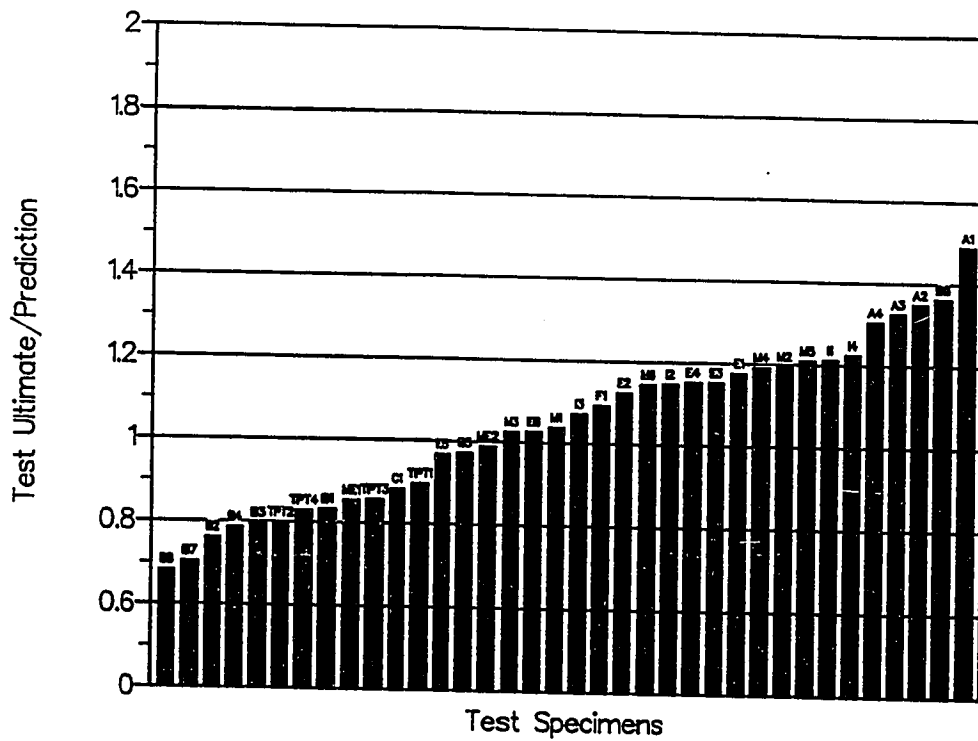


Figure 7.9 Distribution of Results for Modified STM

the compression struts at the node-strut interface or the local zone-general zone interface governed. This is, in essence, a balanced failure.

Table 7.7, Fig. 7.8 and Figs. 7.9 show the results of the modified STM. The average of the test-to-predicted ratios is very close to one (1.04) with a coefficient of variance of 0.19. This coefficient of variance is very close to the value determined by Roberts, 0.15, for her compression capacity equation. Robert's equation determined the compression capacity of the struts. Because the model more closely represents the actual behavior of the specimens, there were several predictions that were unconservative. Of the 36 specimens tested, 15 are predicted unconservatively. Since the modified STM is a plasticity model based on equilibrium, it should still be a lower bound theory and should not be unconservative.

Possible reasons for the unconservative predictions could be a reduced concrete capacity because of the excessive and large cracking, inaccuracies in the strut width approximation, and/or the low effectiveness of long spirals in confining concrete. Since most of the specimens had reinforcement distributions close to the elastic distribution, most cracking within the high compression zones was parallel to the force paths. Therefore, the reduction in concrete strength due to the cracking should be small [151]. The inaccuracies in the strut width approximations are difficult to address since it is a difficult variable to isolate. The general accuracy of the model suggests that the strut width equations are, at least, reasonable. When examining the length of the spirals used in the experimental test program, most were between one and two times the plate width. Since the local zone-general zone interface is influenced directly by the length of the spiral, the effectiveness of spiral length is a major concern. This was addressed in Chapter 3 where many of the specimen predictions discussed were unconservative. Table 7.8, Fig. 7.10 and Fig. 7.11 show the modified STM results altered to limit the depth of

the local zone-general zone interface to one plate width ahead of the loading surface and to limit the compression stress on this plane to $0.7f_c$. This would be a typical length for a spiral in many post-

Table 7.8 Modified STM with Restrictions Results Summary

| Specimen | Failure Mode | Predicted Capacity (kips) | Test Ultimate (kips) | Test/Prediction |
|---|-----------------------|--|----------------------|----------------------|
| A1 | Node-Strut Interface | 199 | 298 | 1.49 |
| A2 | Node-Strut Interface | 204 | 275 | 1.35 |
| A3 | Node-Strut Interface | 200 | 265 | 1.33 |
| A4 | L.Z. - G.Z. Interface | 335 | 437 | 1.30 |
| B1 | L.Z. - G.Z. Interface | 343 | 366 | 1.07 |
| B2 | L.Z. - G.Z. Interface | 305 | 290 | 0.95 |
| B3 | L.Z. - G.Z. Interface | 326 | 331 | 1.02 |
| B4 | L.Z. - G.Z. Interface | 330 | 337 | 1.02 |
| B5 | L.Z. - G.Z. Interface | 201 | 212 | 1.05 |
| B6 | Bearing | 218 | 297 | 1.36 |
| B7 | L.Z. - G.Z. Interface | 327 | 296 | 0.90 |
| B8 | L.Z. - G.Z. Interface | 303 | 276 | 0.91 |
| C1 | L.Z. - G.Z. Interface | 328 | 370 | 1.13 |
| TPT1 | L.Z. - G.Z. Interface | 290 | 310 | 1.07 |
| TPT2 | L.Z. - G.Z. Interface | 311 | 300 | 0.96 |
| TPT3 | L.Z. - G.Z. Interface | 351 | 370 | 1.05 |
| TPT4 | L.Z. - G.Z. Interface | 328 | 332 | 1.01 |
| E1 | Bearing | 404 | 475 | 1.18 |
| E2 | Bearing | 445 | 500 | 1.12 |
| E3 | Bearing | 453 | 522 | 1.15 |
| E4* | Bearing | 434 | 500 | 1.15 |
| E5 | Bearing | 343 | 332 | 0.97 |
| E6 | L.Z. - G.Z. Interface | 333 | 348 | 1.05 |
| M1 | L.Z. - G.Z. Interface | 231 | 304 | 1.32 |
| M2 | L.Z. - G.Z. Interface | 256 | 401 | 1.57 |
| M3 | L.Z. - G.Z. Interface | 236 | 364 | 1.54 |
| M4 | L.Z. - G.Z. Interface | 280 | 411 | 1.47 |
| M5 | L.Z. - G.Z. Interface | 245 | 339 | 1.38 |
| M6 | L.Z. - G.Z. Interface | 262 | 300 | 1.15 |
| ME1 | L.Z. - G.Z. Interface | 328 | 350 | 1.07 |
| ME2 | L.Z. - G.Z. Interface | 330 | 370 | 1.12 |
| F1 | L.Z. - G.Z. Interface | 205 | 248 | 1.21 |
| I1 | L.Z. - G.Z. Interface | 302 | 423 | 1.40 |
| I2 | L.Z. - G.Z. Interface | 335 | 437 | 1.30 |
| I3 | L.Z. - G.Z. Interface | 277 | 375 | 1.35 |
| I4 | L.Z. - G.Z. Interface | 288 | 420 | 1.46 |
| * Longitudinal Edge Tension and Spalling Capacity Ignored | | Average Standard Deviation Coef. of Variance | | 1.19 0.19 0.16 |

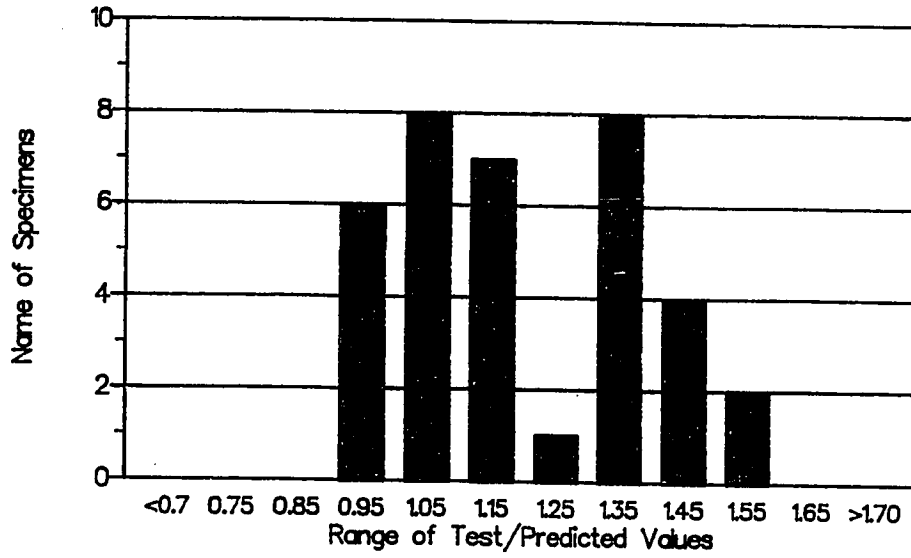


Figure 7.10 Frequency of Occurrence for Modified STM with Restrictions

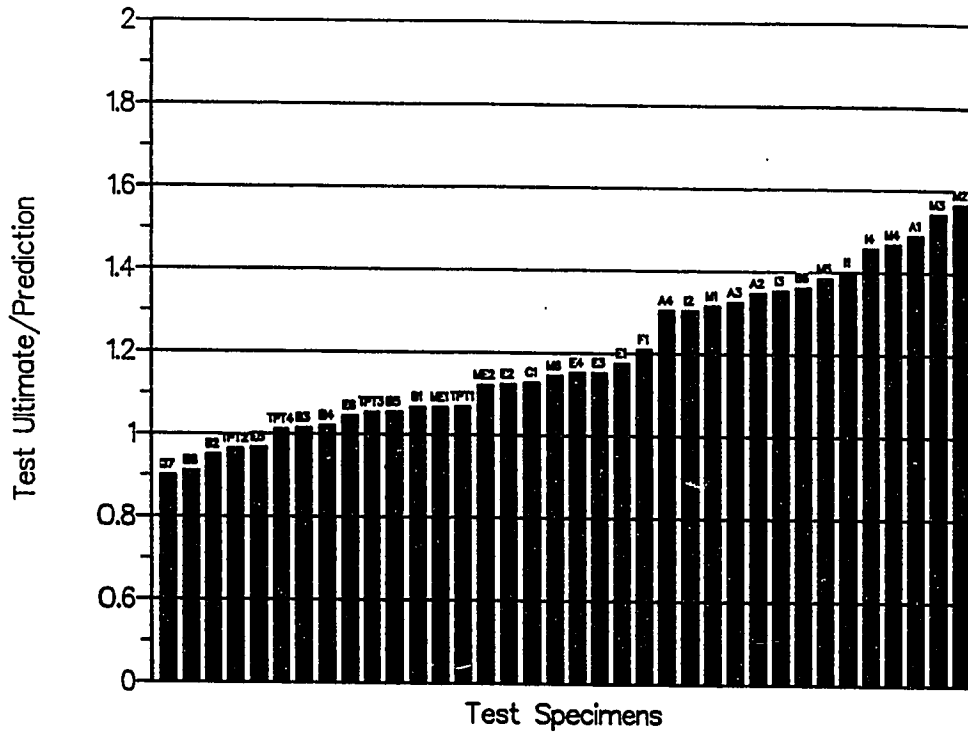


Figure 7.11 Distribution of Results for Modified STM with Restrictions

tensioning applications. The conservatism of the model raises to 1.19 with a coefficient of variance that is slightly lower than the modified STM used previously (0.16 versus 0.19). Only five specimens are unconservative, and they are within ten percent of a value of one. Until further research is conducted, it is recommended that the somewhat arbitrary limit of assuming the critical section at a depth of one plate width ahead of the loading surface and limiting the stress on this plane to $0.7f'_c$ be used when using long spirals. At this time, it is not recommended that the modified STM be used for design. To achieve the additional capacity predicted by the modified STM, substantial additional cracking must occur. This additional cracking would often be unacceptable. The accuracy of the basic STM is sufficient for present design and should, therefore, be used. However, the applicability of the modified STM should continue to be explored.

Reinforced concrete beam design can be used to make a comparison between the basic STM and the modified STM. In reinforced concrete beam design, the design load is based on yielding of the tensile reinforcement occurring before compression failure of the concrete. Beam design is done in this way to provide ductility and warning before failure. Anchorage zone design must also provide some degree of ductility and plenty of warning before failure. Using the basic STM in effect does this by predicting the load at which, without redistribution of forces, the anchorage zone fails. The modified STM predicts the final failure state. In the tests, extensive cracking was typically observed between the failure load predicted by the basic STM and the actual failure load. Table 7.9 and Fig. 7.12 show the relationship between the basic STM predictions and the modified STM predictions. The specimens which were predicted to fail in compression according to the basic STM have failure loads very close to those predicted by the modified STM. The average of modified STM predictions to the basic STM predictions is 1.46. If the modified STM with the restrictions on the depth of the local zone-general zone interface is

used, the average drops to 1.26. This comparison shows that if an anchorage zone is designed for a tension tie failure using the basic STM, the anchorage zone will have some degree of reserve capacity. The

Table 7.9 Comparison between the Modified STM and the Basic STM

| Specimen | Modified STM Predicted Capacity (kips) | Basic STM Predicted Capacity (kips) | Modified STM /Basic STM |
|----------|--|---|----------------------------|
| A1 | 199 | 195 | 1.02 |
| A2 | 204 | 190 | 1.07 |
| A3 | 200 | 204 | 0.98 |
| A4 | 335 | 306 | 1.09 |
| B1 | 440 | 299 | 1.47 |
| B2 | 381 | 292 | 1.30 |
| B3 | 416 | 296 | 1.41 |
| B4 | 429 | 277 | 1.55 |
| B5 | 218 | 218 | 1.00 |
| B6 | 218 | 218 | 1.00 |
| B7 | 421 | 269 | 1.57 |
| B8 | 405 | 252 | 1.61 |
| C1 | 419 | 192 | 2.18 |
| TPT1 | 346 | 180 | 1.92 |
| TPT2 | 376 | 253 | 1.49 |
| TPT3 | 432 | 247 | 1.75 |
| TPT4 | 401 | 235 | 1.71 |
| E1 | 404 | 404 | 1.00 |
| E2 | 445 | 445 | 1.00 |
| E3 | 453 | 453 | 1.00 |
| E4 | 434 | 434 | 1.00 |
| E5 | 343 | 238 | 1.44 |
| E6 | 339 | 259 | 1.31 |
| M1 | 293 | 189 | 1.55 |
| M2 | 336 | 322 | 1.04 |
| M3 | 355 | 290 | 1.22 |
| M4 | 345 | 180 | 1.92 |
| M5 | 280 | 202 | 1.39 |
| M6 | 262 | 104 | 2.52 |
| ME1 | 410 | 226 | 1.81 |
| ME2 | 374 | 261 | 1.43 |
| F1 | 227 | 133 | 1.71 |
| I1 | 349 | 281 | 1.24 |
| I2 | 381 | 223 | 1.71 |
| I3 | 350 | 262 | 1.34 |
| I4 | 343 | 126 | 2.72 |
| | | Average | 1.46 |

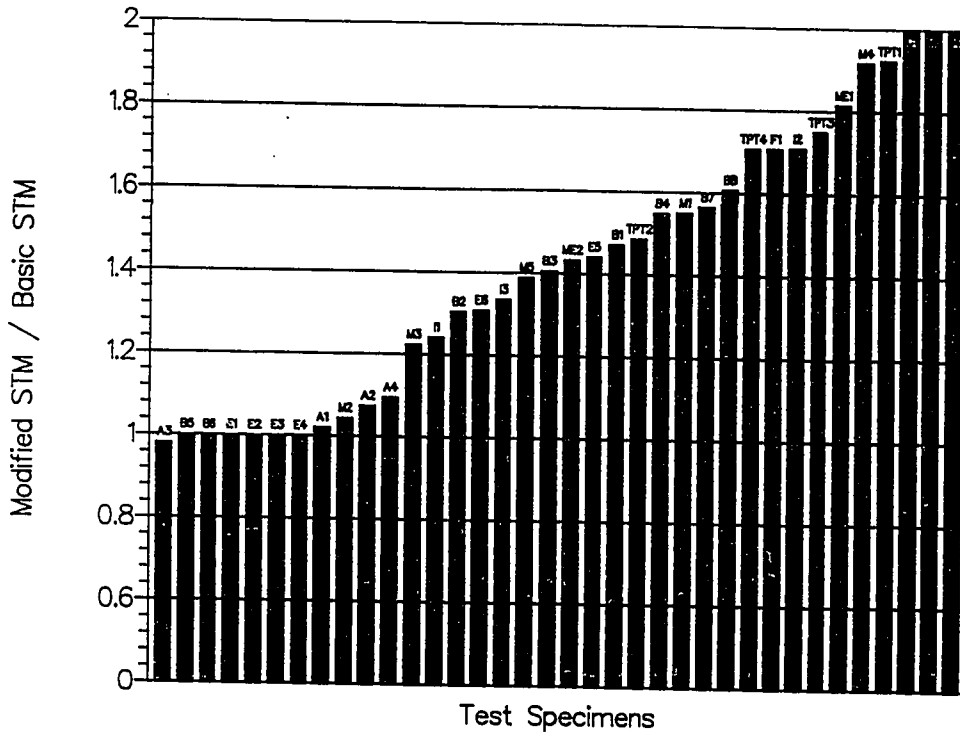


Figure 7.12 Graphical Comparison between the Modified and Basic STM

ductility is provided mainly through redistribution of forces as modelled in the modified STM and not through yielding of the tension ties. Because of the dominance of the concrete in the behavior of the anchorage zone the initial yielding of the ties for most of the specimens did not occur until near the ultimate load of the specimens. Table 7.10 and Fig. 7.13 compare the ultimate load with the load at which first yielding was measured in the tension tie reinforcement. For 72 percent of the specimens first yielding occurred within 15 percent of the ultimate load.

A summary is presented to evaluate the current method for estimating ultimate capacity. The most common method for currently estimating ultimate capacity (as determined from the survey conducted at the start of the project, see Chapter 2) is a combination of

checking the bearing capacity using equations similar to those developed by Roberts and verifying the tension tie capacity with

Table 7.10 Comparison Between Ultimate Load and First Yielding Load

| Specimen | Test Ultimate Load (kips) | First Yield Load (kips) | Ultimate / First Yield |
|----------|---------------------------|-----------------------------|------------------------|
| A1 | 298 | Reinforcement Did Not Yield | - |
| A2 | 275 | | 275 |
| A3 | 265 | | - |
| A4 | 437 | | 437 |
| B1 | 366 | 366 | 1.00 |
| B2 | 290 | 275 | 1.05 |
| B3 | 331 | 240 | 1.38 |
| B4 | 337 | 240 | 1.40 |
| B5 | 212 | No Bursting Reinforcement | - |
| B6 | 297 | | 175 |
| B7 | 296 | | 220 |
| B8 | 276 | | 210 |
| C1 | 370 | 350 | 1.06 |
| TPT1 | 310 | 300 | 1.03 |
| TPT2 | 300 | 280 | 1.07 |
| TPT3 | 370 | 370 | 1.00 |
| TPT4 | 332 | 330 | 1.01 |
| E1 | 475 | 470 | 1.01 |
| E2 | 500 | 495 | 1.01 |
| E3 | 522 | 475 | 1.10 |
| E4 | 500 | 490 | 1.02 |
| E5 | 332 | 325 | 1.02 |
| E6 | 348 | 340 | 1.02 |
| H1 | 304 | 304 | 1.00 |
| H2 | 401 | 300 | 1.34 |
| H3 | 364 | 280 | 1.30 |
| H4 | 411 | 390 | 1.05 |
| H5 | 339 | 325 | 1.04 |
| H6 | 300 | 250 | 1.20 |
| ME1 | 350 | 350 | 1.00 |
| ME2 | 370 | 350 | 1.06 |
| F1 | 248 | 248 | 1.00 |
| I1 | 423 | 310 | 1.36 |
| I2 | 437 | 290 | 1.51 |
| I3 | 375 | 375 | 1.00 |
| I4 | 420 | 380 | 1.11 |
| Average | | | 1.14 |

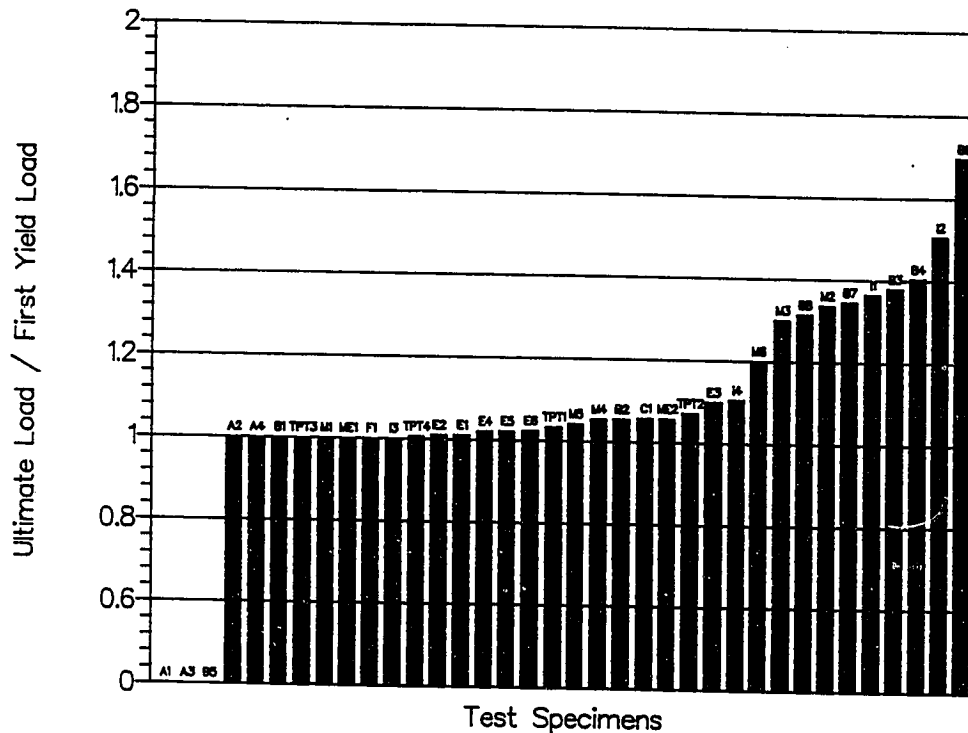


Figure 7.13 Graphical Comparison between Ultimate and First Yielding Load

equations based on Guyon's symmetrical prism method. Table 7.11, Fig. 7.14 and Fig. 7.15 show the results of this type of analysis. The specimens with inclined anchorages and tendon curvatures were not included because the survey results did not indicate a simple current method to design or analyze these types of sections. Most engineers indicated they would use finite element analysis or existing experience to design anchorage zones with tendon curvature or inclined anchorages. Using Guyon's symmetrical prism method coupled with a bearing capacity check is a generally conservative method. Six of the specimens (20 percent) were unconservative, four of which were from the "A" series. When using the STM model these four specimens failed at the node-strut interface, which is not checked with current methods. The method has

an unacceptably large coefficient of variance (0.52). Table 7.11 shows that several specimens were more than 200 percent conservative, while two specimens were more than 20 percent unconservative.

Table 7.11 Current Ultimate Prediction Method Results Summary

| Specimen | Failure Mode | Predicted Capacity (kips) | Test Ultimate (kips) | Test/Prediction |
|---|----------------------|---------------------------|---|----------------------|
| A1 | Bearing | 340 | 298 | 0.88 |
| A2 | Bearing | 340 | 275 | 0.81 |
| A3 | Bearing | 340 | 265 | 0.78 |
| A4 | Bearing | 544 | 437 | 0.80 |
| B1 | Bursting Tension Tie | 342 | 366 | 1.07 |
| B2 | Bursting Tension Tie | 198 | 290 | 1.46 |
| B3 | Bursting Tension Tie | 267 | 331 | 1.24 |
| B4 | Bursting Tension Tie | 287 | 337 | 1.17 |
| B5 | Bursting Tension Tie | 0 | 212 | |
| B6 | Bearing | 218 | 297 | 1.36 |
| B7 | Bursting Tension Tie | 287 | 296 | 1.03 |
| B8 | Bursting Tension Tie | 261 | 276 | 1.06 |
| C1 | Bursting Tension Tie | 258 | 370 | 1.44 |
| TPT1 | Bursting Tension Tie | 164 | 310 | 1.89 |
| TPT2 | Bursting Tension Tie | 239 | 300 | 1.26 |
| TPT3 | Bursting Tension Tie | 345 | 370 | 1.07 |
| TPT4 | Bursting Tension Tie | 312 | 332 | 1.06 |
| E1 | Bearing | 369 | 475 | 1.29 |
| E2 | Bearing | 391 | 500 | 1.28 |
| E3 | Bearing | 399 | 522 | 1.31 |
| E4* | Bearing | 380 | 500 | 1.32 |
| E5 | Bearing | 343 | 332 | 0.97 |
| E6 | Bursting Tension Tie | 147 | 348 | 2.37 |
| M1 | Bearing | 418 | 304 | 0.73 |
| M2 | Bursting Tension Tie | 317 | 401 | 1.27 |
| M3 | Bursting Tension Tie | 314 | 364 | 1.16 |
| M4 | Bursting Tension Tie | 317 | 411 | 1.30 |
| M5 | Bursting Tension Tie | 72 | 339 | 4.69 |
| M6 | Bursting Tension Tie | 152 | 300 | 1.97 |
| ME1 | Bursting Tension Tie | 240 | 350 | 1.46 |
| ME2 | Not Available | | 370 | |
| F1 | Bursting Tension Tie | 177 | 248 | 1.40 |
| I1 | Not Available | | 423 | |
| I2 | Not Available | | 437 | |
| I3 | Not Available | | 375 | |
| I4 | Not Available | | 420 | |
| * Longitudinal Edge Tension and Spalling Capacity Ignored | | | Average Standard Deviation Coef. of Variance | 1.36 0.71 0.52 |

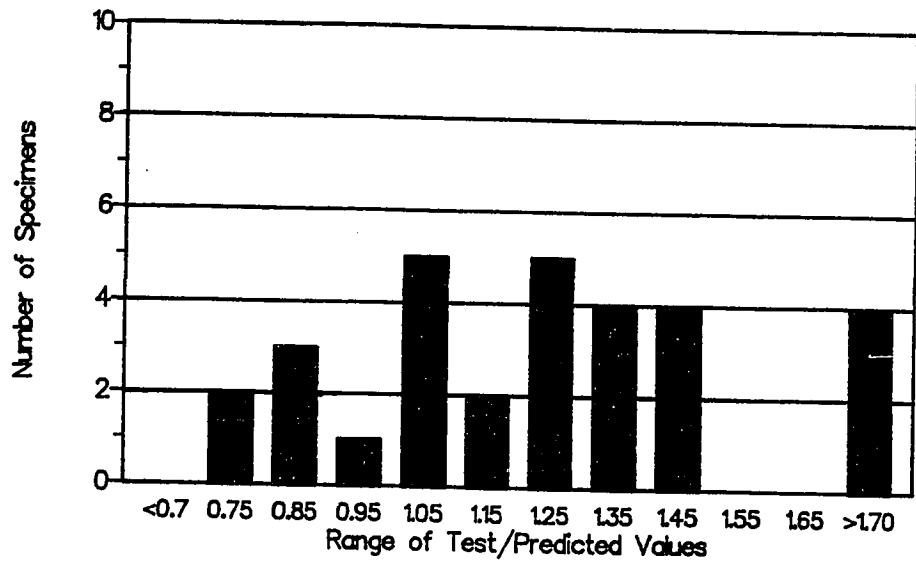


Figure 7.14 Frequency of Occurrence for Current Ultimate Capacity Method

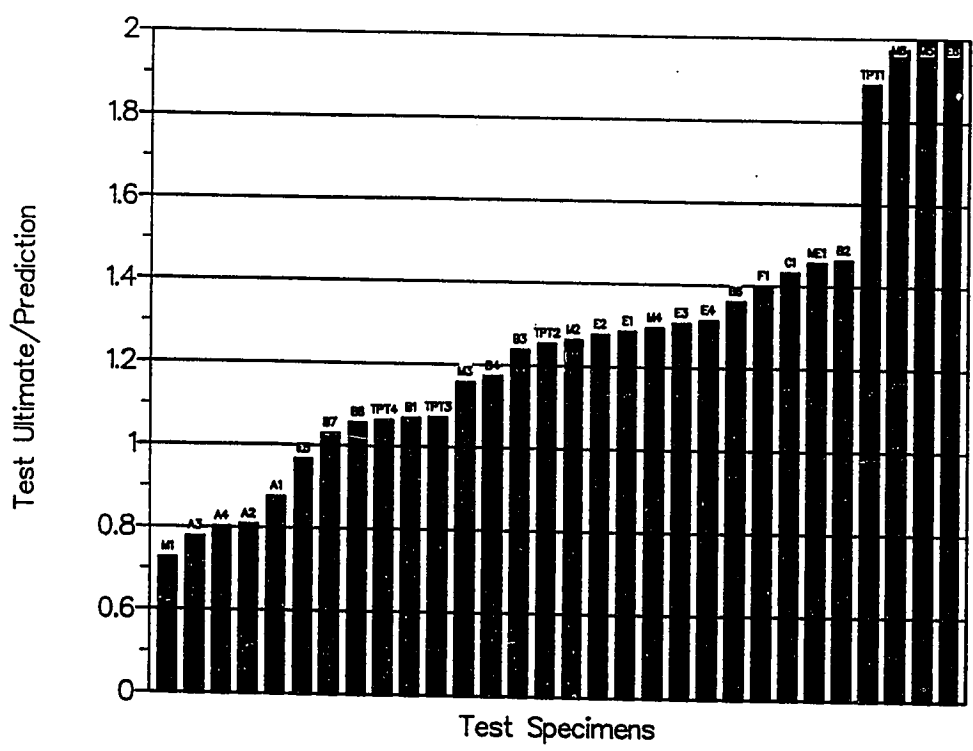


Figure 7.15 Distribution of Results for Current Ultimate Capacity Method

Table 7.12 Ultimate Load versus "GUTS" Capacity

| Specimen | Test Ultimate Load (kips) | Anchorage GUTS Load (kips) | Test Ultimate/GUTS | Specimen | Test Ultimate Load (kips) | Anchorage GUTS Load (kips) | Test Ultimate/GUTS |
|----------|---------------------------|----------------------------|--------------------|----------|---------------------------|----------------------------|--------------------|
| A1 | 298 | 289 | 1.03 | M1 | 304 | 165 | 1.84 |
| A2 | 275 | 289 | 0.95 | M2 | 401 | 165 | 2.43 |
| A3 | 265 | 289 | 0.92 | M3 | 364 | 165 | 2.20 |
| A4 | 437 | 289 | 1.51 | M4 | 411 | 165 | 2.49 |
| B1 | 366 | 174 | 2.10 | M5 | 339 | 289 | 1.17 |
| B2 | 290 | 174 | 1.67 | M6 | 300 | 289 | 1.04 |
| B3 | 331 | 174 | 1.90 | ME1 | 350 | 289 | 1.21 |
| B4 | 337 | 174 | 1.94 | ME2 | 370 | 289 | 1.28 |
| B5 | 212 | 174 | 1.22 | F1 | 248 | 289 | 0.86 |
| B6 | 297 | 174 | 1.71 | I1 | 423 | 289 | 1.46 |
| B7 | 296 | 174 | 1.70 | I2 | 437 | 289 | 1.51 |
| B8 | 276 | 174 | 1.58 | I3 | 375 | 289 | 1.30 |
| C1 | 370 | 289 | 1.28 | I4 | 420 | 289 | 1.45 |
| TPT1 | 310 | 289 | 1.07 | Average | | 1.56 | |
| TPT2 | 300 | 289 | 1.04 | | | | |
| TPT3 | 370 | 289 | 1.28 | | | | |
| TPT4 | 332 | 289 | 1.15 | | | | |
| E1 | 475 | 232 | 2.05 | | | | |
| E2 | 500 | 232 | 2.15 | | | | |
| E3 | 522 | 232 | 2.25 | | | | |
| E4 | 500 | 232 | 2.15 | | | | |
| E5 | 332 | 165 | 2.01 | | | | |
| E6 | 348 | 289 | 1.20 | | | | |

Table 7.12 and Fig. 7.16 are comparisons between the test ultimate and the "GUTS" capacity of the anchors. The "GUTS" capacity of each anchor was shown in Table 7.1. Three of the specimens failed below their "GUTS" capacity and only one of these (Specimen F1) was more than ten percent low. This is not of great concern because these specimens were lightly reinforced and their capacity was predicted correctly by the STM procedure.

In the next section, a proposed specification and commentary suitable for inclusion in AASHTO are presented. In the specification it is proposed to use a load factor of 1.3 for anchorage forces and a

ϕ factor of 0.75. The ϕ factor recommendation resulted from a combination of usual uncertainties about material properties and dimensions, concerns over the somewhat nonductile nature of many of the anchorage failures, and a high level of confidence in the conservatism of the basic STM. This is the same ϕ factor value as used by ACI 318-89 [6] for concrete columns reinforced with spirals. The proposed load factor includes an allowance for possible overstressing above the maximum stressing load (0.81 times "GUTS" for AASHTO Bridge Specification and 0.80 times "GUTS" for ACI 318-89) due to faulty equipment or procedures as well as a modest basic reserve margin for safety. Combining the load factor and the ϕ factor yields a total factor of safety of 1.40, $(1.3 \cdot 0.81 / 0.75)$, in comparison to "GUTS".

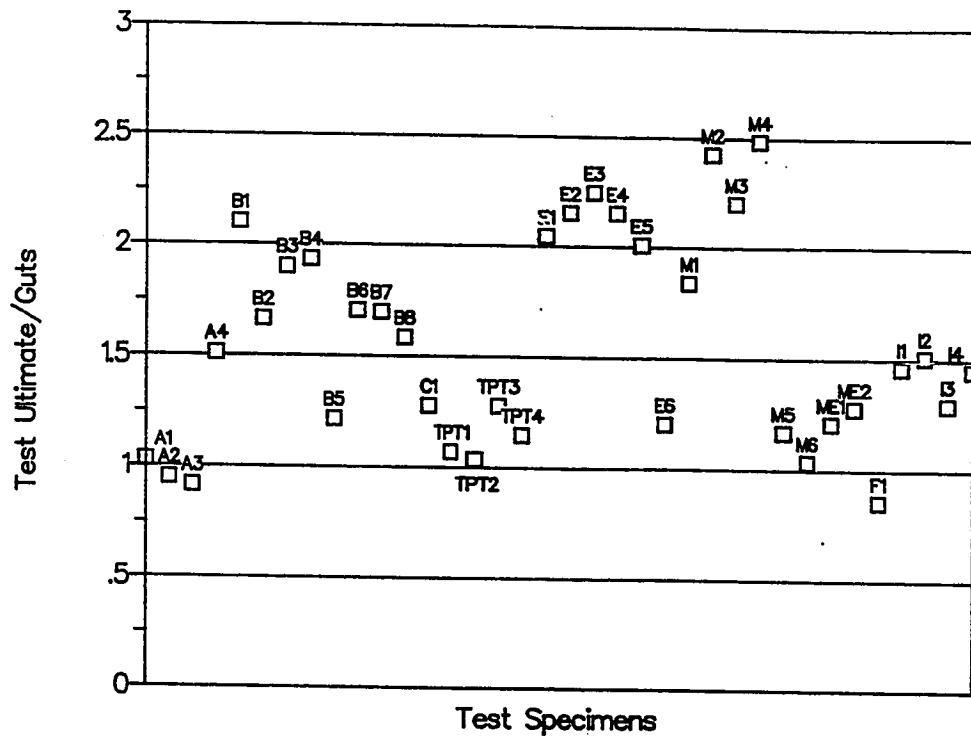


Figure 7.16 Test Ultimate versus "GUTS"

In a laboratory investigation where loads are known, material strengths are known and dimensions are carefully controlled, an appropriate comparison of the factor of safety is to use unity values for ϕ factors and load factors. Thus a basic factor of safety becomes the test ultimate divided by "GUTS" because it would be impossible to place loads higher than "GUTS" on the anchorage. Figure 7.16 shows that the vast majority of specimens tested had resistances greater than the maximum load which could be applied by correctly sized tendons.

7.3 AASHTO Specification and Commentary Proposal

The specification and commentary presented in this section are the result of contributions by the entire NCHRP Project 10-19 research team. Those individuals include Olivier Burdet [25], Dr. John Breen, Dr. Gregory Fenves, Carin Roberts [143], Gregor Wollman [184], and Brian Falconer [55] in addition to the author. The specification was written and critiqued by all the individuals mentioned, reviewed by members of the research sponsor's review panel who provided much valuable insight, revised and is being prepared for presentation to AASHTO at the time of publication of this dissertation. The specification presented in this document should be very close to the final version and is presented in a form suitable for consideration by AASHTO. Numbering of the sections conforms to current AASHTO Bridge Specification numbering. The following two subsections use references that are given at the end of the subsection and have a separate figure numbering from the rest of this dissertation so that they can be used separately from this dissertation.

7.3.1 Proposed Specification.

DIVISION I - DESIGN

9.1.2 Notations [add to current Section 9.1.2]

- F_{pu} - guaranteed ultimate strength of the prestressing tendon, $A_s^* f'_s$
 P_u - factored tendon force

9.1.3 Definitions [add to current Section 9.1.3]

Anchorage Device - The hardware assembly used for transferring a post-tensioning force from the tendon wires, strands or bars to the concrete.

Anchorage Spacing - Center-to-center spacing of anchorage devices.

Anchorage Zone - The portion of the structure in which the concentrated prestressing force is transferred from the anchorage device onto the concrete (Local Zone), and then distributed more widely into the structure (General Zone).

Edge Distance - Distance from the center of the anchorage device to the edge of the member.

End Anchorage - Length of reinforcement, or mechanical anchor, or hook, or combination thereof, beyond point of zero stress in reinforcement. [*Delete remainder of current definition*]

General Zone - Region within which the concentrated prestressing force spreads out to a more linear stress distribution over the cross section of the member (Saint-Venant Region).

Intermediate Anchorage - Anchorage not located at the end surface of a member or segment, for tendons that do not extend over the entire length of the member or segment; usually in the form of embedded anchors, blisters, ribs, or recess pockets.

Local Zone - The volume of concrete surrounding and immediately ahead of the anchorage device, subjected to high local bearing stresses.

Special Anchorage Device - Anchorage device whose adequacy must be proven experimentally in a standardized acceptance test.

9.14 LOAD FACTORS [add to current Section 9.14]

The computed strength capacity shall not be less than the largest value from load factor design in Article 3.22. For the design of anchorage zones and regions of large tendon curvature a load factor of 1.3 shall be applied to the maximum tendon jacking force.

The following strength reduction factors shall be used:

For factory produced precast prestressed concrete members $\phi = 1.0$
 For post-tensioned cast-in-place concrete members $\phi = 0.95$
 For shear $\phi = 0.90$
 For anchorage zones $\phi = 0.75$
 For effects of tendon curvature $\phi = 0.75$

9.21 POST-TENSIONED ANCHORAGE ZONES

9.21.1 Geometry of the Anchorage Zone

9.21.1.1 The anchorage zone is geometrically defined as the volume of concrete through which the concentrated prestressing force at the anchorage device spreads transversely to a more linear stress distribution across the entire cross section at some distance from the anchorage device.

9.21.1.2 For anchorage zones at the end of a member or segment, the transverse dimensions may be taken as the depth and width of the section, but not larger than the longitudinal dimension of the member or segment. The longitudinal extent of the anchorage zone in the direction of the tendon shall be at least equal to the larger of the transverse dimensions of the anchorage zone and shall not be taken as more than one and one-half times that dimension.

9.21.1.3 For intermediate anchorages the anchorage zone also extends in the direction opposite to the anchorage force for a distance at least equal to the larger of the transverse dimensions of the anchorage zone.

9.21.1.4 For design purposes, the anchorage zone shall be considered as comprised of two regions; the *general zone* as defined in Section 9.21.2.1 and the *local zone* as defined in Section 9.21.2.2.

9.21.2 General Zone and Local Zone

9.21.2.1 General Zone

9.21.2.1.1 The geometric extent of the general zone is identical to that of the overall anchorage zone as defined in Section 9.21.1 and includes the local zone.

9.21.2.1.2 Design of general zones shall meet the requirements of Sections 9.14 and 9.21.3.

9.21.2.2 Local Zone

9.21.2.2.1 The local zone is defined as the rectangular prism (or equivalent rectangular prism for circular or oval anchorages) of concrete surrounding and immediately ahead of the anchorage device and any integral confining reinforcement. The dimensions of the local zone are defined in Section 9.21.5.

9.21.2.2.2 Design of local zones shall meet the requirements of Sections 9.14 and 9.21.5 or shall be based on the results of experimental tests required in Section 9.21.5.3 and described in Section 4.33.11 of Division II. Anchorage devices based on the acceptance test of Division II, Section 4.33.11, are referred to as *special anchorage devices*.

9.21.2.3 Responsibilities

9.21.2.3.1 The engineer of record is responsible for the overall design and approval of working drawings for the general zone, including the specific location of the tendons and anchorage devices, general zone reinforcement, and the specific stressing sequence. The engineer of record is responsible for the design of the local zone for anchorage devices based on the provisions of Section 9.21.5.2.

9.21.2.3.2 If special anchorage devices are used, the anchorage device supplier is responsible for furnishing anchorage devices that satisfy the acceptance test requirements of Section 9.21.5.3 and of Division II, Section 4.33.11. The anchorage device supplier shall provide records of the acceptance test by an accredited independent testing agency in conformance with Division II, Section 4.33.11.8 to the engineer of record and to the constructor and shall specify auxiliary and confining reinforcement, minimum edge distance, minimum anchor spacing, and minimum concrete strength at time of stressing required for proper performance of the local zone.

9.21.2.3.3 The responsibilities of the constructor are specified in Division II, Section 4.33.17.

9.21.3 Design of the General Zone

9.21.3.1 Design Methods

The following methods may be used for the design of general zones:

- (1) Equilibrium based plasticity models, generally termed "Strut-and-Tie Models" (see Section 9.21.4)
- (2) Elastic stress analysis (Finite Element Method or equivalent)
- (3) Approximate methods for determining the compression and tension forces given in Sections 9.21.3.4 to 9.21.3.9, where applicable

The effects of stressing sequence and three-dimensional effects shall be considered in the design. Where these three-dimensional effects appear significant they may be analyzed using three-dimensional analysis procedures or may be approximated by considering two or more planes. However, in these approximations the interaction of the planar models must be considered, and the model loadings and results must be consistent.

9.21.3.2 Nominal Material Strengths

9.21.3.2.1 The nominal tensile strength of bonded reinforcement is limited to f_{sy} for non-prestressed reinforcement and to f_y^* for prestressed reinforcement. The nominal tensile strength of unbonded prestressed reinforcement is limited to $f_{se} + 15,000$ psi.

9.21.3.2.2 The effective nominal compressive strength of the concrete of the general zone, exclusive of confined concrete, is limited to $0.7f'_c$. The tensile strength of the concrete shall be neglected.

9.21.3.2.3 Unless otherwise specified, stress shall not be transferred to concrete until the compressive strength of the concrete as indicated by test cylinders, cured by methods identical with the curing of the member, is at least 3,500 psi.

9.21.3.3 Use of Special Anchorage Devices

Whenever special anchorage devices which do not meet the requirements of Section 9.21.5.2 are to be used, additional confinement reinforcement similar in configuration and equivalent in volumetric ratio to that used in satisfying Division II, Section 4.33.11.3 shall be placed in the portion of the general zone ahead of the local zone for that anchorage device.

9.21.3.4 Compressive Stresses

9.21.3.4.1 The compressive stresses in the concrete ahead of the anchorage device shall be checked at a distance measured from the concrete bearing surface equal to the smaller of:

- (1) The depth to the end of the local confinement reinforcement.
- (2) The smaller lateral dimension of the anchorage device.

If these stresses are obtained from an elastic stress analysis, local stress maxima can be averaged over an area equal to the bearing area of the anchorage device. Section 9.21.4.3 defines the critical section if a Strut-and-Tie Model is used.

9.21.3.4.2 In the absence of a more accurate analysis, the concrete compressive stresses can be approximated by Equations (9-32) and (9-33), provided that:

- (1) The cross section of the member is rectangular.
- (2) The minimum edge distance of the anchorage in the main plane of the member is at least one and one-

half times the corresponding lateral dimension, a , of the anchorage device.

$$f_{ca} = \kappa \frac{0.6P_u}{ab \left[1 + a \left(\frac{1}{b} - \frac{1}{t} \right) \right]} \quad (9-32)$$

$$\begin{aligned} \kappa &= 1 + \left[2 - \frac{s}{a} \right] \left[0.3 + \frac{n}{15} \right] \text{ for } a \leq s < 2a \\ \kappa &= 1 \text{ for } s \geq 2a \end{aligned} \quad (9-33)$$

where f_{ca} is the concrete compressive stress ahead of the anchorage device;

κ is a correction factor for closely spaced anchorages;

a is the lateral dimension of the anchorage device measured parallel to the larger dimension of the cross section;

b is the lateral dimension of the anchorage device measured parallel to the smaller dimension of the cross section;

P_u is the factored tendon load;

t is the thickness of the section;

s is the center-to-center spacing of multiple anchorages;

n is the number of anchorages in a row.

If a group of anchorages is closely spaced in two directions, the product of the correction factors, κ , for each direction is used in Equation (9-32).

9.21.3.5 Bursting Force

9.21.3.5.1 The bursting force is the tensile force in the anchorage zone acting ahead of the anchorage device and transverse to the tendon axis. The magnitude of the bursting force, T_{burst} , and its distance from the loaded surface, d_{burst} , can be calculated using the Strut-and-Tie Model procedures of Section 9.21.4 or by integrating the tensile stresses determined from an elastic stress analysis along the tendon path. Three-dimensional effects shall be considered for the determination of the bursting reinforcement requirements.

9.21.3.5.2 In the absence of a more accurate analysis, values for T_{burst} and d_{burst} can be estimated by Equations (9-34) and (9-35) respectively, provided that:

- (1) The member has a rectangular cross section and its

- longitudinal extent is at least equal to the largest transverse dimension of the cross section.
- (2) Only one anchorage device or one group of closely spaced anchorage devices is located in the anchorage zone. Anchorage devices can be treated as closely spaced if their center-to-center spacing does not exceed one and one-half times the width of the anchorage devices in the direction considered.
 - (3) The angle of inclination of the tendon as defined in Equations (9-34) and (9-35) is between -5 degrees and +20 degrees.

In the application of Equations (9-34) and (9-35) the specified stressing sequence must be considered if more than one tendon is present.

$$T_{burst} = 0.25P_u \left[1 - \frac{a}{h} \right] + 0.5P_u |\sin \alpha| \quad (9-34)$$

$$d_{burst} = 0.5(h-2e) + 5e \sin \alpha \quad (9-35)$$

where P_u is the sum of the total factored tendon loads for the stressing arrangement considered;

a is the lateral dimension of the anchorage device or group of devices in the direction considered;

e is the eccentricity (always taken as positive) of the anchorage device or group of devices with respect to the centroid of the cross section;

h is the lateral dimension of the cross section in the direction considered;

α is the angle of inclination of the resultant of the tendon forces with respect to the centerline of the member, positive for concentric tendons or if the anchor force points toward the centroid of the section, negative if the anchor force points away from the centroid of the section.

9.21.3.5.3 Resistance to bursting forces shall be provided by non-prestressed or prestressed reinforcement, in the form of spirals, closed hoops, or well anchored transverse ties. This reinforcement is to be proportioned to resist the total factored bursting force. Arrangement and anchorage of bursting reinforcement shall satisfy the following:

- (1) Bursting reinforcement shall extend over the full width of the member and must be anchored as close to the outer faces of the member as cover permits.
- (2) Bursting reinforcement shall be distributed ahead of

the loaded surface along both sides of the tendon throughout a distance of $2.5 d_{burst}$ for the plane considered, but not to exceed 1.5 times the corresponding lateral dimension of the section. The centroid of the bursting reinforcement shall coincide with the distance d_{burst} used for the design.

- (3) Spacing of bursting reinforcement shall exceed neither 24 bar diameters nor 12 inches.

9.21.3.6 Edge Tension Forces

9.21.3.6.1 Edge tension forces are tensile forces in the anchorage zone acting parallel and close to the transverse edge and longitudinal edges of the member. The transverse edge is the surface loaded by the anchors. The tensile force along the transverse edge is referred to as *spalling force*. The tensile force along the longitudinal edge is referred to as *longitudinal edge tension force*.

9.21.3.6.2 Spalling forces are induced in concentrically loaded anchorage zones, eccentrically loaded anchorage zones, and anchorage zones for multiple anchors. Longitudinal edge tension forces are induced when the resultant of the anchorage forces considered causes eccentric loading of the anchorage zone. The edge tension forces can be determined from an elastic stress analysis, Strut-and-Tie Models, or in accordance with Section 9.21.3.6.4 and Section 9.21.3.6.5.

9.21.3.6.3 In no case shall the spalling force be taken as less than two percent of the total factored tendon force.

9.21.3.6.4 For multiple anchorages with a center-to-center spacing of less than 0.4 times the depth of the section, the spalling forces are adequately approximated by the requirement of Section 9.21.3.6.3. For larger spacings the spalling forces must be determined from a more accurate analysis, such as Strut-and-Tie Models or other analytical procedures.

9.21.3.6.5 If the centroid of all tendons considered is located outside of the kern of the section both spalling forces and longitudinal edge tension forces are induced. The longitudinal edge tension force can be determined from an axial-flexural beam analysis at a section located at one half the depth of the section away from the loaded surface. The spalling force can be taken as equal to the longitudinal edge tension force but not less than specified in Section 9.21.3.6.3.

9.21.3.6.6 Resistance to edge tension forces shall be provided in the form of non-prestressed or prestressed reinforcement located close to

the longitudinal and transverse edge of the concrete. Arrangement and anchorage of the edge tension reinforcement shall satisfy the following:

- (1) Minimum spalling reinforcement satisfying Section 9.21.3.6.3 shall extend over the full width of the member.
- (2) Spalling reinforcement between multiple anchorage devices shall effectively tie these anchorage devices together.
- (3) Longitudinal edge tension reinforcement and spalling reinforcement for eccentric anchorage devices shall be continuous. The reinforcement shall extend along the tension face over the full length of the anchorage zone and shall extend along the loaded face from the longitudinal edge to the other side of the eccentric anchorage device or group of anchorage devices.

9.21.3.7 Intermediate Anchorages

[Text for this section will be furnished after completion of Phase B of Project NCHRP 10-29]

9.21.3.8 Diaphragms

[Text for this section will be furnished after completion of Phase B of Project NCHRP 10-29]

9.21.3.9 Multiple Slab Anchorages

[Text for this section will be furnished after completion of Phase B of Project NCHRP 10-29]

9.21.4 Application of the Strut-and-Tie Model to the Design of Anchorage Zones

9.21.4.1 General

9.21.4.1.1 The flow of forces in the anchorage zone may be approximated by a series of straight compression members (struts) and straight tension members (ties) that are connected at discrete points (nodes). Compression forces are carried by concrete compression struts and tension forces are carried by non-prestressed or prestressed reinforcement.

9.21.4.1.2 The selected Strut-and-Tie Model shall follow a load path from the anchorages to the end of the anchorage zone. Other forces acting on the anchorage zone, such as reaction forces, tendon deviation forces, and applied loads, shall be considered in the selection of the Strut-and-Tie Model. The forces at the end of the anchorage zone can be obtained from an axial-flexural beam analysis.

9.21.4.2 Nodes

Local zones which meet the provisions of Section 9.21.5 or Division II, Section 4.33.11 can be considered as properly detailed and are adequate nodes. The other nodes in the anchorage zone are adequate if the effective concrete stresses in the struts meet the requirements of Section 9.21.4.3 and the tension ties are properly detailed to develop the full yield strength of the reinforcement.

9.21.4.3 Struts

9.21.4.3.1 The effective concrete compressive strength for the general zone shall usually be limited to $0.7\phi f'_{ci}$. In areas where the concrete may be extensively cracked at ultimate due to other load effects, or if large plastic rotations are required, the effective compressive strength shall be limited to $0.6\phi f'_{ci}$.

9.21.4.3.2 In anchorage zones the critical section for compression struts is ordinarily located at the interface with the local zone node. If special anchorage devices are used, the critical section of the strut can be taken as that section whose extension intersects the axis of the tendon at a depth equal to the smaller of the depth of the local confinement reinforcement or the lateral dimension of the anchorage device.

9.21.4.3.3 For thin members the dimension of the strut in the direction of the thickness of the member can be approximated by assuming that the thickness of the compression strut varies linearly from the transverse lateral dimension of the anchor at the surface of the concrete to the total thickness of the section at a depth equal to the thickness of the section.

9.21.4.3.4 The compression stresses can be assumed as acting parallel to the axis of the strut and as uniformly distributed over its cross section.

9.21.4.4 Ties

9.21.4.4.1 Tension forces in the Strut-and-Tie Model are carried uniquely by non-prestressed or prestressed reinforcement. Tensile strength of the concrete shall be neglected.

9.21.4.4.2 Tension ties must be properly detailed and must extend beyond the nodes so that the full tension tie force is developed at the node. The reinforcement layout must closely follow the directions of the ties in the Strut-and-Tie Model.

9.21.5 Design of the Local Zone

9.21.5.1 Dimensions of the Local Zone

9.21.5.1.1 When no independently verified manufacturer's edge distance recommendations for a particular anchorage device are available, the transverse dimensions of the local zone in each direction shall be taken as the larger of:

- (1) The corresponding bearing plate size plus twice the minimum concrete cover required for the particular application and environment.
- (2) The outer dimension of any required confining reinforcement plus the required concrete cover over the confining reinforcing steel for the particular application and environment.

9.21.5.1.2 When independently verified manufacturer's recommendations for minimum cover, spacing and edge distances for a particular anchorage device are available, the transverse dimensions of the local zone in each direction shall be taken as the smaller of:

- (1) Twice the edge distance specified by the anchorage device supplier.
- (2) The center-to-center spacing specified by the anchorage device supplier.

9.21.5.1.3 The length of the local zone along the tendon axis shall be taken as the greater of:

- (1) The maximum width of the local zone.
- (2) The length of the anchorage device confining reinforcement.
- (3) For anchorage devices with multiple bearing surfaces, the distance from the loaded concrete surface to the bottom of each bearing surface plus the maximum dimension of that bearing surface.

In no case shall the length of the local zone be taken as greater than one and one-half times the width of the local zone.

9.21.5.2 Bearing Strength

9.21.5.2.1 Anchorage devices may be either devices meeting the bearing compressive strength limits of Sections 9.21.5.2.2 to 9.21.5.2.4 or special anchorage devices meeting the requirements of Section 9.21.5.3.

9.21.5.2.2 The effective concrete bearing compressive strength f_b used for design shall not exceed that of Equations (9-36) or (9-37).

$$f_b \leq 0.7\phi f'_{ci} \sqrt{A/A_g} \quad (9-36)$$

$$\text{but } f_b \leq 2\phi f'_{ci} \quad (9-37)$$

where f_b is the maximum factored tendon load, P_u , divided by the effective bearing area A_b ;
 f'_{ci} is the concrete compressive strength at stressing;
 A is the maximum area of the portion of the supporting surface that is similar to the loaded area and concentric with it;
 A_v is the gross area of the bearing plate if the requirements of Section 9.21.5.2.3 are met, or is the area calculated in accordance with Section 9.21.5.2.4;
 A_b is the effective net area of the bearing plate calculated as the area A_v minus the area of openings in the bearing plate.

9.21.5.2.3 The full bearing plate area may be used for A_v and the calculation of A_b if the anchorage device is sufficiently rigid. To be considered sufficiently rigid, the slenderness of the bearing plate (n/t) must not exceed the value given in Equation (9-38).

$$n/t \leq 0.07 \sqrt[3]{E_b/f_b} \quad (9-38)$$

where n is the largest distance from the outer edge of the wedge plate to the outer edge of the bearing plate. For rectangular bearing plates this distance is measured parallel to the edges of the bearing plate. If the anchorage has no separate wedge plate, the size of the wedge plate shall be taken as the distance between the extreme wedge holes in the corresponding direction.
 t is the average thickness of the bearing plate.
 E_b is the modulus of elasticity of the bearing plate material.

9.21.5.2.4 For bearing plates that do not meet the requirements of Section 9.21.5.2.3, the effective gross bearing area, A_v , shall be taken as the area geometrically similar to the wedge plate (or to the outer perimeter of the wedge hole pattern for plates without separate wedge plate) with dimensions increased by twice the bearing plate thickness. A larger effective bearing area may be calculated by assuming an effective area and checking the new f_b and n/t values for conformance with sections 9.21.5.2.2 and 9.21.5.2.3.

9.21.5.3 Special Anchorage Devices

Special anchorage devices that do not meet the requirements of Sections 9.21.5.2 may be used provided that they have been tested by an accredited independent testing agency according to the procedures described in Division II, Section 4.33.11 and meet the acceptance criteria specified in Division II, Section 4.33.11.6.

9.22 PRETENSIONED ANCHORAGE ZONES

9.22.1 Vertical stirrups resisting at least two percent of the total factored prestressing force, P_u , shall be placed within the distance of $d/4$ of the end of the beam, the end stirrups to be as close to the end of the beam as practicable.

9.22.2 For at least the distance d from the end of the beam, nominal reinforcement shall be placed to enclose the prestressing steel in the bottom flange.

9.22.3 For box girders, transverse reinforcement shall be provided and anchored by extending the leg into the web of the girder.

9.22.4 Unless otherwise specified, stress shall not be transferred to concrete until the compressive strength of the concrete as indicated by test cylinders, cured by methods identical with the curing of the member, is at least 4,000 psi.

9.29 EFFECTS OF TENDON CURVATURE [new section]

9.29.1 General

Curved tendons induce deviation forces in the plane of tendon curvature. Curved post-tensioning tendons with multiple strands or wires also induce forces perpendicular to the plane of tendon curvature.

9.29.2 In-Plane Forces

[Text for this section will be furnished after completion of Phase B of Project NCHRP 10-29]

9.29.3 Out-of-Plane Forces

[Text for this section will be furnished after completion of Phase B of Project NCHRP 10-29]

DIVISION II - CONSTRUCTION

4.33.11 Post-Tensioning Special Anchorage Device Acceptance Test [add to current Section 4.33.11]

4.33.11.1 The test block shall be a rectangular prism. The dimensions perpendicular to the tendon in each direction shall be the smaller of the minimum edge distance or the minimum spacing specified by the anchorage device supplier, with the stipulation that the cover over any

confining reinforcing steel be appropriate for the particular application and environment. The length of the block along the axis of the tendon shall be at least two times the larger of the cross-sectional dimensions.

4.33.11.2 The reinforcement in the local zone shall be the same as that specified by the anchorage device supplier for the particular system.

4.33.11.3 Any desired reinforcement in the test block outside the local zone shall be specified by the anchorage device supplier, with the limitation that it must be in the form of orthogonal ties or spirals with a volumetric ratio (reinforcement to confined core) of no more than 0.013.

4.33.11.4 The concrete strength at the time of testing shall exceed neither $0.85f'_c$ nor the minimum specified concrete strength at time of tensioning, f_{ci} .

4.33.11.5 Either of two test procedures is acceptable: cyclic loading described in Section 4.33.11.5.1, or sustained loading described in Section 4.33.11.5.2. Measurements shall be reported in accordance with Section 4.33.11.5.3. The loads specified for the tests are given in fractions of the ultimate load F_{pu} of the largest tendon that the anchorage device is designed to accommodate. The specimen shall be loaded in accordance with normal usage of the device in post-tensioning applications.

4.33.11.5.1 In a cyclic loading test, the load shall be increased to $0.8F_{pu}$. The load shall then be cycled between $0.1F_{pu}$ and $0.8F_{pu}$ until crack widths stabilize but for not less than 10 cycles. Upon completion of the cyclic loading the specimen shall be preferably loaded to failure or, if limited by the capacity of the loading equipment, to at least $1.0F_{pu}$.

4.33.11.5.2 In a sustained loading test, the load shall be increased to $0.8F_{pu}$ and held constant until crack widths stabilize but for not less than 48 hours. After sustained loading is completed, the specimen shall be preferably loaded to failure or, if limited by the capacity of the loading equipment, to at least $1.0F_{pu}$.

4.33.11.5.3 Crack widths, patterns, and progression shall be recorded under either test procedure at initial loads of $0.4F_{pu}$, $0.6F_{pu}$, and $0.8F_{pu}$. During loading to failure the final crack measurements shall be recorded at $0.9F_{pu}$. The maximum load shall also be reported. During cyclic loading crack measurements shall be recorded at least at the last three consecutive peak loadings before termination of the test.

During sustained loading crack measurements shall be recorded at least three times at intervals of not less than four hours during the last twelve hours before termination of the test. Crack widths are considered stabilized if they do not change by more than 0.001 in. over the last three readings.

4.33.11.6 The strength of the anchorage zone must exceed $1.0F_{pu}$. The maximum crack width criteria specified below must be met for moderately aggressive environments. For higher aggressivity environments the crack width criteria shall be reduced by at least 50 percent.

- (1) No cracks greater than 0.002 in. at $0.4F_{pu}$.
- (2) No cracks greater than 0.008 in. at $0.8F_{pu}$ after completion of the cyclic or sustained loading.
- (3) No cracks greater than 0.016 in. at $0.9F_{pu}$.

4.33.11.7 A test series shall consist of three test specimens. Each one of the tested specimens must meet the acceptance criteria. If one of the three specimens fails to pass the test, a supplementary test of three additional specimens is allowed. The three additional test specimen results must meet all acceptance criteria of Section 4.33.11.6.

4.33.11.8 Records of the anchorage device acceptance test shall include:

- (1) Dimensions of the test specimen.
- (2) Drawings and dimensions of the anchorage device, including all reinforcement in the local zone.
- (3) Amount and arrangement of reinforcement in the lower portion of the specimen.
- (3) Type and yield strength of reinforcing steel.
- (4) Type and compressive strength at time of testing of concrete.
- (5) Type of testing procedure and all measurements required in Section 4.33.11.6 for each specimen.

4.33.17 Post-Tensioned Anchorage Zones [new section]

The constructor is responsible for the proper placement of all materials and correct performance of all stressing operations according to the design documents of the engineer of record and the requirements stipulated by the anchorage device supplier. Stressing operations may not be initiated before the minimum concrete strengths specified by the engineer of record and the anchorage device supplier are verified. Modifications to the local zone details verified under provisions of Section 9.21.5.3 in Division I and Section 4.33.11 in Division II shall be approved by the engineer of record.

7.3.2 Proposed Commentary.

C.9.14 LOAD FACTORS

The load factor of 1.3 applied to the maximum tendon jacking force means that in many cases the anchorage zone has to be designed to resist a force slightly larger than the nominal ultimate strength of the tendon. This is partly justified by the possibility of an actual tendon strength larger than the nominal strength of the prestressing steel and partly by the desirability of a reasonable safety factor during stressing operations.

The ϕ -factor of 0.75 reflects the importance of the anchorage zone, the brittle failure mode for compression struts in the anchorage zone, and the relatively wide scatter of results of experimental anchorage zone studies.

C.9.21 POST-TENSIONED ANCHORAGE ZONES

Article 9.21 applies to anchorage zones for post-tensioned tendons only. Provisions for anchorage zones in pretensioned concrete are included in Article 9.22.

C.9.21.1 Geometry of the Anchorage Zone

C.9.21.1.1 Within the anchorage zone the usual assumption of beam theory that plane sections remain plane is not valid.

C.9.21.1.2 The definitions of Section 9.21.1.2 (and Section 9.21.1.3) are based on the Principle of Saint Venant. Provisions for members with a length smaller than one of its transverse dimensions were included to address cases such as transverse prestressing of bridge decks (Figure 1).

C.9.21.1.3 For intermediate anchorages large tensile stresses exist locally behind the anchor. These tensile stresses are induced by compatibility of deformations ahead of and behind the anchorage.

C.9.21.1.4 Figure 2 illustrates the distinction between the local zone and the general zone. The region subjected to tensile stresses due to spreading of the concentrated tendon force into the structure is the general zone (Figure 2a). The region of very high compressive stresses immediately ahead of the anchorage device is the local zone (Figure 2b).

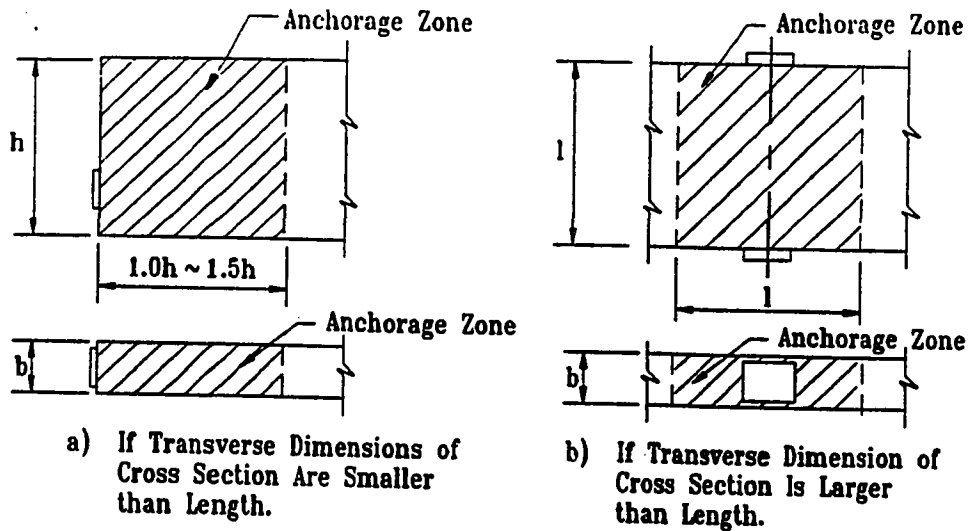


Figure 1 Geometry of the Anchorage Zone

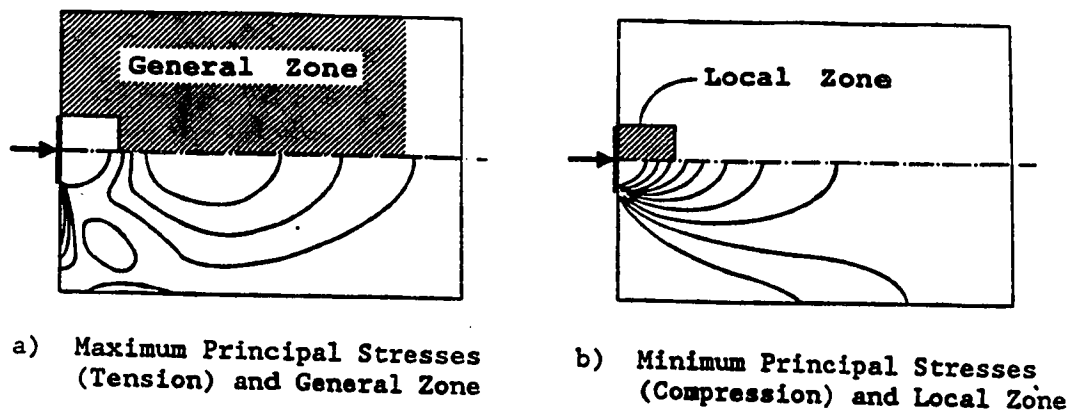


Figure 2 General Zone and Local Zone

C.9.21.2 General Zone and Local Zone

C.9.21.2.1 General Zone

C.9.21.2.1.1 In many cases the general zone and the local zone can be treated separately, but for small anchorage zones, such as in slab anchorages, local zone effects (high bearing and confining stresses) and general zone effects (tensile stresses due to spreading of the tendon force) may occur in the same region.

C.9.21.2.1.2 The main considerations in general zone design are the determination of the reinforcement requirements for the tensile forces in the anchorage zone (such as bursting forces and spalling forces) and the check of the compressive stresses at the interface with the local zone.

C.9.21.2.2 Local Zone

C.9.21.2.2.1 The local zone must resist the very high local stresses introduced by the anchorage device and transfer them to the remainder of the anchorage zone. The behavior of the local zone is strongly influenced by the specific characteristics of the anchorage device and its confining reinforcement, and less influenced by the geometry and loading of the overall structure.

C.9.21.2.2.2 The main considerations in local zone design are the effects of the high bearing pressure and the adequacy of any confining reinforcement to increase the bearing strength. Anchorage devices either have to satisfy the bearing pressure limitations and stiffness requirements of Section 9.21.5 or be accepted manufacturer's special anchorage devices which have to pass an acceptance test by an accredited independent testing agency as described in Division II, Section 4.33.11.

C.9.21.2.3 Responsibilities

C.9.21.2.3.1 The engineer of record has the responsibility to indicate the location of individual tendons and anchorage devices. Should the designer initially choose to indicate only total tendon force and eccentricity he still retains the responsibility of approving the specific tendon layout and anchorage arrangement submitted by a post-tensioning specialist or the contractor. The designer is responsible for the proper design of general zone reinforcement required by the approved tendon layout and anchorage device arrangement.

If ordinary anchorage devices are used, the engineer of record is responsible for the design of the local zone in accordance with Section 9.21.5. If special anchorage devices are used, the anchorage device supplier assumes certain responsibilities as specified in Section 9.21.2.3.2. However, use of special anchorage devices does not relieve the engineer of record from his responsibility to approve the working drawings for the anchorage zone to ensure compliance with the anchorage device supplier's specifications.

C.9.21.2.3.2 The responsibility of demonstrating the adequacy of special anchorage devices and specifying the proper reinforcement of the local zone is assigned to the supplier of the anchorage device. The anchorage device supplier has to provide information on all requirements necessary for the satisfactory performance of the local

zone to the engineer of record and to the constructor. The supplier is also responsible for furnishing the anchorage device proper. Necessary local zone confinement reinforcement has to be specified by the supplier, while design of the general zone reinforcement is the responsibility of the engineer of record. Neither local zone reinforcement nor general zone reinforcement has to be furnished by the anchorage device supplier.

C.9.21.2.3.3 The constructor is responsible for the proper execution of the instructions of both the engineer of record and the anchorage device supplier.

C.9.21.3 Design of the General Zone

C.9.21.3.1 Design Methods

The list of design methods in Section 9.21.3.1 is not meant to, preclude other recognized and verified procedures but includes some methods that have been found acceptable and useful for general zone design.

Different anchorage force arrangements have a significant effect on the general zone stresses. Therefore it is important to consider not only the final stage of a stressing sequence with all tendons stressed but also intermediate stages during construction.

The emphasis on the three-dimensional nature of the spreading of the forces is important, because it was observed that out of major plane transverse reinforcement is often neglected in design. For example, in members with thin rectangular cross sections bursting forces not only exist in the major plane of the member but also perpendicular to it.

C.9.21.3.2 Nominal Material Strengths

Since anchorage zone design is based on an ultimate load approach some plastic concrete deformation is expected. The low value for the nominal concrete compressive strength for unconfined concrete reflects this possibility. For well confined concrete the effective compressive strength could be increased, for example to 0.85 f'c in accordance with column design specifications.

C.9.21.3.3 Use of Special Anchorage Devices

For the acceptance test of special anchorage devices, reinforcement outside the local zone is permitted (Division II, Section 4.33.11.3). Equivalent reinforcement should also be placed in the actual structure. Other general zone reinforcement in the corresponding portion of the anchorage zone may be counted towards this reinforcement requirement.

C.9.21.3.4 Compressive Stresses

C.9.21.3.4.1 The interface between the confined concrete of the local zone and the usually unconfined concrete of the general zone is most critical. The provisions of Section 9.21.3.4 define the location where concrete stresses should be checked.

Results of a linear elastic analysis can be adjusted by smoothing out local stress maxima to reflect the non-linear behavior of concrete at higher stresses.

C.9.21.3.4.2 Equations (9-32) and (9-33) are applicable to rectangular cross sections if the anchorages are not located too close to the edge of the member (Figure 3). The equation is based on a Strut-and-Tie Model for a single anchor with the concrete stresses determined as indicated in Figure 4 (Reference 1). In the figure anchorage plate width, b , and member thickness, t , are equal. Equation (9-32) was modified to include cases with values of b less than t (see also Figure 15).

For multiple anchorages spaced closer than $2a$, a correction factor κ is necessary. This factor is based on an assumed stress distribution at a distance of one anchor plate width ahead of the anchorage device (Figure 5).

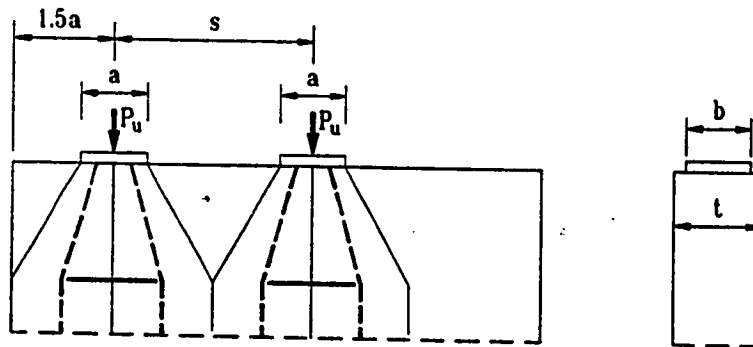


Figure 3 Notations for Equation (9-32)

C.9.21.3.5 Bursting Force

C.9.21.3.5.1 Bursting forces are caused by the lateral spreading of the concentrated prestressing forces.

C.9.21.3.5.2 Equations (9-34) and (9-35) are based on the results of linear elastic stress analyses (Reference 1). Figure 6 illustrates the terms used in the equations.

C.9.21.3.5.3 The guidelines for the arrangement of the bursting reinforcement attempt to direct the designer towards reinforcement

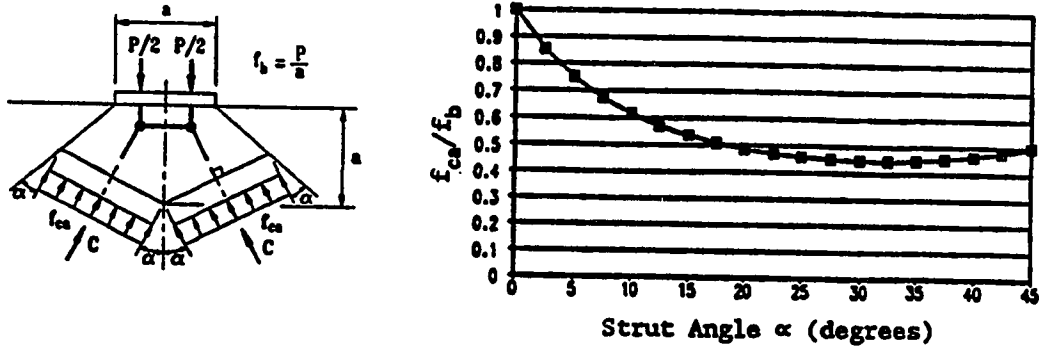


Figure 4 Local Zone and Strut Interface

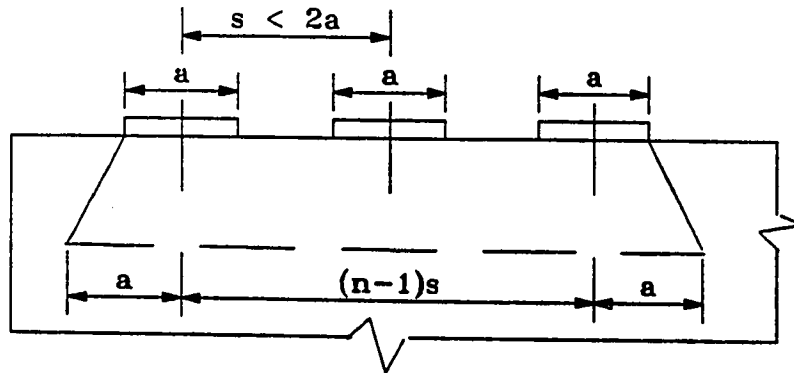
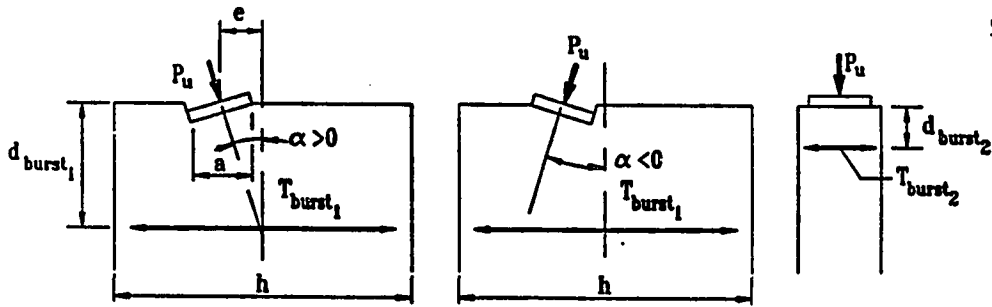
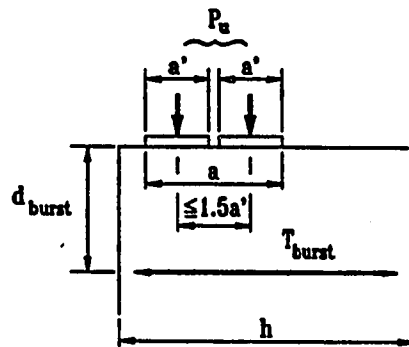


Figure 5 Closely Spaced Multiple Anchorages

patterns which are relatively close to the elastic stress distribution. The experimental test results show that this leads to a satisfactory behavior under service loads by limiting the extent and opening of cracks, and at ultimate by limiting the required amount of redistribution of forces in the anchorage zone (Reference 3). A uniform distribution of the bursting reinforcement with its centroid at d_{burst} is acceptable (Figure 7).



a) Inclined Tendons



b) Closely Spaced Anchorage Devices

Figure 6 Notations in Equations (9-34) and (9-35)

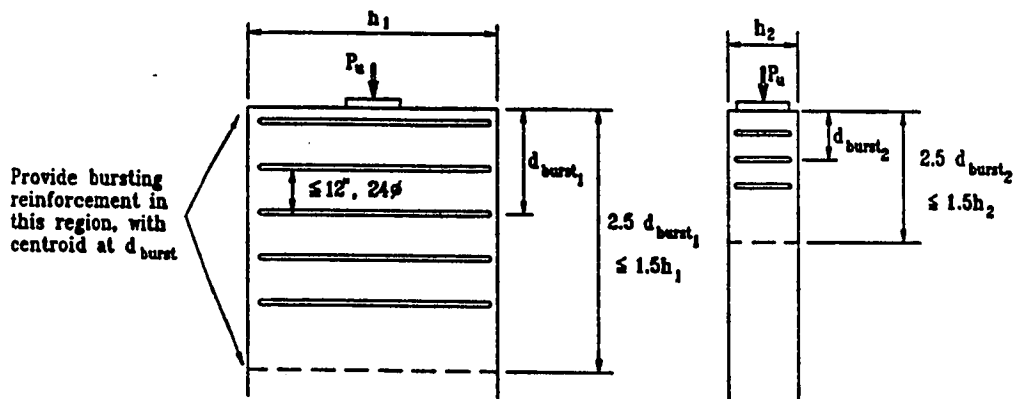


Figure 7 Bursting Reinforcement Arrangement

C.9.21.3.6
C.9.21.3.6.1
forces.

Edge Tension Forces

Figure 8 illustrates the location of the edge tension forces.

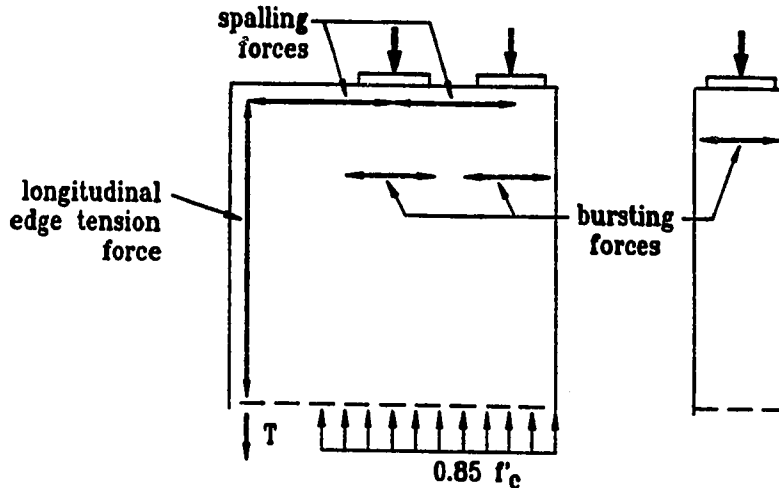


Figure 8 Edge Tension Forces

C.9.21.3.6.3 The minimum spalling force for design is two percent of the total post-tensioning force. This value is smaller than the four percent proposed by Guyon (Reference 2), and reflects both analytical and experimental findings which show that Guyon's values for spalling forces are rather high and that spalling cracks are very rarely observed in experimental studies (References 1,3).

C.9.21.3.6.4 For multiple anchorages the spalling forces are required for equilibrium and provision of adequate reinforcement is essential for the ultimate load capacity of the anchorage zone (Figure 9). These tension forces are similar to the tensile tie forces existing between footings in deep walls supported on individual footings. In most cases the minimum spalling reinforcement of Section 9.21.3.6.3 will control.

C.9.21.3.6.5 The determination of the edge tension forces for eccentric anchorages is illustrated in Figure 10. Either type of axial-flexural beam analysis is acceptable. As in the case for multiple anchorages this reinforcement is essential for equilibrium of the anchorage zone. It is important to consider stressing sequences that may cause temporary eccentric loadings of the anchorage zone.

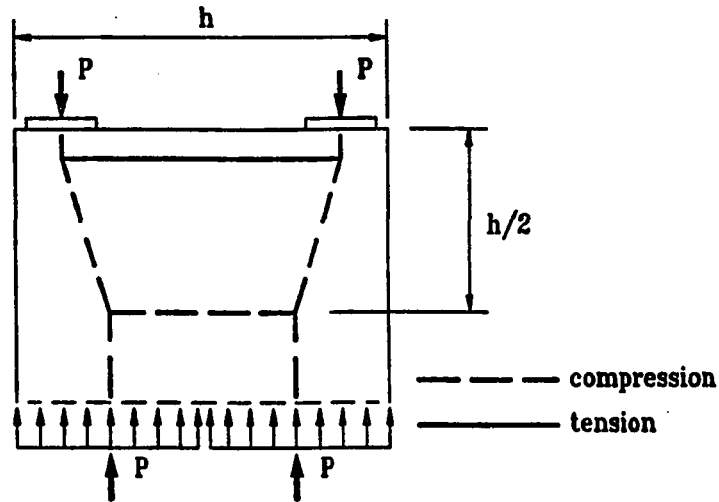


Figure 9 Spalling Forces Between Multiple Anchorages

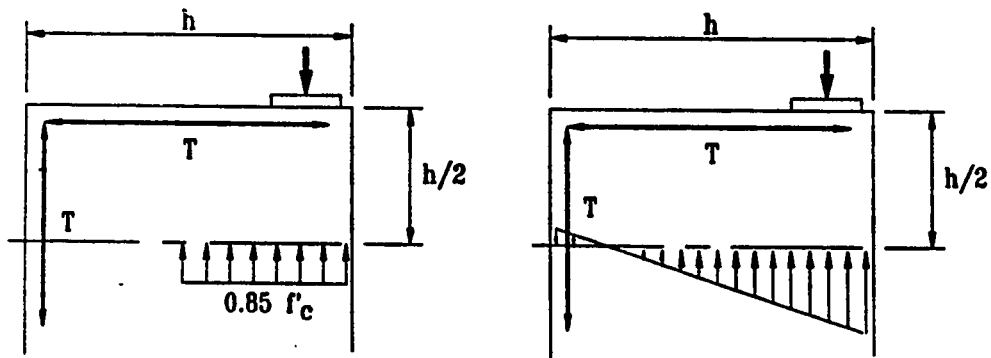


Figure 10 Determination of Edge Tension Forces for Eccentric Anchorages

C.9.21.3.6.6 Figure 11 illustrates the reinforcement requirements of Section 9.21.3.6.6.

C.9.21.3.7 Intermediate Anchorages

Phase B of Project NCHRP 10-29 is currently underway and is scheduled for completion by Fall 1991. The provisions for intermediate anchorages will address problems such as reinforcement

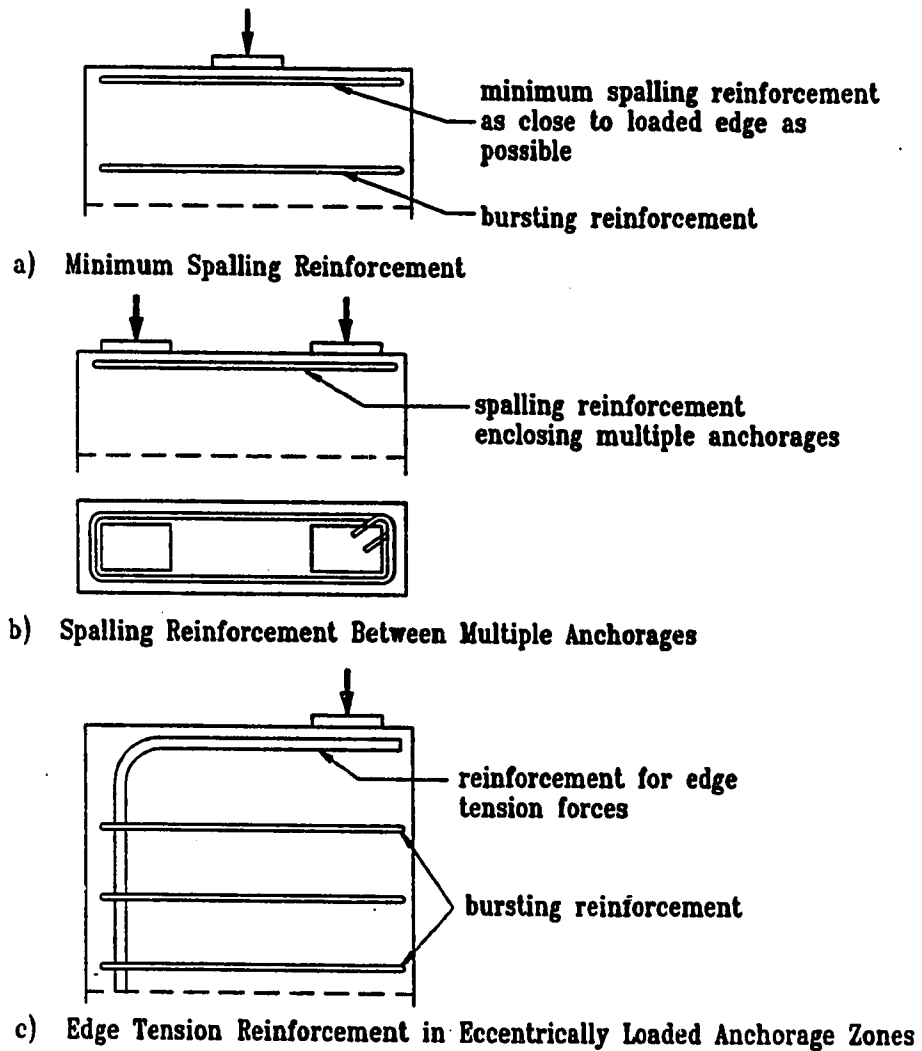


Figure 11 Arrangement of Spalling Reinforcement

requirements to control cracking behind the anchor and local bending stresses at blisters and ribs.

C.9.21.3.8 Diaphragms

Diaphragms are used for the anchorage of external tendons in post-tensioned box girder bridges. The provisions on

diaphragms will address bursting reinforcement requirements for these cases. It is important to note that the provisions of Section 9.21.3.5.2 do not apply to diaphragms (Figure 12).

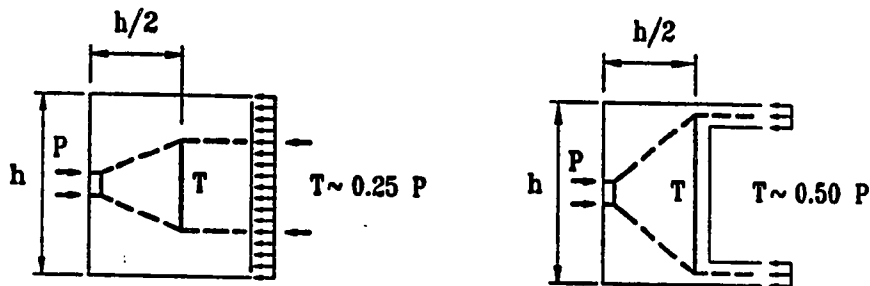


Figure 12 Bursting Force for Member with Rectangular Cross Section and for Diaphragm

C.9.21.3.9 Multiple Slab Anchorages

The provisions on multiple slab anchorages will address stressing sequence and reinforcement requirements.

C.9.21.4 Application of the Strut-and-Tie Model to the Design of Anchorage Zones

C.9.21.4.1 General

C.9.21.4.1.1 A lower bound of the ultimate load that a given concrete structure or member can carry can be obtained by application of the lower bound theorem of the theory of plasticity of structures. Models in which the actual flow of forces in a structure is approximated by a series of straight compression members (struts), and straight tension members (ties) which are connected at discrete points (nodes) are called Strut-and-Tie Models. If sufficient ductility (rotation capacity) is present in the system, Strut-and-Tie Models fulfill the conditions for the application of the above mentioned theorem, and the ultimate load predicted on the basis of a Strut-and-Tie Model will be a conservative estimate of the actual ultimate load of the structure or member. Figure 13 shows the linear elastic stress field and a corresponding Strut-and-Tie Model for the case of an anchorage zone with two eccentric anchors (Reference 4).

C.9.21.4.1.2 In Figure 14 Strut-and-Tie Models for some typical

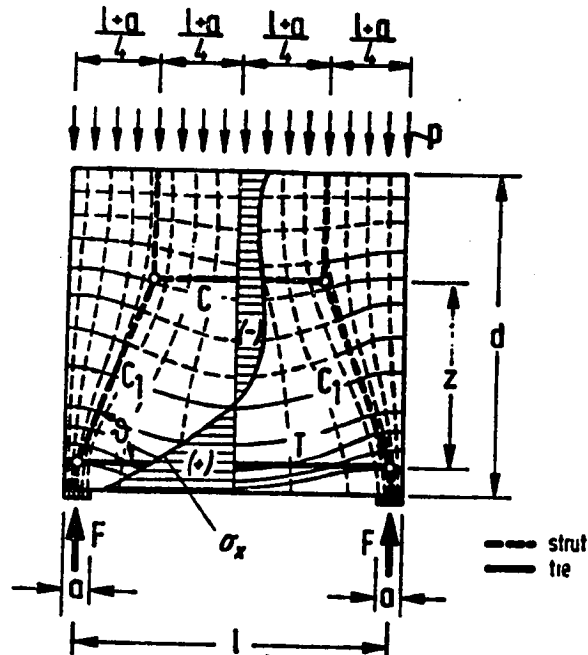


Figure 13 Stress Field and Strut-and-Tie Model (from Reference 4)

load cases for anchorage zones are shown.

C.9.21.4.2 Nodes

Nodes are critical elements of the Strut-and-Tie Model. The entire local zone constitutes the most critical node (or group of nodes) for anchorage zones. In Section 9.21.5 the adequacy of the local zone is achieved by limiting the bearing pressure under the anchorage device. Alternatively, this limitation may be exceeded if the adequacy of the anchorage device is proven by the acceptance test of Division II, Section 4.33.11.

C.9.21.4.3 Struts

C.9.21.4.3.1 For Strut-and-Tie Models oriented on the elastic stress distribution the nominal concrete strength specified in Section 9.21.3.2 is adequate. However, if the selected Strut-and-Tie Model deviates considerably from the elastic stress distribution, large plastic deformations are required and the concrete strength should be reduced. The concrete strength should also be reduced if the concrete is cracked due to other load effects.

C.9.21.4.3.2 Ordinarily the geometry of the local zone node and thus of the interface between strut and local zone is determined by the

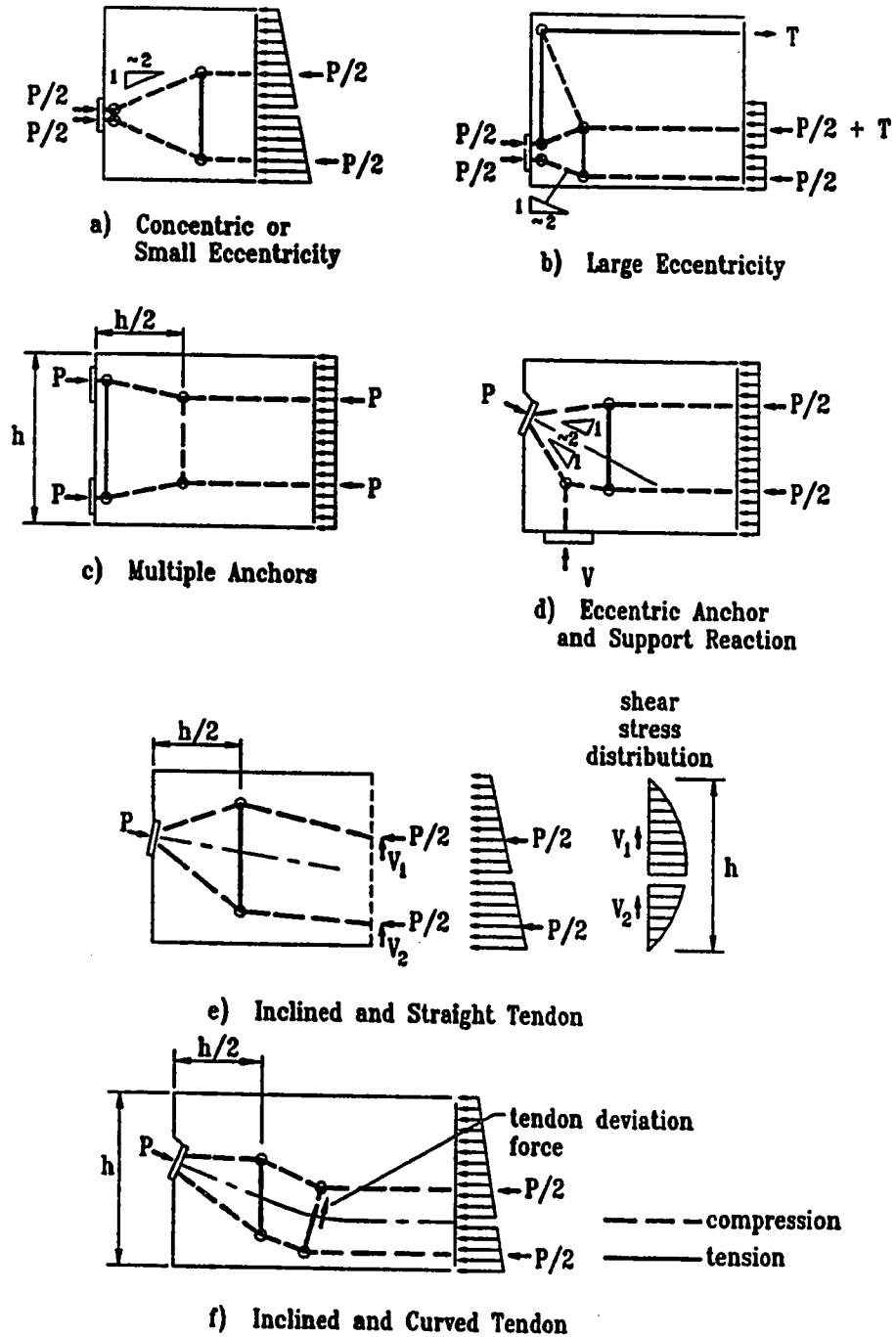


Figure 14 Typical Strut-and-Tie Models for Anchorage Zones

size of the bearing plate and the selected Strut-and-Tie Model, as indicated in Figure 15a. For special anchorage devices based on the acceptance test of Division II, Section 4.33.11, it is suggested to check the stresses at a larger distance from the node, assuming that the width of the strut increases with the distance from the local zone (Reference 1, Figure 15b).

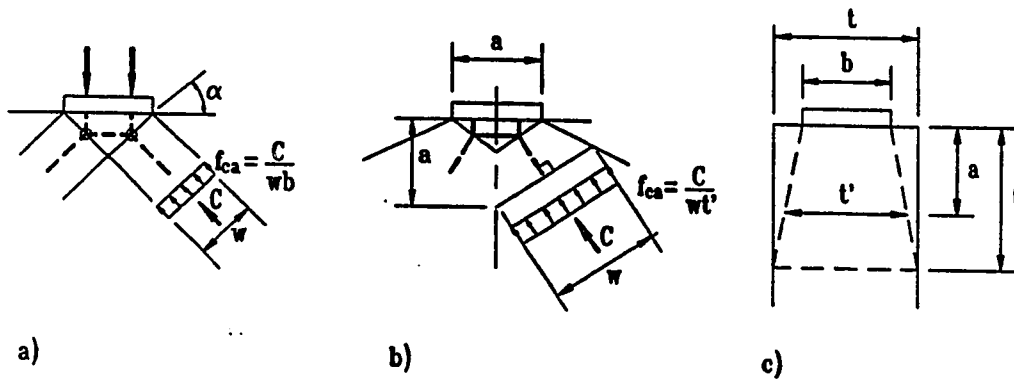


Figure 15 Critical Section for Compression Struts in Anchorage Zones

C.9.21.4.3.3 The determination of the dimension of the strut in the direction of the thickness of the member is illustrated in Figure 15.

C.9.21.4.4 Ties

C.9.21.4.4.1 Because of the unreliable strength of concrete in direct tension, it is prudent to neglect it entirely.

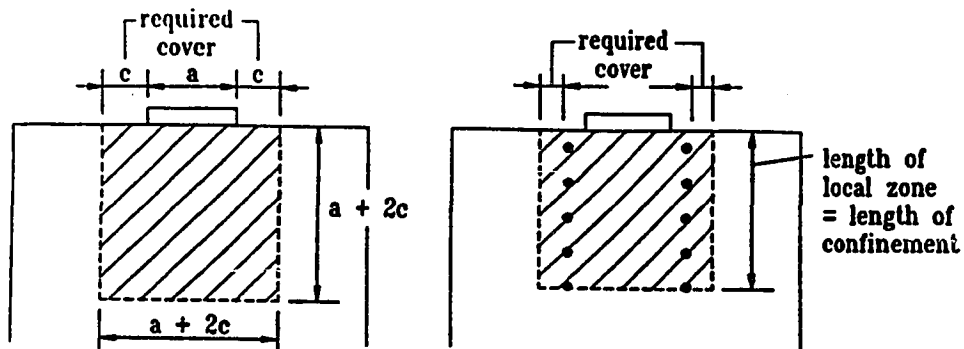
C.9.21.4.4.2 It is important that the reinforcement layout is in agreement with the selected Strut-and-Tie Model. In the selection of a Strut-and-Tie Model practical reinforcement arrangements should be considered.

C.9.21.5 Design of the Local Zone

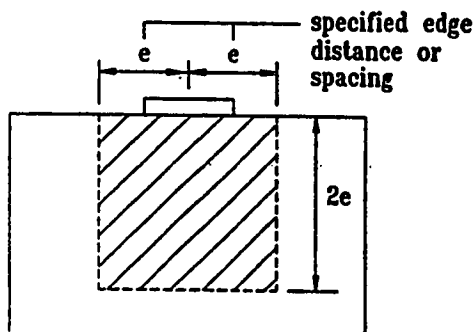
C.9.21.5.1 Dimensions of the Local Zone

The local zone is the highly stressed region immediately surrounding the anchorage device. It is convenient to define this region geometrically, rather than by stress levels. Figure 16 illustrates the local zone definitions of Sections 9.21.5.1.1 to 9.21.5.1.3.

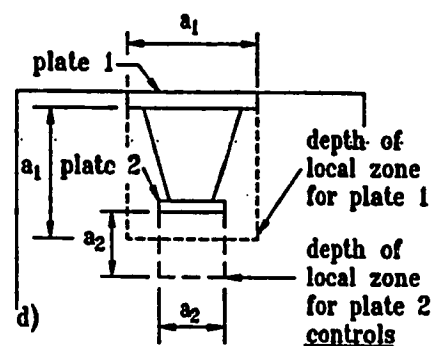
In Section 9.21.5.1.1 knowledge of a minimum cover



a) Manufacturer's Recommendations Available



b) Manufacturer's Recommendations Not Available



c) Length of Local Zone for Multiple Bearing Surfaces

Figure 16 Geometry of the Local zone

requirement over the anchorage bearing plate is needed. AASHTO does not specify any particular concrete cover required for corrosion protection of anchorage devices. In ACI 318-89, Section 6.3.10 a cover of not less than 1-1/2 in for concrete exposed to earth and weather is specified. It is recommended to use this value for Section 9.21.5.1.1 of the proposed specification.

C.9.21.5.2 Bearing Strength

Section 9.21.5.2 provides bearing pressure limits for anchorage devices that are not to be tested in accordance with the

acceptance test of Division II, Section 4.33.11. Alternatively, these limits may be exceeded if an anchorage system passes the acceptance test. Figures 17, 18, and 19, illustrate the specifications of Sections 9.21.5.2.2 to 9.21.5.2.4 (Reference 5).

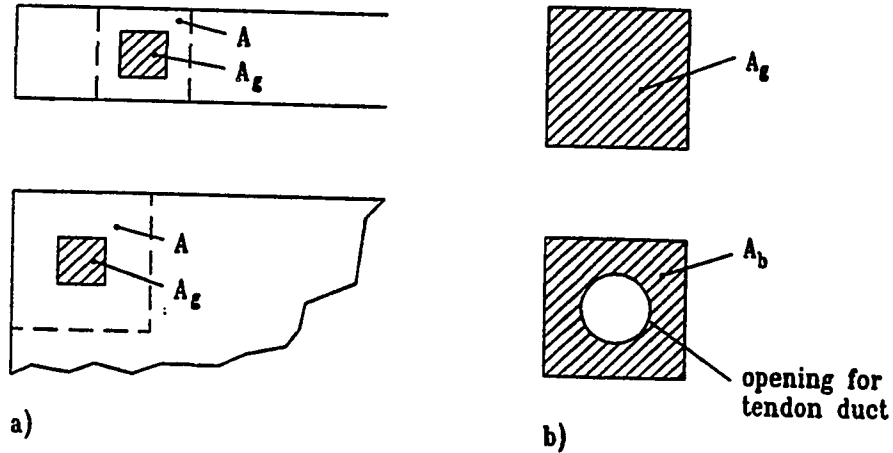


Figure 17 Area of Supporting Concrete Surface in Equation (9-35)

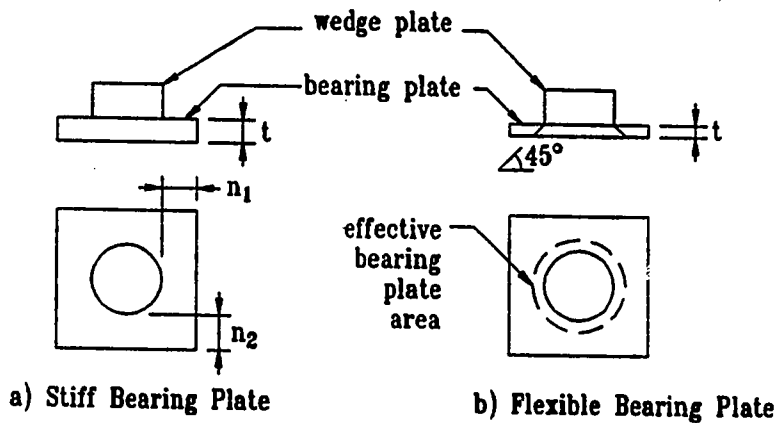


Figure 18 Effective Bearing Plate Area for Anchorage Devices with Separate Wedge Plates

C.9.21.5.3

Special Anchorage Devices

Most anchorage devices fall in this category and have

to pass the acceptance test of Division II, Section 4.33.11. However, many of the anchorage systems currently available in the United States have passed equivalent acceptance tests. The results of these tests may be acceptable if the test procedure is generally similar to that specified in Division II, Section 4.33.11.

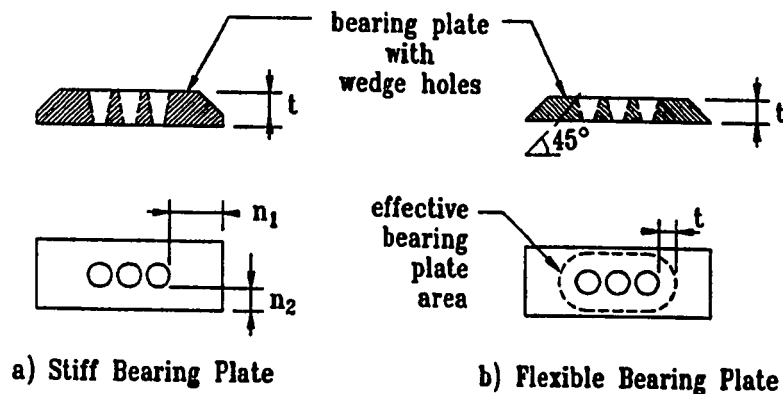


Figure 19 Effective Bearing Plate Area for Anchorage Device Without Separate Wedge Plate

C.9.22 PRETENSIONED ANCHORAGE ZONES

Provisions for pretensioned anchorage zones were beyond the scope of Project NCHRP 10-29, therefore the current AASHTO Standard Specifications for pretensioned concrete were included in this section. Many results for post-tensioned concrete are also applicable to anchorage zones in pretensioned concrete, but some differences exist due to the more gradual force transfer of pretensioning tendons.

C.9.22.1 This provision is roughly equivalent to the provisions of Section 9.21.3 in the current AASHTO specifications, except that the requirements were adjusted for the application of factored load design. Section 9.22.1 of the proposed specifications for pretensioned concrete corresponds to the spalling force provisions in Section 9.21.3.6 for post-tensioned anchorage zones.

C.9.22.2 This provision corresponds to the bursting force requirements of Section 9.21.3.5.

C.9.29 **EFFECTS OF TENDON CURVATURE**
 C.9.29.1 **General**

The formulas to be presented in this section will be simplifications and extensions of formulas originally proposed in References 6 and 7.

C.9.29.2 **In-Plane Forces**

In-plane forces occur for example in anchorage blisters or curved webs (Figures 20 and 21). Without adequate reinforcement the tendon deviation forces may rip through the concrete cover on the inside of the tendon curvature or unbalanced compressive forces may push off the concrete on the outside of the curvature. Small radial tensile stresses may be resisted by concrete in tension.

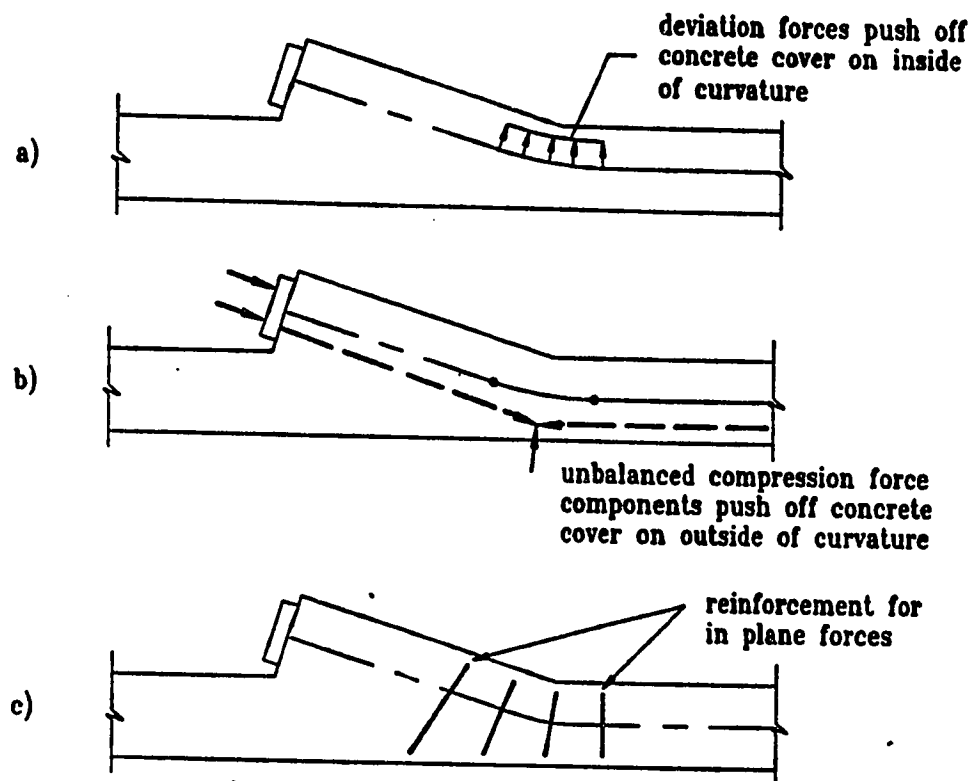


Figure 20 In-Plane Forces in a Blister

C.9.29.3 **Out-of-Plane Forces**

Out-of-plane forces are caused in multi-strand post-tensioning tendons by the spreading of the strands or wires within the

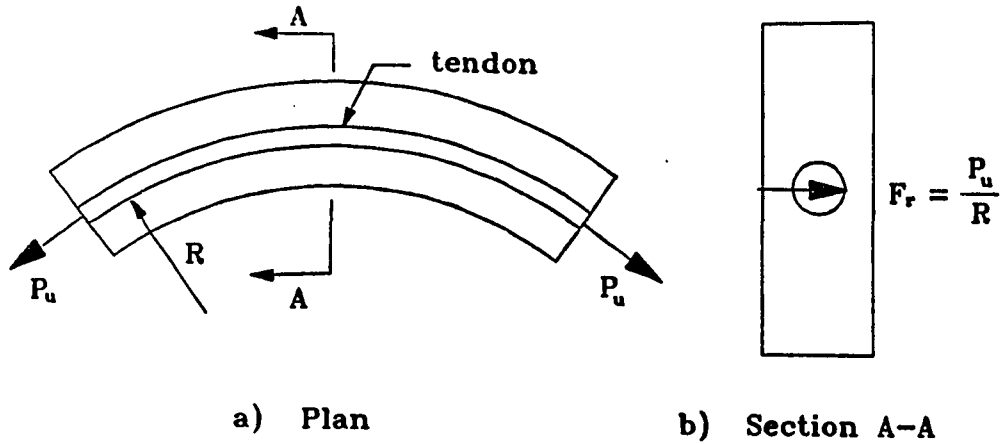
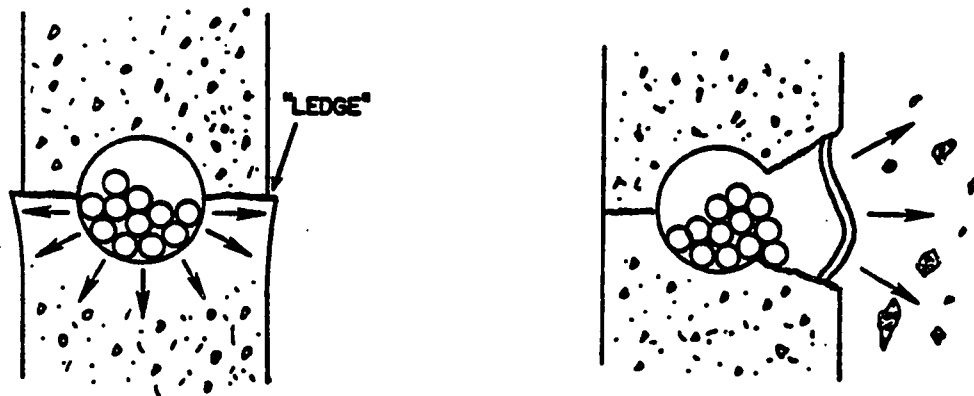


Figure 21 In-Plane Forces in a Curved Member



TENDON AT STRESSING LOAD
 LARGE RADIAL FORCES DUE TO
 "FLATTENING OUT" OF TENDON
 BUNDLE INITIATE CRACKING IN
 VICINITY OF SHARPEST CURVATURE

FAILURE
 SIDE FACE RUPTURE AT
 POINT OF SHARPEST
 CURVATURE

Figure 22 Out-of-Plane Forces (from Reference 6)

duct (Figure 22, References 6 and 7). Small out-of-plane forces may be resisted by concrete in shear, otherwise spiral reinforcement is most effective to resist out-of-plane forces.

DIVISION II - CONSTRUCTION

C.4.33.11 Post-Tensioning Special Anchorage Device Acceptance Test

C.4.33.11.3 Figure 23 shows a local zone specimen with the local zone reinforcement in the upper portion of the specimen and the supplementary reinforcement according to Section 4.33.11.3 in the lower portion of the specimen.

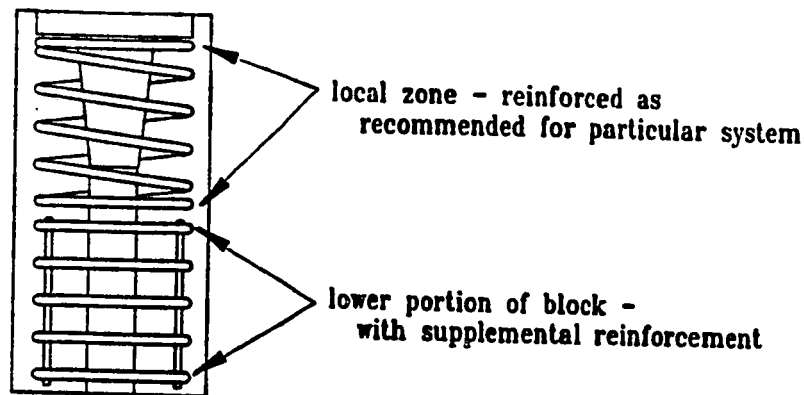


Figure 23 Special Anchorage Device Acceptance Test Specimen

C.4.33.11.5 Long term loading has been found to be more critical for the behavior of the local zone than short term loading. A cyclic loading test gives comparable results to sustained loading tests, but is less time consuming than the sustained loading test (Reference 5).

Loading in accordance with normal usage of the anchorage device in post-tensioning applications means loading through the wedge plate if available, or over an area formed by the perimeter of the wedge hole pattern. It is not required to load the specimen through the tendon.

C.4.33.11.6 The crack width requirements of Section 4.33.11.6 are based on recommendations in Reference 8. A moderately aggressive environment is characterized by moist environments where deicing or sea salts may be present in mists, but where direct exposure to corrosive agents is prevented (Reference 5). This should include most bridge applications.

C.4.33.11.8 Records of the anchorage device acceptance test have to be provided by the anchorage device supplier to the engineer of record and to the constructor.

C.4.33.17 Post-Tensioned Anchorage Zones

Anchorage zones are very critical regions of a structure. Therefore construction should follow exactly the specifications of the engineer of record and the anchorage device supplier. Change of anchorage zone details have to be approved by the engineer of record.

REFERENCES

- (1) Burdet, O.L., "Analysis and Design of Anchorage Zones in Post-Tensioned Concrete Bridges", Ph.D. dissertation, University of Texas at Austin, May 1990.
- (2) Guyon, Y., "Prestressed Concrete", John Wiley and Sons, New York, 1953.
- (3) Sanders, D.H., "Design and Behavior of Post-Tensioned Concrete Anchorage Zones", Ph.D. dissertation, University of Texas at Austin, August 1990.
- (4) Schlaich, J., Schäfer, K., Jennewein, M., "Towards a Consistent Design of Structural Concrete", PCI Journal, Vol.32, No.3, May-June 1987, pp.74 - 151.
- (5) Roberts, C.L., "Behavior and Design of the Local Anchorage Zone in Post-Tensioned Concrete", Master's thesis, University of Texas at Austin, May 1990.
- (6) Stone, W.C., Breen, J.E., "Behavior of Post-Tensioned Girder Anchorage Zones", PCI Journal, Vol.29, No.1, January-February 1984, pp.64-109.
- (7) Stone, W.C., Breen, J.E., "Design of Post-Tensioned Girder Anchorage Zones", PCI Journal, Vol.29, No.1, January-February 1984, pp.64-109.
- (8) Leonhardt, F., "Cracks and Crack Control in Concrete Structures", IABSE Proceedings, P109/87, 1987, pp.25-44.

CHAPTER 8
CONCLUSIONS AND RECOMMENDATIONS

8.1 Introduction

The major objective of this research was to develop a rational and systematic approach to anchorage zone design for post-tensioned structures. One of the first developments was the division of the anchorage zone into a local zone and a general zone. The local zone is defined as the volume of concrete surrounding and immediately ahead of the anchorage device that is subjected to high bearing stresses. The behavior of the local zone is strongly influenced by the specific characteristics of the anchorage device and its confining reinforcement but is less influenced by the geometry and loading of the overall structure. The general zone is defined as the region within which the concentrated prestressing force spreads out to a more linear stress distribution over the cross section of the member (Saint Vénant Region). This division of the anchorage zone into local zone and general zone enabled a division of responsibility. The local zone is the primary responsibility of the anchorage device supplier, while the general zone is the primary responsibility of the engineer-of-record. Responsibilities are also assigned to the constructor.

The definition of the local zone permitted the development of a certification testing procedure for the local zone [143]. The certification test was patterned after existing tests recommended by FIP. By patterning the certification after existing tests that most major manufacturers already follow in Europe, the certification should not present a large burden to anchorage device manufacturers. Certification will be required only for special anchorage devices, which are generally anchorage devices that utilize high bearing stresses and require local confining reinforcement.

Techniques for the design and analysis of the general zone are the emphasis of this dissertation and are continuing to be studied in

a second phase of the overall research project at the University of Texas at Austin. The second phase continues the research on anchorage zones for special post-tensioning applications such as blisters, ribs, diaphragms, and closely spaced deck anchors. The results of the first phase have provided methods for the design and analysis of girder end type anchorage zones with concentric anchorages, multiple anchorages, eccentric anchorages, and inclined anchorages with tendon curvatures. Good correlation was found between these design methods and the tests conducted. In Chapter 7, proposed revisions to the AASHTO Bridge Specification were presented. The new sections implement the division of responsibility within the anchorage zone. The various failure modes of the anchorage zone are described, and analysis and design procedures for the anchorage zone developed in this dissertation and through the research of Burdet [25] and Roberts [143] are presented. The specification provides guidance to those designing the components of the anchorage zones for both the serviceability and ultimate limit states. The following two sections will summarize the findings presented in this dissertation for both prediction of the first cracking load and the prediction of the ultimate strength.

8.2 First Cracking Prediction

The prediction of the first cracking load relied upon the accurate determination of the peak tension stress and the concrete tension capacity. Cracking occurred in the spalling zone, the longitudinal edge tension zone, and the bursting zone. The following methods are recommended for first crack prediction:

- 1) To determine a conservative estimate of the first bursting cracking load, the peak bursting stress should be determined from a two-dimensional finite element analysis. The two-dimensional analysis should be modified using an effective thickness of the cross section equal to the section thickness minus the inside diameter of the duct. The modified analytical stress should be equated to a reduced concrete tension strength equal to $4.2\sqrt{F'_c}$. In the bursting zone, where

compression stresses can be quite high, this tensile strength of concrete is necessary to include the reduced capacity caused by triaxial stress effects. The average of the test-to-predicted first cracking load ratios was then 1.28 with a coefficient of variance equal to 0.17.

2) If a finite element model is not available to estimate the peak bursting stress, the peak bursting stress from Guyon's symmetrical prism can be used in combination with the effective thickness and concrete tension strength as discussed in conclusion 1. Guyon's symmetrical prism was found to be inconsistent relative to the finite element analysis. It did provide conservative results for all but three specimens. These three specimens had test-to-predicted first cracking load ratios of 0.99. The average for all the specimens tested was 1.39, and the coefficient of variance was 0.23.

3) The longitudinal edge tension cracking load can best be determined by predicting the peak stress using beam theory ($P/A \pm Mc/I$) in combination with a concrete tensile strength of $6\sqrt{f'_c}$. The prediction of the first longitudinal edge tension crack was conservative for the three specimens where the resultant force was outside the kern and cracking was observed. Little data is available for verifying the first cracking load prediction method. Longitudinal edge tension cracking was observed in many specimens near the ultimate load due to a redistribution of forces. These cracks were not predicted from the elastic analyses.

4) Test comparisons with the spalling cracking predictions showed that the very high stresses predicted by the finite element analysis near the loading surface do not produce cracking except in eccentric anchorages when the resultant post-tensioning force is outside the kern and in multiple anchorages when the anchors are sufficiently spaced apart to cause a large spalling tension force. Very conservative predictions of the spalling cracking were determined if the stress on the loaded surface fiber estimated by a finite element analysis was

used as the peak spalling stress. The tensile strength of concrete was taken as $6\sqrt{f'_c}$ since compression stresses are very small.

These models help to give an engineer an estimate for the first cracking load. The models were verified only on specimens with isolated anchorage forces, without creep or shrinkage effects, and with no forces other than the post-tensioning force applied to the specimens. In an actual girder, many other forces may exist that could induce cracking. Unfortunately, no data is available for prediction of these cracking forces. Fortunately, the calculation of the first cracking load is rarely critical in a design situation.

8.3 Ultimate Capacity Prediction

Two ultimate strength models based on the strut-and-tie model (STM) were developed: the basic STM and the modified STM. The basic STM assumed that there was an elastic stress distribution at the end of the general zone, while the modified STM permitted a more plastic stress distribution. The modified STM allows the centroids of the compression struts to move toward the tendon axis until the load predicted from the tension tie capacity matched that predicted from the compression strut capacity. Both models are based on the lower bound theory of plasticity. The lower bound theory of plasticity assumes that both internal and external equilibrium are satisfied, and that stresses do not exceed the material yield conditions. The theory also assumes that the system has sufficient ductility to develop the yield conditions.

1) When using the basic or modified STM, it was critical to check the capacity of the tension ties, the bearing capacity, the node compression capacity, the node-strut interface capacity, the local zone-general zone interface capacity and locations of changes in section thickness. The compression capacities (bearing, node, and strut) were determined by using the formula developed by Roberts [143]. If the anchorage device selected in design by the engineer-of-record is a test certified anchorage, it can be assumed that it satisfies node

design requirements. It is, therefore, only necessary to check the tension tie capacity, the local zone-general zone interface capacity, and locations of changes in section thickness.

2) The statistical analyses showed that the basic STM average of the test-to-predicted ratios for ultimate was 1.50 with a coefficient of variance of 0.33. The STM is a lower bound model based on the theory of plasticity; it should be a conservative estimate of the ultimate strength of the specimens.

3) The statistical analysis showed that the modified STM average of the test-to-predicted ratios for ultimate was 1.04 with a coefficient of variance of 0.19. The model predicted 15 of the 36 specimens unconservatively.

4) Because of the use of long spirals in the test specimens and concern regarding the effectiveness of long spirals for confining concrete located more than a plate width ahead of the anchorage device, an analysis using the modified STM was conducted with the local zone-general zone interface assumed to be at a plate width ahead of the loading surface with the stress on that plane limited to $0.7f'_c$. Using these restrictions raised the average of the test-to-predicted ratios for ultimate for the modified STM to 1.19 and actually lowered the coefficient of variance to 0.16.

5) The basic STM is recommended for general use in anchorage zone design and analysis as a conservative and sufficiently accurate model. The modified STM more accurately models the specimens but is not recommended for design. By using the basic STM and forcing the tension ties to control the design, the modified STM indicates that the anchorage zone will have additional capacity over what the basic STM predicts. This additional capacity permits excessive cracking to be a warning sign before failure and provides some additional factor of safety.

6) Specimens which had reinforcement significantly different than that determined from an elastic analysis had additional cracking and

sometimes reduced strength. Therefore, it is recommended that only the reinforcement which is placed within a distance of 1.5 times the section width from the loading surface be considered as effective for the STM calculations, and it is recommended that the centroid of that reinforcement be located close to the pattern that would be indicated by an elastic analysis. This does not mean that an elastic analysis must be performed but that good engineering judgement should be exercised when placing reinforcement so that overly large plastic redistribution of forces is not required.

7) It is important for specimens with curved tendons that tie-back reinforcement be provided. Tie-back reinforcement is modelled in the STM through the use of equivalent forces applied to the compression struts or tension ties. To prevent large cracks and explosive failures, the resulting STM and the portion of the radial forces that are resisted by reinforcement in tension should approximate the elastic stress distribution.

8) The compression struts were assumed to have a width equal to twice the distance from the load axis to the line of action of the strut. The local zone node was also very critical and must be checked if a certification test has not been performed. Most other nodes in the anchorage zone, except the local zone node, are nodes distributed over a large enough distance to prevent high stresses. All nodes should be examined to ensure that this assumption is correct.

9) It is critical to consider anchorage zone analysis and design as a three-dimensional problem. One T-beam section was tested, and the applicability of the STM was quite good. The three-dimensional effects can be considered by dividing the member into multiple two-dimensional planes. The interaction of models used on these planes must be considered, and the model loadings and results must be consistent.

10) Using methods based on Guyon's symmetrical prism to predict the ultimate capacity were not as consistent as the STM and can yield

unconservative results especially for anchorage zones that are more complicated than a concentric anchorage zone.

8.4 Future Research

The research conducted during the first and second phases of the NCHRP research on anchorage zone is a good step towards a better understanding of anchorage zone design and analysis. The purpose of the experimental portion of this research project was to verify the analysis tools developed in this project. No replicate tests and only a few of the many possible anchorage zone configurations were experimentally tested. Therefore, there is much room for further investigation and refinement. Future research should continue to keep the problem in perspective. The major goal is to have safe anchorage zone designs. Though extremely vital to the safety of a post-tensioned structure, the economic cost of reinforcement placed in the anchorage zone is small relative to the total cost of the construction project. Thus, the major goals in the research were a better understanding of the anchorage zone and the development of designs that are consistent and safe. The intent was not necessarily to reduce the reinforcement amounts.

Further research is still needed in the following areas:

- 1) To develop a systematic approach to the distribution of radial forces between tension and compression when curved tendons are used,
- 2) To determine if long spirals are effective in confining concrete at more than a plate width from the loading surface and whether reinforcement can be effectively used to confine compression struts in the general zone,
- 3) To verify the STM theories in actual girders where additional forces other than those caused by the anchorage alone exist,
- 4) To develop guidelines for when reinforcement can be considered fully effective or partially effective,

- 5) To do long-term and fatigue testing of anchorage zones to investigate any adverse effects,
- 6) To develop guidelines for when and how concrete tension capacity can be included in the ultimate strength capacity,
- 7) To investigate anchorage zones with inclined anchorages and straight tendons as well as with section thickness changes, and
- 8) To investigate design of anchorage zones with concrete compressive strength at the time of stressing greater than 7000 psi in view of possible reductions in ductility and/or efficiency of the concrete in carrying the compression struts.

APPENDIX A

SURVEY LETTER



COLLEGE OF ENGINEERING
THE UNIVERSITY OF TEXAS AT AUSTIN

*Bureau of Engineering Research • Phil M. Ferguson Structural Engineering Laboratory
10100 Burnet Road • Austin, Texas 78758-4497 • (512) 471-3062*

March 31, 1987

Dear Mr.

The University of Texas at Austin is currently working under National Cooperative Highway Research Program sponsorship on Project 10-29, "Anchorage Zone Reinforcement for Post-Tensioned Concrete Girders," which is a direct response to an AASHTO-submitted problem statement reflecting concerns with the present AASHTO criteria (see Enclosure 1). The project's basic objectives project are:

- (1) Evaluation of the state-of-the-art for bridge tendon anchorage zone reinforcement techniques.
- (2) Exploration of typical applications through physical tests.
- (3) Development of improved analytical procedures.
- (4) Development of a generalized approach for anchorage zone analysis and proportioning of required reinforcement for both the serviceability (cracking) and strength limit states.
- (5) Development of a draft AASHTO Specification revision.

For the project to be of the most use to AASHTO, we need early input to make sure that major user concerns are addressed. We hope your organization can inform us of what is being done in design and approval of working drawings for anchorage zones.

We are enclosing a general guideline to define some terms and to point out possible areas of concern regarding post-tensioned anchorage zones. We are interested in your specific concerns and difficulties, as well as your evaluation of items which are of no concern or are really not problems.

You will note that we have subdivided the anchorage zone behavior into two areas, which reflect some difference in responsibilities. The first or local zone is that region that closely surrounds the specific hardware device. In this region the manufacturer or supplier often has a proprietary product and is basically interested in the local behavior. Such questions as effective bearing area and very local confinement immediately around the anchor fall into this classification. While the manufacturer or supplier has the prime responsibility, there may be a need for AASHTO criteria to establish

performance requirements or provide checking procedures even for this local problem. The second or general region is the portion of the anchorage zone more remote from the immediate anchorage hardware device. These are the areas subject to spalling or bursting stresses, where the designer and the constructor must ensure that proper confinement or reinforcement are provided to prevent premature failure or unwanted cracking. There obviously needs to be better AASHTO criteria for these general cases.

Could you send us, at your earliest convenience, at least the following:

- (1) A brief statement of problems your organization has encountered in design, checking or inspection of post-tensioned anchorage zones.
- (2) A description of any analysis procedures, evaluation criteria or references you use in design or checking anchorage zones.
- (3) Any criteria that you may use to judge when no special attention has to be paid to the post-tensioning system.
- (4) Any knowledge of specific failures or severe distress in post-tensioned anchorage zones (please include photos or crack pattern sketches).
- (5) Sample plans or details of both commonly used and special anchorage applications.

If you indicate, we will be happy to share the results of the project.

We hope that your organization can provide this highly needed input into the AASHTO specification process. The final result will depend to a large extent on the scope and accuracy of the information submitted.

Sincerely yours,

John E. Breen Gregory L. Fenves
Project Supervisors

Return all replies to:
David H. Sanders
Ferguson Structural Engineering Laboratory
10100 Burnet Road #24
Austin, TX 78758

AASHTO Post-Tensioning Anchorage Provisions

Section 8 REINFORCED CONCRETE

(For information only- Section 8 does not apply to prestressed concrete.)

8.1 APPLICATION

8.1.2 Notations

- A_1 = loaded area (Articles 8.15.2.1.3 and 8.16.7.2)
 A_2 = maximum area of the portion of the supporting surface that is geometrically similar to and concentric with the loaded area (Articles 8.15.2.1.3 and 8.16.7.2)

8.15 SERVICE LOAD DESIGN METHOD (Allowable Stress Design)

8.15.2 Allowable Stresses

8.15.2.1 Concrete

Stresses in concrete shall not exceed the following.

8.15.2.1.3 Bearing Stress

The bearing stress, f_b , on loaded area shall not exceed $0.30 f'_c$.

When the supporting surface is wider on all sides than the loaded area, the allowable bearing stress on

the loaded area may be increased by $\sqrt{A_2/A_1}$, but not by more than 2.

When the supporting surface is sloped or stepped, A_2 may be taken as the area of the lower base of the largest frustrum of the right pyramid or cone contained wholly within the support and having for its upper base the loaded area, and having side slopes of 1 vertical to 2 horizontal.

When the loaded area is subjected to high edge stresses due to deflection or eccentric loading, the allowable bearing stress on the loaded area, including any increase due to the supporting surface being larger than the loaded area, shall be multiplied by a factor of 0.75.

8.31 MECHANICAL ANCHORAGE

8.31.1 Any mechanical device shown by tests to be capable of developing the strength of reinforcement without damage to concrete may be used as anchorage.

8.31.2 Development of reinforcement may consist of a combination of mechanical anchorage plus additional embedment length of reinforcement between point of maximum bar stress and the mechanical anchorage.

Section 9 PRESTRESSED CONCRETE

9.1 APPLICATION

9.1.3 Definitions

End Anchorage—Length of reinforcement, or mechanical anchor, or hook, or combination thereof, beyond point of zero stress in reinforcement; mechanical device to transmit prestressing force to concrete in a post-tensioned member.

End Block—Enlarged end section of member designed to reduce anchorage stresses.

9.15 ALLOWABLE STRESSES

9.15.2 Concrete

9.15.2.4 Anchorage Bearing Stress

Post-tensioned anchorage at
 service load 3,000 psi
 (but not to exceed $0.9 f'_c$)

9.21 ANCHORAGE ZONES

9.21.1 For beams with post-tensioning tendons, end blocks shall be used to distribute the concentrated prestressing forces at the anchorage. Where all tendons are pretensioned wires or 7-wire strand, the use of end blocks will not be required. End blocks shall have sufficient area to allow the spacing of the prestressing steel as specified in Article 9.25. Preferably, they shall be as wide as the narrower flange of the beam. They shall have a length at least equal to three-fourths of the depth of the beam and in any case 24 inches. In post-tensioned members, a closely spaced grid of both vertical and horizontal bars shall be placed near the face of the end block to resist bursting stresses. Amounts of steel in the end grid should follow recommendations of the supplier of the anchorage. Where such recommendations are not available the amount of steel in the grid shall be designed and shall consist of at least No. 3 bars on 3-inch centers in each direction placed not more than 1 1/2 inches from the inside face of the anchor bearing plate.

9.21.2 Closely spaced reinforcement shall be placed both vertically and horizontally throughout the length of the end block in accordance with accepted methods of end block stress analysis.

9.21.3 In pretensioned beams, vertical stirrups acting at a unit stress of 20,000 psi to resist at least 4 percent of the total prestressing force shall be placed within the distance of $d/4$ of the end of the beam, the end stirrups to be as close to the end of the beam as practicable. For at least the distance d from the end of the beam, nominal reinforcement shall be placed to enclose the prestressing steel in the bottom flange. For box girders, transverse reinforcement shall be provided and anchored by extending the leg into the web of the girder.

9.26 POST-TENSIONING ANCHORAGES AND COUPLERS

9.26.1 Anchorages, couplers, and splices for bonded post-tensioned reinforcement shall develop at least 95 percent of the minimum specified ultimate strength of the prestressing steel, tested in an unbonded state without exceeding anticipated set. Bond transfer lengths between anchorages and the zone where full prestressing force is required under service and ultimate loads shall normally be sufficient to develop the

minimum specified ultimate strength of the prestressing steel. Couplers and splices shall be placed in areas approved by the Engineer and enclosed in a housing long enough to permit the necessary movements. When anchorages or couplers are located at critical sections under ultimate load, the ultimate strength required of the bonded tendons shall not exceed the ultimate capacity of the tendon assembly, including the anchorage or coupler, tested in an unbonded state.

9.26.2 The anchorages of unbonded tendons shall develop at least 95 percent of the minimum specified ultimate strength of the prestressing steel without exceeding anticipated set. The total elongation under ultimate load of the tendon shall not be less than 2 percent measured in a minimum gauge length of 10 feet.

9.26.3 For unbonded tendons, a dynamic test shall be performed on a representative specimen and the tendon shall withstand, without failure, 500,000 cycles from 60 percent to 66 percent of its minimum specified ultimate strength, and also 50 cycles from 40 percent to 80 percent of its minimum specified ultimate strength. The period of each cycle involves the change from the lower stress level to the upper stress level and back to the lower. The specimen used for the second dynamic test need not be the same used for the first dynamic test. Systems utilizing multiple strands, wires, or bars may be tested utilizing a test tendon of smaller capacity than the full size tendon. The test tendon shall duplicate the behavior of the full size tendon and generally shall not have less than 10 percent of the capacity of the full size tendon. Dynamic tests are not required on bonded tendons, unless the anchorage is located or used in such manner that repeated load applications can be expected on the anchorage.

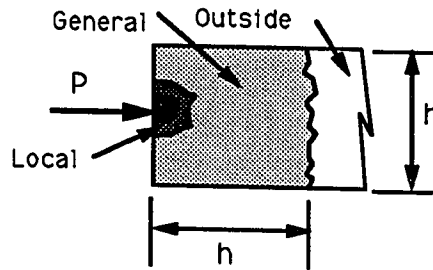
9.26.4 Couplings of unbonded tendons shall be used only at locations specifically indicated and/or approved by the Engineer. Couplings shall not be used at points of sharp tendon curvature. All couplings shall develop at least 95 percent of the minimum specified ultimate strength of the prestressing steel without exceeding anticipated set. The coupling of tendons shall not reduce the elongation at rupture below the requirements of the tendon itself. Couplings and/or coupling components shall be enclosed in housings long enough to permit the necessary movements. All the coupling components shall be completely protected with a coating material prior to final encasement in concrete.

9.26.5 Anchorages, end fittings, couplers, and exposed tendons shall be permanently protected against corrosion.

BRIDGE POST-TENSIONING ANCHORAGE ZONE CLASSIFICATION SYSTEM

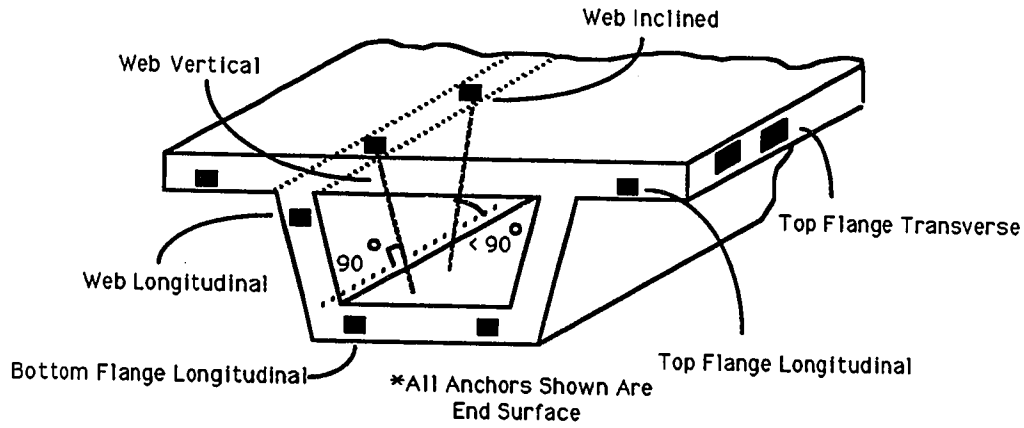
A) Anchorage Zone

- 1) Local
- 2) General
- 3) Outside

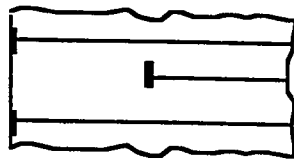
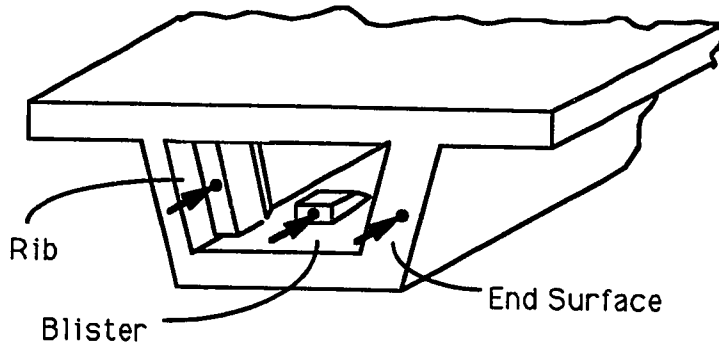


B) Location

- | | |
|---|---|
| <ol style="list-style-type: none"> 1) Direction <ol style="list-style-type: none"> a) Longitudinal b) Transverse c) Vertical or Inclined | <ol style="list-style-type: none"> 2) Position <ol style="list-style-type: none"> a) Web b) Flange c) Diaphragm d) Deck |
|---|---|

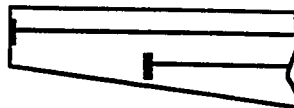


- 3) Entry
 - a) Intermediate or Interior
 - b) Blister or Rib
 - c) End Surface



Plan

Interior

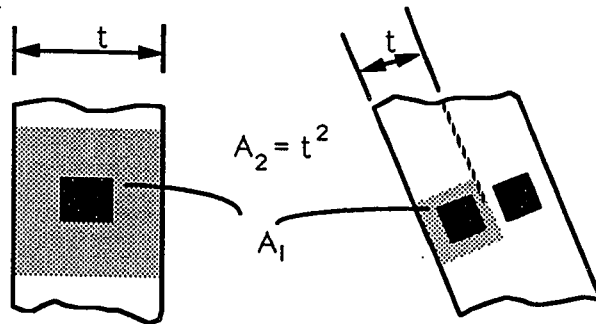
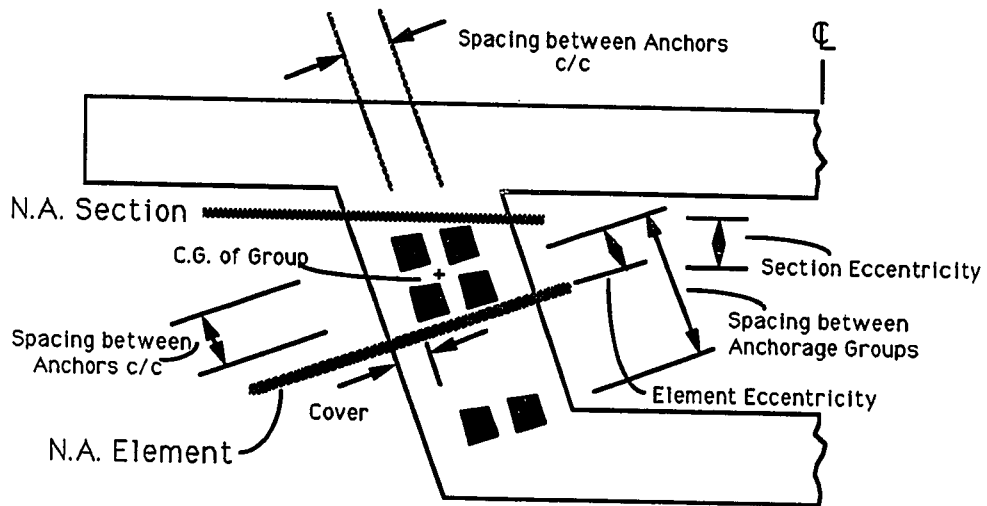


Elevation

C) Geometry

1) Anchorages

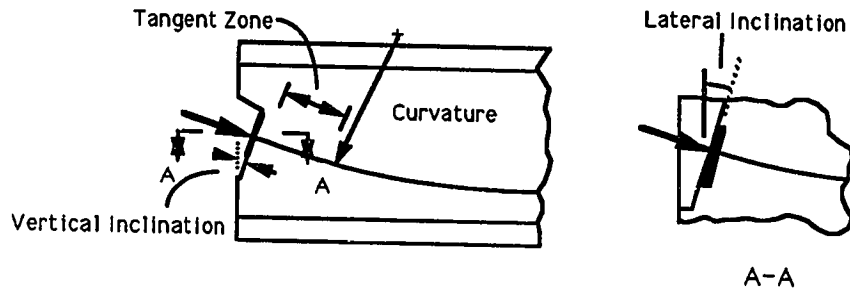
- a) Number
- b) Layout of Multiple Anchorages
 - 1) Spacing between Anchors
 - 2) Spacing between Anchorage Groups
- c) Eccentricity
 - 1) Section
 - 2) Element
- d) Inclination- Vertical and/or Lateral
- e) Proportional Size- Anchor to Effective Confining Concrete (A_1/A_2)
- f) Cover



2) Tendon in Anchor Zone

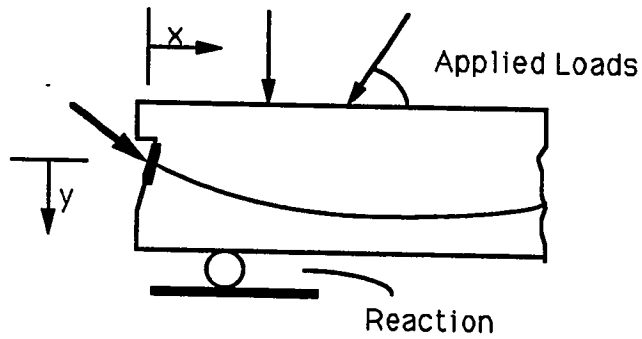
555

- a) Tangent Zone
- b) Curvature
- c) Number of Strands, Bars or Wires



D) Loads

- 1) Prestressing
 - a) Load
 - b) Sequence or Staging
- 2) Other Loads- Magnitude, Angle and Distance from Anchor
 - a) Reactions
 - b) Applied Forces

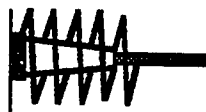


E) Concrete

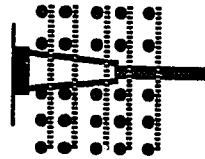
- 1) Type
 - a) Normal
 - b) Lightweight
- 2) Strength
 - a) Initial- at time of prestressing
 - b) Final- at 28 days or other specified age

F) Reinforcement—Amount, Layout and Grade

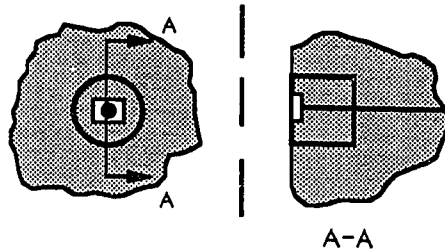
- 1) Local- Reinforcement Surrounding the Anchorage Device for Splitting and Bearing Stresses(See page 1 for sketch)
 - a) Spiral
 - b) Orthogonal
 - c) Confining Sleeve
 - d) Other
- 2) General- Anchor Zone Reinforcement for Bursting and Spalling Stresses(See page 1 for sketch)
 - a) Spiral
 - b) Orthogonal
 - c) Post-Tensioning- Vertical and/or Transverse
 - d) Other



Spiral



Orthogonal



Confining Sleeve

G) Hardware

1) Anchor*

- a) Single Bearing Surface with Trumpet
- b) Multiple Bearing Surface
- c) Flat Bearing Surface
- d) Other

* Fixed End Loop and Strand Anchors, and Couplers excluded from study by NCHRP



Single Bearing Surface
with Trumpet



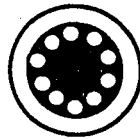
Multiple Bearing
Surface



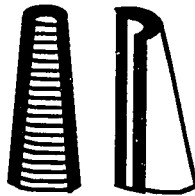
Flat Bearing
Surface

2) Grips

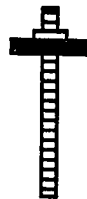
- a) Multiple Strand with Single Central Cone
- b) Wedges
- c) Threaded
- d) Button Head
- e) Other



Multiple Strand with
Single Central Cone



Wedges



Threaded



Button Head

H) Other Design Criteria

- 1) Factor of Safety
- 2) Permissible Crack Width
- 3) Allowable Tensile Stress

BIBLIOGRAPHY

1. Abeles, P.W. and Burdan-Roy; Prestressed Concrete Designer's Handbook, Chapter 10 End Blocks, 3rd Ed.; View Point Publications; 1981; pp 253-279.
2. Adeghe, L.N. and Collins, M.P.; A Finite Element Model for Studying Reinforced Concrete Detailing Problems; Department of Civil Engineering, University of Toronto; Publ. No 86-12; October 1986; pp 66-74.
3. Aldersebaes, J.K. and Wiedner, K.; "Containment Structure for Trojan Nuclear Plant;" ASCE Power Division Journal; Vol 97, No P02; March 1971; paper 7957; pp 351-366.
4. Almasi, J.; "Wieviel Spaltzugbewehrung ist nötig?" IABSE; Vol 35-II; 1975; pp 15-27.
5. American Association of State Highway Transportation Officials (AASHTO); Standard Specification for Highway Bridges; Fourteenth Edition; 1989.
6. American Concrete Institute (ACI) 318-89; Building Code Requirements for Reinforced Concrete; American Concrete Institute; 1989.
7. American Concrete Institute Committee 244; "Control of Cracking;" ACI Manual of Concrete Practice, Part 3, 1983; American Concrete Institute; 1983.
8. American Concrete Institute Committee 443; "Prestressed Concrete Bridge Design;" ACI Journal; Vol 73, No 11; November 1976; pp 597-612.
9. American Concrete Institute-American Society of Civil Engineers Committee 423; "Recommendations for Concrete Members Prestressed with Unbonded Tendons;" Concrete International; Vol 5, No 7; July 1983; pp 61-76.
10. Anderson, R.; "Behavior of CTT Nodes in Reinforced Concrete Strut-and-Tie Models;" M.S. Thesis; University of Texas at Austin; May 1988.
11. Ang, A.H.S.; "Structural Design Analysis and Testing;" ASCE Structural Congress Proceedings; San Francisco; May 1989.

12. Arthur, P.D. and Ganguli, S.; "Tests on End-Zone Stresses in Pretensioned Concrete 'I' Beams;" Magazine of Concrete Research; Vol 17, No 51; June 1965; pp 85-100.
13. Austrian Code for Prestressed Concrete-Road Bridges, Design and Construction; ÖNORM B 4252; December 1975. (German)
14. Austrian Code for Reinforced Concrete Structures, Rules for Design and Construction I; ÖNORM B 4200 Teil 8; August 1979. (German)
15. Austrian Code for Prestressed Concrete, Post-Tensioning Systems; ÖNORM B 4259; December 1979. (German)
16. Bachmann, H.; Stahlbeton II; Institut für Baustatik und Konstruktion; Zurich; 1985.
17. Ban, S., Mugurama, H. and Ogaki, Z.; "Anchorage Zone Stress Distributions in Post-Tensioned Concrete Members;" Proceedings of World Conference on Prestressed Concrete; Univ. of California, San Francisco, CA; 1957; pp 16:1-14.
18. Benabdallah, S. and Ramirez, J.; "Computer Graphics in Truss-Model Design Approach;" ASCE Journal of Computing in Civil Engineering; Vol 3, No 3; July 1989; pp 285-301.
19. Bergmeister K., Breen, J.E., Jirsa, J.O. and Kreger, M.E.; "Detailing for Structural Concrete"; Center for Transportation Research Report No 481-3F; University of Texas at Austin; July, 1989.
20. Bleich, F.; "Der Gerade Stab mit Rechteckquerschnitt als ebenes problem;" Der Bauingenieur (Berlin); No 9; 1923; pp 225-259; No 10; 1923; pp 304-307.
21. Boonman, C.L.F.; "Design of Intermediate Anchorages in Unbonded Tendons;" Magazine of Concrete Research; Vol 32, No 6; June 1980; pp 344-351.
22. Bouadi, A.; "Behavior of CTT Nodes in Structural Concrete for the Strut-and-Tie Model;" M.S. Thesis; May 1990.
23. Breen, J.E., Cooper, R.L. and Gallaway, T.M.; "Minimizing Construction Problems in Segmentally Precast Box Girder Bridges;" Research Report No. 121-6F; Center for Highway Research, The University of Texas at Austin; August 1975.

24. Breen, J.E., Fenves, G., Sanders, D.H. and Burdet, O.; "Anchorage Zone Reinforcement for Post-Tensioned Concrete Girders;" National Cooperative Highway Research Program Interim Report 10-29; University of Texas at Austin; August 1987.
25. Burdet, O.; "Analysis and Design of Post-Tensioned Anchorage Zones Concrete Bridges;" Ph.D. Dissertation; University of Texas at Austin; May 1990.
26. Burgess, J.A., Breen, J.E. and Poston, R.W.; "Anchorage Zone Cracking of Post-Tensioned Bridge Decks with Closely-Spaced Anchors;" To Be Published.
27. Burns, N. and Hemakom, R.; "Test of Post-Tensioned Flat Plate with Banded Tendons;" ASCE Structural Division Journal; Vol 111, No 9; September 1985; pp 1899-1915.
28. Cedolin, L. and Dei Poli, S.; "Finite Element Nonlinear Plane Stress Analysis of Reinforced Concrete;" pp 3-33. (Publication Unknown)
29. Chaikes, S.; Calcul des abouts des poutres en béton précontraint; Congres International du Béton Précontraint a Gand; September 1951; pp B41:1-27.
30. Christodoulides, S.P.; "A Two-Dimensional Investigation of the End Anchorages of Post-Tensioned Concrete Beams;" The Structural Engineer; April 1955; pp 120-133.
31. Christodoulides, S.P.; "A Photoelastic Investigation of Prestressed Concrete Anchorages;" Civil Engineering and Public Works Review; Vol 51, No 603; September 1956; pp 994-997.
32. Christodoulides, S.P.; "The Distribution of Stresses Around the End Anchorages of Prestressed Concrete Beams. Comparison of Results Obtained Photoelastically with Strain Gauge Measurements and Theoretical Solutions;" IABSE Memoirs; Vol 16; 1956; pp 55-70.
33. Christodoulides, S.P.; "Three-Dimensional Investigation of the Stresses in the End Anchorage Blocks of a Prestress Concrete Gantry Beam;" The Structural Engineer; Vol 35, No 9; September 1957; pp 349-356.
34. Collins, M. and Mitchell, D.; Prestressed Concrete Basics, Chapter 9, Design of Disturbed Regions; Canadian Prestressed Concrete Institute; 1987; pp 386-429.

35. Collins, M. and Mitchell, D.; "Shear and Torsion Design of Prestressed and Non-Prestressed Concrete Beams;" PCI Journal; Vol 25, No 5; September-October 1980; pp 32-124.
36. Comité Euro-International du Béton and the Federation Internationale de la Précontrainte (FIP); Model Code for Concrete Structures; English Translation; proposed 1990.
37. Comité Euro-International du Béton; Anchorage Zones of Prestressed Concrete Members; No 181; April 1987.
38. Construction Industry Research and Information Association; A Guide to the Design of Anchor Blocks for Post-Tensioned Prestressed Concrete Members, CIRIA Guide 1; London; June, 1976.
39. Cooks, W.D. and Mitchell D.; "Studies of Disturbed Regions near Discontinuities in Reinforced Concrete Members;" ACI Structural Journal; March-April 1988; pp 206-216.
40. Csagoly, P. and Holowka, M.; Cracking of Voided Post-Tensioned Concrete Bridge Decks; Ministry of Transportation and Communication; January 1975.
41. Csagoly, P. and Holowka, M.; The McCowon Bridge Test; Ministry of Transportation and Communication; December 1974.
42. Csagoly, P. and Holowka, M.; Model Studies for Voided Post-Tensioned Concrete Slab Bridges; Ministry of Transportation and Communication; August 1974.
43. Csagoly, P. and Holowka, M.; Finite Element Computer Program for Analysis of Plates with Bending and In-Plane Stresses; Ministry of Transportation and Communication; November 1974.
44. DeWolf, J.T.; "Axially Loaded Column Base Plates;" ASCE Structural Division Journal; Vol 104, No ST5; May 1978; pp. 781-795.
45. Dilger W.H. and Ghali, A.; "Remedial Measures for Cracked Webs of Prestressed Concrete Bridges," Prestressed Concrete Institute (PCI) Journal; Vol 19, No 4; July-August 1974; pp 76-85.
46. Douglas, D.J. and Trahair, N.S.; "An Examination of the Stresses in the Anchorage Zone of a Post-Tensioned Prestressed Concrete Beam," Magazine of Concrete Research; Vol 12, No 34; March 1960; pp 9-18.

47. Dowrick, D.J.; "Anchorage Zone Reinforcement for Post-Tensioned Concrete;" Civil Engineering and Public Works Review; September 1964; pp 1101-1107.
48. Drew, G.E.; "Post-Tensioning System Surveillance Program;" ASCE Structural Division Journal; Vol 105, No ST2; February 1979; pp 347-357.
49. Egeberg, J.L.; "A Finite Element Investigation of the Anchorage Zones of Prestressed Concrete Beams;" Report No. 363; Department of Civil Engineering, University of California, Berkeley; August 1968.
50. Eibl, J. and Ivanyi, G.; "Untersuchungen an Innenverankerungen im Spannbetonbau;" Deutscher Ausschluß für Stahlbeton; 1966.
51. Eibl, J.; "Innenverankerungen von Spanngliedern;" Béton-und Stahlbetonbau; No 2; 1973.
52. El-Behairy S.; "Zugkrafte in der Naeh der Ankerplatten eines im nneren einer Rechteckscheibe verankerten Spanngliedes;" Béton-und Stahlbetonbau; 1968; S. 135.
53. Erickson, D.A.; "Problems Encountered with Post-Tensioned Unbonded Tendons;" Building Standards; Vol 54, No 5; September-October 1985; pp 4-6.
54. Evans, R.H. and Marathe, M.S; "Micro-Cracking and Stress- Strain Curves for Concrete in Tension;" Materiaux et Constructions; Vol 1, No 1; January-February 1968; pp 61-64.
55. Falconer, B.A.; "Post-Tensioning Anchorage Zones in Bridge Decks;" M.S. Thesis; University of Texas at Austin; May 1990.
56. Fenwick, R.C. and Lee, S.C.; "Anchorage Zones in Prestressed Concrete Members;" Magazine of Concrete Research; Vol 38, No 135; June 1986; pp 77-89.
57. FIP Recommendations for Acceptance and Application of Post-Tensioning Systems; March 1981.
58. Figg, E.C.; "Segmental Bridge Design in the Florida Keys;" Concrete International; Vol 2, No 8; August 1980; pp 17-22.
59. Finite Element Analysis of Reinforced Concrete; State of the Art Report; ASCE; 1982.

60. Florida Department of Transportation Design Criteria.
61. Freyermuth, C.L.; "Post-Tensioning Details for Long Span Concrete Bridges;" PCI Journal; Vol 27, No 6; November-December 1982; pp 48-65.
62. Fujii, M., Miyamoto, A. and Mizuno, H.; "Fundamental Study of Reinforcement of Rib-Anchorage Zone in Prestressed Concrete Member;" Journal of the Society of Materials Science, Japan; Vol 29, No 318; March 1980; pp 299-305. (Japanese)
63. Fujii M., Kitamura, Y. and Araki, T.; "Control of Horizontal Crack Width in Pretensioned Concrete Girders;" Journal of Japan Prestressed Concrete Association; Vol 16; May 1971.
64. Fujii, M., Miyamoto, A. and Kajimura, Y.; "Crack Control Design of Intermediate Anchorage Zone in Prestressed Concrete;" FIP Symposium on Partial Prestressing, Part 1; Romania; September 1980; pp 44-51.
65. Gergely, P. and Sozen, M.A.; "Design of Anchorage-Zone Reinforcement in Prestressed Concrete Beams;" PCI Journal; Vol 12, No 2; April 1967; pp 63-75.
66. Gergely, P., Sozen, M.A. and Siess, C.P.; "The Effect of Reinforcement on Anchorage Zone Cracks in Prestressed Concrete Members;" Civil Engineering Structural Research Series, No. 271; University of Illinois; July 1963.
67. Gerstner, R.W. and Zienkiewicz, O.C.; "A Note on Anchorage Zone Stresses;" ACI Journal; July 1962; pp 970-974.
68. German Building Code; DIN 1045; Sec 17. (German)
69. German Building Code Commentary; Heft 240; Hilfsmittel zur Berechnung der Schnittgrößen und Formänderungen von Stahlbetontragwerken nach DIN 1045; January 1972. (German)
70. Guyon, Y.; Prestressed Concrete; John Wiley and Sons, Inc.; New York; 1953.
71. Guyon, Y.; "Contraintes Dans Les Pieces Prismatiques Soumises a Des Forces Appliquees Sur Leurs Bases, au Voisinage de ces Bases;" International Association for Bridge and Structural Engineering; Vol 11; 1961; pp 165-226 (English Summary).

72. Guyon, Y.; Limit-State Design of Prestressed Concrete, Vol 2, The Design of the Member; John Wiley & Sons; New York; 1974.
73. Hawkins, N.M.; "The Bearing Strength of Concrete Loaded through Rigid Plates;" Magazine of Concrete Research; Vol 20, No 62; March 1968; pp 31-40.
74. Hawkins, N.M.; "The Bearing Strength of Concrete Loaded Through Flexible Plates;" Magazine of Concrete Research; Vol 20, No 63; June 1968; pp 95-102.
75. Hawkins, N.M.; "The Bearing Strength of Concrete for Strip Loadings;" Magazine of Concrete Research; Vol 22, No 71; June 1970.
76. Hawkins, N.M.; "The Behavior and Design of End Blocks for Prestressed Concrete Beams;" Civil Engineering Transactions; Institution of Engineers of Australia; October 1966; pp 193-202.
77. Hawkins, N.M., Srinivasagopalan, V. and Sozen, M.A.; "Anchorage Zone Stresses in Prestressed Concrete Beams;" Structural Research Series No 207; University of Illinois; 1960.
78. Higashida, K. and Nakajima, H.; "Experimental Study on Reinforcement of Multiple Anchorages Zone in Post-Tensioned Concrete Member;" Journal of Japan Prestressed Concrete Engineering Association; Vol 16, extra number; 1974; pp 41-47.
79. Hildebrand, J.F.; "Buttonheads for Tendon Wires of a Prestressed Concrete Reactor Vessel;" PCI Journal; Vol 16, No 5; September-October 1971; pp 78-99.
80. Hiltcher R. and Florin, G.; "Die Spaltzugkraft in einseitig eingespannten am gegenüberliegenden Rande belasteten rechteckigen Scheiben;" Bautechnik; Vol 39, No 10; October 1962; pp 325-328.
81. Huang, T.; "Anchorage Take-Up Loss in Post-Tensioned Members;" PCI Journal; Vol 14, No 4; August 1969; pp 30-35.
82. Huang, T.; "Stresses in End Blocks of a Post-Tensioned Prestressed Beam;" ACI Journal; Vol 61, No 5; May 1964; pp 589-601.

83. Iyengar K.T.S.R.; "Über den Spannungszustand in einem elastischen Halbstreifen;" Österreichisches Ingenieur Archiv; Vol 16, No 3; 1962; pp 185-199.
84. Iyengar, K.T.S.R. and Prabhakara, M.K.; "Anchor Zone Stresses in Prestressed Concrete Beams;" ASCE Structural Division Journal; Vol 97, No ST3; March 1971; pp 807-824.
85. Iyengar, K.T.S.R.; "Two-Dimensional Theories of Anchorage Zone Post-Tensioned Prestressed Beams;" ACI Journal; Vol 59, No 10; October 1962; pp 1443-1446.
86. Iyengar, K.T.S.R. and Yogananda, C.V.; "A Three-Dimensional Stress Distribution Problem in the Anchorage Zone of a Post-Tensioned Concrete Beam;" Magazine of Concrete Research; Vol 18, No 55; June 1966; pp 75-84.
87. Jofriet, J.C., McNeice, G.M. and Csagoly, P.; "Finite Element Analysis of Prestressed Concrete Voided Bridge Decks;" PCI Journal; Vol 18, No 3; May-June 1973; pp 51-66.
88. Jones, T.R. Jr. and Stephenson, H.K.; "Properties of Lightweight Concrete Related to Prestressing;" Proceedings of World Conference on Prestressed Concrete; Univ. of California, San Francisco, CA; 1957; pp A6.1-A6.12.
89. Kozak, J. and Bezouska, T.; "Twenty Five Years of Prestressed Concrete Bridges;" PCI Journal; Vol 21, No 5; September-October 1976; pp 90-111.
90. Komendant, A.E.; Prestressed Concrete Structures; McGraw-Hill; 1952; pp 172-173.
91. Kruger, U.; "The Analysis of Patented Anchor Heads of Steel Wire Cable;" Der Bauingenieur; Vol 52, No 5; March 1977; pp 105-111. (German)
92. Kupfer H.; "Bemessung von Spannbetonbauteilen;" Beton-Kalender; 1981; Teil 1 S. 1102.
93. Kammenhuber, J. and Schneider, J.; "Arbeitsunterlagen für die Berechnung vorgespannter Konstruktionen;" Stahlton; Zurich; 1974.
94. Lee, S.C.; "Bursting Stresses in the End Block of a Post-Tensioned Prestressed Beam;" Library School of Engineering, Report No 321; University of Auckland; January 1983.

95. Lenschow, R. and Sozen, M.A.; "Practical Analysis of the Anchorage Zone Problem in Prestressed Beams;" ACI Journal; November 1965; pp 1421-1437.
96. Leonhardt, F.; Prestressed Concrete--Design and Construction; Wilhelm Ernest and Son; Berlin; 1964.
97. Leonhardt F.; "Das Bewehren von Stahlbetontragwerken;" Béton-Kalender; von Wilhelm e. & Sohn; 1973.
98. Leonhardt F.; "Vorlesungen über Massivbau, Teil 2;" Sonderfaelle der Bemessung im Stahlbetonbau; Springer Verlag; 1986.
99. Leonhardt F.; "Vorlesungen über Massivbau, Teil 5;" Spannbeton; Springer Verlag; 1980.
100. Libby, J.; "Critique of a Post-Tensioned Roof Slab Failure;" Concrete International; Vol 7, No 10; October, 1985; pp 28-32.
101. Libby, J.R.; "Segmental Box Girder Bridge Superstructure Design;" ACI Journal; Vol 73, No 5; May 1976; pp 279-290.
102. Lin, T.Y. and Redfield, C.; "Some Design Issues for American Constructors;" Proceedings of the Segmental Concrete Bridge Conference PC-7; Kansas City, MO; 1982.
103. Littlejohn, G.S.; "Rock Anchor - State of the Art, Part 1:Design;" Ground Engineering; Vol 8, No 3; August 1975.
104. Losinger, LTD; "Technical Documentation, Einleitung der Vorspannkrafte in den Béton;" Bern; October 1985.
105. Losinger, LTD Bern: "VSL End Block Design in Post-Tensioned Concrete;" Bern; November 1975.
106. Ly, K.T.; "Effet des forces de précontrainte concentrée dans les poutres caisson;" Rapport de recherche du Laboratoire des Ponts et Chaussées; No 68; September 1977.
107. Magnel, G.; Prestressed Concrete; McGraw-Hill; New York; 3rd Ed.; 1954.
108. Marti, P.; "Basic Tools for Reinforced Concrete Beam Design;" ACI Journal; January-February 1985; pp 46-56.

109. Marti, P.; "Truss Models in Detailing;" Concrete International; December 1985; pp 66-73.
110. Marti, P.; "Zur plastischen Berechnung von Stahlbeton;" Report No 104; IBK ETH Zurich; 1980.
111. Meyer, C. and Okamura, H., editors; Finite Element Analysis of Reinforced Concrete Structures; ASCE; 1986.
112. Meyerhof, G.G.; "The Bearing Capacity of Concrete and Rock;" Magazine of Concrete Research; Vol 4, No 12; April 1953; pp 107-116.
113. Middendorf, K.H.; "Anchorage Bearing Stresses in Post-Tensioned Concrete;" ACI Journal; November 1960; pp 580-584.
114. Middendorf, K.H.; "Practical Aspects of End Zone Bearing of Post-Tensioning Tendons;" PCI Journal; Vol 8, No 4; August 1963; pp 57-62.
115. Mitteilungen des Instituts für Bautechnik, 7; Jg. 1976; Heft 5; Berlin 1976. (German)
116. Mordecci, V.S.; "The Progress of Post-Tensioning Concrete;" Concrete, Journal of Concrete Society; Vol 18, No 10; October 1984.
117. Mörsch, E.; "Über die Berechnung der Gelenkquader;" Béton-und Eisen; No 12; 1924; pp 156-161.
118. Müller R.K. and Schmidt, D.W.; "Zugkräfte in einer Scheibe, die durch eine zentrische Einzellast in einer rechteckigen Öffnung belastet wird;" Die Bautechnik; 1964 S. 174 (IABSE); Vol 11 pp 165-226.
119. Nawy, E.G; "Crack Control in Reinforced Concrete Structures;" ACI Journal Proceeding; Vol 65, No 10; October 1968; pp 825-836.
120. Niyogi, S.K.; "Bearing Strength of Reinforced Concrete Blocks;" ASCE Structural Division Journal; Vol 101, No ST5; May 1975.
121. Niyogi, S.K.; "Bearing Strength of Concrete-Geometric Variations;" ASCE Structural Division Journal; Vol 99, No ST7; July 1973; pp 1471-1490.
122. North Carolina Department of Transportation Design Criteria.

123. Ontario Highway Bridge Design Code; 1983.
124. Ontario Highway Bridge Design Commentary; 1983.
125. Ottosen, N.S.; "A Failure Criterion for Concrete;" ASCE Journal of Engineering Mechanics; Vol 104, No EM4; Aug 1977; pp 527-535.
126. Paes Filho, W.; "The Behavior of Post-Tensioned Anchorage Zone Models of Thin Web Members;" M.S. Thesis; University of Texas at Austin; December 1979.
127. PCI Segmental Construction Committee; "Recommended Practice for Segmental Construction in Prestressed Concrete;" PCI Journal; Vol 20, No 2; March-April 1975; pp 22-41.
128. PCI Bridge Committee; "Tentative Design and Construction Specification for Precast Segmental Box Girder Bridges;" PCI Journal; Vol 20, No 4; July-August 1975; pp 34-42.
129. Picket, G. and Iyengar, K.T.S.R.; "Stress Concentration in Post-Tensioned Prestressed Concrete Beams;" Journal of Technology; Bengal; Engineering College; Vol 1, No 2; December 1956; pp 105-112.
130. Podolny, W.; "The Cause of Cracking in Post-Tensioned Concrete Box Girder Bridges and Retrofit Procedures;" PCI Journal; Vol 30, No 2; March-April 1985; pp 82-139.
131. Podolny, W. and PCI-Post Tensioning Institute (PTI) Comm.; "Recommended Practice for Precast Post-Tensioned Segmental Construction;" PCI Journal; Vol 27, No 1; January-February 1982; pp 15-61.
132. Post-Tensioned Box Girder Bridges, Design and Construction; Western Concrete Reinforcing Steel Institute, PCI and Concrete Reinforcing Steel Institute, 1969.
133. Post-Tensioned Box Girder Bridge Manual; PTI; 1978.
134. Post-Tensioning Institute Ad Hoc Committee for Unbounded Single Strand Tendons; PCI Journal; Vol 30, No 2; March-April 1985; pp 22-39.
135. Post-Tensioning Institute; "Design and Construction Specification for Segmental Concrete Bridges;" February, 1988.

136. Post-Tensioning Manual, 4th Ed.; PTI; 1986.
137. "Prestressing Part 2-Anchorage and End Blocks;" Concrete, Journal of the Concrete Society; Vol 13, No 6; June 1979; p 41.
138. Ramaswamy, G.S. and Goel, H.; "Stresses in End Blocks of Prestressed Beams by Lattice Analogy;" Proceeding of World Conference on Prestressed Concrete; San Francisco; July 1957; pp 23.1-23.4.
139. Rasheeduzzafar, I.M.A. and Al-Saadoun, S.S.; "A Photoelastic Investigation of Anchorage Bearing Stresses;" Magazine of Concrete Research; Vol 36, No 127; June 1984, pp 81-91.
140. Rejcha, C.; "Simplified Bearing Plate Computations for Post-Tensioning Anchorages;" PCI Journal; Vol 20, No 4; July-August 1975; pp 102-111.
141. Richart, F.E., Brandtzaeg, A. and Brown, R.L.; "A Study of the Failure of Concrete under Combined Compressive Stresses;" Research Bulletin No 185; University of Illinois Engineering Experimental Station; 1928.
142. Rhodes, B. and Turner, F.H.; "Design of End-Blocks for Post-Tensioned Cables;" Concrete; Vol 1, No 12; December 1967; pp 431-434.
143. Roberts, C.; "Behavior and Design of the Local Anchorage Zone in Post-Tensioned Concrete;" M.S. Thesis; University of Texas at Austin; May 1990.
144. Rowe, R.E.; "End Block Stresses in Post-Tensioned Concrete Beams;" The Structural Engineer; Vol 41, No 2; February 1963; pp 55-67.
145. Rowe, R.E. and Zielinski, J.; "Distribution of Stress in Anchor Blocks;" Engineering; Vol 189, No 4899; March 11, 1960; pp 347-348.
146. Rüsç H.; Spannbeton-Erläuterungen zu DIN 4227: Richtlinien für Bemessung und Ausfuering. Berlin, Wilhelm Ernst und Sohn, 1954.
147. Rüsç H. and Kùpfer, G.; Bemessung von Spannbetonbauteilen, Beton-Kalender; von Wilhelm e. & Sohn; 1974.

148. Rydezewski, J.R. and Whitbread, F.J.; "Short End Blocks for Prestressed Beams;" The Structural Engineer; Vol 41, No 2; February 1963; pp 41-53.
149. Sargious, M.; "Beitrag zur Ermittlung der Hauptzugspannungen am Endauflager vorgespannter Betonbalken;" Ph.D. Dissertation; Technische Hochschule; Stuttgart; July 1960.
150. Schechter, E. and Boecker, H.C.; "Wedge Anchorage System for Strand Post-Tensioning;" PCI Journal; Vol 16, No 4; July-August 1971; pp 49-63.
151. Schlaich, J., Schäfer, K. and Jennewein, M.; "Toward a Consistent Design of Reinforced and Prestressed Concrete Structures;" PCI Journal; Vol 32, No 3; May-June 1987; pp 74-151.
152. Schlaich, J. and Schäfer, K.; "Konstruieren in Stahlbetonbau;" Beton-Kalender, Part 2; 1989; pp 563-715. (German)
153. Schlaich, J. and Scheef H.; Concrete Box-Girder Bridges; Structural Engineering Documents, 1e; IABSE; 1982.
154. Schlaich, M.; "Computeruntersetzte Bemessung von Stahlbetonscheiben mit Fachwerkmodellen;" Ph.D. Dissertation; ETH Zurich; 1989. (German)
155. Schlee, L.K.; "The Stress Pattern at the Support of a Prestressed Concrete Beam;" Beton-und Stahlbetonbau; Berlin; Vol 58, No 7; July 1963; pp 157-171. (German)
156. Schupack, M.; "Large Post-Tensioning Tendons;" PCI Journal; Vol 17, No 3; May-June 1972; pp 14-28.
157. Seible, F.; "Coupling Joints of Prestressing Tendons in Continuous Post-Tensioned Concrete Bridges." (To be Published)
158. Seible, F., Kropp, Y. and Lathan, C.T.; "Stress State in Coupling Joints of Post-Tensioned Concrete Bridges;" Department of Applied Mechanics and Engineering Sciences, University of California, San Diego.
159. Sievers, H.; "Über den Spannungszustand im Bereich der Ankerplatten von Spanngliedern vorgespannter Stahlbetonkonstruktionen;" Bauingenieur; Vol 31; April, 1956; pp 134-135.

160. Smith, M.A.; "Anchorage Design with Finite Element Techniques;" Concrete; Vol 17, No 7; July 1983; pp 25-26.
161. Soliman, M.T.M. and Yu, C.W.; "The Flexural Stress-Strain Relationship of Concrete Confined by Rectangular Transverse Reinforcement;" Magazine of Concrete Research; Vol 19, No 61; December 1967; pp 223-238.
162. Som, P.K. and Ghosh, K.; "Anchor Zone Stresses in Prestressed Concrete Beams;" ASCE Structural Division Journal; Vol 90, No ST 4; August 1964; pp 49-62.
163. Soroushian, P., Ahmadi, P., Navas, F. and Haji, M.N.; "Transfer of Column Pressure to Concrete Footings;" Concrete International; Vol 8, No 12; December. 1986; pp 38-42.
164. Stone, W.C. and Breen, J.E.; "Analysis of Post-Tensioned Girder Anchorage Zones;" Center for Transportation Research Report No 208-1; University of Texas at Austin; January 1981.
165. Stone, W.C. and Breen, J.E.; "Behavior of Post-Tensioned Girder Anchorage Zones;" Center for Transportation Research Report No 208-2; University of Texas at Austin; January 1981.
166. Stone, W.C. and Breen, J.E.; "Behavior of Post-Tensioned Girder Anchorage Zones;" PCI Journal; Vol 29, No 1; January- February 1984.
167. Stone, W.C. and Breen, J.E.; "Design of Post-Tensioned Girder Anchorage Zones;" Center for Transportation Research Report No 208-3F; University of Texas at Austin; January 1981.
168. Stone, W.C. and Breen, J.E.; "Design of Post-Tensioned Girder Anchorage Zones;" PCI Journal; Vol 29, No 2; March-April 1984.
169. Stone, W.C.; "Measurement of Internal Strain in Cast- Concrete Structures;" Experimental Mechanics; Vol 23, No 4; December 1983; pp 361-369.
170. Suzuki, K. and Nakatsuka, T.; "Estimation of Bearing Strength of Reinforced Anchorage Zone in Post-Tensioned Prestressed Concrete Members;" Technical Report, Osaka Univ; Vol 32, No 1652-1683; October 1982; pp 419-428.
171. Swiss Code for Concrete; Betonbauteile; SIA code 162.

172. Taylor, S.J.; "Anchorage Bearing Stresses;" Conference on Prestressed Concrete Pressure Vessel, Group H, March 13-17, 1967, London; The Institution of Civil Engineers; London; 1968.
173. Taylor, S.J.; Discussion of the paper. "A Three Dimensional Stress Distribution Problem in the Anchorage Zone of a Post-Tensioned Concrete Beam;" Magazine of Concrete Research; Vol 19, No 58; March 1967; pp 54-57.
174. Tesar, M.; "Determination expérimentale des tensions dans les extrémités des pièces prismatiques munies d'une semi-articulation;" IABSE Memoirs; 1932; pp 497-506.
175. Thürlimann, B., Marti, P. et al.; "Anwendung der Plastizitätstheorie auf Stahlbeton, Institut für Baustatik und Konstruktion;" Zurich; 1983. (German)
176. Thürlimann B.; "Plastizitätstheorie im Stahlbetonbau, Institut für Baustatik und Konstruktion;" Zurich; 1986. (German)
177. Trinh, J.; "Résistance du béton aux forces concentrées, première partie: cas du béton non armé;" Annales de l'Institut Technique du Batiment et des Travaux Publics, No 439; November 1985. (French)
178. Trinh, J.; "Resistance du Béton Leger Aux Efforts D'Ancrage De Cable Post-Tendu;" Proposition De publication dans les Annales de l'ITBTP; Paris; 1987. (French)
179. Vaughn, S.D.; "An Exploratory Photoelastic Investigation of Post-Tensioned Concrete Anchorage Zone Bursting Stresses;" M.S. Thesis, The University of Texas at Austin; August 1977.
180. Virlogeux, M.; "Analyse de quelques problemes specifiques au calcul des ponts par encorbellements successifs;" Annales de l'Institut Technique du Batiment et des Travaux Publics, No 391; February 1981. (French)
181. Welsch, W.A. Jr and Sozen M.A.; "Investigation of Prestressed Reinforced Concrete Highway Bridges, Part 2, Analysis and Control of Anchorage Zone Cracking in Prestressed Concrete;" Engineering Experimental Station Bulletin No 497; University of Illinois, Urbana; 1968.
182. Williams, A.; "The Bearing Capacity of Concrete Loaded Over a Limited Area;" Technical Report 526; Cement and Concrete Association; 1979.

183. Wium, D. and Buyukozturk, O.; "Problems in Designing Prestressed Segmental Bridges;" Massachusetts Institute of Technology; March 1984.
184. Wollmann, G.; "Analysis and Design of Anchorage Zones;" Ph.D. Dissertation; University of Texas at Austin; To be Published.
185. Woodward, R.J.; "Cracks in a Concrete Bridge;" Concrete; Vol 17, No 7; July 1983; pp 49-45.
186. Wurm, P. and Daschner, F.; "Teilflächenbelastung von Normalbeton Versuche an bewhrten Scheiben;" Deutscher Ausschuß für Stahlbeton; Heft 344; Berlin; 1983. (German)
187. Wurm, P. and Daschner, F.; "Versuche über Teilflächenbelastung von Normalbeton;" Deutscher Ausschuß für Stahlbeton; Heft 286; Berlin; 1977. (German)
188. Yankelvski, D.Z. and Reinhardt, H.W.; "Uniaxial Behavior of Concrete;" ASCE Journal of Structural Engineering; Vol 115; January, 1989; pp 166-182.
189. Vecchio, F.S. and Collins, M.P.; "The Modified Compression Field;" ACI Journal; March-April 1986; pp 219-231.
190. Yettram, A.L. and Robbins, K.; "Anchorage Zone Stresses in Axially Post-Tensioned Members of Uniform Rectangular Section;" Magazine of Concrete Research; Vol 21, No 67; June 1969; pp 103-112.
191. Yettram, A.L. and Robbins, K.; "Anchorage Zone Stresses in Axially Post-Tensioned I-Section Members with End-Blocks;" Magazine of Concrete Research; Vol 23, No 74; March 1971; pp 37-42.
192. Yettram, A.L. and Robbins, K.; "Anchorage Zone Stresses in Post-Tensioned Uniform Members with Eccentric and Multiple Anchorages;" Magazine of Concrete Research; Vol 22, No 73; December 1970; pp 209-218.
193. Yong, Y.K., Gadugbeka, C. and Nawy, E.; "Anchorage Zone Stresses of Post-Tensioned Prestressed Beams Subjected to Shear Forces;" ASCE Structural Division Journal; Vol 113, No 8; August 1987; pp 1789-1805.

194. Zielinski, J.L. and Rowe, R.E.; "The Stress Distribution Associated with Groups of Anchorages in Post-Tensioned Concrete Members;" Research Report No 13; Cement and Concrete Association; London; October 1962.
195. Zielinski, J.L. and Rowe, R.E.; "An Investigation of the Stress Distribution in the Anchorage Zones of Post-Tensioned Concrete Members;" Research Report No 9; Cement and Concrete Association; London; September 1960.
196. Zielinski, J.L. and Scibak, W.; "Anchorage Zone of Post-Tensioned Concrete Members, Recent Tests and Design Provisions;" FIP-10th International Congress; New Dehli; February, 1986; pp 281-288.

VITA

David Howard Sanders was born in Urbana, Illinois, on December 6, 1961, the son of Wallace Wolfred Sanders Jr. and Julia Beth Sanders. After graduating from Ames High School, Ames, Iowa, in 1980, he entered Iowa State University in Ames, Iowa. During his years at Iowa State University, he worked for the Engineering Research Institute at Iowa State University and for the Chicago Bridge and Iron Company in Oakbrook, Illinois. Upon completion of his Bachelor of Science in Civil Engineering from Iowa State University in May, 1984, he entered the Graduate School at The University of Texas in Austin. He received his Master of Science Degree in Structural Engineering from the University of Texas at Austin in May, 1986 under the guidance of Dr. Joseph Yura. In August, 1986 he married Tina Zoe Rasmussen. He began his studies for the Doctor of Philosophy degree in the June, 1986. He is currently a professor of Civil Engineering at the University of Nevada, Reno.

Permanent address: Department of Civil Engineering
 University of Nevada, Reno
 Reno, NV 89557-0030

This dissertation was typed by the author.